Proceedings of:

The Ninth Annual Meeting

The American Society for Precision Engineering

October 2-7, 1994
Hyatt Regency Cincinnati
Cincinnati, Ohio

The American Society for Precision Engineering (ASPE) is a multidisciplinary professional and technical society concerned with research and development, design, manufacture and measurement of high accuracy components and systems. ASPE activities encompass relevant aspects of mechanical, electronic, optical and production engineering, physics, chemistry, and computer and materials science. Membership is open to anyone interested in any aspect of precision engineering.

Founded in 1986, ASPE provides a new focus for a diverse but important community. Other professional organizations have covered aspects of precision engineering, always as a sideline to their principal goals. ASPE is based on the core of generic concepts necessary to achieve precision in any application; independent of discipline, ASPE intends to be the focus for precision technology — and to represent all facets from research to application.

ASPE — The American Society for Precision Engineering
401 Oberlin Road, Suite 108
P.O. Box 10826
Raleigh, NC 27605-0826
Phone (919) 839-8444 Fax (919) 839-8039

Preface

This book comprises the proceedings of the 1994 Annual Meeting. The contributions reflect the authors' opinions and are published as presented to ASPE, without change. Their inclusion in this publication does not necessarily constitute endorsement by the ASPE, or its editorial staff.

Individual readers of this book and nonprofit libraries acting for them are permitted to make fair use of the material contained in this book to be used in teaching or research; provided they copy said paper in total, as written by the author. Permission is granted to quote excerpts from the scientific or technical works in this book with proper acknowledgement of the source to include: the author's name, the book name, and the ASPE tag line. Reproduction of figures and tables is likewise permitted from the contents of this book, provided that the same acknowledgment of the same source and content is printed.

Any other type reproduction, systematic copying or multiple reproduction of any material in this book is expressly prohibited except with the written permission of the ASPE editorial staff, addressed to the Society's headquarters.

Printed in the United States of America
AMERICAN SOCIETY FOR PRECISION ENGINEERING

ISBN 1-887706-12-7

Corporate Members of the ASPE

COMPANY	CONTACT	LOCATION
3M Company	William J. Bryan	Petaluma, CA
ADE Technologies, Inc.	John Morgello	Newton, MA
Bausch & Lomb	Donald E. Morrison	Rochester, NY
Brown & Sharpe	David H. Genest	North Kingstown, RI
Chardon Tool & Supply Co.	Weldon Bennett	Chardon, OH
Contour Fine Tooling, Inc.	Jeffrey Tomlin	N. Swanzey, NH
Cranfield Precision Engineering, Ltd.	Patrick A. McKeown	Cranfield, England
Dover Instrument Corporation	John R. Hero	Westboro, MA
Fabreeka International, Inc.	Robert P. Haley	Stoughton, MA
Lawrence Livermore National Lab.	Daniel C. Thompson	Livermore, CA
Moore Tool Company, Inc.	E. Ray McClure	Bridgeport, CT
Precitech, Inc.	Donald Brehm	Keene, NH
Professional Instruments Company	Ted J. Arneson, Jr.	Minneapolis, MN
Rank Pneumo, Inc.	Leonard E. Chaloux	Keene, NH
Tencor Instruments	Graham J. Siddall	Mountain View, CA
Zygo Corporation	Carl A. Zanoni	Middlefield, CT

Cooperating Sponsors

Butterworth-Heinemann

Chardon Tool & Supply Co., Inc.

Contour Fine Tooling, Inc.

Federal Products Corporation

Laser Focus World

Photonics Spectra

Rank Pneumo, Inc.

Zygo Corporation

Technical Exhibitors

ADE Technologies, Inc.
Alson E. Hatheway, Inc.
Chardon Tool & Supply Co., Inc.
Contour Fine Tooling, Inc.
Cranfield Precision, Inc.
Dover Instrument Corporation
Fabreeka International, Inc.
Lawrence Livermore National Laboratory
Lion Precision
Micro Surface Engineering, Inc.
Moore Tool Company, Inc.
Precision Engineering Center — N. C. State University
Precision Engineering Laboratory — University of N. C. at Charlotte
Precision Engineering Research Laboratory — Boston University
Precitech, Inc.
Professional Instruments Co., Inc.
Queensgate Instruments
Rank Pneumo, Inc.
Tencor Instruments
The Timken Company
Zygo Corporation

Program

1994 ASPE Annual Meeting

Time	Sun., Oct. 2	Mon., Oct. 3	Tues., Oct. 4	Wed., Oct. 5	Thurs., Oct. 6	Fri., Oct. 7
8:00			Continental Breakfast			
9:00	Tutorials	Tutorials	Technical Session 1	Technical Session 4	Technical Session 6	Technical Tours
10:00			Break	Break	Break	
11:00			Poster Session 1 + Exhibits	Poster Session 2 + Exhibits	Open Forum	
12:00			Lunch + Committee Meetings	Lunch + Business Meeting	Lunch	
1:00						
2:00	Tutorials	Tutorials	Technical Session 2	Technical Session 5	Technical Session 7	
3:00			Break	Break	Break	
4:00			Technical Session 3	Commercial Session	Technical Session 8	
5:00						
6:00			Distinguished Lecture			
7:00		Welcome Reception	Dinner			
8:00						
9:00			Hospitality Suite			

Other Technical Sessions

Distinguished Lecturer

Tuesday, October 4, 6:00

Daniel B. DeBra

Dan DeBra is the Edward C. Wells Professor of Aeronautics and Astronautics at Stanford University. Before joining Stanford in 1964, he spent eight years at Lockheed Missiles and Space Company working on attitude control, dynamics and guidance during the development of the Agena Spacecraft. He was the manager of the first drag-free control system which was flown on TRIAD, one of the Navy navigation satellites in 1972. He has been involved with satellite design and instrument development for physics experiments like the Stanford Gyro Test of Relativity (GP-B), the Space Test of the Equivalence Principle (STEP), and vibration isolation and stabilization of experiments such as gravity wave detectors requiring an unusual degree of attenuation of environmental disturbances.

In 1978 he enjoyed a part of his sabbatical leave as a guest of R. V. Jones at Aberdeen. Starting in 1979 he began helping Jim Bryan at the Lawrence Livermore National Laboratory with the design of Diamond Turning Machine Number Three, which continued for ten years. He also pursues research in quiet hydraulics for application to precision machines and instruments.

Professor DeBra is a member of the National Academy of Engineering and a fellow of the AIAA, AAS and SME. He has received the Thurlow Award from the ION and the Industrial Research Award 100 for the successful flight of a drag-free satellite in 1973.

When not absorbed in precision engineering, he can usually be found on a bike, skis or otherwise enjoying the wonderful world we live in.

Commercial Session

Wednesday, October 5, 3:30-5:00

Session Chair: William J. Bryan, 3M Company

The commercial session will take place on Wednesday afternoon, from 3:30 to 5:00 p.m. In this special afternoon session company representatives are invited to make brief presentations on new products associated with precision engineering. You will have the opportunity to hear about limitations of performance of existing approaches, new approaches relevant to precision engineering and advances that can be expected in the future.

Open Forum

Thursday, October 6, 10:30-12:00

Session Chair: John B. Byrd, III, OTHY, Inc.

This year we have also scheduled a very special open forum, which will focus on problems (or challenges) in precision engineering. In this Thursday morning session, authors will request the assistance of the precision engineering community in formulating a solution to several specific dilemmas.

Fred Gray, DePuy
"Problems associated with the manufacture and measurement of super tapers for hip stems"

John Nemecheck, TROPEL Corporation
"Challenges of developing the next generation of photolithography equipment"

David Koester, MCNC
"Opportunities in the use of microelectronic devices"

Technical and Poster Paper Index

The technical program for the 1994 ASPE Annual Meeting contains over 110 papers on current research from Asia, Australia, Europe, India, South America and the U.S. Authors from national laboratories, universities and industry will share their ideas and conclusions on a variety of topics.

Papers that lent themselves to significant verbal interaction, concise but important discoveries, or strongly visual or tactile subjects have been selected for the poster session. This year the poster papers will be close to both the exhibits and the technical sessions for the duration of the conference, and authors will be present to discuss their work on Tuesday, October, 4 and Wednesday, October 5, from 10:00 a.m. to 12:00 p.m.

Once again, in addition to ten technical sessions, a special Open Forum and a Commercial Session will be offered.

Session I
Scanning Probe Microscopy

Tuesday, October 4, 1994, 8:30 - 10:00 a.m. — *Session Chair: Phillip E. Russell (North Carolina State University)*

1. ***Force Calibrations in the Nanonewton Regime***
   L. P. Howard and E. C. Teague (National Institute of Standards and Technology) . . . . . *page 13*
2. ***A Near-field Infrared Scanning Microscope***
   B. D. Boudreau, J. Raja, J. Patten and R. J. Hocken (University of North Carolina at Charlotte) . . . . . *page 18*
3. ***A Metrological Scanning Force Microscope***
   Y. Xu, T. Judge (University of Warwick), S. T. Smith (University of North Carolina at Charlotte), and P. D. Atherton, R. Jones (Queensgate Instruments Ltd., UK) . . . . . *page 23*
4. ***Hertzian Contact Resonances***
   J. Kramar, T. McWaid, J. Schneir, E. C. Teague (National Institute of Standards and Technology) . . . . . *page 29*

Session II
Ultraprecision Machining

Tuesday, October 4, 1994, 1:30 - 3:00 p.m. — *Session Chair: Don A. Lucca (Oklahoma State University)*

1. ***Measurement of Tool Tip Temperature in Micro Cutting by Infrared Radiation Pyrometer with Optical Fiber***
   T. Ueda, T. Sugita (Kanazawa University), and M. Sato (Toyama Prefectural University) . . . . . *page 33*
2. ***Use of Force Feedback for Dynamic Error Correction in Diamond Turning for Surface Roughness Improvement***
   Q. Ma , P. I. Ro (North Carolina State University) . . . . . *page 37*
3. ***Effects of Feedrate and Tool Rake Angle in the Single Point Diamond Turning of PVD Silicon***
   A. C. Miller, Jr. (Oak Ridge National Laboratory) . . . . . *page 41*
4. ***Generation of Rotationally Asymmetric Optical Surfaces Using a Fast Tool Servo***
   G. M. Moorefield II, K. P. Garrard, K. J. Falter, L. W. Taylor, T. A. Dow (North Carolina State University) . . . . . *page 45*
5. ***Design of Nanometric Cutting Instruments***
   S. Balasubramaniam, R. J. Hocken (University of North Carolina at Charlotte), and D. A. Lucca (Oklahoma State University) . . . . . *page 49*

Session III

Precision Machine Design

Tuesday, October 4, 1994, 3:30 - 5:00 p.m. *Session Chair: Thomas A. Dow (North Carolina State University)*

1. ***Application of Electrorheological Fluid for the Improvement of Dynamic Characteristics of Machine Tool Table Systems (Basic Analysis of the Dynamic Characteristics of Table Systems)***
   M. Ishiyama, T. Aoyama (Keio University), and K. Edamura (Fujikura Kasei Co., Ltd.) . . . . . page 53
2. ***Ceramic Machine Tool Axis with Self-compensated, Water-hydrostatic Linear Bearings***
   A. Slocum, P. Scagnetti, N. Kane (Massachusetts Institute of Technology) . . . . . page 57
3. ***Two-axis Force Sensing Knife to Obtain Dynamic Information***
   M. Nakao, I. Eguchi, Y. Hatamura (The University of Tokyo) . . . . . page 61
4. ***Precision Magnetic Bearing Six Degree of Freedom Stage***
   M. E. Williams, D. L. Trumper (Massachusetts Institute of Technology) . . . . . page 65

Session IV
Machine Tools

Wednesday, October 5, 1994, 8:30 - 10:00 a.m. *Session Chair: Robert G. Wilhelm (University of North Carolina at Charlotte)*

1. ***Thermal Error Models for Software Compensation of Machine Tools***
   J. A. Soons, H. A. Spaan, P. H. Schellekens (Eindhoven University of Technology) . . . . . page 69
2. ***Measurement of Machine Tool Parametric Errors Using the Laser Ball Bar***
   J. C. Ziegert (University of Florida) . . . . . page 76
3. ***Precision Roll Measurement Using a Polarization Reference***
   S. R. Patterson, D. M. Schmidt (University of North Carolina at Charlotte) . . . . . page 80
4. ***Straightedge Metrology in a Wet Environment***
   S. B. Peirce, D. B. DeBra (Stanford University) . . . . . page 84
5. ***Improving the Machine Accuracy Through Machine Tool Metrology and Error Corrections***
   J. S. Chen, C. C. Ling (National Chung Cheng University) . . . . . page 88

Session V
Precision Grinding

Wednesday, October 5, 1994, 1:30 - 3:00 p.m. *Session Chair: W. Keith Kahl (Oak Ridge National Laboratory)*

1. ***Dressing of Metal Bonded Diamond Wheel by Use of Loose Abrasive Lapping for Ductile Mode Grinding of Brittle Materials***
   F. Inaba, A. Kanai and M. Miyashita (Ashikaga Institute of Technology) . . . . . page 92
2. ***Material Effects in Grinding Response of Hot Isostatically Pressed Silicon Nitrides****
   C. J. Evans, L. K. Ives, R. S. Polvani and S. Jahanmir (National Institute of Standards and Technology) . . . . . page 96
3. ***Mechanical, Thermal, Diffusional, and Geometrical Length Scales in Polishing and Grinding***
   J. C. Lambropoulos (University of Rochester) . . . . . page 97
4. ***Modeling the Wheel/Work Interface in Precision Grinding***
   M. H. Miller and T. A. Dow (North Carolina State University) . . . . . page 101
5. ***Cup Wheel Grinding Geometry***
   G. E. Storz II and T. A. Dow (North Carolina State University) . . . . . page 105

** Extended abstract not available at press time.*

Session VI
Component Fabrication

Thursday, October 6, 1994, 8:30 - 10:00 a.m. — *Session Chair: Donald Golini (University of Rochester)*

1. ***Optical Polishing of Hydrophilic Polymer Materials***
   J. Sun, L. C. Zhang, Y-W. Mai (The University of Sydney), and M. Hogg, S. Payor (Eycon Lens Laboratories Pty. Ltd.) . . . . . page 109
2. ***Ultraprecision Grinding of Brittle Hard Disk Substrates***
   P. Bierden and T. Bifano (Boston University) . . . . . page 113
3. ***Machinability of PMMA in the Near-cryogenic Region***
   C. R. Friedrich and K. Visvanathan (Louisiana Tech University) . . . . . page 117
4. ***Integrated Ion Beam Milling and Coating for Precision Optical Fabrication***
   C. M. Egert, K. W. Hylton, and K. A. Thomas (Oak Ridge National Laboratory) . . . . . page 121
5. ***Testing System of Mechanical Properties of Magnetic-optical Disk for Higher Density Storage***
   E. Tokutomi, H. Aoyama, T. Santo, and T. Kubo (Shizuoka University) . . . . . page 125

Session VII
Metrology I — CMMS

Thursday, October 6, 1994, 1:30 - 3:00 p.m. — *Session Chair: John C. Ziegert (University of Florida)*

1. ***Development of Subpixel Edge Probe with High Resolution and Application for Coordinate Measuring Machine***
   K. Maruyama, H. Tsuji, and K. Hashimoto (Tokyo Institute of Technology) . . . . . page 129
2. ***A Small CMM Design, Not Just Scaling Down***
   M. M. P. A. Vermeulen, P. C. J. N. Rosielle, and P. H. J. Schellekens (Eindhoven University of Technology) . . . . . page 133
3. ***Verification of Form Tolerances Using Point Data***
   K. Carr (Ford Research Laboratory) and P. Ferreira (University of Illinois at Urbana-Champaign) . . . . . page 137
4. ***A Simple and Effective Method to Account for Tilt and Eccentricity in Roundness Measurements***
   V. Jayaraman and J. Raja (University of North Carolina at Charlotte) . . . . . page 141
5. ***Micro-electro-mechanical Actuator Arrays for Deformable Mirrors***
   T. Bifano (Boston University) . . . . . page 145

Session VIII
Metrology II — Sensors

Thursday, October 6, 1994, 3:30 - 5:00 p.m. — *Session Chair: Anthony E. Gee (Cranfield University)*

1. ***Angle Measurement Based on the Internal-reflection Effect Using Right-angle Prisms***
   P. S. Huang (State University of New York at Stony Brook), and J. Ni (The University of Michigan) . . . . . page 149
2. ***Development of a New Ultrasonic Sensor for Displacement Measurement***
   K. Mitsui (Keio University), M. Koike (Fuji Photo Film Co., Ltd.), and H. Tsukamoto, M. Yajima (Mitsubishi Heavy Industries, Ltd.) . . . . . page 153
3. ***Design of an Ultra Sensitive Force Transducer for Biomedical Experiments***
   P. V. Pistecky and E. van Dop (Delft University of Technology) . . . . . page 157
4. ***Development of a Measuring Laser System with Nanometer Accuracy***
   S. F. Wetzels, P. H. Schellekens (Eindhoven University of Technology) . . . . . page 161

Poster Session I

Tuesday, October 4, 1994, 10:30 a.m. - 12:00 p.m.

Metrology

SPM

1. ***Characterization of Micromachined Surfaces by Atomic Force Microscopy***
   V. Scherer, U. Rabe, W. Arnold (Fraunhofer-Institute for Nondestructive Testing), R. Fechner, A. Schindler (Institute for Surface Modification e.V.), and O. Riemer, W. R. Preuß, E. Brinksmeier (University of Bremen) . . . . . *page 167*
2. ***The Design of an Atomic Force Microscope for Metrology***
   T. H. McWaid and J. Schneir (National Institute of Standards and Technology) . . . . . *page 174*

Machine Tool Metrology

1. ***Correlating Machine Tool Accuracy with Part Features***
   N. Srinivasan, F. Farabaugh, R. G. Wilhelm and R. J. Hocken (University of North Carolina at Charlotte) . . . . . *page 178*
2. ***Accuracy Improvement of Machine Tool by WORFAC (3rd Report)—Investigation and Elimination of Uncontrollable Point***
   Y. Uda, T. Kohno and T. Yazawa (Tokyo Metropolitan Institute of Technology) . . . . . *page 182*

Sensors

1. ***Various Dynamic Micro Tribological Phenomena Under SEM Observation Measured by a High-rigid Multi-axis Force Sensor***
   H. Hachiuma, M. Nakao and Y. Hatamura (The University of Tokyo) . . . . . *page 186*
2. ***Torque Measurement Using a Photoelastic Coating Method***
   M. Hasegawa (Mitsubishi Electric Corporation) . . . . . *page 190*
3. ***What Can Lasers Do For You?***
   S. Case, M. E. Riddle and T. Skunes (CyberOptics Corporation) . . . . . *page 194*
4. ***First Look at an Angle Multiplying Angle Generator***
   S. K. Smith (Air Force Measurement Standards Laboratory) . . . . . *page 198*
5. ***A Method for the Spatial Calibration of a Commercial Phase Measuring Interferometer—Practical Implementation***
   P. Sullivan and C. Evans (National Institute of Standards and Technology) . . . . . *page 202*
6. ***The Automation of Measurement for Length Scales***
   W. L. Yang, S. H. Lu, R. H. Hsu, C. J. Chen and H. C. Huang (Industrial Technology Research Institute) . . . . . *page 206*

Surface Topography

1. ***Evaluation of Topography of Precision Engineering Part Surfaces with the Employing of Representative Mathematical Methods***
   J. Mandak (Foreign Students Institute—Military Academy of Brno) . . . . . *page 210*

CMMS

1. ***Optimizing Metrology and Control in a C.I.M. Environment by Prediction and Design***
   M. Mestre and H. Abou-Kandil (Ecole Normale Supérieure de Cachan - L.U.R.P.A.) . . . . . *page 214*
2. ***Some Considerations for a Measurement Strategy for Circular Features***
   H. Harary (National Institute of Standards and Technology), and C. Buchard, P. L'Heritier, J-O. Dufraigne and P. Chollet (Centre d'Etudes Supérieures des Techniques Industrielles) . . . . . *page 218*
3. ***Calibration and Real Time Compensation of Errors Introduced by Measurement Probe and Machine Geometry in a Commercial CMM***
   H. Pahk and K. Lee (Seoul National University) . . . . . *page 222*
4. ***The Research on the High Precision Measurement Method and System of Diameter of Large Scale Hole***
   Y. Zheng (Tsinghua University) . . . . . *page 226*

Surface Finishing

1. ***Design of a Three-dimensional Surface Profiler***
   V. G. Badami, S. T. Smith, J. Raja and R. J. Hocken (University of North Carolina at Charlotte) . . . . . page 230
2. ***Surface and Subsurface Characteristics of Ultraprecision Ground Silicon Wafers***
   M. Kerstan, H. Lundt, A. Huber, P. O. Hahn and M. Brohl (Wacker Chemitronic GmbH) . . . . . page 234

Design

Precision Mechanisms

1. ***Collaborative Precise Operation by Two Miniature Robots—Single Diamond Cutting with Local Position Feedback***
   H. Aoyama, H. Nakano, A. Sasaki, J. Fukaya, F. Iwata and T. Kubo (Shizuoka University) . . . . . page 238
2. ***Miniature Linear Actuator Using Piezoelectric Elements***
   T. Goto, S. Tawara (Mitsubishi Heavy Industries, Ltd.), and K. Mitsui, N. Suzuki (Keio University) . . . . . page 242
3. ***Metrology for Characterizing Actuators with Sub-atomic Repeatability***
   A. E. Hatheway (Alson E. Hatheway, Inc.) . . . . . page 246
4. ***Development of an Automatic Fixturing Design System***
   K. Ikezoe and T. Aoyama (Keio University) . . . . . page 250
5. ***An Intelligent Positioner Realizing Precise Positioning and a Wide Working Range through an Internal Monitoring System***
   M. Nakao, Y. Hatamura, S. Tanaka (The University of Tokyo), and M. Watanabe, K. Kaneko (THK Co., Ltd.) . . . . . page 254
6. ***Application of Flexure-hinged Displacement Amplifiers for Piezo-actuators***
   W. Xu and T. King (The University of Birmingham) . . . . . page 258

Bearings

1. ***Design and Manufacture of a Hydrostatic Bearing for Production Precision Machining****
   V. Delbrugge and W. Hockenberger (Precision Grinding and Manufacturing Corporation), and F. Titcomb (DevTek, Ltd.) . . . . . page 262
2. ***Analyses of the Rotating Accuracy of Externally Pressurized Air Bearings Considering the Roundness Errors of Spindle and Bearing***
   D-C. Han and S-S. Park (Seoul National University) . . . . . page 263
3. ***Experimental Analysis of Force-operated Feed Mechanism of Slide on Plain Bearing Guideways for Long Travel Range***
   J. Hisada (Sumimoto Heavy Industries, Ltd.), and A. Kanai, M. Miyashita (Ashikaga Institute of Technology). . . . . page 267
4. ***Step Response Characteristics of Air-lubricated Slideways for Ultraprecision Machine Tools***
   S. Kato (Nippon Institute of Technology) . . . . . page 271
5. ***Low Noise Fluid Circuit Design Method for Hydrostatic Bearing Systems***
   P. Scagnetti, A. Slocum and N. Kane (Massachusetts Institute of Technology) . . . . . page 275
6. ***Characteristics of Aerostatic, Hydrostatic and Rolling Element Spindles and Slide Systems and Their Influence on the Machining Accuracy***
   M. Weck, J. Luderich, A. Wieners and M. Vos (Fraunhofer-Institut für Produktionstechnologie) . . . . . page 281

Machine Tools

1. ***Development of Approach and Real Pressure in Multiple Contact Loading Process***
   A. Polijaniuk (Polish Academy of Sciences) . . . . . page 285
2. ***Design and Analysis of a New Type Multi-functional Machine Tool***
   N. Sugimura (University of Osaka Prefecture), S. Ueno (Technical Research Institute of JSPMI), N. Mishima (AIST, MITI), and S. Hachiga (Japan Machine Tool Builders' Association) . . . . . page 289
3. ***The Bulging Effects of Bolted Machine Tooled Guideways***
   Z. Q. Zhu and B. Zhang (University of Connecticut) . . . . . page 293

* *Extended abstract not available at press time.*

Materials

1. ***Measuring Method to Determine Dimensional Changes on Ion Nitrided Steels***
   G. Ascanio, R. Nava, R. Trejo and J. Rickards (Universidad Nacional Autónoma de México) . . . . . *page 297*
2. ***Scratch Test of Glass Slides***
   K. Li, Y. Shapiro and J. C. M. Li (University of Rochester) . . . . . *page 301*
3. ***Effect of Temperature and Load Rate on Brittle-ductile Transition of Silicon Single Crystal***
   N. Morita and Y. Yoshida (Chiba University) . . . . . *page 305*
4. ***A Model for Predicting Grinding Damage in Ceramics***
   B. Zhang (University of Connecticut) . . . . . *page 309*

Poster Session II

Wednesday, October 5, 1994, 10:30 a.m. - 12:00 p.m.

Controls

Manufacturing

1. ***The Implementation of Visual Sensory Data in a Closed Loop Video Feedback Manufacturing Environment***
   B. R. Mackie (DI/MAC Technologies, Inc.) . . . . . *page 313*
2. ***Manufacturing Error Flow and its Modeling***
   Z. Luo (Tsinghua University), Y. Rong (Southern Illinois University at Carbondale), and Y. Zhu (Beijing Institute of Machinery Industry) . . . . . *page 317*
3. ***Integration of Tolerances and Process Capability for Concurrent Engineering***
   R. Wilhelm (University of North Carolina at Charlotte) . . . . . *page 322*

Error Compensation

1. ***Nonlinear Effects in Ball Screw Actuators***
   J. F. Cuttino and T. A. Dow (North Carolina State University) . . . . . *page 326*
2. ***Control Method for Thermal Displacement of a Hydrostatic Air Spindle***
   N. Mishima, K. Mizuhara and Y. Okazaki (AIST, MITI) . . . . . *page 330*
3. ***Accuracy Improvement of Machine Tools by Computer Real-time Control***
   C. Zhang, F. Margrave and A. Bradshaw (Lancaster University) . . . . . *page 334*

Machine Tool

1. ***Automatic Acquisition of Machining Conditions: Towards a Self-evolving Machining Center***
   M. Mitsuishi, S. Warisawa, T. Ohta and T. Nagao (The University of Tokyo) . . . . . *page 338*
2. ***Non-circle Cutting by an NC Lathe Using DNC System***
   Y. Morimoto, K. Hirosaki (Industrial Research Institute of Ishikawa), and T. Yasui, T. Tsubono (Kanazawa University) . . . . . *page 342*

Processing

Turning

1. ***Development of Thermally Stabilized Aluminum Mirrors for the Composite Infrared Spectrometer***
   S. C. Fawcett (NASA/Marshall Space Flight Center) . . . . . *page 346*
2. ***Study of Process Parameters in Diamond Tool Manufacturing—Influence of Scaife Material***
   K. Horio, T. Kasai, and H. Takei (Saitama University) . . . . . *page 350*
3. ***A Micro Feeding Tool Post (MFTP) with Optical Fiber Displacement Feedback for Diamond Turning Machines***
   X. M. Lu , W. B. Lee, T. P. Leung (Hong Kong Polytechnic), and Z. J. Yuan (Harbin Institute of Technology) . . . . . *page 354*
4. ***The Development of a Non-contact Diamond Tool Alignment and Measuring System***
   J. Schaefer, S. Kaiser and T. Carrington (Texas Instruments, Inc.) . . . . . *page 358*

Grinding

1. ***Evaluation and Application of Precision Contour Grinding for a RBSiC Off-axis Spherical Mirror***
   W. K. Kahl (Oak Ridge National Laboratory) . . . . . *page 362*
2. ***Design Strategies of an Ultraprecision Surface Grinding Machine for Ductile Mode Surface Finishing of Brittle Materials***
   M. Daito (Nissin Machine Works Co., Ltd.), and A. Kanai, M. Miyashita (Ashikaga Institute of Technology) . . . . . *page 366*
3. ***Mechanics and Materials Issues in Optics Manufacturing***
   J. C. Lambropoulos, P. D. Funkenbusch, D. J. Quesnel, S. M. Gracewski and R. F. Gans (University of Rochester) . . *page 370*
4. ***Correlation Between the Properties of Ceramics and Grinding Mode Mechanism****
   I. D. Marinescu (University of Connecticut)
5. ***Effect of Grinding Energy on Wheel Speed and Surface Finish***
   M. H. Miller, G. E. Storz, T. A. Dow and Ronald O. Scattergood (North Carolina State University) . . . . . *page 374*
6. ***Effect of Elevated Wheel Surface Speed in the Internal Grinding Process***
   K. Yasui, I. Inasaki (Keio University), and M. Hatakeyama (Okamoto Machine Tool Works, Ltd.) . . . . . *page 378*
7. ***Grinding Induced Damage in Ceramics***
   B. Zhang (University of Connecticut) . . . . . *page 382*
8. ***An Experimental Study of Thermal Aspects of Cylindrical Grinding***
   S. Zhou and J. Webster (University of Connecticut) . . . . . *page 386*
9. ***An Experimental Investigation of Workpiece Out-of-roundness in Centerless Grinding***
   S. S. Zhou and J. R. Gartner (University of Connecticut) . . . . . *page 390*

Polishing

1. ***The Influence of Polish Particle Size Distribution on Speed and Surface Quality in the Precision Polishing of Glass***
   D. J. Bell (Optical Surface Technologies) . . . . . *page 394*
2. ***Sub-surface Damage in ULE from Loose Abrasive Grinding and Polishing***
   L. Lombardo, J. Nemechek (TROPEL Corporation), and A. Lindquist (University of Rochester) . . . . . *page 398*
3. ***Twin Surface Lapping and Single Surface Polishing of Silicon Wafers for the Electronics Industry***
   P. Wright (Speedfam Ltd.), and K. Leaf (Speedfam, S.G., USA) . . . . . *page 402*

Models

1. ***Development of a Tool Force/Surface Finish Model for Diamond Turning***
   T. A. Dow and C. Arcona (North Carolina State University) . . . . . *page 404*
2. ***Validation of a Dynamic Grinding Model***
   T. R. Kurfess, H. E. Jenkins (Georgia Institute of Technology) and S. J. Ludwick (Carnegie Mellon University) . . . . . *page 408*
3. ***Computer Simulation of Transmission and Side Sputterings by Monte Carlo Method***
   I. Miyamoto, A. Kuroda and K. Yoshimura (Science University of Tokyo) . . . . . *page 412*
4. ***Finite Element Modeling of Ultraprecision Machining of Copper***
   B. C. Rao and R. X. Gao (Louisiana Tech University) . . . . . *page 416*
5. ***A Practical Guide to Theoretical Modeling of Contour Grinding***
   G. E. Storz II and T. A. Dow (North Carolina State University) . . . . . *page 420*

Other Processing

1. ***Ion Figuring of Small Optics***
   T. W. Drueding, T. G. Bifano (Boston University), and S.C. Fawcett (NASA Marshall Space Flight Center) . . . . . *page 424*
2. ***Biochemical Machining of Plastics***
   T. Kaneeda, H. Morioka (Okayama University of Science), S. Yokomizo, A. Miwa, K. Mitsuishi (Industrial Technology Center of Okayama Prefecture), and Y. Uno (Okayama University) . . . . . *page 428*
3. ***Development of a Micro Machining/Testing System with a Fixed View/Operational Point***
   M. Mitsuishi, K. Kobayashi, T. Watanabe, H. Nakanishi and T. Nagao (The University of Tokyo) . . . . . *page 432*

** Extended abstract not available at press time.*

4. ***Focused Ion Beam Machining of Diamond Probes—Simulation for Profile Change of Probes***
I. Miyamoto, S. Kiyohara and M. Ide (Science University of Tokyo) . . . . . *page 436*

5. ***Analytic and Experimental Investigation on Deep Hole Formation Process of Covalent Bond-ceramics Using Pulsed YAG Laser***
N. Morita, T. Watanabe and Y. Yoshida (Chiba University) . . . . . *page 440*

6. ***Manufacturing Economics and Removal Mechanisms in the Forming and Finishing of Reflective Optical Surfaces***
A. J. Vieira Porto and J. G. Duduch (Universidade de Sao Paulo), and A. E. Gee (Cranfield University) . . . . . *page 444*

7. ***Electrochemical Discharge Machining —A New Approach***
V. Raghuram (Indian Institute of Technology Kanpur), and T. Pramila (Christ Church College) . . . . . *page 449*

8. ***Abrasive Wear Characteristics Under Three-body Conditions of CFRP in Vibratory Environment***
S. Teraoka (Kanazawa Technical College), and K. Ishikawa, T. Nakagawa (Kanazawa Institute of Technology) . . . . . *page 453*

9. ***A New Biological Machining Technique with Chemolithotrophic Bacteria***
Y. Uno, A. Okada, T. Yoshimura (Okayama University), T. Kaneeda (Okayama University of Science), and S. Yokomizo (Industrial Technology Center of Okayama Prefecture) . . . . . *page 457*

Micro Electro Mechanical Systems (MIMS)

1. ***Deflection Compensation Model for the Machining of Microshafts (Initial Results)***
C. R. Friedrich and B. Kithiganahalli (Louisiana Tech University) . . . . . *page 461*

Technical Papers

FORCE CALIBRATIONS IN THE NANONEWTON REGIME

L.P. Howard and E.C. Teague
NIST Precision Engineering Division, Micrometrology Group
Bldg. 220, Rm. A117
Gaithersburg, MD 20899

Introduction

In the emerging nanotechnology, force measurement plays a key role in the understanding of atomic and molecular phenomena. Biological manipulations, nanomachining, tribology, micromechanics, nanohardness and atomic force microscopes (AFMs) are all somewhat dependent upon accurate observations of extremely small forces, ranging anywhere from millinewtons to piconewtons and even lower. The recent commercialization of AFMs has made the nanonewton a casually mentioned physical unit. Casual, that is, until an accurate assessment of measurement uncertainty is required.

Often, force is measured by observing the strain of a calibrated spring. In the case of AFMs, the spring in question is a cantilever. The cantilever stiffness can be estimated by measuring the geometry and then assuming good conformance to simple beam bending theory. Experience has shown that batch fabricated micro cantilevers are often subject to residual stresses and warpage, thus complicating any stiffness calibrations. Fig. 1 shows typical distortions in a commercial AFM cantilever. Other methods using the shift in resonance frequency due to small applied mass have been developed with good results[1].

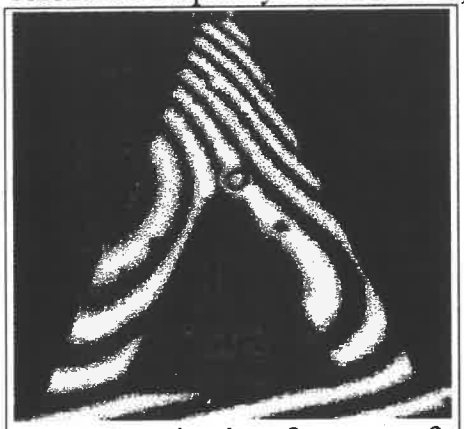

Figure 1. Microinterferogram of a Si_3N_4 AFM cantilever.

From an uncertainty standpoint, it is desirable to characterize a single standard instrument, using it to calibrate other force measuring instruments. Also, any instrument used in this fashion should have a much higher stiffness than the cantilever spring under test to prevent back-action loading effects. These two requirements seem to eliminate spring observation methods, despite their high resolution and simplicity. Our balance derives its stiffness from a control system, applying an opposite restoring force to the balance platen through a force actuator. This paper describes our efforts to build and test a microbalance suitable for AFM calibration.

Null force balance

A balance based upon an earlier design by Smith and Howard[2] was designed and constructed. Planned resolution was from 10^{-4} to 10^{-9}N. Since the preliminary results of the first generation balance were vibration limited, this second generation instrument was designed to be insensitive to external vibrations. In this newer design, two nearly identical balances were used differentially, one exposed to external forces and the other as a reference (Fig. 2). In the figure, displacements x_2 and x_1 are monitored differentially by a capacitance bridge. Restoring forces are applied to each balance through a magnet and

coil actuator. The modified control system was designed so that the reference balance and the measurement balance have the same AC characteristics. For static forces (below a few Hz), only the measurement balance has a DC response. Otherwise, control offsets would be generated to make the reference balance track the applied forces on the main balance. Since both balances have essentially the same response to AC forces, they should null out any external forces due to vibrations. Both balances are vertically colinear along a vee groove to reduce susceptibility to tilting motions. The entire assembly is located in an acoustically dead enclosure on a pneumatically isolated optical table.

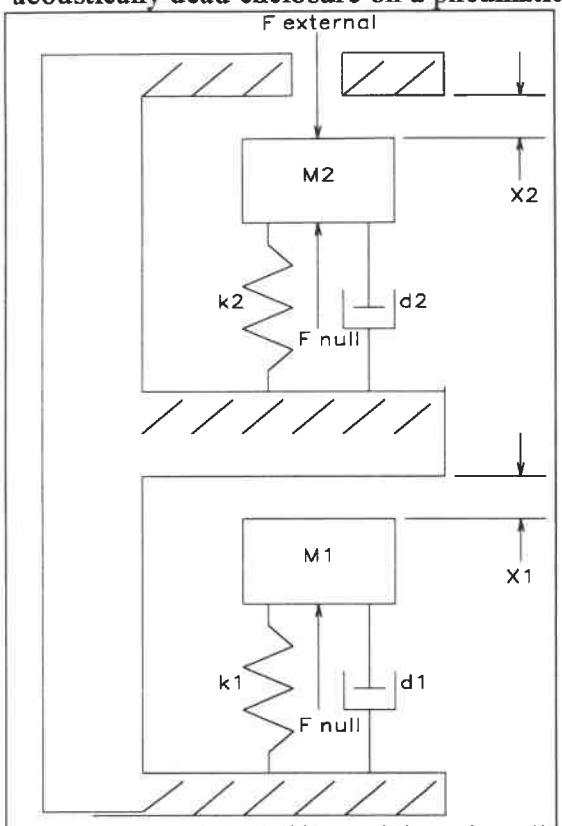

Figure 2. Model of differential mode null balance.

Force balance calibrations

If the volume, density and local gravity are well known, dead weights are a good force standard. Since mass scales with volume, smaller dead weights are extremely tiny and thus, more difficult to handle. With the unaided eye, it is difficult to work at levels below 10^{-6} N, thus making it difficult to characterize an instrument over its entire range of operation. Consider the case of a force balance operating over five decades from 10^{-9} to 10^{-4} N. At the upper range of operation, 1 and 10 mg dead weights will suffice for calibration. It is highly undesirable to assume that the balance will be linear in operation over the other three decades, down to the noise floor of the instrument. For these low forces, applying micro-dead weights would become necessary. Polyester micro sphere particle standards were explored for use as micro dead weights. Handling such spheres in large discrete numbers proved to be a painstaking process however, due in part to the presence of capillary forces arising from surface water layers. Ultimately, the difficulty of handling individual microspheres led to the use of the following calibration method.

Electro-dynamic measurements

The issue of artifact mass standards has been recently visited by one branch of workers who are striving to redefine the kilogram in terms of reproducible SI units[3]. Applying the conservation of energy, to a first order, mechanical power, (force times velocity) is equivalent to electrical power, (volts times amperes), or

$$F V = \varepsilon i. \qquad (1)$$

The SI electrical watt is well defined by the Josephson junction voltage standard and standard resistances referenced to calculable capacitors or quantum Hall resistance measurements. So, to measure force from first principles, we must be able to observe voltage, current and velocity. A two part measurement scheme thought to be originally proposed by Kibble[4], allows experimenters to first calibrate a coil using a motional emf,

and then use the coil in a null balance measurement with a dead weight. The experiment proceeds in two parts: First, an observation is made of the motional emf produced by moving the magnet or coil at a certain relative velocity. The emf produced is dependent upon many geometrical factors, including coil geometry, magnet geometry and their mutual interactions. A second observation is made of the amount of coil current required to balance an applied force (from a dead weight). Again, this current is dependent upon the *same geometrical factors* as the first measurement. By comparing the ratios of emf and velocity to force and current, the geometrical factors cancel out.

By Faraday's law, the electromotive force (ε) produced by a magnet and coil system is

$$\varepsilon(t) = -\frac{\partial \Phi}{\partial t}, \tag{2}$$

where the coil is presumed to be moving through a constant flux gradient (reasonable for small displacements in our geometry). In such a situation we can write

$$\varepsilon(t) = -\frac{\partial \Phi}{\partial z}\frac{dz}{dt} \quad \text{where} \quad -\frac{\partial \Phi}{\partial z} = \frac{\varepsilon(t)}{(dz/dt)}. \tag{3) and (4}$$

The flux gradient (or the geometrical factor) is called the back emf constant of the actuator and is the observable outcome of the first part of the measurement. The back emf constant is actually dependent upon many degrees of freedom, but is assumed to be constrained here to only one. The Lorentz force produced by that same coil on a magnet is then

$$F(t) = -i\frac{\partial \Phi}{\partial z} \text{ where } \quad i = mg \Big/ -\left(\frac{\partial \Phi}{\partial z}\right). \tag{5) and (6}$$

So, a second observation can be made to compare the expected outcome of the first observation against the actual current required to balance a known force. In the kilogram experiments, this known force is generated by a mass standard in a gravitationally well characterized locale. To be of use for AFM calibrations, such measurements will need to be made on a scale that starts six orders of magnitude lower, working with nanowatts of electrical and mechanical power. The force balance, having a magnet and coil force actuator and a capacitance gage to measure displacement, was used as a test bed for these types of measurements.

Nano electrodynametic calibrations

In these calibrations, the force balance was operated in a single-ended mode, with the reference balance replaced by a fixed reference capacitor. To determine the back emf constant of the magnet and coil actuator, a Queensgate DPT[5] actuator was placed on top of the balance and adjusted to make contact with the balance platen. The DPT was first used to make static displacements of several micrometers to calibrate the force balance capacitance gage. Next the DPT was actuated with a 100 Hz sine wave of not more than several micrometers peak-to-peak. Coil emfs were stepped-up using an instrument transformer and amplified by an instrument amplifier with a nominal gain of 10,000 ±0.1%. The instrument transformer was characterized at 100 Hz by comparing it to a 7 digit ratio transformer in a bridge measurement, using a lock-in amplifier as a null detector. The transformer ratio was measured as 51.2 ±1.0%. Eight hundred data points

each were collected from the DPT drive signal, the balance capacitance gage and the coil emf at a nominal rate of 30 kHz using a 16 bit A/D converter. Next, the DPT drive signal was changed to a trianglar waveform at the same frequency and the process repeated.

Data were obtained and analyzed for two different displacement waveforms, triangular and sinusoidal. For the trianglar excitation, the displacement data from the balance capacitance gage were numerically differentiated and the outlying points of high acceleration were removed because they exceeded the measurement bandwidth. A least squares line was fit to emf(t) -vs- velocity(t). The slope of this line is the back emf constant (the geometrical constant). For the sinusoidal data, time dependence was removed by numerically integrating the motional emf and dividing by the total one-cycle displacement to again yield the back emf constant.

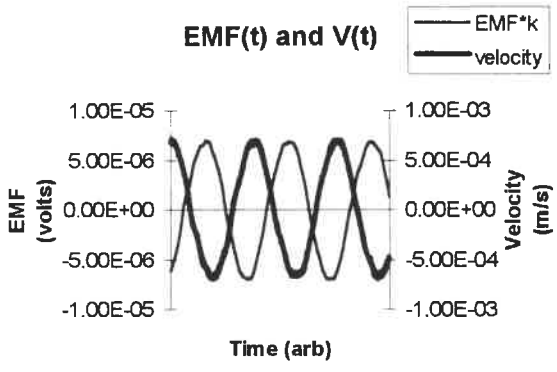

Figure 3. 100 Hz motional emf data.

Part two of the experiment involved measuring the force and current interaction by connecting the coil actuator to a current amplifier and PID controller, servoing the balance to a fixed point on the z axis. In this mode, the coil current is proportional to the external applied force on the balance platen. Dead weights of 10 mg were repeatedly dropped from a small vacuum chuck mounted to the DPT actuator. For each drop, the net change in coil current was the observable.

The expected results from the first part of the experiment were compared with the actual balance current observed in the second experiment. For the motional emf experiment, a current/force ratio of 97.161 AN^{-1} was predicted for the sine wave measurement and 103.3 AN^{-1} predicted for the triangle wave. For ten drops of a 10 mg dead weight, a mean balance current/force ratio of 99.868 AN^{-1} was recorded with a standard deviation of $\sigma=\pm 1.542$ AN^{-1}. This comparison results in an accuracy of 2.71% for the trianglar waveform and 3.32% for the sinusoid. Estimations of total uncertainty included the amplification chain, null current measurement, velocity measurement and displacement measurement.

Subsystem	Type A uncertainty	Type B uncertainty
EMF amplification	1 nN	1%
Null current measurement	1 nN	0.1%
Velocity measurement	10 nN	1%
Displacement measurement	10 nN	1%
Quadrature combination	±14.2 nN	±1.73%

Total uncertainty is obtained by combining the type A and type B uncertainties in quadrature. Since the type B uncertainties are expressed as coefficients of variation (CV), the combined standard uncertainty is then

$$u_c = \sqrt{u_A^2 + (CV \cdot F)^2} \qquad (7)$$

and is shown in Fig. 4.

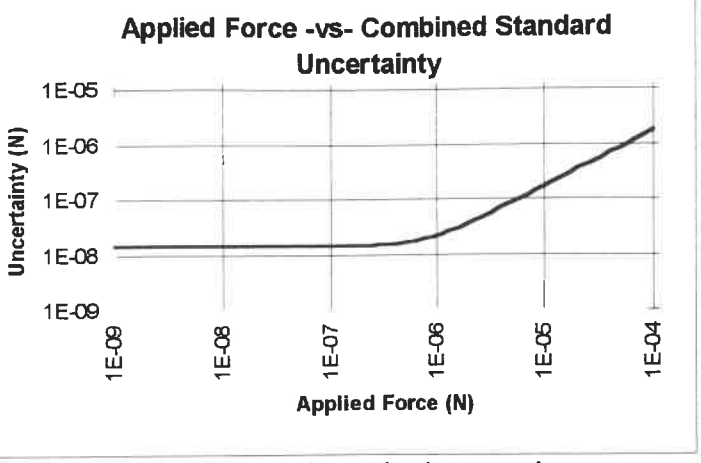

Fig. 4. Graph of combined standard uncertainty showing combination of both random and systematic errors.

These initial results are rather encouraging, suggesting that electrodynamic measurements have a potential for calibrating nanonewtons of force to at least several percent. With better dimensional and electrical metrology, the type B uncertainties could be greatly reduced, hopefully to the same order as the type A uncertainties. A preliminary analysis of fundamental noise limits in voltage, current and displacement measurements indicates that type A uncertainties at room temperature could be reduced to beyond the thermal noise level of the mechanical system, which is currently about 10^{-17} N for the best cantilever spring measurements.

Acknowledgments

The authors wish to acknowledge Nile Oldham and Gerry Stenbakken of the Electronics and Electrical Engineering Laboratory (EEEL) and many other NIST colleagues for their useful discussions. In particular, one of the authors (LPH) would like to thank Tom Olsen of EEEL for sharing his watt experiments and Stuart Smith for providing the initiative and early balance designs.

---

[1] J.P. Cleveland, S Manne, D. Bocek and P.K. Hansma, "A nondestructive method for determining the spring constant of cantilevers for scanning force microscopy", Rev. Sci. Instrum., **64**(2), pp. 403-405, (1993).

[2] S.T. Smith and L.P. Howard, "A precision, low-force balance and its application to atomic force microscope probe calibration", Rev. Sci. Instrum., **65**(4), pp. 903-909, (1994).

[3] P.T. Olsen, W.L. Tew Jr., E.R. Williams, R.E. Elmquist and H. Sasaki, "Monitoring the mass standard via the comparison of mechanical to electrical power",. IEEE Trans. Instrum. Meas, **40**(2), pp. 115-120, (1991).

[4] B.P. Kibble, "A measurement of the gyromagnetic ratio of the proton by the strong field method", Atomic Masses & Fundamental Constants 5, J.H. Sanders & A.H. Wapstra , eds., Plenum Press, NY, pp. 575-551, (1975).

[5] The identification of commercial product names is for identification purposes only and does not constitute an endorsement by the National Institute of Standards and Technology.

A NEAR-FIELD INFRARED SCANNING MICROSCOPE

B.D. BOUDREAU, J. RAJA, J. PATTEN AND R.J. HOCKEN

DEPARTMENT OF MECHANICAL ENGINEERING AND ENGINEERING SCIENCE
UNIVERSITY OF NORTH CAROLINA AT CHARLOTTE
CHARLOTTE, NC 28223

1.0 INTRODUCTION

Optical microscopy has become an increasingly important measurement instrument in many industries due to its non-destructive nature. Unfortunately, conventional microscopy with its far-field optics is diffraction limited to 200nm ($\approx\lambda/2.3$) resolution. A relatively new technique called near-field microscopy utilizes initially collimated radiation emanating from a subwavelength aperture to image objects significantly smaller than this limit. Using visible light, near-field microscopes have obtained images with 10-15nm spatial resolution [1]. Due to the long wavelengths involved, infrared imaging of objects is currently limited to 500nm of spatial resolution. Near-field microscopy with its enhanced resolution imaging capabilities offers a chance to substantially improve the imaging of miniature infrared sources, e.g. integrated circuits, light emitting diodes, and laser diodes.

This paper describes the results of an ongoing research project to develop a near-field infrared scanning microscope (NISM). The reported development primarily involved redesigning the standard fiber-optic or pipette based near-field probe and detector system of a visible near-field microscope [2] as a fiber-optic radiometer. Due to the low energy and wide variation of the wavelengths involved with self-emitted radiation, special attention was required in the design of the optical system and the selection of the components.

2.0 FIBER-OPTIC RADIOMETRY

Infrared imaging involves the use of either radiometry or pyrometry. These two fields are concerned with the measurement of the radiation being emitted by surfaces. In the case of pyrometry this measurement is further processed to determine the temperature of the surface. Both of these fields rely on the simple principle that the thermal radiation emitted from a surface will continually increase with temperature. In this research we are only concerned with imaging the radiation emanating from the surface in the near-field zone.

Pyrometers and radiometers are available in a wide variety of configurations. The structural configuration of near-field microscopes however favors the use of a fiber-optic based device. As a result, the aperture/detector system was designed as a total radiation fiber-optic radiometer with a near-field aperture at one end (figure 1). The advantage of this configuration is that it simply replaces the standard visible near-field probes and uses many of the same fabrication procedures developed for the visible near-field probes [2]. The primary disadvantage of fiber-optic based radiometers is that they further limit the already low intensities involved with infrared radiation measurements. For this reason, fiber-optic radiometers commonly include a chopper to reduce the noise bandwidth of the

measurement. The total radiation configuration was selected to maximize the available signal strength.

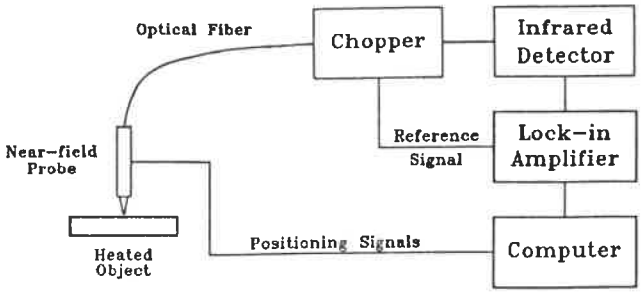

Figure 1 - Fiber-optic pyrometer.

3.0 INFRARED NEAR-FIELD MICROSCOPE

The infrared near-field microscope (figures 2 and 3) developed in this study was built using the structural and positioning components from a visible near-field microscope described in a previous paper [2]. This approach provided components whose functional performance was previously verified. The infrared microscope could therefore be developed using components whose function was assured.

3.1 MICROSCOPE MODULE

The integration of the infrared optical system into the visible near-field microscope required minor modifications to the microscope structure (figure 2). These modifications primarily resulted from the repositioning of the sample and aperture within the microscope. The near-field probe now approaches the sample from above. This change provides easier viewing of the aperture/sample region and therefore a simplified setup procedure. Except for the inclusion of a coarse aperture positioning device, the microscope module still retains all of the positioning devices describe previously. In the infrared microscope, the coarse vertical aperture positioning was required to compensate for the unknown and often varying height of the imaging sample. This stage is only required to place the aperture within the 1.5mm range of the fine Z-axis sample adjustment stage. Another feature that was not included in the visible microscope is an infrared laser diode in the mounting base. This laser allows the microscope to be operated in either self-illumination or collection imaging modes. The laser's primary function is to serve as a high intensity source that can be used to identify the target and to position the aperture within the near-field zone. This action increases the stability of the microscope by avoiding excessive operation of the thermal imaging device prior to imaging.

3.2 OPTICAL SYSTEM

A diagram of the infrared microscope system is shown in figure 3. An examination of this figure shows that only three primary components are located within the optical path through the system. These components are an aperture/wavequide, indium antimonide detector, and elliptical mirror.

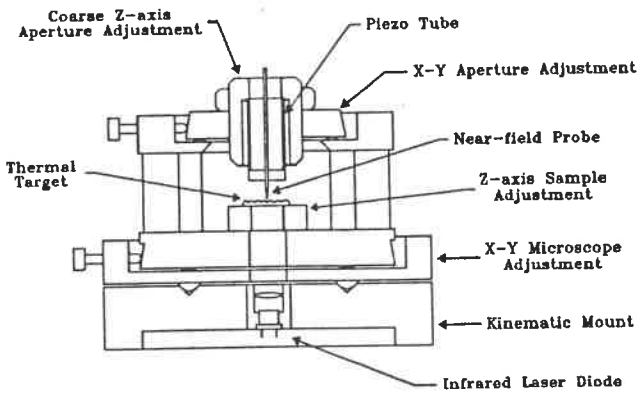

Figure 2 - Microscope module.

The near-field apertures currently being used are fabricated from 1mm

diameter quartz micropipettes. The aperture is produced using standard micropipette fabrication techniques and then overcoating with an opaque film of aluminum (≈200nm). Silver or gold would be the preferred coating material for infrared wavelengths, but aluminum is more readily available and yet still retains >95% reflectivity. The 0.5mm inner diameter of the micropipette tube serves as a hollow core waveguide to direct the collected radiation outside of the microscope structure. Near-field apertures in the range of 1-2μm are currently being projected for use with this microscope.

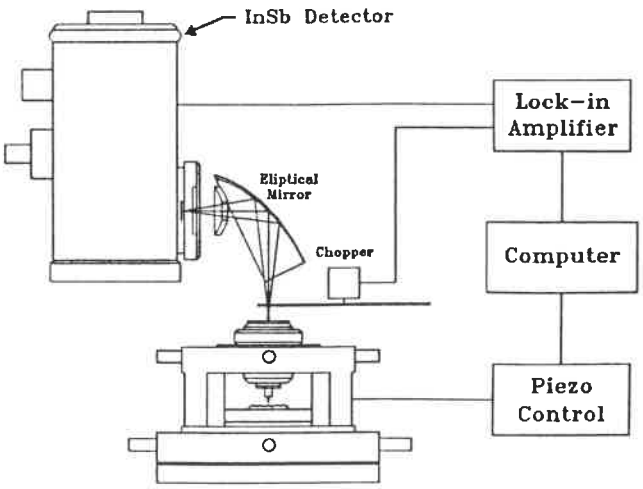

Figure 3 - Microscope system.

A 0.5mm liquid nitrogen cooled indium antimonide detector was selected to monitor the collected infrared radiation. This detector's sensitivity region extends from 2 to 5.5 microns with a peak sensitivity around 5 microns. This wavelength range has the advantage that it coincides with a window of relatively low atmospheric and water absorption. Two field-of-view limiting devices have been included to reduce background noise sources. The first device is a 45° cold stop that is internal to the detector package, while the second is a cored spherical mirror that has the detector at its center of curvature. This mirror further limits the field-of-view to 30°. The external mirror is not as effective as the internal cold stop but has the advantage that it's adjustable to match the optical conditions.

The optical system is now complete except for an optical element to focus the collected radiation onto the infrared detector. An elliptical mirror was chosen for this application. The use of a mirror avoids both chromatic aberration, and the reflection and absorption losses associated with a lens system. The elliptical mirror however causes significant image distortion. This possible loss mechanism was eliminated by selecting a mirror that produced a 50% reduction in image size. The entire image of the exit aperture of the waveguide can therefore be imaged onto the detector.

4.0 INFRARED IMAGING TARGET

The quality of a microscope is gauged by the resolution of the images that it produces. Image resolution is important because it ultimately governs the minimum observable feature size and eventual applications of the microscope. On this point near-field microscopy is no different. Near-field microscopy however is capable of much higher image resolution. Finding an imaging target capable of challenging the resolution capabilities of near-field microscope can therefore be difficult. This proved to be especially true while trying to find a micron scale thermal target for use with the infrared microscope. The following section describes the features and characteristics of a thermal imaging target developed for this research.

The thermal imaging target developed for this study is a micron scale resistive heater type device. A simple sketch of the imaging target is shown in figure 4. The entire target consists of two large connection pads (4mm X 4mm) with 1mm wide lead wires that connect to the imaging conductors. The actual imaging region consists of a parallel array of ten imaging conductors spaced 10μm apart. Each individual conductor is 2μm wide and 100μm long. The spacing values were adopted to form a 0.1 X 0.1mm imaging area where at least one conductor will always be within imaging range of the scanning tube. The width of the imaging conductors was chosen to match the minimum linewidth capabilities of our fabrication process. Unfortunately, the width of these lines is on the same order as the diffraction limit. Signal contrast and edge definition will primarily be used to evaluate the microscope resolution capabilities.

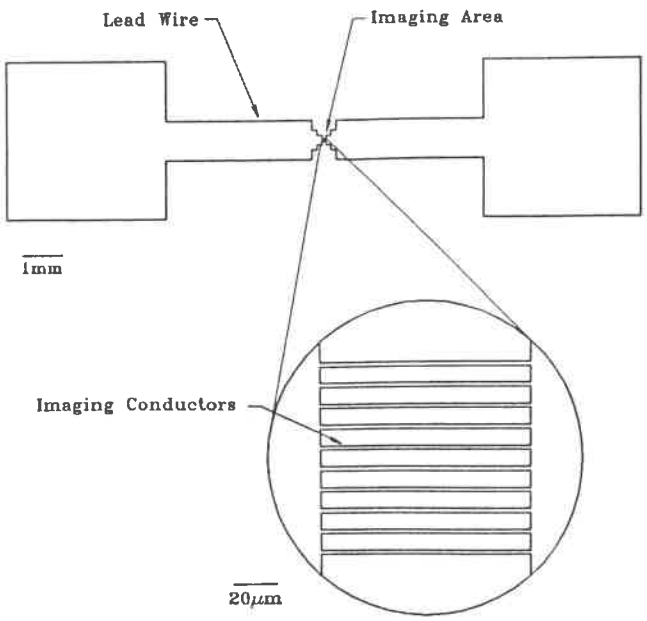

Figure 4 - Thermal imaging target.

The heater elements themselves were photolithographically etched into a 200nm thick thin film of NiCr (60-40) on a sapphire substrate. Nichrome was selected as the conductor material because it has a high resistivity (110$\mu\Omega$·cm), and excellent resistance to corrosion and oxidation when used in air. Nichrome also exhibits a range of fairly high emissivities from 0.67 for a bright surface to 0.98 oxidized [3]. The sapphire substrate was primarily chosen for its low emissivity (<0.20) and high melting point, but it also possesses a high hardness and chemical inertness. Not all of these properties are important to the function of the device but were vital during the photolithographic fabrication process. The low emissivity of the substrate was chosen to ensure high contrast between the thermal conductors and background.

Several experiments were performed on the thermal imaging targets. These tests found that the thermal targets could conduct up to 140mA and dissipate 1W within the imaging conductors before failure. Unfortunately, the lifetime of the targets at this level was only 30 to 60 minutes. A significant increase in target lifetime was observed at lower current levels. Finite element analysis indicated that the imaging conductors would radiate $\approx$900W/m^2 while the substrate would be emitting $\approx$200W/m^2 at 100mA conductor current. The finite element model also found that the emission is linear to within several percent over each region and that sufficient contrast should exist for imaging.

5.0 CONCLUSIONS

A near-field infrared microscope capable of imaging micron scale thermal emitters

has been designed and built. The structure and positioning devices of this microscope have been patterned after a visible near-field microscope. The optical system has been designed to operate as a total radiation fiber-optic radiometer. This configuration has the advantages that it simply replaces the fiber-optic based visible near-field probes while maximizing the available signal strength. A micron scale thermal imaging target for use with the infrared near-field microscope has also been described. Additional development and characterization of this microscope continues.

ACKNOWLEDGEMENTS

This research effort is being supported by a three year National Science Foundation Grant: DDM-9019776. The authors wish to thank Todd Cloninger and Senthil Balasubramaniam for their help in the development of the near-field microscopes at UNC-Charlotte.

REFERENCES

1. E. Betzig, J.K. Trautman, T.D. Harris, J.S. Weiner, and R.L. Kostelak, "Breaking the Diffraction Barrier: Optical Microscopy on a Nanometric Scale", *Science* **251** 1468 (1991).

2. B.D. Boudreau, T. Cloninger, J. Raja, J. Patten and R.J. Hocken, "A Near-field Scanning Optical Microscope Module," *Proceedings from ASPE 1992 Annual Meeting*, **6** 173 (1992).

3. E.A. Avallone and T. Baumeister eds., Marks' Standard Handbook for Mechanical Engineers, 9th Edition, McGraw-Hill, New York, p. 4-69, (1987).

A metrological scanning force microscope

Y. Xu, S.T.Smith*, P.D.Atherton**, T.Judge and R.Jones**
Centre for Nanotechnology and Microengineering
University of Warwick, Coventy,CV4 7AL, UK
* Precision Engineering Laboratory, University of North Carolina at Charlotte
Charlotte, NC 28223, USA
** Queensgate Instruments Ltd
Silwood Park, Ascot, Berkshire SL5 7PW, UK

1 Introduction

A large number of scanning probe microscopes (SPMs) have been developed, mainly based on either tunneling or atomic force with other techniques such as capacitance, magnetic, thermal, stiffness, acoustic, ion conductance and near-field optical techniques [1]. Both scanning tunneling microscope (STM) and scanning force microscope (SFM) are capable of nanometer or subnanometer lateral and vertical resolution. Many of this generation SPMs have successfully produced surface topographical images with atomic resolution, which is approaching the physical limits of this technique. However, as SPM is increasingly used for industry applications, the requirement has extended from high resolution to high accuracy. The new generation of SPM should be able to produce not only topographic images of specimens with subnanometer resolution, but also function as a metrological measurement tool with similar accuracy or perform microfabricating tasks at this level.

At present, almost all SPMs use piezoelectric (PZT) actuators for both X-Y scanning and Z profiling. A major problem with these is their inherent lack of precision which is caused by the nonlinear voltage/strain characteristic, hysteresis and creep of piezoelectric elements and coupling between the motions in x, y and z axes. Many strategies have been reported to reduce these errors. One way is to linearize the extension of piezoelectric actuator by providing nonlinear compensatory drive voltage using a predetermined algorithm [2]. Alternatively a charge drive can be used [3] which, in principle should reduce these errors although present efforts are not adequate for the more demanding applications. A more satisfactory method is to directly monitor the tip or specimen position with high sensitivity transducers to reduce the errors to insignificant levels either by post-scan image correction or closed loop feedback control [4] – [10]. The later technique has been adopted for the instrument design of this paper.

2 Instrument

A schematic diagram of the metrological scanning force microscope instrument is shown in **Fig. 1**. This consists of a capacitance based force probe attached beneath a vertical Z piezoelectric

translation system, a precision X-Y scanning stage and an X-Y coarse positioning mechanism. The specimen is mounted on the platform of the horizontal X-Y flexure stage machined from a single aluminium monolith, Queensgate Instruments S220 precision X-Y stage. In this, two piezoelectric actuators are used to drive a lever mechanism with a ratio of four to one resulting in a 50 μm range while maintaining a natural frequency of above 500 H_z in both axes. Two capacitance sensors, Queensgate Instruments NanoSensors ^{TM} , are incorporated in the stage for *in-situ* monitoring of platform position. The NanoSensor ^{TM} is capable of resolving better than 0.02 $nm\ H_z^{-\frac{1}{2}}$ (RMS), with a linearity of better than 0.2 %. In this particular stage the outputs from the sensors are used as feedback for closed-loop control resulting in low crosstalk and hysteresis. Scanning is controlled by a PC computer via a digital servo and PZT driver module for each x and y axis control.

Fig. 2 shows a line diagram of the mechanical system of the SFM. Three dimensional imaging is achieved by positioning a custom built force probe, a capacitance based force sensor, above the specimen and orthogonal to the scanning plane of the X-Y stage. The force probe is mounted on a linear translator, Queensgate Instruments Digital Piezoelectric Translator or DPT in the vertical, or z, axis. The translator consists of a stacked, tubular piezoelectric actuator with an integral capacitance sensor along its central axis to monitor the actual extension. The output from the force sensor is maintained at constant value by again feeding it through a servo controller to the vertical translator. While the X-Y stage is scanning, the force probe will follow the contour of constant force which is interpreted as the mechanical surface height at the point of contact. This DPT translator has a linear extension range of 15 μm with a resolution of less than 0.1 nm and a bandwidth of 5 kH_z. Calibrated with x-ray interferometry, the capacitance gauges have been shown to exhibit accuracies of better than a tenth of a nanometer [11]. Because of their hardness and well defined geometry a diamond tip is used for the probe. With this kind of probe, contact forces can be controlled over a wide range from 10^{-5} to 10^{-8} N, covering the entire force range generally encountered with atomic force microscopes and precision stylus profilers.

The Z translator on which the force probe is attached is, in turn, mounted on a three axis coarse positioning device. Three mechanical micrometers are used as positioners providing a coarse adjustment range of 25 mm in x, y, and z axes with resolution of approximately 10 μm. The scanning and data acquisition of the microscope are controlled by a PC computer using in-house software to provide stage positioning, data sampling and image processing under a Windows environment. A National Instruments PC-DIO-96 card was used to match the PAR parallel interface of the system that allows the system to be controlled by a computer via a high speed parallel I/O bus.

For the first prototype of the metrology SFM, the base, frame and most of other components are made of aluminium alloy because of its ease of manufacturing and favorable mechanical and thermal properties. While the high thermal diffusivities can rapidly dissipate the effects of thermal shock resulting from manual operation and therefore reduce the settling time, it also makes the instrument very susceptable to environmental temperature changes. Therefore the instrument has been used in a temperature-controlled laboratory. For vibration isolation, the instrument is mounted on a general metrology table consisting of a heavy granite plate supported by a steel frame of six leveling feet with 10 mm thick rubber pads underneath. No obvious effects from ground and airborne vibration have been observed in our experiments.

3 Performance evaluation

The X-Y specimen scanning stage was calibrated using a Hewlett Packward 5505A laser interferometer system. Extrapolating from this calibration it was possible to achieve a minimum step displacement of 0.425 nm through a 14 bit fine control D/A converter over the 50 μm range. The Z translator has a resolution of 0.21 nm corresponding to one bit of A/D converter using a commercial Queensgate Instruments Digital Piezoelectric Translator.

While the tip is in contact with a stationary silica specimen under full closed-loop control, peak-to-peak and RMS noise levels of less than 4 nm and 1.016 nm were observed in the output of Z translator. To increase the resolution, a simple box-car averaging filter was adopted at each increment during data acquisition. **Fig. 3** plots averaging times, noise level and sampling speed and these show clearly that as the averaging times increases, the noise level reduces accordingly. After 500 averages the noise level drops to approximately 0.18 nm (RMS) see **Fig. 3**. After this, improvements in noise will result in unacceptably high scan times. Averaging 2000 times at each data point results in a noise level of 0.105 nm (RMS), implying a precision of one part in 10^5 with a full DPT vertical range of 15 μm, albeit at the expense of scan speed.

The noise magnitudes of the X-Y scanning stage while stationary were recorded by monitoring the output from the two integral sensors. The noise level of the stage is measured to have a peak-to-peak magnitude of 5 nm and a RMS value of 1.586 nm which is comparable with that of the probe system. With a full scanning range of 50 μm, a precision of better than one part in 30,000 can be achieved over this relatively broad bandwidth and using similar filters to those mentioned it would be expected that a precision of better than 1 in 10^5 is achievable.

To demonstrate the repeatability of the stage, two repeat meander scans over a small area of 44 $\times$ 44 nm are shown in **Fig. 4** for a scan rate of about 80 nm/s. The sampled data is plotted without any artificial processing or filtering. In **Fig. 4**, the individual bits of the output of capacitance gauge are clearly visible, and it is obvious that the peak-to-peak magnitude of the trace fluctuation is within 3 bits of the output of A/D converter with each bit corresponding to a displacement of 0.875 nm. By comparing these two scans, the maximum position error between the corresponding lines (line 1 in scan 1 to line 1 in scan 2, ...) comes out to be 0.25 nm. These indicate that the X-Y stage is capable of positioning and scanning with a repeatability at subnanometer levels. The linearity error of the scanning stage is too small to be detected with the laser interferometer. Thus, it can be considered linear to better than $\pm 2.5nm$ over the full scan range of 50 μm with errors of less than 1 nm potentially achievable.

To assess the repeatability of the instrument in vertical axis, two repeat profiles of an optical grating surface are plotted in **Fig. 5**, which have been obtained from a continuous forward and backward scan. The data was sampled from the z translator while the stage was scanning. Again no filtering has been applied. From these data, the mean point-to-point vertical error between the two profiles is 0.21 nm, resulting in a relative error of 0.4 % over 45.06 nm. This includes the effects of directional dependence of the probe sensor, drift, mechanical and electronic noise and, therefore, represents a worst case error.

4 Surface measurement results and discusion

Fig. 6 shows a 3D plot of integrated electronic components on a silicon chip for a scan range of 30 $\times$ 30 μm and showing peak-to-valley height variations of $\approx$ 2 μm. **Fig. 7** presents an image

of an optically polished Zerodur flat . Several scratches with depths of 3 or 4 nm can be clearly seen on the surface and these are believed to be produced during polishing. From this data, R_q and R_a values of the surface roughness were calculated to be 0.67 nm and 0.53 nm. Using a Rank Taylor-Hobson Nanostep a similar portion of the surface was measured to have an R_q of 0.72 nm and an R_a of 0.58 nm over a 12.5 μm sample length, showing an agreement between these two techniques.

References

[1] H.K. Wickramasinghe, edited, 1992, *AIP conference proceedings 241*, American Institute of Physics, New York

[2] D.R. Baselt, S.M. Clark, M.G. Youngquist, C.F. Spence and J.D. Baldeschwieler, 1993, *Rev. Sci. Instrum.*, **64** *(7)*, 1874 - 1882

[3] C.V. Newcomb I. Flinn, 1982, Electron. Lett., **18**, 442 - 443

[4] J.E. Griffith, D.A. Grigg, M.J. Vasile, P.E. Russell, and E.A. Fitzgerald, 1992, *J. Vac. Sci. Technol.*, **B10***(4)*, 674 - 679

[5] R.C. Barret and C.F. Quate, 1991, *Rev. Sci. Instrum.*, **62***(6)*, 1393 - 1399

[6] J.E. Griffith, G.L. Miller and C.A. Green, 1990, *J. Vac. Sci. Technol.*, **B8***(6)*, 2023 - 2027

[7] H. Yamada, T. Fujii and K. Nakayama, 1989, *Jpn. J. Appl. Phys.*, **28**, 2402 - 2404

[8] E.C. Teague, R.D. Young, F. Scire, and D. Gilsinn, 1988, *Rev. Sci. Instrum.*, **59***(1)*, 67 - 73

[9] E. C. Teague, 1989, *J. Vac. Sci. Technol.*, **B7***(6)*, 1896 - 1902

[10] T.H. McWaid and J. Schneir, 1994, The proceeding of ASPE 1994 Spring Topical Meeting.

[11] S.T. Smith, D.G. Chetwynd and D.K. Bowen, 1991, SPIE, Vol. **1573.**, 225 - 236

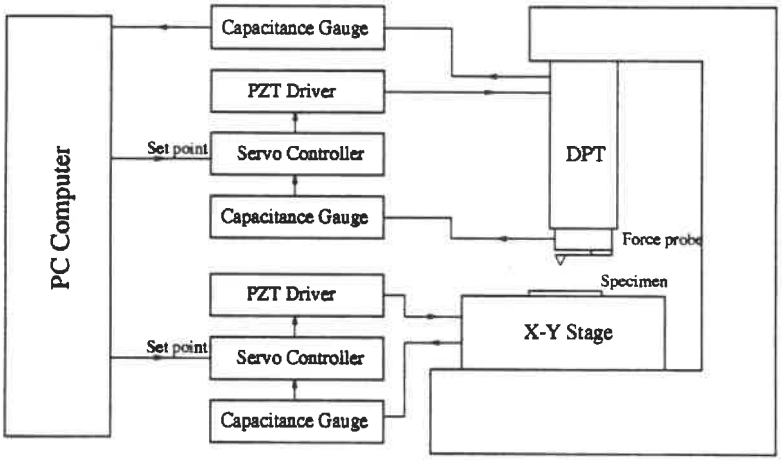

Figure 1: Schematic working principle diagram of SFM system

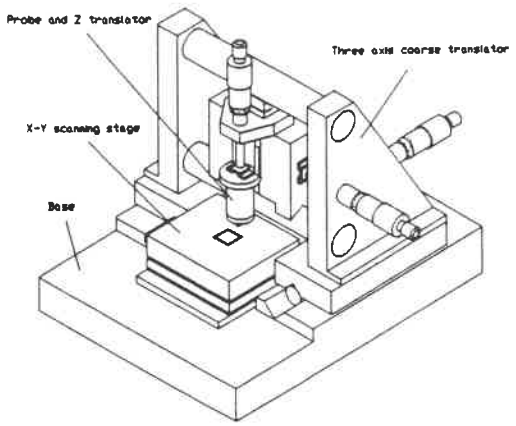

Figure 2: Isometric sketch of the metrological SFM

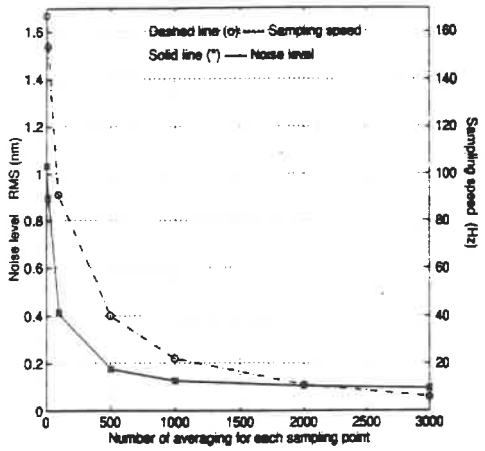
Dashed line (o) ---- Sampling speed
Solid line (*) —— Noise level
Noise level RMS (nm)
Sampling speed (Hz)
Number of averaging for each sampling point

Figure 3: Noise level and speed of data acquisition vs. averaging times

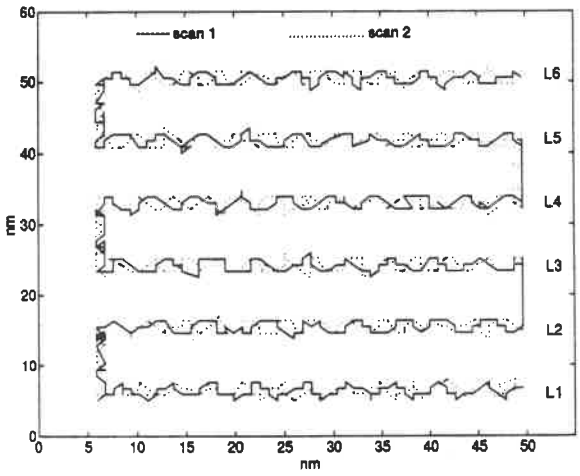

Figure 4: Plots of two meander pattern scans

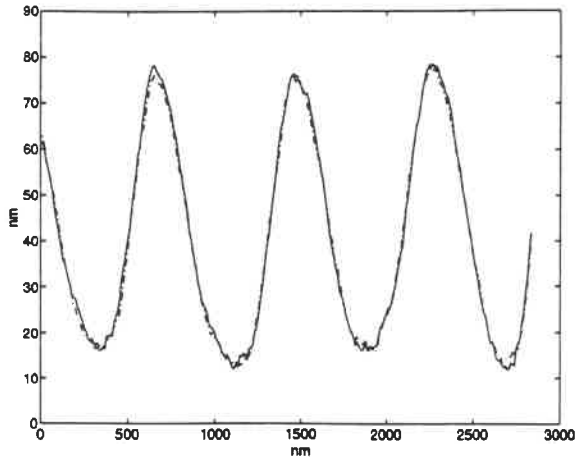

Figure 5: Plot of two optical grating surface profiles obtained from a continuous forward and backward scan

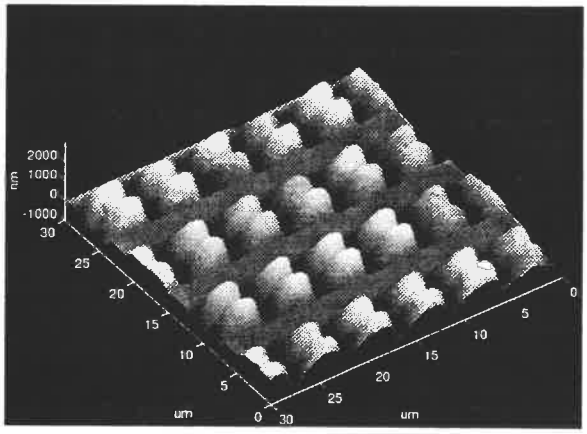

Figure 6: 3D image of electronic components on a silicon chip

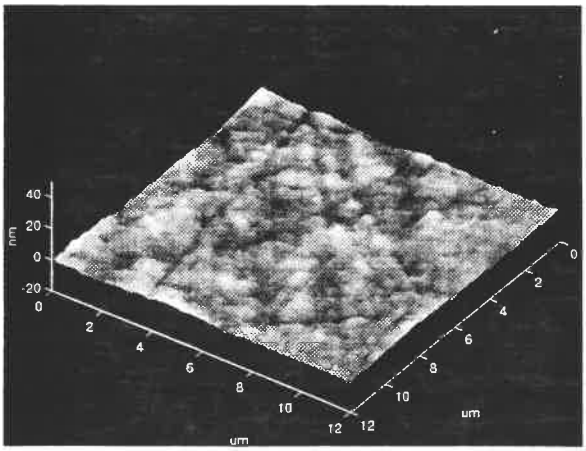

Figure 7: Image of polished Zerodur flat

Hertzian Contact Resonances

J. Kramar, T. McWaid, J. Schneir, E.C. Teague
National Institute of Standards and Technology
Gaithersburg, MD 20899

Abstract

The resonant frequency of a sphere in contact with a flat surface was measured as a function of loading force for contacting materials with different elastic moduli. Comparisons were made with predictions based on the Hertzian theory of elastic deformation. With a 4 mm radius, stainless steel ball on a ground stainless steel flat supporting an inertial mass of 180 g, the measured resonant frequencies ranged from 970 Hz to 1.73 kHz as the loading force was increased from 0.85 N to 23 N. This compares favorably with the theoretical predictions which range from 930 Hz to 1.62 kHz. For a 4 mm radius ruby ball on a sapphire flat, where the inertial mass was 200 g, the resonant frequencies ranged from 1.34 kHz to 1.81 kHz compared to a theoretical range of 1.09 kHz to 1.98 kHz as the loading force was increased from 0.87 N to 31 N.

Introduction

In many implementations of precision machine design, a kinematic mounting or repositioning scheme is utilized wherein the mating elements come into contact through balls resting on flats or on multiple flats (*e.g.*, vees). Familiar examples of six-degrees-of-freedom, spatial fixturing are three vees, oriented at 120° to each other, and the Kelvin clamp (trihedron, flat and vee). Whereas these methods of mounting provide well-studied advantages with respect to repeatability, they are also relatively compliant. Often they are found to be the weakest link in the structural loop, and the source of the lowest resonant frequencies. This seems to be particularly true in many popular embodiments of scanning tunneling and atomic force microscopes.

A theoretical treatment of the elastic deformation of a sphere of diameter D in contact with a flat as a function of loading force, F, was given by Hertz[1] in the late 1800's. The combined deformation of the sphere and flat is

$$\alpha = \frac{1}{2}\left[3\left(V_1 + V_2\right)\right]^{2/3}\left[\frac{F^2}{D}\right]^{1/3}, \qquad (1)$$

where $V = (1-\upsilon^2)/E$, and E and υ are the Young's modulus and Poisson's ratio for the contacting materials. From this equation, a contact stiffness can be defined, $\frac{dF}{d\alpha}$, which is essentially a non-linear spring that scales as the cube root of F. The complete solution of the equation of motion for a system composed of this spring loaded with a mass, m, is not trivial.[2] However, for small amplitudes of motion, it is sufficient to use a linear approximation of the spring constant about its static deformation point to define a resonant frequency for the system,

$$f_{res} = \frac{1}{2\pi}\left(\frac{3DF}{m^3\left(V_1 + V_2\right)^2}\right)^{1/6}. \qquad (2)$$

We have examined the validity of this linearized Hertzian model experimentally under conditions relevant for kinematic mounting and have investigated the dependence of the resonant frequency on material properties, loading force, and driving amplitude. All prior work on Hertzian resonances that we are aware of has focused on rolling or sliding contacts.[3]

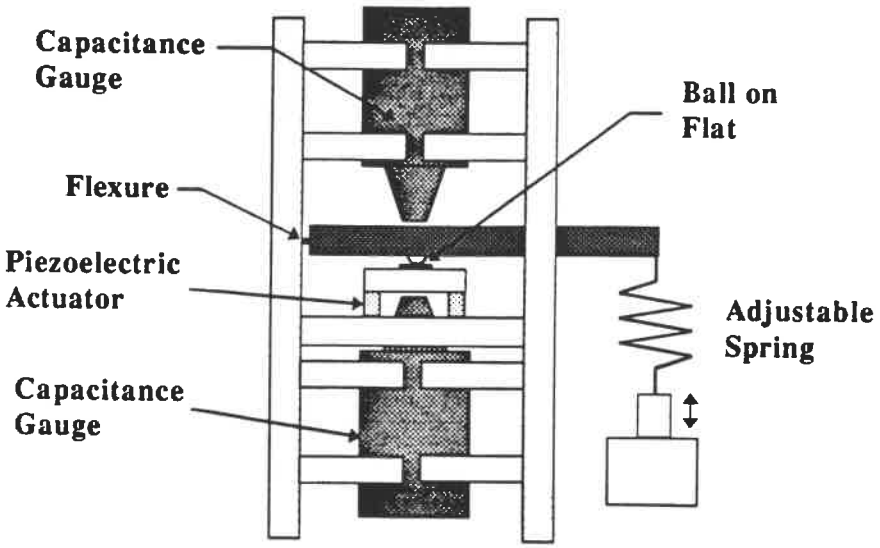

Figure 1. Schematic drawing of the test structure used for measuring the contact resonances of a ball on a flat. The ball is attached to the bottom of a hinged cantilever. The hinge is a flexure made from a thin metal shim. The motion of the back of the cantilever is measured using a capacitance gage. The flat to be measured is attached to the top of a plate that is supported and driven by three piezoelectric actuators. The motion of the back of the plate is also measured using a capacitance gage. A variable loading force is applied through a spring that is attached to the end of the cantilever.

Experimental

The test system, sketched in Fig. 1, is a single ball on a flat where the orientation and position of the ball is maintained by means of a hinged cantilever. The cantilever hinge is made from a weak flexure so as to avoid stiction effects and minimize its contribution to the loading force on the contact. The ball itself is actually a hemisphere. It is bonded to the cantilever through its flat surface by means of a threaded stud in the case of the stainless steel ball, and by means of a cyanoacrylate adhesive in the case of the ruby ball. The contact load is a combination of the moment of the cantilever about the hinge axis and an additional load applied through a spring connected to the end of the cantilever. The inertial mass, which in combination with the contact stiffness defines the resonant frequency, is the moment of inertia of the cantilever about the hinge axis divided by square of the distance from the hinge to the contact point. The flat is driven in the vertical, contact axis by piezoelectric actuators, and the displacement of both the flat and the ball are measured with capacitance gages so that the transfer function can be obtained. This is key, since in this way interference from other resonances and compliances in the test structure are excluded. To wit, as the frequency of the oscillation is swept through the Hertzian resonance, very little increase in the amplitude of the ball-supported cantilever motion is observed, but instead the motion amplitude of the driven flat drops to near zero as its energy is coupled into the ball. This is an example of a tuned frequency vibration absorber.[4] Nevertheless, when the ratio of amplitudes is taken in the transfer function, the resonance peak is clearly defined.

It is also important to limit the amplitude of the test excitation to a small fraction of the total static Hertzian deformation. This allows the use of a linear approximation to the spring stiffness about the static deformation value. For higher-amplitude excitations, the nonlinear effects are observed first as a shift of the resonance to lower frequency, as is expected for a softening spring of which this is an example. We then observe a marked increase in higher-order harmonics in the cantilever motion, and finally an audible rattle when contact is broken and the ball begins to bounce on the surface. The total shift in resonant frequency with increasing amplitude before loss of contact is small, typically less than 5 percent.

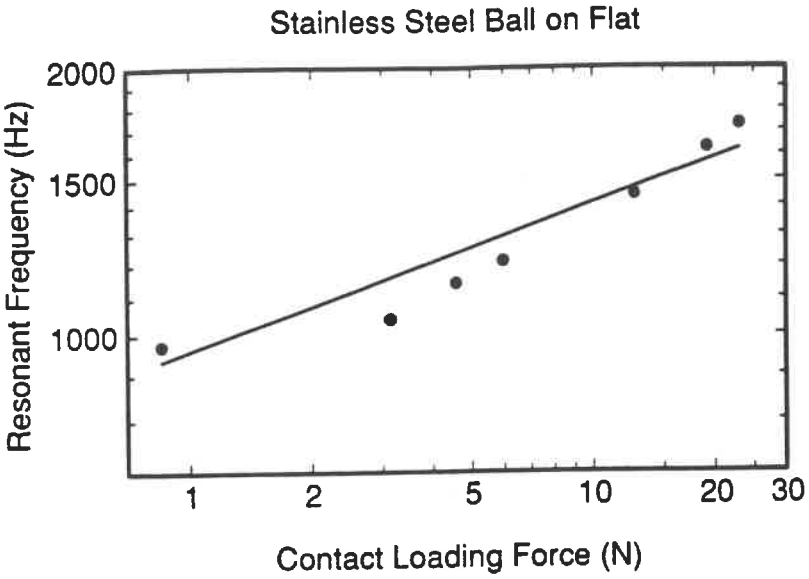

Figure 2. Log-log plot of resonant frequency as a function of loading force for a 180 g inertial mass supported by a 4 mm radius stainless steel ball on a ground stainless steel flat. The solid line is a theoretical curve based on the Hertzian elastic deformation model using a modulus of 196 GPa and a Poisson's ratio of 0.30 for both ball and flat.

Results and Discussion

For the systems and ranges of parameters we tested, the Hertzian model successfully predicts the approximate frequency of the contact resonance as well as the trends in the resonant frequency as a function of loading force and material properties. As expected, higher modulus materials or increased loading force result in a stiffer contact and a higher resonant frequency.

The measured resonant frequency as a function of loading force for a 180 g inertial mass supported by a 4 mm radius stainless steel ball on a ground stainless steel flat is shown in Fig. 2. The theoretical curve based on Eq. (2) is shown in the plot as a solid line. The measured data is fairly well predicted by the theoretical curve, with a maximum discrepancy of about 10%. This agreement demonstrates the utility and potential level of applicability of the Hertzian model for practical design.

For a 4 mm radius ruby ball on a sapphire flat, the resonant frequency as a function of contact loading force is presented in Fig. 3. In this case the inertial mass was 200 g. Note that for this higher modulus material, the resonant frequency at a given loading force is increased relative to the stainless steel system. Once again, the model predicts the approximate resonant frequency. In this case, the maximum discrepancy is about 25% and there is a clear trend for the measured data to have a lower slope. Also, in both this data and the stainless steel data, there appears to be a tendency for the data to have an upward curvature. Based on the systematic deviation of the experimental data from the theoretical curve, we suspect that the model that we have been using is incomplete in some significant detail. In this regard, we are examining the possible effects of any compliance between the ball and the cantilever, as well as any possible effects of cantilever bending. We are also exploring the possible effects of subsurface damage in the contacting elements themselves.

Figure 3. Log-log plot of resonant frequency as a function of loading force for a 200 g inertial mass supported by a 4 mm radius ruby ball on a sapphire flat. The solid line is a theoretical curve based on the Hertzian elastic deformation model using a modulus of 370 GPa and a Poisson's ratio of 0.22 for both ball and flat.

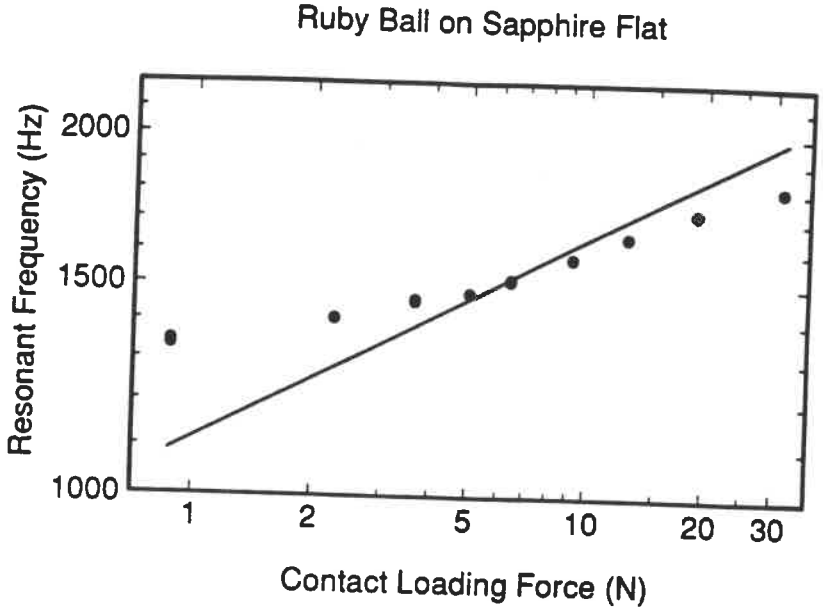

Conclusion

Despite some lack of conformity of our data to the precise form of the linearized Hertzian model, we nonetheless find that the model is a good starting point in understanding the trends and the approximate magnitudes of ball-flat resonances. These studies confirm that Hertzian contact resonances are typically in a structurally significant regime—in the hundreds of hertz—and should be given due attention in precision machine design. Because of the weak dependence on all other parameters, the most effective way of raising the resonant frequency is by decreasing the supported mass, followed by changing the contacting elements to materials with higher elastic moduli. While mathematically less significant, entering only as the $1/6$ power, increasing the loading force is also often an expedient means of raising the resonant frequency as a consequence of its practical accessibility.

References

1. *see, for example:* J.L. Lubkin, "Contact Problems," ch. 42, *Handbook of Engineering Mechanics*, W. Flügge, ed., McGraw-Hill, NY, 1962; S.P. Timoshenko, J.N. Goodier, *Theory of Elasticity*, 3rd ed., pp. 409-414, McGraw-Hill, NY, 1970.
2. P.R. Nayak, "Contact Vibrations," *Journal of Sound and Vibration*, **22**(3), pp. 297–322, 1972.
3. *for example:* R.M. Carson, K.L. Johnson, "Surface Corrugations Spontaneously Generated in a Rolling Contact Disc Machine," *Wear*, **17**, pp. 59–72, 1971; A. Soom, C. Kim, "Interactions Between Dynamic Normal and Frictional Forces During Unlubricated Sliding," *ASME Journal of Lubrication Technology*, **105**, pp. 221–229, 1983.
4. W.T. Thomson, *Theory of Vibration With Applications*, pp. 149–151, Prentice-Hall, Englewood Cliffs, NJ, 1981.

Measurement of Tool Tip Temperature in Micro Cutting by Infrared Radiation Pyrometer with Optical Fiber

Takashi Ueda*, Masahiko Sato** and Tadaaki Sugita*

*Kanazawa University, Faculty of Mechanical Systems Engineering

Kodatsuno 2-40-20, Kanazawa 920, Japan/**Toyama Prefectural University

1. Introduction

Temperature of a cutting tool is a significant factor in the investigation of the cutting mechanism and the lifetime of the cutting tool. However, it is very difficult to measure the tool tip temperature correctly using the thermocouple technique and so on.

Recently, authors have investigated a new type of infrared radiation pyrometer in which an optical fiber accepts the infrared flux radiated from the object and transmits it to an infrared detector. The flexibility of the optical fiber whose diameter is about one hundred micrometer makes it possible to enter into an intricate part and to measure the temperature of the very small area. In the grinding operation, this pyrometer was applied to measure the temperature of cutting grains on the wheel surface and the temperature distribution in the workpiece of ceramics[1-3].

In the present study, the temperature at the tip of a conical tool after cutting is measured using this pyrometer. Measurement accuracy of this pyrometer when applying to the experiment is investigated theoretically. Applying the heat transfer theory to the experimental results, the cooling characteristics of the tool after cutting is then investigated.

2. Experimental Procedure

2.1 Experimental set-up and Experimental conditions

The experimental set-up is illustrated schematically in Fig.1. A conical tool whose conical angle is 120 ° and nose diameter is 200 μm is mounted on the disk of the air spindle. The material of the conical tool is silicon nitride (Si_3N_4). The workpiece of 6 mm length is fixed on a piezo-type dynamometer. The cutting forces of normal and tangential components are measured by the dynamoneter. The materials of the workpiece are titanium and molybdenum. The thermal properties of tool and work materials are summarized in Table 1. The cutting speed is 1350 m/min and the depth of cut is 30 μm.

The position of a optical fiber can be adjusted to any points around the circumference of the disk. In order to investigate the effect of cooling on the temperature of tool tip, the fiber is fixed at any angles from the cutting point. The incident face of the fiber is set up by using the microscope and the micrometer at a distance of 50 μm from the top of cutting tool. The central axis direction of the fiber is coincide with that of the conical tool.

The fiber can accept the infrared rays radiated from the tip of the conical tool, which was heated by cutting action, when it passes through the target area. The infrared energy is

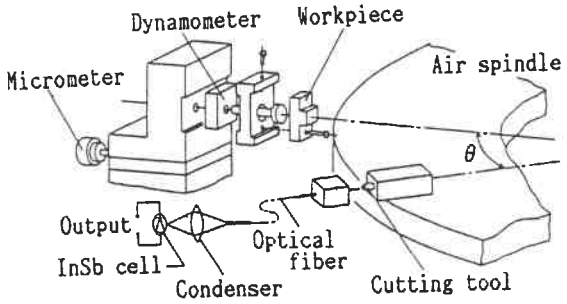

Fig.1 Schematic illustration of experimental arrangement

Table 1 Thermal properties of tool and work materials

	Si_3N_4	Ti	Mo
Specific heat J/(kg · K)	8.00×10^2	5.22×10^2	2.48×10^2
Thermal conductivity W/(m · K)	28.0	21.9	138.0
Density kg/m³	3.23×10^3	4.5×10^3	10.2×10^3
Thermal diffusivity m²/s	1.08×10^{-5}	9.31×10^{-6}	5.44×10^{-5}
Melting point ℃	------	1668	2620

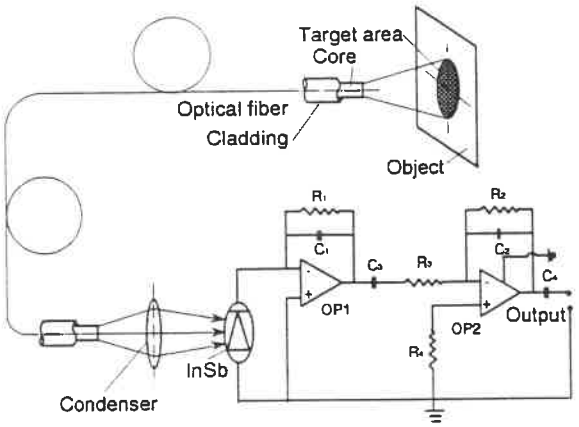

Fig.2 Pyrometer system

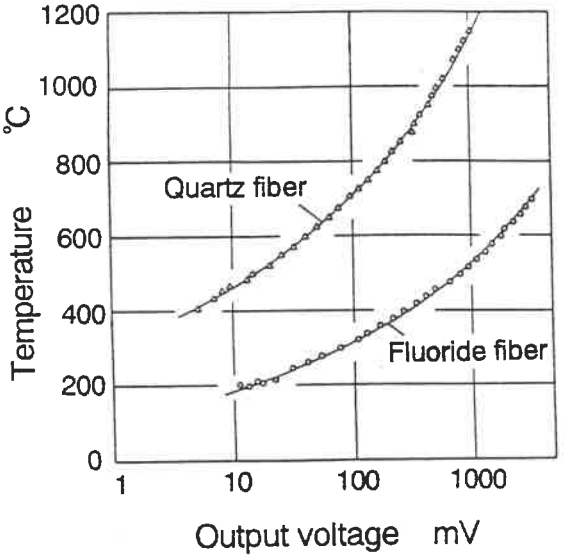

Fig.3 Calibration curves

transmitted to the detector and changed to the electric signal. The output voltage is stored in a digital memory (sampling time is 0.5 μs) and analyzed by a micro computer.

2.2 Temperature measurement

The basic system of the pyrometer is shown in Fig.2. The infrared rays radiated from the object are accepted and transmitted by the fiber, and led to the detector InSb through a condenser. The response speed of this pyrometer is approximately 5 μs [1]. Two kinds of optical fiber, quartz fiber and fluoride fiber, are used. The upper limit of the wavelength of light transmission of fluoride fiber is about 4 μm and that of quartz fiber is about 2 μm. The calibration curves of the pyrometer are obtained experimentally and shown in Fig.3.

Only rays which are incident on the face of fiber with an angle less than the acceptance angle can be transmitted. So, the target area and the acceptable energy of the I.R.P. are influenced by both the setting location of the fiber face and the temperature distribution of the object (tool tip). Therefore measurement accuracy of this pyrometer when applying to the experiment is investigated theoretically. Figure 4 shows the model to calculate the energy accepted by a fiber. The object is assumed to be a circular plane (radius Rb) which has the temperature distribution of 2nd power. The total energy E accepted by a fiber is

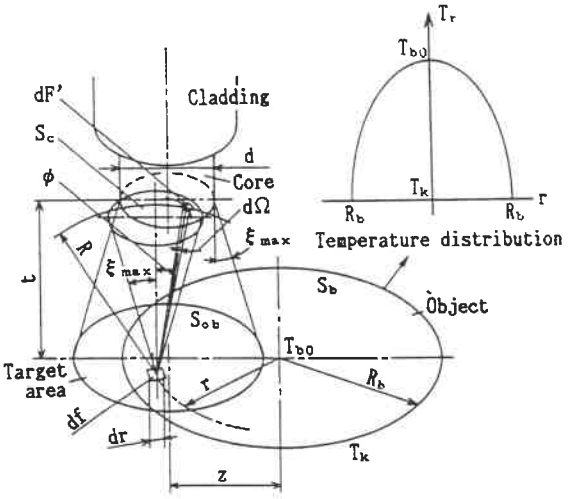

Fig.4 Model to calculate energy

$$E=\frac{C_0}{t^2}\int_{S_{ob}} dr \int_{S_c} dF' \int_{\lambda_1}^{\lambda_2} J_{\lambda n}(\lambda, T_r) \times r \cdot \frac{\cos^2\phi}{R^2} \cdot d\lambda \quad (1)$$

where, $J_{\lambda n}(\lambda, T_r)$ is the normal spectral radiant intensity, T_r is the temperature, and $\lambda_1 \sim \lambda_2$ is measurable range in wavelength of the pyrometer.

In the case of t=50 μm, Tb0=1300K, Tk=300K and Rb=250 μm in Fig.4, the calculated result of Eq.(1) is shown in Fig.5. The height of pulse is 97.1 % of Em, so that the temperature measured is almost equal to 1300K. The broken line indicates the result when the object has the uniform temperature of 1300K. In this case the temperature measured is 1300K. In the cases of Rb=100 μm and 400 μm, the heights of pulse are 83.4% and 98.8% of Em, respectively. The 80% of acceptable energy means that the temperature measured is lower by about 5 % than the real one from Fig.3. Consequently, the output voltage of the pyrometer corresponds to the maximum temperature of the object with more than 95 % accuracy.

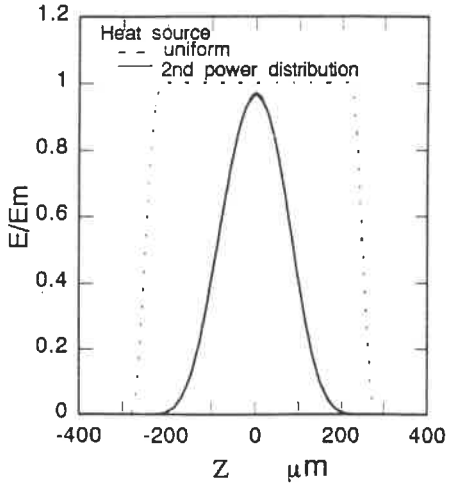

Fig.5 Appearance of energy accepted

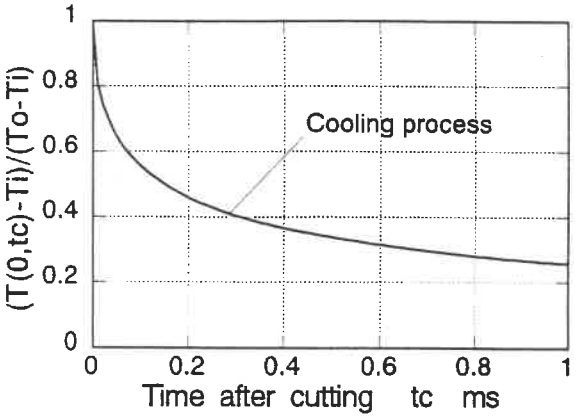

Fig.6 Cooling characteristics of tool tip

3. Heating and Cooling of Tool Tip

Thermal action of tool tip is analyzed by one dimensional unsteady state heat transfer theory, namely, it is assumed that the heat flows only to the direction of the central axis (x axis) in the tool. Because the size of heat source is much larger than the size to be analyzed.

In the cutting process, it is assumed that the quantity of heat flowing into the tool is constant. When the quantity of heat q_a per unit time and unit area is flowing into the tool, the temperature distribution in the tool at time t_h is

$$T(x,t_h) - T_i = \frac{q_a \xi}{k}\left[\frac{1}{\sqrt{\pi}}\exp\left\{-\left(\frac{x}{\xi}\right)^2\right\} - \frac{x}{\xi}\,\mathrm{erfc}\left(\frac{x}{\xi}\right)\right] \quad (2)$$

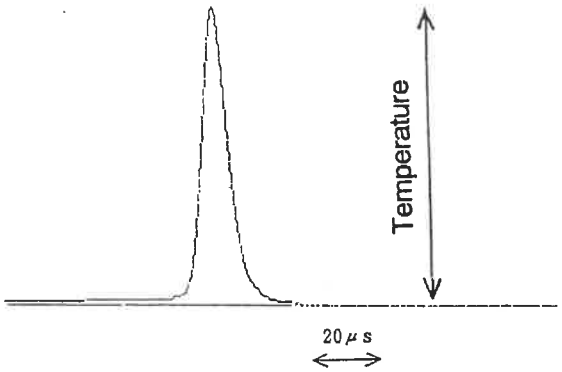

Fig.7 Output wave

where, x is the distance from the surface of the tool, $\xi=2\sqrt{\alpha t_h}$, α is thermal diffusivity and k is thermal conductivity [4].

After cutting, the tool tip cools rapidly, because the heat is transferred by conduction to the inner region of tool and convection to the air at the surface of tip. Therefore, the temperature at the surface of the tool tip at time t_c (t_c=0 is when the cutting process is finished) is

$$\frac{T(0,t_c)-T_i}{T_0-T_i}=\exp\left(\frac{\gamma}{\eta^2}\right)\cdot\left(\zeta+\frac{1}{\eta}\right)\times\left[\exp\left(\frac{\gamma}{\eta^2}\right)\left\{\frac{\zeta}{\zeta^2-\frac{1}{\eta^2}}-\frac{\frac{1}{\eta}}{\zeta^2-\frac{1}{\eta^2}}\operatorname{erf}\left(\frac{\sqrt{\gamma}}{\eta}\right)\right\}-\frac{\zeta}{\zeta^2-\frac{1}{\eta^2}}\exp\left(\zeta^2\gamma\right)\left\{1-\operatorname{erf}\left(\zeta\sqrt{\gamma}\right)\right\}\right] \quad (3)$$

where, $\zeta=h/k$, h is heat-transfer coefficient and $\gamma=\alpha\, t_c$.

The calculated results from Eq.(3) for the tool of Si_3N_4 is shown in Fig.6. From this figure, it is found that the tool tip temperature decreases to one half of the maximum temperature only 0.15ms(=t_c) after cutting.

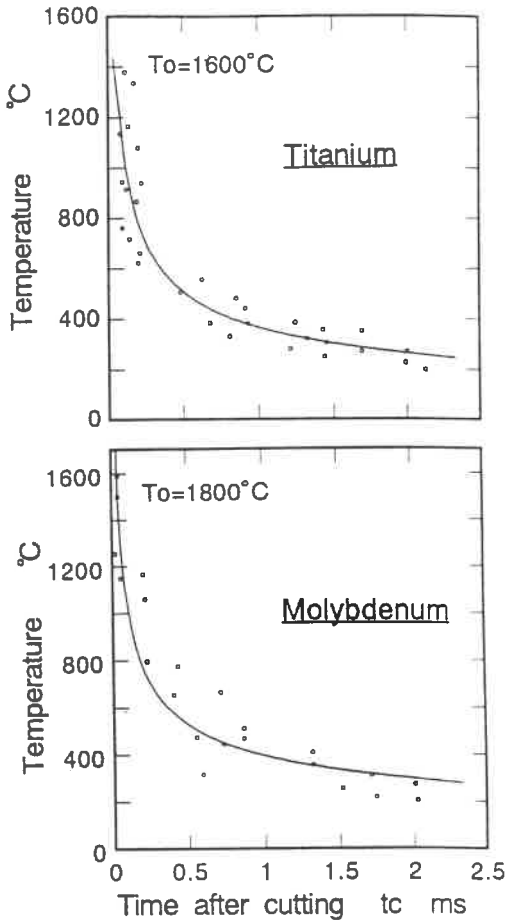

Fig.8 Tool tip temperature after cutting

4. Experimental Results and Discussions

Figure 7 shows an example of the output wave of the pyrometer. The height of pulse represents the temperature and the width represents the size of the heat source.

In Fig.8, the measured and the calculated temperatures of the tool tip after cutting are plotted as a function of cooling time t_c. The curve is calculated from Eq.(3) and the value of T_0 is chosen so as to minimize the difference between the measured temperatures and the calculated ones. The maximum temperature measured is 1380℃ for titanium and 1590℃ for molybdenum. The temperature of the tip of the tool just after cutting is estimated to be 1600 ℃ for titanium and 1800℃ for molybdenum. 1600℃ is close to the melting point of titanium.

References

1. Ueda,T.,Hosokawa,A.,Yamamoto,A. "Studies on Temperature of Abrasive Grains in Grinding-Application of Infrared Radiation Pyrometer." ASME Jour. Ind. for Eng., 1985, 107, 127-133.

2.Ueda,T.,Hosokawa,A.,Yamamoto,A. "Measurement of Grinding Temperature Using Infrared Radiation Pyrometer with Optical Fiber."ASME Jour. Ind. for Eng., 1986, 108, 247-251.

3. Ueda,T.,Yamada,K.,Sugita,T. "Measurement of Grinding Temperature of Ceramics Using Infrared Radiation Pyrometer with Optical Fiber."ASME Jour. Ind. for Eng., 1992, 114, 317-322.

4. Ueda,T.,Hosokawa,A.,Yamamoto,A. "Thermal Analysis of Active Grains in Surface Grinding."Jour.of Japan Society of Precision Engineering, 1985, 58, 1732-1737.

USE OF FORCE FEEDBACK FOR DYNAMIC ERROR CORRECTION IN DIAMOND TURNING FOR SURFACE ROUGHNESS IMPROVEMENT

Quan Ma, Graduate student **Paul I. Ro**, Associate Professor
Precision Engineering Center
North Carolina State University, Raleigh, NC 27695-7918

1 Introduction

Tool force contains rich dynamic information that can be utilized to ascertain the quality of a diamond turned surfaces. As the requirement for surface accuracy becomes more stringent, the addition of tool force feedback may improve the control of the diamond turning process.

Two control schemes utilizing the force feedback have been investigated and compared. These schemes are different in the way the force information is utilized. The first approach makes use of an admittance model, which relates the cutting force to tool-interface relative motion error, whereas the second approach is an observer-based state feedback approach that requires the force to be a direct measurable state of the machining process. For the first approach, several admittance models have been developed including a chip-geometry based model and a model based on empirical date. The accuracy of the models plays a significant role in the performance of the overall control. For the second approach, a Luenberger type observer and a Kalman filter were both developed to estimate the tool motion based on the output force, and the full-state feedback scheme is employed to close the loop on the tool position. Advantages and limitations of both schemes are examined and tested through computer simulation.

2 Admittance Model Based Approach

2.1 Force/Tool motion (Admittance) model based on chip geometry

An admittance model gives the relationship between cutting force and the normal tool variation. A chip geometry based model which relates the dynamic motion errors to the dynamic variations in tool forces has been introduced by Abler and Ro[1]. This model relates the variations in forces to the change in depth of cut error on successive revolutions of the spindle. It is developed for overlapping cutting where only the dynamic term is considered. The model can be expressed as

$$F(k) = K(X_i(k) - X_o(k)) + B\dot{X}_i(k) \qquad (1)$$

where $X_i(k)$ and $X_o(k)$ are current and previous surface variations(also known as inner and outer modulations). K and B are dynamic stiffness and damping coefficients. They are determined by the cutting process parameters such as tool radius and the areas of contact between the tool and workpiece. An assumption was made by Jeong and Ro[2] that there is only a time shift, d, between the two modulations,

$$X_o(k) = X_i(k)Z^{-d} \qquad (2)$$

Substitute $X_o(k)$ into (1), the admittance model can be expressed as

$$F(k) = K(1 - Z^{-d})X_i(k) + B\dot{X}_i(k) \qquad (3)$$

$X_i(k)$ could be estimated provided $F(k)$ is measured.

2.2 Control system structure and simulation result

A flow diagram of the admittance model-based control system is shown in Figure 1. The desired input X_i which represents the current tool/workpiece relative motion is zero. The major disturbance input is X_o which represents the previous surface variation. The role of the admittance model in the feedback path is to map the relationship between cutting force variation and surface to obtain an accurate X_i. Simulated 50 nm step response is shown in Figure 2.

3 Full State Feedback Approach

3.1 System modeling

To use cutting force to improve the surface finish in diamond turning, a force measurement based Fast-Tool-Servo(FFTS) that incorporates a high sensitivity force sensor measuring the dynamic variation of thrust force has been designed and

fabricated. It also has two eddy current probes for tool position measurement. The schematic of the FFTS is shown in Figure 3. It can be seen from Figure 3 that the FFTS is a fourth order system. If the measured force signal is chosen as a direct state of the system, cutting force is also a feedback signal when full state feedback is applied. The four states of the system are chosen as X_t , $\dot{X}_t$, F_f , $\dot{u}$ which are tool position, tool velocity, force measured by the force sensor and velocity of the sensor holder, respectively. The system model in state space form is developed as

$$\dot{X} = \begin{bmatrix} 0 & 1 & 0 & 0 \\ 0 & 0 & \frac{K_{1f}}{M_t K_f} & 0 \\ 0 & -K_f & 0 & K_f \\ \frac{K_{fp}}{M_h} & 0 & -\frac{K_a}{M_h K_f} & \frac{B}{M_h} \end{bmatrix} X + \begin{bmatrix} 0 \\ 0 \\ 0 \\ \frac{K_{fp}}{M} \end{bmatrix} r$$

$$y = [1\ 0\ 0\ 0]\, x$$

3.2 Control system structure and simulation result

Since the measurable states are only tool force and tool position, an observer has to be designed to estimate the other two states to use full state feedback for pole placement of the closed loop system. The diagram of the control system is shown in Figure 4. For the simulation, two types of observers have been used in state estimation, one is a Lunberger type observer and the other is a Kalman filter. Simulated 50 nm step responses are shown in Figure 5. Under the same noise and disturbance inputs, Figure 5 indicates that the system with a Kalman filter as the observer is much more robust to disturbance and insensitive to noise compared to the system with a Lunberger type observer.

4 Conclusion

Use of force feedback in diamond turning is investigated. Two specific schemes have been developed and the performances have been tested through simulation. To implement the control schemes developed, a PZT-based Fast Tool Servo (FST) system that incorporated a high-sensitivity single-axis force sensor (Kistler Model 9207) is designed and built. The tool motion is measured with two eddy current sensors. The two control schemes are being tested experimentally on a Rank Pneumo's ASG 2500 diamond turning machine. It is hoped to generate some general guidelines concerning force feedback control of diamond turning process.

Reference

[1] Abler, J.A.,. and Ro, P.I. , "Development and Verification of Dynamic force Model in Diamond Turning", PEC 1994 Interim Report.

[2] Jeong, S. and Ro, P.I. , "Cutting Force-Based Feedback Control Scheme for Surface Finish Improvement in Diamond Turning", PEC 1992 Annual Report, Vol. X, pp.201-208, 1993.

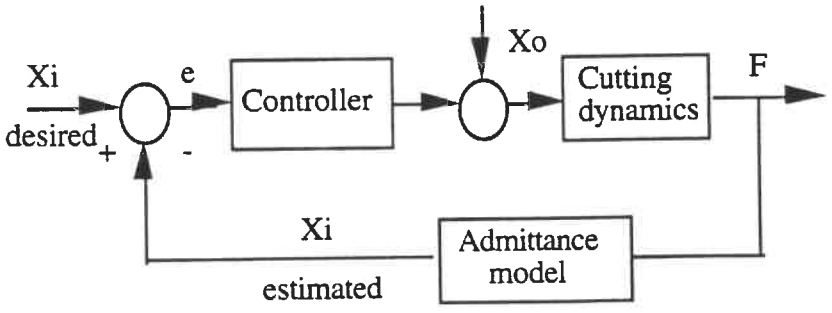

Figure 1 : Admittance model-based control system

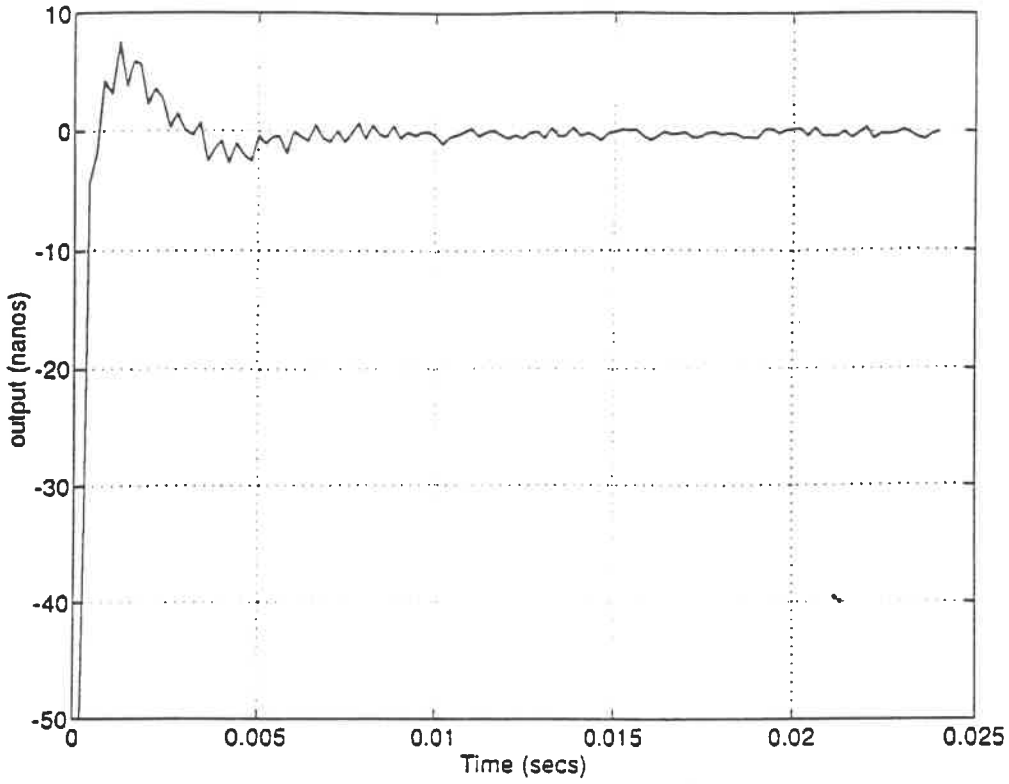

Figure 2 : Simulated 50 nm step response

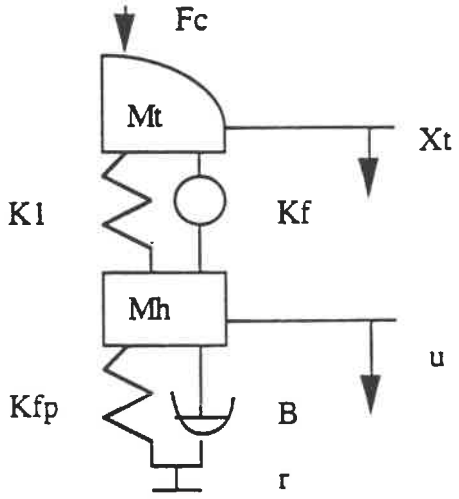

Figure 3 : Schematic of the FFTS

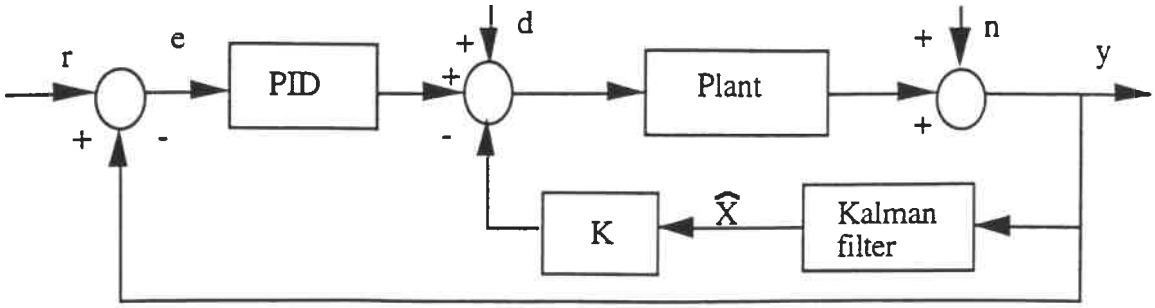

Figure 4 : Structure of the full state feedback control system

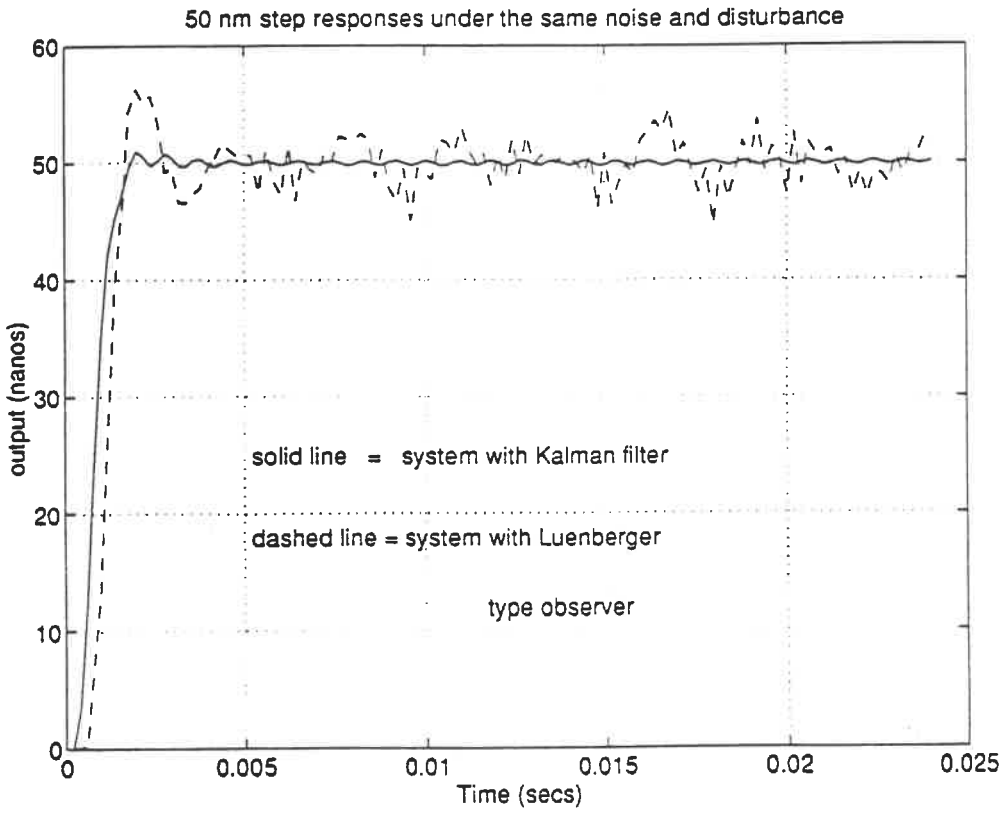

Figure 5 : Step responses of the FFTS system with different observers

Effects of Feedrate and Tool Rake Angle in the Single Point Diamond Turning of PVD Silicon

Arthur C. Miller, Jr. *
Oak Ridge National Laboratory
Oak Ridge, Tennessee 37831-8039

Introduction

High-performance materials such as Silicon Carbide (SiC) are being investigated for optical components that must be used in space applications. Consequently, cost-effective processing methods must be developed which provide low-scatter, highly accurate front surface reflectors. Prior attempts to directly single point diamond turn physical vapor deposited (PVD) claddings on SiC resulted in severe tool wear and surfaces characterized by microcracks. This paper discusses a single point turning experiment performed in conjunction with United Technologies Optical Systems where feedrate and tool rake angle parameters were analyzed in machining PVD silicon claddings on SiC coupons. These experimental parameters were measured with respect to the coupon surface roughness and diamond tool edge wear.

The intent of our experiment was to optimize a limited set of the possible diamond turning parameters with respect to the resulting surface finish and tool wear. As the edge breaks down, high spatial frequency flaws are immediately produced in the surface, and eventually unacceptable surface figure errors are introduced as edge recession becomes excessive. By measuring the amount of tool edge recession, we hoped to show that scatter produced by residual microcracks could be reduced with post polishing techniques and still preserve the accuracy of the machined aspheric surface.

Some information is available on the diamond turning of single crystal silicon (1-3), but processing of polycrystalline front surface silicon cladding has not been extensively reported. A statistical design was used in the experiment that covered the expected range of operating conditions. Initial parameters used in the experiment were based on the available single crystal machining data. Roughness and tool wear data were fitted to a reduced second order model to predict the response surfaces for PVD Si claddings.

Machinability Study

Sample preparation proved to be a key issue, since it is difficult to obtain damage-free starting surfaces after roughing operations. Highly polished 36 mm diameter flat coupons were used in the study in conjunction with a precision tilting fixture for alignment. Samples were placed in an off-axis position and tilted so that a single 2.5 μm depth of cut pass would cut the entire surface. The depth of cut was maintained at 2.5 μm on each run, and surfaces were remachined for subsequent runs when possible. Testing followed a full factorial design with three levels for tool rake angle and feedrate parameters. Values are shown in Table 1:

Factor	Level
Tool Rake Angle (deg)	-17, -39, -60
Feedrate (μm/rev)	0.25, 1.39, 2.54

Table 1. Factor levels for response surface design.

** Research sponsored by the Ballistic Missile Defense Organization, through the System Integration, Command and Control Directorate, Integration Support Division, under Interagency Agreement No. 1855-1562-A1 under Martin Marietta Energy Systems, Inc. contract DE-AC05-84OR21400 with the U.S. Department of Energy.*

Including replicates, 13 runs were used in the experiment. Double conic, negative rake geometry diamond tools were supplied by Edge Technologies. These tools would hold significant advantages to standard tools in production since they allow a wider use of the available tool edge and eliminate recalculation of machining coordinates when the tool is rotated. In machining of contoured surfaces, tool wear rates are expected to be high in the PVD silicon, and frequent rotation of the tool is likely. An oil stream coolant was used in the machining. Surface finish measurements were made on a Chapman MP 2000 instrument with a 50 μm spatial filter.

Tool Wear Measurement

We were interested in resolving possible degradation of the surface figure due to tool edge wear that was extensive enough to result in nose recession and subsequent loss of figure accuracy. Traditional tool wear methods employ microscopic examination of the flank face. However, to achieve the much higher resolution (0.03 μm) required for this study, we chose a variation of the nose replication method described in (4). Scanning electron microscope images were impractical to analyze due to charging of the edge and the difficulty in locating wear zones.

Tool nose edge recession was measured by replicating the edge profile in a soft metal substrate. The profile was recorded by a single 25 μm deep plunge cut in a Udalyte Bright Acid Copper (UBAC) coated sample before and after each machining run. The 25 μm depth provided approximately a 3:1 ratio in worn edge to unused edge for comparison. Example profiles of low and high wear runs are shown in Figures 1. and 2. after appropriate offsets were applied to allow matching the pre- and post-cut profiles.

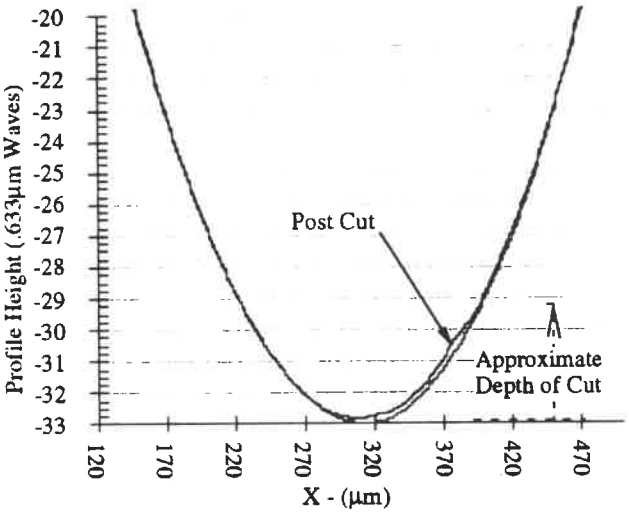

Figure 1. Tool Edge Recession - Low wear

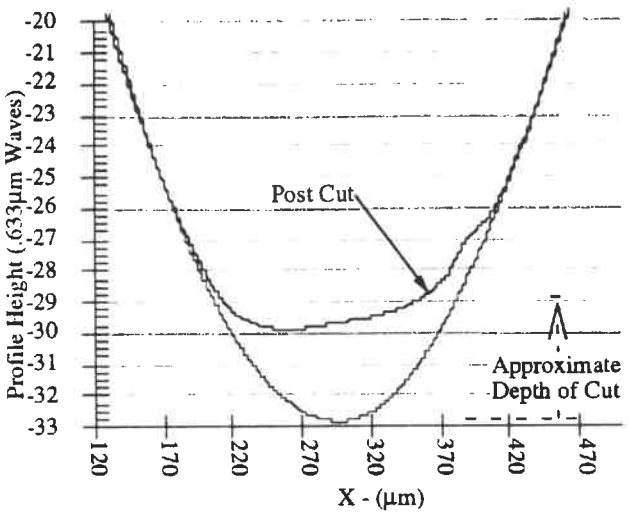

Figure 2. Tool Edge Recession - High wear

A photograph of the corresponding low tool wear sample is shown in Figure 3. This highly reflective sample is contrasted by the high wear sample, Figure 4., where a chatter mechanism has placed regular marks approximately 3 μm deep in the surface. Based on the surface speed, a frequency of between 50 and 80 Khz would be necessary to cause the regular features. An explanation for this oscillation is still under investigation, although at the high frequency observed, resonance in the diamond crystal is a distinct possibility. Note that the chatter lines radiate from the machining center of rotation which indicates that the cause is process related. The fact that the replicate run did not exhibit chatter marks also suggests that process parameters or cladding properties may be important.

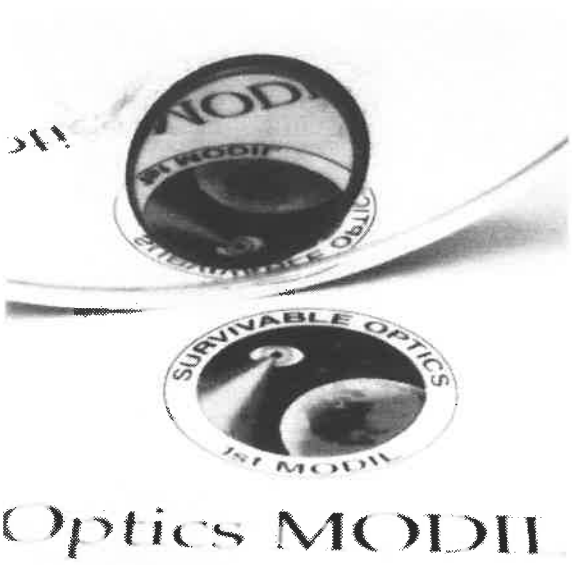

Figure 3. Low-wear Sample

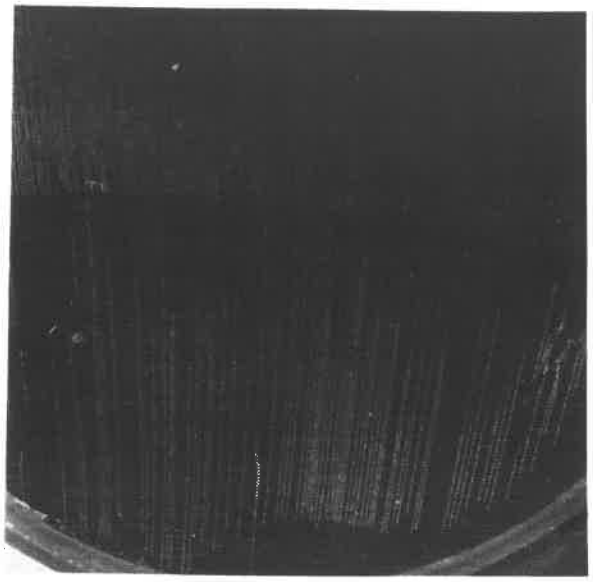

Figure 4. High-wear sample with chatter marks (2X)

Machinability Study Analysis

The expected value of the response (either RMS roughness or tool wear) was modeled as a second-order polynomial in terms of rake angle and feedrate:

$$E(Y) = \beta_0 + \beta_1 X_1 + \beta_2 X_2 + \beta_{12} X_1 X_2 + \beta_{11} X_1^2 + \beta_{22} X_2^2 + \varepsilon \qquad [1]$$

Where: Y = Response, X_1 = rake angle, X_2 = feedrate, ε = experimental error

The coefficients β_0-β_{22} were estimated by a least-squares regression, and a reduced model was obtained by eliminating statistically non-significant (<10% significance level) terms.

Figure 5. shows the reduced response surface of [1] for RMS roughness with respect to rake angle and feedrate. The fitted response surface has a minimum expected value when rake angle = -40° and feedrate = 2.54 μm/rev. Approximately 30% of the runs exhibited severe tool edge breakdown and damaged surfaces. Interestingly, the response surface indicates that faster feedrates and/or less steep negative rake angles minimize surface roughness. The response for tool wear (Figure 6.) also suggests further experimentation at faster feedrates. Coefficients for the response surfaces are as follows:

Y = RMS roughness,	β_{12} = 0.15027	β_{11} = 0.185975	β_{22} = 0.028979
Y = Tool wear,	β_0 = 1.36218	β_2 = −0.00833	

Optimized parameters in the machinability study were subsequently used in an experiment to machine a typical contoured mirror. A 200 mm by 88 mm Si cladded SiC mirror with a spherical surface was machined off-axis to evaluate the results of the study. Prior to machining the mirror surface, an estimate of the tool edge recession was obtained by repeatedly machining small coupons on the same tool edge until an area equal to the test mirror was covered. After an area equal to approximately 75% of the mirror area was covered, tool edge breakdown had caused significant damage in the surface. Despite the increased surface roughness, tool edge recession was minimal (< 0.16 μm).

A great deal of care was taken to align and balance the mirror for diamond turning. During the several roughing passes, it became obvious that an additional optimization study would be needed to speed fabrication of contoured surfaces. Since each roughing pass produces new damage as well as removing damage from the previous cut, careful planning is necessary to approach a damage-free final state and still preserve enough cladding for the required surface. The mirror roughing-in process produced chatter marks and excessive microfracture damage that were not adequately removed when the diamond turning operation was completed. The roughness of the mirror's surface prevented interferometric analysis.

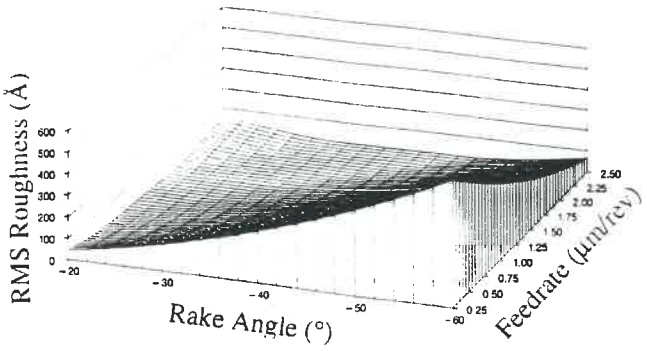

Figure 5. Response surface for surface roughness

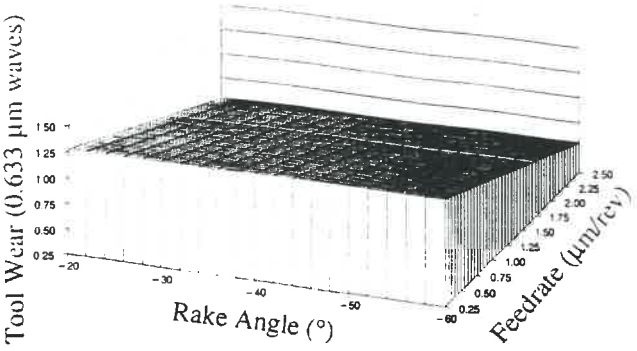

Figure 6. Response surface for tool wear

Summary

The experimental data show that PVD silicon can be successfully diamond turned with a high quality surface finish on small (36 mm diameter) flat coupons. Tool edge recession measurement by the nose replication technique produced a high resolution evaluation of possible figure errors introduced by excessive tool wear. Surface roughness as low as 24 Å RMS (Chapman MP 2000 with 50 µm spatial filtering) was observed with less than 0.16 µm ($\lambda/4$) tool edge recession. However, chatter mechanisms, not well understood at this point, caused defects in the surface when the optimized machinability results were used to diamond turn an off-axis, contoured mirror surface and prevented the demonstration of high-quality surface production. Further investigation into the issues of cladding and surface preparation is needed before a reduction or elimination of polishing will be possible through single point turning of PVD Si cladding.

The author gratefully acknowledges the efforts of Joe Cunningham in diamond turning and Richard Counts in statistical design and analysis.

(1) Syn, C.K., "Diamond Turning of Silicon, Glass, and Beryllium", Fabrication Technology, Vol 4, pp 19-25.
(2) Bifano, T.G., et al., "Precision Finishing of Ceramics", Proceedings of the SPIE, Vol. 803, 1987, pp 12-22.
(3) Blake, P.N., and Scattergood, R.O., "Ductile-Regime Machining of Germanium and Silicon", J. American Ceramics Society, Vol 73,[4], 1990, pp 949-957.
(4) Syn, CK, et al., "Diamond Tool Wear vs Cutting Distance on Electroless Nickel Mirrors", Proceedings of the SPIE, Vol. 676, (1986) pp 128-140.

GENERATION OF ROTATIONALLY ASYMMETRIC OPTICAL SURFACES USING A FAST TOOL SERVO

G. M. Moorefield, II, K. P. Garrard, K. J. Falter, L. W. Taylor, and T. A. Dow
Precision Engineering Center
North Carolina State University, Raleigh, NC

INTRODUCTION

A laser relies on an optical system for feedback that will enhance the stimulated emission of photons and control the output. An annular laser cavity such as shown in Figure 1 has distinct advantages over the more common cylindrical configuration, including efficient laser excitation by internal pumping and large discharge surfaces for diffusion cooling for high-power applications [1]. However, the shape required for such optical surfaces is much more complicated than their cylindrical counterparts. The optical system must drive the geometric rays toward the coupling aperture (i.e., the output slot) while preventing them from "walking" toward a larger radius. As suggested in the sketch, this can be accomplished with a curved surface on the face of a helical mirror which causes the optical path to increase with θ and forces the rays toward the coupling aperture.

The technology key to producing these mirrors is the integration of a fast tool servo (FTS) with a diamond turning machine (DTM). The PEC recently completed a contract with an industrial client to machine a set of mirrors for a 1 kW diffusion cooled CO_2 laser. The surfaces were machined using the movement of the DTM axes and the fast tool servo which were controlled and coordinated by a custom high-speed digital signal processor (DSP) based controller [2].

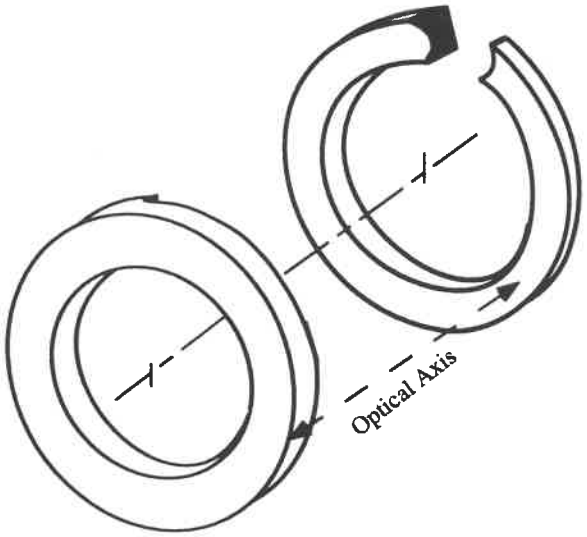

Figure 1: Annular Laser Cavity.

DESCRIPTION OF MIRROR SET

The mirror set consisted of two annular (45.5 mm ID, 62 mm OD) workpieces with mirror-image surfaces designated as the "right-hand" and "left-hand" mirrors. The mirror surfaces differ in that the azimuthal angle, θ, increases in the counterclockwise direction for the right-hand mirror while θ increases in the clockwise direction for the left-hand mirror. The surfaces were fabricated from oxygen-free, high-conductivity copper. The surfaces are defined by the following expression.

$$z(r,\theta) = -K\theta + K\frac{2}{r_s}(r - r_s)\theta + \frac{(r - r_s)^2}{2R} \tag{1}$$

Variables:

z = surface height (m)

r = radius (m); 0.0475 m $\leq r \leq$ 0.0555 m

θ = azimuthal angle (rad)

Constants:

R = radius of radial curvature (3.0 m)

r_S = radial position of parabola's vertex (0.0515 m)

K = height/angle variation constant (2.0 µm/rad)

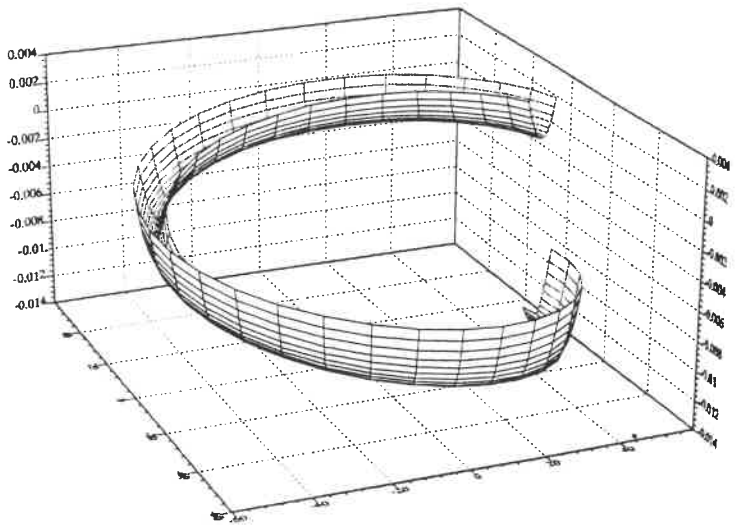

Figure 2: Workpiece Surface.

Figure 2 reveals that the 8 mm wide annular parabolic cross-section spirals in the Z-direction as a function of radius and azimuthal angle, with a discontinuity occurring at θ=0. The maximum single-revolution surface height variation (i.e., the maximum required stroke of the FTS) was 15 µm. The surface finish was to be less than 300 nm PV and the form error limit was specified to be +/- 300 nm.

DESCRIPTION OF EQUIPMENT AND PROCEDURE

The DTM used in this project is a Rank Pneumo ASG2500 Aspheric Generator. This DTM features T-base configured hydrostatic bearing slides, an aerostatic bearing workpiece spindle, and laser interferometer position feedback. The PEC's custom DTM controller uses DSP architecture to provide the high-speed operation necessary for real-time control [2]. C-language software developed at the PEC provides the DTM's user interface, controls the slide and servo positions, and manages the ancillary machine functions.

The FTS used in this fabrication process has a range of approximately 16 µm, a natural frequency of greater than 7 kHz, and a usable bandwidth of 1 kHz [3]. The principal elements comprising the FTS are the body, the 18 mm long hollow cylindrical piezoelectric stack, the capacitance gage for position feedback, and two annular plate flexures to guide the motion of the moving mass (i.e., the diamond tool, the tool holder, etc.) and to preload the moving mass against the stack (see Figure 3). When coupled with the controller and its I/O, the capacitance gage, and the high voltage amplifier, the FTS is capable of closed-loop positioning in increments of approximately 13 nm. The FTS was mounted to the tool post on the DTM's X-axis carriage.

The workpiece was mounted to the spindle on the DTM's Z-axis carriage. To adapt the annular mirror/mirror mount assemblies to vacuum chuck mounting, each assembly was bolted to a mounting

plate which was then vacuum-mounted to the vacuum chuck. The mirrors required centering for radial alignment and, because of the lack of rotational symmetry, also required angular alignment. This angular alignment involved the registration of a fiducial (on the mirror) with the diamond tool while the spindle was rotated such that the rotary encoder's index pulse was triggered. The specified angular alignment of the optical surface with the fiducial was +/- 0.08 radians.

The spindle speed was 200 rpm, clockwise for the left-hand mirror, counterclockwise for the right-hand mirror. With the spindle rotating counterclockwise, the tool was centered via iterative machining and interferometric analysis of a spherical test plug [4,5]. Because of the low spindle speed, shifting of the spindle centerline (due to reversing the spindle's direction of rotation) was assumed to be small and therefore the tool was not re-centered when the spindle's direction of rotation was reversed.

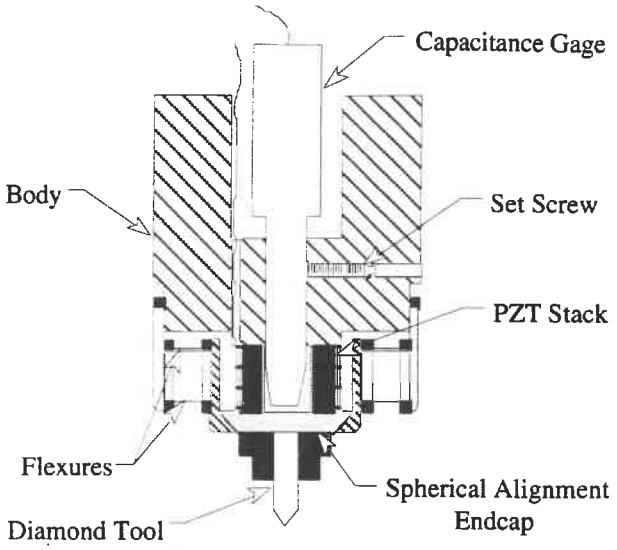

Figure 3: Fast Tool Servo (section view, no scale).

Each surface was separated into a symmetric component to be provided by the X and Z axes of the DTM and an asymmetric component to be produced by the FTS (Figures 4a and 4b). The DTM axes were programmed to sweep out the last term in Equation (1), a parabola with a vertex radius of 3 m. Because of the small radius (1.5 mm) of the tool, the large vertex radius of the parabola, and the small angle through which the tool was swept, no tool geometry corrections were required.

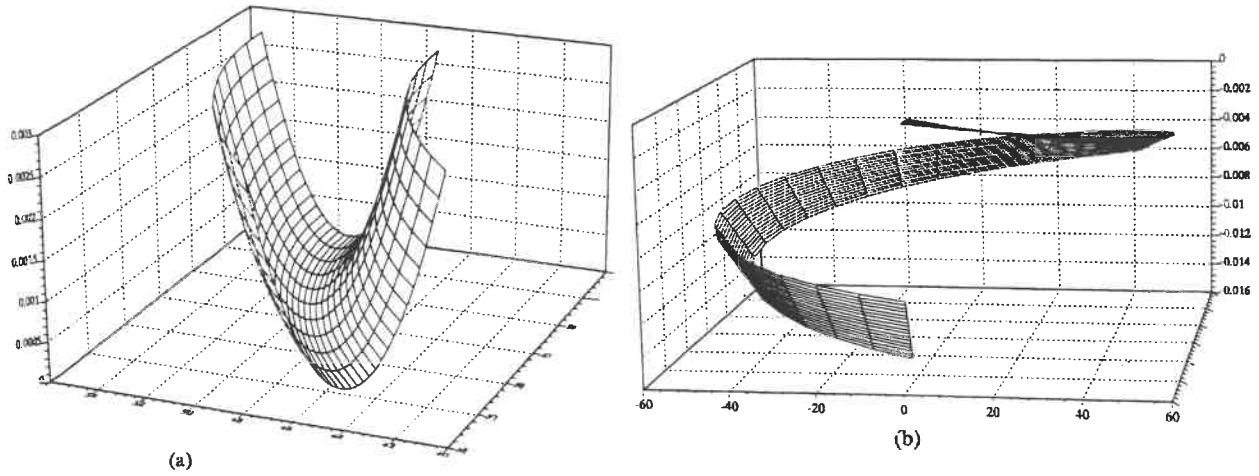

Figure 4: (a) Section of Symmetric Component of Surface; (b) Asymmetric Component of Surface.

The FTS commands were generated "on-the-fly" by computing the value of the first two terms in Equation (1). The resulting positions form a gradual spiral down into the surface of the workpiece

(i.e., the tool is extended) until θ=0, the point at which the tool is rapidly withdrawn. Because of the dynamics associated with this step and the anticipated degradation of the surface finish, a noncritical zone of +/- 0.08 radians was specified around the step transition at θ=0.

Initially, the FTS position change at θ=0 was commanded as a single step with a limit on the maximum voltage increment per controller cycle to protect the amplifier and piezoelectric stack. The first machined mirror surface exhibited considerable surface roughness after the transition, even beyond the noncritical zone. Examination of the laser interferometer and capacitance gage data revealed no obvious periodicities. However, spectrum analysis data from an accelerometer mounted on the rear of the FTS revealed a large peak at 450 Hz, which is approximately the torsional natural frequency of the tool post. To minimize the excitation of the tool post by the FTS motion, a two-step digital control algorithm was implemented. This algorithm employs two separate output steps per feedback sample to control the motion of an underdamped second order system in response to a step input. The first step reduces the following error and the second step negates the oscillatory behavior created by the first step [6]. The amplitude and timing of the two steps are based on the damping and natural frequency of the system.

RESULTS

Surface finish measurements on the final mirror surfaces were performed using a Zygo Maxim 3D Laser Interferometric Microscope. The measurements showed that the 300 nm PV surface roughness requirement was met except in the region several degrees past the noncritical zone (after the θ=0 transition) where the dynamics had not sufficiently decayed and the PV surface roughness was approximately 400 nm. The form accuracy of the mirrors allowed the client to build a resonator that provided the high efficiency (>10%) and high beam quality necessary for successful operation [1].

REFERENCES

[1] "Stable-Unstable Resonators for Annular Gain Media", personal communication with Hans-J. Meister, Rocky Mountain Instrument, GmbH, April 20, 1994.

[2] Allen, W. D., K. P. Garrard, L. W. Taylor, and R. J. Fornaro, "H^2ART Multiprocessor Control for a Diamond Turning Machine", *Precision Engineering Center Annual Report*, North Carolina State University, 1992, Volume X.

[3] Falter, P. J., "Diamond Turning of Nonrotationally Symmetric Surfaces", PhD. Dissertation, North Carolina State University, 1990.

[4] Rasnick, W. H. and R. C. Yoder, "Diamond-Turning Tool Setting by Interferogram Analysis", Department of Energy, Oak Ridge Y-12 Plant, October, 1980.

[5] Gerchman, M. C., "Optical Tolerancing for Diamond Turning Ogive Error", Reflective Optics II, *Proceedings of SPIE Conference*, 1989, Volume 1113.

[6] Bifano, T. G. and T. A. Dow, "Application of a Novel Two Step Digital Control Algorithm for Precision Actuation", *Precision Engineering Center Annual Report*, North Carolina State University, 1984, Volume II.

DESIGN OF NANOMETRIC CUTTING INSTRUMENT

S.BALASUBRAMANIAM, Dr. R. J. HOCKEN AND Dr. DON A. LUCCA*
Department of Mechanical Engineering and Engineering science
Precision Engineering Group
University of North Carolina at Charlotte

*Department of Mechanical Engineering
OKLAHOMA STATE UNIVERSITY

Introduction

There is an ever increasing interest in the ability to manufacture to dimensional accuracies in the nanometer range and to attain surfaces with atomic level smoothness, free of residual stresses and metallurgical defects. To achieve this, it is necessary to understand the mechanics governing ultra-precision machining. Single point diamond turning has been extensively developed to achieve sub-micrometer accuracies and to investigate the sub-micrometer depths of cut, but process mechanics at the nanometer scale are difficult to study with commercially available diamond turning machines. A specialized instrument is being built for this purpose.

The instrument is basically a single point diamond "planer". The instrument uses a piezo-electric tube for positioning. The instrument is designed to have sample access and replacement, optical and visual access to cutting zone, depth of cut control, feed control, coarse positioning, cutting and thrust force measurement and vacuum compatibility. The instrument is designed to have a cutting range of approximately ±5 μm with a depth of cut variation of 2.5 μm to 1 nm. Initially a cutting speed of 0.3 m/min will be used.

Design

Force Tripod

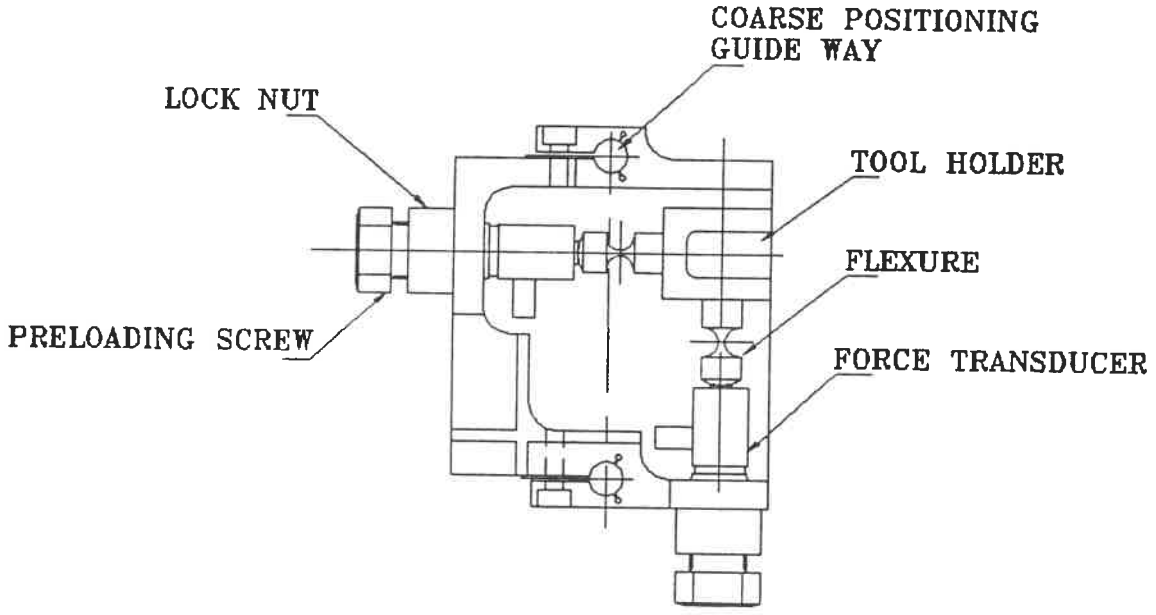

Fig 1. Force Tripod

The instrument has two modules, the force tripod and the horizontal slide. The force tripod is shown in Fig. 1. The force tripod houses the tool and the force transducers. The tool is mounted in the tool holder with its face in the vertical plane. This orientation will allow the cutting mechanics to be observed from the top. The tool holder is held in place by dual axis flexures. Extrapolation from the previous experimental data indicates that the cutting force and the thrust force are approximately 0.08 N/mm and 0.06 N/mm at a depth of cut of 1 nanometer[1]. To measure this force, two single component force transducers with a range of 0.49 mN to 21.5 N and a resolution of 0.22 mN are used. The force transducers are purchased from PCB Piezotronics. One of the force transducer is oriented along the direction of depth of cut and the other along the direction of feed motion. The two transducers are preloaded against the tool holder with a two axis flexure between them. The dual axis flexure is designed to have an axial stiffness of 60 MN/m, which is greater than the stiffness of the piezo-electric tube. The dual axis flexure is used to decouple the cutting and the thrust force measurement. A hysteritic drive is used to coarse position the force tripod in the vertical direction. The drive can be decoupled after positioning the force tripod by taking it out of the structural loop.

Horizontal Slide

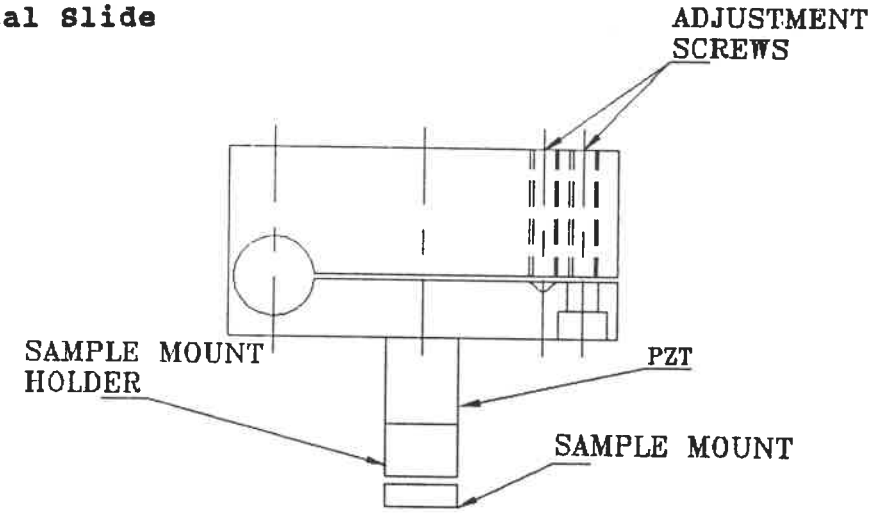

Fig 2. Horizontal Slide - Single Axis Flexure

The horizontal slide is essentially a single axis flexure housing a piezo-electric tube. The sample is glued to the sample mount, which is mounted kinematically on the piezo-electric tube. A Maxwell (three V grove) coupling designed to have a stiffness of 7.5 MN/m is used to mount the sample mount to the piezo-electric tube. The sample mount is made of Macor in order to reduce the mass on the piezo electric tube. The piezo electric tube with the sample mount is estimated to have a resonance frequency of 10 KHz, which is much higher than the driving frequency. The desired depth

of cut is obtained by moving the sample towards the tool. This is achieved by controlling the voltage applied to the center electrode of the piezo-electric tube. The feed motion is achieved by controlling the voltages applied to the two outer, opposite electrodes of the piezo-electric tube. The PZT is driven using the circuits designed for the UNCC's near-field scanning microscopy project[2]. The depth of cut is monitored by a LVDT placed inside the piezo electric tube. The sample mounted on the PZT is made perpendicular to the tool by adjusting the horizontal slide - single axis flexure. The horizontal slide also has a coarse positioning system.

Structure

A box type structure houses the force tripod and the horizontal slide. All the components in the instrument are designed to be flat there-by reducing the height of the instrument. The height of the instrument is 60 mm and can be conveniently placed under a high power optical microscope. Figure 3 shows the force tripod and horizontal slide assembled in the structure.

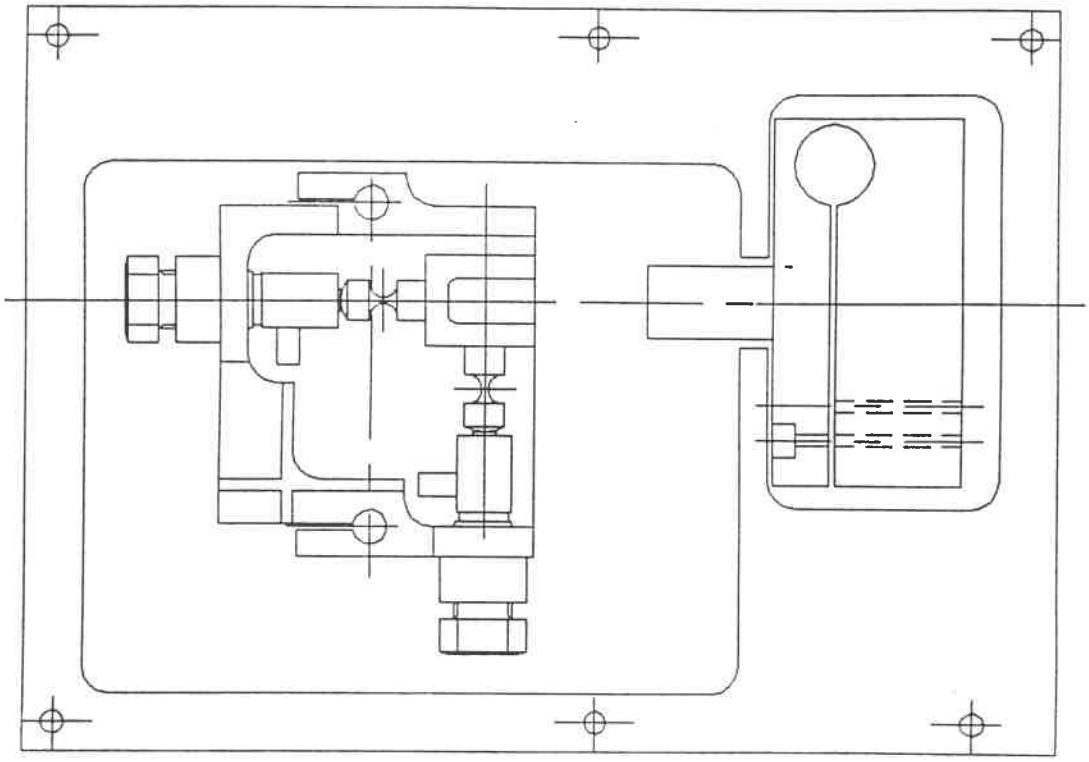

Fig 3. Force Tripod and Horizontal Slide assembled in structure

The coarse positioning of the sample will be done with the aid of a calibrated eyepiece. Fine positioning and depth of cut will be set using the PZT. Initial experiments will be performed with a high-powered optical microscope.The mechanics of cutting can be observed by focusing on the stationary tool. Based on the outcome of this experiment the design will be revised, if necessary.

Work in Progress

Based on the above design a prototype is being built. The force tripod has been manufactured and assembled. It has to be tested and calibrated. The LVDT calibration is being done. For calibration purpose the LVDT is mounted in the similar way as it will be mounted in the instrument. A modified plain mirror interferometer is being used to calibrate the LVDT. This calibration set up will also be used to determine the electrical interference between the LVDT and PZT. The horizontal slide is also manufactured. The instrument structure will be manufactured after the LVDT calibration. Finally the instrument will be interfaced to a computer.

References

1. Dr. D.A.Lucca, Y.W.Seo, "Effect of tool edge geometry on energy dissipation in ultraprecision machining, Annals of CIRP Vol. 42/1/1993.
2. Boudreau,B.D., et al., "A near-field scanning infrared microscope", Proc. of 1992 NSF design and mfg. sys grantees conf., The Georgia Institute of Tech.

Application of Electrorheological Fluid for the Improvement of Dynamic Characteristics of Machine Tool Table Systems

(Basic Analysis of the Dynamic Characteristics of Table Systems)

Makoto ISHIYAMA*, Tojiro AOYAMA* and Kazuya EDAMURA**

* Department of Mechanical Engineering, Keio University
3-14-1, Hiyoshi, Kouhoku-ku, Yokohama, 223, JAPAN
** Fujikura Kasei Co., Ltd.
2-6-15, Shibakoen, Minato-ku, Tokyo, 105, JAPAN

1. Introduction

Sliding guideways have been conventionally employed by machine tool table systems because of their high damping ability. The sliding guideways, however, have some demerits such as high temperature rise during high speed feeding and the occurrence of stick-slip motion during positioning operations. These problems are due to the high frictional resistance of sliding guideways, and they can be solved by employing rolling guideways instead of sliding guideways. Practically, the rolling guideways have been widely applied to the machine tool table systems. A weak point of rolling-guided tables is their low damping ability which causes the chatter vibration during machining, and it results in the decrease of machining accuracy and productivity of machine tools[1]. One of the effective method to improve the damping ability of rolling-guided tables is to apply an additional damping force to the tables when it is required[2].

In order to improve the damping ability of the rolling-guided tables, a new variable damping mechanism is proposed. The additional damping force should be controllable in response to the mode of table operations. The high damping force is required during cutting operation while it becomes a nuisance in the high speed feeding operation. In this research, an ER(electrorheological) fluid is applied to the proposed mechanism in order to control the additional damping force.

2. Structure of proposed damping mechanism

The structure of the proposed damping mechanism is illustrated in Fig.1. The mechanism is a kind of the fluid film damper which consists of a moving plate inserted in a slot filled with an ER fluid. The effective viscous damping force is obtained when the inserted plate moves along the slot. The magnitude of the damping force depends on the viscosity of the ER fluid. The ER fluid is a colloidal suspensions whose apparent viscosity strongly depends on an applied electric field. It may be, therefore, possible to control the damping force by charging the electric field between the inside faces of slot and the moving plate.

When ER fluid is exposed to an electric field, it quickly responds by forming fibrous structures parallel to the applied electric field as shown in Fig.2. Since an additional force is necessary to shear these fibrous structures of ER fluid between the electrodes, the apparent viscosity of the fluid effectively increases[3], [4]. The ER fluid used in this research is a mixture of 80wt.% nonconductive silicone oil and 20wt.% inorganic/organic composite ER particles. The ER particles consist of spherical cores of organic polymers covered with electrorheological inorganic substances, and their diameter is about 15μm. There is no fear of electrodes being eroded by the ER particles because of their soft cores of polymer, and their low specific gravity may suppress sedimentation. This ER fluid

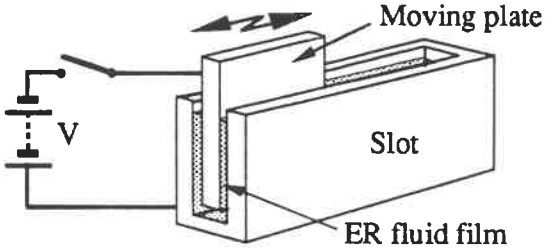

Fig.1 Structure of ER fluid film damper.

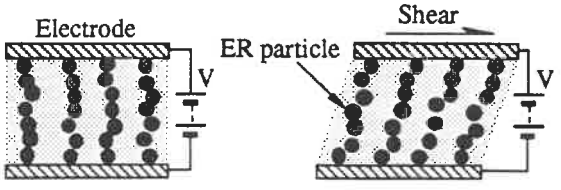

Fig.2 Mechanism of the ER effect.

works on a low current, because the particles display a high electric resistance[5]. The apparent viscosity of the ER fluid remarkably increases as the electric field intensity increases. Fig.3 shows the relationship between the shear rate and the shear stress under different electric fields.

The damping characteristics of the rolling-guided table system can be controlled by changing the viscous friction of proposed ER fluid film damper attached to the table system. A high damping ability is required to the table systems during machining and positioning operations. In this case, the additional damping force(i.e., the additional viscous friction) is generated by charging an electric field to the ER fluid filled in the slot of fluid film damper. On the other hand, the low frictional resistance is desirable during high speed feeding operation, and the additional damping force is unnecessary. In this case, the additional damping force is rapidly reduced to a minimum by switching off the electric field.

3. Evaluation of the performances of the ER fluid film damper

3-1. Experimental devices and evaluation method

In order to evaluate the fundamental performances of the proposed ER fluid film damper, a simple testing stand of a rolling-guided table is prepared, and the ER fluid film damper is installed to it. The structure of the testing stand is illustrated in Fig.4. The testing table is supported by a piece of linear bearing element. The moving plate, which is a part of the ER fluid film damper, is fixed to the table, while the slot filled with the ER fluid is equipped parallel to the direction of the table feed. The gap between the moving plate and the inside faces of slot is adjustable. The cartesian coordinate system (X, Y and Z) is defined as indicated in Fig.4.

The effects of the proposed ER fluid film damper on the dynamic performances of the testing table are evaluated by means of the impulse force response method. The experimental setup for the measurements of the dynamic compliance is explained in Fig.5. The table is connected to the base plate by a plate spring instead of a ball screw in order to give the stiffness in the direction X.

3-2. Experimental results

The results of the impulse force response tests are summarized in Fig.6. The ER fluid used in this experiment is produced by mixing 20wt.% ER particles into 10cSt silicone oil. The dynamic compliances in direction X, Y and Z are shown in Fig.6(a), (b) and (c) respectively. The peak values of the dynamic compliance decrease with the increase

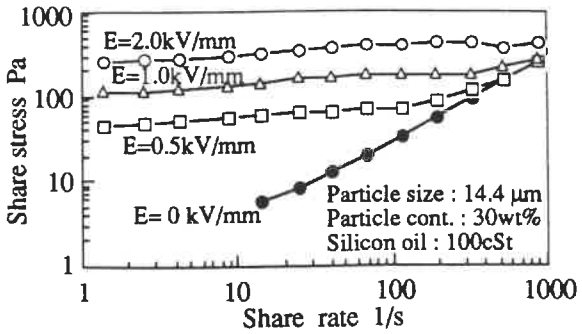

Fig.3 Increase in apparent viscosity of the ER fluid.

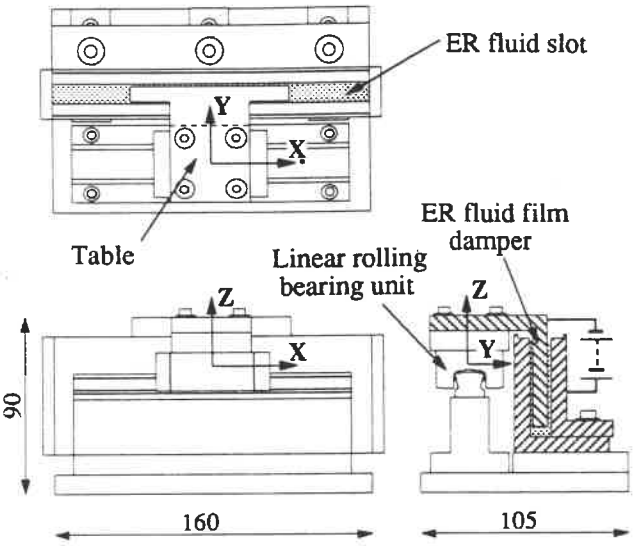

Fig.4 The testing stand of rolling-guided table with the ER fluid film damper.

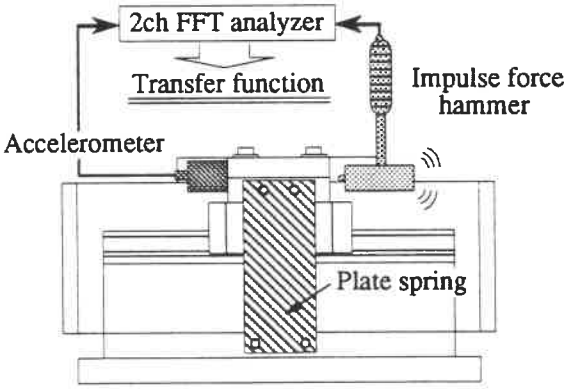

Fig.5 Experimental setup.

of applied electric field. The effects of the proposed ER fluid damper are obtained not only in the direction X but also in the direction Y and Z. For example, the peak value of the dynamic compliance in the direction X decreases to about 50% by

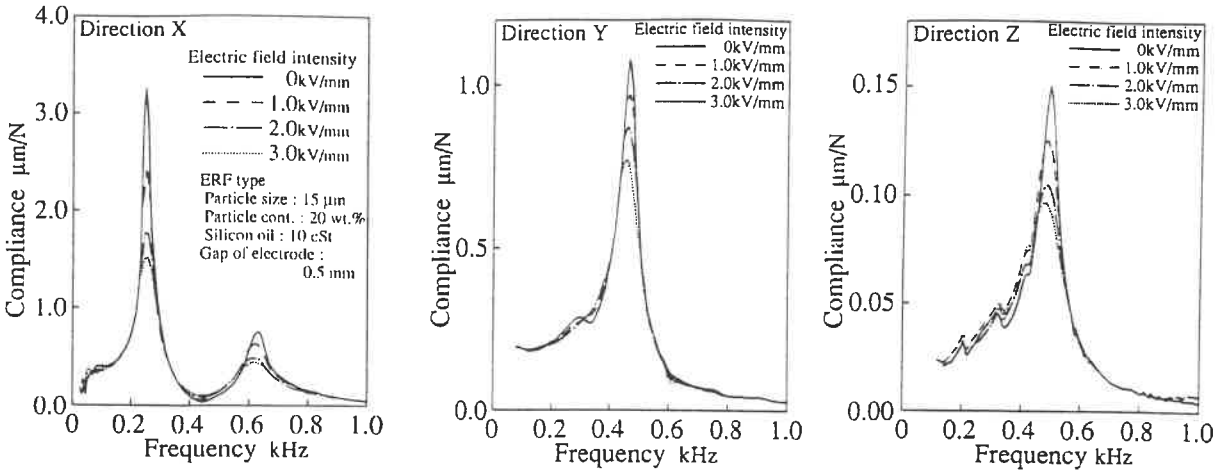

(a) Direction X (b) Direction Y (c) Direction Z

Fig.6 The results of the impulse forece response tests.

charging the electric field up to 3.0kV/mm. The dynamic stiffness of the testing table is successfully increased in proportion to the applied electric field intensity. Therefore, the damping ability of testing table is considerably improved in all directions. These results suggest that the proposed ER fluid film damper is effective to control the dynamic performance of the rolling-guided table systems.

The effect of the basis oil viscosity on the dynamic characteristics of the testing table is shown in Fig.7. It is confirmed from the results that the characteristics of the ER fluid film damper is significantly influenced by the basis viscosity of the ER fluid. The higher damping force can be obtained by employing the basis oil with higher viscosity. However, the controllable range of dynamic compliance also decreases by increasing the viscosity of basis oil. The relatively high viscous friction may still remains irrespective of the ER effects. In order to change the viscous friction adapting the mode of table operation, it is suitable to chose the low viscosity oil which gives the wide controllable range of apparent viscosity (i.e., the wide range of dynamic compliance).

In order to evaluate the response time of the ER fluid film damper, a step response test is carried out in the following manner. The testing table is forced to vibrate in the direction X at the resonance frequency by the electro-dynamic exciter. The dynamic displacement in the direction X was measured by the eddy current type displacement sensors. Fig.8 shows the response of the table displacement in the direction X. An electric field of magnitude 4.0kV/mm is suddenly applied at time=0ms. The amplitude of the table vibration

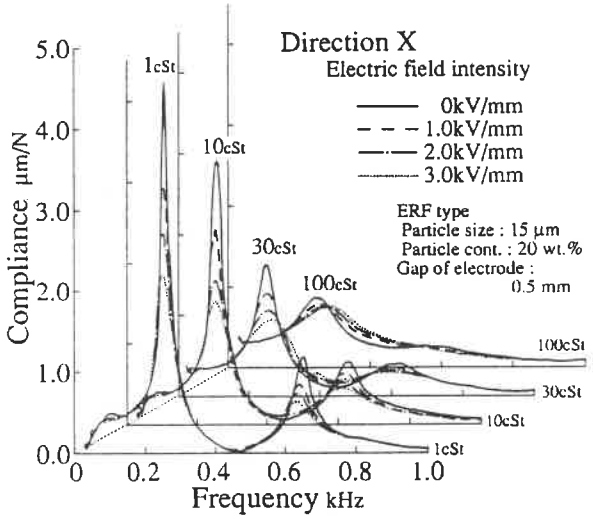

Fig.7 Effect of basis oil viscosity on dynamic characteristics.

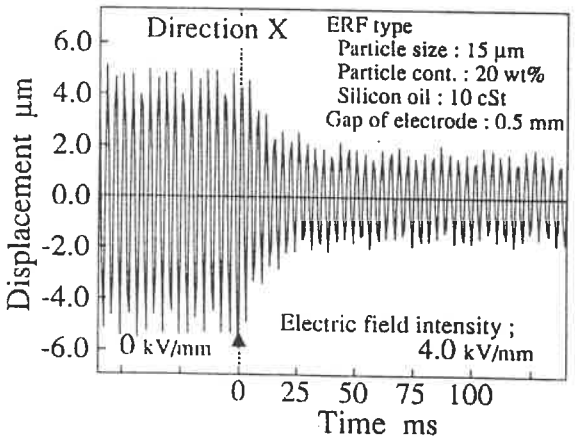

Fig.8 Response of the ER fluid film damper.

decreases in response to the charged electric field. It is estimated from the result that the rise time(from 10% to 90%) of the ER fluid film damper is less than 30ms, which will be enough short for practical applications.

3-3. Evaluation with the improved testing table

All of the above results indicate that the proposed ER fluid film damper is effective to improve the dynamic performances of machine tool table systems. However, a special attention should be paid to the dynamic stiffness of the testing table before installing the ER fluid film damper. The commercially available table systems most likely have much higher dynamic stiffness than the testing table, especially in the direction X. This difference is due to the plate spring used instead of the ball screw for the testing table system. In order to evaluate the effect of ER fluid film damper under practical condition, the testing stand is improved so that the higher stiffness in the direction X is obtained. The structure of the improved testing stand is illustrated in Fig.9. Improvements are made on the following points : (i) the table is supported by two pieces of linear bearing elements; (ii) the higher stiffness in the direction X is attained by replacing the plate spring with a ball screw of 4mm in the diameter; and (iii) the additional damping force is increased by two sets of the ER fluid film damper.

The experiments were carried out in the same manner. The results of the impulse force response tests in the direction X is shown in Fig.10. The peak compliance value of the improved testing table under no ER effect is decreased to about 30% of that of the previous testing table (Fig.6(a)). The peak compliance values decrease in response to the increase of applied electric field. The same results are also obtained for the direction Y and Z. The dynamic performances of the testing table are successfully improved.

4. Conclusion

In order to improve the dynamic performance of the rolling-guided tables for machine tools, a new variable damping mechanism was developed by applying the ER fluid to the fluid film damper. In the proposed system, the damping force is controllable by adjusting the electric field charged to the ER fluid film. A testing table with the ER fluid film damper was prepared and the effects of the ER damper were evaluated by means of the impulse force response method. The results show that the proposed damper is effective to improve the dynamic characteristics of rolling-guided table systems.

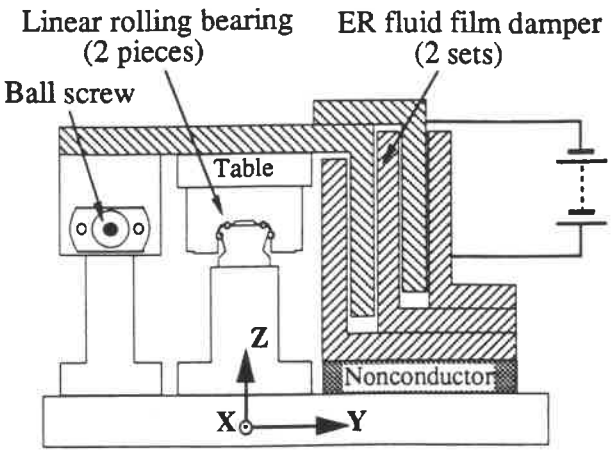

Fig.9 The improved testing stand.

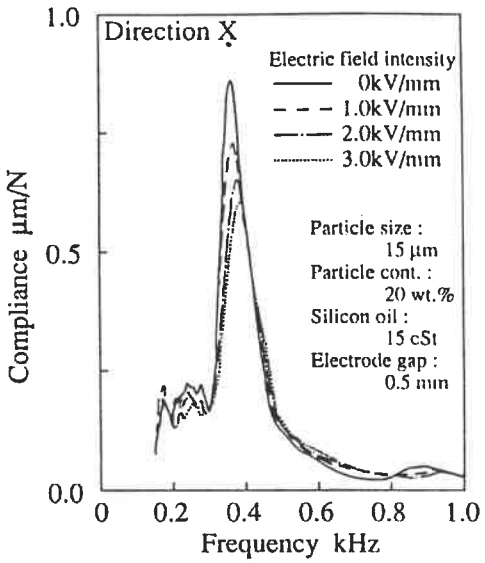

Fig.10 Dynamic compliance of the improved table.

References

1. T. Itoh, T. Aoyama and I.Inasaki, Dynamic Characteristics of Machine-Tool Tables, Proceedings of the KSME/JSME Vibration Conferenc, (1987), P.138.
2. T.Aoyama and I.Inasaki, Developement of Hybrid Table System (Rolling Guideway with Variable Frictional Force), Trans. of NAMRI/SME, (1990), P.334.
3. Thomas C. Halsey, Electrorheological Fluids, Science, Vol.258, (1992), P761.
4. D.J.Klingenberg and C.F.Zukoshi IV, Studies on the Steady-Shear Behavior of Electrorheological Suspensions, Langmuir, Vol.6, (1990), P.15.
5. Fujikura Kasei Co., Ltd., New Electro-Rheological Fluid Technology, JETRO, December, (1993), P16.

CERAMIC MACHINE TOOL AXIS WITH SELF-COMPENSATED, WATER-HYDROSTATIC, LINEAR BEARINGS

ALEXANDER SLOCUM, PAUL SCAGNETTI, NATHAN KANE
PRECISION ENGINEERING RESEARCH GROUP
DEPARTMENT OF MECHANICAL ENGINEERING
MASSACHUSETTS INSTITUTE OF TECHNOLOGY

Conventional machine tools lack the stiffness, damping, and durability required for machining ceramics. They have less than half the lifetime of a similar machine used to machine metals because their performance degrades quickly due to sub-micron ceramic particles which permeate the manufacturing environment. Consequently, next generation machines for grinding of ceramic materials will require improvements in structural components, actuators, and bearings as well as a means to address the inability of seals to effectively prevent rapid wear of the machine components.

Accordingly, this paper investigates a new design theory and methodology (DTM) for the development of machines for precision finishing of ceramic components. The new DTM is discussed in the context of the design of a new machine tool axis prototype. The prototype brings together two new precision machine tool design strategies: (1) self-compensated, water-hydrostatic bearings, and (2) ceramic structural materials. In the future, the prototype will be able to incorporate (1) replicated internal shear dampers and (2) integral structural cooling passages. These innovations will result in increased bearing and structural stiffness, improved the vibration damping, reduced thermal errors, and increased durability towards ceramic dust.

Hydrostatic bearings form the centerpiece of the design approach because generally they provide a superior stiffness, and damping, and the positive outflow of fluid will keep them clean. The principle drawbacks of conventional hydrostatic bearings are the ergonomic problems associated with oil as a working fluid, tuning the restrictors, and prevention of restrictor clogging. Although there have been many self-compensated, hydrostatic bearing designs in the past, the approach taken here allows for water to be used without fear of long-term degradation due to deposits or bacteria growth. The new bearing pad design[1], uses an environmentally friendly fluid (water), requires no hand-tuning of restrictors, and is insensitive to manufacturing errors. In addition, the smallest passage is typically 3-5 mm in diameter which eliminates clogging of the hydrostatic passages.

Historically, wood machines wore quickly when used to machine cast iron, whereas cast iron machines lasted for a long time when machining iron. Similarly, to address the issue of erosive wear of components, ceramic materials will be used in the structure. To address the issues of low material damping in ceramics, replicated internal shear dampers will be placed inside hollow cell ceramic structural beams. The shear dampers will be made from hollow tubes which will then serve as heat exchanger pipes, so a more uniform temperature can be maintained in the machine.

[1] United States Patent # 5,104,237, Alexander Slocum.

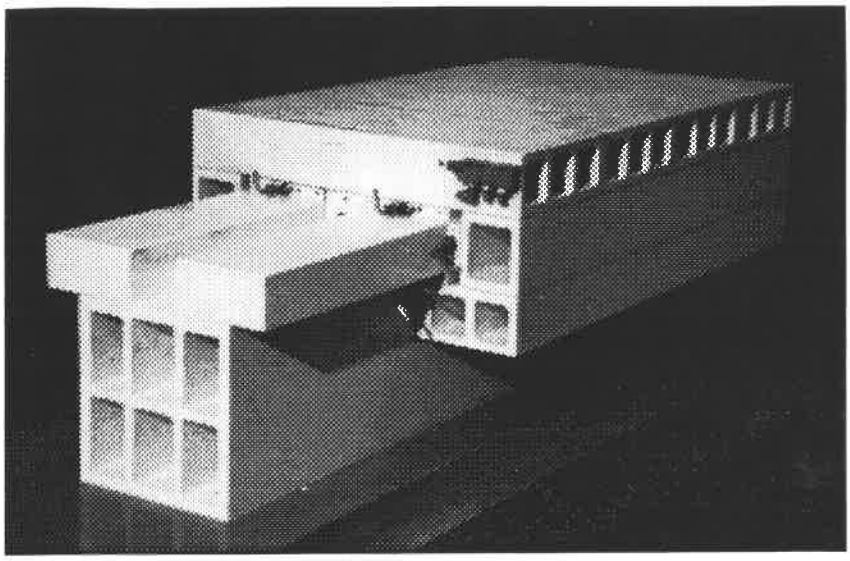

Figure 1: Photograph of the prototype ceramic machine tool axis[2]. The axis was mounted to an isolated granite table for measurement purposes. Hydraulic supply lines are not shown in this photograph.

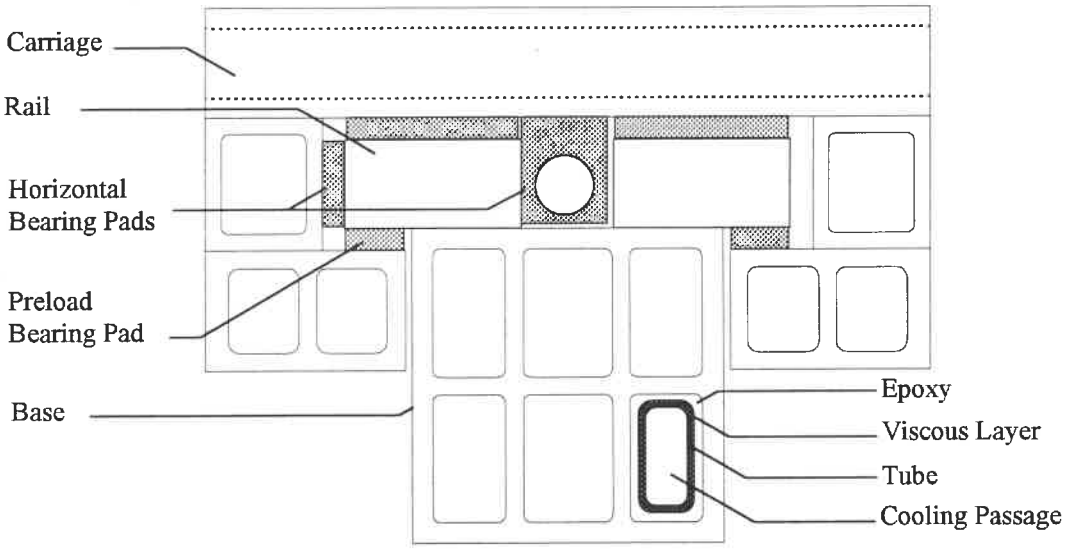

Figure 2: Diagram of the prototype machine tool axis. The gray areas indicate the location of bearing pads. All components were constructed of 96% alumina. The design of the replicated internal damping tubes and cooling passages (as shown in the bottom right core of the base) could be applied to each core in the structure and the carriage[3].

[2] Assembled at M.I.T. from alumina components built by Wilbanks International, Hillsboro, OR. Design assistance provided by Reg Maas, Wilbanks International. Hydrostatic bearing pads replicated into assembly by Drew Devitt, Devitt Machinery, Ashton, PA.

[3] See A. Slocum, E. Marsh, and D. Smith, "A New Damper Design for Machine Tool Structures: the Replicated Internal Vicous Damper", Precision Engineering, vol. 16, no. 3, June, 1994, p. 174-183.

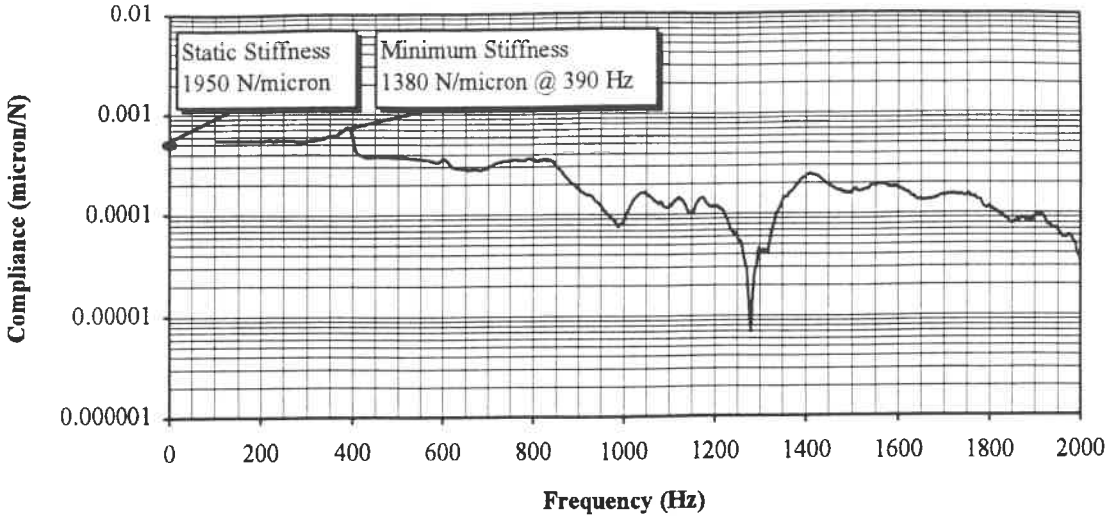

Figure 3: Plot of dynamic compliance as a function of frequency for the prototype ceramic machine tool axis system.

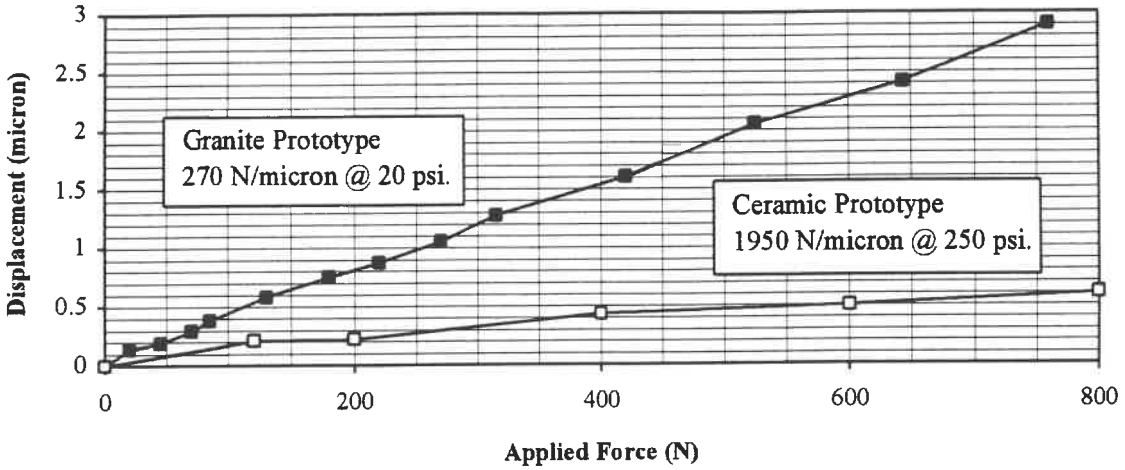

Figure 4: Plot of force versus displacement[4] for the granite[5] and ceramic prototypes. The static stiffness can be estimated by using a best fit line on the data. The spreadsheets used to design the ceramic machine tool axis prototype predicted 2000 N/μm.

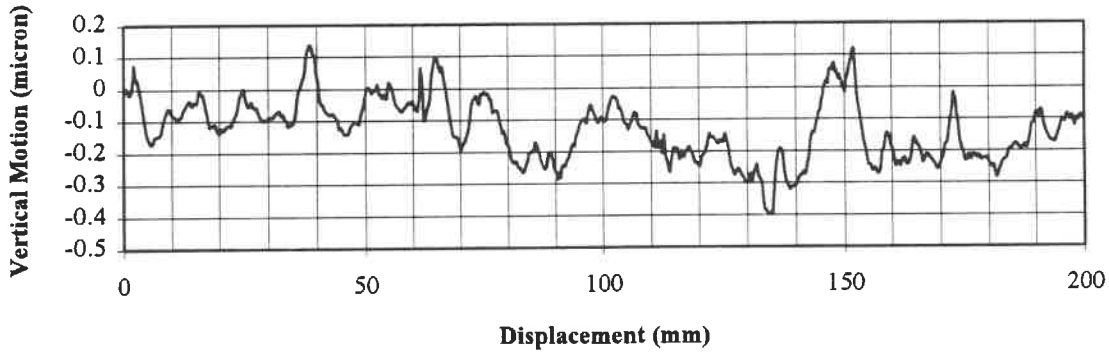

Figure 5: Plot of vertical straightness of the axis over 200mm travel[5]. The overall vertical motion is approximately .55microns. The data is characteristic of straightness measurements over the entire length.

[4] Displacement measured with 3910 capacitance probe system from A.D.E. Corporation, Newton, MA, Technical assistance provided by Michael Bahtiarian of A.D.E..

[5] Measurement performed with a ZMI1000 laser interferomter system from Zygo Corporation Middlefeld, CT., Technical assistance provided by Ned Bennett.

The design of the prototype system can be divided into three smaller sub-projects. First, the bearing pads design is analyzed using the governing fluid circuit equations. Spreadsheets, based upon these deterministic equations, are the primary design tool for bearing pad design. Second, the structure of the axis must be designed in order to support the bearing pads with respect to the rail even when the bearing pressure is high. The main design issues are the elasticity of the structure and the required tolerances. Third, the pressure supply system, must supply high pressure bearing fluid without adding pressure induced vibrations into the system.

Although the supply system can be designed almost independently, the structural and bearing pad designs are strongly coupled. The main performance goals of the overall design are high stiffness, high damping, low straightness error, low noise level, and thermal stability. Table 1 is a summary of the main performance goals and the design issues which they depend upon.

Table 1: List of bearing characteristics and the related design decisions.

Characteristic	Typical Value	Related Design Issues
Stiffness	2000 N/μm	• Bearing pad geometry • Bearing gap • Pressure supply system
Damping	$\zeta = .5$	• Bearing pad geometry • Bearing gap
Straightness	Total Vertical Motion (Δz) = .5μm over 100mm of axial travel	• Rail straightness • Bearing pad geometry • System geometry
Noise Level	$\Delta z = .05$ μm	• Pressure supply system • Bearing pad geometry
Thermal Stability		• Structural material • Pressure supply system

In designing the bearing pads, there is a trade-off between "designing for stiffness and damping" and "designing for low noise levels". In order to design a bearing for high stiffness and damping, increasing the pressure supply and bearing pad area, and decreasing the nominal gap are effective choices. However, these choices make a bearing which is more sensitive to pressure supply noise. Fortunately, the issue of noise can be precluded by properly designing the fluid supply circuit with accumulators[6].

Measurements of the prototype's stiffness indicate an order of magnitude improvement in stiffness compared with the previous prototype[7]. Figures 3, 4, and 5 show the frequency response, static stiffness, and straightness of the prototype respectively. The improvements in stiffness are mainly due to the ability of the prototype to withstand higher supply pressures. The improved damping is a result of the new design of the bearing pads.

---

[6] See P. Scagnetti, A. Slcoum, N. Kane, "Low Noise Fluid Circuit Design for Hydrostatic Bearings", Proceedings of the American Society for Precision Engineering 1994 Annual Conference.

[7] The previous prototype was constructed of granite with stainless steel bearing pads. See A. Slocum, P. Scagnetti, N. Kane, C.Brunner, "Design of Self-Compensated, Water-Hydrostatic Bearings", to be published, Precision Engineering.

Two-axis Force Sensing Surgery Knife to obtain Dynamic Information

Masayuki Nakao, Ikuko Eguchi
and Yotaro Hatamura
Department of Engineering Synthesis,
the University of Tokyo
Hongo 7-3-1,Bunkyo-Ku, Tokyo, Japan

1. Introduction

During the past several years, endoscopic surgery has largely replaced conventional open surgery for removal of the gallbladder, and has begun to find applications in other procedures as well. However, endoscopic surgery has two problems. First, dexterity and force feedback of endoscopic surgery instruments are quite poor compared with those of open surgery instruments. This is attributed to the reason as follows: Surgeon's hand is far from the surgical site with long grip tools and the depthless video image scarcely supplies a surgeon with 3-dimensional information. Secondly, micro operating for a long time with the awkward tools exhausts the surgeon seriously. Endoscopic surgery commonly constitutes up to three hours after routine surgical procedures for several hours. For solution of these problem, endoscopic surgery needs some robotic applications.

Dynamic information of surgery is indispensable to design these applications. However, there are few researches on dynamic information analysis in open surgery, still less in endoscopic surgery, because kinetic sensation, such as hard, soft, elastic, sticky, etc., is more important for surgeons than dynamic information, such as force, displacement, velocity, etc..

As a first step of this analysis, the authors quantified the cutting force of open surgery. This paper introduces a novel "Two-axis Force Sensing Surgery Knife (Force Sensing Knife)," developed to quantify the cutting operation.

2. Function of Force Sensing Knife

In surgery operation, a surgeon cuts with a surgical knife as shown in Fig.1-(a). Force sensing needs two-axis, because the knife has two degrees of freedom in cutting movement. The cutting force requires two coordinates: one is on cutting object to evaluate mechanical property of it(object coordinate), another is on the knife to evaluate the surgeon's kinetic sensation(knife coordinate).Here the axes of these coordinates and the cutting force in each axis are determined as shown in Fig.1-(b). Now the surface of the cutting object is assumed to be a horizontal plane.

Knife coordinate can convert into object coordinate by grip inclination(in Fig.1-(b)). However, grip inclination changes every moment as a surgeon cuts with his or her wrist turning. Therefore, measurement of ever-changing grip inclination is necessary for transformation of two coordinates.

The cutting force and the force of inertia by wrist turning and hand trembling are measured as one at the same time. Measurement of inertia is also necessary for cancel this influence from force outputs.

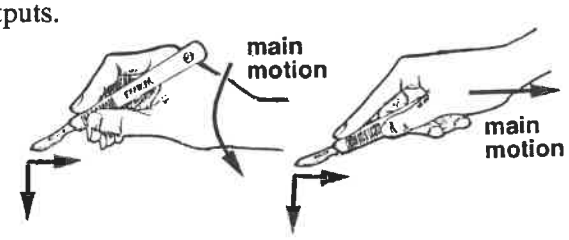

(a) The way of holding a surgery knife and cutting motion

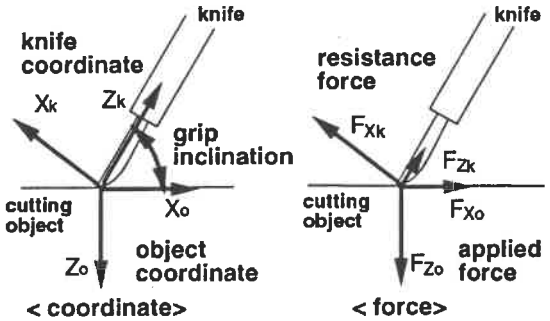

(b) Axis and force in two coordinate and grip inclination

Fig.1 Schematic of cutting operation in surgery

As mentioned above, Force Sensing Knife requires functions as follows: (i) two-axis force measuring, (ii) grip inclination measuring, (iii) two -axis inertia measuring.

3. Mechanism and structural elements of detectors

For realization of functions, Force Sensing Knife has X_k (represented in Fig.1-b) and Z_k-axis force sensors and X_k and Z_k-axis accelerometers. Each force sensor has a parallel plate structure that have a couple of thin plates. Each accelerometer has a one thin plate structure with a mass on its top. Four strain gauges are glued on the roots of thin plates, and amplify the deformation of plates caused by the cutting force and acceleration. These accelerometers also have a role of clinometer to measure the grip inclination.

4. Structure of Force Sensing Knife

We synthesized these elements as Force Sensing Knife in Photo.1. This sensing knife has a disposable blade made of stainless steel on its top and a removable sensor cover made of aluminium anodized alloy. Fig.2 illustrates the structure of Force Sensing Knife in section. The cutting force transmits in order: surgeon's hand → sensor cover → sensor block → blade → cutting object. Force Sensing Knife weighs 46g, about twice of an actual surgical knife.

5. Evaluation of Force Sensing Knife

5-1 Evaluation of sensors

5-1-1 Force sensors

The relation between two-axis forces and sensor outputs were measured by loading on the top of the blade as shown in Fig.3. From this figure, these force sensors have small interference from the other axis force and good linearity within 2%.

5-1-2 Accelerometers

For measurement of the relation between acceleration of gravity and accelerometer outputs, grip inclination was changed as shown in Fig.4. From this figure, these accelerometers have good linearity within 5%.

5-2 Measurement of wrist turning

Wrist turning is detected as grip inclination changing. Fig.5 shows the relation between grip

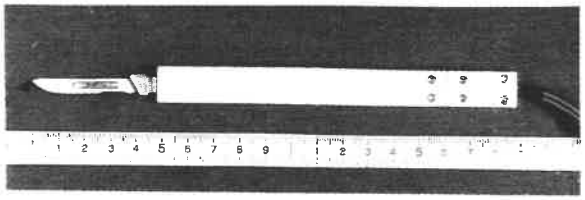

Photo.1 appearance of Force Sensing Knife

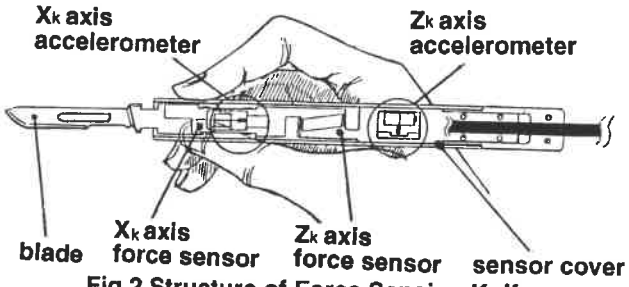

Fig.2 Structure of Force Sensing Knife

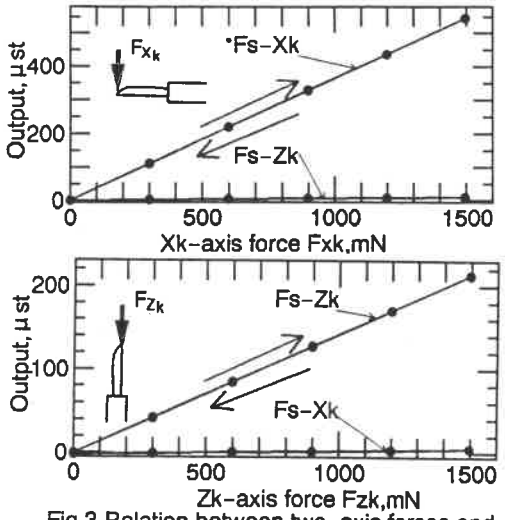

Fig.3 Relation between two-axis forces and outputs of force sensors(Fs-Xk,Fs-Zk)

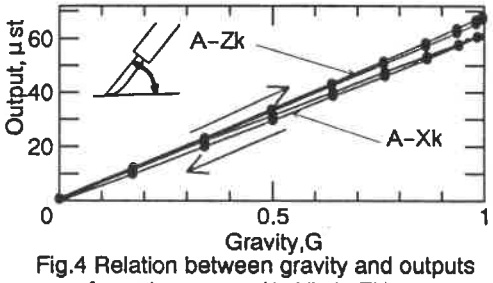

Fig.4 Relation between gravity and outputs of accelerometers(A-Xk,A-Zk)

inclination and outputs of sensors. On the basis of the result in Fig.5, grip inclination and the influence of grip inclination in force sensors are detected from outputs of accelerometers.

Fig.6-(a) shows outputs of X_k and Z_k-axis accelerometers(Ax_k, Ax_k) in wrist turning without hand trembling. From the result in Fig.6-(a), the output of Az_k was decided to use for grip

inclination conversion, because Az_k detected the influence of wrist turning less than Ax_k.

In this measurment, we tried another device using a tracking machine system to confirm the accuracy of this metnod. This tracking machine system has two CCD cameras to monitor two LEDs attached to the sensor cover, and calculates grip inclination. The error of grip inclination by tracking was within 1 degree. Fig.6-(b) shows the result of grip inclination conversion by Az_k(**Ia**) and grip inclination by tracking(**It**). **Ia** nearly coincided with **It**. From this result, grip inclination by accelerometer is correct and this value can cancel the influence of grip inclination in force sensors.

5-3 Measurement of hand trembling

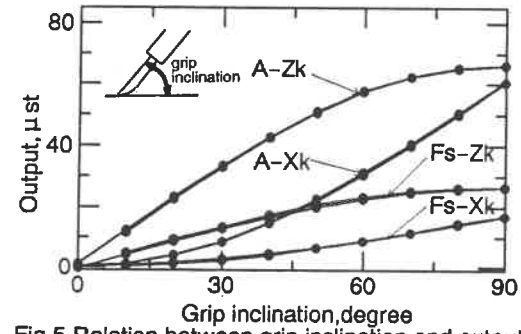

Fig.5 Relation between grip inclination and outputs of force sensors(Fs-Xk,Fs-Zk) and accelerometers(A-Xk,A-Zk)

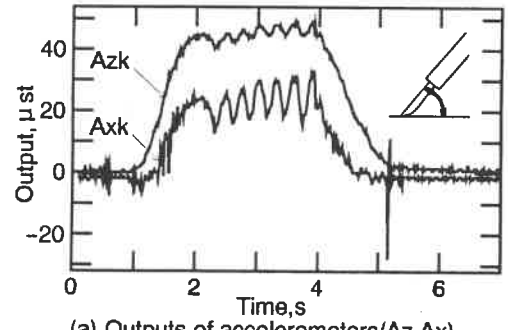

(a) Outputs of accelerometers(Az,Ax)

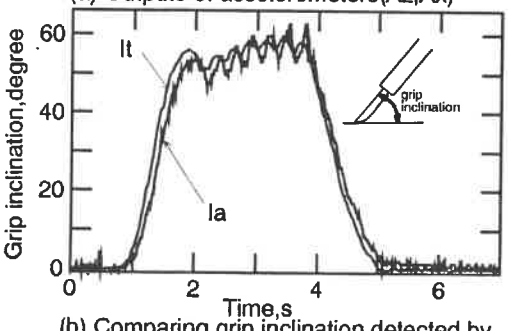

(b) Comparing grip inclination detected by accelerometer(Ia) with by tracking(It)

Fig.6 Grip inclination in wrist turning

Fig.7 shows the hand trembling by holding in hand and sliding arm in the air. As a result, the influence of hand trembling inertia is negligible on each sensors.

5-4 Force transformation

The cutting force was transformed in knife coordinate into that in object coordinate by **Ia**. A loaf of meat was cut on a three-axis force sensing table(1) to evaluate the accuracy of transformed cutting force. The transformed cutting force (**Fxo**, **Fzo**) coincided with the result by the sensing table(**Fxt**, **Fzt**) as shown in Fig.8. From this result, the transformed cutting force is correct, and **Fxo** and **Fzo** can tell the mechanical properties of cutting object.

6. Trial usage of Force Sensing Knife

6-1 Measurement in surgery

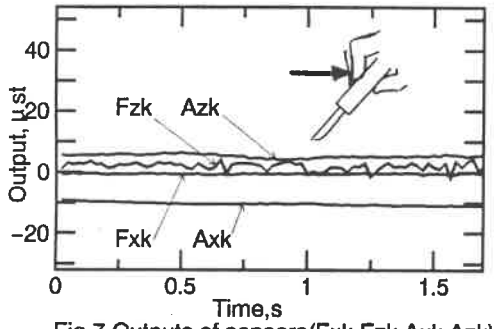

Fig.7 Outputs of sensors(Fxk,Fzk,Axk,Azk) by hand trembling in sliding in the air

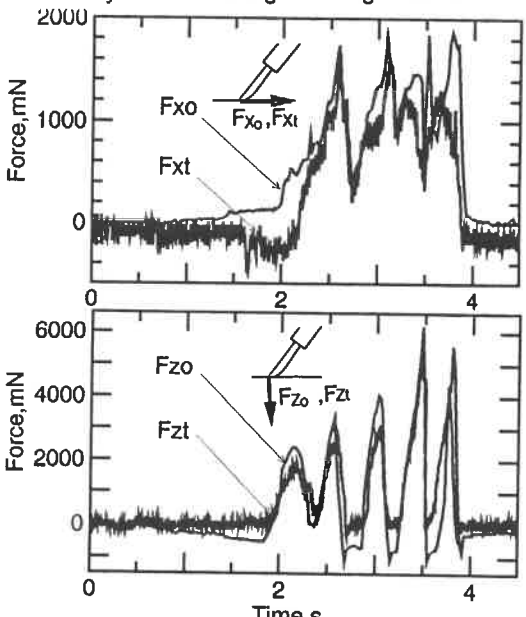

Fig.8 Cutting force measured by Three-axis Force Sensing Table(Ftx,Ftz) and Force Sensing Knife(Fzo,Fzo)

Force Sensing Knife was applied for surgery, and measured the force in human skin cutting at the back of the auricle. Photo.2 shows the scene of measuring/cutting, and Fig.9-(a) shows the result of the cutting force measured in knife coordinate (Fx_k, Fz_k). From this result, the surgeon provided his cutting force constantly to the knife. Fig.9-(b) shows the change of grip inclination in the measurement. By the result of grip inclination, Fx_k and Fz_k were transformed into the cutting force in object coordinate(Fx_o, Fz_o) as shown in Fig.9-(c). This figure informs as follows: The knife only touched the skin and from 1.5s to about 3s, and began to cut at a peak in 3.2s. In this figure, Fx_o and Fz_o are about 1000mN.

As mentioned above, Force Sensing Knife proved to be able to quantify the cutting operation, and to correct the dynamic information in surgery.

6-2 Effect of force measurement in surgery

The authors have measured the relation between the break force and the deformation of the tympanic membrane, and have connected the mechanical properties of tympanic membrane with the disease(2). In the same way, the relation between the mechanical properties of organs and diseases will be collected.

In the measurement during surgery, the surgeon could get information of the cutting force on a monitor simultaneously. He also could obtain the relation between the cutting force and cutting motion. Using this system, an experienced surgeon can initiate the skill of cutting into a beginner. Thus this knife can not only collect dynamic information of cutting but find applications in medical training.

7. Conclusions

This paper introduced a "Two-axis Force Sensing Surgery Knife" newly designed and produced to obtain dynamic information in surgery. This knife can measure two-axis force and acceleration and grip inclination. This knife was applied for surgery and could quantify the cutting operation.

Acknowledgment

The authors wish to thank Prof.Tetsuo Ishii and Prof.Mikiko Takayama of Tokyo Women's Medical College for help in using our sensing knife in surgery.

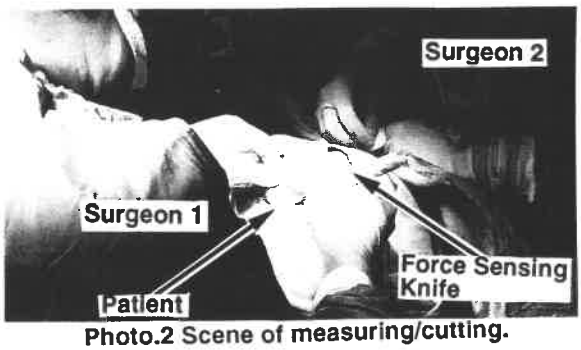

Photo.2 Scene of measuring/cutting.

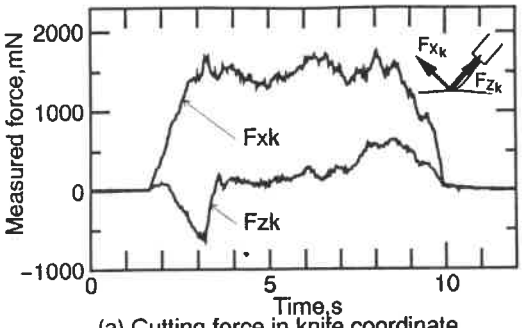

(a) Cutting force in knife coordinate

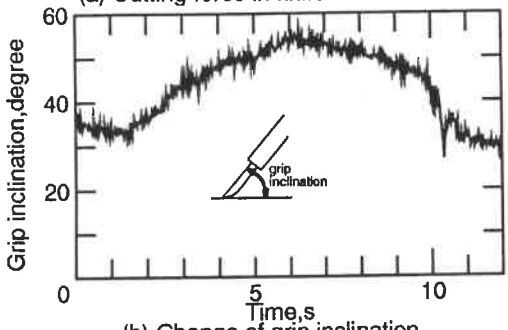

(b) Change of grip inclination

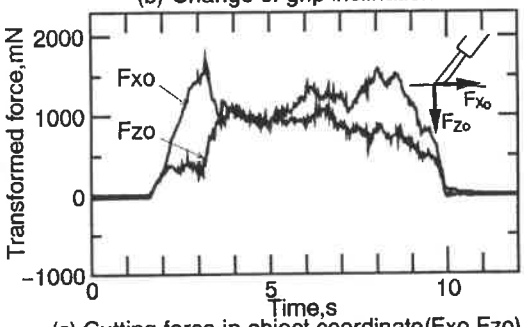

(c) Cutting force in object coordinate(Fxo,Fzo)

Fig.9 Cutting force in surgery

References

(1) Hatamura, Y. "Multi-axis Force Sensors and Their Applications" Journal of Automation Technology Vol.4 No.4 1992

(2) Hachiuma, H., et.al. "Measurement of Mechanical Properties of Tympanic Membrane Using Force Sensing Operation Knife and Micro Testing System," proceeding of 1993 annual meeting of ASPE, pp142-145.

Precision Magnetic Bearing Six Degree of Freedom Stage

M.E.Williams, D.L.Trumper

Dept. of Mechanical Engineering
Massachusetts Institute of Technology
Cambridge, Mass. 02139

Magnetic bearings are capable of applying force and torque to a suspended object without rigidly constraining any degrees of freedom. Additionally, the resolution of magnetic bearings is limited only by sensors and control, and not by the finish of a bearing surface. For these reasons, magnetic bearings appear to be ideal for precision wafer positioning in lithography systems. Lithography steppers currently produced use a combination of mechanical stages to achieve control of the wafer location in six degrees of freedom. In these stages, the wafer is carried on a fine stage which provides six degree of freedom control with approximately 100 μm travel. This fine stage is mounted on a coarse mechanical stage which provides X-Y positioning with approximately 200 mm travel. The fine stage is typically comprised of multiple piezo-actuators and or voice coil drives which are used to position a platen on flexures. These mechanical stages generally suffer from poor dynamics, a result of the compound flexures used. This method of X-Y positioning can become very complicated and could be approaching its maximum resolution capabilities. In comparison magnetic bearings can provide speed and simultaneous control of six degrees of freedom, thus eliminating the complicated flexures and mechanical actuators used in current designs. To demonstrate this capability, a magnetically suspended linear bearing has been constructed which uses variable reluctance actuators to control the motion of a 13 kg platen in five degrees of freedom (three rotational and two translational). A Lorentz type linear motor controls motion of 50 mm in the long travel direction. Laboratory tests of this linear bearing verify that the positioning requirements of photolithography can be met with a magnetic bearing system [1,2]. These results have provided the motivation for the design and construction of an advanced stage which refines the design concepts developed in the first prototype. This paper focuses on the design and construction of the next generation magnetic bearing stage.

This next generation stage has 220 mm travel in the X-Y plane allowing exposure over any portion of a 200 mm wafer. For fine focusing the stage can provide 300 μm of travel normal to the wafer surface and miliradian rotations around three axes. The stage utilizes variable reluctance actuators to control five degrees of freedom of a 13.5 kg platen, and a unique permanent magnet Lorentz type linear motor to position the platen 200 mm in the sixth degree of freedom (X). The linear motor consists of a permanent magnet Halbach array attached to the underside of the platen and a planar, ironless, six phase stator fixed in the machine frame [3,4]. A conventional mechanical linear slide will be used to provide 200 mm of travel in the Y direction. This design increases power efficiency and yields increased performance by capitalizing on the typical operation of a lithography X-Y stage. Typical operation of a stage is to step in the X direction 10 - 20 times along a row of die sites, before a single step is made in the Y direction to the next row of die sites. Since the stage operation is dominated by X positioning, this mechanical-magnetic bearing stage design results in a simple magnetic bearing structure while simultaneously increasing the stage precision and throughput.

The electromagnetic actuators that comprise the magnetic bearings consist of "E" type laminations and a single copper coil. This actuator coil configuration is power efficient and the laminated core minimizes eddy current losses. The dimensions of the core laminations also optimize force by sizing the pole face area in relation to the core window length and width. Thus, for an optimum square pole face area the maximum force is obtained for a given power level. With these power optimizing refinements the total platen power dissipation is reduced and is calculated to be 1-2 watts during a 0.5 g lateral platen acceleration. These low power levels will minimize any thermal distortions of the platen. The lamination material is a 49% nickel and soft iron alloy and was selected for its negligible hysteresis and high saturation flux density [5]. Negligible hysteresis is critical to ensure that the actuator force is single valued on the control current. Because the actuators are non-linear, they are characterized for their force-current-airgap relationship and real time linearized by the digital controller [5].

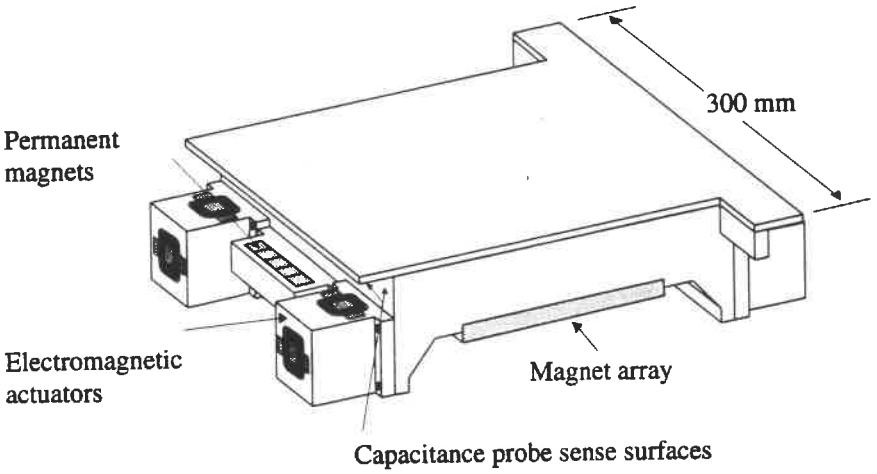

Figure 1: Assembled platen with actuators, lift magnets, and magnet array

The actuators are located on the moving platen to provide a constant force relative to the platen center of gravity. Located at each corner of the platen is a housing which contains three E-core and coil assemblies. The actuators are arranged at 90° intervals in each housing and together total six pair of opposed push-pull actuators which provide five-degree of freedom control of the platen. The actuators have a nominal bearing air gap of 300 μm with displacements of ± 150 μm from the nominal in the Y and Z translational direction. Rotations of one miliradian are possible around all three axes. These translational and rotational ranges are sufficient to provide the local focusing required of typical lithography equipment. The actuator control current is passed to the moving platen through highly flexible flat conductor which rolls under the platen. The bend radius of the flexible conductor is consistent throughout the platen travel to help minimize the disturbance force.

Located between the actuator housings on each side of the platen, are rare earth permanent magnet Halbach arrays. These lift magnets offset the mass of the platen and allow the vertical actuators to dissipate power only for platen position control. The permanent

lift magnets are operated at a relatively large airgap so the force is not a strong function of position. This results in a slow open loop time constant associated with the lift magnets allowing the actuators easier stabilization of the system. The actuators and the lift magnets act upon a laminated magnetic material target rail that runs the length of the machine base. The machine base is mounted on three points and is kinematically constrained using a system of brackets and Belleville washer stacks.

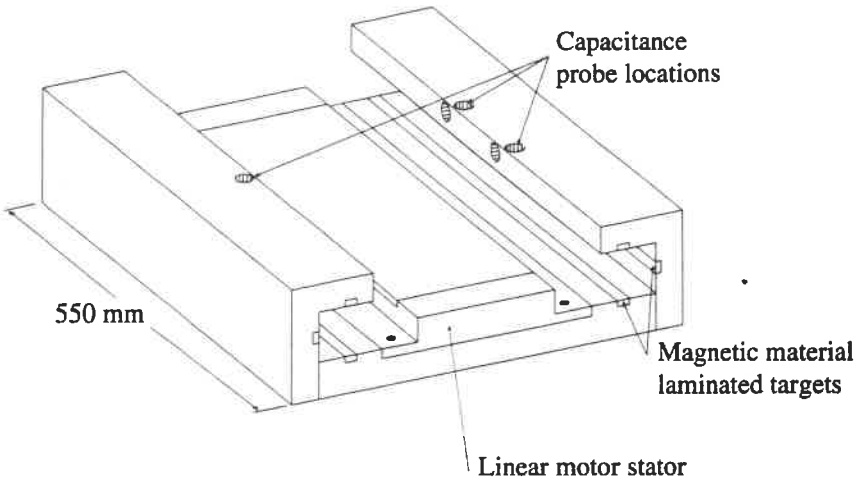

Figure 2: Stage base with linear motor stator base

Since five platen degrees of freedom are controlled by the actuators, five independent position measurements are required. This is achieved by locating capacitance probes in the stationary frame which sense upon a ground surface located on the platen. Laser interferometry is used to measure platen displacement along the X-axis. For lithography operations the stage would be positioned and locally focused using six axes laser metrology.

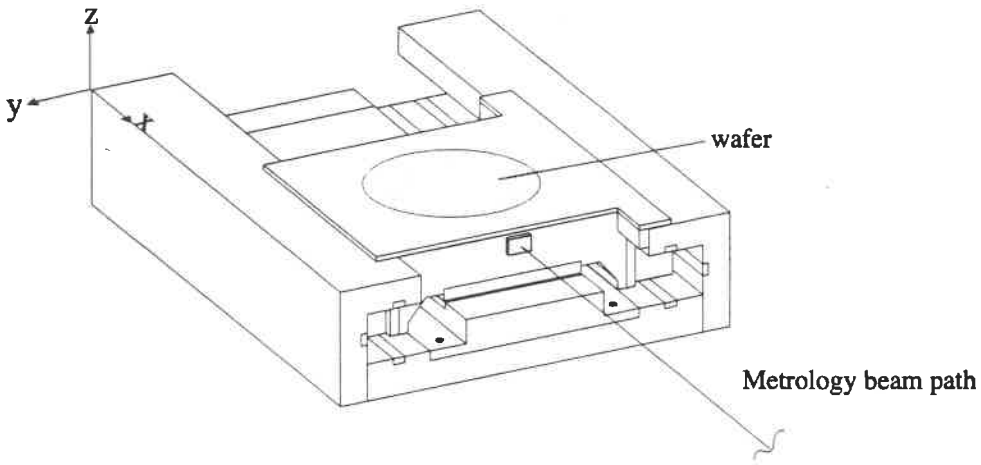

Figure 3: Suspended platen in base

To further reduce the stage power dissipation the linear motor stator winding thickness is power optimized and a Halbach type magnet array is used which doubles the power efficiency of the motor. The key concept in the Halbach array is that the magnetization vector should rotate as a function of distance along the array. In fact if the vector rotates continuously, the field on one side of the array will be identically zero, while the field strength on the other side of the array is doubled relative to an array with a sinusoidally varying purely vertical magnetization. While the ideal case calls for continuous rotation, in practice it is not possible to construct magnetic material with a continuously rotating easy axis. Therefore, the magnet array is constructed of four uniform blocks of magnets, square in cross section each rotated by 90°. This geometry achieves 90% of the ideal continuously rotating field and is easily manufacturable. The magnet sections are sized to provide one full rotation in one spatial period of the stator winding. The magnet array is 150 x 250 x 12.7 mm in size and is constructed of sixty individual rare earth magnet elements. The linear motor and the linear magnetic bearing are digitally controlled using a C30 floating point digital signal processor implemented on a VME chassis.

We have introduced the design and construction of a magnetic suspension X-Y stage and have shown that magnetic suspension technology has the capability to improve the state of the art in lithography systems through increased resolution and wafer throughput.

References

[1] Trumper, D.L., "Magnetic Suspension Techniques for Precision Motion Control," Ph.D. Thesis, Dept. of Elec. Eng. and Comp. Sci., M.I.T., Camb., Mass., Sept., 1990.

[2] Trumper, D.L., and Slocum, A. H., "Five-Degree-of-Freedom Control of an Ultra-Precision Magnetically-Suspended Linear Bearing," NASA Workshop on Aerospace Applications of Magnetic Suspension Technology, NASA Langley Research Center, Hampton, VA, Sept. 25–27, 1990.

[3] Trumper, D.L and Williams, M.E., Nguyen,T.H. "Magnet Arrays for Synchronous Machines" IEEE Industrial Applications Society 28th Annual Meeting, Toronto, Canada, October 3–8, 1993.

[4] Halbach, K., "Design of Permanent Multipole Magnets with Oriented Rare Earth Cobalt Material," Nuclear Instruments and Methods, 169, 1980, pp. 1–10, North-Holland Publishing Co.

[5] Williams, M.E. and Trumper, D.L "Materials for Efficient High Flux Magnetic Bearing Actuators" NASA International Symposium on Magnetic Suspension, Seattle, WA, Aug 1993. VA, Sept. 25–27, 1990.

Thermal Error Models for Software Compensation of Machine Tools

J.A. Soons, H.A. Spaan, and P.H. Schellekens
Precision Engineering Group
Eindhoven University of Technology, Eindhoven, The Netherlands

This abstract summarizes our experiences in the application of both new and existing methods to predict the thermal errors of machine tools, especially for software error compensation. The models are analytical or empirical. Special attention is paid to the capability of a model to describe deformations under transient conditions and at different positions in the workspace. Promising modelling techniques are applied to predict and compensate the thermal errors of a five-axis milling machine. The work was part of a European Community project[3] on methods for the software compensation of machine tools, in which the PTB, Philips and Maho participated.

1 The analytical model

The analytical model is based on an assumed stress-free thermal deformation of the structural loop. This approach was pioneered by Yoshida[5] and successfully used by e.g. Trapet[4] to model the thermal errors of a CMM. The temperature distribution is approximated by piecewise linear interpolation of temperatures measured by sensors distributed over the structural loop.

In the analysis we consider the structural loop as several beam-like structures that can expand without mutual interaction. Stress-free deformation occurs when the temperature distribution of such an element is linear with respect to a rectangular Cartesian co-ordinate frame. Neglecting the effect of lateral contraction and using the classical Bernoulli-Euler beam theory, this restriction can be relaxed by allowing any variation of the average temperature and orthogonal thermal gradients along the main beam axis. It may be argued that these restrictions limit the usefulness of the method. On the other hand, practical limits on the number sensors often results in a modelled temperature distribution that belongs to the stress-free class.

Stress-free thermal deformation can be calculated from global geometric entities (e.g. the length of a beam is important but not the nature of its cross section). Pitch and yaw errors are obtained by integration of the orthogonal thermal gradients along the beam. Dependent on the guideway configuration, the effect of thickness variations along the beam is sometimes included. Straightness errors are approximated as integrated angular errors. Stress-free torsional rotation of beam cross-sections does not exist. However, roll errors may occur if there is a lateral gradient variation. For example, a carriage supported by two horizontal guideways each with a different vertical temperature gradient will experience a roll error. If this setup is rotated 90 degrees about its main axis, the same temperature distribution yields an opposite roll error. Hence roll errors are dependent on the guideway configuration. Thermal stresses introduced in any effective cross section of the guideway will significantly reduce the roll errors. In our model these errors are not included.

The analytical model of the five axis milling machine depicted in Figure 1 requires 35 temperature sensors (Pt-100's). To verify the model, eddy-current transducers are used to monitor the errors in the orientation and position of a cylinder mounted in the tool holder during characteristic load cycles of the spindle. Some results are shown in Figures 2 and 3.

A major problem of this and other models is tool expansion. If coolant is used, effective models could be obtained by assuming that the tool has the same temperature as the coolant. If no coolant is used, the tool temperature is significantly affected by forced convection and the temperature of the spindle bearings. When the spindle is stopped, the temperature of the tool increases rapidly even though the temperature of the spindle head decreases. This effect is clearly indicated in

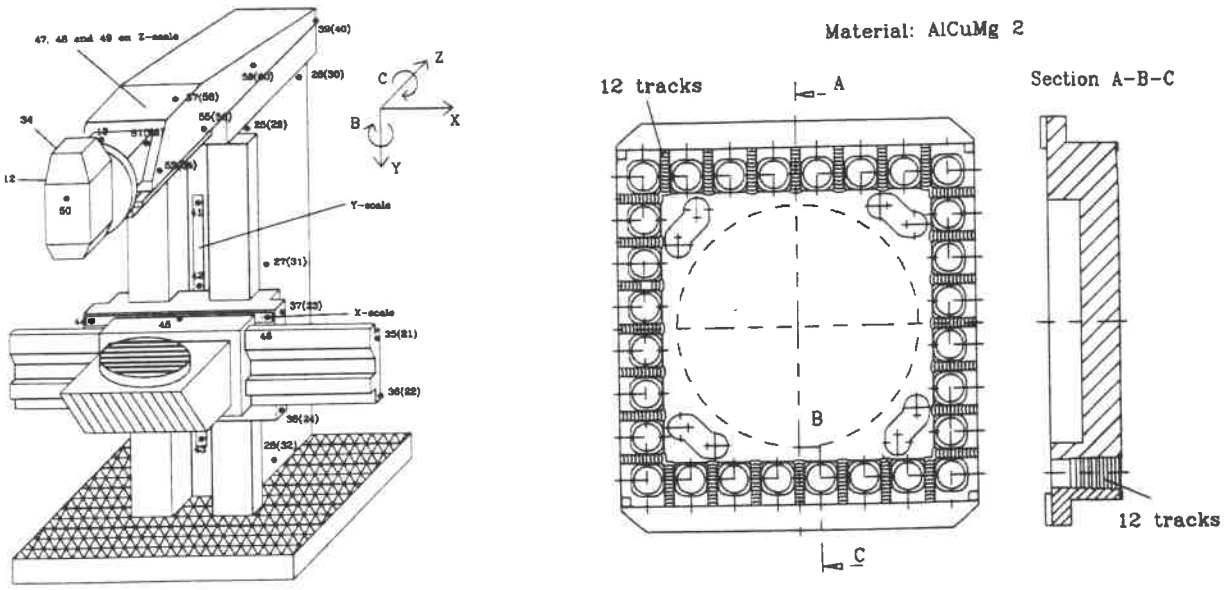

Figure 1: The studied five-axis milling machine and the temperature sensors. The right figure shows the workpiece used to validate the software compensation.

figures 2 and 3. For this machine the effect is very profound due to the large temperature increase of the spindle head (35 degrees at 6000 rpm). Furthermore, the invar bars that connect the Z-axis scale to the spindle head enhances the visibility by causing a relatively slow retraction of the spindle head when the spindle is stopped. As a first approach, tool expansion was modelled using a 'classical' analytical model for the temperature distribution of a rotating cylinder with forced convection dependent on the spindle speed and the cabin environment. Somewhere along the tool axis its temperature is approximated as that of the first spindle bearing. Parameters of the model where estimated using the observed diameter change of the tool. The validity of this model for real tools, tool changes, and cutting conditions is expected to be limited.

Although the principles of the analytical model are relatively simple, its application is time consuming and requires specific knowledge on the construction of the machine (e.g. the used scale mounting and the configuration of the spindle bearings). Due to the large number of underlying assumptions and approximations, especially regarding the complex temperature distribution of the Z-axis ram, several iterations were required to derive an acceptable model.

A significant advantage of the analytical model is that it yields parametric errors. Thus the errors of the machine are described at any position of the machine axes. The use of many temperature sensors furthermore makes the model valid for moving axes, various operating conditions, and environmental conditions. The small number of dominant heat sources in the milling machine allows a reduction of the number of sensors by identifying leverage sensors and extrapolating their effect. This will however reduce the model's capability to describe the errors under any condition, especially regarding transient conditions and changes in the environment.

2 Empirical models

Empirical models can be divided into two groups: static models that relate machine errors at a certain instant to e.g. the temperatures of certain sensors at that instant, and dynamic models that take the history of the model input into account. The data used to estimate the models should describe the machine's errors in response to switching the machine on, a changing environment, and variations in operating conditions. We focused our efforts on the latter errors. Of particular interest was the spindle drive, which is by far the major heat source of the studied machine.

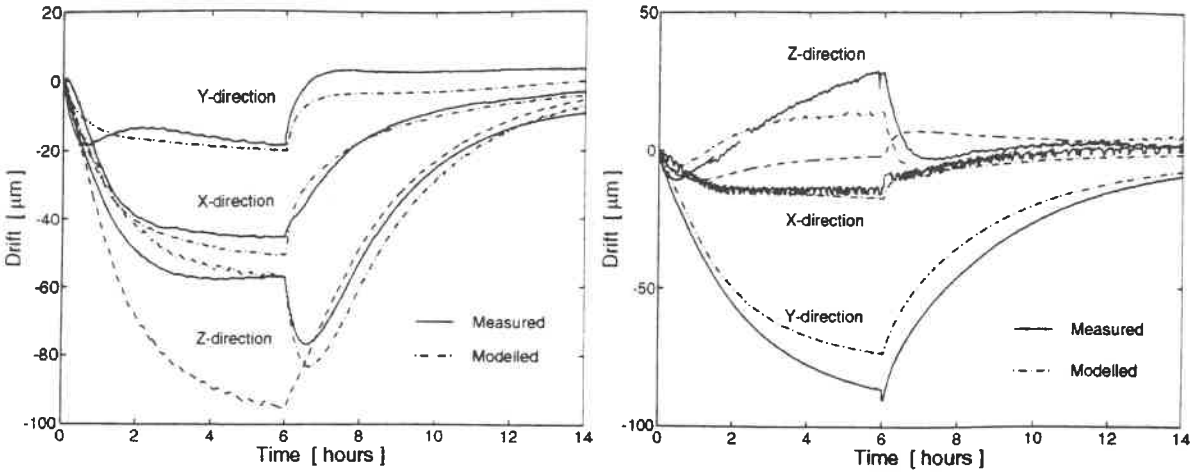

Figure 2: Drift of the tool during a spindle load of 6000 rpm for six hours (horizontal spindle, no coolant, left figure: Z-axis extracted, right figure: Z-axis retracted). For errors in the Z-direction an additional model is shown based on the (naïve) assumption that the tool temperature equals that of the front spindle bearing. Analytical model.

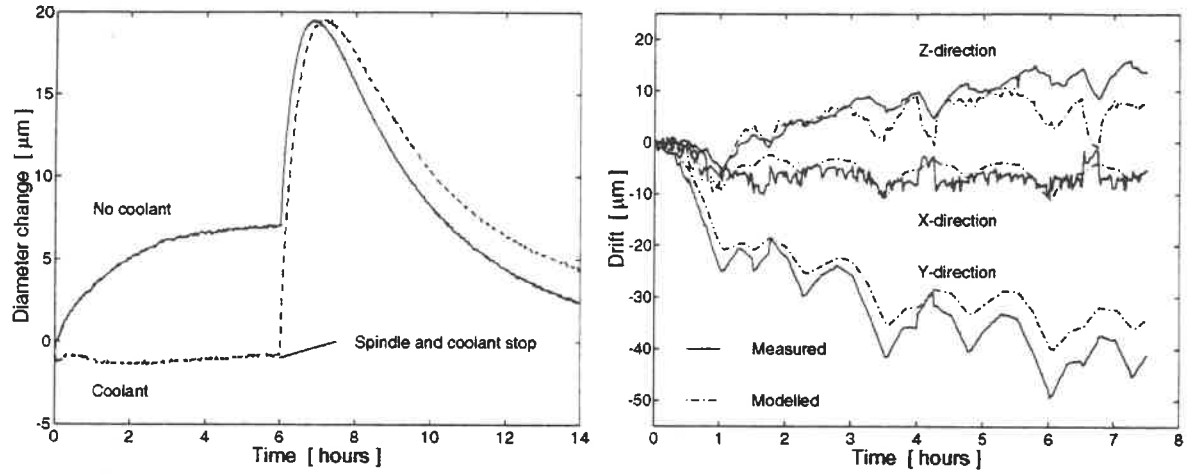

Figure 3: Observed diameter change of the tool during a spindle load of 6000 rpm for six hours. The right figure presents the drift of the tool during a spindle load according to DIN 8602 (horizontal spindle, no coolant, Z-axis retracted). Analytical model.

The estimation data is obtained by measuring the drift of the tool and the temperature distribution at a fixed position of the machine axes. These tests were conducted for various spindle loads and at various machine positions, especially along the Z-axis of the machine (the positions of the Y- and X-axes have a minor effect on the observed errors). Although a sweep test is more effective to assess the error variation along an axis, it was not used. The main reasons are the very fast change of machine errors whenever the spindle speed is changed, the added complexity caused by the significant (dynamic) effect of a different axis position on the temperature distribution of the machine, and the sensitivity of the required equipment to temperature and coolant.

2.1 The static model

The static model relates the temperature elevation of identified significant sensors to the observed drift of the tool at a certain axis position. Models for the variation of the responsible parametric errors along an axis are derived by interpolation. Various modelling techniques based on this principle have been reported (see e.g.[1]), including neural networks and GMDH type modelling techniques. The latter two techniques have the advantage that often very complex models are

automatically' proposed. We prefer relatively simple models where the observed errors are estimated as linear combinations of the temperature elevations of significant temperature sensors using linear least squares regression. Although the number of sensors can be reduced by including higher order terms, the resulting models were usually not very robust against conditions that differ from those used in the model estimation.

The selection of the significant model parameters (i.e. temperature sensors) is critical, not only to reduce this number but also to avoid overfitting. Several parameter selection techniques were studied. Selection of sensors based on their correlation with the observed drift proved difficult. Since all temperature elevations origin in a limited number of heat sources they show a high degree of interdependence. Including one sensor into the model can dramatically change the relative significance of the other sensors. Also the grouping of sensors with identical patterns was hazardous, since a slight difference between two sensors can determine an important gradient. Stepwise regression techniques are an accepted method to deal with such problems, but we obtained the best results by brute force methods that evaluate all possible combinations of a certain number of temperature sensors. The significant parameter analysis is executed for all errors and axis positions simultaneously. To avoid nonsense relations the use of estimation and validation datasets proved to be very important.

In addition to the strong correlation between the sensors there also exists the problem of near linear dependencies. This problem is known as multicolinearity. It not only causes problems in the selection of the parameters but also in the stability of the parameter estimation. The application of Principle Components analysis showed improvements in the robustness of the obtained error models by lowering the absolute values of the model coefficients. However, in some cases a slight loss in the predictive power of fast changing errors was observed.

It is important to note that although these models are static, they can implicitly describe transient conditions. Usually this is not achieved by identifying the leverage sensors that determine the relevant temperature distribution of the machine, but by including sensors at different distances from the major heat sources. The effect of different axis positions on the temperature distribution is often modelled by including a sensor near the carriage. Although this implicit dynamic nature has the advantage that less sensors are required, it limits the application of the model to conditions represented by the estimation dataset. We currently use an experiment where the spindle is loaded with a constant speed followed by a cool down period, and one where the spindle loaded with a 'random' spectrum of speeds including spindle stops.

For the studied machine good models were obtained using 16 sensors, including 2 sensors for each scale. A major problem in the sensor selection was the significant effect of the environmental temperature on both the distribution and intensity of the temperature elevations near the spindle head, probably due to changes in preload. Except for spindle head and tool, the effects of coolant were relatively small, since the machine structure is well protected by splash guards.

2.2 The dynamic model

The used dynamic model is based on the Lumped-Parameter description developed by McClure[2]. McClure showed that the temperature elevation at each point in a fixed structure with fixed heat-source configuration, and hence the resulting thermal drift, can be described by a parallel series of first order dynamic systems that take the heat flow variation in time as input. Instead of using operating conditions as a measure of the heat flows, we use various temperature sensors located as close as possible to the main heat sources. The sensors are chosen regarding their position and the nature of the observed temperature elevation during characteristic load cycles. Models were improved by including zero order terms, which corresponds to an area of uniform temperature near the sensor.

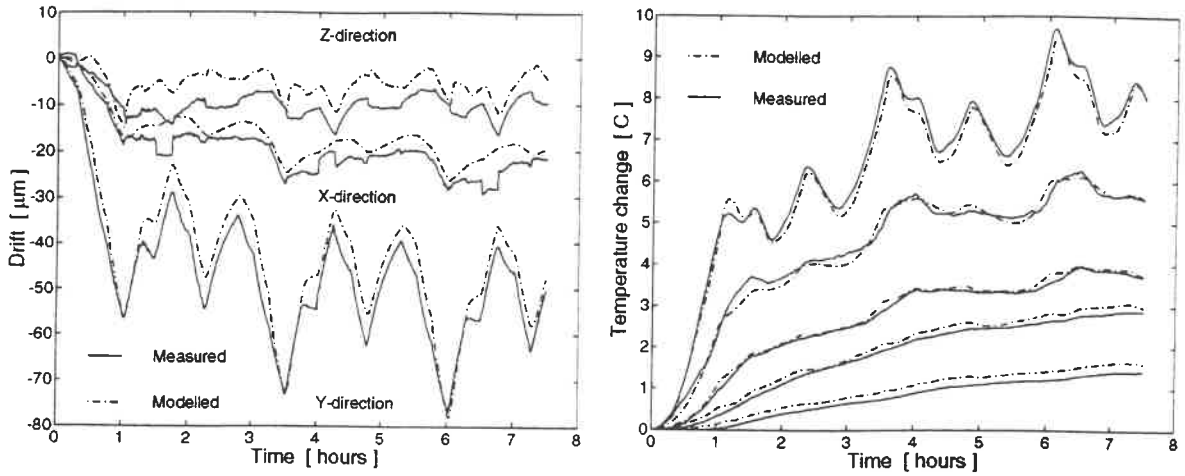

Figure 4: Drift of the tool during a spindle load according to DIN 8602 (horizontal spindle, no coolant, Z-axis in center position). Dynamic model. The right figure presents the temperature elevations of some sensors. Hybrid model.

The system can be efficiently described by a standard linear state space model. Here both the model and the estimation of its parameters (time constants and gains) benefit from the extensive amount of techniques developed in this field. The same time constants (three) are used for all the significant sensors (three, located close to the horizontal and vertical spindle) and the errors that have to be described. Only for the tool additional model terms are required to describe the tool expansion. Good models were obtained using only a constant spindle speed test for their estimation (see e.g. Figure 4). At this moment, different axis positions are modelled by changes in the gains, which yields reasonable results at fixed axis positions. In accordance with the next section, it is expected that the use of extra sensors near the carriages will also enable the modelling of the dynamic effects of axis movement, provided that suitable experiments are executed.

3 The hybrid model

This method is a two step approach consisting of an empirical model to predict the thermal state of the machine and the discussed analytical model to describe the resulting machine errors. The purpose of this approach is twofold: first to reduce the large number of experiments required to assess the parametric errors at various conditions, and second to incorporate the dynamic effect of axis movement on the thermal state of the machine.

The structural loop is divided into several bodies, each separated by a kinematic element. For each body, a model is estimated that relates its temperature distribution to the temperatures measured by sensors near its internal heat sources and sensors near the boundary with other bodies. The latter sensors describe the heat sources and heat sinks embodied by these neighbours. To estimate the model for the temperature distribution, additional sensors are temporarily attached to the machine. These sensors are the same as those used in the analytical model. Based on the measured temperature elevations during characteristic duty cycles of the machine and, in principle, characteristic changes in environmental temperature and gradients, a dynamic model similar to that discussed in the previous section is estimated. This model relates the temperatures of the additional sensors to the fixed sensors and environmental conditions. The additional sensors can than be removed from the machine, although some can be retained to evaluate the validity of the model during operation. Each body has its own set of time constants. This is difficult to achieve in the former dynamic method since the observed machine errors on which the estimation is based result from the behaviour of the complete structural loop. Compared with the analytical model

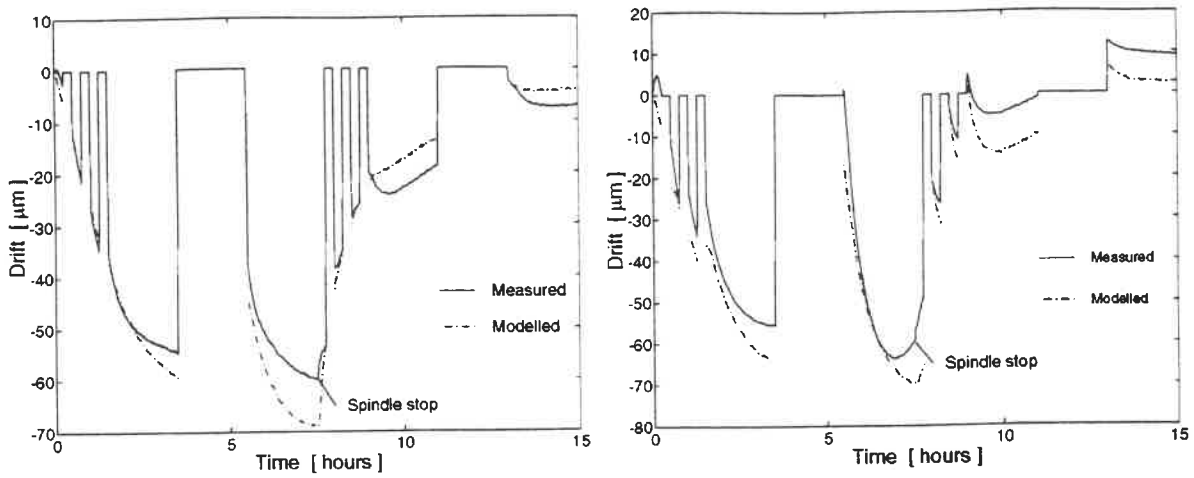

Figure 5: Drift of the tool in X- (left figure) and Y-direction (right figure) during a spindle load of 6000 rpm for 7.5 hours. (vertical spindle, no coolant, measurement at extracted position Z-axis). No errors are measured when the Z-axis is retracted. Hybrid model.

that uses all the sensors, the resulting model showed no significant loss of predictive power at stationary axis positions.

Besides by generating heat, axis movement represents two additional sources of transient effects. First the structural loop changes, resulting in different heat-flow pathways, time constants, and overall surface geometry. This causes a transient change to a different temperature distribution. Second, a carriage acting as a heat sink at a certain location may, after movement to a cooler area of the machine, act as a heat source in that area. Thus axis movement represents a special mode of heat transfer. These effects will be profound if a machine element containing the main heat sources of the machine (the Z-axis for our machine) is infrequently moved. They can result in significant differences between the results of fixed-station and sweep tests to assess machine errors. Frequent movement of such a carriage will generally have an averaging effect on the heat distribution.

To determine the importance of this "effect of memory of previous environment"[2] and the model's capability of describing it, the following experiment is conducted. The drift of the tool is measured with the ram fully extended during a spindle load of 6000 rpm for $7\frac{1}{2}$ hours. For periods of initially 15 minutes and later two hours the ram is fully retracted. During the cool down period the same process is repeated. Figure 5 shows the observed and modelled drift.

4 Implementation and validation

Preliminary versions of a software compensation based on the analytical and static empirical models were implemented in the five-axis milling machine. Every minute a PC records the temperature sensors and updates the parametric errors of the machine. These are then downloaded as error tables to the machine controller. The controller applies spatial and time dosing of the compensation values to avoid limit cycles and visible marks on the workpiece surface. In the first version of the controller only zero- point drift, squareness, and scale errors were compensated.

Figure 1 shows the prototype of a test workpiece developed by the PTB that was used to validate the error compensation. The machined tracks embody a square grid of three dimensional points spaced at 34 mm intervals. A single workpiece contains twelve of these grids that can be machined at different instances. By machining four workpieces in three different planes, the thermal parametric errors of the machine can be assessed. Figure 6 shows some results obtained under finishing conditions.

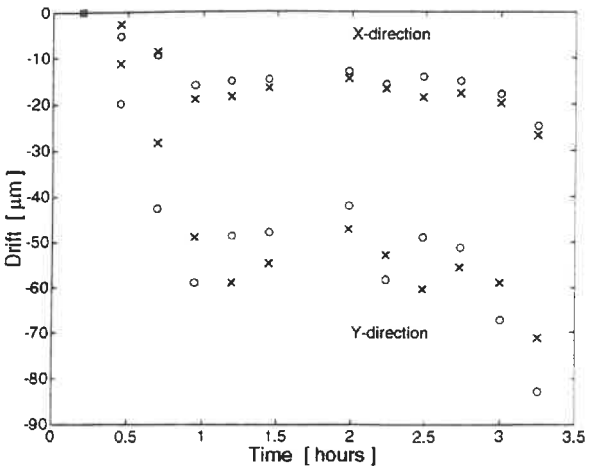

Conditions	XY,DIN	XZ,6000	XZ,DIN
Uncompensated	91 μm	144 μm	73 μm
Analytical	29 μm	39 μm	29 μm
Static	24 μm	32 μm	22 μm

Figure 6: Predicted (x) and measured (o) errors in the average position of the workpiece holes during a spindle load according to DIN 8602 (horizontal spindle, coolant, center workspace, finishing conditions, analytical model). The table shows the maximum errors observed in workpieces milled with and without compensation. The workpieces span 200 minutes of operation.

5 Conclusions

A major advantage of the analytical model is that it results in parametric errors, thus avoiding extensive error assessment. Furthermore it can describe the machine errors resulting from various conditions, including axis motion and environmental effects. Its major defects are the large number of sensors required and its difficult construction. Both empirical models are relatively easy to estimate but require many experiments. The dynamic model requires fewer sensors and experiments than the static model. The hybrid approach shows promise in reducing the amount of experiments and modelling the dynamic effect of axis motion. The latter can, in principle, also be achieved by the static and dynamic models, provided that suitable experiments are included in the estimation. A key factor that determines the quality of all models are experiments that yield error data representative of conditions encountered during operation.

References

[1] M. A. Donmez. *"A General methodology for machine tool accuracy: theory, application and implementation"*. PhD thesis, Purdue university, 1985.

[2] E. R. McClure. *"Manufacturing accuracy through the control of thermal effects"*. PhD thesis, Lawrence Livermore National Laboratory, 1969.

[3] P. H. Schellekens et al. "Final project report". In *"Development of Methods for the Numerical Error Correction of Machine Tools"*. Bureau Communautaire de Référence, 3320/1/0/160/89/8-BCR-NL, Brussels, 1993.

[4] E. Trapet and F. Wäldele. "Koordinatenmeßgeräte in der Fertigung — Temperatureinflüsse und erreichbare Meßunsicherheit". *VDI Berichte*, (751):209–227, 1989.

[5] Y. Yoshida and F. Honda. "Thermal deformations of machine tool structure — the bed of a lathe". *Annals of the CIRP*, 15(1):337–344, 1967.

Acknowledgment

The research of the principal author has been made possible by a fellowship of the Royal Netherlands Academy of Arts and Sciences.

MEASUREMENT OF MACHINE TOOL PARAMETRIC ERRORS USING THE LASER BALL BAR

John C. Ziegert
Department of Mechanical Engineering
University of Florida
Gainesville, FL

1.0 Introduction

The laser ball bar (LBB) was developed to facilitate rapid measurement of machine tool errors. The LBB consists of a heterodyne laser displacement interferometer whose measurement axis is aligned between the centers of two precision spheres joined by a telescoping tube assembly. The spheres ride in trihedral magnetic sockets carried by the tool holder and machine table. A quick and easy initialization procedure allows the absolute length of the LBB to be known so that it can be used to measure the absolute distance between any pair of magnetic sockets. In use, three sockets are carried on the machine table and a fourth is carried in place of the tool. These four sockets form the vertices of a tetrahedron. If the lengths of all six sides of the tetrahedron are measured with the LBB, then the spatial coordinates of the tool socket with respect to the table sockets can be determined by trilateration.

The LBB measures spatial coordinates of the moving tool socket with respect to the LBB native coordinate system, which is fixed to the three base sockets on the table. The measured spatial coordinates of the tool socket can be transformed into the machine coordinate system and compared to the commanded coordinates to determine the machine positioning accuracy if the coordinate transformation matrix the LBB system and the machine coordinate system is known. This transformation can easily be found by moving two of the machines axes, one at a time, and measuring the LBB coordinates of points along these lines. Straight lines are fit to these data points using a least squares technique, and the direction cosines of these lines are computed. One of the straight lines is chosen as a reference machine axis direction. Since the two lines may not be perfectly orthogonal due to squareness errors in the machine, the second machine axis direction is formed as the normalized vector product of the unit vectors along each of the two lines. The third machine axis is then formed as the vector product of the first two. This yields the direction cosines of unit vectors along the three machine axes in LBB coordinates, which is what is needed to form the transformation. This rotation matrix is then used to transform all LBB measured coordinates into machine coordinates for comparison to the commanded positions and evaluation of the positioning accuracy. Transformation of coordinates allows the LBB base sockets to be placed at convenient locations on the table and makes it unnecessary to attempt to align them with the machine axis motions.

Although the LBB has the ability to rapidly and directly measure the tool position, it is still desirable to be able to determine the axis parametric errors to reduce the time needed for machine metrology and to aid in machine diagnostics. If one were to measure a 10X10X10 grid of points over the machine workspace from all possible combinations of axis motion directions, there would be 8000 points to measure. Even with an automated system such as the LBB, the time required is substantial. If the parametric errors can be measured using the LBB, then a rigid body kinematic error model of the machine can be used to

estimate the volumetric accuracy. In the case where the machine accuracy is found to be inadequate, knowledge of the axis parametric errors helps in diagnosis of the root causes of the inaccuracy. Parametric error fall into four groups; translational errors, tilt errors, axis alignment errors, and spindle errors. The LBB is capable of making measurements from all of these groups.

2.0 Translational Error Motions

When a linear slide is actuated, the actual motion of the moving body consists of the intended motion plus 6-DOF of unwanted error motions. The three translational error motions are commonly called the linear displacement error or scale error, and two straightness errors in two axis directions perpendicular to the nominal direction of motion. If we assume the axis being measured is the X-axis, then the scale error is $\delta_x(x)$, and the two straightness errors are $\delta_y(x)$ and $\delta_z(x)$. To measure these error functions using the LBB the X-axis of the machine is actuated while the Y and Z axes are held stationary. The machine is stopped at selected points along the X travel, and the spatial coordinates of the tool socket are measured using the LBB. These points are then transformed into the machine coordinate system. The vector difference between pairs of nominal and actual coordinates represents the position error vector at each measured point, E(x). The scale and straightness errors are simply the components of the error vector as shown in Figure 1. Typical results are shown in Figure 2.

$$\begin{aligned} \vec{E}(x) &= \vec{P}_{meas}(x) - \vec{P}_{nom}(x) \\ \delta_x(x) &= E_x(x) \\ \delta_y(x) &= E_y(x) \\ \delta_z(x) &= E_z(x) \end{aligned} \qquad (1)$$

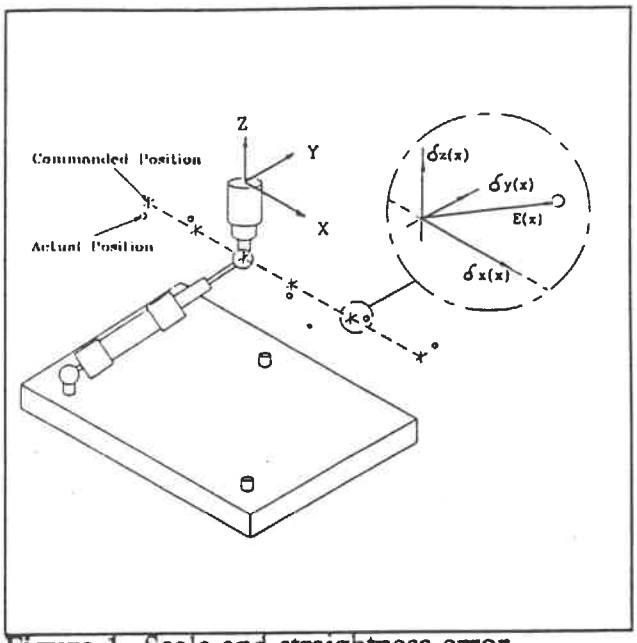

Figure 1. Scale and straightness error measurement.

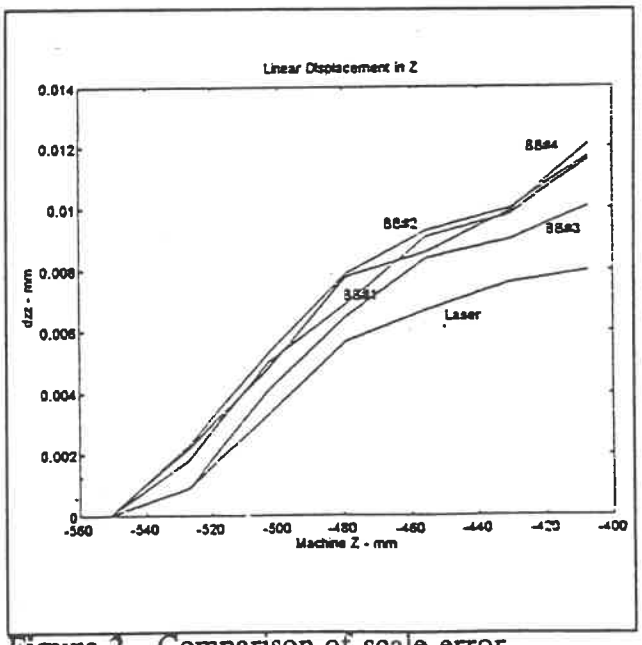

Figure 2. Comparison of scale error measurement with LBB and direct interferometry.

3.0 Tilt Motions

The tilt motions of a linear slide are also commonly referred to as the roll, pitch, and yaw motions. When any single axis of a machine is actuated, the tool point becomes an extension of that single moving body. It is not possible to measure rotational motions of a rigid body by measuring positions of a single point on the body. Therefore, if we wish to measure the tilt (rotational) error motions of the moving slide, we must measure the spatial positions of at least three points on the moving body. To accomplish this, an L shaped fixture which holds three magnetic sockets is carried by the tool holder. These sockets are arranged so that socket A is on the spindle centerline, while sockets B and C are displaced parallel to the axis directions. The spindle must be fixed from rotation during these tests. The test setup is shown in Figure 3. As the axis is actuated to selected points along its travel, the spatial position of each of the sockets is measured. After transforming into the machine coordinate system, the position error components of pairs of sockets are compared to obtain the tilt parametric errors.

For small rotations, the tilt parametric errors are related to the error motions of each socket by the relations given in Equation 2. The distance between sockets, d_{AB} and d_{AC}, is obtained from the magnitude of the vector difference between the spatial coordinates of sockets A, B, and C at any single axis position.

$$\epsilon_x(x) = \frac{E_{Az}(x) - E_{Cz}(x)}{d_{AC}}$$

$$\epsilon_y(x) = \frac{E_{Az}(x) - E_{Bz}(x)}{d_{AB}} \qquad (2)$$

$$\epsilon_z(x) = \frac{E_{Ay}(x) - E_{By}(x)}{d_{AB}} = \frac{E_{Ax}(x) - E_{Cx}(x)}{d_{AC}}$$

Note that there is some redundancy in the error equations. This is a reflection of the fact that we have taken nine measurements (three leg lengths for each socket) to obtain the components of the 6-DOF error motion. The three measurements to socket A give the three translational DOF. It should not require six more measurements to obtain the remaining three tilt DOF. If we deleted one leg length measurement to each of the sockets A, B, and C, then the measurement setup becomes kinematically equivalent to a Stewart Platform. Unfortunately, the forward positonal solution for this type of Stewart Platform has sixteen separate assembly configurations. Therefore, there is a computational cost associated with determining the position and orientation of the tool fixture, and there may be some ambiguity in choosing the proper solution if we attempt to use the minimal number of measurements.

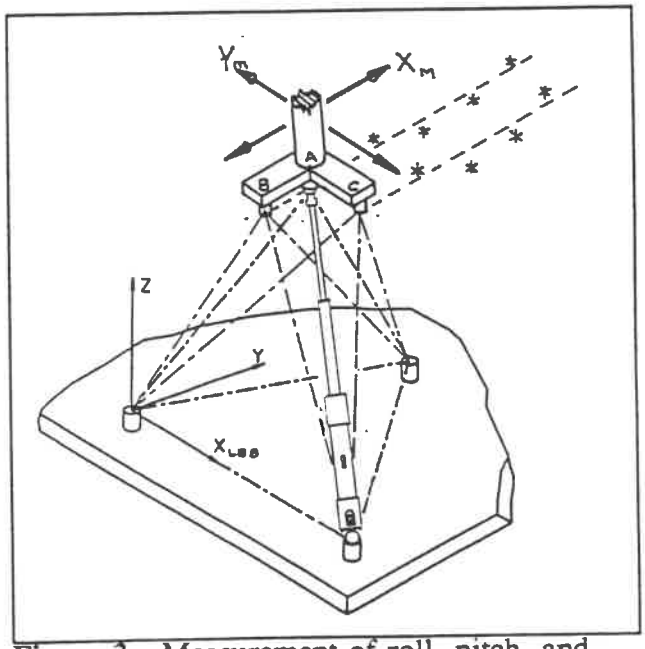

Figure 3. Measurement of roll, pitch, and yaw.

4.0 Axis Alignment errors

The squareness error between any pair of axes is easily measured using the LBB. The spatial coordinates of the tool socket are measured at selected points as each axis is actuated. A best fit line is found for each data set and the angle between these two lines is computed. Any deviation from 90° represents a squareness error between the two axes.

5.0 Spindle Error Motions

For conventional machine tools, the radial, axial, and tilt error motions of the spindle are expected to be on the order of 0.1μm. Since the LBB has a spatial measurement accuracy on the order of 1μm, the LBB is not accurate enough to measure the synchronous and asynchronous error motions of the spindle. However, the thermal drift motions of the spindle for typical machine tools are often on the order of 10 - 100μm. The LBB can be used to measure these thermal drift motions if a rotary encoder is attached to spindle shaft. The setup for the measurements is shown in Figure 3. A socket is mounted eccentrically to the spindle axis, and the spindle is rotated at a very slow speed, typically 1-2 rpm. The LBB is fixtured between base socket 1 and the spindle socket, and the output of the encoder is used to initiate data capture at specified rotary positions. The LBB is then moved to base sockets 2 and 3, and the procedure is repeated. After processing the data, the coordinates of the points measured represent the trajectory of the moving socket, which is very nearly a circle in space. A circle is fit to the data using a least squares technique. The line in space which is normal to this circle and through its center represents an *average* axis of rotation for the spindle. To measure thermal drift motions of the spindle, the LBB is removed and the spindle is rotated at a working speed. After a suitable period of time, the spindle is stopped and the trajectory of the socket is measured as before. Axial and radial drift motions of the spindle will show up as spatial translations of the center of the circle, while tilt motions will be indicated by changes in the direction of the normal line through the center.

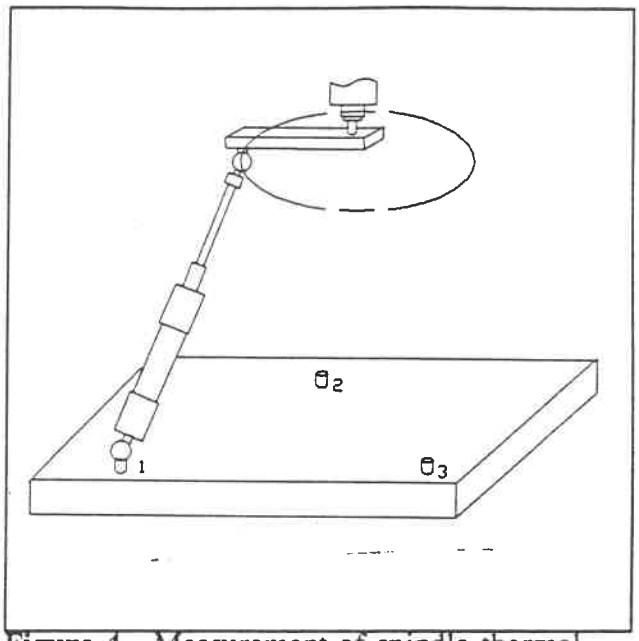

Figure 4. Measurement of spindle thermal drifts using the LBB.

References:

1. Bryan, J.B., "A Simple Method for Testing Measuring Machines and Machine Tools, Part I: Principles and Applications", *Precision Engineering*, v. 4/2, 1982, pp. 61-69.
2. Ni, J., Huang, P.S., and Wu, S.M., "A Multi-Degree-of-Freedom Measuring System for CMM Geometric Errors", *ASME Journal of Engineering for Industry*, v.114, 1992, pp. 362-369.

This work was supported in part by National Science Foundation Grant #DDM-9017293 and NSF Young Investigator Grant #DDM-9358138.

Precision roll measurement using a polarization reference

Steven R. Patterson, David M. Schmidt

University of North Carolina at Charlotte

Charlotte, NC 28223

Introduction

Historically, roll has been one of the more difficult machine metrology measurements to accomplish. Currently accepted methods for evaluating roll[1] use either the constant direction of local gravity as a reference (differential level technique) or a precision artifact (differential straightness). The use of a gravitational reference is limited to horizontal axes, and measurements made with differential levels are subject to seismic noise. The use of an artifact for differential measurement is subject to the availability of a suitable artifact, and becomes more difficult and expensive as the length of axis travel increases. It can be shown that the average polarization state of an optical beam remains constant as it propagates. This makes the polarization state of a linearly polarized optical beam an appropriate physical reference for angular rotation about the axis of propagation.

Detection method and noise limits

It has been previously shown[2,3] that roll may be measured with a precision of one microradian by using a linearly polarized laser beam as shown in figure 1.

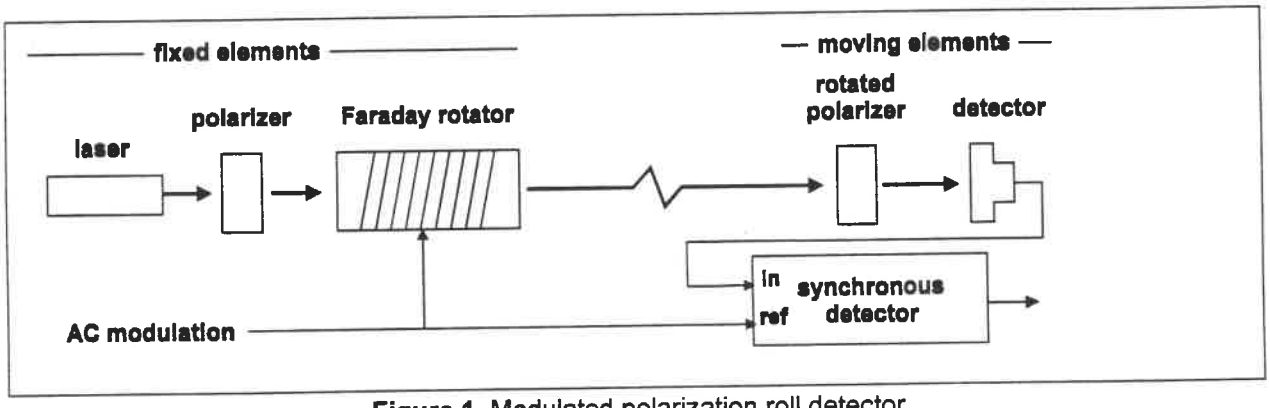

Figure 1 Modulated polarization roll detector

A linearly-polarized incident beam with amplitude **A** (intensity A^2) is used as the polarization reference. The modulating signal in the Faraday rotator induces a rotation of that polarization axis of $\varepsilon \cos \omega_m t$. The beam then passes through a linear polarizer rotated at the angle to be measured, ϕ. The resulting signal from the detector is

$$I_d = A^2 \sin^2(\phi + \varepsilon \cos \omega_m t) + \sigma = \frac{A^2}{2}(1 - \cos 2(\phi + \varepsilon \cos \omega_m t)) + \sigma \qquad (1)$$

where σ, a stochastic function of **t**, is the noise-equivalent-power of the detector assembly. The result of synchronously detecting the $\cos\omega_m t$ component of this intensity produces an output signal

$$s = A^2 \sin 2\phi J_1(2\varepsilon) + \frac{\sigma\{\omega_m\}}{\sqrt{2}} \tag{2}$$

where $\sigma\{\omega_m\}$ indicates noise which is frequency shifted by the modulation frequency and the factor of square root 2 arises from the synchronous demodulation.

For sufficiently small ε and ϕ, the measured angle, ϕ_m, derived from this signal will be

$$\phi_m = \frac{s}{2A^2\varepsilon} \approx \phi + \frac{\sigma\{\omega_m\}}{2\sqrt{2}\,A^2\varepsilon} \tag{3}$$

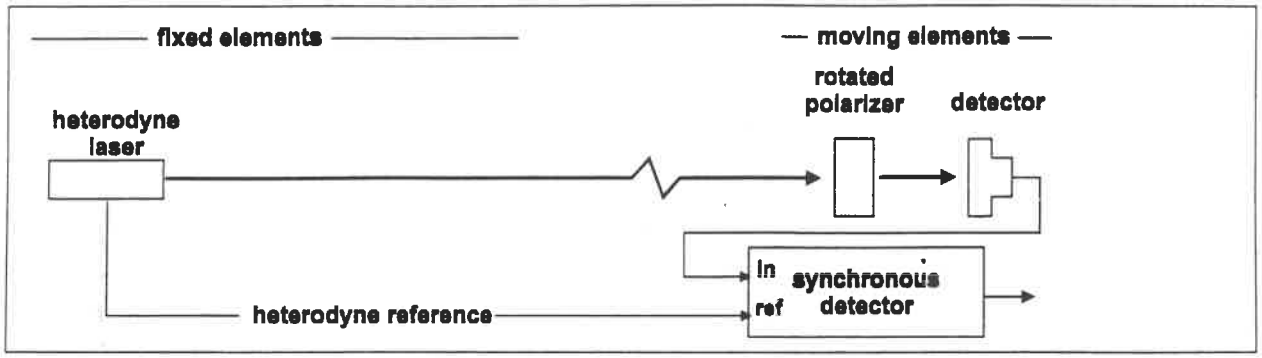

Figure 2 Heterodyne roll detector

A polarization-based measurement of rotation may also be made using a polarization analyzer and a two-color laser source of the sort used for conventional heterodyne distance measuring interferometery.[4] Such a configuration is shown schematically in figure 2. In this case, the beam of intensity $\mathbf{A^2}$ is partitioned between s- and p-polarized beams with amplitude $\mathbf{A/\sqrt{2}}$ and optical frequencies ω_1 and ω_2. If a polarization analyzer is placed at rotation angle ϕ with respect to the plane of p-polarization then the transmitted wave has amplitude and power ($\omega_m = \omega_1 - \omega_2$)

$$\begin{aligned} A_t &= \frac{A}{\sqrt{2}}(\sin\phi e^{i\omega_1 t} + \cos\phi e^{i\omega_2 t}) \\ I_t &= |A_t|^2 = \frac{A^2}{2}(1 + \sin 2\phi \cos\omega_m t) \end{aligned} \tag{4}$$

Adding detector noise-equivalent-power and applying the same small angle and synchronous demodulation assumptions leading to eq (3) produces the analogous result

$$\phi_m = \phi + \frac{\sigma\{\omega_m\}}{\sqrt{2}\,A^2} \tag{5}$$

While the heterodyne technique appears to have a advantage in realizable sensitivity, it suffers from a larger shot noise component due to the DC signal on which the modulation occurs. This shot noise is approximately given by the expression[5]

$$\sigma_{shot} = A\sqrt{\frac{h\nu}{\eta}} \tag{6}$$

where $\mathbf{h}$ is Plank's constant, ν is the optical frequency of the photon and η is the quantum efficiency of the photodetector. For a typical photodetector with $5\text{x}10^{-14}$ watt/$\sqrt{\text{Hz}}$ noise-equivalent-power, and 0.74 quantum efficiency at 670 nm wavelength[6], the equivalent angle noise for both methods is shown in figure 3. While the actively rotated system shows a lower noise limit in the region of common laser source power (greater than 50 microwatt), both methods appear capable of achieving noise less than 0.1 microradian/$\sqrt{\text{Hz}}$. Experimental measurements of a heterodyne roll detector using a 50 microwatt beam at 633 nm wavelength and a somewhat noisier detector have yielded an angle noise density of 1

microradian/√Hz, in approximate agreement with the calculated limit.

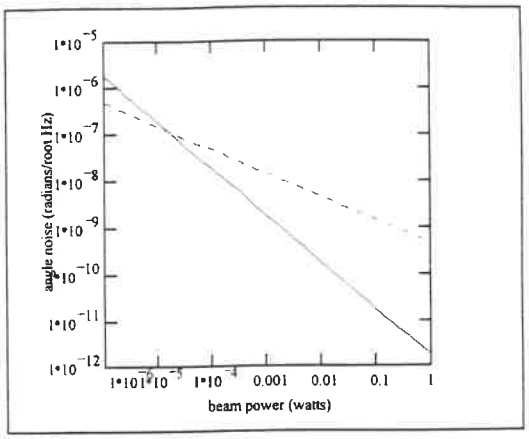

Figure 3 Photodetector limits to roll noise for modulated (solid) and heterodyne (dotted) detection methods

Straightness-roll coupling

Systematic errors in polarization-based roll measurement can also arise from coupling between straightness and roll due to imperfect performance of the polarization analyzing optics used. The overall performance of a roll measurement instrument based on a polarized beam reference will be more strongly limited by this error than the extinction ratio of the polarizers used. This coupling between polarization axis and position may be reduced by employing very high-precision polarizers, but at the expense of increased instrument cost.

To quantify this coupling, we have measured polarization axis variation as a function of position in two different kinds of polarizers: a low-cost polymeric sheet polarizer and a high-quality Glan-Thompson prism polarizer. The measurement method used is an adaptation of the well-known straightedge reversal technique[7] used to separate straightedge errors from axis motion errors. Using the roll detector shown in figure 1, the angle of the analyzer polarization axis with respect to the source is measured as a function of position, **x**, along an axis perpendicular to the optical axis of the system. This measurement reflects the sum of polarizer and positioning slide pitch errors.

$$\phi_+(x) = \phi_p(x) + \phi_s(x) \tag{7}$$

The polarizer is then rotated 180 degrees about an axis parallel to the x-axis and passing through the midplane of the polarizer and the system optical axis, reversing the entrance and exit faces of the polarizer while leaving the correlation between slide position and spot position on the polarizer unchanged. In this orientation, the sign of the polarizer error contribution is reversed, so that a second measurement of polarization axis yields the composite value

$$\phi_-(x) = -\phi_p(x) + \phi_s(x) \tag{8}$$

Given these functions, it is straightforward to calculate both the slide error and the polarization analyzer axis error

$$\begin{aligned} \phi_p(x) &= \tfrac{1}{2}(\phi_+(x) - \phi_-(x)) \\ \phi_s(x) &= \tfrac{1}{2}(\phi_+(x) + \phi_-(x)) \end{aligned} \tag{9}$$

The results of these measurements over a 4 mm region of the Glan-Thompson polarizer are shown in figures 4 and 5. For comparison purposes, the slide pitch error was measured independently using a Renishaw angle interferometer.

Measurements were also made over a larger region of a low-cost polymer sheet polarizer. The polarization axis variation of the sheet polarizer is shown in figure 6. The greater variability of the sheet polarizer is readily apparent. However, it should be noted that there are limited regions in the sheet polarizer over which the variation in polarization axis is substantially less than the average value for the range. For some applications, the use of careful mapping and region selection would allow the use of sheet polarizers in roll measurement devices at a substantial reduction in component cost.

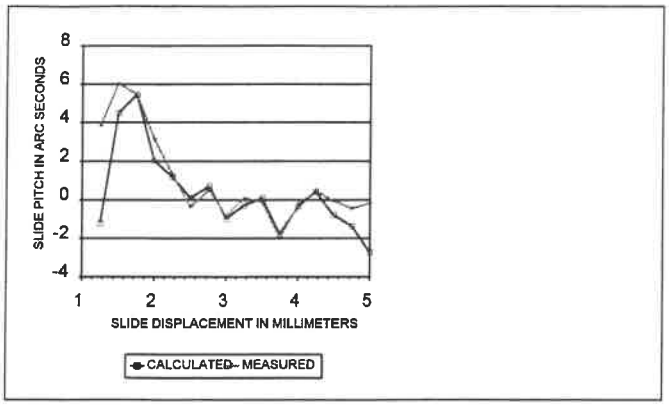

Figure 4 Measured slide pitch using interferometer (measured) and polarization axis (calculated)

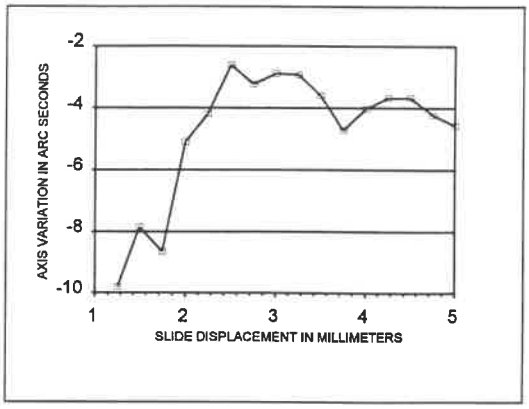

Figure 5 Measured polarization axis variation for Glan-Thompson polarizer

Summary

The average polarization axis of an optical beam may be used as an effective reference for roll measurement. Both explicit modulation of the axis of a reference beam or the modulation which results from the frequency difference of a heterodyne laser beam may be used to derive a measurement of relative changes in the axis direction by synchronous demodulation of transmitted intensity. Such a measurement technique is independent of low-frequency fluctuations of the beam or electronics, and exhibits a noise limit less than 1 microradian/√Hz for practical choices of lasers and detectors.

Systematic errors arising for coupling between straightness of travel of the measurement head and polarization axis variations in the analyzer have been measured for Glan-Thompson and polymer sheet polarizers. While the sheet polarizers show substantially greater variation of axis direction with position, some restricted regions show more than an order of magnitude smaller errors than the average variation for the polarizer.

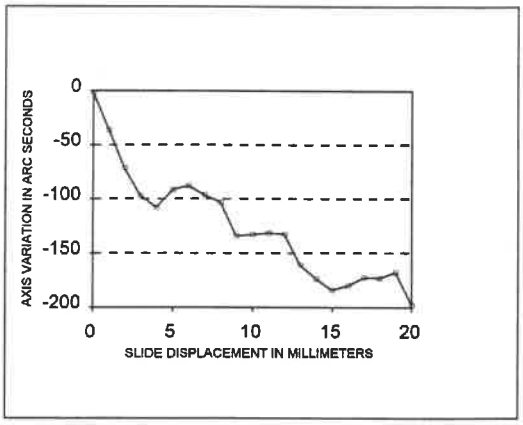

Figure 6 Measured polarization axis variation for sheet polarizer

References

1. *Methods for Performance Evaluation of Computer Numerically Controlled Machining Centers*, ASME B5.54-1992, American Society of Mechanical Engineers, 1993.
2. Hocken, Raja, Caskey, Fang, Hurst, Kumaran, Shelnutt, Nicholson, Suter, Trumper and Poovey, "Research in Precision Engineering," *Proceedings of the 1993 NSF Design and Manufacturing Systems Conference*, 1993.
3. Z. Fang, *Precision Laser Roll Detector for Instrument and Machine Tool Metrology*, PhD dissertation, Tianjin University, 1993.
4. C. R. Steinmetz, "Sub-micron position measurement and control on precision machine tools with laser interferometry", *Precision Engineering* **12** 1, 12-24 (1990).
5. P.H. Sydenham (editor), *Handbook of Measurement Science Vol 2*, John Wiley and Sons, 1983.
6. BKC Semiconductors BKCP 1043 PV-B diode, catalog values.
7. ASME B5.54-1992 *op. cit.*

Straightedge Metrology in a Wet Environment

Scott B. Peirce, Daniel B. DeBra
Department of Aeronautics and Astronautics
Stanford University, Stanford, CA

Abstract
We have been developing actuation and sensing techniques based on quiet hydraulics to take advantage of the improved thermal control possible with hydraulic technology. The devices are designed to operate at low Reynolds number to avoid turbulence which could disturb the machine function. This paper describes a new method of non-contacting straightedge detection, called a "differential oil gauge." We are integrating the technique into our quiet hydraulics testbed to correct for motion of the carriages. The actuation is provided by slideway bearings which modulate their gap as the means of non-straightness and yaw correction.

Differential Oil Gauge Design
Since no slideway is perfectly straight, there must be provision for measuring and correcting error motion if additional accuracy is needed. We are developing and have built a novel hydraulic sensor for measuring non-straightness and yaw called a "differential oil gauge". A differential oil gage can be thought of as a pair of opposed externally pressurized bearings. There is an external resistance between the supply and the pocket and a variable resistance to flow between the lands and the surface of the straightedge. The resistance is a function of the gap, h, between the lands and the surface of the straightedge. By measuring the differential pressure between the two pockets over a small range of motion, one can arrive at a linearized relationship with the deviation of the head from the nominal centered position (See Figure 1). A differential oil gauge measurement has no probe contact: There is neither lift off nor surface contamination. Furthermore, since the oil gauge measurement averages over the straightedge surface, sensitivity to errors with short correlation distance is reduced.

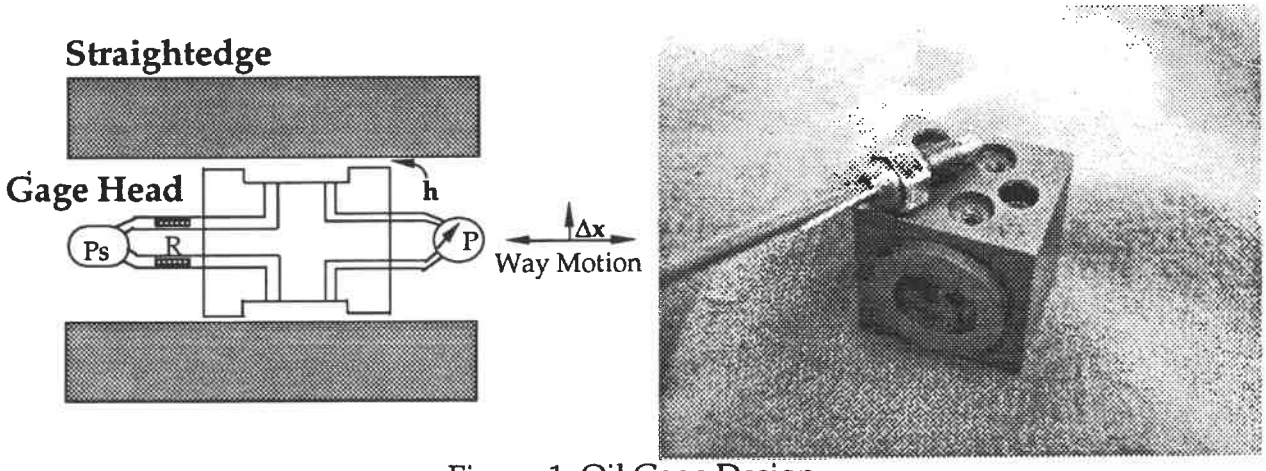

Figure 1: Oil Gage Design

While the sensor uses the same technology as an externally pressurized bearing, its function and requirements are much different. The oil gage should have low stiffness and net force levels in order to minimize the disturbances to the rest of the system. However the net force is also proportional to the signal sensitivity so we must be careful not to throw out the signal with the disturbance. With the geometry of our initial design, we have experimentally measured a sensitivity of 1.1 psi/μm (7.55 GPa/m) and a stiffness of 2.07 MN/m. The force levels can be reduced in later designs by one or more of three approaches: reducing the area, reversal with the forces modeled, and force cancellation. The larger forces in the prototype are more appropriate for evaluating their effect. Although it is possible with brute force designs to make the machine tool extremely stiff, this is not a practical solution and we will make future units with smaller areas. We are studying reversal methods in the presence of a force with the current design.

Initial evaluations of the differential oil gauge straightedge detector are consistent with the theoretical model on which the design is based (See Figure 2). This technology has the potential of being both more robust and less expensive than the use of LVDT's or optical devices as straightedge sensors in a oil shower environment.

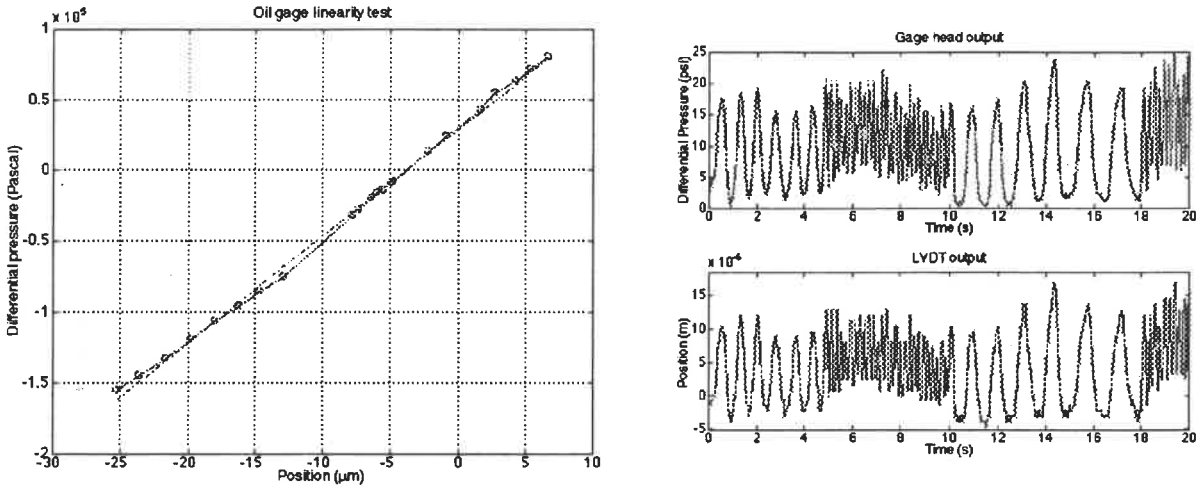

Figure 2: Experimental Data from Prototype Oil Gauge

We are also developing a compensated detector which maintains high signal sensitivity but cancels the force through a unique compensating geometry. The new design uses two bearing surfaces per side instead of one and has additional resistive connections between the two sides. This design is still in the process of being developed and evaluated experimentally.

Straightness and Yaw Actuation

The correction of non-straightness could be done by the machine tool controller, but there are advantages in correcting the error in the ways. For example, the controller is simpler and one can utilize a commercial unit without modification. We vary the

external resistance of the externally compensated way bearings which allows us to modulate the gap and thus control the position of the ways. This is done at the front and rear for both sensing and correction, thus providing independent correction of non-straightness and yaw.

We have built hydraulic slideways based on Kraakman's [1969] design. Kraakman's slideway design results in a very compact carriage supported by externally pressurized hydrostatic bearings (see Figure 3). These slideways have a total travel of approximately 130 mm and have a built-in means of correction for non-straightness and yaw motion. As shown in the cross sectional view, the design incorporates an opposed pad caliper bearing. Two pairs of pads are actuated. One pair acts at the front of the carriage and one at the rear. A lateral translation of the carriage can be achieved by actuating these together and a small rotation can be achieved by actuation in opposition. The total range of motion available is ±30 μm about the nominal centered position. This range is sufficient to deal with the expected non-straightness of the ways, which is on the order of ±5 μm. Differential flapper valves are used to control the fluid flow to the bearings. As assembled, the measured lateral stiffness is approximately 36 MN/m without feedback. [Peirce et al. 1992]

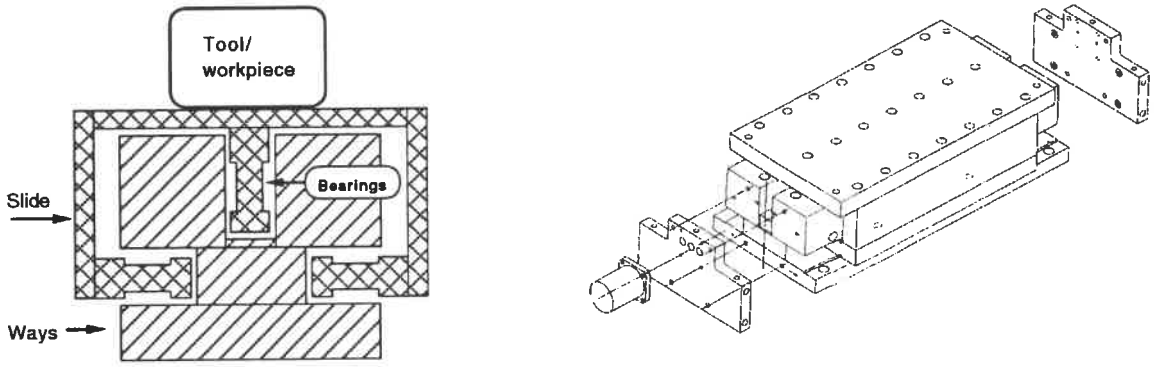

Figure 3: Kraakman Slideway Design

Straightness and Yaw Feedback

The straightness measurement system consists of a pair of differential oil gauges and a reference straightedge. The common-mode signal from the oil gauges provides information about the non-straightness and the differential signal provides information about the yaw in the motion of the carriage (Figure 4). This information will be used in conjunction with data from optical scales which will measure the long-stroke motion of the carriage. The reference straightedge is imperfect and must be mapped out using reversal. These data are then used in the form of a look-up table to correct the measurements as a function of the carriage position along the ways.

The feedback control of straightness and yaw is the next concern to be handled. A high bandwidth dedicated analog controller will command the actuators. The straightedge correction command input to this regulator will come from a digital controller. The controller uses the carriage position along the ways as entry to the look-up tables. The

look-up tables contain a map of the irregularities of the straightedge. External disturbances will be compensated for by the analog controller. The look-up table corrections will be handled by the lower bandwidth digital controller, which is adequate for the relatively slow feed rates required in precision turning or grinding.

This design is consistent with a fail-operate/fail-safe philosophy and serves to present a machine tool with perfect actuation to a generic commercial machine tool controller when the straightness and yaw control system is working. Without the computer commands, the system performance degrades to the errors inherent in the straightedge, and if the servos fail, the errors then become the errors in the carriage ways.

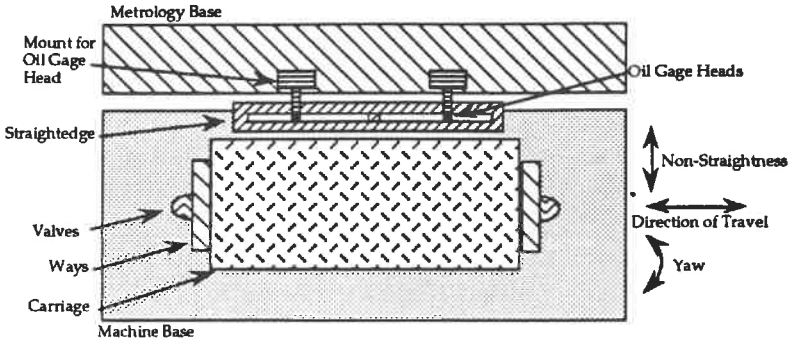

Figure 4: Straightness and Yaw System Schematic

Conclusion and Acknowledgements

The current oil gauge prototype performs within its design predictions. It has demonstrated a good signal to noise ratio and adequate linearity, but has a high stiffness. We are taking three approaches to solve this problem. The first is simply to reduce the area of the pockets. The second is to include a model of the net disturbance force in the straightedge reversal process. The third approach is a redesign of the oil gage sensor to minimize the net disturbance force.

We would like to acknowledge the support of the National Science Foundation (NSF-DDM-8914232) and the contributions of John Kietzman and Michael Wiedemann.

References

Bryan,J. B. . International Status of Thermal Error Research. *Keynote Paper, Annals of the CIRP Vol. 39/2.* 1990.

Campbell, P., John Kietzman, and Dennis Schissler, "External Resistance Network," ME119 Class Project, Stanford University, 1994.

Donaldson,R., *A Simple Method for Separating Spindle Error from Test Ball Roundness Error.* In CIRP Annals Vol. 21, 1972.

Kraakman,H. J. J. and J. G. C. deGast. A precision lathe with hydrostatic bearings and drive. *Philips Technical Review*, 30(5), 1969.

Peirce,S., Kahn,R, and Rischer D., *Design of an Oil Gage.* ME119 Class Project, Stanford University, 1992.

Peirce, S., Tran, H., Wiedemann, M., and DeBra,D., "Quiet Hydraulics for Ultraprecision Actuation,"ASPE 1994 Spring Topical Meeting, Tucson Az.

Improving the Machine Accuracy Through Machine Tool Metrology and Error Corrections

Jenq Shyong Chen and Cheng Chang Ling
Department of Mechanical Engineering
National Chung Cheng University, Taiwan, R. O. C.

Abstract Improving the positioning accuracy and contouring accuracy of a vertical machining center using the machine tool metrology and in-house error correction techniques has been studied. Contouring errors due to the servo lag and friction of servo-drive systems at high speed feedrates are calibrated using circular test and then reduced by tuning the servo driver the CNC controller to match the dynamic characteristics of the servomechanism and external load. It has been proved that feedforward velocity control and friction torque compensation are very effective to reduce the radial and protrusion errors during high speed contouring. The dynamic thermal errors generated during machining are predicted on line using a neural network based thermal error. Thermal error model is calibrated through a quick set-up and multiple D.O.F. measurement system consisting of spindle-mounted probe and artifacts where thermal effects from the spindle and three feed-drive systems can be calibrated at the same time. Positioning errors caused by static geometric errors and thermal effects are reduced in real time by a PC based software error compensation scheme which is integrated with the CNC controller through digital communication. Test results have shown that more than 70% of positioning errors and contouring errors has been reduced after compensation and servo-drive tuning.

Introduction To the required level of modern machine accuracy, a precision machine tool must get all supports from the mechanical design, manufacturing, CNC developments and servo-drive control techniques if optimum performance is to be achieved. The machine should have great design making the machine with the highness stiffness-to-weight ratio while maintaining good thermal and damping characteristics. Excellent manufacturing is also required to secure a right geometry and proper preloading of the machine. The NC controller should be able to correct for mechanical inaccuracies such as compensation for linear accuracy, backlash, and squareness errors. The servo-driver of the feed axes should perform accurate path-following, automatic acceleration/deceleration control in sudden starts and stops, and compensation for friction and spring effect due to external load. Machine accuracy, however, will also depend on the additional factors of environmental effects and operating methods which are not usually under the designer's control. Great machine accuracy also relies on applying in-house servo-drive tuning and software error compensation to correct errors produced from installation, environment and operating where the machine tool metrology plays a critical role.

Machine tool metrology serves the dual purpose of providing both error calibration and error correction. Calibration of a machine should include, at least, static geometric accuracy, quasistatic thermal effects, and dynamic contouring accuracy. For a multi-axis machine, calibration of geometric errors and thermal effects should include both the displacement accuracy of a slide along an axis and the geometric framework of three axes, i.e. the straightness, angular errors and squareness/parallelism. Geometry and thermal effects of a machine are important to the positioning accuracy and long-term repeatability in point-to-point cutting. On the other hand, the contouring test with which a cutter moves along a specific profile at specific feedrates by the simultaneous movement of two or more axes, is carried out to reveal problems in numerical control and servomechanism at high speed contouring.

Positioning errors caused by geometric and thermal errors can be corrected by software error compensation where the CNC controller of a machine injects additional positioning signals into the servo control loops of feed axes. Compensation of the angular errors and dynamic thermal errors, however, is difficult, because the resultant positioning errors at the cutting edge will depend on the machine's kinematic configuration and temperature status which vary in time during machining. By the aid of an external PC, researchers have achieved the real-time error

compensation by NC part program modification [3], analog feedback signal modification [4], and CNC error register modification [1,2]. Reported improvement by a factor of ten after compensation is not unusual on a turing or milling machine [1, 2, 3].

Contouring errors, by their dynamic nature, should be eliminated at servo control level to secure a highly accurate and fast-response feed system. Traditional servo drive controls, where position, speed and current are controlled based on feedback signals in a cascade form for each axis individually, have been shown to be insufficient for overcoming these problem at high-speed applications. More powerful servo control techniques, such as feedforward control [7] and cross-coupling control [5]. Feedforward control and nonlinear friction compensation features are now available on commercial CNC controllers [6].

Pre-Process Servo-Drive Tuning In the old day, contouring feedrates were slow enough to make the cutter motion a quasistatic problem so that the dynamics of the servomechanism can be ignored. At high speed machining, the servo lag of the servo-drive based only on the feedback control becomes unacceptable. Time delay due to exponential acceleration/deceleration control (ACC/DCC) after interpolator by the CNC controller also creates a path-following lag. Protrusions are usually formed on a workpiece at quadrant cutting due to the friction in servomechanism. In this research, the circular test using magnetic ball bar is applied to assess and diagnose the contouring errors of machine tools. Fig. 1. plots the circular tests of x and y axes under a 4000 mm/min feedrate.

Although the radial error caused by the servo lag can be reduced by increasing the gain of the servo drive, the concern in stability has prevented these measures. In machine tool applications, because the desired signals are known in advance, the controller does not have to be constrained to work only on the error signals from the feedback position and velocity. The feed forward velocity control is to pre-read the velocity of the desired signal and then feed an additional signal to the velocity loop to recover delays caused by dynamics of feed drives. Radial contouring errors caused by the exponential ACC/DCC control after interpolator can be improved if linear or bell-shape ACC/DCC control is used. Moreover, if the ACC/DCC control can be executed before interpolator, the radial error caused by the time delay can be avoided. Fig. 2 shows the circular test after feedforward control and ACC/DCC tuning.

When a feed axis reverses its direction of movement during arc cutting, the friction torque applied to a servo motor also reverses. The output torque generated by the servo motor, however, does not immediately reverse due to the integrator of the velocity control loop. Protrusion is then happened in a time in which the feed axis stops moving according to a command because the torque of the motor is less than the friction. The protrusion can be eliminated by a feedforward torque compensation function offered by the digital servo-driver of the CNC controller. The torque feed-forward control adds an appropriate value to the value specified by the velocity command and enable the integrator in a digital servo system to reverse at high-speed. The degree of torque compensation has been designed to consider variations in cutting speed and axis friction. Fig 3. plots the circular test after torque compensation.

In conclusion, traditional servo drive controls based on feedback signals in a cascade form have been shown to be insufficient for overcoming servo-lag, friction and external load at high-speed applications. It has been shown that a pre-process servo drive tuning can improve the contouring errors of the machine significantly. Reductions of the radial error from 46μm to 2μm, jump motion error from 10μm to 1μm and spike error from 28.7μm to 10μm at a 4000 mm/min feed rate test have been gained.

Real-Time Positioning Error Compensation Quasistatic geometric errors caused by thermal effects, in many cases, are considered as the largest error sources of positioning accuracy. To compensate for thermal errors in real time, involved works include an innovative calibration system for identifying multiple thermal error sources simultaneously, a neural network based technique for monitoring dynamic thermal errors on line, and a PC-based error compensation system to upgrade the CNC controller for correcting machine errors in real time.

For a vertical machining center, resultant thermal errors at the cutting edge are the combination of the expansion of the spindle, the distortion of the cantilever arm, the expansion of three leadscrew and the distortion of the machine column (Fig. 4). These error sources have different thermal response characteristics highly dependent on cutting conditions. In this research, a quick set-up and multiple D.O.F. measurement system consisting of an on-machine probe and artifacts has been developed to accelerate and simplify the thermal error calibration. Seven measurement points scattered over the entire working zone are designed to calibrate the thermal effects at different cutting points. One point on the center of the working table is designed to calibrate the combined thermal effects at this particular cutting point. Other six points, which parallel to three feed axes, are designed to calibrate the thermal effects at near the start and end points of each travel. Thermal effects at any location of the working zone are linearly interpolated by these seven measurements. Feature of the calibration system is that thermal effects from the spindle and three feed-drive systems can be calibrated at the same time in one setup. Calibrating multiple errors simultaneously not only accelerates the thermal error calibration significantly but also enhances the calibration accuracy by considering the interaction effects among thermal error sources.

To monitor thermal errors on line, artificial neural network (ANN) based technique has been developed. An ANN based thermal error model has been established in advance by mapping thermal errors to temperature measurements at some critical points on machine structures. Measured temperatures, along with the thermal error model, then provide as a control signal for on-line thermal error prediction. One advantage of the ANN is that multiple thermal errors can be easily modeled together. That means all of the calibrated thermal error sources of a machine can be modeled and predicted with only one ANN model. In this research, a three-layer backpropagation network has been develop to model the calibrated thermal effects from the spindle and three feed-drive systems. The ANN thermal error model has been obtained by a supervised backpropogation training algorithm where a training set of data at several cutting conditions were collected. Test result has shown that the ANN not only fits the data set well but also can predict thermal effects well even when new cutting conditions not included in the learning set has been conducted (see Fig. 5).

To upgrade the CNC controller for real-time error compensation, a PC based compensation controller has been developed and integrated with the CNC controller through digital communication. That means machine errors can be compensated for in real time without any hardware modification to the hardware of the machine and CNC controller. Fig. 6 plots the architecture of the compensation controller. Positions of three machine slides and temperature status of the machine are monitored on line by the compensation controller. The resultant positioning errors of any cutting point within the working zone can be calculated through an error synthesis module. The PC then feeds the compensation value into the CNC controller in real time through the digital I/O communication port of the PLC card. Manipulated by the PLC control software, these compensation values are continuously put into the coordinate reference registers of the machine axes. According to the specifications of the FANUC 0M controller, the compensation of three axes can be done by 48 ms which is fast enough for real-time thermal error compensation. Fig. 7 shows that the resultant thermal drifts of the cutting edge at the z direction have been improved from 40 μm to within 5μm after compensation.

In conclusion, the study has demonstrated that the machine accuracy can be much enhanced through software error compensation. Test result shows that a 70 to 90% reduction of thermal errors have been gained after compensation.

References

[1]. Chen, J. S., Yuan, J. X., Ni, J., and Wu, S. M., "Real-time Compensation of Time-variant Volumetric Error on a Machining Center", ASME Transactions, Journal of Engineering for Industry, Vol. 115, Nov. 1993

[2]. Donmez, M. A. et al., "A general methodology for machine tool accuracy enhancement by error compensation", Precision engineering, Oct. 1986

[3]. Fan, K. C., Lin, J. F., and Lu, S. S., "Measurement and Compensation of Thermal Error on a Machining Center", 29 MATADOR Conf., England, April/1992
[4]. Gavin, R., and Yee, K., "Implementing Error Compensation on Machine Tool", Quality control/Quality Improvement, Southern Manufacturing Technology Conference, 1989
[5]. Koren, Y., and Lo, C. C., "Variable-Gain Cross-Coupling Controller for Contouring", Annals of the CIRP, Vol. 40/1/1991
[6]. Sakamoto, K., Matsubara, S., and Iwashita, Y., "High-Precision Digital Servo Control", FANUC Tech. Rev., Jan 1991
[7]. Tung, D. E., Anwar, G., and Tomizuka, M., "Low Velocity Friction Compensation and Feedforward Solution Based on Repetitive Control", ASME Transactions, Journal of Dynamic Systems, Measurement, and Control, June 1993

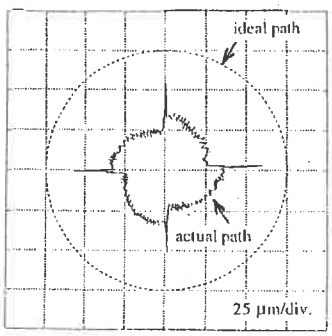

Fig. 1: Before servo tuning

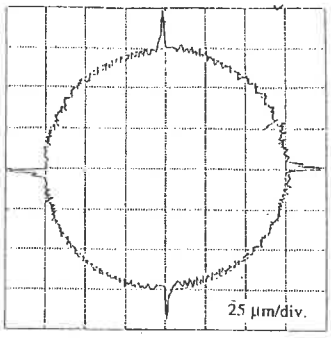

Fig. 2: After feedforward control

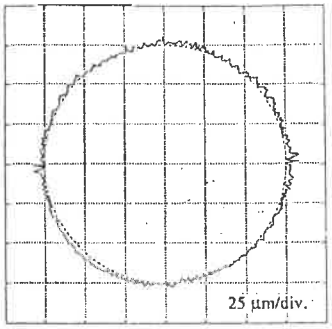

Fig. 3: After friction compensation

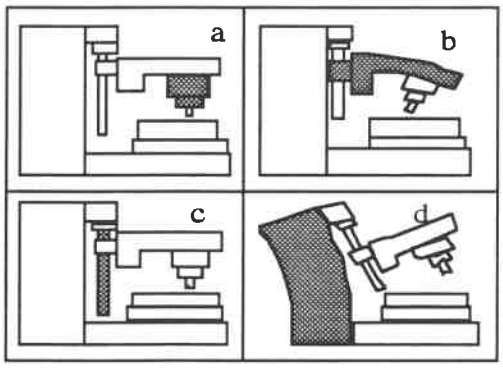

Fig. 4: Thermal error sources

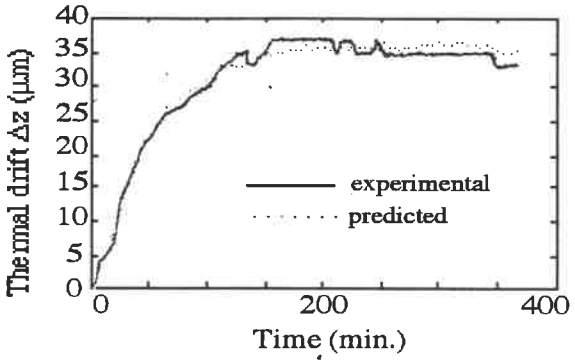

Fig. 5: Predicted result of the ANN model

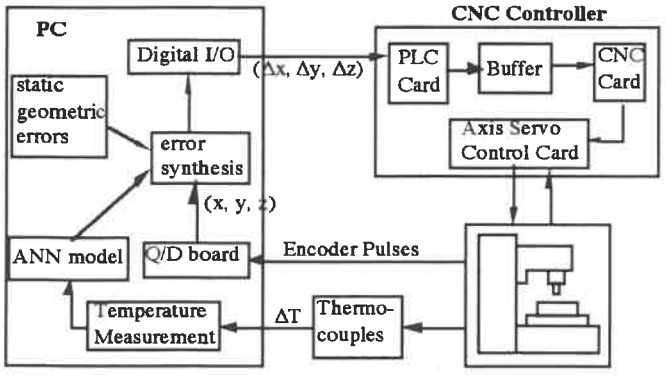

Fig. 6: Architecture of the compensation controller

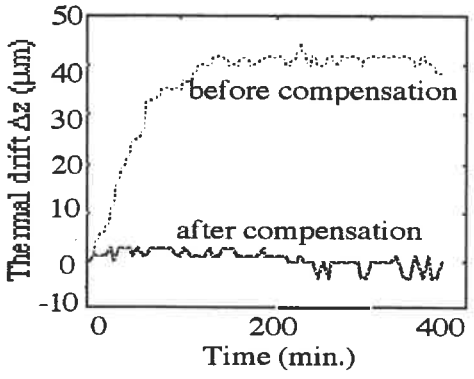

Fig. 7: Before and after compensation

DRESSING OF METAL BONDED DIAMOND WHEEL BY USE OF LOOSE ABRASIVE LAPPING FOR DUCTILE MODE GRINDING OF BRITTLE MATERIALS
-- CONTROL TECHNOLOGY OF ACTIVE GRAIN PROTRUSION --

Fumio INABA, Akira KANAI, Masakazu MIYASHITA
Ashikaga Institute of Technology Mechanical Engineering Dept.
268-1 Ohmae-Cho Ashikaga-City Tochigi Pref. 326 JAPAN

1. Introduction
For replacing the traditional abrasive machining processes such as lapping and polishing in the field of ultraprecision machining, the grinding process has to realize the material removal resolution corresponding to them. The material removal resolution with the grinding wheel as a multi-point cutting tool is a resolution of grain depth of cut. The requirement for achieving ductile mode grinding of brittle materials is to keep the resolution of grain depth of cut no more than the ductile to brittle transition in uncut chip thickness.
Generally, there are the following two ways for upgrading the resolution of grain depth of cut:
(1) to apply finer abrasive grain wheel, or
(2) to make height distribution of cutting edges on active wheel surface smaller.
For improving the resolution of grain depth of cut with the second way, the following processes of truing and dressing are considered:
(1) truing as ductile mode machining of grinding wheel to remove random distribution of cutting height,
(2) dressing realizing specified protrusion height of cutting edges to give uniformity of chip pockets over the active wheel surface and to keep reduction of the grain hold strength minimum.
The present paper aims at developing the dressing technology for achieving the above function.

2. Proposal of loose abrasive dressing for controlling protrusion height of cutting edges
For realizing ductile mode grinding of brittle materials, it has to keep the grain depth of cut smaller than the ductile to brittle transition in uncut chip thickness d_c, for example, 100nm. Height distribution of cutting edges on the conventional wheel surface is random and far wider comparing with the d_c. In such case, the grain depth of cut is dominated by the height distribution Δh and the maximum value d_{gmax}:

$$d_{gmax} \leq \Delta h$$

Therefore, in truing process the wheel surface has to be machined in the ductile mode to realize the random distribution of cutting heights smaller than the d_c. Fig.1 shows an example of the ground surfaces of diamond pellets for this purpose with the newly designed ultraprecision surface grinding machine. The function of dressing process is to remove only the bond material for giving chip pockets uniformly without the resulted deterioration of cutting height distribution. That is , it is required to develop the dressing technology capable to give a specified protrusion height of cutting edges.
In this paper, the loose abrasive dressing technology is proposed for this purpose.
Criterion of the dressing performance is:
(1) how to achieve a specified protrusion height of cutting edges, and
(2) how to remove only bonding material without any damage on cutting edges.
From a series of the experimental analyses, a guideline to the optimum conditions to achieve the above performance of the loose abrasive dressing is introduced in the following.

3. Experimental conditions
Metal bond diamond pellets instead of diamond grinding wheels are dressed with loose abrasive grains. The experimental conditions are shown on Table 1. As for dressing performance, the protrusion height of cutting edges is measured with the contact stylus profilometer and the chipping and the dropping out of the cutting edges are observed with SEM images. The test examples are shown in Fig.2.

4. Experimental result and Consideration

4.1 Protrusion height of cutting edges

Fig.3 shows the lapping distance to protrusion height of cutting edges relationship for the case of loose abrasive dressing with five different grain sizes of SiC abrasives. In the range of experiments, the protrusion height has a stationary value, which is approximately same as the grain size of lapping powders. However, in case of the diamond pellet with the diamond grains of 20μm in diameter, it is observed that the protrusion height can not arrive at the stationary one similar to the size of lapping powders as shown in Fig.4, in which the grain size of lapping powders is similar to the one of diamonds. It is caused because the grain size of lapping powder is not sufficiently small comparing with the distance between the cutting edges on the pellet.

From Fig.3 and 4, it is generally concluded as follows:

if the grain size of lapping powders is selected sufficiently small comparing with the distance between the cutting edges on the pellet, the protrusion height of cutting edges with the loose abrasive dressing has a stationary value approximately equal to the grain size of the lapping powders.

4.2 Damage of cutting edges

Damage of the cutting edges caused by the dressing is classified into chipping and dropping out of the cutting edge. The typical examples of damage are shown in Fig.5 and 6. The chipping and the dropping out of the cutting edges observed with SEM images are additionally indicated by the black marks to Fig.3 as shown in Fig.7. In the case of the size of the lapping powders to the one of the cutting edges, the dropping out starts before the protrusion height arriving at the stationary state. And in the case of the grain size of the lapping powders being no more than one third of the one of the cutting edges, continued dressing causes the damage of cutting edges after the protrusion height arriving at the stationary state. Therefore, the lapping distance is preferable to be limited. One of the predominant parameters of the damage of the cutting edges is the lapping pressure. Fig.8 shows the influence of lapping pressure on the damage. The higher lapping pressure causes the damage at the shorter lapping distance. In the range of the experiments, 10 to 20kPa is moderate.

Next, the lapping abrasive grain is also one of the predominant parameters. Fig.9 is a comparison of the effect of the abrasive grain on the damage between SiC and Al_2O_3. The figure shows that Al_2O_3 is preferable to SiC because of the difference of hardness.

5. Guidelines to loose abrasive dressing

The guidelines to the optimum conditions of the dressing performance are:

(1) abrasive grain with lower hardness is preferable among abrasives suitable to remove bond material of grinding wheel,

(2) grain size of lapping powders is preferable to be sufficiently small comparing with diamond cutting edges as far as specified protrusion height allows,

(3) lapping pressure has much effect on damage of cutting edges and 10 to 20kPa is preferable in practice, and

(4) after protrusion height arriving at stationary state continued dressing causes damage of cutting edges, and lapping distance is to be limited to the minimum.

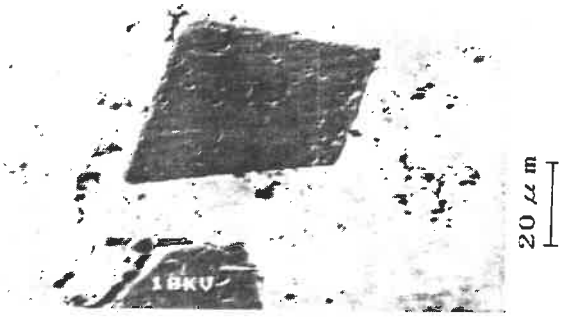

Fig.1 Diamond grains after truing with ultraprecision surface grinder

Grinding wheel	:SD230N75M
Wheel speed	:13m/sec
Table speed max	:3.8m/min
Grinding method	:Plunge
Feed rate	:0.1μm/work rev

Table 1 Experimental Conditions

Lapping Machine	•Type	: Two-lap lapping machine
	•Tool	:Lapping plates of cast iron
Lapping Conditions	•Lapping plate	: ϕ 180 × ϕ 80
	•Lapping pressure	:10kPa, 20kPa, 40kpa, 80kpa
	•Lapping speed	:6.5m/min (in Average)
Diamond Pellet	•Pellet size	: ϕ 20 × 3mm
	•Grain size	:10 μm, 20 μm, 60 μm diameter
	•Bond	:Bronze
	•Concentration	:75
Abrasive Grain	•Material	:Silicon carbide, Alumina abrasive
	•Grain size	:60 μm, 30 μm, 20 μm, 11.5 μm, 5.5 μm, 3 μm
	•Slurry	:90%w Water + 10%w Abrasive

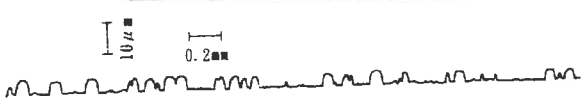

(a)Lapping distance 100m

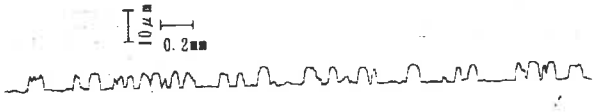

(b)Lapping distance 275m

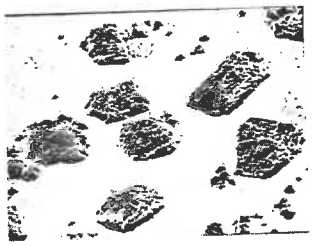

Abrasive size :5.5μm
Lapping pressure :10kPa

100 μm

Fig.2 Surface profiles and SEM images

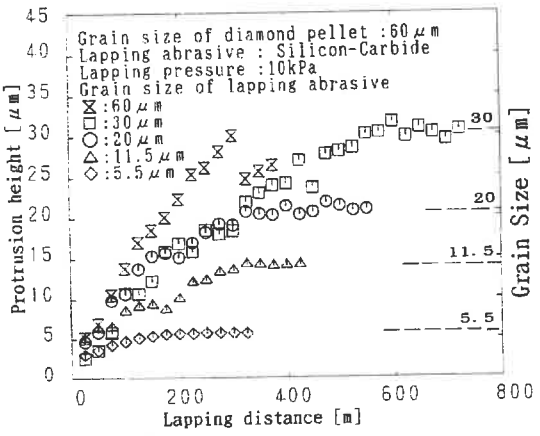

Fig.3 Influence of abrasive size on protrusion height

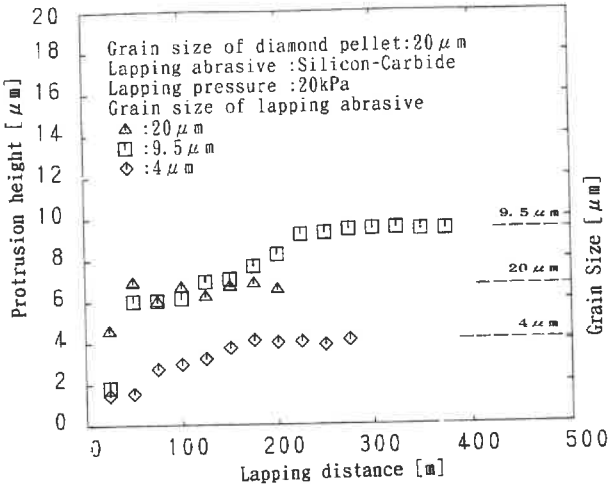

Fig.4 Influence of abrasive size on protrution height

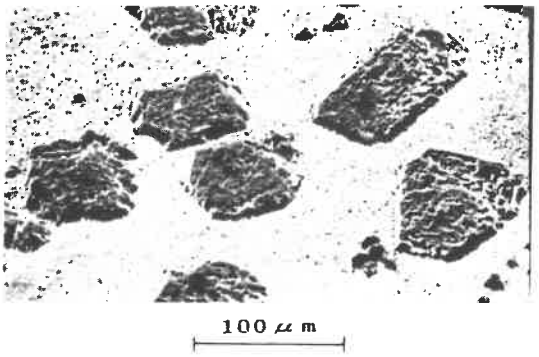

Fig.5 Chipping of cutting edges

Grain size of pellet :60μm
Abrasive grain size :5.5μm
Abrasive material :SiC
Lapping distance :275m
Lapping pressure :10kPa

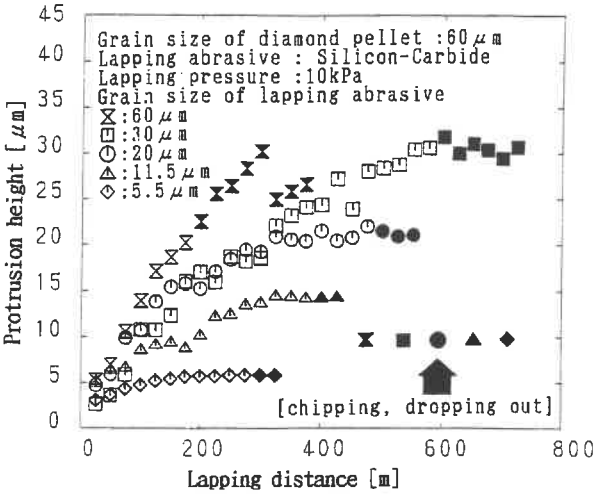

Fig.7 Optimum conditions of lapping distance

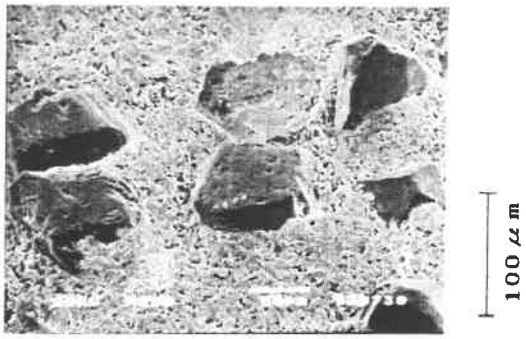

Fig.6 Dropping out of cutting edges

Grain size of pellet :60μm
Abrasive grain size :20μm
Abrasive material :SiC
Lapping distance :100m
Lapping pressure :40kPa

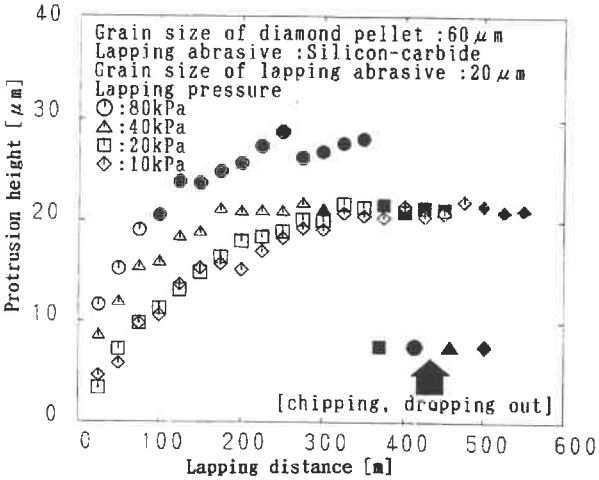

Fig.8 Optimum conditions of lapping pressure

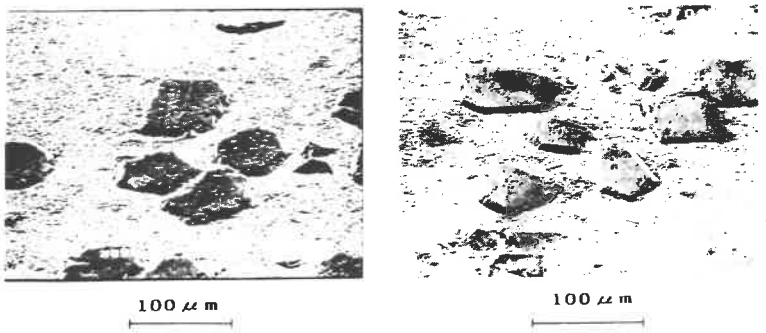

(a) SiC Slurry (b) Al_2O_3 Slurry

Fig.9 Comparison of abrasive materials

Grain size of pellet :60μm
Grain size of abrasive:5.5μm
Lapping distance :100m
Lapping pressure :10kPa

Materials Effects in Grinding Response of Hot Isostatically Pressed Silicon Nitrides

Chris J. Evans, Lewis K. Ives, Robert S. Polvani, and Said Jahanmir

National Institute of Standards and Technology
Gaithersburg, Md 20899

Keywords: grinding, ductile grinding, silicon nitride

Most research and development in ductile regime grinding has focussed on issues such as process parameters, machine design, wheel selection, dressing and truing. The literature frequently describes work materials simply with generic descriptions such as "HIPped silicon nitride". The purpose of this paper is first to illustrate the importance of materials characteristics and secondly to present a simple methodology for their study.

Surface condition of ground ceramics is affected by an array of factors. As an alternative to large numbers of repetitions, we have chosen to grind samples of various materials simultaneously. In surface grinding, samples are arranged in line on the table, while on an aspheric generator the samples are arranged azimuthally on the face plate. Thus if there is no variation in the sample characteristic of interest in the direction normal to the grinding lay, then differences between samples (ie along the grinding lay) cannot be attributed to process variations.

Samples of several hot isostatically pressed silicon nitrides have been ground under a variety of conditions using this methodology and the resulting surface characteristics compared with variations that would be expected from bulk materials properties. Bifano *et al* have shown for a number of materials that surface morphology correlate with a critical depth of cut given by:

$$d_c = (E/H)(K_{Ic}/H)^2$$

where E is Young's modulus, K_{Ic} is fracture toughness and H is hardness. The materials used in this study have a reasonable range of values of d_c . In processes giving reasonably ductile surfaces, percentage of areal fracture and fracture size show no correlation with d_c.

MECHANICAL, THERMAL, DIFFUSIONAL, AND GEOMETRICAL LENGTH SCALES IN POLISHING AND GRINDING

J. C. Lambropoulos

Department of Mechanical Engineering & Center for Optics Manufacturing (COM)
University of Rochester, Rochester, NY 14627

ABSTRACT: Deterministic microgrinding and polishing are processes characterized by a complex interaction of mechanical, thermal, and diffusional length scales. There are also imposed axial and transverse length scales, arising from the infeed rate or the abrasive/surface contact size

Mechanical length scales describe the elastic, plastic, or cracking mode of deformation of the optical surface. The presence of friction between abrasive and glass gives rise to a thin, localized layer of large tensile stresses and hydrostatic tension underneath an abrasive particle. The extent of the region in tension is another mechanical length scale which is controlled by the size of the contact between abrasive and glass and by the coefficient of friction. The diffusional length scale is described as a competition between diffusion of water in the glass surface, which is strongly influenced by temperature and stress, and the rate of material removal. The thermal length scales are described in terms of the Peclet numbers for the optical surface (usually very large for typical operating conditions) and for the bound abrasive medium (considerably lower).

I. ELASTIC LENGTH SCALES

For simplicity, we consider a simple model for the contact between an abrasive particle and the surface of a brittle solid [Cook, 1990]. Conical shapes have also been examined, leading to significantly more complicated expressions for the stresses [Hanson, 1993]. The abrasive particle is assumed to be a sphere of radius R, pressed into contact (total normal force P and tangential or shear force $Q = \mu P$, μ being the coefficient of friction) with an isotropic, elastic half-space. The area of contact, a circle of radius a, is determined by using Hertz contact theory [Johnson, 1985]. To a good degree of approximation, the contact size a is determined only by the normal force P, and is thus independent of the coefficient of friction. The relevant length scales are the size $a = (3\ P\ R\ /\ 4\ E^*)^{1/3}$ of the contact region, and the resulting depth of penetration $\Delta = a^2/R = (9\ P^2\ /\ 16\ R\ E^{*2})^{1/3}$ of the indenting particle into the brittle surface, where $1/E^* = (1-\nu_1^2)/E_1 + (1-\nu_2^2)/E_2$, with E_1 the Young's modulus of the abrasive particle, E_2 that of the optical component, and ν denotes the Poisson ratio [Johnson, 1985]. Since the pressure scales with the contact size a, the stress distribution within the elastic solid also scales with a.

The introduction of the coefficient of friction μ in the stress distribution near the contact region alters significantly the stress pattern [Hamilton, 1983], some features of which have been discussed by Lawn and Wilshaw [1975] and applied to polishing by Cook [1990]. Now, a large tensile stress parallel to the free surface of the half-space develops at the trailing edge of the abrasive particle. Fig. 1 shows the mean hydrostatic tension in the vicinity of the trailing edge, the maximum value of which depends linearly on μ, and Fig. 2 the variation of the spatial extent of tensile stress σ_{xx} on μ. A length scale of relevance in optics manufacturing is introduced via friction: the spatial extent of the region near the trailing edge of the particle under tensile stresses. Such tensile stresses enhance the brittle response of the solid at the expense of its elastic and plastic responses [Sharp et al., 1993].

II. ELASTIC–PLASTIC LENGTH SCALES

The measurement of the hardness by microindentation in many brittle optical solids exhibits the indentation size effect (ISE) in which the hardness increases as the applied load P or indentation diagonal D is diminished. Instead of describing the ISE by Meyer's law $H=A/D^n$, which does not allow the existence of a unique length scale, we use the form proposed by Li and Bradt [1992]

$$H=\frac{\alpha_1}{D}+\alpha_2=H_\infty\left(\frac{D_0}{D}+1\right)=H_\infty\left(\frac{L_{p,0}}{L_p}+1\right) \qquad (1)$$

where L_p is the depth of the residual impression (L_p = D/7 for the Vickers geometry). The material properties H_∞, D_0, and $L_{p,0}$ are the load independent hardness at large loads, the critical diagonal size, and the critical depth size below which the ISE dominates the hardness of the solid. Typical data from the literature, for example Bifano [1988], give values for D_0 in the range of 4-10 μm.

The previous analysis neglects the elastic spring-back accompanying the reduction of load from its maximum value at maximum penetration. Fig. 3 shows the results of finite element modeling of indentation using material constants typical of optical glass. It is seen that the maximum and residual penetrations are different, and that their relative difference increases at lower loads.

In addition to surface features of the plastically deformed zone, there is the elastic-plastic boundary, a location of high residual tensile stresses following unloading, where nucleation and growth of subsurface flaws occurs [Lawn and Evans, 1977]. Its radial distance b from the surface indentation site is found by using the model of an expanding spherical cavity in an infinite solid [Chiang et al., 1982]

$$\left(\frac{b}{a}\right) \approx \left(\frac{E}{H}\right)^m, \quad m = 0.4 - 0.5 \tag{2}$$

At low loads the response of the material is elastic-plastic. The model of Lawn et al. [1975] provides an estimate for the indentation size D that must be exceeded for cracking to be manifested as a deformation mechanism

$$D = \xi \left(\frac{K_c}{H}\right)^2 \tag{3}$$

where K_c is the fracture toughness of the material, and ξ a geometrical constant. This analysis, in spite of its simplifying assumptions that only a radial crack develops (i.e. $P \sim c^{3/2}$) and that the hardness is constant, clearly shows that at low loads or penetrations any brittle material will deform by plastic flow. Similar analyses have developed the concept of critical depth of cut dc, below which the material removal mechanism is by plastic deformation rather than microcracking [Bifano et al., 1991].

We have measured by microindentation the hardness H and fracture toughness K_c of many optical glasses and crystals. To emphasize the presence of length scales in correlating surface deformation features (such as the indentation diagonal D or residual depth L_p=D/7) we write

$$c = -c_0 + m D = c_0 \left(-1 + \frac{D}{D_*}\right) = c_0 \left(-1 + \frac{L_p}{L_{p,*}}\right) \tag{4}$$

D_* is the critical diagonal and $L_{p,*}$ the critical permanent depth below which no well-defined crack can be observed. High values of m = dc/dD imply a high sensitivity of the crack length c to the indentation diagonal D. In our measurements, m is in the range $1 < m < 3$, $5\ \mu m < c_0 < 25\ \mu m$, $1.5 < D_* < 15\ \mu m$, $0.2 < L_{p,*} < 2\ \mu m$.

III. CHEMOMECHANICAL LENGTH SCALES

The diffusivity D of water in glass is affected by stress and temperature, being higher for tensile stresses [Nogami and Tomozawa, 1984; Tomozawa and Tomozawa, 1989]

$$D = D_0 \exp\left[\frac{-\Delta E + \Delta V_D(\sigma_{kk}/3)}{R_g T}\right] \tag{5}$$

where D_0 is a pre-exponential, $\sigma_{kk}/3$ is the mean hydrostatic tension, R_g is the universal gas constant , and T is the absolute temperature. ΔE is the activation energy, and ΔV_D is the activation volume.

A model of steady-state uniaxial diffusion while the free surface (maintained at the water concentration c_0) is itself moving at the rate V_0 (the infeed rate), gives for the concentration c(x)

$$c(x, t) = c_0 \exp\left(-\frac{x - V_0 t}{D/V_0}\right) \tag{6}$$

The decay length scale for the water concentration profile into the glass surface is D/V_0. The stress under a sliding abrasive particle is on the order of the hardness of the glass, and tensile (due to friction), say in the range 0.2 to 0.8 GPa. With an infeed rate of 12 μm/min, we find that, for no rise in temperature, D/V_0 is from 1A to 1 μm, whereas for a 100 °K rise it is in the range 1A to 20 μm.

IV. THERMAL LENGTH SCALES

Since the temperature rise near the contact of an abrasive particle with an optical surface has a significant impact on the diffusion of water near that surface, we can determine the maximum temperature rise from [Tian and Kennedy, 1994]

$$\Delta T_{max} = \frac{\zeta \mu a p_{ave} U}{k_1 \sqrt{1.25+Pe_1} + k_2 \sqrt{1.25+Pe_2}} \tag{7}$$

where 1 and 2 denote the abrasive particle and optical material, ζ is a numerical factor (1.1-1.3 depending on the heat distribution during contact), a the radius of contact, p_{ave} the average contact pressure, U the relative velocity, k the thermal conductivity, and $Pe=Ua/2\kappa$ the Peclet number, $\kappa = k/(\rho c_p)$ being the thermal diffusivity.

Typically for microgrinding U = 40 m/s, a = 1 μm, for the glass ($\kappa = 6 \times 10^{-7}$ m^2/s) $Pe_2 >> 1$, whereas for single crystal diamond ($\kappa = 5 \times 10^{-4}$ m^2/s) $Pe_1 << 1$. Using $\mu = 0.3$, and $p_{ave} \approx H$ (say, 5 GPa), we find that $\Delta T_{max} \approx 60$ °K. A polycrystalline diamond, or other ceramic abrasives, would have a much lower thermal diffusivity κ, thus leading to even higher localized temperatures.

ACKNOWLEDGEMENTS: The author acknowledges the support and encouragement provided by the Manufacturing Sciences Group in the Center for Optics Manufacturing, and the support by the National Science Foundation under Grant MSM-8857096.

REFERENCES

T.G.Bifano, 1988, Ductile regime grinding of brittle materials, PhD thesis, North Carolina State University.

T.G. Bifano, T.A. Dow, and R.O. Scattergood, 1991, Ductile-regime grinding: A new technology for machining brittle materials, J. Engin. for Industry, Trans. ASME 113, 184-189.

S.S. Chiang, D.B. Marshall, and A.G. Evans, 1982, The response of solids to elastic/plastic indentation, I. Stresses and residual stresses, J. Appl. Phys. 53, 298-311.

L.M. Cook, 1990, Chemical processes in glass polishing, J. Non-Cryst. Solids 120, 152-171.

G.M. Hamilton, 1983, Explicit equations for the stresses beneath a sliding spherical contact, Proc. Instn Mech. Engineers, 197c, 53-59.

M.T. Hanson, 1993, The elastic field for a sliding conical punch on an isotropic half-space, J. Appl. Mech. 60, 557-559.

B.R. Lawn and A.G. Evans, 1977, A model for crack initiation in elastic/plastic indentation fields, J. Mater. Sci. 12, 2195-2199.

B. R. Lawn and R. Wilshaw, 1975, Review; Indentation fracture: principles and applications, J. Mater. Sci. 10, 1049-1081.

H. Li and R.C. Bradt, 1992, The indentation load/size effect and the measurement of the hardness of vitreous silica, J. Non-Crystall. Solids 146, 197-212.

M. Nogami and M. Tomozawa, 1984, Effect of stress on water diffusion in silica glass, J. Amer. Ceram. Soc. 67, 151-154.

S.J. Sharp, M.F. Ashby, and N.A. Fleck, 1993, Material response under static and sliding indentation loads, Acta metall. mater. 41, 685-692.

X. Tian and F.E. Kennedy, Jr., 1994, Maximum and average flash temperatures in sliding contacts, J. Tribology 116, 167-174.

H. Tomozawa and M. Tomozawa, 1989, Diffusion of water into a borosilicate glass, J. Non-Cryst. Solids 109, 311-317.

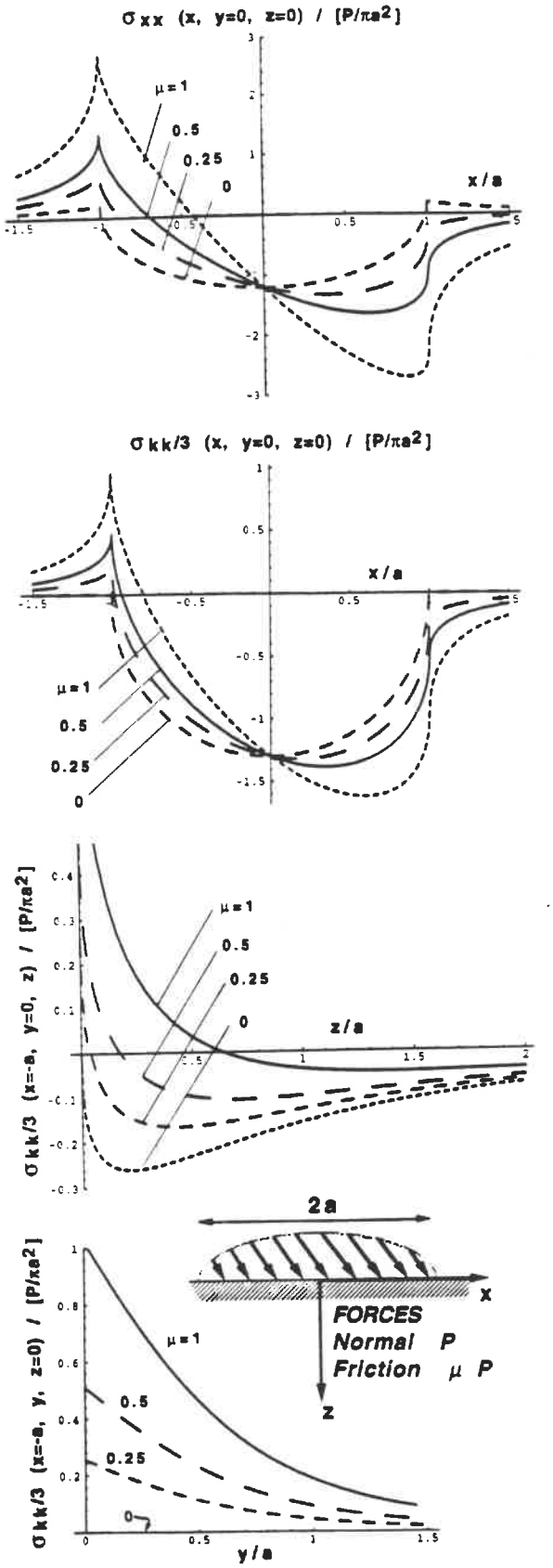

FIGURE 1. Variation of tensile stress σ_{xx} and mean hydrostatic tension $\sigma_{kk}/3$ near an abrasive particle sliding on a half-space (ν=0.25). $\sigma_{zz} = -(3P/2\pi)\sqrt{a^2-r^2}$, $\tau_{zx} = \mu\,\sigma_{zz}$, and $\tau_{zy} = 0$ for $r^2 = x^2+y^2 \le a^2$ at z=0.

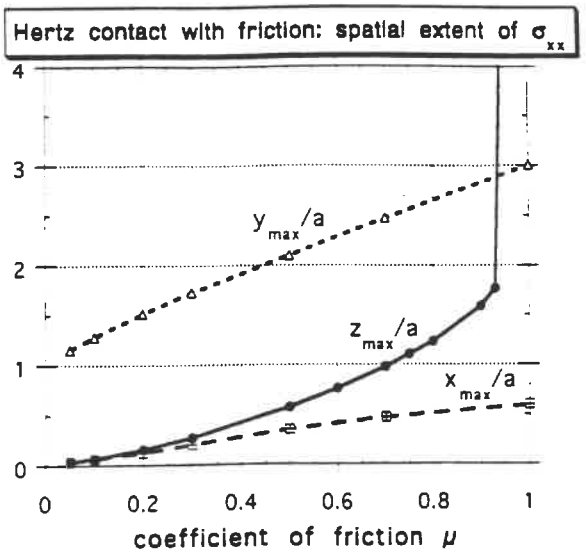

FIGURE 2. Spatial extent over which stresses σ_{xx} are tensile near sliding abrasive particle. x_{max} is along line (x, y=0, z=0), y_{max} along line (x=-a, y, z=0), and z_{max} along line (x=-a, y=0, z).

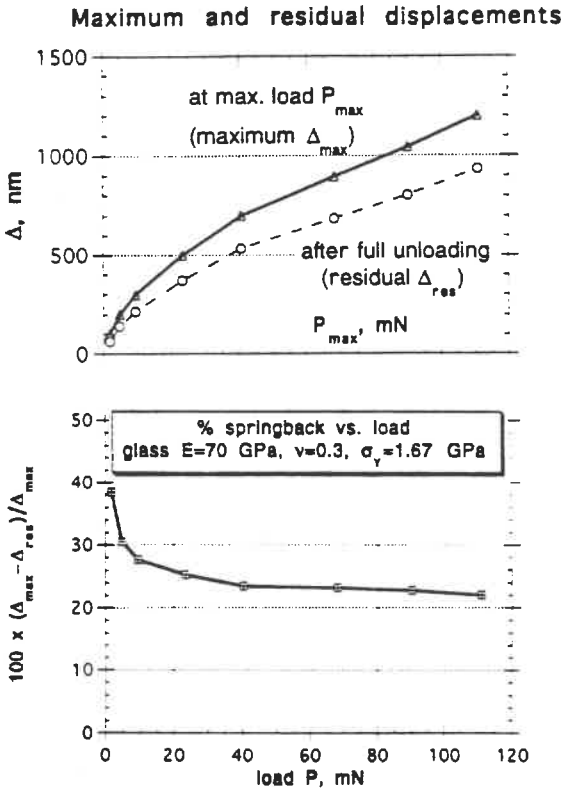

FIGURE 3. The maximum Δ_{max} and residual Δ_{res} displacements underneath a rigid indenter on glass (the uniaxial yield stress is σ_Y). The indenter is conical with a total cone angle of 120°, and radius of curvature of 1 μm at its tip.

MODELING THE WHEEL/WORK INTERFACE IN PRECISION GRINDING

Michele H. Miller, Thomas A. Dow
Precision Engineering Center, N. C. State University
Raleigh, NC 27695-7918

1 Introduction

Fixed abrasive grinding has an important role to play in the spectrum of precision finishing operations and is preferable to diamond turning or polishing for certain applications--for instance, machining an asphere into a brittle material. However, grinding brittle materials in the ductile regime requires careful selection and control of grinding conditions. The motivation for developing a model is to identify the factors at the wheel/work interface which influence the process and thereby develop guidelines for improving performance.

The critical depth of cut model[1], based on indentation fracture research, describes how the critical infeed for ductile grinding varies with workpiece properties but does not account for variable grinding wheel parameters. During one revolution, the grinding wheel does not remove material as a single chip. Multiple indentation-like events occur during a revolution, each with the potential of causing fracture. To account for variable grinding wheels, the basic material removal unit under consideration has been reduced from the volume removed during a wheel revolution to the volume removed by an individual cutting grain. A kinematic approach is used to identify the relationships between chip size and grinding wheel parameters.

2 Model

Simulation Program An algorithm was developed to simulate the kinematics of the plunge grinding process. The key geometric features of the process are represented in Figure 1. The grinding wheel has been "unwrapped," and the infeed/rev and wheel circumference form a slope which is similar to a broaching tool.

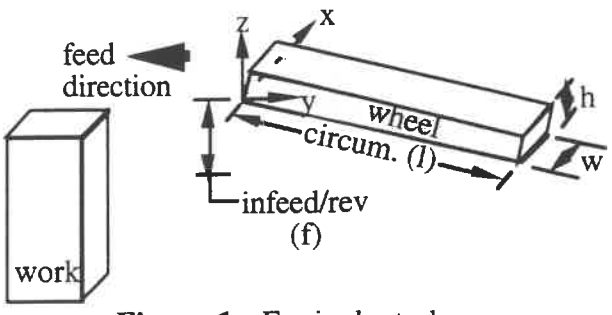

Figure 1: Equivalent plunge grinding geometry

All of the cutting grits are assumed to be spheres of radius r_g which are randomly distributed throughout the binder matrix. The number of potential cutting grits N (at a volume fraction f_v) in the wxl xh volume is then $(3f_v wlh)/(4\pi r_g^3)$.

The surface of the workpiece is represented by a discrete grid in two dimensions and initially is a flat surface. Cutting grits are identified as those whose projected area (in the X-Z plane) overlaps with the 2-D representation of the workpiece surface. Figure 2 shows how a cutting grit moving in the Y direction (into the paper) would modify the workpiece surface grid. The succeeding grit is then tested for overlap with the modified surface. This testing and grid modifying process is repeated N times. The thickness and area of a removed chip are calculated by subtracting new Z grid coordinates from old ones.

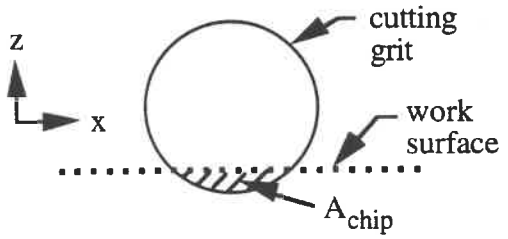

Figure 2: How cutting grit modifies workpiece grid

Because they relate to grit force, chip thickness and area should be key parameters in the prediction of fracture. Simulations yielded

[1] Bifano, T. G., "Ductile Regime Grinding of Brittle Materials," *PhD Dissertation*, N. C. State Univ., 1988.

thickness and area data for a variety of wheel/work parameters and infeed rates. The effects of grit size and abrasive concentration were determined by assuming a rigid binder matrix with no grit deflection. To identify the effects of binder modulus and workpiece hardness, grit deflection estimates were incorporated into the plunge simulation algorithm.

The repeatability of grit locations from revolution to revolution turned out to be an important consideration in the simulations. Simulations were performed with both "static" grits (in which the locations are assumed constant) and "dynamic" grits (in which the locations are randomized between each revolution). "Static" grits would be appropriate for plunge grinding conditions only where grit pullout is minimal and asynchronous error motion in the lateral direction is small. Re-arranged or "dynamic" grits may be a realistic model for grinding geometries such as contour or crossfeed, in which the cutting grit trajectories are not replicated in the following pass of the wheel.

2.1 Grit Size and Concentration Effects

Repeatable Cutting Points Simulations were conducted in which grit radius r_g, abrasive volume fraction f_v, and circumference l, were varied. Plotting average chip area A_{chip} or thickness t_{chip} versus feed f on a log-log scale results in bi-linear relationships such as those shown in Figures 3(a) and (b). Note that the area and thickness data fall into two regimes. The following expressions were found to fit the simulation data:

$$\frac{A_{chip}}{r_g^2} = \begin{cases} 2.28\left(\frac{f_v l}{r_g}\right)^{0.65}\left(\frac{f}{f_v l}\right) & f \le f_c \\ 1.94\left(\frac{f}{f_v l}\right)^{0.6} & f \ge f_c \end{cases} \quad (1)$$

where $$f_c = 0.67\left(\frac{r_g}{f_v l}\right)^{0.625} r_g$$

and

$$\frac{t_{chip}}{r_g} = \begin{cases} \frac{f}{r_g} & f \le f_c \\ 1.17\left(\frac{f}{f_v l}\right)^{0.4} & f \ge f_c \end{cases} \quad (2)$$

where $$f_c = 1.30\, r_g \left(\frac{r_g}{f_v l}\right)^{0.67}$$

The solid lines in Figures 3(a) and (b) were generated with these expressions. The close fit to the simulation data indicates that average chip area and thickness can accurately be calculated without conducting the simulation.

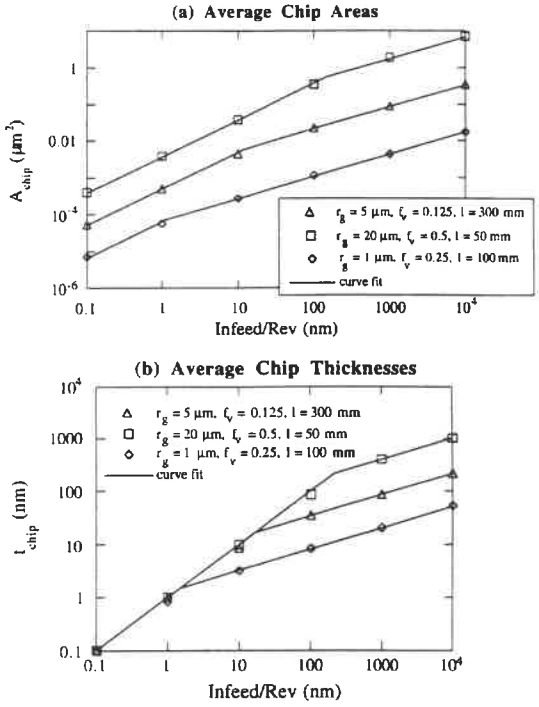

Figure 3: Relationship of (a) average chip area and (b) average chip thickness to infeed

Non-Repeatable Cutting Points Average chip area results for "dynamic" cutters are shown in Figure 4 along with corresponding data for "static" cutters. Note that at high feedrates the static and dynamic wheels yield the same average chip areas. In the low feedrate region, the dynamic wheels yield larger chip areas. The chip thickness data shows the same behavior. Therefore, with non-repeatable cutting points all of the data falls into one regime and can be described by the high feedrate ($f \ge f_c$) relationships in Equations (1) and (2).

The difference between static and dynamic cutters at low feedrates relates to the degree of correlation between wheel and workpiece. At low feedrates the number of cutting grits is small enough that evidence of every cutting grit is visible after each revolution. For a static wheel each cutting grit interacts with the cutting

groove that it formed on the previous revolution whereas for the dynamic wheel re-located grits interact with an uncorrelated surface. This leads to differences in surface roughness and chip size between the two types of wheels.

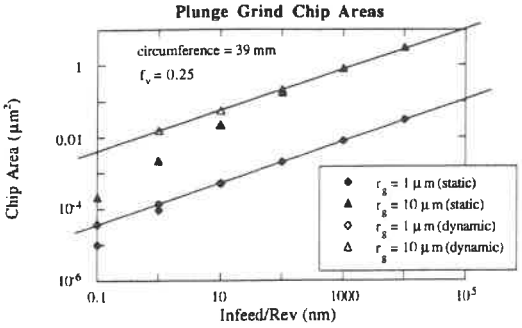

Figure 4: Comparison of average chip areas for "static" and "dynamic" cutters

2.2 Binder Stiffness and Work Hardness Effects

The cutting process exerts tangential and normal forces on the cutting grits. The normal force causes the cutting grains to deflect into the binder. Significant deflections change the chip sizes and the number of cutting grits. The equilibrium grit deflection δ_g can be calculated by balancing the normal cutting force exerted by the workpiece material F_{work} and the elastic spring force of the wheel binder F_{binder}:

$$F_{work} = F_{binder} \tag{3}$$

$$H_w A_{contact}(\delta_g) = 2/(1-\nu^2)\, E_b\, r_g\, \delta_g \tag{4}$$

H_w, E_b, and ν represent workpiece hardness, binder modulus of elasticity, and Poisson's ratio, respectively. With this type of force balance the outermost grits deflect the most, and the effect of grit deflection is to increase the abrasive concentration near the edge of the wheel.

Simulations were run with dynamic cutting grits to find how A_{chip} and t_{chip} vary with E_b and H_w. Curve fitting techniques were used to find that average area and thickness decrease with decreasing E_b and increasing H_w according to the following:

$$\frac{A_{chip}}{r_g^2} = 1.91\left(1 - e^{-\sqrt{E/H}}\right)\left(\frac{f}{f_v l}\right)^{0.6} \tag{5}$$

$$\frac{t_{chip}}{r_g} = 1.17\left(1 - exp\left(\frac{-\sqrt{E/H}}{0.786}\right)\right)\left(\frac{f}{f_v l}\right)^{0.4} \tag{6}$$

Critical Infeed Equations (5) and (6) may be useful for predicting the effect of wheel parameters on the critical infeed for fracture onset. For instance, if an A_{crit} could be determined from workpiece material properties, then the critical infeed would be:

$$f_{crit} = 0.337\,\frac{f_v l\, A_{crit}^{1.67}}{r_g^{3.3}\left(1 - e^{-\sqrt{E/H}}\right)^{1.67}} \tag{7}$$

Likewise, if a t_{crit} could be determined, the critical infeed would be:

$$f_{crit} = 0.675\,\frac{f_v l\, t_{crit}^{2.5}}{r_g^{2.5}\left(1 - e^{-1.27\sqrt{E/H}}\right)^{2.5}} \tag{8}$$

For both relationships, the critical infeed is proportional to abrasive concentration ($\approx 4 f_v$) and wheel circumference. It is also strongly dependent on grit size and moderately dependent on binder modulus and workpiece hardness.

3 Experiments

Because the chip sizes involved in the grinding of brittle materials are small, experimental verification of Equations (5) and (6) is difficult. However, an indirect measure of average chip area is possible by experimentally measuring the number of cutting grits. (In plunge grinding, the cross-sectional area removed equals average chip area times number of cutting grits N_{cg}.)

Plunge grinding tests were conducted with a special "fly" grinding wheel[2] which limits the size of the abrasive region to about 5 mm for a 320 mm circumference. The number of grinding scratches on surfaces plunge ground with this wheel were counted and taken as an estimate of the number of cutting grits which created the surface. Figures 5(a) and (b) show comparisons of N_{cg} calculated from simulation and measured experimentally. The figures show that grit size has a significant effect on N_{cg} while abrasive volume fraction and binder stiffness have moderate effects.

[2] Pellet inserts provided by American Diamond Tool.

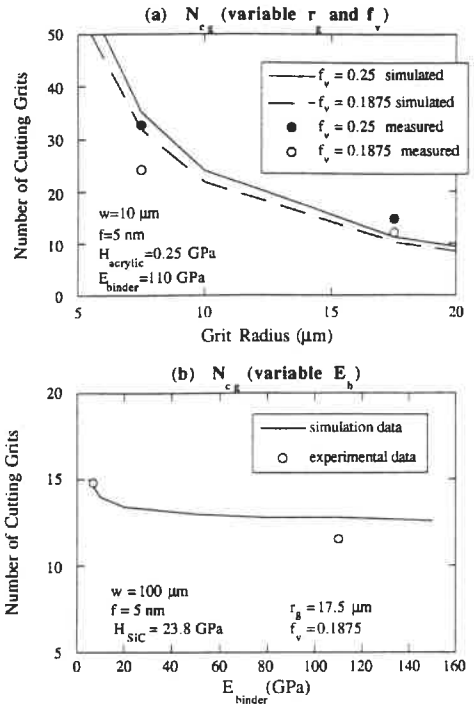

Figure 5: Comparison of number of cutting grits from simulation and experiments

Further experiments were conducted to test the validity of Equations (7) and (8). Feed/rev was varied in a "crossfeed" test[3], and fracture for each feed region on the resulting surface was measured. Note that this geometry is different than the plunge geometry, but it allows the variation from low to high feeds in a single test. Figure 6 shows the results for tests on soda lime glass in which metal wheels with different grit size and concentration are compared.

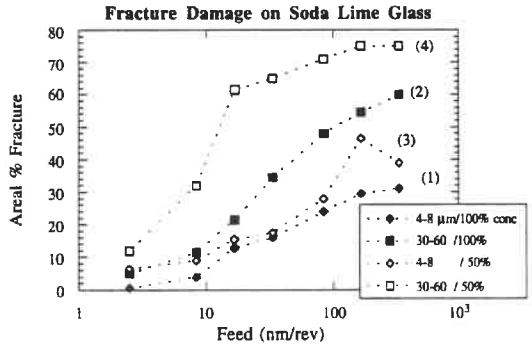

Figure 6: Fracture measurements of ground soda lime glass

[3] Miller, M. H., Dow, T. A., "Effect of Wheel Characteristics on Ductile Regime Grinding of Brittle Materials," *Proceedings of the ASPE Annual Meeting*, 1993.

Using 10% areal fracture as the criterion for transition from the ductile to the brittle regime, the critical feedrates were determined and are shown in the table below.

wheel	f_{crit}(nm)	ratio (meas)	ratio (model)
1	14	7	308
2	7	3.5	2
3	10	5	154
4	2	1	1

From Equations (7) and (8) ratios of critical infeeds for variable wheel parameters can be determined. For instance, Equation (8) predicts that f_{crit} increases by a factor of 154 when r_g is decreased from 22.5 μm to 3 μm. The table also shows these measured and predicted ratios of f_{crit} to a reference f_{crit} (wheel number 4 in this case).

Comparing the measured and predicted ratios shows that the model overestimates the effect of grit size. Several explanations are possible. Since Equations (7) and (8) are based on *average* chip area and thickness, it neglects larger chips that could initiate significant fracture. Also, actual grinding wheels have a range of grit sizes that the model does not account for. Finally, chip area and thickness, without consideration for chip shape, may not be appropriate fracture criteria.

4 Conclusions

In its attempt to quantify the effects of wheel characteristics on the critical depth of cut for ductile grinding, the model described above provides insights into the material removal geometry at the wheel/work interface. It shows, for instance, how grit size, abrasive concentration, and wheel circumference affect the number of cutting edges. It elucidates the inverse effects of work hardness and binder stiffness on grit deflection and force distribution. In addition, the results for repeatable versus non-repeatable cutting points indicate that critical depth of cut values obtained from plunge grinding experiments may not always translate to other grinding geometries.

CUP WHEEL GRINDING GEOMETRY

Gene E. Storz II, Thomas A. Dow
Precision Engineering Center
North Carolina State University, Raleigh, NC

INTRODUCTION

Cup wheel grinding is a precision fabrication technique used to create convex or concave spherical surfaces. In this process a rotating part is centered below the inner edge of a rotating cup wheel and then feed into the wheel. The angle between the axes of the wheel and part determine the radius of the spherical surface.

Through both theoretical and empirical research, several generalized rules and methods have been determined to suggest preferable grinding conditions to obtain high quality surfaces. Unfortunately, a model of the process showing how the surface and chips are generated has yet to be developed due to the complexities of the wheel-workpiece interaction.

This paper proposes a new method of modeling the geometry of cup wheel grinding derived from techniques developed by Storz[1]. From the geometry, both the surface and chips are generated for use in calculations of several surface quantities. The model is based on the geometry of the interacting surfaces and the assumption that the wheel cuts only once per revolution. These assumptions are general enough to allow more complex cutting problems to be modeled through further development.

GEOMETRY OF CUP WHEEL GRINDING

Cup wheel grinding is described by a rotating cup wheel with its edge centered above a rotating part which is feed into the wheel. This type of operation produces a radius of curvature, Rc, in the part as determined by the radius, R, and the orientation, θ, of the cup wheel. The relationship is given in Equation (1).

$$R_c = \frac{R}{sin(\theta)} \tag{1}$$

Figures 1(a) shows a cross section of the cup wheel grinder during the infeed process that generates the curvature of the part. Figure 1(b) shows the cupwheel grinder after the curvature of the workpiece has been generated. Nw and Np represent the rotational speeds

of the cupwheel and part, respectively, and D is the diameter of the part. If the cup wheel was tilted at a larger angle, the radius of curvature will decrease.

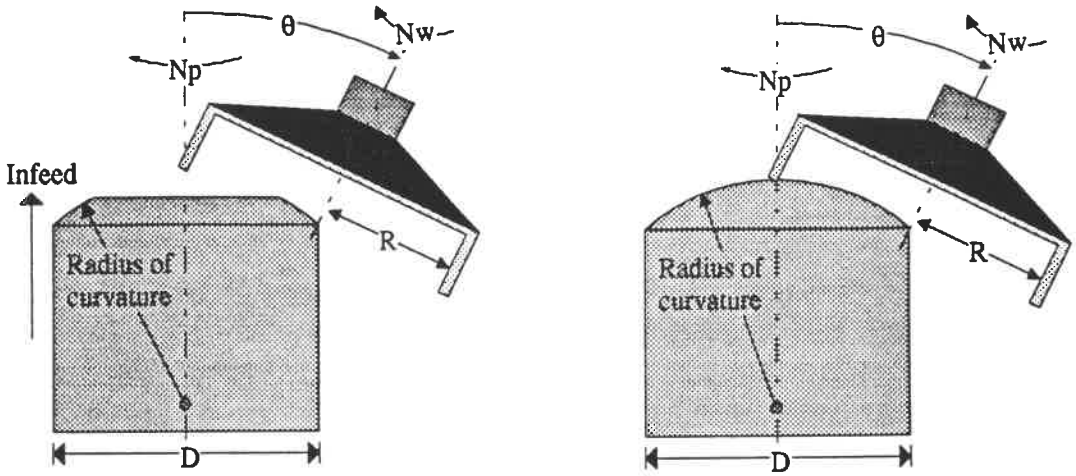

a) Infeed process

b) Dwell

Figure 1: Cross section of workpiece and cup wheel tilted at a rotation angle θ

METHOD OF OPERATION

The grinding process can be divided into two stages. The first stage is the infeed process in which the part is shaped with the radius of curvature determined by Equation (1). The second stage of the process occurs once the center of the part makes contact with the grinding wheel. This process is called the dwell (also known as spark out).

The infeed process begins with only the edge of the cylindrical workpiece being cut as shown in Figure 1(a). As the workpiece feeds into the wheel, the cuts extend towards the center of the part. Once the center of the workpiece contacts the wheel, the grinding to form the curvature of the part is complete. The second stage of the grinding process is the dwell as illustrated in Figure 1(b). Both the wheel and part continue to rotate while they are held at a constant position. The dwell first removes artifacts created during the infeed process and then continues to smooth the surface and create a better surface finish.

MODEL OF THE CUP WHEEL GRINDER

To understand how the final surface is formed and where damage occurs, a model must be developed to simulate the entire process. The difficulty lies in visualizing the geometry of the wheel-workpiece interactions and then determining a means to model them accurately. The complexities occur because a single point on the surface of the part

may be changed several million times before the part is completed. These interactions are three dimensional and must be calculated over the whole surface since that surface is changed with each revolution of the part. As an additional complication, the process goes through two stages of grinding before the part is completed. Each stage is different and requires different modeling techniques.

Modeling the Infeed Process The infeed operation has two geometries to be modeled. The first is the intersection between one cut of the wheel with the next which are separated by a small arc length determined by the grinding conditions. The second geometry is the intersections between the cuts made at the current location of the wheel with those of the wheel on the opposite side of the part.

The first geometry to model is the intersection between the previous cut of the wheel just made and the current cut of the wheel. As the part feeds into the wheel, an impression of the wheel is made on the part the shape of which is dependent upon the grinding conditions specified. Assuming the wheel removes one chip from the workpiece per revolution, then the part will rotate by a fractional amount called the upfeed between cuts. This action moves the impression made on the part by one upfeed distance. Another cut is then made by the wheel producing another impression on the part. Since the upfeed distance is not large enough to move the previous cut out of range of the current cut, an intersection occurs between the current cut into the material and the previous cut. The intersection between these two cuts forms a surface dependent upon the grinding conditions and the current infeed position of the part. This process occurs on both sides of the part where it intersects the wheel.

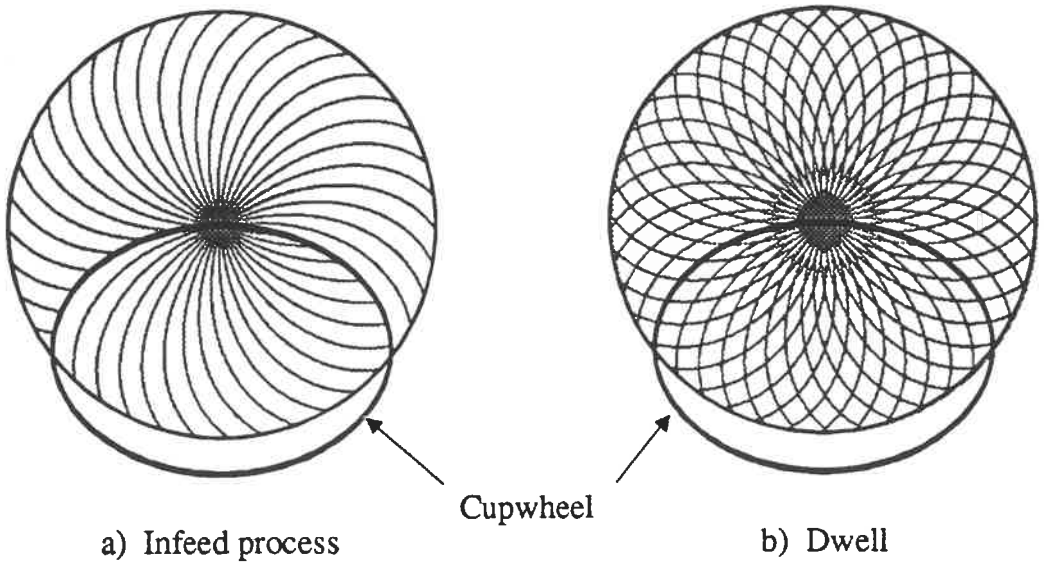

Figure 2: Top down views of infeed process and dwell

The second geometry to model are for the cuts which are made on one side of the part and then rotate around to the other side to intersect with the wheel. This process is caused by rotation of the part and the infeed of the part into the wheel. After impressions are made on the surface of the part by the wheel and are intersected as stated above, they continue to travel around the part with each upfeed. With each upfeed movement, the part also moves up into the cupwheel by some infeed distance. When these impressions intersect the cutting surface of the wheel on the opposite side, the part has moved in the infeed direction such that these features are higher with respect to the cutting surface of the wheel. Therefore, each cut rotated around the part from the opposite side is removed once it comes into contact with the cupwheel. Figure 2(a) shows a diagram from the top down view of this process occurring.

Modeling the Dwell Once the center of the part contacts the cupwheel, the infeed stops and the dwell process begins. The dwell process first removes the impressions remaining from the infeed process because they are higher on the surface than the dwell cuts. When the surface features created by dwell cuts travel around the part, they intersect with the wheel and are modified, but are not removed. The dwell cuts remain because each impression made by the wheel is at the same depth, therefore a crisscross pattern is generated on the surface as shown in Figure 2(b). Within each of the small rectangular areas shown in Figure 2(b), a pyramidal shape is formed.

The surface patterns formed during both the infeed and the dwell are dependent upon phase. The phase indicates how many times the part must rotate before a steady state removal rate is reached and no more material is removed. If the phase is 0 or 1, the part rotates once before cuts begin overlapping previous cuts. If the phase is 0.5, two revolutions are required before a steady state is reached.

CONCLUSIONS

A model of the cupwheel grinding process has been developed. The model will allow cup wheel grinding process to be visualized and the resulting material removal process characterized. The cupwheel grinding model is based on the geometry of the grinding operation only, but other theoretical aspects can be included upon further development such as the fracture mechanics process leading to surface damage.

REFERENCES

[1] Storz, G.E., *Theoretical Modeling of Contour Grinding,* MS Thesis, North Carolina State University (1994).

Optical Polishing of Hydrophilic Polymer Materials

J. Sun†, L.C. Zhang†, Y-W Mai†, M. Hogg††, and S. Payor††
†Centre for Advanced Materials Technology
Department of Mechanical & Mechatronic Engineering
The University of Sydney, NSW 2006, Australia
††Eycon Lens Laboratories Pty. Ltd.
296 Burns Bay Road, Lane Cove, NSW 2066, Australia

Keywords: *polishing; hydrophilic polymer materials; spherical surface; ultra precision.*

INTRODUCTION

The polishing of spherical surfaces of hydrophilic polymer materials is a complex material removal process. It involves interactions of the work material, polishing tool, polishing agent and substrate. The setting of polishing parameters such as loading pressure and the combination of rotating and sliding motions significantly affect the quality of a polished surface. The optimisation of these parameters is therefore critical. Unfortunately, there is very little literature available on this subject, although some studies have been carried out regarding the mechanical properties of this type of materials [1-4]. The mechanics and mechanisms of spherical surface polishing of hydrophilic polymer materials are not yet well understood. The present work aims to gain an in-depth understanding of the polishing technique and mechanisms of material removal of the polishing process with small radius.

EXPERIMENTAL DETAILS

The polishing process was conducted in a slurry form. The polishing system was illustrated schematically in Fig.1a. Loose abrasive grains (Al_2O_3 particles with 0.3μm average diameter), suspended in an oil based polishing cream, were applied to a lap (a micro polishing cloth). To generate a desired optical surface (the surface roughness shall be less than 150nm) and minimise the heat damage to the surface layer, the polishing pressure $\boldsymbol{P}$ and polishing time $\boldsymbol{t}$ were varied over a range ($\boldsymbol{P}$ = 6, 9, 12, 15 kPa; $\boldsymbol{t}$ = 0 - 180 seconds), while the rotation speed (1500 rpm) and sliding velocity (4m/min) were kept constant. Three typical hydrophilic polymers with hydration water of 38%, 45% and 55% were studied. The materials were polished in the dry state, at a relative humidity of 65% and an ambient temperature of 20°C.

The temperature during polishing was recorded using a low mass, rapid response thermocouple (type K, bonded foil, 12.7μm thickness) and a Fluke Model 51 digital thermometer. The thermocouple was placed between the polishing tool and the workpiece immediately after stopping the polishing machine. The time needed to measure the temperature was 5 seconds. A small correction based on the measured temperature T_m was therefore necessary:

$$T_c = c_t T_m$$

where T_c was the real temperature and c_t was the correction coefficient given by

$$c_t = \exp\{[t_1/(t_2-t_1)]\ln(T_1/T_2)\}$$

which was obtained by fitting the data from our cooling experiment. T_1 and T_2 were the temperature readings at instants t_1 and t_2 (5 and 30 seconds after stopping the machine).

An Atomic Force Microscope (AFM), (Autoprobe, Park Scientific Instruments), was used to measure the surface roughness. The hardness, elastic modulus and other mechanical properties of the materials were measured using a UMIS 2000 Ultra Micro Indentation System. In addition, the material removed was measured by an electronic balance of resolution 0.1 μg.

Table 1. Mechanical and physical properties of the hydrophilic polymer materials

Material (Content of hydration water)	Hardness UMIS 2000 (GPa)	Elastic Modulus (GPa)	Strain Index UMIS 2000	Density ρ (gram/mm^3)	Temperature correction coefficient ct
A (38%)	0.20	4.10	1.167	1.2789×10^{-3}	1.022
B (45%)	0.11	2.60	0.452	1.2831×10^{-3}	1.033
C (55%)	0.13	2.57	0.553	1.3152×10^{-3}	1.030

RESULTS AND DISCUSSION

Layer removal rate

Assuming that the material was removed uniformly from the polished spherical surface, a surface of radius r before polishing will become $r+\Delta h$, see Fig. 1b, where Δh is the layer thickness removed. Since the weight loss, ΔW, was measured, Δh could easily be calculated by the following equation derived from geometrical consideration:

$$\Delta h^3 + \frac{3}{2}(h + r)\Delta h^2 + 3hr\,\Delta h - \frac{3\Delta W}{2\pi\rho} = 0$$

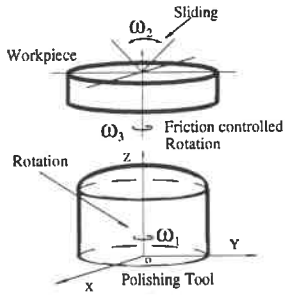

Figure 1a. Polishing tool

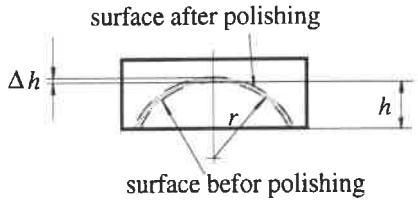

Figure 1b. The workpiece

With Δh calculated above, the layer removal rate in terms of types of material and pressure levels could be obtained. In our experiments, r was 7.00mm and h was 3.008mm.

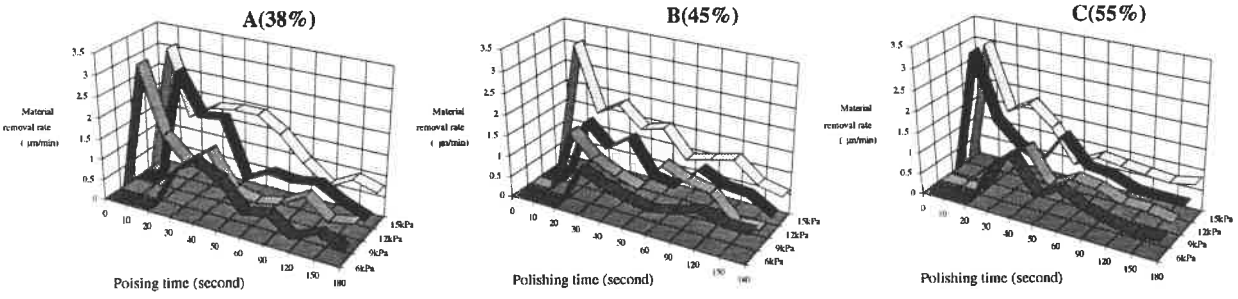

Figure 2. Layer removal rate vs polishing time under four different polishing pressure

Fig. 2 shows the layer removal rate for materials A, B and C respectively. Basically, for a given type of material, the layer removal rate is an increasing function of the applied polishing

pressure. Obviously, the content of hydration water and polishing pressure played an important role. Polishing was found to be efficient only in the first 40 - 50 seconds. There are several reasons for this. Firstly, the lathe marks (ridges) were removed largely at the beginning (Fig. 3a). Secondly, as the surface roughness became smaller, the real contact area became larger so that the real polishing pressure was smaller (Fig. 3b). Finally, loaded chips also reduced the material removal ability of the polishing grains.

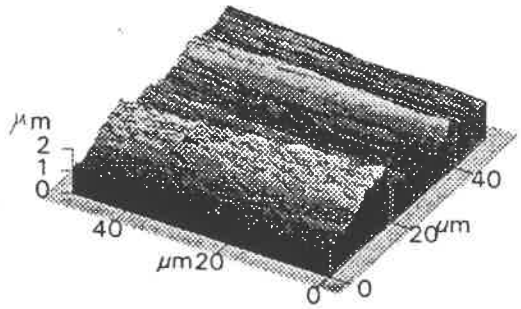

Figure 3a. Unpolished surface

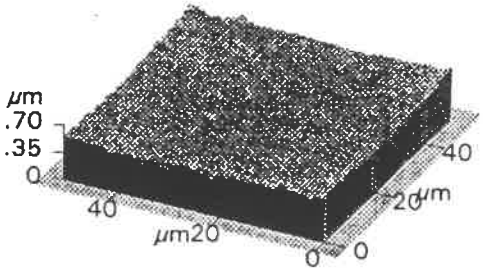

Figure 3b. Polished surface

Our experimental observations indicate that the polishing process of hydrophilic polymer material is a combination of micro fracture and plastic cutting. Initially, micro-fracture could be the dominant mechanism. The AFM surface image showed that the surface before polishing had a "hill and valley" structure with an average profile height of 1.3μm as shown in Fig. 3a. Such a topography was changed rapidly in 40 to 50 seconds to an optically desired structure with an average profile height of 0.1μm (Fig. 3b). Fractured and plastically cut chips were found on the lap surface using a high resolution microscope. However, the change of the content of hydration water alters the variation rule of the material removal rate. A sharp change of the rate was observed when the polishing pressure was 9kPa for type A material, in the range of 12 to 15kPa for type B material and in the interval of 9 to 12kPa for type C material. The mechanism for causing this is not clear so far.

Temperature Generation

A significant temperature rise was observed during polishing. The surface temperature rose rapidly from ambient to 35°C - 50°C in 60 seconds. It then increased slowly to about 60°C in 180 seconds.

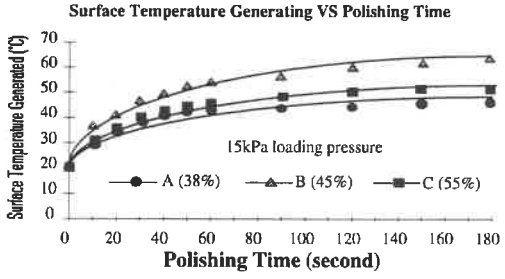

Figure 4. Surface temperature generation vs polishing time

It is clear that a larger hardness of a material gives a lower heat generation rate. If the hardness is considered to be an indication of the yield stress of a material, a higher hardness indicates a greater yield stress and hence implies less plastic deformation under a constant polishing pressure. This may explain to a certain extent the behaviour of temperature generation for the different types of materials as shown in Fig. 4.

Fig. 5 shows the pressure effect on the temperature generation in the first 60 seconds. It shows that the temperature rise is a strong increasing function of polishing pressure for all the materials.

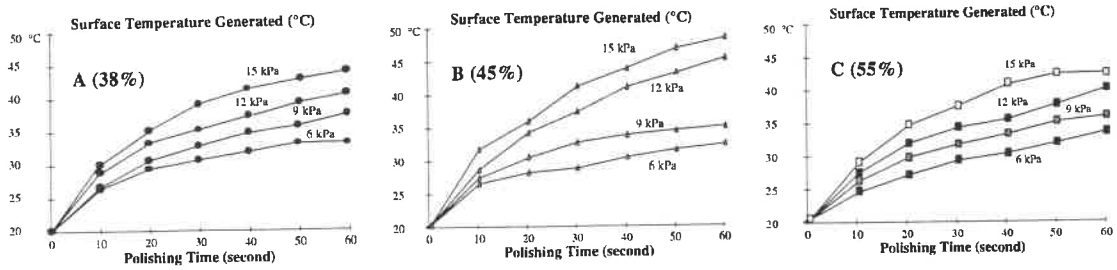

Figure 5. Surface temperature generated vs different polishing time for material A, B and C

Theoretical investigations have indicated that when the temperature increases, the equilibrium water content of hydrophilic polymer materials decreases. The essential effect of water in a hydrophilic polymer is to act as an internal plasticiser allowing the polymer chains to move easily with respect to one another [5]. If the equilibrium water content decreases, the hydrophilic polymer dehydrates and leads to a change of mechanical properties of the material such as an increase of hardness and shear strength [6]. Accordingly, a temperature rise would decrease the layer removal rate to a certain extent. This is consistent with the trends of the surface temperature (Figs. 4 and 5) and layer removal rate (Fig. 2).

CONCLUSIONS

In ultra precision polishing of hydrophilic polymer materials with small radius, the layer removal rate is very dependent upon polishing pressure, surface temperature rise and the content of hydration water. An optical surface with reasonable dimension accuracy is usually generated in 60 - 90 seconds. The material removal mechanism in the first 60 second is a combination of micro-fracture and plastic cutting.

ACKNOWLEDGMENTS

The authors would like to thank the Australian Research Council and Eycon Lens Laboratories Pty. Ltd. for providing the financial support for this project. Also thanks to Dr. A. Bushby of The University of Sydney, Mr. T. Bell of CSIRO and Mr. D. Mackay of Eycon Lens Laboratories Pty. Ltd. for their assistance to some of the experiments.

REFERENCES

1. Tighe, B.J. and Ng, C.O., The Mechanical Properties of Contact Lens Materials, *The Ophthalmic Optician*, pp. 394-402, May 1979
2. Hosaka, S, Yamada, A. and Tanzawa, H., Momose, T., Magatani, H. and Nakajima, A., Mechanical Properties of the Soft Contact Lens of Poly(methyl methacrylate-*N*-vinylpyrrolidone), *Journal of Biomedical Materials Research*, Vol. 14 pp. 557-566, 1980
3. Migliaresi, C., Nicodemo, L., Nicolais, L. and Passerini, P., Water Sorption and Mechanical Properties of 2-Hydroxyethyl - Methacrylate and Methylmethacrylate Copolymers, *Journal of Biomedical Materials Research*, Vol. 18 pp. 137-146, 1984
4. Fatt, I., Elasticity of Rigid GP Materials, *Optician -contact lens monthly*, pp. 42 - 45, September 1988
5. Ruben, M, Soft Contact Lenses: clinical and applied technology, *Baillière Tindall, London,* 1978.
6. Stone, J. and Phillips, A. J., Contact Lenes, *Butterworths, London*, 1981.

Ultraprecision Grinding of Brittle Hard-Disk Substrates

Paul Bierden and Thomas Bifano, Precision Engineering Research Laboratory
Aerospace and Mechanical Engineering Department
Boston University, 110 Cummington St., Boston, MA 02215

Introduction:

There has been a major change in the computer hard disk industry over the past several years. The substrate material chosen for new product development is frequently ceramic or glass instead of the traditional nickel coated aluminum. There are a number of reasons for this change, principally increased memory capacity and decreased weight achievable with these alternate substrates. This change is having a major effect on the industry. While there are clear advantages to be obtained by using brittle materials that are capable of withstanding high annealing temperatures, there is also one disadvantage: brittle glass and ceramic substrates are more difficult to machine than conventional Al/NiP substrates. We have begun a program at Boston University to identify cost effective, deterministic machining processes suitable for manufacturing brittle substrates to the shape and surface finish required by the hard disk industry. Table 1 lists five substrate materials and some relevant properties of those materials. Nickel-phosphorous coated aluminum (Al/NiP) is the conventional substrate material. The other materials listed are borosilicate glass, Canasite™ (a glass/ceramic blend), glassy carbon (an amorphous brittle carbon), and silicon carbide (a polycrystalline ceramic). The four new materials developed for substrate use are all currently being investigated by major hard disk manufacturers. While each of the materials listed has advantages and disadvantages as a substrate material, the high purity low density, and high softening temperature of the glassy carbon make it a leading choice as a substrate material for the next generation of hard disks, provided that it can be economically machined to the tolerances and surface finish required.

Hard Disk Substrate Properties:

The properties listed in Table 1 are those that affect the material's performance as a substrate material (softening temperature, density, elastic modulus) and those that effect machinability (hardness and critical depth of cut). In addition, a relative ranking of substrate cost, based on supplier information, is tabulated for each material. The approximate cost of these materials in a rough substrate shape ranges from more than $10 to less than $1 per substrate. In the following paragraphs each of these properties will be analyzed with respect to how they affect substrate performance and/or substrate machinability.

Table 1: Properties of Hard Disk Substrate Materials[1]

	Al/NiP	Borosilicate glass	Canasite	Glassy Carbon	SiC
Softening Temp, (°C)	280	500	500	1200	2500
Density, (gm/cc)	2.7	2.5	2.7	1.6	3.21
Elastic Modulus, (GPa)	72	85	85	35	461
Hardness, (kg/mm^2)	500	650	610	500	2500
Critical Depth of Cut, (nm)	(ductile)	27	32	44	180
Substrate Cost	low	low-medium	medium	medium	high

[1] Most properties listed here are taken directly from manufacturer's data sheets. Because the hardness of Al/NiP and glassy carbon will be shown to be critically important in developing an appropriate substrate fabrication process, these were measured directly using a Vickers dPH system.

• *Softening temperature* : After machining, a magnetic thin film is deposited on the surface of the hard disk substrate. This film is the media upon which information is written and stored. After the media has been deposited, the hard disk undergoes an annealing process. The annealing temperature directly affects the final coercivity of the magnetic media, which in turn directly affects the amount of storage on the disk. (Higher coercivity allows more disk storage density). For a typical magnetic film, the maximum coercivity is a achieved in disks that have been annealed at 600-700° C. One can increase the *storage density* of a hard disk by choosing a substrate that can withstand such annealing temperatures without deforming permanently. Of the substrates listed in Table 1, the four brittle materials can all withstand temperatures in excess of that achievable with Al/NiP, but only glassy carbon and SiC can withstand the annealing temperatures required for optimum coercivity,

• *Density :* As computers shrink to enhance portability, increasing demands for lightweight components are made by the hard disk industry. The substrate density is of particular concern, since a lighter disk permits smaller mechanical drive components. For the materials listed in Table 1, glassy carbon is the lightest by a significant margin.

• *Elastic Modulus:* While density is important in making lightweight components, one must also consider the relative *rigidity* of a material, characterized by the elastic modulus. For components with the same size and shape, E is a measure of the elastic rigidity. The elastic modulus of SiC is far greater than that of any of the other materials listed in Table 1.

One way to characterize "lightweight" materials (that is, those that are rigid in combination with low mass) is to compare specific stiffness, or E/ρ. For the materials listed in Table 1, SiC is the has the largest specific stiffness, with no significant differences among the remaining four. (Glassy carbon has the *lowest* specific stiffness of all these materials)

• *Hardness and Critical Depth of Cut:* Hardness is important because it directly influences the efficiency with which a material can be machined in a lapping or polishing process (which are conventionally used for substrate machining). Harder materials are not more difficult to lap or polish, they simply require more time to achieve a specified surface finish than softer materials. A study by N. Brown at Lawrence Livermore National Laboratory found that SiC can take as much as 20 times longer than glass to lap to a given surface roughness under identical conditions.

Critical-depth-of-cut is a parameter that is important in *fixed abrasive* grinding (as opposed to loose abrasive lapping and polishing). The critical-depth-of-cut is defined as the maximum chip thickness that can be removed in a machining process without introducing fracture in the machined material. If the cutting chip thickness exceeds the critical-depth-of-cut, fracture will occur on the surface of the material. Materials with large critical depths of cut are more amenable to damage free grinding, as would be required for hard disk substrates.

• *Cost:* There are two main concerns when considering cost of the hard disk substrate. The first is the cost of the substrate material itself. From left to right in Table 1 there is an increase in material cost. But there is also a cost consideration for processing. With nickel coated aluminum, there is a well established manufacturing method for producing the desired surface by diamond belt grinding, a relatively inexpensive process. For borosilicate glass and Canasite, loose abrasive lapping and polishing are conventional processes well-suited to the geometry and finish requirements of hard disks. Glassy carbon and CVD SiC have been found to be difficult to polish. To make the processing of SiC and Glassy Carbon economically feasible, alternative processes should be considered for feasibility and cost effectiveness. In the remainder of this paper, we describe a series of fixed-abrasive grinding experiments on glassy carbon substrates.

Development of Disk Grinding Machine:
A primary goal of this project is to develop an ultraprecision machine tool and process steps for fixed abrasive grinding of brittle computer hard disk substrates. A specially built ultra precision machine tool was used in this research. The machine uses orthogonal stacked double "vee" slideways to achieve infeed and crosfeed motions of a 100 mm diameter cup-shaped grinding wheel mounted on an air bearing spindle. The workpiece is mounted on a vacuum chuck attached to a second air bearing spindle. The two horizontal spindle axes are parallel at the same vertical level, allowing two possible grinding processes: plunge grinding (the cup wheel edge overlaps workpiece center, allowing generation of a flat surface on the disk substrate using only infeed motion and workpiece rotation), and crossfeed grinding (the cup wheel is advanced a fixed amount, then translated in the crosfeed direction to remove material from the rotating workpiece). All motion control for the ultraprecision grinding apparatus is achieved through a microcomputer, an analog to digital converter, and a binary input/output board. This controller was built specifically for the hard disk substrate grinding test. Controllable parameters are detailed in Table 2.

Table 2: Disk substrate grinding machine parameters

Axial Stiffness	**50 N/μm**	
Grinding Wheels	**6A2 cup, 6 mm rim, 100 mm diameter, diamond grit**	
Coolant	**Water**	
Motion Range/Resolution	**Resolution**	**Range**
Coarse Infeed Steps	2.5 μm	0.1 m
Fine Infeed Steps	15 nm	5 μm
Crossfeed Rate	0.5 mm/min.	0-170 mm/min.
Grinding Spindle Speed	10 RPM	0-3500 RPM
Workpiece Spindle Speed	10 RPM	0-1000 RPM

Process Convergence:
A series of grinding passes on several glassy carbon substrates yielded the desired finish and contour accuracy, as shown in the bar graphs in Figure 1. Because the conditions of grinding were specified to be conservative with respect to subsurface damage generation and machining rate, the processing time listed for each successive grinding wheel change is relatively arbitrary. Specifically, the processing time can be reduced in each of the last three operations without compromising surface flatness or finish. At this time, production-scale experiments are underway to demonstrate the achievable reductions in processing time.

The comparison of grinding time to workpiece flatness shows that the surface can be shaped to the required flatness specifications (8μm P-V) in a small amount of time (~5min). Further processing produces an ultimate flatness of 3μm. The flatness of the workpiece does not improve after 30 minutes. The convergence rate for surface roughness of the hard disk substrate is more gradual, requiring all four successively finer grinding operations and a total of 320 minutes to achieve the required 8nm RMS roughness (150μm scan, 2μm stylus profilometer, no filter).

These results are currently being used as the basis for an economic and technical assessment of fixed abrasive grinding for hard disk substrates. Current research directions include three process modifications:

- **Scale-up** – Use multiple disk workpiece holders
- **Speed-up** – Use a single plunge as opposed to multiple crossfeed passes
- **Hand-off** – Use coarse grinding for flatness generation followed by polishing for surface finish generation.

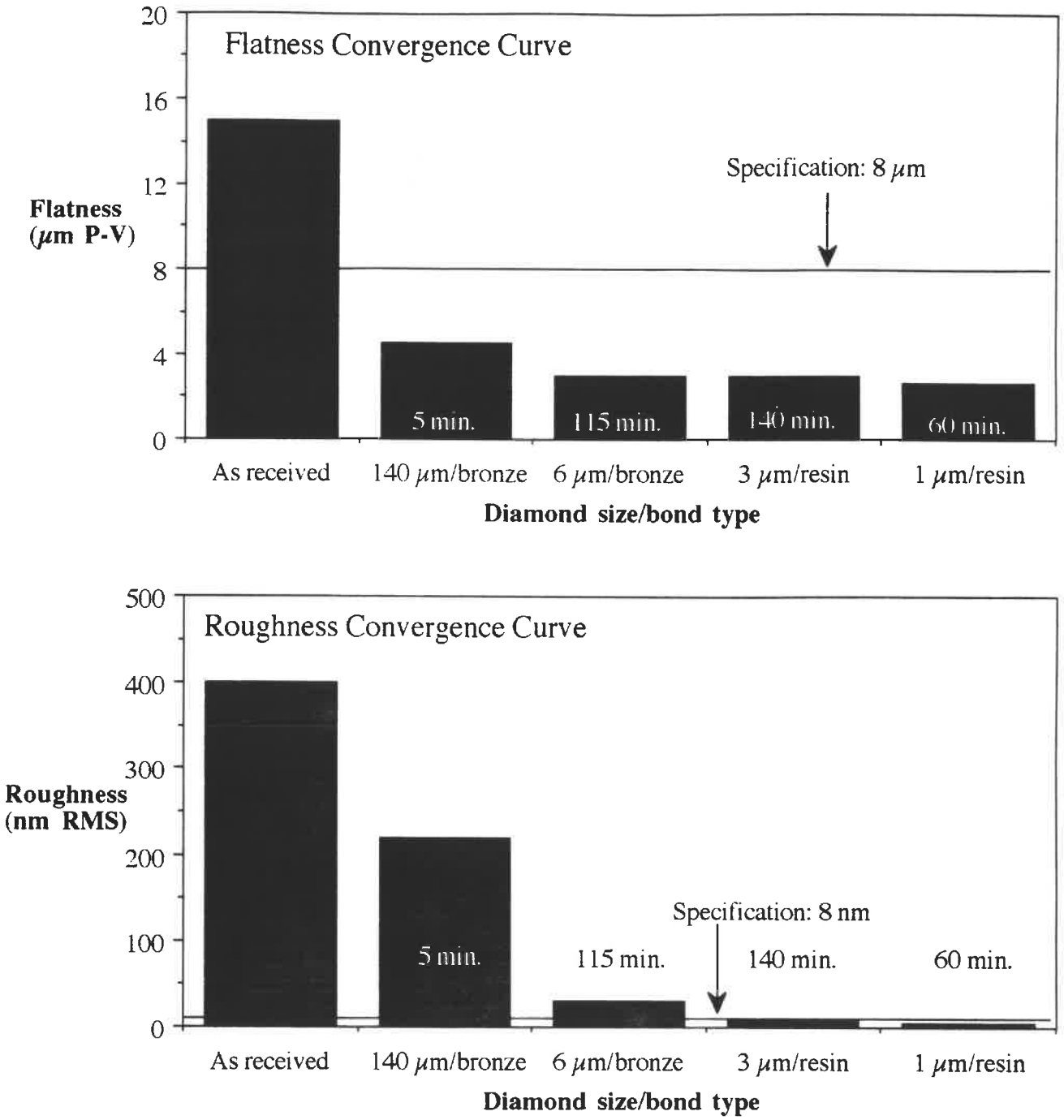

Figure 1: Flatness and roughness convergence curves for four successive fixed-abrasive grinding processes on glassy carbon hard disks. Process 1, with a 140μm grain size, bronze-bonded cup wheel was a 5 minute plunge-grinding operation. All subsequent grinding cycles were achieved using multiple crossfeed passes with a fixed infeed. Process times for each cycle are indicated on the bar graph data.

Acknowledgments
This work was supported by grants from KAO Infosystems Inc., and the National Science Foundation (DDM9202377).

MACHINABILITY OF PMMA IN THE NEAR-CRYOGENIC REGION

by
Craig R. Friedrich and Karthik Visvanathan
Complementary Micromachining Processes Laboratory
Institute for Micromanufacturing
Louisiana Tech University
Ruston, LA 71272 USA

INTRODUCTION

The fabrication of microelectromechanical systems (MEMS), using electroplating for the formation of microstructures, requires that cavities be made in a support material. The support material serves a similar function as a sand, or other type mold in conventional casting. In the electroplating process however, the metal is not melted so the process takes place at close to room temperature. In MEMS, the mold material has often been PMMA because it absorbs well at x-ray wavelengths and therefore is an excellent photoresist. The exposure of PMMA is typically carried out by x-ray lithography. The x-rays are not used because of the very high resolution possible with them but rather because of their penetrating power. This allows for the fabrication of high aspect ratio structures. This is a very expensive process requiring a synchrotron costing tens-of-millions of dollars.

The structure sizes for typical MEMS devices (accelerometers, fiber optic connectors, etc.) are in the 10 μm to 100 μm range. Because of these sizes, it may well be possible to fabricate prototypes of many of these cavities with precision micromachining techniques such as microdrilling and micromilling. Because the development and plating processes using PMMA are also somewhat mature, the use of PMMA as a molding material is continuing. This does present at least one difficulty when performing micromachining. The machinability of the PMMA changes when passing through the glass transition temperature of approximately 105 C. Because the cutting tools are so small, the machining speed is very low and the machining temperature can greatly vary. This may result in machining either in the brittle or ductile regions, or both. For example, a 22 μm endmill cutter recently developed at the CMPL has a cutting speed of only 0.7 m/minute when cutting at 10,000 rpm. Although machining above the glass transition is preferred, not knowing the cutting conditions may result in uncertainty of the cutting forces and the inability to adequately predict the results. Therefore, it was decided to perform a somewhat esoteric investigation into the variability of the cutting forces at the macroscale due to cooling the PMMA down to -55 C.

EXPERIMENTS

A workpiece was made of commercial PMMA extruded sheet and was 6 mm thick and 127 mm in diameter. The piece was made as two semicircular halves and mounted with a 6 mm gap. This was done to eliminate cracking of the workpiece due to stress resulting from mounting and to re-excite the piezoelectric transducer used in the cutting force dynamometer. The workpiece was mounted on a PMMA thermal spacer which was attached to a 100 mm diameter air spindle. The spacer was required to eliminate condensation inside the air spindle due to conduction. The workpiece was also contained inside a thermally insulated steel housing which had openings for the diamond cutting tool, an air bearing LVDT, and a fill port for liquid nitrogen. This setup is shown in Fig. 1. The tool was a single crystal diamond with a nose radius of 762 μm (0.030"). The shank of the tool was rigidly clamped in a tool fixture. The fixture used a PCB Piezotronics 290A02 long time constant force transducer mounted near the cutting

edge of the tool. The cantilever fixture was calibrated using dead weights and found to have a very linear response. The entire tool holder was moved by computer controlled X-Y stages as shown in Fig. 2. The air bearing LVDT (Rank-Pneumo MP-077B) was used to determine the location of the workpiece surface both before and after cooling. This difference was required to compensate for workpiece shrinkage to help assure a proper depth of cut. A brass rod was used between the LVDT and the workpiece experiments.

A cutting test consisted of locating the surface of the workpiece at room temperature by making a setup cut with the diamond tool. The radial coordinate of the tool was noted. The surface was also located with the LVDT, and the radial coordinate noted. The tool tip and the LVDT were not referenced to the same global system. Liquid nitrogen was then slowly poured into the fill port so that it took 5 to 10 minutes to reduce the workpiece temperature to the desired value. This was done to eliminate cracking due to high thermal gradients in the workpiece and to help assure a uniform, steady state temperature within the outer periphery of the workpiece. The surface temperature was periodically checked with a hand held thermocouple-based thermometer. When the desired temperature was reached, the surface was again located with the LVDT and the shrinkage compensated for in the tool positioner software. The spindle was then rotated and the cut was made. The transducer output was read from, and stored on, an Ono-Sokki CF-910 FFT analyzer. A typical readout is shown in Fig. 3. After the cut, the surface temperature was again recorded and the average was used for analysis. The final value for each cut was the mean of the six cutting voltages from each trace. Each cut consisted of five traces, therefore approximately 30 data points were analyzed for each cut.

Because of the limited space, it is not possible to show all experimental results. A total of five experiments were performed at room temperature. Three of these were to determine if the test apparatus was performing as expected. Speed, feed, and depth of cut were varied and the response was as expected. The cutting force varied linearly with depth of cut over the range of 2 to 10 μm and the cutting pressure increased exponentially as the chip thickness got smaller. One test was performed under the cutting conditions reported by Carr and Feger [1] and by Kobayashi [2]. No direct comparison with their results is possible. Carr and Feger measured resulting surface roughness and Kobayashi used conventional tooling.

RESULTS

The next 6 experiments were conducted at various lower temperatures and at various combinations of speed, feed, and depth of cut. Spindle speed varied from 500 to 1200 rpm. The feedrate varied form 50 μm/sec to 1.33 mm/sec and the depth of cut varied from 2 μm up to 10 μm. Workpiece temperature varied form room temperature (approximately 25 C) down to -55 C. The effect of workpiece temperature on specific cutting energy, from a single experiment, is shown in Fig. 4. Because the cutting conditions were the same for all temperatures in this experiment (constant chip cross section), the data was also indicative of the cutting force and cutting pressure at these machining conditions. There was a relatively rapid increase as the temperature was lowered from room temperature to 0 C. At lower temperatures, the cutting energy still increased but at a lower rate.

The effect of workpiece temperature on cutting forces, at various speeds, is shown in Fig. 5. In these results the feed and depth of cut were constant. As cutting speed was increased, the cutting forces showed a mixed result with a general increase in cutting speed. This may be due to material non-linearity even when cooled.

Finally, the specific cutting energy derived from 5 of the 6 experiments is shown in Fig. 6. This data is

taken from a wide range of machining conditions and therefore shows variability. However, it is clear that there is a somewhat linear relationship between specific cutting energy and workpiece temperature.

CONCLUSIONS

The experiments showed that machining speed is indeed important when attempting to predict cutting forces in cooled PMMA. The speeds used were far removed form those which are encountered in micromachining but the results indicate that the microscale cutting speed may well influence the material behavior, the predicted cutting forces, and probably the resulting surface finish.

EXPERIMENTAL UNCERTAINTY

Because of the atypical nature of the experiments performed, sources of uncertainty must be addressed. For all data values, the 95 % confidence limit criteria was used. For the room temperature experiments, this ranged form +/-0 % to a maximum of +/-12.7 %. The average uncertainty for all room temperature experiments was +/-7.8 % for 20 sets of data. For the experiments utilizing a cooled workpiece, the uncertainty ranged from +/-0 % to a maximum of 56.1 %. The average uncertainty for the cooled experiments was +/-11.9 % for 31 sets of data.

Another concern was warming of the workpiece during machining. The data was taken at approximately equal intervals over the total cut so as to reduce effects due to lower temperature at the faces of the disk. The temperatures reported on the graphs were the average temperature prior to and just after the cut was completed. The average temperature rise in the surface of the workpiece was approximately 10 C. Warming of the workpiece and the tool apparently were not a factor or negated each other. The force values at the end of a cut were essentially the same as at the beginning of a cut and varied by only several percent. Nearly all the uncertainty came about because of multiple cuts at various cutting conditions.

REFERENCES

1. Carr, J. W. and Feger, C. "Ultra Precision Machining of Polymers," *J. of Precision Engr.*, {15,4,1993}, pp. 221-237.
2. Kobayashi, A. K., Machining of Plastics, McGraw-Hill, New York, 1967.

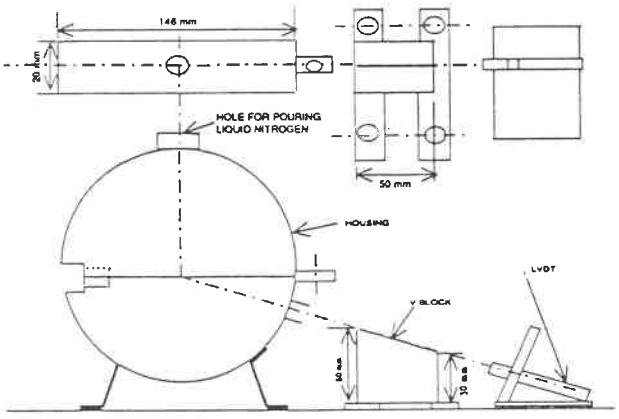

Figure 1 Setup

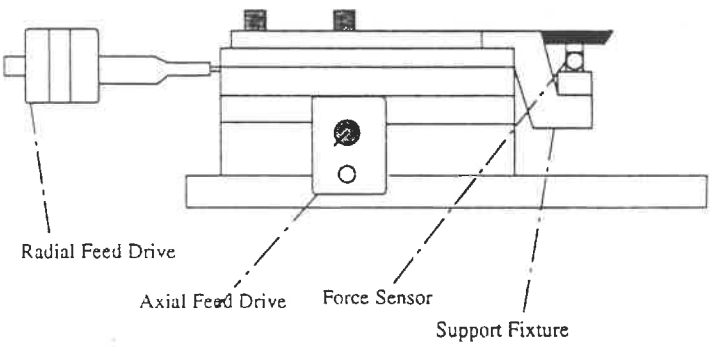

Figure 2 Dynamometer

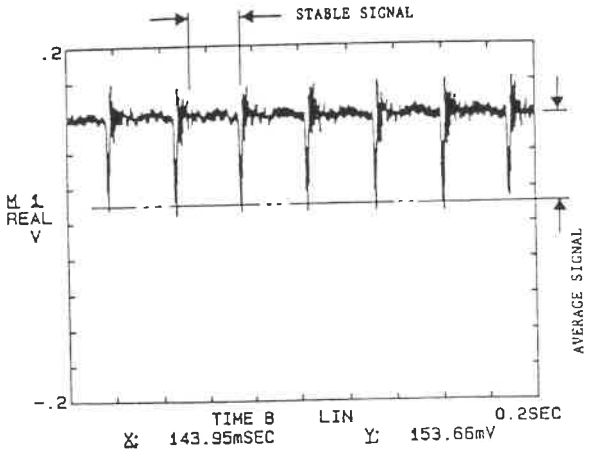

Figure **3** Typical Trace

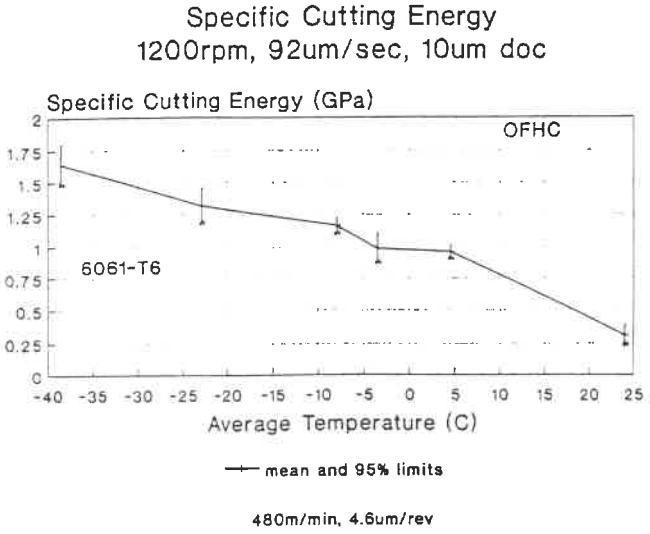

Figure **4** Specific Cutting Energy

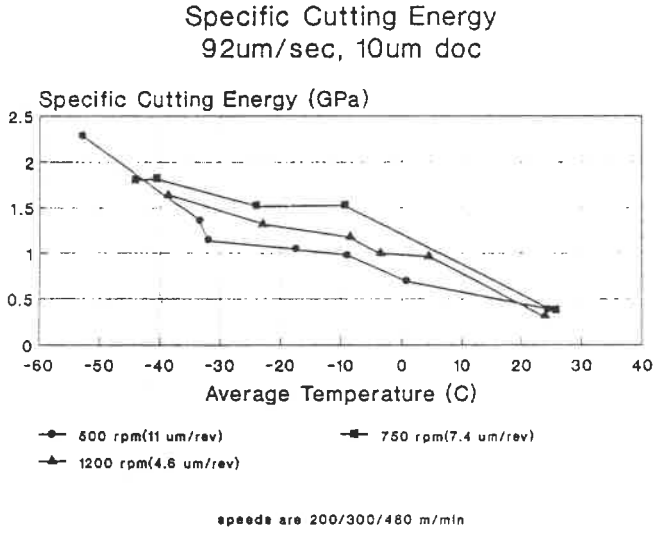

Figure **5** Specific Cutting Energy

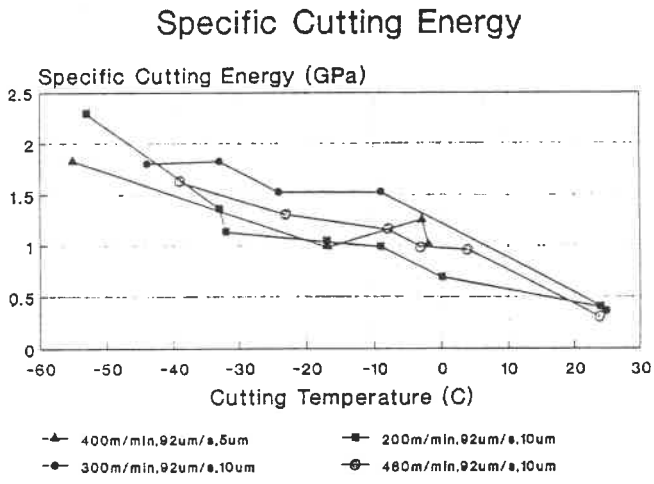

Figure **6** Specific Cutting Energy

Integrated Ion Beam Milling and Coating for Precision Optical Fabrication

C. M. Egert, K. W. Hylton and K. A. Thomas
Ultra-precision Manufacturing Technology Center
Oak Ridge National Laboratory

Abstract

An ion beam milling system, used for precision optical fabrication, was modified to easily allow deposition of thin films onto the same optics within a single vacuum operation. A series of coating experiments were performed to assess this approach to integrated ion milling and optical coating. Attempts were made to maximize the deposition rates while maintaining a narrow 'beam' of coating material to provide the optimum total process time. A conical shaped sputter target was found to maintain high deposition rates compared to a flat target, but without having the desired effect of narrowing the material distribution. Apertured shields did produce narrow material distributions, but at the expense of significantly lowering the deposition rates. Despite these limitations, thin optical films can be produced by this approach.

1. Introduction

Ion beam milling uses an energetic ion beam to removal material from a surface and is used as an advanced fabrication process capable of correcting or aspherizing optical surfaces. Ion beam milling has demonstrated figure correction of a variety of optical surfaces including fused silica,[1] ULE,[2] silicon carbide,[3] and even metal mirrors.[4] This versatility and the deterministic nature of ion milling make it a potentially valuable optical fabrication process. Ion beam milling promises to be even more versatile and efficient if it can be integrated with another important optical manufacturing process: thin film deposition.

There are several good reasons for integrating ion beam milling and coating operations. First, final figure correction or aspherizing is the last material removal operation prior to applying any required thin films to the optical surface; greater manufacturing efficiency can therefore be realized by combining these operations in a single, versatile ion milling/coating system. The ion milling process is performed under vacuum, as is thin film deposition; thus, integrating these two process eliminates the need to break vacuum and refixture the optical component in a coating chamber. The ion milling process also cleans the surface producing an atomically clean surface and eliminating the need for any cleaning operations between final figuring and coating. Finally, thin film thickness can be arbitrarily controlled in much the same way that material removal is controlled giving another degree of freedom to the optical manufacturer.

This paper describes a novel means of integrating these two processes and results of preliminary experiments evaluating this method. In this approach the same ion source used to remove material during fabrication of the optical surface is used to sputter deposit material onto the surface. During ion milling the ion source is directed normal to the optical surface; for coating operations the ion source is rotated by 90° and is directed onto a sputter target positioned at a 45° angle with respect to the optical surface and the ion gun axis as illustrated schematically in Fig. 1. The sputter target is attached to the ion gun carriage allowing the ion source-sputter target assembly to be rastered over the optical surface during coating in the same way as when ion milling. This ability to raster the coating source allows deposition of uniform coatings or allows precise variation in coating thickness with position on the optical surface.

For integrated coating to be an efficient process it is necessary to maximize the coating deposition rate on the optical surface while maintaining a relatively narrow spread in the distribution of coating material. However, these two criteria are inversely related: a narrow coating material distribution results in a lower deposition rate and vice versa. The experiments reported here concentrate on understanding the deposition rates and on the distribution of sputtered coating material achievable by an integrated ion beam coating process.

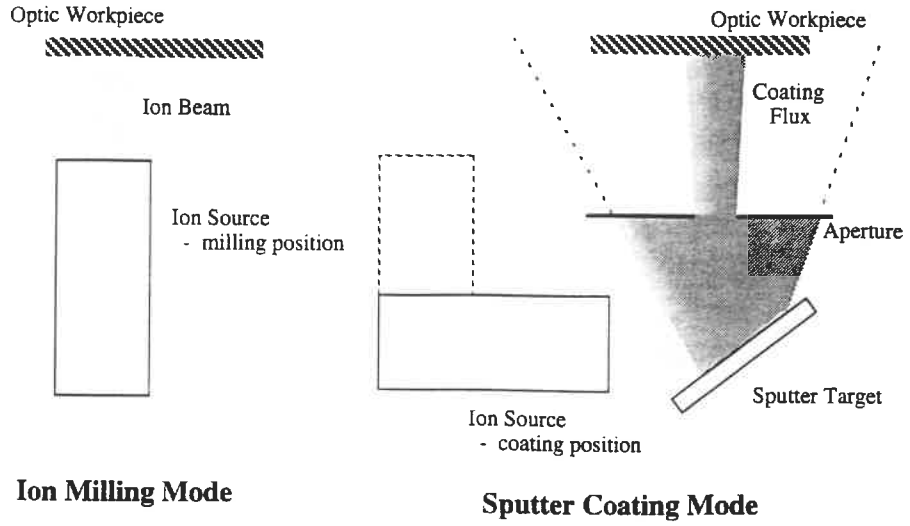

Fig. 1 Schematic diagram of the ion gun mount in ion milling and coating modes.

2. Experimental Setup and Procedures

The basic ion milling system used in these experiments has been described in detail elsewhere.[4] The system uses a 3 cm Kaufmann ion source (with 1.7 cm diameter grids) mounted on a vertical x-y stage capable of rastering over a 60 cm diameter optical surface. For these experiments the ion source mount was modified to allow rotation by ± 90° with respect to optical surface normal. A single sputter target fixture was also attached to the ion source mount. This fixture holds a 10 cm diameter sputter target at a 45° angle about 12 cm from the ion source. Note that the capability to rotate the ion source through ± 90° provides for the possibility of adding a second sputter target, opposite the first target, thus allowing the deposition of multi-layer thin films. In addition to these changes made to the ion source mount, a quartz crystal thin film deposition monitor was attached to the optics mounting fixture to monitor deposition rates during the coating experiments.

A first set of experiments were designed to determine the effect of curvature of the sputter target on the coating material distribution and deposition rate. It was thought that perhaps a conical target could 'focus' the sputtered material resulting in a narrow coating material distribution without significantly affecting deposition rates. The distribution of material and the effective deposition rates were measured by stepping the sputtering fixture over the quartz crystal thickness monitor. The total material deposited onto the monitor for a given time interval was used to calculate the deposition rate at that location with respect to the sputter target.

Another set of experiments were conducted to determine the effect of aperturing the coating flux on deposition rate and material distribution. The smaller the distribution of sputtered material, the less time must be spent dwelling off the optic. A 1 cm and a 2.5 cm aperture were tested. The

apertures were made of copper and mounted at an angle of 45 degrees to the sputter target (parallel to the optical surface) as shown schematically in Fig. 1.

3. Results

The coating material distributions for flat and conical sputter targets at the optic surface are shown in Fig. 2. In this figure the local deposition rate is plotted as a function of position measured from the maximum of the distribution. The greatest deposition rate, 2.4 Å/s was obtained using the flat sputter target. The conical target produced somewhat lower deposition rate of 1.6 Å/s. These distributions for both flat and conical sputter targets were nominally Gaussian-shaped and found to be essentially the same - all with a full width at half maximum (FWHM) of approximately 11 cm. The flat target

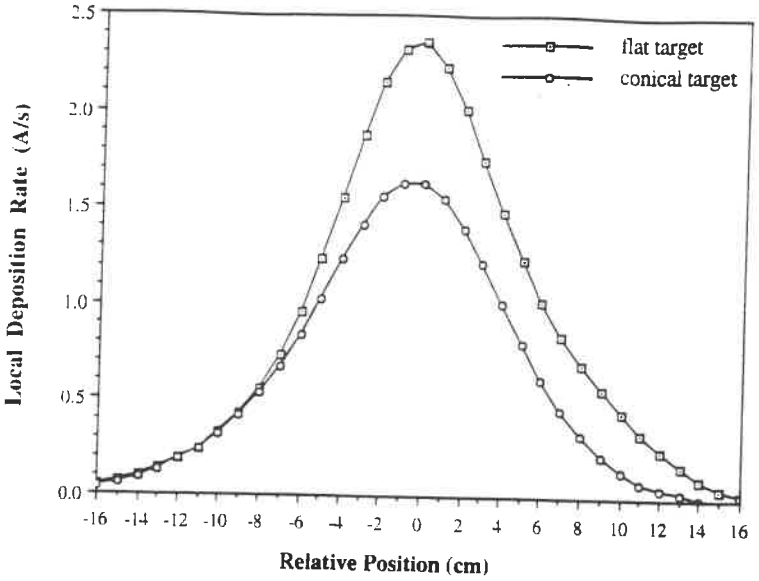

Fig. 2 Coating Material Distribution curves for flat and conical sputter targets.

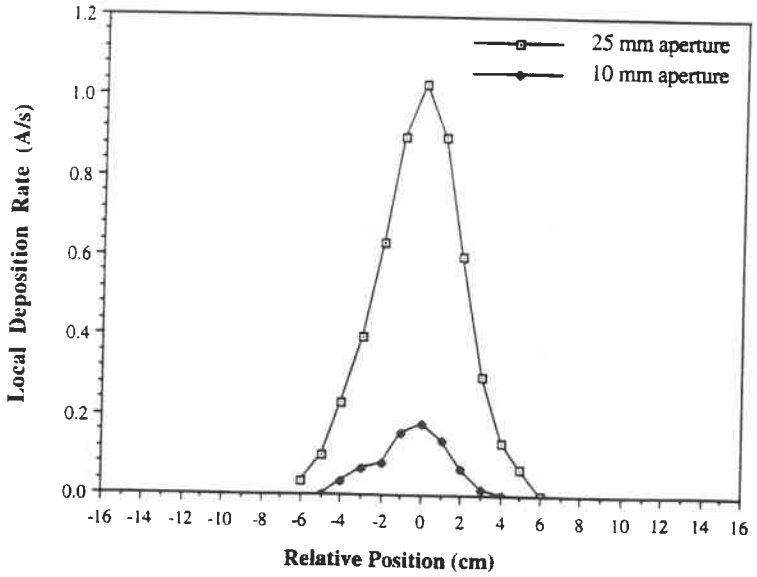

Fig. 3 Coating material distributions for 25 mm and 10 mm diameter apertures.

functioned superior to the others probably due to the increased surface area covered by the ion beam on the flat surface. The hypothesis that a shaped target could be used to focus the beam was not verified in these experiments.

Two different apertures, 10 mm and 25 mm diameter, were used in the second set of experiments in an attempt to reduce the size of the sputtered material distribution. Comparison of material distributions produced using these apertures and without an aperture are shown in Fig. 3. A broad distribution (FWHM of 11 cm) and a high deposition rate was obtained when no aperture was used. A much narrower distribution was achieved with the 10 mm diameter aperture. This coating material distribution has a FWHM of ~3.5 cm; however with a maximum deposition rate of only 0.18 Å/s. The 25 mm aperture produced a distribution with a FWHM of ~5 cm, but with a somewhat larger maximum deposition rate of 1.03 Å/s.

4. Conclusions

Experiments performed here showed that shaped sputter targets, while maintaining high maximum deposition rates, were not effective in narrowing the material distribution sizes. The use of apertures did narrow the material distributions, while decreasing the maximum deposition rates. These experiments did not identify an optimum aperture size to provide an optimum tradeoff between distribution width and deposition rate; although such an optimum size is probably 25 mm or larger.

These experiments have demonstrated the feasibility of depositing optical coatings after ion milling by an integrated ion beam sputtering process described here. Hence, final figuring by ion milling can be integrated with subsequent thin film deposition processes. While deposition rates for integrated coating are somewhat low, they are large enough to allow efficient coating of thin films onto substrates of moderate size. For example, assuming a 2 Å/s deposition rate, a 100 nm metallic film can still be applied to a small surface area in under 10 minutes. However, larger surface areas requiring rastering of the sputter source and thicker multi-layer films will still require several hours to deposit.

Acknowledgements

Parts of this research were sponsored by the Ballistic Missile Defense Organization under Interagency Agreement No. 1855-1562-A1. Oak Ridge National Laboratory is managed by Martin Marietta Energy Systems Inc., for the U. S. Department of Energy under contract DE-AC05-84OR21400.

References

1. S. R. Wilson and J. R. McNeil, "Neutral Ion Beam Figuring of Large Optical Surfaces," *Proc. Soc. Photo Opt. Instrum. Eng.*, vol. 818, p. 320, 1987.

2. L. N. Allen et al., "Final Surface Error Correction of an Off–Axis Aspheric Petal by Ion Figuring," *Proc. Soc. Photo Opt. Instrum. Eng.*, vol. 1333, p. 22, 1991.

3. K. W. Hylton, et al., "Ion Beam Milling of Silicon Carbide Optical Components," *Proc. Soc. Photo Opt. Instrum. Eng.*, vol. 1994, p. 16, 1993.

4. C. M. Egert, et. al., " Ion Beam Milling As Part of a Deterministic Approach to Optical Fabrication," *Proc. Optical Fabrication and Testing Workshop*, vol. 24, p. 212, 1992.

Testing System of Mechanical Properties of Magnetic-Optical Disk for Higher Density Storage

E.Tokutomi, H.Aoyama, T.Santo and T.Kubo
Department of Precision Engineering
Shizuoka University
3-5-1,Johoku, Hamamatsu, Shizuoka 432, Japan

1.Introduction

Recently technologies for multi-media processing such as optical fiber cable, optical component and high performance micro-computer become much more important because audio visual information should be processed quickly to spread it widely. Device and media which have plenty of capacity of storage are a key of the technologies and optical disk storage system is well-known to provide high density of storage on a disk of special substrate. New technique such as the phase-change method has been developed to improve the storage density[1] and also an optical disk of 5 inch size with capacity of 2.0GB will be almost merchandized in the market. On the other hand, ISO standards of measurement and evaluation methods for characterizing such equipments and optical disks have been considered to maintain the interchangeability. However it must be noted that optical disk storage system is composed of several components which are mechanical parts, electronics and optical elements, and the standard which is currently available may not keep up with the newly improved system. Furthermore, precise equipments for information processing such as a MO disk and a CD-ROM can no longer employ the special facilities which are implemented intentionally in the manufacturing machines since they are produced mainly for consumer products where cost benefit is essential, and therefore the quality control for mechanical components such as spindle,

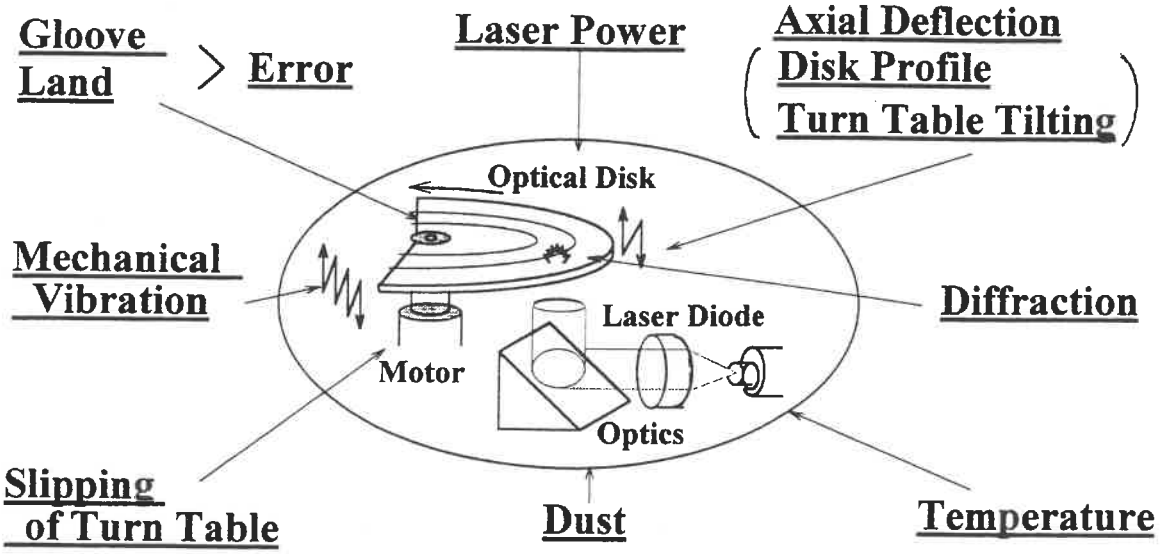

Fig.1 Factors Contributing to the Performance of Optical Storage System

such as spindle, turn table and disk must be also significant. The aim of this project is to construct a testing system which investigates various factors to affect on the performance of optical disk storage system. It is pointed out that the performance of optical disk system should depend on the microscopic profile of pit hole, optical beam characteristics, electronics, spindle runout, disk flatness, dust, temperature change as shown in **Figure 1**. We are developing the testing system for the optical disk equipment to investigate quantitatively several factors which cause the read/write errors. Mechanical properties which are dynamic axial and radial runouts of a track, tilt and profile of the disk surface are also essential factors because they are significant to tracking and focusing servo achievements. And measurement and evaluation method for some of them have been proposed by ISO and JIS standards[2]. In regard to the axial deflection, the displacement of an objective lens of optical pick-up which is controlled may be measured by the capacitance or the optical gauges[3] otherwise the current to magnet actuator be monitored, and the peak to peak of deflection and the maximum acceleration are to be evaluated. However the deviation of disk profile can not be distinguished from the titling of turn table due to the lack of measuring scheme by using the convensional method. And slipping between the turn table and the disk which are clamped by a magnet chuck occurs when the spindle is accelerated and therefore this movement also must be investigated to obtain higher reliability. In this report, the testing system which we developed to measure the slipping and the tilting motion for the optical storage equipment and the experimental results will be described.

2 Measurement System of Slipping and Titling

2.1 Slipping measurement

Figure 2 shows the schematics of measurement and evaluation system for mechanical properties of an optical disk equipment which includes a DC spindle motor, turn table, optical pick-up, electronics. Optical rotary encoder which can generate 200 plus signal per revolution is implemented on the spindle axis as well as on the surface of a sample

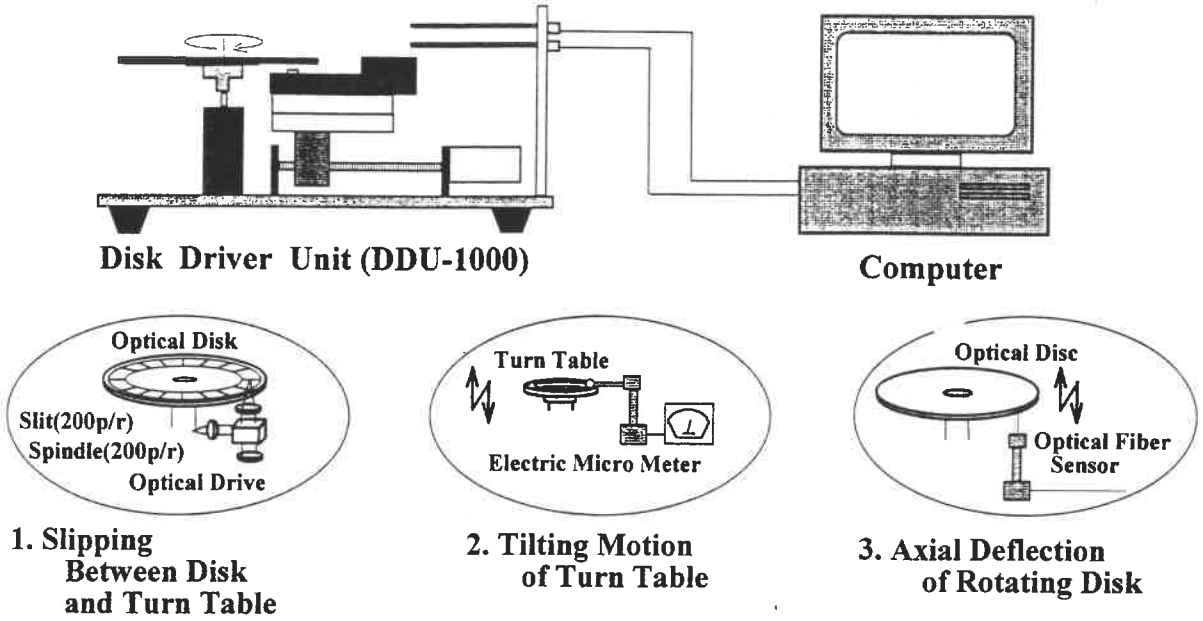

Fig.2 Schematic of Developed Testing System

optical disk. Slipping motion between the turn table and the sample disk, which is not considered in the ISO standard yet, can be monitored as the difference of rotating angle of two encoders, which is to be processed by the responsible computer for a few seconds. When testing the slipping motion, the relation between slipping phase vs acceleration time and the slipping phase vs rotating spindle angle are to be given graphically at various conditions of acceleration and cramping force.

2.2 Tilting measurement

Considering the tilt motion which is measured as axial deflection of the disk track by single probe, it must be cared that the measured deflection is the combination of turn table tilting and fluctuation of disk surface profile. As target area of the turn table is limited due to narrow width of the ring plate and roughly machined, the axial deflection is at first measured by an electric micrometer with a contact probe and sampled at 1.8 degree of spindle rotation. In addition the axial deflection of rotating disk which is set on the rotating turn table is also sampled by an optical fiber displacement probe and scanned over radius direction. Since microscopic grooves are etched on the substrate of optical disk which is coated by polycarbonate, contactless probe with non-focused optical beam is selected to gauge the axial deflection on the disk. Of course these two probes are employed after careful calibration. Finally, the profile of disk can be estimated after several raw data sampled on the disk surface are processed by using simple linear correction based on turn table tilting. It seems that this measuring scheme is rather simple to explore both the turn table tilting and the disk profile for practical use.

3. Experiment

3.1 Slipping motion

Figure 3 shows typical result of the relation between the time vs slipping rate of the accelerated disk. Slipping motion occurs in a second at the beginning of acceleration when the clamping force is not sufficient, namely less than 3N. Similar results which indicate that slipping motion is also depending on the rate of acceleration have been obtained. This means that the optimal clamping force and spindle acceleration should be governed when improving the density of storage by using such constant linear velocity control(CLV) scheme and the reliability of clamping material.

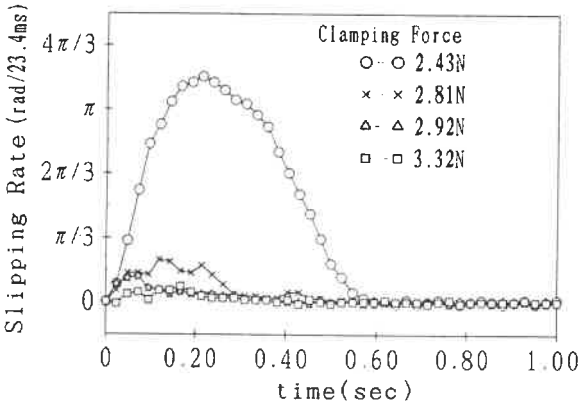

Fig.3 Slipping Rate and Time

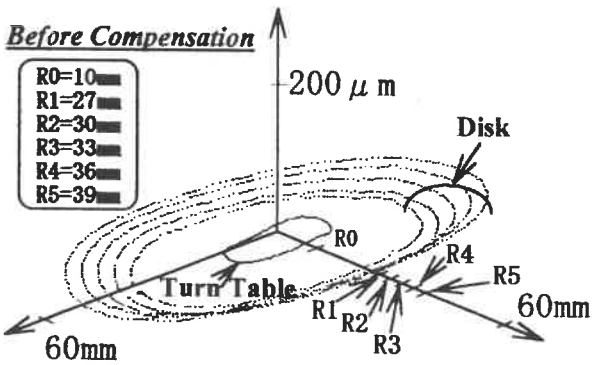

Fig.4 Axial Deflection of Optical Disk (Before Compensation)

3.2 Tilting motion

Figure 4 shows axial deflection which is sampled at the turn table and several radius of the optical disk of 90mm diameter by using single probes, the topography of which is also depicted in **Figure 5**. It is obvious that the axial deflection measured on the disk surface is strongly affected by the turn table tilting. Indeed we did distinguish them by using simple linear compensation technique on turn table tilting to estimate the profile of the disk as shown in **Figure 6**, where the profile of sample disk was concave. These results can easily provide the design criterion for the dimension of components as well as for the performance of optical pick-up servo in manufacturing processes to achieve the high quality production. Moreover we measured the axial deflection at every 20 degrees of clamping angle, which means the phase between the turn table and the disk, and evaluated the maximum range of deflection. Maximum axial deflection of the combination of the examined turn table and disk could be estimated about at 180μm.

4. Summary and future work

In this report, we described the testing system for mechanical properties of slipping and tilting of the optical disk. In the primary experiment, the results showed slipping motion occurred under certain condition, i.e. clamping force of less than 3.0N at the rotating acceleration of 860 rad/s^2. And profile of the optical disk is possibly estimated by linear correction based on the turn table tilting by using single displacement probes on the equipment, without the special testing machine. Currently we endeavor to improve measuring accuracy and to automate the system with other measuring tasks.

The authors thank Prof.S.Hara for his useful suggestions and Mr.N.Kubota, T.T.Centre, Kato Spring Manufacturing Corp., Tokyo and Mr.T.Kinoshita, PULSTEC INDUSTRIAL Corp., Hamamatsu for experimental advices. This work was supported by Shizuoka Science and Technology Foundation.

References

1)T.Ohta et al; "Million cycle overwritable phase change optical disk media, Proc.SPIE,1078(1989)27.

2)ISO/IEC,JTC1/SC23 Document; " Proposed measuring methods for the characteristics of 90mm rewritable/read-only optical disk cartridges(April, 1993)

3)S.Hara and T.Yoshizawa, "Measuring method of optical disk mechanical characteristics, Optical Mass storage II, Proc. SPIE,965(1986)pp.26-32

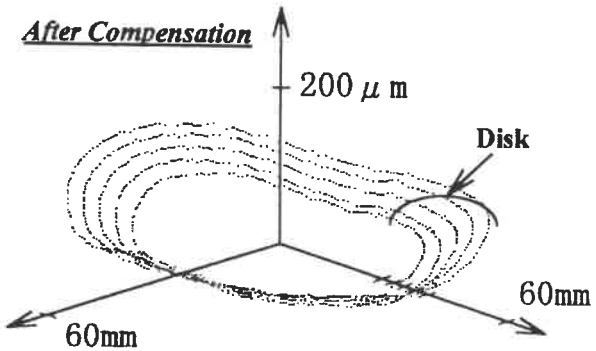

Fig.5 Axial Deflection of Optical Disk (After Compensation)

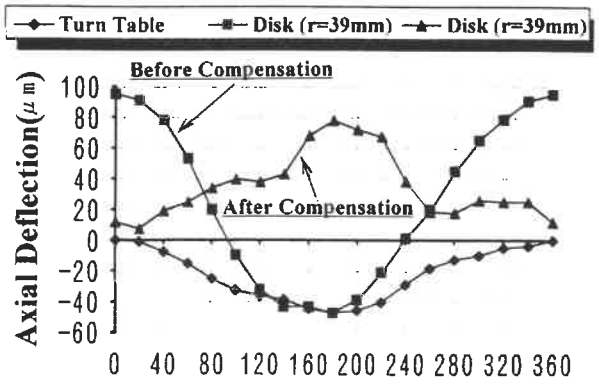

Fig.6 Axial Deflection and Spindle Rotation Angle

Development of Subpixel Edge Probe with High Resolution and Application for Coordinate Measuring Machine

Kazuo MARUYAMA, Hirokazu TSUJI, and Katsuro HASHIMOTO

Precision and Intelligence Laboratory, Tokyo Institute of Technology,
4259 Nagatsuta-cho Midori-ku, Yokohama 227, JAPAN

1. Introduction

In order to measure the profile of complex machine elements with high speed and high accuracy, a CNC non-contact-type coordinate measuring machine (CMM) have been developed on trial by us[1)], which used a photoelectric probe. However, the photoelectric probe requires many times in the measurement of profile of machine elements because it must detect the coordinates at many points moving along the profile.

In this study, a new non-contact-type subpixel edge probe is developed with the intention of variety in measurement, and applied to CMM and the measurement accuracy for the screw thread profile are discussed.

2. Subpixel Edge Probe

2.1 Principle and Construction

Figure 1 shows the principle of the subpixel edge probe which is developed in order to detect the edge profile error of an object with high resolution. The light from the illuminator goes to an object to be measured, the real image of the object is focused on the screen by an object lens, and its picture is taken by a CCD camera, memorized in frame memory board (640 × 400 pixels × 8(RGB)bit) in a personal computer (NEC PC-9801). The size of a pixel corresponds to the area of about 1.5 × 1.5 μm^2 on the object. However, the resolution of detection for the location of edge position is not enough by only two-levels image processing. Therefore the subpixel image processing is carried out in order to locate the edge position with the order of subpixel. This device is called a subpixel edge probe hereafter. This probe is attached on the non-contact-type CMM developed by us, and detects the edge profiles of objects.

2.2 Algorithms for Subpixel edge location

Figure 2 shows the distribution of pixel values in the neighborhood of the profile edge. Supposing that the change of pixel values is maximum at the profile edge as shown in Fig. 2 (b), the

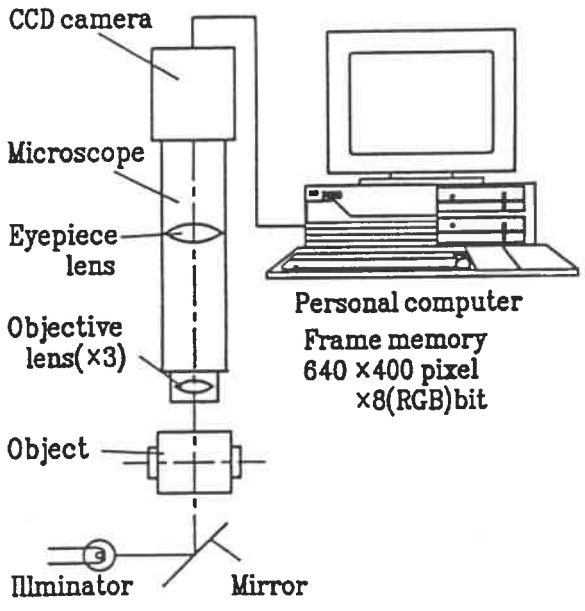

Fig. 1 Principle of subpixel edge probe

position where the change of pixel values is maximum is located as the position of profile edge, using the pixel values surrounding the profile edge.

The following algorithms for subpixel edge location are evaluated;

(1) Center of mass of relative signal[2] for 3 pixels;

$$x_c = \begin{cases} \dfrac{f_{-1} - f_{+1}}{2f_{+1} - f_0 - f_{-1}} & \text{if } f_{-1} > f_{+1} \\ \dfrac{f_{+1} - f_{-1}}{2f_{-1} - f_0 - f_{+1}} & \text{if } f_{-1} \leq f_{+1} \end{cases} \quad (1)$$

(2) Parabolic interpolation[2];

$$x_h = \frac{f_{+1} - f_{-1}}{2(2f_0 - f_{+1} - f_{-1})} \quad (2)$$

(3) Gaussian interpolation[2];

$$x_g = \frac{\log f_{+1} - \log f_{-1}}{2(2\log f_0 - \log f_{+1} - \log f_{-1})} \quad (3)$$

(4) P. Seitz's Gaussian interpolation [2];

$$x_{max} = \frac{\{\exp(-a^2)\}(f_{+1} - f_{-1}) + 2\{\exp(-4a^2)\}(f_{+2} - f_{-2})}{f_0} \quad (4)$$

(5) Center of mass over threshold;

This algorithm is our proposal. Figure 3 shows the principal concept, which is derived by improving the expectation of first-order derivatives[3]

$$x_f = \frac{\sum_{i=1}^{n} [i \cdot \{f_i - T\}]}{\sum_{i=1}^{n} \{f_i - T\}}, \quad T\text{: Threshold level} \quad (5)$$

Using the same pixel values, accuracy of edge detection are evaluated. The edge is a high precision straight edge pattern of chromium mask. One edge is fixed parallel to the Y-axis and another is parallel to the X-axis.

2.3 Accuracy of Subpixel edge location

Table 1 shows the accuracy of edge detection in various subpixel edge location algorithms. The accuracy is expressed by standard deviation in 100 times detections of the same edge. Table 2 shows the accuracy of linearity of edge detection in various subpixel edge location algorithms.

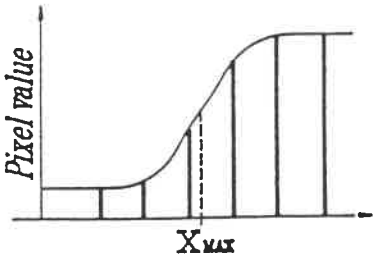

(a) Pixel values

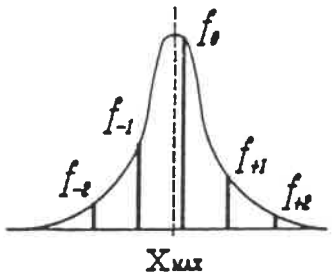

(b) Difference of pixel values

Fig. 2 Change of pixel values at edge

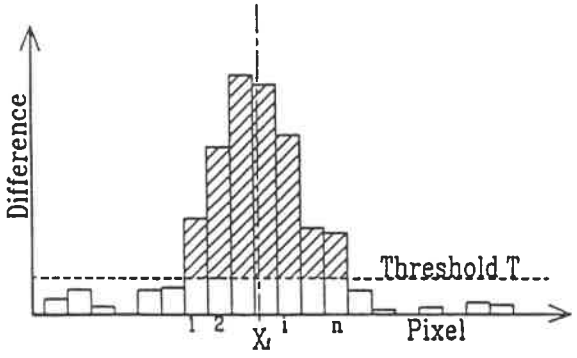

Fig. 3 Center of mass over threshold

Table 1 Accuracy of edge location (n = 100)

Scanning direction / Algorithm	X (pixel)	Y (pixel)
Mass of center (3 pixels)	0.72	0.70
Parabolic interpolation	0.48	0.50
Gaussian interpolation	0.47	0.48
P.Seitz's Gaussian int.	0.47	0.42
Mass of center (threshold)	0.09	0.14

Table 2 Accuracy of straight edge location

Scanning direction / Algorithm	X (pixel)	Y (pixel)
Mass of center (3 pixels)	0.62	0.56
Parabolic interpolation	0.46	0.58
Gaussian interpolation	0.45	0.60
P.Seitz's Gaussian int.	0.44	0.53
Mass of center (threshold)	0.15	0.19

The accuracy is expressed in standard deviation of the deviation from the least square approximate straight line for the same edge pattern. The algorithm proposed by us has the highest accuracy of edge location. Therefore the subpixel edge probe using our algorithm is applied to the non-contact-type CMM.

3. Application to Non-Contact-Type CMM

As an example of application of subpixel edge probe, the measurement of thread profile is carried out by CMM[1] as shown in Fig. 4, which is produced on trial by reconstructing a toolmaker's microscope. Though the origin of X-Y coordinates relatively moves by inclining the Z-column according to the lead angle of screw thread, a chromium mask fixed on the X-Y stage is used as an reference origin. In comparison of the movements of edge pattern in the probe coordinate system with those in the machine coordinate system (by the laser measurement system), the probe coordinate system is calibrated and transformed to the machine coordinate system by the soft wares. The transformation accuracy is 0.24 μm for X-, and 0.22 μm for Y-coordinate in the neighborhood of probe center, and 0.79 μm for X-, and 0.57 μm for Y-coordinate in the neighborhood of probe edge, in standard deviation, respectively.

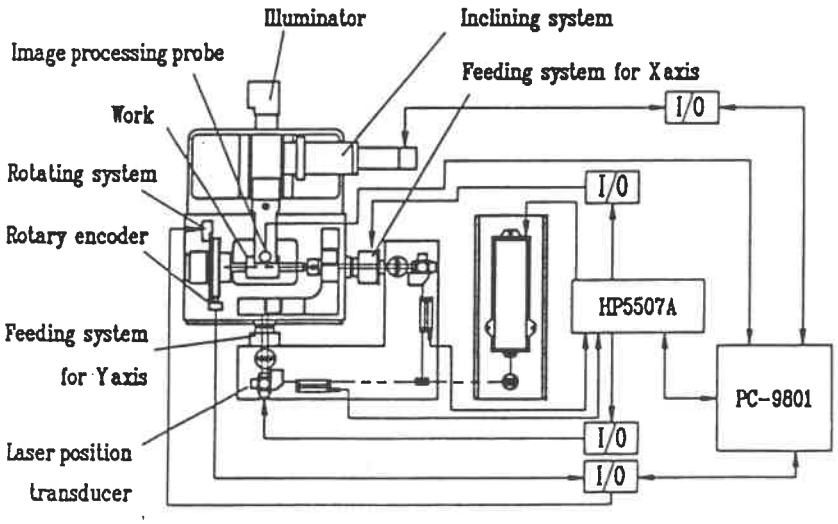

Fig. 4 Construction of the non-contact-type CMM

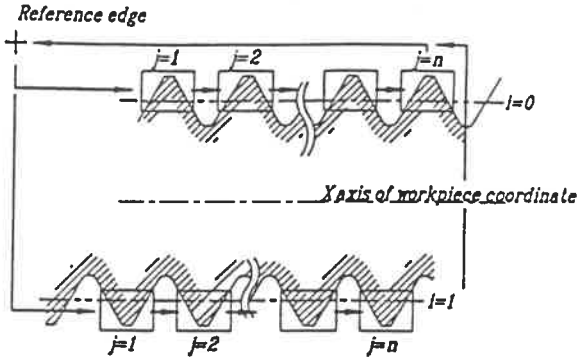

Fig. 5 Procedure of measurement

Figure 5 shows schematically the traveling path and the image area of the subpixel edge probe. Firstly, the subpixel edge probe travels at the position of screw thread of $j = 1 \sim n$ for the screw threads of $i = 0$ in turn, and next for the screw threads of $i = 1$ similarly. At that time, from each image of screw thread, straight lines which express the edge profile of major diameter, of each flank are obtained as least square approximate line for 25 detective edge points, respectively. Figure 6 shows the points for calculation of the factors of screw threads profile.

4. Results of Measurement and Consideration

The designation of screw thread used in this experiment is M10 x 1.25. Figure 7 shows the comparison of the result of measurement for the cumulative pitch error by this measuring machine with that by SIP UMM. They show a good agreement with each other. The accuracy of measurement is 0.08 μm in standard deviation for repeatability in this measuring machine and 0.57 μm in the SIP UMM.

Figure 8 shows the comparison of the result of measurement for the pitch diameter. The trend of their measured values shows a good agreement with each other. The accuracy of measurement is 0.12 μm in this machine and 0.47 μm in the three wires method.

Table 3 shows the results of measurement for whole factors. In comparison with the results of measurement by the conventional methods, the trend of their measured values shows a good agreement with each other except the factors related to the radial ones and the accuracy of measurement are improved. The time used for the whole measurement is about 14 minutes.

5. Conclusion

The main results are summarized as follows;

1) A new subpixel edge probe with high resolution is developed and applied to CMM.
2) The detective accuracy of probe is 0.13 μm (X) and 0.20 μm (Y) for the edge of chromium mask in standard deviation.
3) The accuracy of measurement for M10 x 1.25 screw thread are 0.16 μm for major diameter, 5 arc-min for half flank angle, 0.08 μm for cumulative pitch error, and 0.12 μm for pitch diameter, in standard deviation.
4) The values of measurement in this machine show fairly good agreement with ones in the conventional methods.

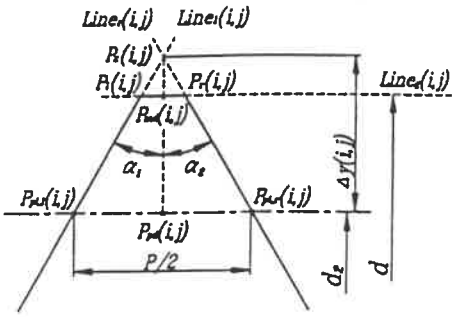

Fig. 6 Points for calculation

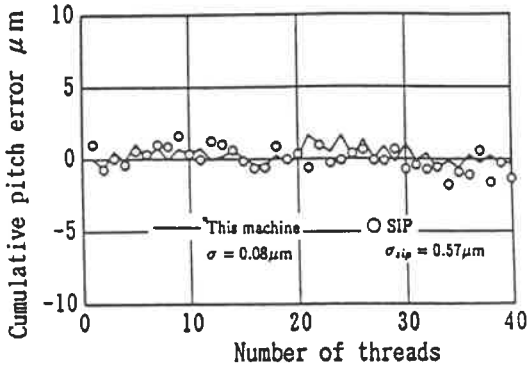

Fig. 7 Cumulative pitch error

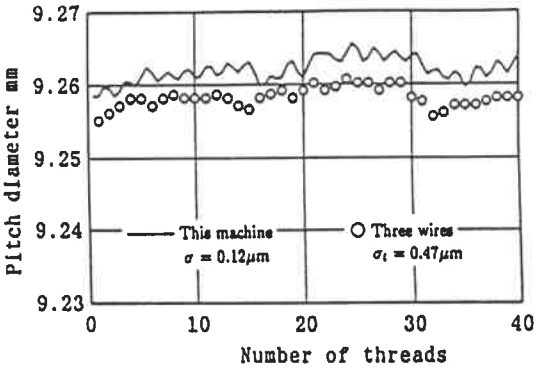

Fig. 8 Pitch diameter

Table 3 Accuracy of measurement

Factor		CMM	Conventional
Major dia.	μm	0.16	0.46 (Micro m.)
Half ang.	min	5	11 (SIP UMM)
Cumul. pitch	μm	0.08	0.57 (SIP UMM)
Pitch dia.	μm	0.12	0.47 (3 wires)

References

1) K. Maruyama et.al.: Development of Non-contact-type Coordinate Measuring Machine, Proceedings of 8th Annual Meeting ASPE, 74
2) P. Seitz: Optical superresolution using solid-state cameras and digital signal processing, Optical Engg, 27-7(1988), 535
3) G. Hu and X. Cao: A Subpixel Edge Detector Using Expectation of First-Order Derivatives, SPIE., Vol. 1657(1992), 415

A SMALL CMM DESIGN, NOT JUST SCALING DOWN

Marc M.P.A. Vermeulen, P.C.J.N. Rosielle, P.H.J. Schellekens
Precision Engineering section
Faculty of Mechanical Engineering
Eindhoven University of Technology (Netherlands)

Introduction

To measure relatively small products, table size CMM's are often used. On a smaller machine more accurate measurements would be obtained. For instance a down scaled version of an existing CMM could be made by reducing xyz-travel, guide lengths etc. This would not only reduce inertia but also tilt errors. Such a machine could meet the demand for accurate measurements in Precision Engineering. The design group of the Eindhoven Precision Engineering section presents an alternative approach for a high precision CMM[1)]: By satisfying fundamental principles of measurement like the Abbe and Bryan principle[2)] many tilt errors are prevented, so a higher measuring accuracy near to 0.1 μm is feasible with less effort on software compensation. The machine has a measuring volume of 100x100x100mm. It should function as a platform for a large variety of probes, both contact and non-contact versions, for the measurement of shapes and surface roughness.

Design

In CMM's Abbe errors often introduce quite large systematic errors. In the proposed design, of which a top view is schematically shown in fig. 1, much attention is paid to satisfying the basic Abbe principle: Measuring without any Abbe errors in three directions is realised in the horizontal mid-plane of the machine, (i.e. fig. 1). This is possible using separate intermediate bodies in x- and y-direction and crossing beams. The scales, used in the measuring systems, are always aligned with the probe motion, so machine tilt angles do not influence accuracy. Outside the mid-plane only small errors appear in x- and y-direction, (offset equals the vertical travel). This structure also satisfies the Bryan principle in two directions making the machine nonsusceptible for straightness errors of the scale supporting beams.

In fig. 1, x- and y-scales are supported each on orthogonal beams, which are connected to the probe by a moving xy-platform. The beams each move through their respective intermediate body, which carries a measuring head. The intermediate bodies are each separately driven along their respective guiding beam, which is mounted on a base. From this base, a table for the products to be measured is suspended. A statically determined design is shown in fig. 2.

Expanding this design to a machine, that would satisfy both principles of measurement in three directions, would introduce six intermediate bodies causing a high complexity and unfavourable dynamic behaviour. The much simpler design of fig. 1 and 2, has a vertical slide in the xy-platform, with an internal z-scale, satisfying the Abbe principle.

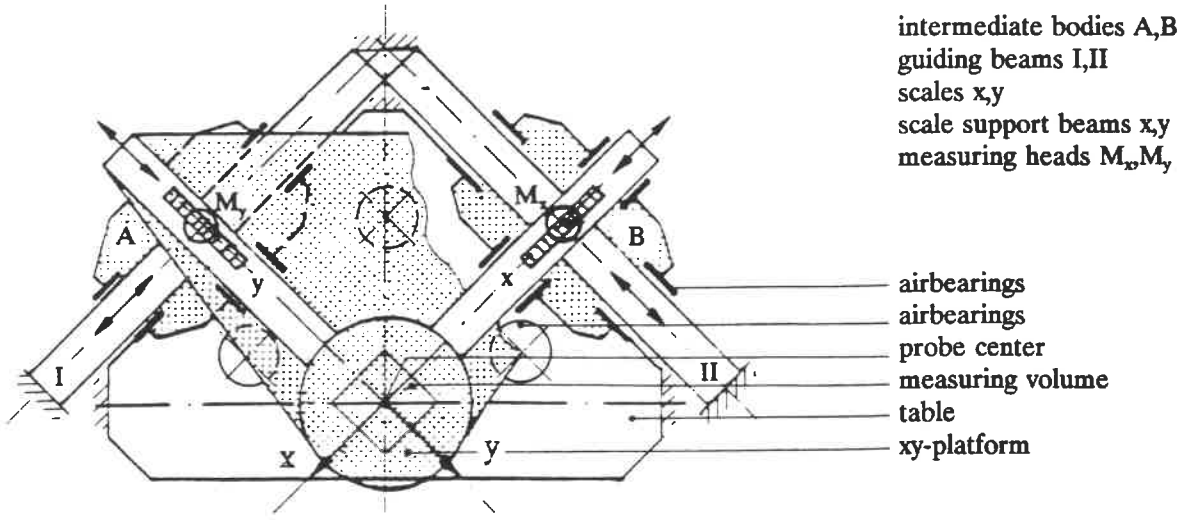

fig. 1: top view of CMM with intermediate bodies satisfying Abbe and Bryan principles.

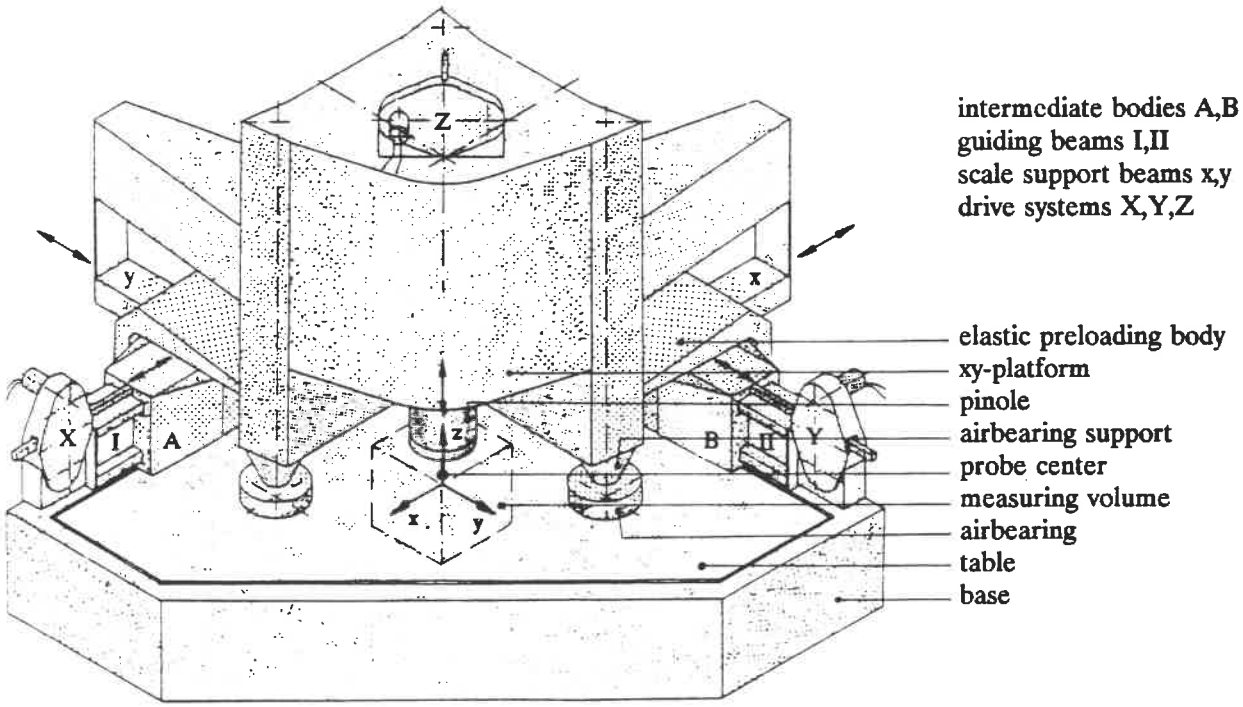

fig. 2: 3D CMM with intermediate bodies satisfying Abbe and Bryan principles.

Construction details

A ceramic table plate (500x500x200 mm) is chosen instead of the usual granite for four reasons: it's good thermal behaviour, it's high Youngs-modulus, it's fine structure and it's good flatness. The table plate is suspended in a statically determined way from the base on three hinged leafsprings providing a thermal center. The base is supported by three pneumatic isolators.

Airbearings were chosen for all slides resulting in high guiding accuracy and reproducebility, high stiffness and negligible friction. All airbearings are placed in opposite pairs to prevent bending of the guides. A separate elastic body is used to preload the three airbearings on the table. Thereby the machine frame is free of force transmission. A special compact airbearing support with high axial stiffness compared to the bearing stiffness, low hysteresis and low pad tilt force is developed. This support is made by wire electrical discharge machining (EDM) of tungstencarbide.

The machine frame is a closed plate construction of several compontents that are glued and bolted together after finishing. These components are CNC milled out of massive blocks preventing loss of stiffness and conduction in the plate connections. Aluminium is chosen for excellent thermal behaviour and mass reduction.

Zerodur scales are used with 5 nm resolution. Their negligible expansion and maximum velocity of 40 mm/s for high digital interpolation together with a high accuracy of 0.1 μm over 100 mm travel make them suitable measurement systems.

The vertical slide is a circle-cilindrical pinole moving in two radial airbearings with a rotation prevention. Weight compensation is realized by three constant force spring devices, preventing damage in case of power failure.

Each slide is driven by it's own single stage low ratio friction wheel drive. The design is based on the harmonic drive system. Favourable properties of friction wheel drives in general are combined with a low transmission-ratio (1:230) from a single stage.

Error analysis

Machine accuracy is optimized by several measures:

- Influence of heat sources is minimized by temperature stabilisation, remote operation and placing the drive systems on the outside of the machine. Additionally, extensive use of aluminium with it's high conductivity and thermal capacity favours a uniform temperature distribution. Integrated thermal length compensation for all principal axes and coinciding thermal centers make the machine nonsusceptible to general temperature changes, without using neither zerodur nor other exotic materials in this concept.

- This machine concept with intermediate bodies limits the influence of geometry errors of the machine guides. The following errors will be software compensated: the straightness and squareness of the guiding beams, the straightness of the pinole and the flatness of the table.

- Inspite the use of intermediate bodies and the out of center of gravity driving, also found in classical designs, construction principles on geometry and assembly of machine components result in high statical stiffness ($3 \cdot 10^6$ N/m) and favourable dynamic behaviour (lowest frequency of 70 Hz).

An extensive error analysis has been made to predict the total machine errorbudget. The following can be concluded: Measurement errors caused by thermal behaviour and finite stiffness of the machine parts are negligible compared to geometrical errors and inaccuracy of the measurement systems. The reached measurement uncertainty depends on the used probe type, the probe position in the workspace and the movement direction. By calibration with a laser interferometer measurement system a measurement uncertainty of 0.12 μm can be reached for the entire measuring volume.

Realization

During 1994 the realization phase of this project will commence on the mechanical component manufacturing at Eindhoven University of Technology Technical Services (CTD) with the support of NMI (Dutch Metrology Institute). Motion control, error compensation and calibration have to be prepared to precede the envisaged use in the metrology group of the Precision Engineering section.

Conclusions

The design process involved the generation and the selection of alternatives and lead to a CMM design different from conventional CMM's. An extensive analysis of dynamical, geometrical, gravitational and thermal errors has been made. Although it is anticipated, that error compensation methods will be required to get down to 0.1 μm accuracy, the objective was to get as close as possible by sound mechanical design and maximum use of the capabilities of the instrument construction group of the Eindhoven University.

The principles employed in this small high-end machine are to a large extend transferable to medium size machines. Large machines are likely to remain the same in general layout, although mechanical details can be improved without cost increase.

References

1) Vermeulen, M.M.P.A.: Ontwerp van een kleine carthesische 3D-meetmachine met submicron-meetonnauwkeurigheid, *Masters Thesis TUE,* (1994), (in Dutch)

2) Bryan, J.B., Carter, D.L.: Design of a new error-corrected coordinate measuring machine, *Precision Engineering,* 1979, 1(3), 125-128

Verification of Form Tolerances Using Point Data

Kirsten Carr
Research Engineer
Ford Research Laboratory
Dearborn, Michigan

Placid Ferreira
Associate Professor
Department of Mechanical and Industrial Engineering
University of Illinois at Urbana-Champaign

Introduction

Mass production depends on the use of interchangeable parts which are produced with sufficiently small variations to ensure they are functionally equivalent in the final assembly. Designers indicate the allowable amount of variation in a part with tolerance specifications that are defined in the ANSI Y14.5 National Standard on Dimensioning and Tolerancing [2]. During the production of interchangeable parts, a measurement method which determines if the parts conform to the tolerance specifications is required. With the increasing demand for flexibility on the factory floor, a programmable inspection tool, known as the coordinate measuring machine (CMM), has become popular for the measurement of parts. A CMM is programmed to collect point data information from the surface of the part. The point data information is analyzed by verification algorithms to determine if the measured part conforms to the tolerance specifications.

In 1988, a Government-Industry Data Exchange Program (GIDEP) [11] alert was issued which indicated that different verification algorithms produced different results given the same set of point data. This problem is especially true for form tolerances, which control how close to perfect-form a feature must be. The ANSI Y14.5 Standard [2] definition for form tolerances requires the form error of a surface to be less than some set limit. However, most inspectors are interested in the minimum form error, known as the minimum zone solution. The minimum zone solution minimizes the maximum error between the data points and a reference feature. Current CMM verification algorithms are based on the least-squares solution, which minimizes the sum of the squared errors, resulting in a possible over estimation of the form tolerance. Therefore, while CMM algorithms successfully reject bad parts, they may also reject some good parts.

Current Verification Methods

A mathematical formulation of the form tolerance verification problem results in a nonlinear optimization problem. In the cases of flatness and cylindricity, the tolerance zones can be geometrically described as two parallel infinite planes and two coaxial cylinders of infinite length. A verification algorithm must search for the optimal location and orientation of these tolerance zones such that all the data points are between the two planes or two cylinders.

The most popular verification methods that attempt to fit perfect-form geometry to the data points are based on the second norm or L_2-norm solution, obtained using least squares algorithms. Unfortunately, these methods do not compute the minimum zone solution, which is a L_∞-norm problem. Direct search verification methods for determining the L_∞-norm solution are discussed by Murthy [8], Kanada [7], and Tsukada [10]. These algorithms employ the simplex search method, Nelder-Mead simplex method, or Powell's method to search the solution space. Computational geometry based methods, which utilize the convex hull of the data set, are discussed by Traband [9]. Exchange algorithms, which start with a random set of points and uses exchange rules to add and delete points from the set until a minimum solution is found, are discussed by Fukuda [5], Chetwynd [4], Huang [6], and Anthony [3].

Proposed Verification Algorithm

The basic verification algorithm proposed in this work solves a sequence of linear programs that converge to a local solution of the non-linear problem. Given adequate initial conditions, this solution will be the minimum zone solution. To increase the robustness, efficiency, and accuracy of the algorithm, the linear program is solved in a preferred coordinate system. The results are then transformed back to the original coordinate system and tested for convergence. The basic algorithm is shown in Figure F.1. Since the algorithm is based on solving linear programs, it can be easily implemented when a library of optimization subroutines is available. The linear programs required for a flatness algorithm and cylindricity algorithm are discussed below.

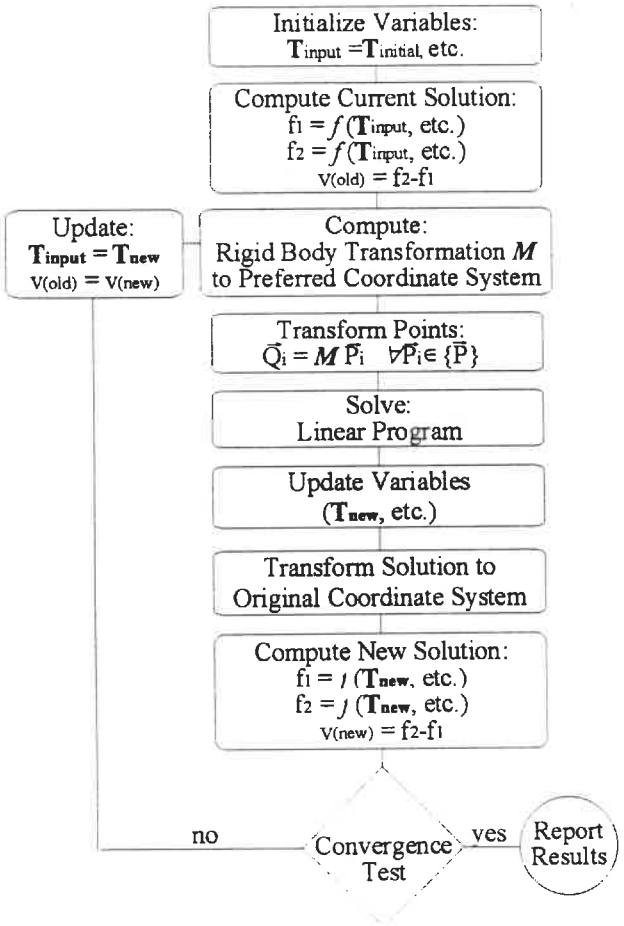

Figure F.1: Basic Verification Algorithm

Flatness Verification Method

The flatness problem can be modeled as searching for a normal vector $\mathbf{T}$ of a reference plane through the origin such that the difference between the distances of the points farthest and closest to the reference plane is minimized. The only nonlinear equation in the resulting optimization problem is the constraint requiring $\mathbf{T}$ to be a unit vector ($T_x^2 + T_y^2 + T_z^2 = 1$). This constraint prevents the reduction of the objective function by the rescaling of the coordinate space. By transforming the optimization problem to a coordinate system where $\mathbf{T}_{input}$ coincides with $(1/\sqrt{3}, 1/\sqrt{3}, 1/\sqrt{3})^T$, the nonlinear constraint can be replaced by $T_x + T_y + T_z \geq 1$.

Flatness Linear Program

Determine value for the variables $(T_x, T_y, T_z, d_1, d_2)$ that satisfy:

$$\text{Min } \{d_2 - d_1\} = v$$

$$\text{s.t.} \quad \mathbf{T} \bullet \vec{Q}_1 \geq d_1$$
$$\vdots$$
$$\mathbf{T} \bullet \vec{Q}_n \geq d_1$$
$$\mathbf{T} \bullet \vec{Q}_1 \leq d_2$$
$$\vdots$$
$$\mathbf{T} \bullet \vec{Q}_n \leq d_2$$
$$T_x + T_y + T_z \geq 1$$
$$T_x \geq 0, \quad T_y \geq 0, \quad T_z \geq 0$$

where $\mathbf{T} = (T_x, T_y, T_z)^T$ = *parallel planes zone normal direction vector*

d_1 = *distance from reference plane to one zone plane*

d_2 = *distance from reference plane to other zone plane*

n = *number of points in the data set*

Since the improved normal vector computed by the linear program is not a unit vector, it must be normalized before the next linear program. This vector is also transformed into the original coordinate system so flatness can be computed using the original data.

Cylindricity Verification Algorithm

The cylindricity problem can be modeled as searching for an axis (direction vector $\mathbf{T}$, locating position vector $\vec{\mathbf{L}}$) such that the difference between the distances of the points farthest and closest to the axis is minimized. The resulting optimization problem has a linear objective function and nonlinear constraints. These constraints are linearized using the small-displacement screw model, where $\mathbf{T}$ and $\vec{\mathbf{L}}$ are replaced by functions of the input axis ($\mathbf{T}_{input}$, $\vec{\mathbf{L}}_{input}$) and the incremental variables $(\Delta\alpha, \Delta\beta, \Delta\gamma, \Delta x, \Delta y, \Delta z)$:

$$\mathbf{T} = \begin{bmatrix} 1 & \Delta\alpha & -\Delta\beta \\ -\Delta\alpha & 1 & \Delta\gamma \\ \Delta\beta & -\Delta\gamma & 1 \end{bmatrix} \mathbf{T}_{input} = \begin{bmatrix} T_{input_x} + \Delta\alpha T_{input_y} - \Delta\beta T_{input_z} \\ -\Delta\alpha T_{input_x} + T_{input_y} + \Delta\gamma T_{input_z} \\ \Delta\beta T_{input_x} - \Delta\gamma T_{input_y} + T_{input_z} \end{bmatrix}$$

$$\vec{\mathbf{L}} = \vec{\mathbf{L}}_{input} + \begin{bmatrix} \Delta x \\ \Delta y \\ \Delta z \end{bmatrix} = \begin{bmatrix} L_{input_x} + \Delta x \\ L_{input_y} + \Delta y \\ L_{input_z} + \Delta z \end{bmatrix}$$

To prevent scaling problems, r_1 and r_2 are also incrementally changed: $r_1 = r_{1,input} + \Delta r_1$, $r_2 = r_{2,input} + \Delta r_2$. In order to simplify the resulting linear program and increase the efficiency and robustness of the algorithm, the linear program is solved in a preferred coordinate system where $\mathbf{T}_{input}$ parallels the Z-axis and $\vec{\mathbf{L}}_{input}$ coincides with the origin.

The missing incremental variables represent translations along and rotations about the Z-axis, which do not effect the value of cylindricity in the preferred coordinate system. The results of the linear program are used to incrementally improve the current solution axis. This new axis is transformed into the original coordinate system so cylindricity can be computed using the original data.

Implementation and Results

The above verification algorithms were implemented on an IBM RS/6000 computer using IBM's Optimization Software Library (OSL) package. The algorithms were tested using both published data sets and generated data sets with the initial conditions set to either the nominal or the least-squares parameters. For the flatness algorithm, results indicate that the above flatness algorithm successfully equals or betters published results. For the cylindricity algorithm, published data sets were unavailable. Therefore, generated data sets with known cylindricity form errors were tested using various initial conditions. The algorithm computed the correct cylindricity using initial conditions of $\mathbf{T}_{initial}$ tilted up to 40^0 from the solution axis and $\vec{\mathbf{L}}_{initial}$ translated away from the solution locating position, indicating that the algorithm is robust. Next, data sets with unknown cylindricity were generated and tested. For these data sets, the cylindricity algorithm improved upon both the

Cylindricity Linear Program

Determine values for the variables $(\Delta\beta, \Delta\gamma, \Delta x, \Delta y, \Delta r_1, \Delta r_2)$ *that satisfy:*

Min $\{\Delta r_2 - \Delta r_1\} = v$

s.t. $2Q_{l_x}Q_{l_z}\Delta\beta - 2Q_{l_y}Q_{l_z}\Delta\gamma - 2Q_{l_x}\Delta x - 2Q_{l_y}\Delta y - 2r_{l_{input}}\Delta r_1 \geq r_{l_{input}}^2 - Q_{l_x}^2 - Q_{l_y}^2$

$2Q_{n_x}Q_{n_z}\Delta\beta - 2Q_{n_y}Q_{n_z}\Delta\gamma - 2Q_{n_x}\Delta x - 2Q_{n_y}\Delta y - 2r_{l_{input}}\Delta r_1 \geq r_{l_{input}}^2 - Q_{n_x}^2 - Q_{n_y}^2$

$2Q_{l_x}Q_{l_z}\Delta\beta - 2Q_{l_y}Q_{l_z}\Delta\gamma - 2Q_{l_x}\Delta x - 2Q_{l_y}\Delta y - 2r_{2_{input}}\Delta r_2 \leq r_{2_{input}}^2 - Q_{l_x}^2 - Q_{l_y}^2$

$2Q_{n_x}Q_{n_z}\Delta\beta - 2Q_{n_y}Q_{n_z}\Delta\gamma - 2Q_{n_x}\Delta x - 2Q_{n_y}\Delta y - 2r_{2_{input}}\Delta r_2 \leq r_{2_{input}}^2 - Q_{n_x}^2 - Q_{n_y}^2$

$-limit_{angular} \leq \Delta\beta, \Delta\gamma \leq limit_{angular}$

$-limit_{linear} \leq \Delta x, \Delta y \leq limit_{linear}$

$-\infty \leq \Delta r_1, \Delta r_2 \leq \infty$

where: n = *number of points in the data set*

nominal axis and the least square axis solutions. The efficiency of the algorithms was also studied. Test results indicate that the number of loops required before convergence depends upon the initial conditions and the efficiency of each loop in terms of CPU seconds is a linear function of the number of data points.

Conclusions

The increase in use of CMMs as inspection tools has necessitated the development of fast and accurate verification methods for determining the concurrence of an actual part to tolerance specifications. This paper proposes a basic verification algorithm that solves a sequence of linear programs which converge to a solution that, given adequate initial conditions, is the minimum zone solution. A coordinate transformation is employed to obtain a linearization of the nonlinear optimization problem which will result in an efficient and robust algorithm. The linear programs for flatness and cylindricity are shown above. Linear programs for straightness, minimum circumscribed cylinder, and maximum inscribed cylinder can be obtained in a similar manner. For example, the minimum circumscribed cylinder linear program is derived from the cylindricity linear program by removing r_1 from the objective function and removing the constraints containing r_1. These algorithms are relatively easy to implement. In this work, we have used a commercially available optimization engine, namely OSL, to demonstrate the good performance of these algorithms with the minimum amount of specialized programming.

Bibliography

1. *ANSI Y14.5.1M-Draft Mathematical Definition of Dimensioning and Tolerancing Principles,* ASME, New York, NY, 1993.
2. *ANSI Y14.5M-1982 Dimensioning and Tolerancing,* ASME, New York, NY, 1982.
3. Anthony, G., et al., "**Chebyshev Best-Fit Geometric Elements,**" *NPL Report DITC 221/93*, 1993.
4. Chetwynd, D. G., "**Application of Linear Programming to Engineering Metrology,**" *Proc of Inst Mech Eng*, V199, N B2, 1985, pp. 93-100.
5. Fukuda, M., et al., "**Algorithms for Form Evaluation, Methods of Minimum Zone and Least Squares,**" *Proc of Int'l Symp on Metrology for Quality Prod*, Tokyo, 1984, pp. 197-202.
6. Huang, S. T., et al., "**A New Minimum Zone Method for Evaluating Flatness Errors,**" *Precision Engineering*, V15, N1, 1993, pp. 25-32.
7. Kanada, T., et al., "**Evaluation of Minimum Zone Flatness by Means of Nonlinear Optimization Techniques and Its Verification,**" *Precision Engineering*, V15, N2, 1993, pp. 93-99.
8. Murthy, T. S. R., et al., "**Minimum Zone Evaluation of Surfaces,**" *Int'l J. Machine Tool Design and Research*, V20, 1980, pp. 123-136.
9. Traband, M. T., et al., "**Evaluation of Straightness and Flatness Tolerances Using the Minimum Zone,**" *Manufacturing Review*, V2, N3, 1989, pp. 189-195.
10. Tsukada, T., et al., "**Minimum Zone Evaluation of Cylindricity Deviation by Some Optimization Techniques,**" *Bul. Jap Soc Prec Eng*, V19, N1, 1985, pp. 18-23.
11. Walker, T., "**GIDEP Alert No. X1-A-88-01,**" Government-Industry Data Exchange Program, August, 1988.

A Simple and Effective Method to Account for Tilt and Eccentricity in Roundness Measurements

V.Jayaraman and Jay Raja
Precision Engineering Laboratory
Dept. of Mechanical Engineering and Engineering Science
University of N. Carolina at Charlotte, Charlotte, NC

1.0 Introduction

In roundness and cylindricity measurements using an extrinsic datum (a precision spindle) the accuracy of assessment depends on the alignment of workpiece axis with the spindle axis. The misalignment could be due to eccentricity or a combination of tilt and eccentricity. The roundness and cylindricity measurements essentially result in radius suppressed and magnified data. The radius suppressed data gets distorted in the presence of eccentricity and/or tilt. In other words the data does not resemble an eccentric circle instead it more resembles a limacon. The equation for an eccentric circle is non-linear. The linearised equation of eccentric circle is also the equation of a limacon. The mathematics behind this apparent distortion is shown in section 2.0. In the presence of low eccentricity, a limacon is a good reference figure for assessing the roundness. Actually the eccentricity over radius of workpiece (e/r) ratio is the limiting factor, rather than the eccentricity itself. In other words as the radius of the workpiece becomes smaller even low eccentricity values can lead to a large e/r ratio. An e/r value of less than 0.008 is considered to be a good limit within which limacon is an acceptable reference figure [1]. Also in such low e/r cases, the other option currently prevalent is to suppress the second harmonic obtained through fast fourier transform. However in the presence of large e/r ratios, the above methods would be inadequate. Such a scenario would arise when small diameter high precision parts are to be measured in large volumes. For a workpiece of diameter 1mm, 4 microns eccentricity will mean an e/r of 0.008 as against 400 microns eccentricity for a workpiece of 100 mm in diameter. Such requirements will mean centering the smaller diameter parts to very low eccentricity values which in turn takes more time and will result in reduced throughput. Relaxing the centering requirements would increase the throughput, provided the distortion in data is corrected mathematically. This possibility of mathematically correcting the data which in turn could lead to increased throughput is the motivation for current work. The idea behind the correction is to bring the distorted data within the limacon regime so that limacon can be used as a reference figure. The highly distorted (e/r value larger than 0.008) data is corrected by an amount equivalent to the second order term of the equation of eccentric circle. This correction is called the 'second order correction' for eccentric circles [2].

Tilt is the other form of misalignment which can lead to inaccurate results. A circular section looks like an ellipse when it is tilted. The larger diameter of this ellipse is equal to secant(α) times the diameter of workpiece, where α is the angle of tilt. Tilt becomes important for large diameter part because its effect is directly proportional to diameter. This is in contrast with the eccentricity where it is the smaller diameter part which has to be centered well. The current practice to correct the tilt misalignment is to use the tilt adjustment table to align the workpiece as best as possible. Instead, we propose correcting it mathematically similar to eccentricity correction. Parametric equation of a cylinder represents a section of cylinder (a circle) in space i.e. it has terms accounting for orientation in addition to translation (eccentricity). A review of the second order term of the cylinder equation shows that it accounts for both tilt and eccentricity and hence is deemed to be a more appropriate term for use in second order correction of roundness measurements. This method is explained in the subsequent sections.

2.0 Linear equations of circle and cylinder

In the Figure 1, the datum circle with center o is shown by dashed lines. The profile, a circle with o' as center, is eccentric with respect to the center of the datum. The angle of eccentricity is ϕ and the magnitude of eccentricity is e_o. The radius of the profile, from its center (o') be r and the radial distance of the profile at angle θ from the datum center be $R(\theta)$. The displacement of the stylus will be proportional to the distance ε.

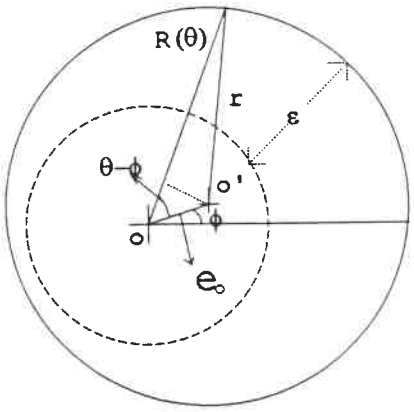

o	Center of datum
o'	Center of profile
r	Radius of profile
ϕ	Angle of eccentricity
ε	Measured displacement
$R(\theta)$	Radial distance of profile from datum center
e_o	Magnitude of eccentricity

Figure 1: Eccentric Circle

From the triangle oo'p,

$$R(\theta) = e_o \cos(\theta - \phi) + \sqrt{r^2 + e_o^2 \sin^2(\theta - \phi)} \tag{2.1}$$

Expanding the second term in Equation 2.1 binomially,

$$R(\theta) = e_o \cos(\theta - \phi) + r - \frac{1}{2}\frac{e_o^2}{r}\sin^2(\theta - \phi) + \frac{1}{8}\frac{e_o^4}{r^3}\sin^4(\theta - \phi) - \cdots \tag{2.2}$$

The equation derived expresses an eccentric circle in instrument coordinates. The limacon is given by the equation,

$$\rho(\hat{\theta}) = A + B\cos\hat{\theta} \tag{2.3}$$

The linear portion of equation 2.2, $r+e_o\cos(\theta-\phi)$, resembles the limacon equation 2.3. At low eccentricities the second and higher order terms of the equation 2.2 becomes negligible and the eccentric circle can be approximated to a limacon (limacon approximation). Notice that the second order term ($e_o^2 \sin^2(\theta-\phi)/2r$)only accounts for eccentricity.

Now expanding the first term of equation (2.2) and substituting $a = e_o\cos\phi$ and $b = e_o\sin\phi$ the equation becomes,

$$R(\theta) = a\cos\theta + b\sin\theta + r - \frac{1}{2}\frac{e_o^2}{r}\sin^2(\theta - \phi) + \frac{1}{8}\frac{e_o^4}{r^3}\sin^4(\theta - \phi) - \cdots \tag{2.4}$$

The following equation for cylinder is more comprehensive in describing a circular section in space.

A cylinder oriented in space can be viewed as having a set of points (on the surface) equidistant radially from the axis of the cylinder which has a specific orientation. This description of a cylinder has an implicit assumption of rigid body theory. Consider Figure 2. 'X' is a point on the cylinder surface with coordinates (x,y,z). 'X_o' with coordinates (a_o,b_o,0) is the center of the section of the cylinder lying on the XY plane and is referred to as bottom section in further paragraphs. The cylinder axis is tilted with respect to Z axis by angle α. The bottom section is eccentric at angle ϕ. Let the direction cosine of the axis be (a,b,c). The direction ratio of the axis can be designated as (a_1,b_1,1) where a_1 = a/c, and b_1 = b/c. The following equation of cylinder represent only upto second order terms.

$$R(\theta) = (a_o + a_1 z)\cos\theta + (b_o + b_1 z)\sin\theta + R_o - \frac{R}{2}(a_1\cos\theta + b_1\sin\theta)^2 + \frac{1}{2R}\left[(a_o + a_1 z)\sin\theta - (b_o + b_1 z)\cos\theta\right]^2 \quad (2.5)$$

Comparison of linear portion of the above cylinder equation with that of the linear portion of the equation of an eccentric circle (equation 2.4) reveals a striking similarity. The coefficient of cosθ 'a_o+a_1z' is the measure of X component of the eccentricity of the section of cylinder at height 'z' and the coefficient of sinθ 'b_o+b_1z' is the Y component of eccentricity of cylinder at height 'z' just as in the case of coefficients of the first two terms of equation of eccentric circle. Consider the second order terms of,

the cylinder $\Rightarrow -\frac{R}{2}(a_1\cos\theta + b_1\sin\theta)^2 + \frac{1}{2R}\left[(a_o + a_1 z)\sin\theta - (b_o + b_1 z)\cos\theta\right]^2$ and

the circle $\Rightarrow -\frac{1}{2}\frac{e_o^2}{r}\sin^2(\theta - \phi)$

It can be seen that the first term (of second order terms) of cylinder has a_1 and b_1 in it. These are the direction ratio terms and they give a clue to the tilt of the cylinder axis with respect to the 'Z' axis. The second term (of second order terms) of cylinder have the X and Y components of the eccentricity of that particular section at that height z. In contrast the second order term in the equation of eccentric circle, has terms that only account for eccentricity. Thus a correction based on cylinder second order terms will be more comprehensive than second order term of the equation of eccentric circle. The next section describes the measurement process to use the cylinder second order term for correcting the roundness data.

3.0 Computer Simulations and Experimental Validation

Generally all tilt adjustment tables have a point in space, at a height from its top, about which they tilt. This point is called the table focal point. One trace of the workpiece is taken at this height (refer Figure 3). Then a second trace, at the section where roundness is to be determined (measured section), is taken. An estimate of eccentricities of the first section and measured section is obtained from the respective traces. Direction cosine of the axis of the cylinder can be estimated from the eccentricity estimates and the knowledge of height between the two traces. The second order term of the cylinder equation is calculated and used to correct the raw data. Then a limacon is fit to this corrected data and the out of roundness value is computed. Simulation results show this correction to be very effective. Experiments to validate this is being carried out using a 12.7 mm diameter pin gage and a 9.0 mm diameter part. The workpiece is centered as well as possible. The measured section is at a height above the table focal point (5 mm above the table focal point for results given in Table 1). The table focal point in this case is 50.8 mm above the table top. Out of roundness of the measured section in well centered condition is measured and taken as the reference out of roundness value. Then tilt is introduced in steps of 25 micrometers upto a total of 150 micrometers in the measured section. Table 1 gives a comparison of out of roundness of the pin gage at the measured section in the presence of tilt when the radius suppressed data is corrected for both tilt and eccentricity versus correction for eccentricity only. The out of roundness value of raw data when tilt is

The tilt corrections will be more useful when the part diameter is large, in the range of 50 mm and above. The accuracy in estimating the center of a section influences the effectiveness of second order corrections, a better estimate of the center leads to a more effective correction.

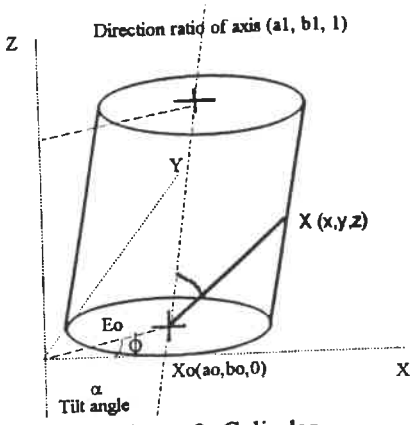

Figure 2: Cylinder

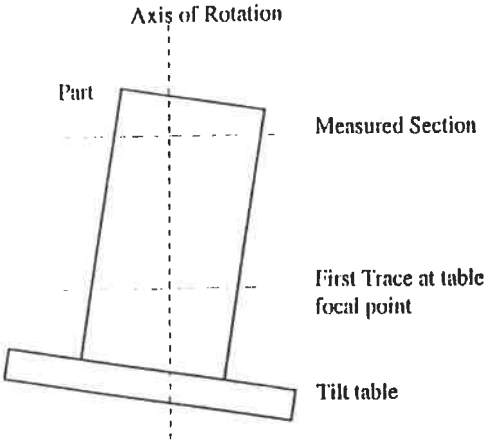

Figure 3: Tilt & Eccentricity correction in roundness measurement.

Tilt introduced at 5mm above table focal point in 12.7 mm dia. pin gage (μm)	Out of roundness value of raw data (μm)	Out of roundness value of data corrected for eccentricity only (μm)	Out of roundness value of data corrected for both tilt & eccentricity (μm)
0	1.1023*	-	-
50	1.0834	0.9974	1.1076
75	1.4888	1.1851	1.1757
100	2.1946	1.4451	1.1741
125	2.8961	1.7560	0.9623
150	3.9986	2.3501	0.9919

* Reference out of roundness value.

Table 1: Experimental results for 12.7 mm diameter pin gage with tilt introduced at 5 mm above table focal point

References:
1. Chetwynd D. G., Roundness measurement using limacons - Precision Engineering 1, 1979.
2. Chetwynd D. G., Ph. D. Thesis, Dept. of Engineering, University of Leicester, UK 1980.
3. ANSI B89.3.1 American National Standards: Measurement of Roundness. ASME, 1972.
4. Reason R. E., Report on the measurement of roundness, 1966.
5. Whitehouse D. J., A best fit reference line for use n partial arcs, J. Phys. E. Sci. Instrum. 6, 1973.
6. BS 3730 Assessment of Departures from roundness, BSI 1974.

Micro-electro-mechanical Actuator Arrays for Deformable Mirrors

Thomas Bifano, Associate Professor, Precision Engineering Research Laboratory
Aerospace and Mechanical Engineering Department, Boston University, Boston MA 02215

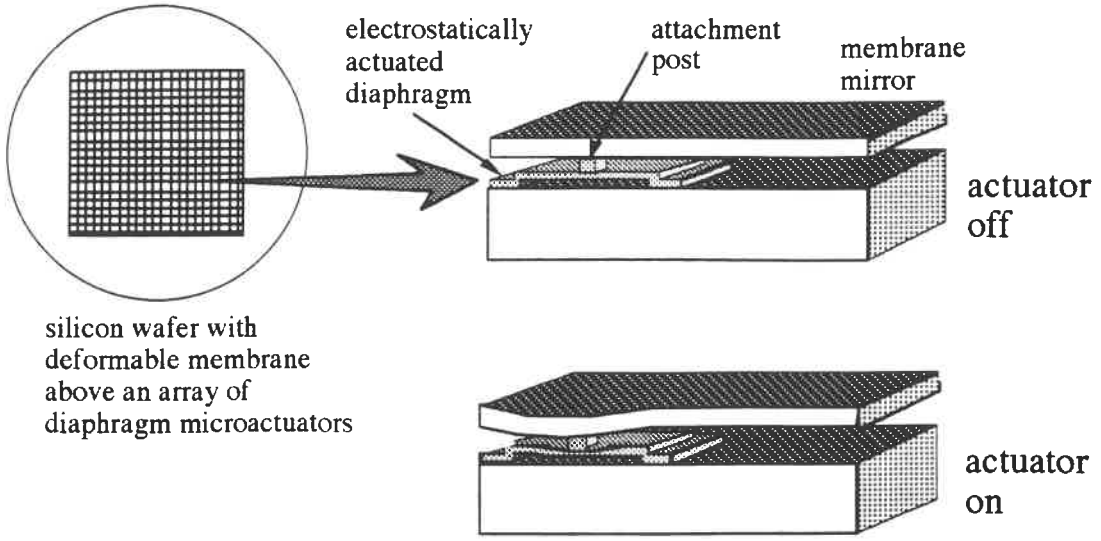

Figure 1: Concept schematic: microelectromechanical deformable mirror device using an array of electrostatically actuated diaphragms. A continuous mirror membrane spans hundreds of actuators. At right is a schematic of a small section of the device. When on, *an individual actuator locally deflects the membrane mirror by a prescribed amount. Several working actuator arrays have been fabricated and tested for this project.*

Introduction

Microelectromechanical systems (MEMS) offer a new approach to the production of reliable, high-tolerance mechanical components. Semiconductor fabrication technology has enabled the *miniaturization* of a variety of sensors and, more recently, a variety of actuators. Of equal significance is the enabling of *large numbers* of such sensors and actuators, all fabricated at the same time and on the same substrate. Furthermore, the common fabrication technology enables *integration* of these sensors, actuators, and electronics into monolithic, closed-loop controlled devices with superior performance and lower cost than discretely assembled devices. At Boston University, we have begun a project aimed at exploiting the large numbers and integration of semiconductor fabrication to develop massively parallel, interconnected micro-actuators coordinated to achieve precision actuation and control at a of a macroscopic structure. We designed, fabricated, and tested several prototype MEMS actuator arrays to demonstrate their feasibility. The arrays consist of electrostatically actuated diaphragms capable of surface-normal deflection, which will be used as a basis for developing a deformable mirror device. Beyond its value as a demonstration project for MEMS arrays, the deformable mirror project represents a significant advance in the field of adaptive optics: an inexpensive, easily reproduced, non-piezoelectric, low-power device for correction of optical wavefront aberrations.

Demonstration Project: Deformable Mirror Actuator Array

There are several important applications for deformable mirrors, primarily in adaptive optical (AO) systems, which correct aberrations in an optical system through active control of mirror geometry. The most common AO systems use nominally flat, deformable secondary mirrors, whose shape is adjusted to compensate for aberrations in an optical wavefront. One important application of AO is compensation of aberration due to atmospheric turbulence in astronomical telescopes. The process is called phase conjugation, and requires that each of

the deformable mirror's many segments or zones is controlled in real-time. With AO, the achievable image resolution is greatly enhanced. A recently published review of AO research noted that the largest research system implemented to date uses 241 separate piezoelectric actuators (individually manufactured and mounted, with an integral cooling system required to eliminate excess heat). By using *MEMS technology*, the image resolution of an adaptive optical system can be improved while reducing manufacturing time, actuator cost, and assembly complexity.

The primary variables to be specified in a deformable mirror system are the *number of actuators, the control bandwidth, and the maximum actuator stroke*. For astronomical observations, these design parameters can be estimated based on the desired strehl ratio[1], the optical wavelength of interest, the characteristics of the optical disturbance (e.g. intensity of atmospheric turbulence) and the optical system aperture, using theoretical turbulence and photonic models. For example, based on assumptions of moderate turbulence, near-infrared light (λ=1.0μm), a 1m diameter primary mirror, and a strehl ratio of 0.5 (roughly 5 times better than non-adaptive optical performance), a deformable mirror would require 500 actuators, a bandwidth of 600Hz, and a stroke of 2μm. These parameters will serve as design goals for the proposed MEMS actuator array project.

The proposed MEMS deformable mirror is made up of a planar array of ~500 small electrostatically actuated diaphragms arranged in a square grid pattern beneath a thin membrane mirror. Each actuator is a ~2μm thick silicon diaphragm measuring ~350μm x ~350μm. The diaphragms are oriented with their surfaces parallel to the surface of the substrate, and are, anchored to the substrate material (a 750μm thick silicon wafer) along two of their edges. The gap between diaphragm and substrate is ~2μm. Actuation is achieved by imposing opposite polarity electric charge between the diaphragm surface and the substrate, which generates an electrostatic force in the direction normal to the diaphragm surface, thereby deflecting the diaphragm. A 2μm thick membrane mirror is supported above the array of diaphragms, also oriented with its surface parallel to the substrate. Its span of 10mm x 10mm allows it to completely cover the actuator grid. The membrane mirror is supported by small (50μm square, 2μm tall) attachment posts at the center of each actuator diaphragm. After fabrication, the front surface of the membrane mirror will be electroplated and lapped to optical quality. The optical correction strategy will use open loop voltage control of each of the actuators to achieve local mirror deflections of 0-2μm with 20nm resolution and a 1kHz bandwidth. In this paper, we report only on diaphragm actuator array characteristics. Fabrication runs with integral membrane mirrors have not yet been completed.

The actuator array design envisioned for this demonstration project depends on a proven MEMS actuation scheme: surface-normal arrays of electrostatically actuated silicon diaphragms. Two critical technology issues that have to be addressed to demonstrate the feasibility of the proposed parallel micro-actuation arrays are:

- Actuator Performance - Theoretically, the diaphragm actuators should be able to achieve the required resolution (20nm), stroke (2μm), and frequency bandwidth (1000Hz), but these performance criteria have never been demonstrated in an actual diaphragm array.

- Process Reliability - A process yield of >90%, with fault tolerant design rules will be necessary for implementing coordinated actuation arrays, though current MEMS production runs usually yield 40-60%.

[1]Strehl ratio, S, is a common measure of optical system imaging performance. S is the ratio of the on-axis intensity of an aberrated image to the on-axis intensity of an unaberrated image.

We have completed a research program aimed at these two technology issues. By joining in two multi-project MEMS fabrication cycles at the Microelectronics Center of North Carolina (MCNC), we were able to fabricate arrays of surface normal diaphragms on several dozen sample wafers. Evaluation of the performance of these wafers has provided essential feedback for the development of acceptable surface-normal actuator arrays. The MCNC project permits inexpensive prototype development of MEMS devices, offering semi-annual production runs using a standardized set of semiconductor fabrication processes. Basically, the design rules allow user-specified two-dimensional patterning of any or all of the following layers, which are sequentially deposited on a doped silicon wafer:

Layer	Thickness	Comments
Silicon nitride	100 nm	electrically insulating
Silicon dioxide1	2.0 μm	sacrificial layer
polycrystalline silicon 1	2.0 μm	structural, doped
Silicon dioxide 2	0.5 μm	sacrificial layer
Polycrystalline silicon 2	1.5 μm	structural, doped

In the first fabrication cycle, constructed a series of polycrystalline silicon wafer diaphragms varying in size from 125 μm square to 500 μm square, with as many combinations of diaphragm thickness and gap thickness as were permitted by the MCNC design rules (e.g. diaphragm thicknesses of 1.5 μm, 2.0 μm, and 3.5 μm were achievable by using either or both polycrystalline silicon layers). Our plan was to choose the best of these evaluation designs for use in the actuator array. A simplified schematic of common actuator design features is shown in Figure 1. To fabricate this device, the following sequence of processes were performed at MCNC. A full layer of silicon nitride was deposited on a doped silicon wafer, patterned only where subsequent ground pads would be used to make electrical contact with the silicon base wafer. Silicon dioxide was deposited on top of the silicon nitride and patterned to produce a series of islands with square footprints. Polycrystalline silicon was then deposited and patterned on top of the oxide, with rectangular footprints of the same width as the underlying silicon dioxide islands, but slightly (~50 μm) longer, to create walls for the double-cantilevered diaphragms. Holes were patterned into each diaphragm to allow subsequent acid etching to remove the sacrificial oxide layer. The silicon nitride serves to electrically isolate each diaphragm from the others and from the silicon substrate, which serves as a ground plane. To actuate a diaphragm a voltage was applied (through a pair of micro-probing electrodes) between the diaphragm and the ground pad, generating an electrostatic force that caused elastic deflection of the diaphragm. Five hundred copies of this pattern were reproduced on each of fifteen wafers that were fabricated in this production run. The dynamic and static response of each diaphragm was tested using a displacement measuring interferometer. This commercially available device uses a focused laser beam to measure normal displacement with a resolution of 0.6 nm, a range of 1-2 mm, a frequency bandwidth of 0-130kHz, and a lateral sampling area of several micrometers.

The best performance was obtained with diaphragms that were 350 μm square, 2.5 μm thick, with a 2.0 μm gap. With these diaphragms, voltages of 40-60 V were sufficient to achieve full deflection. Deflection of the center of the diaphragm scaled nonlinearly but predictably with applied voltages below this threshold. Smaller diaphragms could not be deflected with voltages under 100 V, and larger diaphragms were often "stuck down" without any applied voltage, probably due to the residual stresses left by deposition and etching of the polycrystalline silicon (this is a common problem with larger MEMS devices).

In a second MCNC production cycle, an array of 360 of the diaphragm actuators were fabricated on each of four 10 mm x 10 mm silicon wafers to test performance, uniformity, and yield of this optimized diaphragm design.

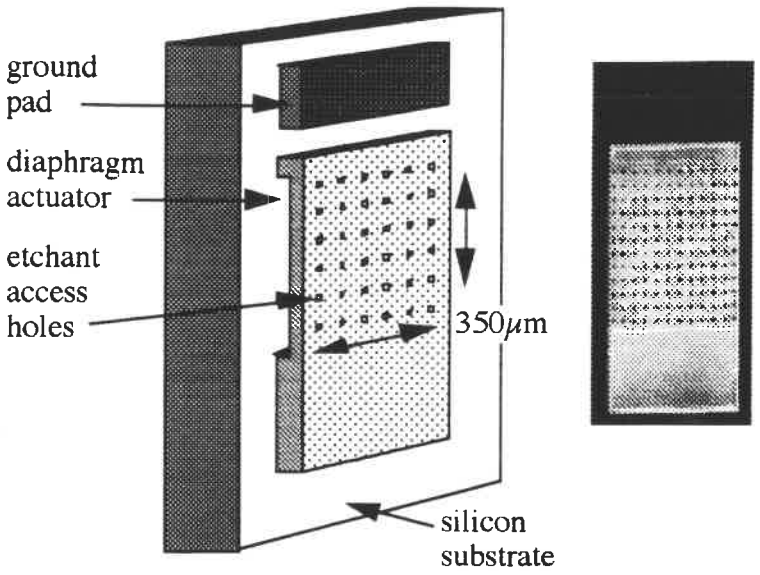

Figure 2: Schematic (left) and scanning electron microscope image (right) of an electrostatic diaphragm actuator fabricated at the Microelectronics Center of North Carolina for this project. The diaphragm surface deflects toward the substrate when an electrostatic charge is applied between the substrate and the diaphragm.

Previous MEMS research has demonstrated that the average yield for individual actuator designs is 40-60%. It reasonable to expect that the simpler design and layout of the diaphragm surface-normal actuator arrays will lead to higher yields, and in fact that is what we found. In our prototype wafers, we tested each diaphragm on four 10 mm x 10 mm samples (a total of 1440 actuators) and found a yield of 98% useful, working electrostatic actuators.

When subjected to a slowly increasing voltage (0-100V) the diaphragms began to deflect when the voltage reached 40 V, and the deflection increased nonlinearly but quite repeatably until the voltage reached 60 V at which time the diaphragm was deflected by approximately 0.7 μm. Above this critical voltage, the diaphragm would undergo the well-known electrostatic actuator phenomenon called "snap through instability", instantaneously deflecting all the way to the substrate. It was found that there was a 10% variability (1σ) in critical voltage among the actuators tested, but less than 0.1% variability in the critical voltage for a given actuator subjected to repeated deflections. This suggests that the actuators in a given array could be used in an open loop actuation control scheme, provided that each actuator's characteristic critical voltage was previously measured. The actuators were able to respond to frequencies from 0-10kHz (the bandwidth of our driving amplifier) without attenuation. The actuators were found to draw no measurable current, which implies that the array is thermodynamically reversible, as expected for an electrostatic system.

The next step in this prototype actuator array development program is to include a face sheet, and to test actuator coupling as a result of the mechanical attachment to the sheet (electrical coupling has been found to be nonexistent). This design is currently being fabricated in a third MCNC MEMS production run.

Acknowledgments

Experimental testing and numerical simulation were performed by Boston University undergraduate students Laura Rennie and Jody Koch. Funding was provided by the NSF through a *Small Grant for Exploratory Research* # DDM9317937.

Angle measurement based on the internal-reflection effect using right-angle prisms

P. S. Huang
Department of Mechanical Engineering
State University of New York at Stony Brook
Stony Brook, NY 11794-2300

J. Ni
Department of Mechanical Engineering and Applied Mechanics
The University of Michigan
Ann Arbor, MI 48109-2125

1. Introduction

Small-angle measurement is conventionally performed by using interferometers and auto-collimators. Recently Huang *et al.* developed a new method, namely, Angle Measurement based on the Internal-Reflection Effect (AMIRE)[1], which showed some unique features. AMIRE basically consists of a beam splitter for splitting the incident beam into two for differential detection, a pair of prisms for transforming the angular displacement into the change of beam intensities, and a pair of photodiodes for detecting the beam intensities. For high-resolution measurement, a multiple-reflection scheme has been proposed to increase the measurement sensitivity, using a pair of elongated critical-angle prisms as the reflection prisms[1,2]. While the measurement sensitivity is greatly increased by this method, the use of elongated critical-angle prisms results in some complexity in constructing the sensor because elongated critical-angle prisms are customer designed components and require higher geometric accuracy.

To solve this problem, a pair of right-angle prisms are used to substitute for the elongated critical-angle prisms. Since right-angle prisms are inexpensive, commercially available components, such a design entails simpler optics and lower cost. Also, right-angle prisms are smaller than elongated critical-angle prisms, which makes the sensor more compact. Theoretical analysis and experimental results are presented in this paper.

2. Theoretical Analysis

Figure 1 shows how a light beam propagates through a right-angle prism when the light is incident on the entrance face of the prism. There are three reflections and refractions before the light beam traverses out of the exit face of the prism. If we assume that the light source is *p*-polarized and denote the reflectances at the entrance face, hypotenuse face and exit face as R_1, R_2 and R_3 respectively, we obtain the Fresnel's equations in the following forms:

$$R_1 = \left(\frac{\tan\theta_1 - \tan\theta_2}{\tan\theta_1 + \tan\theta_2} \right)^2 \qquad (1)$$

$$R_2 = \left(\frac{\tan\theta_3 - \tan\theta_4}{\tan\theta_3 + \tan\theta_4} \right)^2 \qquad (2)$$

$$R_3 = \left(\frac{\tan\theta_5 - \tan\theta_6}{\tan\theta_5 + \tan\theta_6} \right)^2 \qquad (3)$$

where θ_1, θ_3 and θ_5 are the angles of incidence, and θ_2, θ_4 and θ_6 are the angles of refraction at the entrance face, hypotenuse face and exit face respectively. From the symmetry of the refractions at the entrance face and the exit face, we can readily see that $\theta_1 = \theta_6$ and $\theta_2 = \theta_5$, and therefore $R_1 = R_3$ (see Eqs. (1) and (3)). The total reflectance of the light beam traversing through the prism is then given by

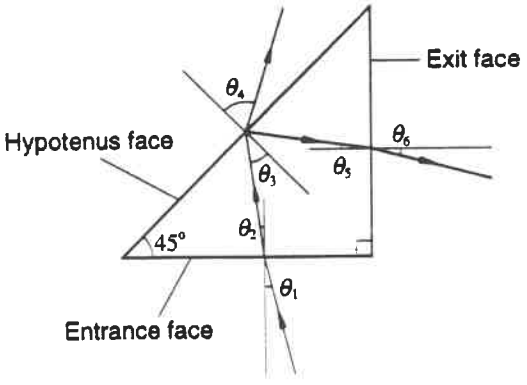

Figure 1 Light reflection at a right-angle prism.

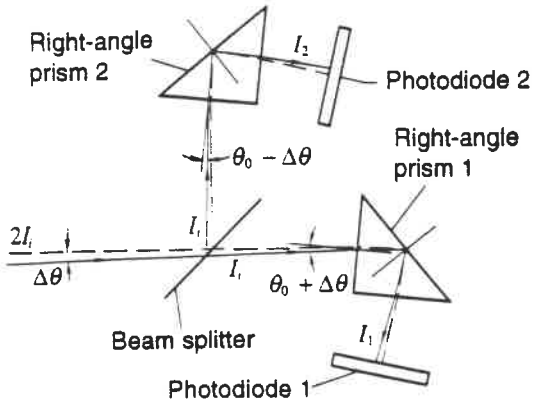

Figure 2 Optical layout of the differential detection method.

$$R = (1 - R_1)R_2(1 - R_3)$$
$$= (1 - R_1)^2 R_2 \qquad (4)$$

In the case when light incidence at the entrance face is near normal, R is mainly determined by R_2 because R_1 is small (approximately 0.04 when n_i = 1.5 and n_t = 1.0) and remains virtually unchanged.

Figure 2 shows the optical layout of the differential detection method when a pair of right-angle prisms are used as the reflection prisms. Here we have assumed that the angle of incidence θ_1 is equal to $\theta_0 + \Delta\theta$, where θ_0 is the initial angle of incidence and $\Delta\theta$ is the angular displacement from θ_0. From the definition of linearized reflectance[1], we can calculate the linearized reflectance R_l crresponding to the reflectance R as follows:

$$R_l(\Delta\theta) = \frac{R(\Delta\theta) - R(-\Delta\theta)}{R(\Delta\theta) + R(-\Delta\theta)} \qquad (5)$$

where $R(\Delta\theta)$ and $R(-\Delta\theta)$ are the reflectances at prism 1 and prism 2 respectively. Now from the same figure, we can see that $R(\Delta\theta)$ and $R(-\Delta\theta)$ can be represented as follows:

$$R(\Delta\theta) = I_1 / I_i \qquad (6)$$
$$R(-\Delta\theta) = I_2 / I_i \qquad (7)$$

where I_1 and I_2 are the intensities measured by photodiode 1 and photodiode 2 respectively, and I_i is half of the incident intensity (here the beam splitting ratio of the beam splitter has been assumed to be 50%:50%). Substituting the above equations into Eq. (5), we obtain another expression of the linearized reflectance R_l as

$$R_l(\Delta\theta) = \frac{I_1 - I_2}{I_1 + I_2} \qquad (8)$$

Table 1 Optimal angles and sensor performance

Light source	Optimal angle (deg)	Optimal reflectance (%)	Nonlinearity error (%)	Sensitivity (1/deg)	Measurement range (deg)
s-polarized	37.845	5.590	0.041	0.031	32.237
	12.150	22.263	0.013	0.102	6.542
p-polarized	6.396	28.210	0.015	0.779	0.788
unpolarized	16.141	7.954	0.004	0.080	10.533
	9.152	19.046	0.014	0.196	3.544

While Eq. (5) is used for the following theoretical analysis, Eq. (8) is used for the experiment described in the following section.

As we know from previous studies[1, 2], the linearity of $R_l(\Delta\theta)$ as a function of $\Delta\theta$ depends on the initial angle of incidence θ_0. To find the θ_0 at which the nonlinearity error of $R_l(\Delta\theta)$ becomes minimal (the optimal angle), we substitute different values for θ_0 and then calculate the nonlinearity error at each θ_0 by linear curve fitting. Table 1 shows the results. Here we have assumed that the glass material is BK7 and its refractive index is 1.51509 (at the wavelength of 632.8 nm). For *p*-polarized light, there is one optimal angle 6.396° at which the nonlinearity error becomes minimal. The measurement sensitivity and range at this optimal angle are 0.779 (1/deg) and 0.788° respectively. For *s*-polarized or unpolarized light, there are two optimal angles at which larger measurement ranges with excellent linearity can be realized.

3. Experimental Results

A prototype sensor has been developed to verify the results obtained from the theoretical analysis. The laser beam for the sensor is from a single-mode fiber beam delivery system which provides a *p*-polarized, collimated laser beam with high pointing stability[3]. The right-angle prisms are made of BK7 glass with a roof angle tolerance of ± 3 arcmin. The beam splitter is a cube beam splitter with an all-dielectric non-polarizing partial reflection coating. The photodiodes are silicon photodiodes for precision photometry. The angular displacement for the calibration is provided by a rotary stage driven by a micrometer. The signals from the photodiodes are first amplified and conditioned and then sent to a computer via a data acquisition system for further signal conditioning as well as

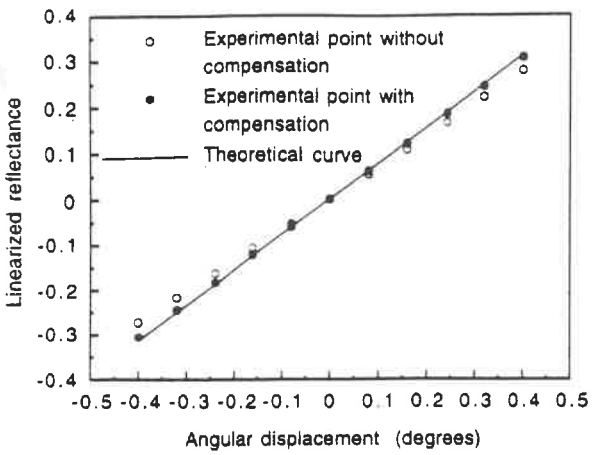

Figure 3 Calibration results compared with the theoretical curve.

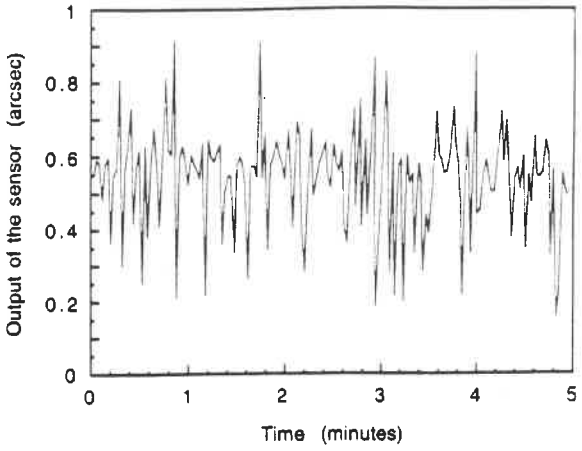

Figure 4 Noise and drift.

the calculation of linearized reflectance. As the reference of the calibration, a laser interferometer (HP5528A from Hewlett-Packard) is used, which provides a measurement resolution of 0.1 arcsec, a measurement accuracy of ± 0.2% and a measurement range of ± 1°.

For minimal sensor nonlinearity, the initial angle of incidence θ_0 needs to be set precisely at the optimal angle. To do this, one simple method is to set the initial reflectance to the optimal reflectance because the reflectance can be easily monitored by measuring the light intensities using the photodiodes. Once the angular position of the first prism is determined, the optimal position of the second prism can be found by rotating the prism until the output of the sensor, or the linearized reflectance, becomes zero.

Figure 3 shows the calibration result of the sensor in a range of ± 0.4° along with the theoretical curve for comparison. Here the experimental points without compensation is obtained by calculation using Eq. (8), while the experimental points with compensation is obtained by calculation using the following equation:

$$R_l(\Delta\theta) = \frac{I_1 / I_{i1} - I_2 / I_{i2}}{I_1 / I_{i1} + I_2 / I_{i2}} \qquad (9)$$

where I_{i1} and I_{i2} are the intensities of the laser beams right after the beam splitter. Ideally, I_{i1} and I_{i2} should be equal and independent of the angle of incidence at the beam splitter, as has been assumed in deriving Eq. (8). However, we found that this assumption did not hold for the beam splitter we used. To compensate for the change of I_{i1} and I_{i2} with the angle of incidence at the beam splitter, we modified Eq. (8) to Eq. (9). Notice that I_1/I_{i1} and I_2/I_{i2} in Eq. (9) represent the reflectances at two right-angle prisms and are obviously independent of the angle of incidence at the beam splitter. In this experiment, I_{i1} and I_{i2} as a function of the angle of incidence at the beam splitter was measured prior to the calibration of the sensor and stored in the computer for later calculation of the linearized reflectance. In the future, a beam splitter whose beam splitting ratio is relatively insensitive to the angle of incidence, for example, a cube beam splitter with a hybrid, metal-dielectric partial reflection coating, could be used to eliminate the need for compensation.

As can be seen in Figure 3, the calibration result agrees well with the theoretical curve once the change of I_{i1} and I_{i2} is compensated. Also, linear regression analysis showed that the nonlinearity error for this sensor is approximately ± 0.1% after compensation. Although this nonlinearity error is still much larger than that of the theoretical value, it is already within the accuracy limit of HP5528A, the calibration reference. A more accurate reference instrument is needed if higher accuracy calibration is to be performed.

Figure 4 shows the noise and drift of the sensor over a time period of five minutes. The peak-to-peak fluctuation, which is mainly due to the electronic noise, is approximately 0.75 arcsec. There is no apparent drift during the time period.

To see if the same sensor is suitable for higher resolution measurement, we further amplified the signals electronically so that the measurement range became approximately ± 50 arcsec, and then repeated the calibration experiment and linear regression analysis. The result is

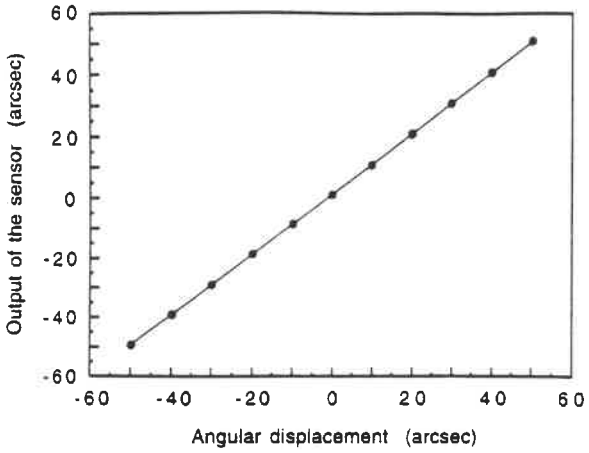

Figure 5 Calibration result in a small range with linear curve fitting.

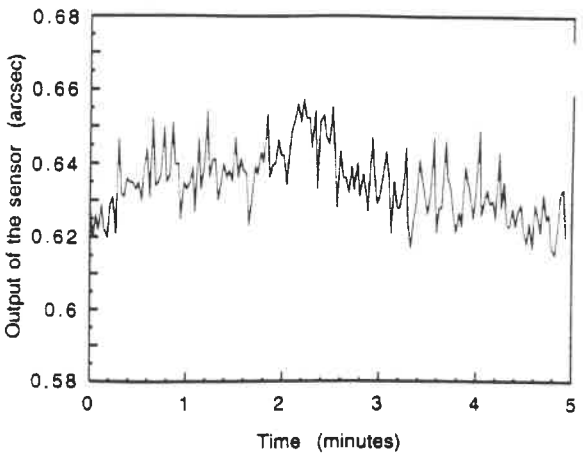

Figure 6 Noise and drift when the sensor is set for high-resolution measurement.

shown in Figure 5. The nonlinearity error is found to be approximately ± 0.12%. To check the resolution in this case, the same five-minute noise and drift test was performed and the result is shown in Figure 6. We see that the peak-to-peak fluctuation is reduced to approximately 0.04 arcsec. We also performed a one-hour drift test in this case which resulted in a peak-to-peak fluctuation of less than 0.1 arcsec. This long-term drift is mainly due to the temperature variation of the environment.

From these results, it is appropriate to say that the same sensor is suitable for both general alignment applications and high-resolution small angle measurement applications, as long as a high S/N ratio for the electronics of the sensor is guaranteed.

4. Conclusions

We have presented the theoretical analysis and experimental results of the recently developed method of angle measurement, Angle Measurement based on the Internal-Reflection Effect (AMIRE), when a pair of right-angle prisms are used as the reflection prisms to simplify the optics. Theoretical analysis showed that sensors based on this principle can be easily designed for applications with different measurement ranges by selecting light sources with different polarization states, such as *s*-polarized, *p*-polarized and unpolarized light. For all these light sources, the sensor design can be optimized by choosing the initial angle of incidence so that the nonlinearity error of the sensor becomes minimal. In our prototype sensor, *p*-polarized light was chosen as the light source. As a result, the sensor demonstrated a measurement range of ± 0.4° and a resolution of approximately 0.75 arcsec. The same sensor can also be used for higher resolution applications if the measurement range is limited to a smaller value. One experiment showed that a resolution of 0.04 arcsec with a measurement range of ± 50 arcsec can be easily achieved by simply electronically amplifying the signals.

In summary, angle measuring sensors based on the principle of AMIRE with a pair of right-angle prisms can outperform conventional angle measuring instruments, such as interferometers and autocollimators, with additional benefits of compact size, simple optics, and low cost. Also, if light sources other than *p*-polarized light are used angle measuring sensors with measurement ranges of tens of degrees are possible, which are usually difficult with the conventional methods.

References

1. P. S. Huang, S. Kiyono, and O. Kamada, "Angle measurement based on the internal-reflection effect: a new method," Appl. Opt. 31, 6047-6055 (1992).
2. P. S. Huang and J. Ni, "Angle measurement based on the internal-reflection effect: multiple reflections," (submitted to Appl. Opt. for review).
3. P. S. Huang, "Laser optical measurement systems and their application to the on-line error compensation of coordinate measuring machines," Ph.D. Dissertation, The University of Michigan, Ann Arbor, 131-135 (1993).

Development of a New Ultrasonic Sensor for Displacement Measurement

Kimiyuki MITSUI*, Makoto KOIKE**,
Hidehiko TSUKAMOTO*** and Minoru YAJIMA***

*Department of mechanical Engineering, Keio University, 3-14-1 Hiyoshi, Kohoku-ku, Yokohama, 223 Japan
**Fuji Photo Film, Ltd., 200 Ohonakazato, Fujinomiya, Shizuoka, 418 Japan
***Mitsubishi Heavy Industries, Ltd.,4-6-2 Kannon Shin-machi, Hiroshima, 733 Japan

1. Introduction

In order to improve dimensional accuracy of workpieces, in-process measurement is considered the best. As for accurate dimensional deviation measurement, some optical measuring methods including commercially available have been developed[1]-[3], but optical methods are not suitable using in wet condition such as turning or grinding operations. Measuring method using ultrasonic wave can be used even in such a severe environment.

This study deals with development of ultrasonic sensor for displacement measurement based on astigmatic focus error detection. First, the measuring principle is described. Then, the experimental results that show the validity of the principle are shown.

2. Measuring principles

The measuring principle of astigmatic focus error detection[4] is illustrated in Fig.1. The backward-traveling collimated ultrasonic wave beam

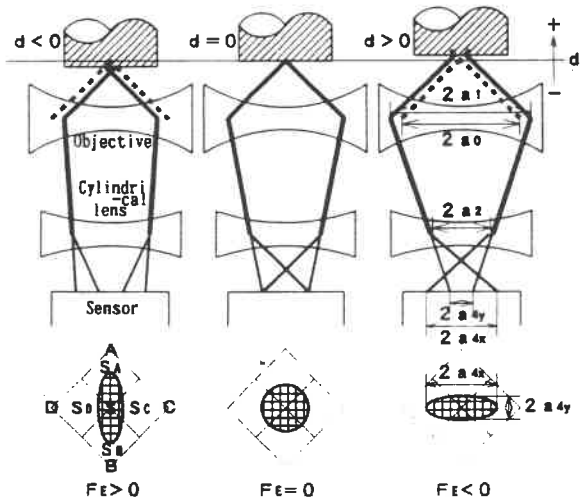

Fig.1. Principle of astigmatic focus error detection

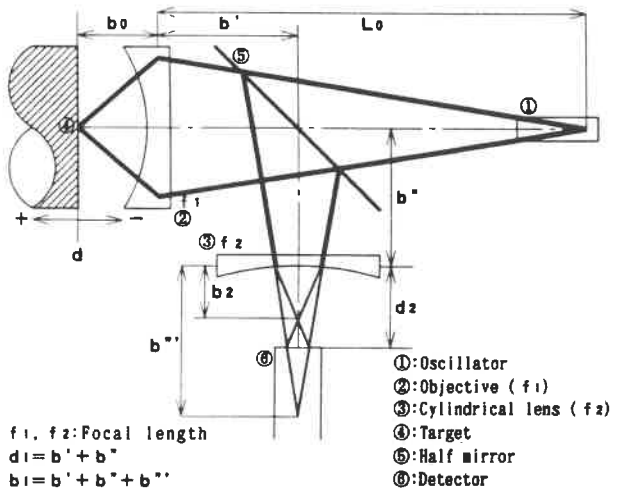

Fig.2. System layout of the ultrasonic sensor

makes an image on the quadrant type ultrasonic wave sensor. A cylindrical ultrasonic lens is placed between objective and sensor to give th astigmatism. The quadrant ultrasonic sensor is placed in the position where a convergent beam profile becomes circular. When the target surface position changes, the form of the image on the sensor becomes an ellipse, as shown in the figure. The signal corresponding to the target surface displacement is given by

$$F_E = \frac{(S_A + S_B) - (S_C + S_D)}{S_A + S_B + S_C + S_D} \qquad (1)$$

Where S_A-S_D represent output signal of a quadrant sensor elements.

Figure 2 shows the system layout of ultrasonic displacement sensor. The relationship between system output and focus error can be calculated with the aid of geometric optics. Here, the objective and the cylindrical lens are assumed as single thin lens. Main parameters are written as following.

f_1: focal length of objective lens
f_2: focal length of cylindrical lens
d_1: distance between objective and cylindrical lens
d_2: distance between cylindrical lens and recieving sensor
d: displacement of target surface
L_0: distance between focus point of the ultrasonic transducer and objective lens

Figure 3 shows an example of calculated result. In the astigmatic focus

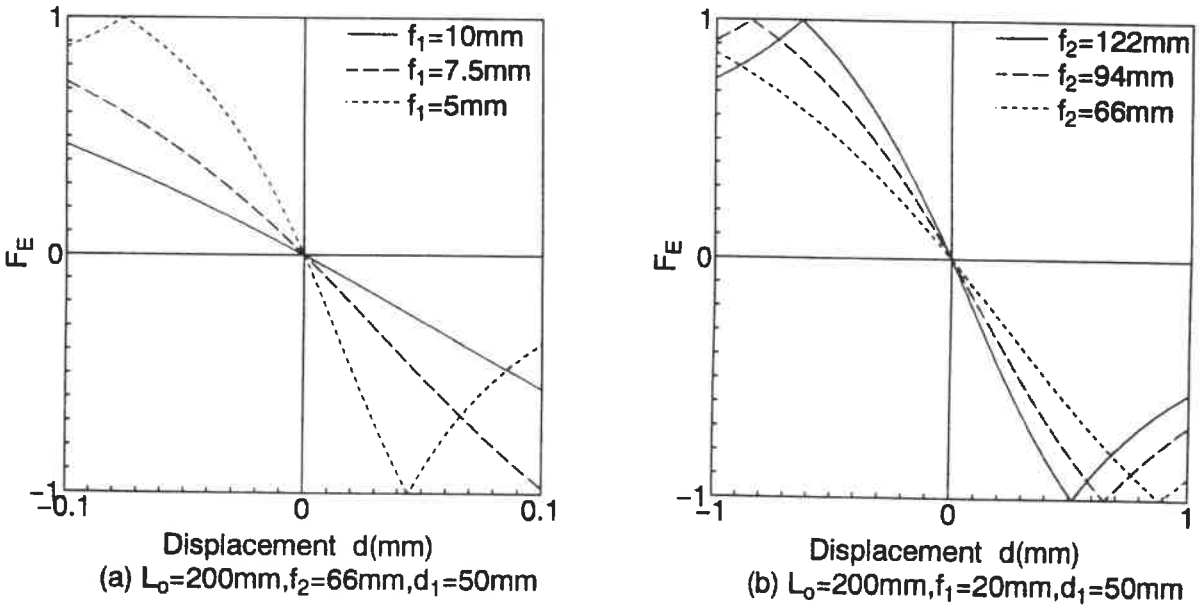

Fig.3. System output and focus error (calculation)

error detection method, the focal length of the objective and cylindrical lenses, the distance between these two lenses, and the position of the quadrant sensor can be chosen as variables in the system design. This allows the equipment to have any sensitivity and linear range.

3. Experimental results

Parameters of the experimental apparatus are f_1=20mm, f_2=66mm, d_1=50mm, d_2=70.2mm and L_0=200mm. Oscillating frequency of the transducer is 7.5MHz and its diameter is 10mm. The half mirror is made of acrylic resin plate of thickness 0.5mm. The objective lens is plano-concave lens of curvature 10mm, and the curvature of the cylindrical lens is 33mm. Both lenses are made of acrylic resin. As for target surface, edge of micrometer head is used. All measuring equipment was sunk in a water tank and the receiving sensor was connected with ultrasonic flaw detector. The signal intensity was obtained by reading the display.

The relationship between the displacement of target surface and system output was measured. The target surface, edge of micrometer head, was positioned every 0.1mm, and the output of each element of the quadrant sensor was connected to the ultrasonic flaw detector in order.

Figure 4 shows the output A+B, C+D and A+B+C+D. Also, a similar measuring result by the establishment which removed cylindrical lens is shown in Fig.5. Furthermore, characteristic of F_E calculated from equation (1) is shown in Fig.6. A calculated result, a measuring result and the corrected result which is explained later on are shown in Fig.6. While A+B almost coincided with C+D in Fig.5 where the cylindrical lens was removed, the relation is reversed in Fig.4 which include cylindrical lens. As a result of this, it was clarified that displacement measurement by a way of astigmatic focus error detection is effective also for ultrasonic wave.

In addition, the sum total of output of all elements is biger in Fig.5 than in Fig.4. The reason is considered that input power to the quadrant sensor becomes larger when cylindrical lens does not exist, because attenuation and reflection of ultrasonic wave is caused by cylindrical lens.

Minimal value of A+B and C+D are not 0V in Fig.4. Ultrasonic wave turns into the elliptical form which has a certain degree of width in fact even the case where a beam spot form must turn into a linear focus, because ultrasonic wave does not converge perfectly by a lens. Then, F_E was shown in Fig.6 as the corrected result. Corrected F_E was obtained by subtracting each minimal value of A+B and C+D from measured value respectedly. By This operation, sensitivity may improve because value of F_E enlarges. But, for analog calculation of F_E, operation such as subtracting certain value from output signal of each receiving sensor elements is needed.

4. Conclusion and Acknowledgement

Development of a new ultrasonic displacement measuring method was tried

in this research, and it was verified experimentally that displacement measurement by a way of astigmatic focus error detection is effective als for ultrasonic wave.

The authors gratefully acknowledged the many comments and suggestions made by Messrs.Hiroaki Shimazutu and Takayuki Goto of Mitsubishi Heavy Industries ,Ltd.

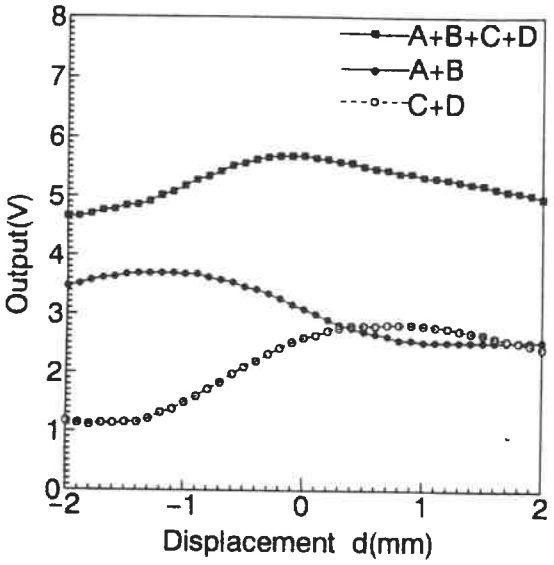

Fig.4. Measuring result(f2=66mm)

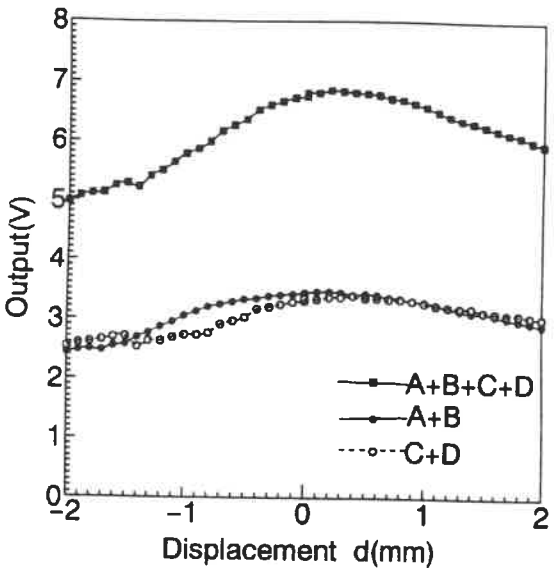

Fig.5. Measuring result (without cylindrical lens)

References

1)M.Shiraishi:Control of workpiece dimension in turning, J. of The JSPE,45-2, (1979)88. (in Japanese)

2)K.Takesa,H.Sato and Y.Tani:Measurement of Diameter Using Charge Coupled Device (CCD),Annals of theCIRP,33-1(1984)377.

3)S.Taneda, K.Miyazawa, I.Katayama and K.Yanagi: Optical Measurement System of Diametrical Dimension by the Synchronous Pitch Signal with a Parallel Scanning Laser Beam, J. of The JSPE,59-2(1993)227. (in Japanese)

4)K.Mitsui, M.Sakai and Y.Kizuka: Development of a high resolution sensor for surface roughness,Optical Engineering, 27-6(1988).498.

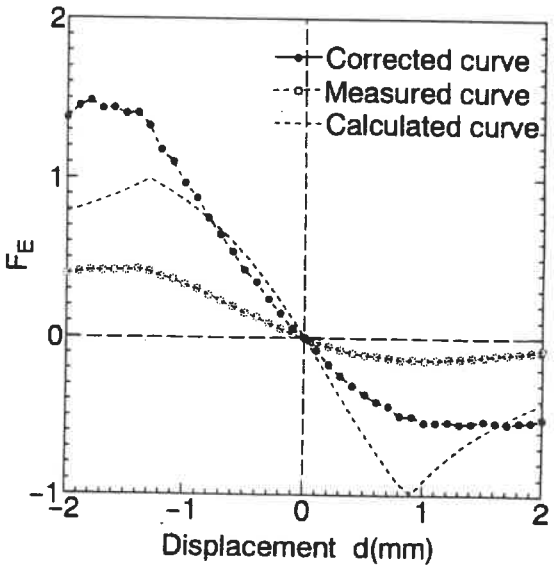

Fig.6. Output and focus error

Design of an Ultra Sensitive Force Transducer for Biomedical Experiments

P.V.Pistecky, E. van Dop
Delft University of Technology, Laboratory for Micro Engineering
2628 CD Delft, The Netherlands

Introduction

Some biomedical experiments require measurements of extremely small forces exerted by isolated single muscle cells during an artificial stimulation of their contraction [1,2]. One of the possible fields of research, where the knowledge of muscle cell behavior is of extreme importance, is the investigation of urological aberrations of the human bladder.

The average muscle cell of a bladder has a length of 300 μm and a diameter of 20 μm. The maximum active force during the cell contraction is in the order of 5 μN. For a meaningful analysis of the cell behavior, the force transducer must have very high resolution in the order of 20 nN.

There are two major kinds of force measurements on isolated single muscle cells under laboratory conditions, the isometric mode and the isotonic mode. In the isometric mode, the length of the muscle cell must remain nearly constant during the contraction. Therefore, the stiffness of the force transducer must be relatively high, at least 50 N/m. The isotonic measurements, on the other hand, allow for some cell length shortening, preferably with a programmable speed.

Force transducers known from literature [3,4] do not meet all the criteria necessary for investigation of cell behavior. The new transducer is based on a known principle of the electromagnetic actuator with force balancing, using feedback control of the transducer position. This transducer is developed for the benefit of biomedical research at the Department of Urology of the Erasmus University in Rotterdam. Tests performed on the first prototype of the force transducer show that it meets all major requirements for the cell force measurements.

Design of the force actuator

In order to realize the required high transducer stiffness, it was almost impossible to use elastic deformation of a spring as a measure for the exerted force. Therefore, an electromagnetic actuator principle with force balancing, using closed loop control of the transducer position, was chosen. The heart of the transducer is formed by an electrical coil placed in a permanent magnetic field. The flat coil is mounted on a miniature leaf spring parallel guiding to guarantee its linear movement. Figure 1 shows an exploded view of the transducer. During the cell contraction, the cell force tries to displace the moving coil from its zero position. Any displacement of the coil larger than several nanometers, measured by a displacement sensor, leads to an increase of the electric current through the coil. This prevents any further displacement of the coil. As a consequence, the electric current through the coil is a very precise measure of the exerted external force.

Precision etching technique was used to manufacture the electric coil and the coil parallel guiding, being the most important parts of the instrument. The coil is a flat, copper based structure placed on a flexible insulation foil. The leaf spring guiding is etched as one integral piece from a 30 μm thick stainless steel foil. By folding the four spring legs in parallel direction the desired structure of the guiding is given.

Design of the zero position detector

The required resolution of the detector depends on the mechanical stiffness of the overall measurement system. The total passive spring stiffness is the sum of the average muscle cell stiffness (~ 2N/m) and the stiffness of the actuator parallel guiding (~ 1.5N/m). In order to achieve the required resolution of 20 nN,

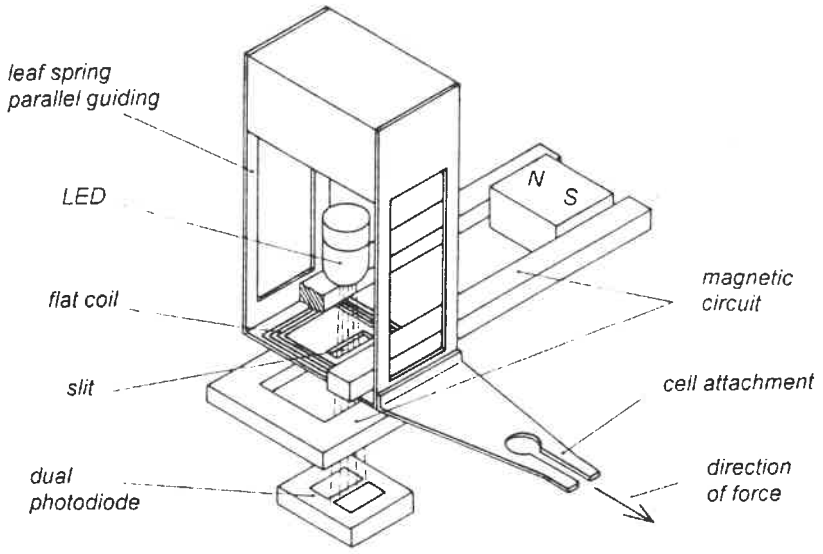

Fig. 1. Exploded view of the force transducer showing the most important parts.

the position detector needs to possess a displacement resolution of 6 nm! Because only slight movements of the actuator from its zero position need to be detected, the linearity of the displacement detector is of minor importance. To obtain good dynamic behavior, the movable parts of the sensor have very low mass, less than 0.01 g.

It was found that the best performance can be achieved with a contactless optical sensor. This sensor consists of a light emitting diode (LED), a movable slit and a sensing dual photodiode as shown in Figure 1. The light from the LED passes through the slit and falls on the photodiode. In the zero position of the coil both sensing areas of the photodiode obtain an equal quantity of the light energy. As a consequence, the difference of both photodiode output signals is equal to zero. Any movement of the coil from the zero position causes a measurable signal difference and can therefore be detected very easily. The minimum width of the movable slit is restricted by the signal/noise ratio of the electrical circuit. Calculations and experiments lead to a slit width of 65 μm.

The optical sensor has been tested using a laser interferometer. It was found that the sensor has a range of ±8 μm and it possesses a very good linearity within a range of ±2 μm. The sensitivity is equal to 1.13 V/μm with a resolution of 6 nm. There is no measurable hysteresis.

Design of the feedback control

Regular feedback control was applied to keep the force actuator during the measurement in the zero position with sufficient accuracy and with the desired system stiffness. The isometric measurements require a static stiffness of at least 50 N/m and a bandwidth of 10 Hz.

To set up the PID controller, measurements on the open loop system were performed to determine the necessary parameters. By applying the Ziegler-Nichols controller tuning method, the three basic parameters should have the following values: proportional gain = 60, integral time = 0.003 s, derivative time = 0.0008 s. However, extended computer simulations of the total transducer system, using the VISSIM program, showed that both integral time and derivative time need to be five times larges than initially predicted.

Cell attachment

Several cell attachment methods are in use in biomedical experiments. One of the possibilities is to catch both ends of a single cell between a pair of tweezers. Given the extremely small dimensions of the cells, the tips op the tweezers should have comparable dimensions. Additionally, one of the tweezers needs

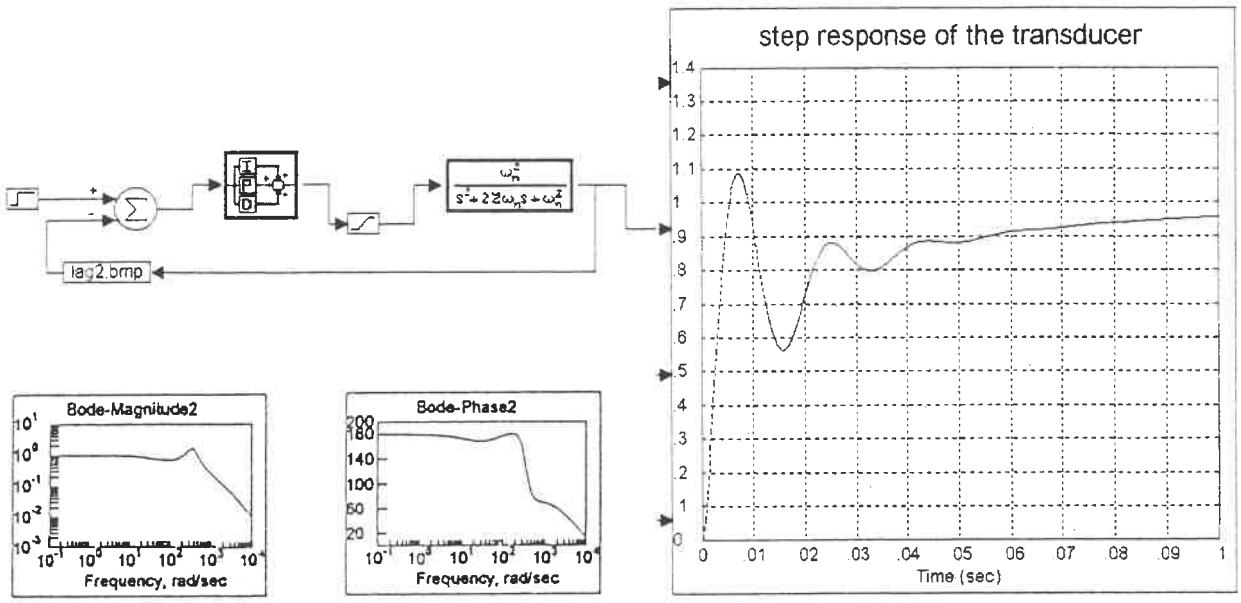

Fig. 2. VISSIM simulation of the dynamic behavior of the transducer.

to be attached to the force transducer and, as a consequence, should have a very small mass. There have been several prototypes of the tweezers built using the precision etching technique. Figure 3 shows one of the prototypes. The first experiments showed reasonable suitability of this tool, however, some improvements are still needed.

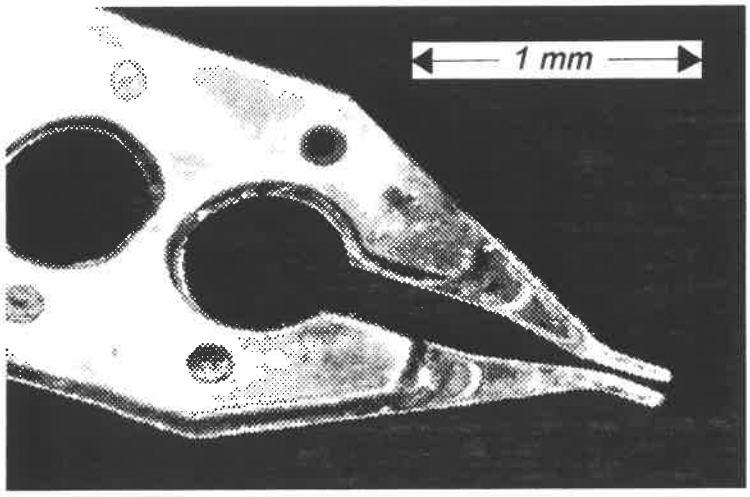

Fig. 3. Photograph of a prototype of the cell attachment tweezers. The maximum opening of the tips is 40 μm in order to catch the very small muscle cells.

Calibration of the force transducer

The common method of calibration of force transducers is the use of gravity forces exerted by known calibrated masses. However, in this case the masses should be extreme small. For example, a gravity force of 100 nN requires a piece of brass of 0.001 mm^3. Therefore, the mass of the instrument itself was used to

exert the necessary forces for the calibration. As the movable coil is actually supported like a pendulum, a small angle rotation away from the equilibrium position causes a very small known gravitational force component in the coil moving direction. Figure 4 gives the results of the calibration.

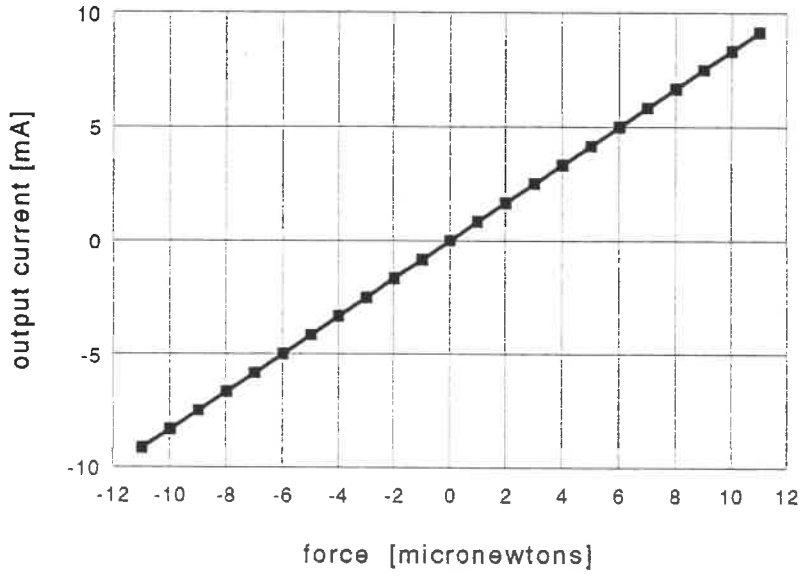

Fig. 4. Calibration of the input/output relationship of the force transducer.

Extended tests showed the following transducer properties. Forces up to 50 μN can be measured with a resolution of 10 nN. The measured repeatability is better than 2 % of the maximum force. The transducer has a bandwidth of 10Hz. Due to the leaf spring guiding, the actuator does not possess any measurable hysteresis. The input/output signal ratio is equal to 1.2 μN/mA. The closed loop transducer stiffness is better than expected and equal to 135 N/m.

Conclusions

Tests performed on the first prototype of the force transducer show that it meets all the major requirements for the cell force measurements. The transducer can measure forces up to 50 μm with a resolution of 10 nN. The transducer principle applied also allows, with some modifications, for isotonic measurements on cells. Some further development might be necessary to improve the repeatability and the temperature stability of the instrument.

References:

[1] Glerum, J.J., R. van Mastrigt and A.J. van Koeveringe: *Mechanical properties of mammalian single smooth muscle cells.* Journal of muscle research and cell motility 11 (1990), 453-462.

[2] Warschaw,, D.M. and F.S. Fay: *Cross-bridge elasticity in single smooth muscle cells.* The journal of general physiology 82 (1983), 157-199.

[3] Cecchi, G.,F.Colomo, C.Pogessi and C.Tesi: *A simple method to measure isometric twitch tension in single frog cardiac cells.* Poster on XVIIIth European Conference on muscle and motility, 1989.

[4] Iwazuma, T.: *High-speed ultrasensitive instrumentation for myofibril mechanics measurements.* American Journal of General Physiology 21(1987), 253-262.

DEVELOPMENT OF A MEASURING LASER SYTEM WITH NANOMETER ACCURACY

S.F. Wetzels, P.H. Schellekens
Eindhoven University of Technology
Eindhoven, The Netherlands

Introduction

Increased accuracy requirements in metrology have resulted in displacement sensors with resolutions at the nanometer and subnanometer level. Until recently the calibration of these sensors was very difficult. Therefore we have developed an instrument that enables traceable calibrations at nanometer level. It is called a measuring laser. The final goal is an accuracy and resolution at the nanometer level over a measuring range of at least 100 μm.

The Basic Principles

Since its development in 1961, the HeNe-laser has found many applications. Due to the definition of the I_2-stabilized HeNe-laser as the international standard of length in 1983, the HeNe-laser is also well established in the field of Precision Engineering. The main elements of a typical HeNe-laser are shown in Fig. 1.

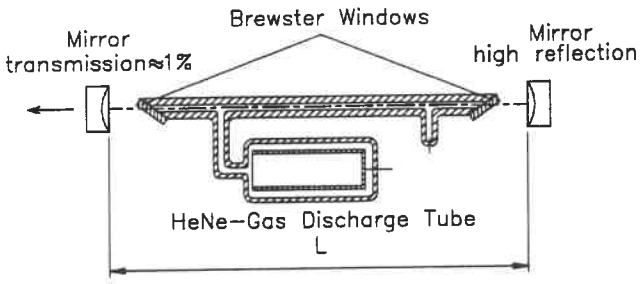

Fig. 1

The gas discharge tube is filled with a 6:1 He-Ne mixture at a total pressure of 400 Pa. Inversion is reached by sending some mA electrical current through the gas. The mirrors with a radius of 600 mm form a cavity with a length of 115 mm.
The most important property of the laser is that it emits light in a very narrow frequency band. The centre frequency f of this band is given by:

$$f = \frac{kc}{2nL}. \qquad (1)$$

here c is the speed of light, L the distance between the mirors, also called the cavitylength, n the refractive index of the medium inside of the cavity and k the mode-number of the laser. Within the (relatively narrow) working range of a laser (≈1500 MHz) a number of modes can be supported at the same time, depending on the cavitylength. This is called multi mode oscillation of the laser. For our purpose the laser must work in only one mode at the same time, so the cavitylength must be optimized.
The relation between the frequency and the cavity length is used to measure length. If one

of the laser mirrors is translated, the resulting frequency shift can be measured. With formula (1) the exact translation of the mirror can then be calculated. If the translation of the mirror is coupled to a sensor, this sensor can be calibrated.
From formula (1) it can be seen that the frequency shift of a laser with a cavitylength of 115 mm, as is used here, is 4 MHz per nanometer translation. As frequency changes down to 10 kHz can be detected, a resolution of less than 0.01 nm is achievable.
It should be pointed out here that spontaneous length changes of the cavity, not due to controlled mirror displacements, also change the laserfrequency and will thus reduce the accuracy of the measurement.
In order to measure the frequency changes a measurement setup like that shown in Fig. 2 is required.

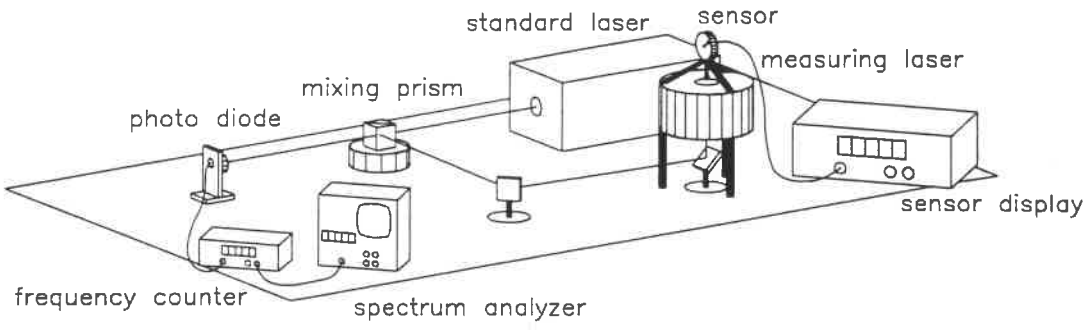

Fig. 2

In this setup the frequency is measured by mixing the frequency of the measuring laser with that of an I_2-stabilized He-Ne laser. This results in a beat frequency of the order of magnitude of some 100 MHz which can be detected with a photo diode and is measured by a frequency counter. The measured frequency change can be converted into a displacement and is compared with the read out of the sensor.
Due to the integration of the laser length standard into the measurement setup the calibration is directly traceable to this standard.

The Laser Design

To get the optimum conditions for the calibration setup we have formulated a set of critical specifications:
- single frequency laser design over the whole measuring range to minimize the effects of the mode jumps
- very stable laser cavity to get minimal and corrigible drift during the measurement (<1 nm/15 min)
- minor error effects of mirror adjustment

For these specifications we have developed a small laser cavity (length 115 mm) which allows single frequency operation over several mm of mirror adjustment. The cavity is designed nearly insensitive to temperature effects.
Fig. 3 shows a cross-section of the laser. The laser is built in a vertical way to get the optimum condition for the calibration of the sensors.

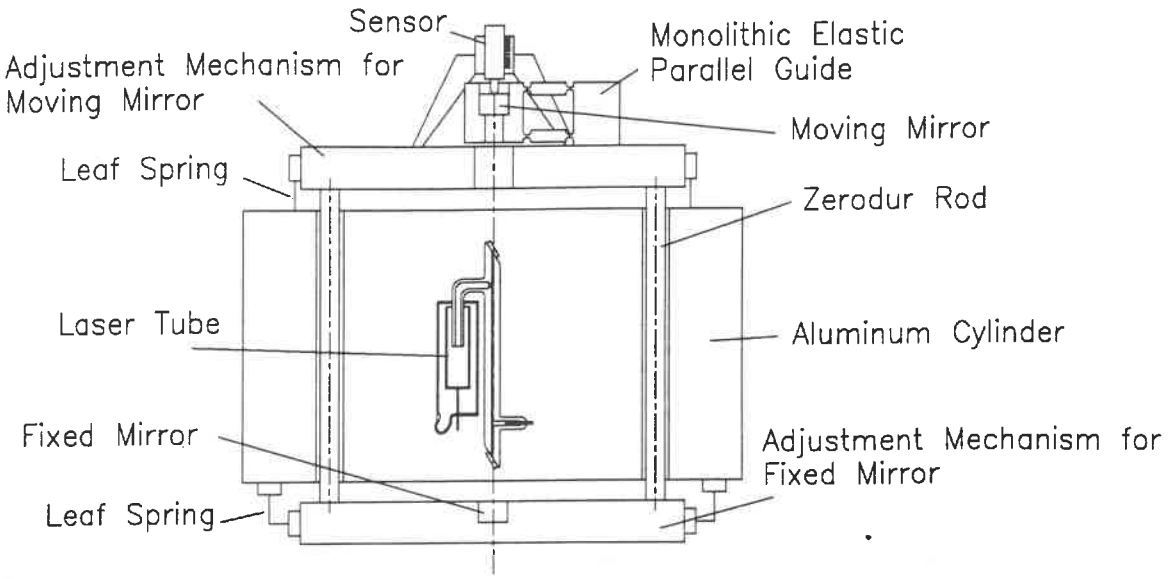

Fig. 3

The heart of the measuring laser is formed by an aluminum cylinder to which all components of the laser are connected. Inside the cylinder the lasertube is mounted. The dissipated heat of the lasertube is distributed uniformly over the construction due to the excellent thermal conductance of the aluminum. On top of the construction a calibration platform is mounted on three leaf springs. This platform holds the specially designed parallel movement mechanism driven by a piezo. The platform also incorporates an adjustment mechanism for the alignment of the mirror. On the platform the sensor to be calibrated can be positioned.
On the bottom side of the aluminum cylinder another adjustment mechanism for the fixed mirror is mounted. This mechanism is connected to the cylinder by three leaf springs.
The distance between the mirrors is fixed by three zerodur rods. Due to the application of leaf springs in the construction, expansion differences between zerodur and aluminum can be absorbed in the leaf springs, causing no deformation of the construction.

Experiments

While this design is under construction, first experiments to test this measurement principle have been carried out with an existing home built laser cavity in a measurement setup similar to that shown in Fig. 2. The frequency shift caused by the translation of one of the laser mirrors was compared with the registration of a high resolution laser interferometer, which directly measured the displacement of the mirror. Fig. 4 shows the results of the measurement.
The laserfrequency is lineair with the displacement of the mirror only for about 300 nm because of the narrow bandwidth of the laser. When the frequency change is so large that it runs out of the working range of the laser, the laser jumps sharply into the next mode which differs exactly half a wavelength from the previous mode. Because the size of the jump is exactly known for this type of laser this doesn't cause a deviation in the measurement.

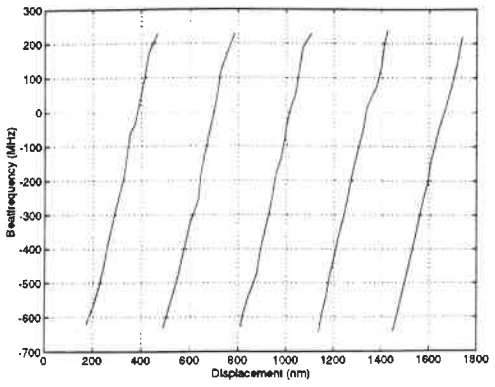

Fig. 4

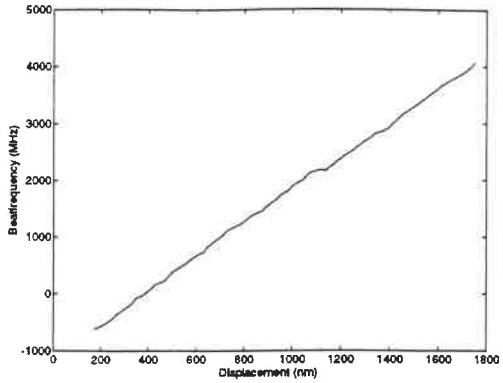

Fig. 5

The measurement data can be corrected for the mode jump. This results in a calibration curve as shown in Fig. 5. The maximum deviation between interferometer and measuring laser is 30 nm. This is due to drift effects of this cavity and measuring effects of the laserinterferometer. Thermal drift of the cavity used in this experiment was measured to be about 2.5 nm during the measuring period.

Conclusion

The measuring laser proposed here offers a traceable way of calibrating sensors at nanometerlevel. First tests show the high resolution that can be obtained with this principle. The desired accuracy is not achieved with the provisional measurement setup used here but the final design should offer the stability needed for this measurement in order to obtain nanometer accuracy.
In principal the measurement range can be extended to the mm level using the design under construction at Eindhoven University.

Literature

Wetzels S.F., 1994.
Development of a Measuring Laser for Calibrations at Nanometer Level (Dutch)
Masters thesis, Eindhoven University of Technology

Schellekens P.H., 1986.
Absolute Accuracy of Technical Interferometers (Dutch)
Ph.D. thesis, Eindhoven University of Technology

Schellekens P.H., 1979.
Frequency Stabilisation of He-Ne Lasers by Saturated Absorption of I_2 (Dutch)
Masters thesis, Eindhoven University of Technology

Ottmann S., Sommer M., 1989.
Absolute Length Calibration of Microindicators in the Nanometer Range
VDI Berichte Nr. 761

Poster Papers

Characterization of Micromachined Surfaces by Atomic Force Microscopy

V. Scherer[1], U. Rabe[1], R. Fechner[2], A. Schindler[2],
O. Riemer[3], W. Preuß[3], E. Brinksmeier[3] and W. Arnold[1]

[1] Fraunhofer-Institute for Nondestructive Testing,
University, Bldg. 37, D-66123 Saarbrücken
[2] Institute for Surface Modification e. V.,
Permoser Straße 15, D-04303 Leipzig
[3] University of Bremen, Production Engineering Department,
Badgasteiner Straße 1, D-28359 Bremen

The limiting factor for the finish of a diamond turned surface is the response of the workpiece material to the cutting action of the diamond tool. Atomic force microscopy has become a powerful method for accessing extremly fine surface features which is an essential prerequisite for relating machining parameters to surface finish.

The two examples discussed in this paper relate to the machining of brittle semiconductors and ductile metals. In the last chapter we are proposing a polishing technique for further improvement of diamond turned metal surfaces.

1 Monocrystalline silicon

Diamond turning of monocrystalline silicon in the ductile mode can yield excellent surfaces with roughness values below 2 nm rms. If a perfectly cut silicon surface is examined with an AFM, the repulsive force image does not show any topographic anisotropy below a scan area of approx. 1 μm^2 which is well within a single turning groove. The lateral force image, however, reveals a granular structure with an average diameter of 100 nm (Fig. 1).

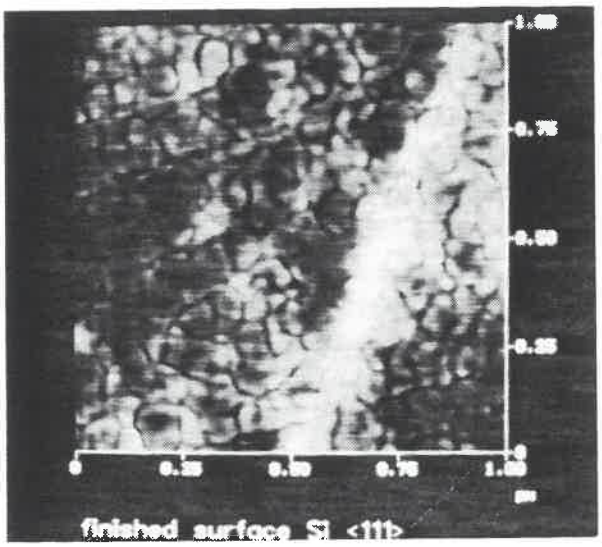

Figure 1:
Lateral force image of granular structure of a silicon {111} surface.

scan area: A = 1 μm^2

surface preparation:
diamond turning
feed: f = 3 µm/rev.
depth of cut: a_p = 4 µm

diamond tool:
rake angle: γ = -45°
nose radius: r_ε = 3 mm

The origin of this structure can hardly be understood within the existing models of ductile machining [1]. Therefore we have revisited the ductile to brittle transition using the inclined plunge-cut method described earlier [2]. Cuts were performed with constant speed along the <221> direction of a diamond turned {111} surface with a 0° rake, r = 0.76 mm diamond tool at an inclination of approx. 0.057° (Fig. 2). Cutting forces were recorded with a Kistler 9251A piezo-electric force transducer. The resulting cutting grooves were examined with a Nomarski and an atomic force microcope.

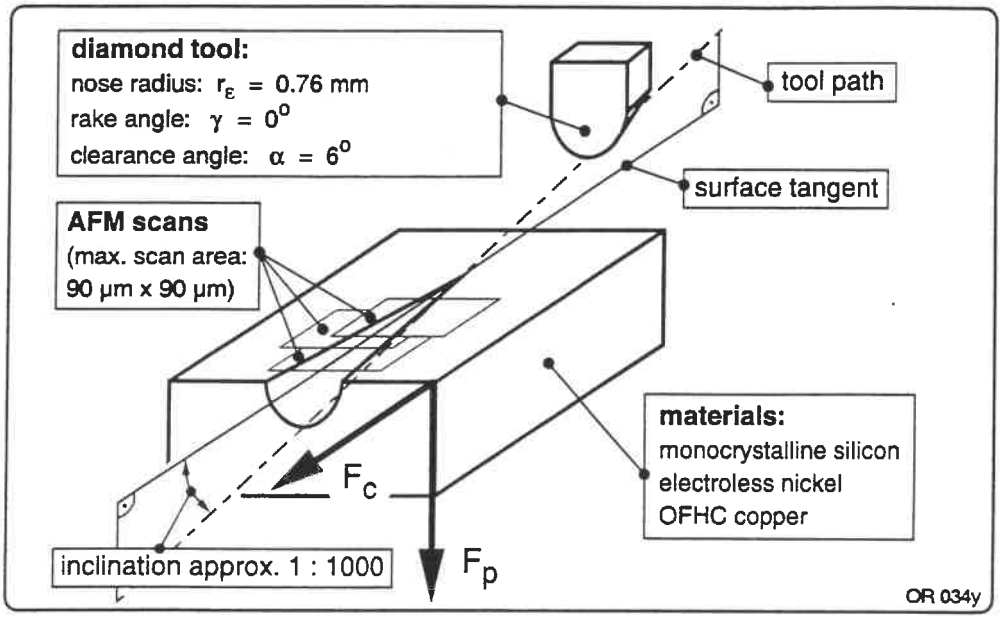

Figure 2: Principle of plunge-cut experiments.

Four regimes of material response could be distinguished (Fig. 3):

(1) elastic regime, identified by a steady increase of thrust force without any trace of damage detectable by Nomarski or atomic force microscopy,

(2) plastic regime, identified by a change of interference contrast without any alteration of topography larger than 1 nm,

(3) ductile regime, defined by the appearance of a cutting groove deeper than 1 nm, and

(4) brittle regime, defined by crack initiation (Fig. 4).

From the existance of these four regimes we conclude that even machining in the ductile mode leads to sub-surface damage. This is confirmed by recent results obtained by Zhang and Howes [3] from scratch tests of ceramic materials. The structure seen in the lateral force image of Fig. 1 could be attributed to dislocation bands or partial amorphization of a thin sub-surface layer during machining.

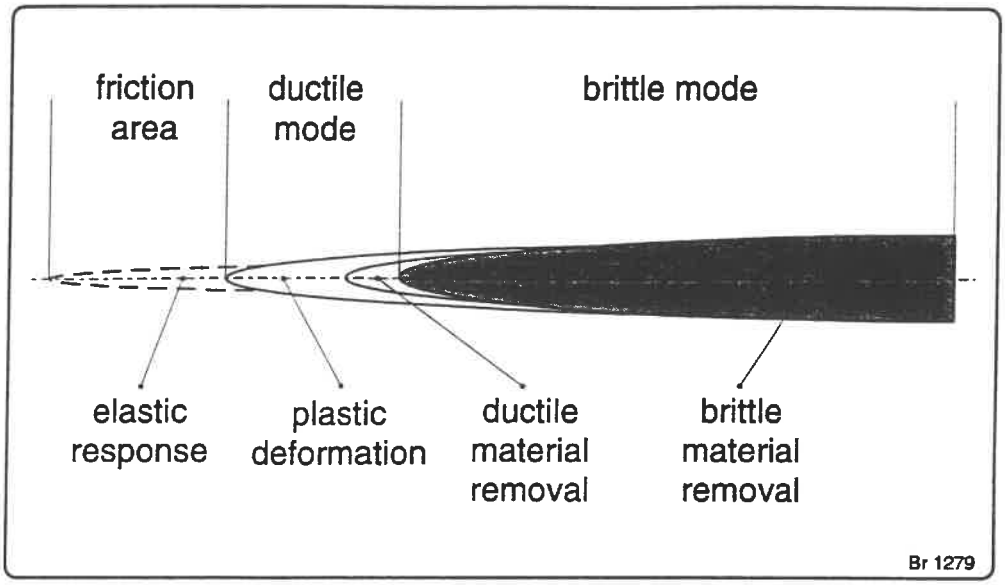

Figure 3: Four regimes of material response found in inclined plunge-cut experiments of monocrystalline silicon.

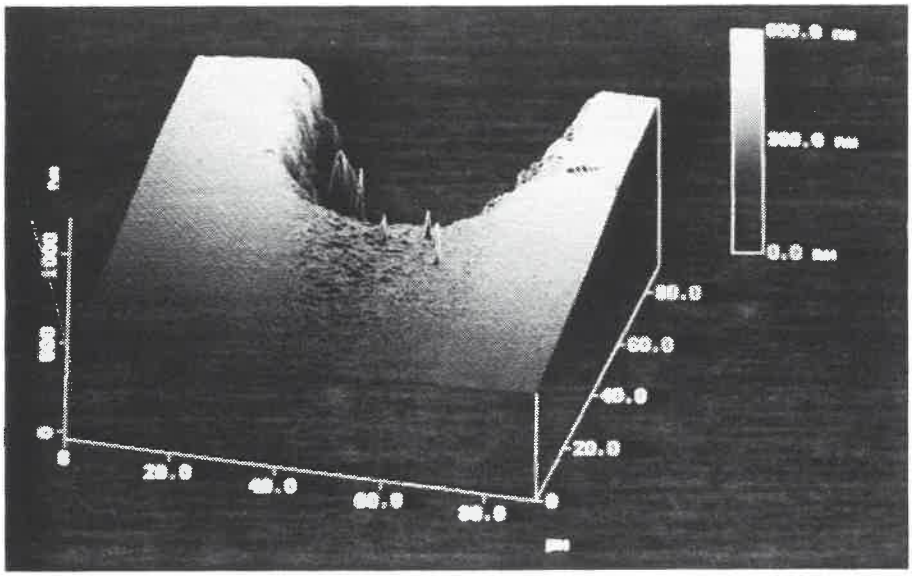

Figure 4: AFM image of brittle to ductile transition along a plunge-cut groove in monocrystalline silicon.

diamond tool: nose radius: r_ε = 0.76 mm, rake angle: γ = 0°
cutting speed: v_c = 20 mm/min

depth of groove before crack initiation: approx. 30 nm
depth of groove after crack initiation: approx. 500 nm

2 Electroless nickel and OFHC copper

It is well known that the surface finish of diamond turned polycrystalline metals is restricted by the unequal elastic and plastic response of individual grains due to their random crystallographic orientation [2, 4, 5]. This limitation does not occur with amorphous metals. Fig. 5 shows the AFM image of the bottom of a plunge-cut groove cut into electroless nickel. The height of the ripples forming an elongated cellular structure is only 1 to 3 nm. Undoubtedly, they bear witness of the chip separation process.

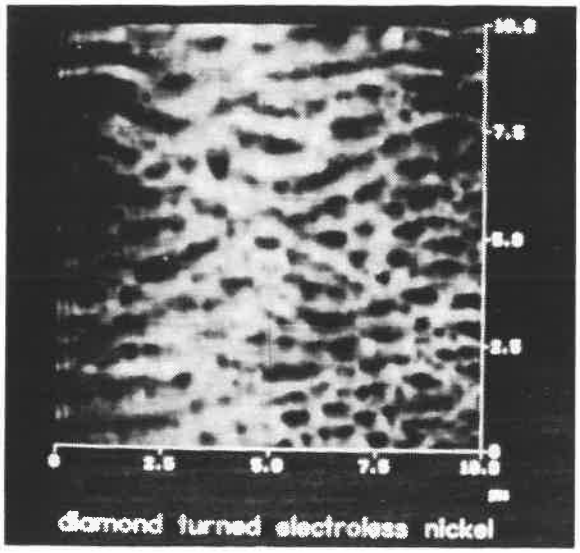

Figure 5:
AFM image of cellular structure at the bottom of a plunge-cut groove in electroless nickel.

scan area: $A = 100\ \mu m^2$

diamond tool:
rake angle: $\gamma = 0°$
nose radius: $r_\varepsilon = 0.76$ mm

cutting speed: $v_c = 1000$ mm/min

Inclined plunge-cuts with 0° rake tools on ductile metals cannot resolve different regimes of material response, since the transition from frictional contact to chip removal is almost instantaneous. However, an analysis of the size-effect suggests the existance of a characteristic depth of cut a_c where the energy associated with plastic deformation starts to dominate other energy dissipation channels.

Fig. 6 shows the specific cutting forces measured in inclined plunge-cut experiments of electroless nickel and OFHC copper as a function of depth of cut which were determined with a laser profilometer. Note that the specific cutting forces increase rapidly at a depth of cut much larger than the edge radius of the diamond tool [6] which is in the order of 0.01 µm.

As a first coarse approximation let us assume that the forces associated with friction around the cutting edge (F_E) and with surface creation (F_S) are proportional to the effective length l of the cutting arc, $F_E + F_S \sim l$, while the forces associated with plastic deformation (F_D) and with friction on the rake face (F_R) are proportional to the cross-section q of the plunge-cut groove, $F_D + F_R \sim q$. Since in the case of a round nose tool, $l \sim a_p^{1/2}$ and $q \sim a_p^{3/2}$ where a_p is the depth of the groove, we arrive at the following relationship for the ratio of the forces

$$(F_E + F_S) / (F_D + F_R) = a_c / a_p.$$

The value of a_c can be found from a fit to the total specific cutting forces, yielding $a_c \approx 1$ µm for electroless nickel and $a_c \approx 4.5$ µm for OFHC copper. These values reflect the fact that plastic deformation takes place much easier in OFHC copper than in electroless nickel. Moreover, there is substantial material side flow as exemplified by the AFM image in Fig. 7.

process:	plunge-cut	rake angle:	$\gamma = 0^o$
cutting speed:	$v_c = 20$ mm·min^{-1}	clearance angle:	$\alpha = 6^o$
inclination:	$\lambda = 0.0573^o$	nose radius:	$r_\varepsilon = 0.76$ mm
lubricant:	petroleum		

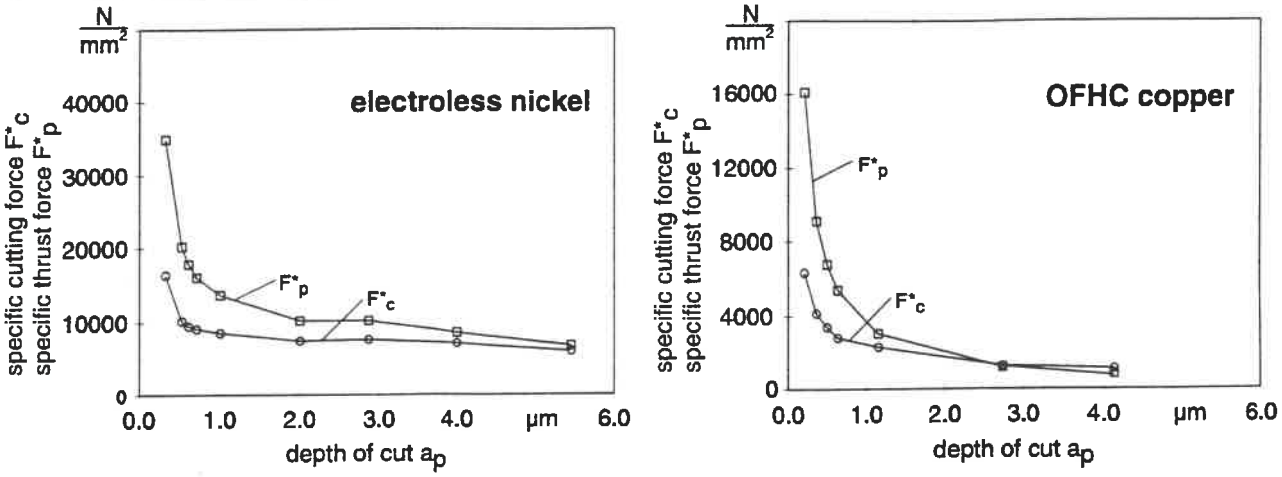

Figure 6: Specific cutting forces measured in inclined plunge-cut experiments with electroless nickel and OFHC copper.

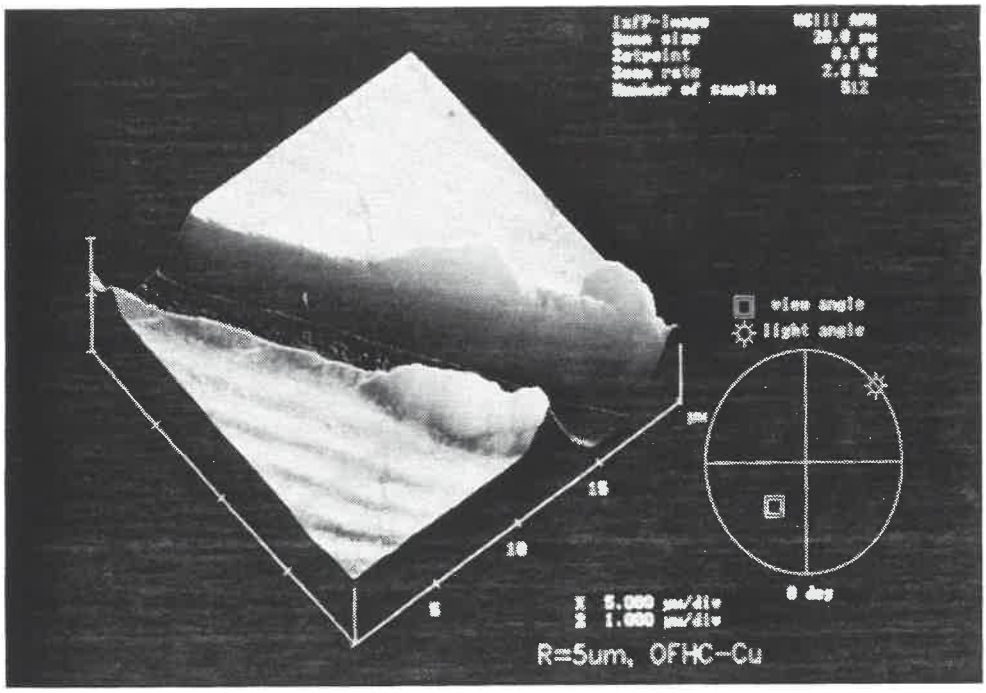

Figure 7: AFM image of burred material behind a grain boundary in OFHC copper. Cutting direction from left to right. Grain boundary running from upper to lower corner.

diamond tool:	nose radius: $r_\varepsilon = 0.005$ mm, rake angle: $\gamma = 0°$
cutting speed:	$v_c = 1000$ mm/min

3 Argon ion etching of diamond turned metal surfaces

Although material response sets an ultimate limit to the surface finish achievable with a diamond turning process, further reduction of surface roughness is possible with post polishing techniques [7]. An argon ion etching technique also applicable to non-plano surfaces has been developed at the Institute for Surface Modification e. V., Leipzig. In a first step, the ion etching rate of the metal is determined as a function of angle of incidence of the ion beam. Prior to ion machining, a polymer resist is applied which equilizes the roughness profile of the metal surface. The angle of incidence is chosen so that the etching rate of the metal equals the etching rate of the resist. Thus, the extremely smooth surface of the polymer resitst is transferred into the metal substrate.

sample		rms-roughness [nm]		
material	original surface	before ion beam polishing	after first ion beam polishing	after second ion beam polishing
electroless nickel	diamond turned	4,38	1,90	1,51
electroless nickel	diamond turned with post polishing	2,92	1,27	1,01
OFHC copper	diamond turned	6,53	4,28	—

Figure 8: Surface finish improvement of diamond turned metal surfaces achieved by ion beam polishing.

Talystep measurement parameters:

diamond stylus:	0.1 µm x 2.5 µm
scanning force:	20 µN
profile length:	1 mm
cut-off wavelength:	0.08 mm

Fig. 8 summmarizes the finish improvements which could be achieved with this method. In the second row the average of three electroless nickel samples is given which were hand polished with diamond paste after diamond turning.

As can be seen from Fig. 8, the finish of electroless nickel surfaces can be reduced in successive polishing steps while the grain structure of OFHC copper gives rise to varying etching rates which makes ion beam polishing less effective. In any case, a comparison between the amplitudes of spacial frequencies before and after ion beam etching (Fig. 8) shows that the method is well suited for eliminating spacial frequencies higher than approx. 30 mm^{-1}. Waviness, however, cannot be reduced.

Acknowlegdement

The work presented in this paper was partially funded by the Deutsche Forschungsgemeinschaft (DFG).

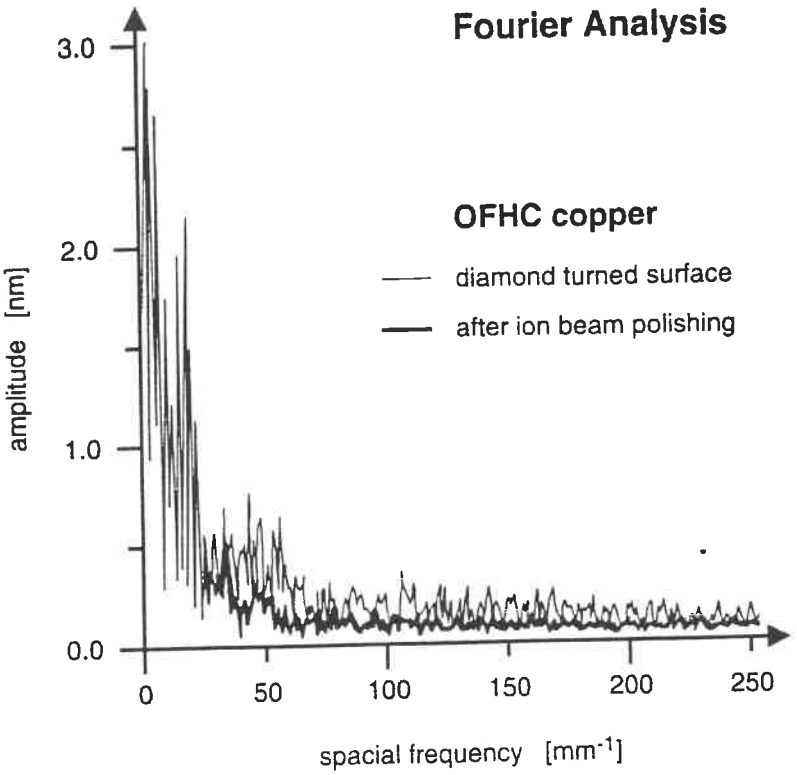

Figure 9: Spectral density function before and after ion beam polishing.

References

[1] Blackley, W. S. and R. O. Scattergood. "Chip Topography for Ductile-Regime Machining of Germanium". Transactions of the ASME, Journal of Engineering for Industry, Vol. 116, May 1994: p. 263-266.

[2] Brinksmeier, E; W. Preuß; O. Riemer. "From Friction to Chip Removal. An Experimental Investigation of the Microcutting Process". Proceedings of the 3rd International Conference on Ultraprecision in Manufacturing Engineering, Aachen, Germany, May 1994: p. 393-400.

[3] Zhang, B. and T. D. Howes. "Material-Removal Mechanisms in Grinding Ceramics". Annals of the CIRP Vol. 43, 1/1994: p. 305-308.

[4] Spenrath, M. "Technologische Aspekte zum Feinstdrehen von Kupferspiegeln". Dissertation, RWTH Aachen, 1991.

[5] Yuan, Z. J; W. B. Lee; Y. X. Yao; M. Zhou. "Effect of Crystallographic Orientation on Cutting Forces and Surface Quality in Diamond Cutting of Single Crystal". Annals of the CIRP Vol. 43, 1/1994: p. 39-42.

[6] Lucca, D. A; R. L. Rhorer; R. Komanduri. "Energy Dissipation in the Ultraprecision Machining of Copper". Annals of the CIRP Vol. 40, 1/1991: p. 69-72.

[7] Parks, R. E. and C. J. Evans. "Rapid Post-Polishing of Diamond-Turned Optics". Precision Engineering Vol. 16, No. 3, July 1994: p. 223-227.

The Design of an Atomic Force Microscope for Metrology

T.H. McWaid and J. Schneir
National Institute of Standards and Technology
Precision Engineering Division
Gaithersburg, MD 20899

ABSTRACT

Atomic force microscopy (AFM) is a rapidly evolving technique which has been used in numerous academic studies since its invention eight years ago. AFM manufacturers are now marketing instruments for industrial metrology applications. The National Institute of Standards and Technology (NIST) is developing a specially designed calibrated AFM (C-AFM) system that will be capable of calibrating artifacts which, in turn, can be used to calibrate commercial AFMs.

The need for calibration artifacts for the AFM community is first developed. The C-AFM system design goals are then summarized. The critical electro-mechanical and metrology issues involved in the design, construction and operation of the C-AFM are then discussed. Finally, the current status of the instrument is summarized, and preliminary measurements are presented.

INTRODUCTION

Atomic force microscopes can be used to obtain very highly resolved three-dimensional images. The semiconductor, optical and magnetic storage, razor blade and photographic film industries are investigating the use of AFM for improving the precision and accuracy of their manufacturing process control measurements. Suitable calibration standards must be developed and properly utilized before the metrological potential of AFM can be realized.

Most AFMs utilize piezoelectric (PZT) actuators to produce, and measure, the motion of a probe relative to the surface being imaged. There are two approaches one can take to obtain a linear scan from the piezoelectric actuators: 1) Drive the actuators in a (nonlinear) manner that results in a linear response; and, 2) Use independent transducers to measure the displacements. Both techniques have been utilized [1,2,3].

Regardless of which type of linearization scheme is utilized, AFMs should be calibrated using NIST-traceable pitch and height standards. Presently, there are neither NIST-traceable sub-micrometer pitch standards nor sub-ten nanometer height standards suitable for calibrating scanning probe microscopes. Researchers are developing specimens with features of this size that may prove suitable for the calibration of AFMs; however, NIST does not yet have the capability for performing calibrations at the required levels of precision and accuracy. We are developing a calibrated AFM (C-AFM) in order to overcome this limitation. Unless AFM is one of the metrology tools used to measure the calibration artifacts used with atomic force microscopes, methods divergence between AFM and whatever other tool is used to calibrate the artifact will increase the calibration uncertainty [4].

DESIGN

We have set the following performance specifications for the C-AFM: 1) Measurements are to be made in air in order to maximize measurement throughput; 2) A scan range of at least 50 μm; 3) A lateral resolution of 2 nm; 4) A lateral accuracy of 3 nm; 5) A vertical resolution of 0.1 nm; 6) A vertical accuracy of 1 nm.

Commercially-available components and subsystems have been utilized in order to minimize the development time and cost, and to maximize the upgradeability of the C-AFM. The precision and accuracy of commercial metrology equipment have improved considerably over the last five years. We expect the requirements of ultraprecision metrology to continue to drive this trend, thereby influencing the evolution of the C-AFM.

The various components and subsystems that comprise the C-AFM have been described in the literature [5,6]. To summarize, we use a flexure stage driven by piezoelectric actuators for scanning; heterodyne interferometers to measure the lateral displacements (ΔX and ΔY) of the sample; a capacitance sensor to measure the vertical displacement (ΔZ) of the sample; an integrated piezoresistive force sensor/probe; and a commercially-available AFM control system. The control system utilizes two feedback loops which read from the X and Y interferometers and adjust the PZT actuator voltages to maintain the desired XY scan position. Images can be acquired in contact, non-contact and intermittent-contact imaging modes.

The mechanical design of our system is based on the principles developed by Teague et al. [7,8]. Teague has identified, and developed, the following set of 13 patterns inherent to the successful design of a precision instrument: repeatability, workspace metric, metrology frame, alignment (Abbé) principal, probe/tool knowledge, error budget, kinematic mounting, structural loop, isolation, kinematic drives, symmetry, materials selection, and energy flow. These patterns have been realized to a significant degree in the C-AFM; we plan on publishing an in-depth review of the system in view of these patterns sometime in the near future. The major deviation of the C-AFM from Teague's patterns concerns the Z-axis metrology.

The Z stage is mounted in the center, scanned portion, of the X-Y flexure stage. It consists of a commercially available PZT actuator and an integrated capacitance sensor. The capacitance sensor will be calibrated using interferometry. Similar capacitance gauges have reportedly been calibrated with x-ray interferometry to uncertainties of a tenth of a nanometer [9,10].

The Z-axis capacitance sensor violates the principle of a metrology frame: the measurement transducer is not referenced to the C-AFM metrology frame, but rather to the Z-stage. Since the Z-stage and the flexure stage are fabricated out of zerodur and/or invar (materials characterized by very small coefficients of thermal expansion) we do not expect this deviation from the ideal to prevent us from meeting the Z-axis performance specifications of the C-AFM.

PRELIMINARY MEASUREMENTS

The C-AFM is presently operating in a so-called Phase II configuration. All major subsystems, save the acoustic/thermal isolation box, have been integrated into the assembly. The system has been aligned such that all Abbé offsets are less than 1 mm. The system is supported on a vibration isolation system and located in a temperature-controlled room with 0.1 °C stability over several hours. The Z-axis capacitance gauge has not yet been calibrated at NIST using interferometry; we have obtained a scale factor for the gauge based on the nominal heights of measured artifacts. We have conducted a number of experiments in order to characterize the performance of the C-AFM system in the Phase II configuration.

The first AFM calibration artifact calibrated with the C-AFM will be a combined pitch and height standard. We are presently developing calibration strategies for calibrating this type of artifact. An image of a commercially-available pitch and height surface topography artifact is shown in Figure 1. This image was obtained with the C-AFM operating in contact imaging mode. The nominal pitch of this specimen is 3 μm. Measurements of two adjacent pitches yielded pitch values of 3.010 and 3.006 μm, respectively. These are preliminary measurements, performed in order to trouble-shoot the C-AFM system, and develop viable calibration schemes. A thorough uncertainty analysis will have to be performed before the C-AFM can be used to calibrate AFM artifacts; all calibration values obtained with the C-AFM will be reported with a quantitative statement of uncertainty.

The pitch values were determined using a novel technique. This technique relied on the fact that the controller displays, and stores, the center position of each image in the global coordinate system defined by the X- and Y-interferometers. First we took a 0.6 μm image with an edge centered vertically in the field of view. Next, we took a similar image of an adjacent line edge. We then best-fit vertical (constant X) lines along each edge using the controller software. The X-coordinate of the vertical lines is given in the local (image) coordinate system. The average pitch is found by subtracting the sum of

the center and the vertical line coordinates corresponding to one edge from the respective sum corresponding to the second edge. This technique was utilized in an effort to minimize the influence of scanner following errors on the pitch measurements.

We have also imaged a specimen fabricated using laser focused atomic deposition [11]. The nominal pitch of this specimen is 212.78 nm [11]. A 4 μm image of the specimen obtained in intermittent-contact imaging mode is presented as Fig. 2. This figure is interesting for several reasons. First, the straightness and parallelism of the lines indicate that the C-AFM scan control system is functioning fairly well. Second, one sidewall of each line appears significantly sharper than the other. This is because the tip axis is oriented approximately 20° off the normal to the surface. This tip orientation allows us to image one sidewall of a line.

Based on a cursory analysis of a profile crossing normal to the specimen features, the nominal height of the deposited features is about 6 nm, and the fundamental peak of the Power Spectral Density (PSD) function is located at a spatial wavelength of 214 nm. While this analysis does not prove that the C-AFM is working at its design specifications, these preliminary data are very encouraging.

SUMMARY

The National Institute of Standards and Technology (NIST) has initiated the development of a calibrated AFM that will be used to perform highly-resolved measurements that are directly traceable to the wavelength of light in all three axes of motion. The C-AFM will be used to measure standard reference materials that can be purchased by industry. These reference artifacts will enable customers to calibrate their own atomic force microscopes with traceability to a national standard. In this paper we have summarized the industrial need for a calibrated AFM and standard reference artifacts, presented a brief overview of the critical electro-mechanical and metrology issues involved in the design and construction of the C-AFM, and presented preliminary images.

ACKNOWLEDGEMENTS

This work was supported in part by SEMATECH. Both T.M. and J.S. wish to thank Ted Vorburger and Clayton Teague for helpful discussions, and Jabez McClelland for providing the specimen fabricated using laser focused atomic deposition. Brian Renegar's valuable assistance in the laboratory is greatly appreciated. Finally, we also wish to thank Ned Bennett of Zygo for assisting with the alignment of the system.

REFERENCES

1. J.E. Griffith, G.L. Miller, C.A. Green, D.A. Grigg and P.E. Russell, J. Vac. Sci. Technol. B **8** (6), 2023 (1990).
2. J. Fu, R.D. Young and T.V. Vorburger, Rev. Sci. Instrum., **63** (4), 2200 (1992).
3. R.C. Barrett and C.F. Quate, Rev. Sci. Instrum., **62** (6), 1393 (1991).
4. T.H. McWaid, T.V. Vorburger, J. Fu, J.F. Song and E. Whitenton, Nanotechnology **5**, 33 (1994).
5. J. Schneir, T. McWaid and T.V. Vorburger, SPIE Vol. 2196, 166 (1994).
6. T.H. McWaid, J. Schneir and T.V. Vorburger, Proc. 3rd Intl. Conf. UME, 342 (1994).
7. E.C. Teague, J. Vac. Sci. Technol. B7, 1898 (1989).
8. E.C. Teague and D. Swyt, Tutorial Notes, ASPE, Orlando, FL (1982).
9. S.T. Smith, D.G. Chetwynd and D.K. Bowen, SPIE Vol. **1573**, (1991).
10. S. Harb, S.T. Smith and D.G. Chetwynd, Rev. Sci. Instrum. **63** (2), 1680 (1992).
11. J.J. McClelland, R.E. Scholten, E.C. Palm and R.J. Celotta, Science, **262**, 877 (1993).

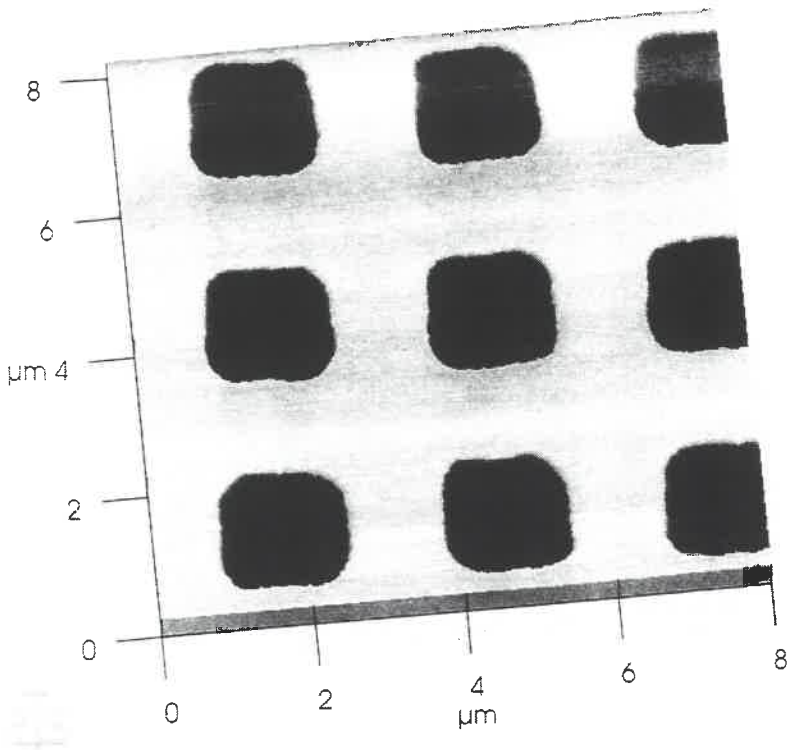

Fig. 1 C-AFM image of a commercial 3µm pitch grid artifact

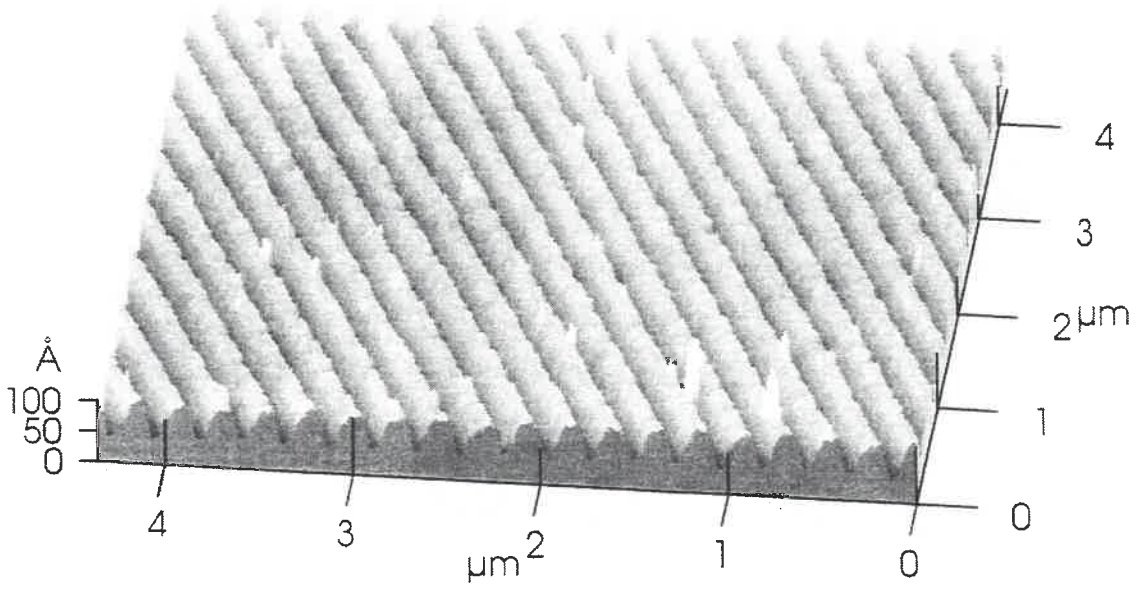

Fig. 2 C-AFM image of an artifact fabricated using laser focused atomic deposition

Correlating Machine Tool Accuracy with Part Features

Nandakumar Srinivasan, Fred Farabaugh,
Dr. Robert G. Wilhelm, Dr. Robert J. Hocken
The University of North Carolina at Charlotte
Charlotte, NC 28223

Metal removal machine tools are widely used in manufacturing processes. The accuracy of machine tools, mainly Computer Numerically Controlled machine (CNC) tools, is a prime consideration because they run without any operator intervention. Increasing technical advances continually place more stringent demands on the accuracy of machine tools. Improvement in accuracy translates directly into lower cost and higher quality by reducing scrap parts and providing higher performance products. With higher accuracy of machine tools, future inspection can be reduced. Prediction of variations in the geometry of the part produced by a specific machine tool can contribute significantly to accuracy improvement in precision manufacturing processes.

Several approaches have been used by precision engineers to significantly improve the performance of the machine tool. A Geometric - Thermal (G-T) model has been developed using machine measurements by Donmez to successfully compensate for machine tool errors [1]. Raja and Salsbury used mathematical models and parametric machine measurements to develop a quantitative relationship between the measured work piece and the machine errors [2]. In most cases, for each machine, these models require extensive instrumentation, testing, and measurement, requiring significant investment in time and resources. The characterization and development of the model has to be done for each machine, which is a time-consuming and expensive process. Moreover, such G-T models that are used to characterize machine tools may not be accurate over a period of time and hence the machine must be tested and recharacterized regularly. Our research focuses on development of fast and cost effective methods for improvement of machine tool accuracy.

Our research work aims to develop a methodology for machine tool accuracy improvement with the aid of simple and standardized machine tool performance tests. A feature-based analysis technique correlates errors of the machine tool with errors of the machined part. To test the machine tool, our approach uses the standard tests specified in the ANSI/ASME B5.54 standard - "Methods for Performance Evaluation of Computer Numerically Controlled Machining Centers" [3]. The machine performance evaluation tests include linear displacement accuracy tests, spindle errors and contouring performance tests using telescoping ball bar. The results of our research will correlate the variations in the performance of the machine tool with the variations that can be expected in the accuracy of the part produced by the machine tool. The advantage of this approach is that these performance tests can be completed in a few hours, when compared with other approaches which may require days or weeks of parametric measurements.

Machining experiments with standard geometric features [4] are used to develop the correlation model. To aid in the design of experiments, a set of diagnostic rules that relate the errors of the machining centers and errors of the part are being developed. Similar work has already been done by Donmez [5] for a two-axis turning center. Deriving diagnostic rules for a machining center (milling machine) is more complicated because of the number of motions possible and the different tool orientations involved. The performance tests specified in the ANSI/ASME B5.54 Standard for performance evaluation of CNC machining centers are performed to determine the errors of the machine tool. Working from the knowledge of errors in a particular machine tool, a series of simple test parts are designed to isolate the error effects caused by one or a combination of error components of the machine. At the initial stage, the analysis includes only a limited number of features and operations, specifically excluding those that are tool dominated such as tapping.

To illustrate the types of parts that will be used to isolate the effects of machine errors, three types of parts are initially considered (Fig. 1). They are

(a) Parts with prismatic features,
(b) Parts with prismatic and cylindrical features, and
(c) Parts with contour features.

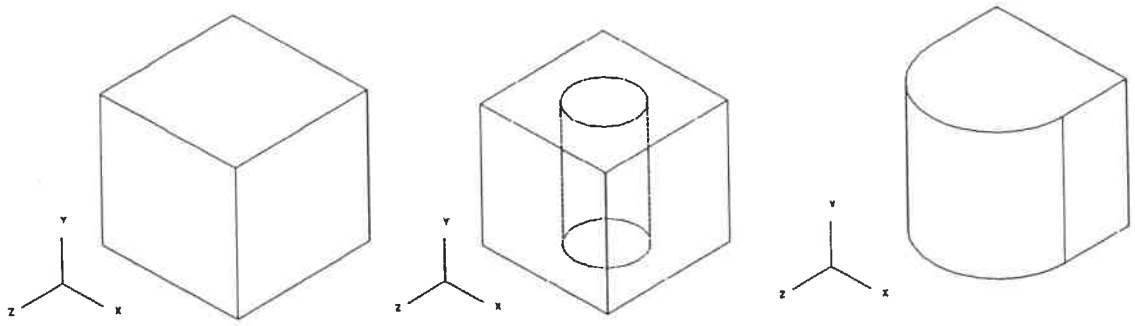

Figure 1. Three types of test parts

Parts with prismatic features have been designed to isolate the errors associated with prismatic features such as flatness, straightness, squareness, parallelism, and positioning. The sources of machine errors and their effect on each of the part errors are analyzed in detail. In machining prismatic features, it is assumed that the motion of the tool follows one of the three principal axes of the machine tool.

Parts with prismatic and cylindrical features are used to isolate part errors associated with cylindrical features. A typical part is a prismatic part with internal cylindrical holes. With the knowledge of the errors in prismatic parts, the machine error sources that contribute only to cylindrical features can be identified. The various errors of the part associated with cylindrical features are circularity, cylindricity, squareness, parallelism, contouring, positioning, and concentricity. The analysis on each of these errors is done so as to reveal the effect of machine error on cylindrical features. It is assumed that the motion of the

tool follows one (two in the case of counterboring etc.) of the three principal axes of the machine tool.

The last type of part includes simple contour features which are machined using the A and B axes (rotary axes) of the machining center. Only the principal X, Y and Z axes have been used for machining the prismatic parts and prismatic parts with cylindrical features. This part needs use of the A and B axes of the machining center only and, hence, the errors associated with these axes can be isolated.

For each type of part, the theoretically derived diagnostic rules are used to design test parts. The diagnostic rules help to identify simple parts that correlate one or two machine errors with one part feature. CAD models of the test parts are developed, test parts are machined and inspected, and part variations due to machine errors are determined by correlating part errors to machine runoff results.

To illustrate the analysis and diagnostic rules, we consider a prismatic part. A variety of tolerance features were analyzed and it was observed that flatness is dominated by angular errors and compliance. If the roll and pitch of the machine table on which the part is placed are each 12 arcseconds, each angular error could cause a variation of 17.97 μm in the flatness of the part over a length of 0.3 m. In the worst case, the effect of roll and pitch would combine and vary flatness by 36 μm (1.5 thousandths of an inch). Similarly, compliance would also affect flatness considerably. These analyses lead us to conclude that a flat prismatic part will be useful for correlation studies related to compliance and angular errors. The test part is then machined and inspected to gather data for the correlation study. Such analyses are performed for each geometric feature and part type.

Using these test parts, an adaptive algorithm, shown in Fig. 2, is being developed to improve the accuracy of CNC machine tools. A CAD model of the part to be manufactured is developed. The part is then machined using a B5.54-tested CNC machining center and measured using a software-corrected coordinate measuring machine. Repeated machine tool performance measurements, cutting tests, and measurements of the part are done to collect the data used for deriving the correlation. The data obtained from measurements is compared with the CAD model and variations in accuracy of the test part are determined. The results obtained from the standard tests specified in the ANSI/ASME B5.54 Standard for performance evaluation of CNC machining centers should predict variations of the machine tool. The variations of the machine tool and variations of the test part are used to derive a predictor that correlates variations in the measured geometry with variations in machine's performance. The results will then be fed back to the CAD model to increase the accuracy of the part produced by altering the design of the test part.

The predictor developed can be used for many different parts since most parts can be decomposed into a set of basic features. The predictor could be used to determine whether a part, composed of a set of basic features, could be manufactured by a particular machine within the specified tolerances. This would considerably reduce the time required for traditional post-process quality control operations and the amount of scrap material,

while increasing the production rate. Also, the machine performance tests could be used to determine changes that would improve the accuracy of the machining process. The dominant errors of the machine tools also give an indication of the repairs or maintenance necessary to improve the accuracy of the machine tool. As well, since the predictor relates machine errors to part features, the correlation matrix could be used to guide designers in the selection of tolerances. In this way designs might be developed to avoid the dominant errors of the machine tool.

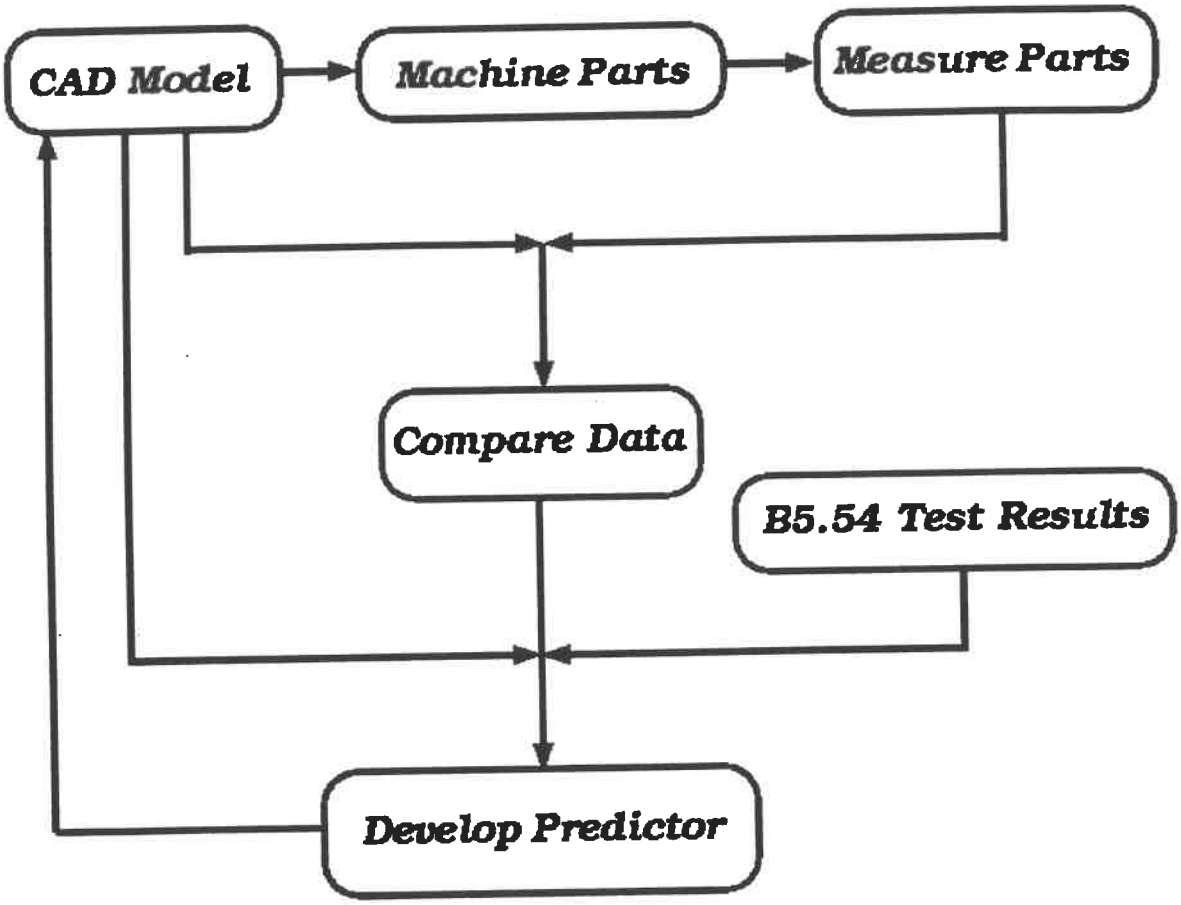

Figure 2. Adaptive Algorithm

1. M.A. Donmez, "Development of a New Quality Control Strategy for Automated Manufacturing", Proceedings of Manufacturing International 1992, D. Durham, ed., ASME, NY, 1992.
2. J.G. Salsbury, "Development of a Methodology correlating machine tool errors to work piece geometry", M.S. Thesis, University of North Carolina at Charlotte, 1991.
3. ASME B5.54-1992, "Methods for Performance Evaluation of Computer Numerically Controlled Machining Centers", The American Society of Mechanical Engineers, 1992.
4. ANSI Y14.5M-1982, "Dimensioning and Tolerancing", ASME, NY,1982.
5. J. Mou, M.A. Donmez and S. Cetinkunt, "An Adaptive Error Correction Method using Feature-based Analysis Techniques for Machine Performance Improvement - Part I : Theory Derivation", Accepted for publication in ASME Journal of Engineering for the Industry.

ACCURACY IMPROVEMENT OF MACHINE TOOL BY WORFAC (3RD REPORT)

- Investigation and elimination of uncontrollable point -

Yutaka Uda, Tsuguo Kohno, Takanori Yazawa

Tokyo Metropolitan Institute of Technology
6-6 Asahigaoka, Hino, Tokyo 191 Japan

1.Introduction

In ultraprecision machining technology, manufacture of more precise and larger elements is expected. The author proposed a new system, called the workpiece-referred form accuracy control system (WORFAC), and confirmed an effectiveness of this manufacturing method[1]. In the first report[2], two matters were found out: the effectiveness of simulation for estimating the formed accuracy, and the new function of the corrective servo by changing the feedback volume such that the error is multiplied by the corrective servo coefficient m ($0 \leq m \leq 1$). In the second report[3], the effects of the coefficient m for disturbance elimination and for remained error convergency were cleared. Then the existence of such a special point (SP) as uncontrollable for form accuracy improvement was found.

In this study, (1)the existence of SP, (2)the elimination of SP, and (3)the influence of the extra sensor's setting error are investigated.

2.Principle of the research

The WORFAC is based on a concept that form accuracy is determined by the relative displacement between the workpiece and the cutting tool. Hence this method is a way of controlling the depth of microcutting via in-process measurement of the distance between the tool and the workpiece. The experimental system of cylindrical turning is illustrated in Fig.1. A microtool servo (MTS) and noncontact optical surface sensor (HIPOSS) are attached rigidly on the same post, and the workpiece is placed between the MTS and HIPOSS.

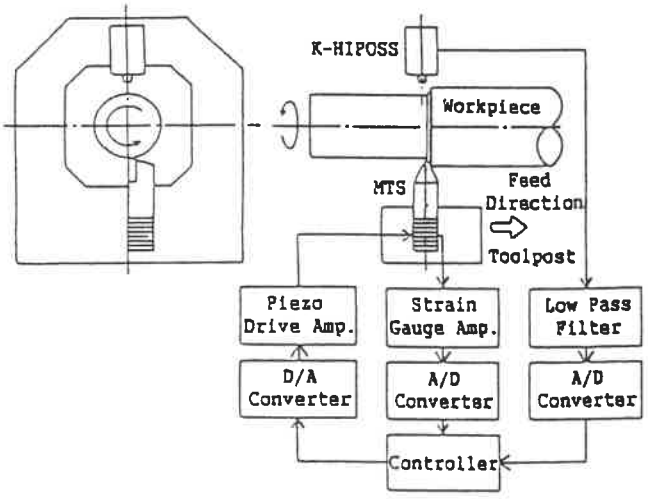

Fig.1 Block diagram of WORFAC experiment

3.The existence of the special point

For simulation of this system, the mechanism is modeled as

shown in Fig.2. The X-axis is defined as the direction of workpiece's axis, and x means the position of cutting point. The tool post motion to the radial direction of workpiece will be appeared as an error $T_0(x)$. In the case of servo-off turning, the amount of displacement of the cutting tool and the sensor, as well as the cutting workpiece figure, are all same as $T_0(x)$. In the case of servo-on turning, the motion of the tool and the figure change from $T_0(x)$ to $T(x)$ but the motion of sensor is still $T_0(x)$. If the axial distance between the cutting point and the sensing point is x_g, the figure at the sensing point is $T(x-x_g)$.

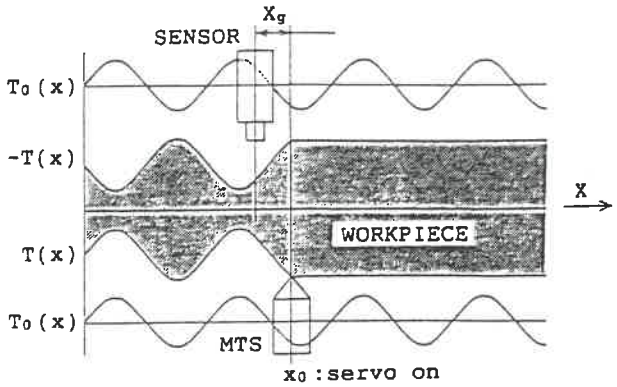

Fig.2 Simulation model of the experiment

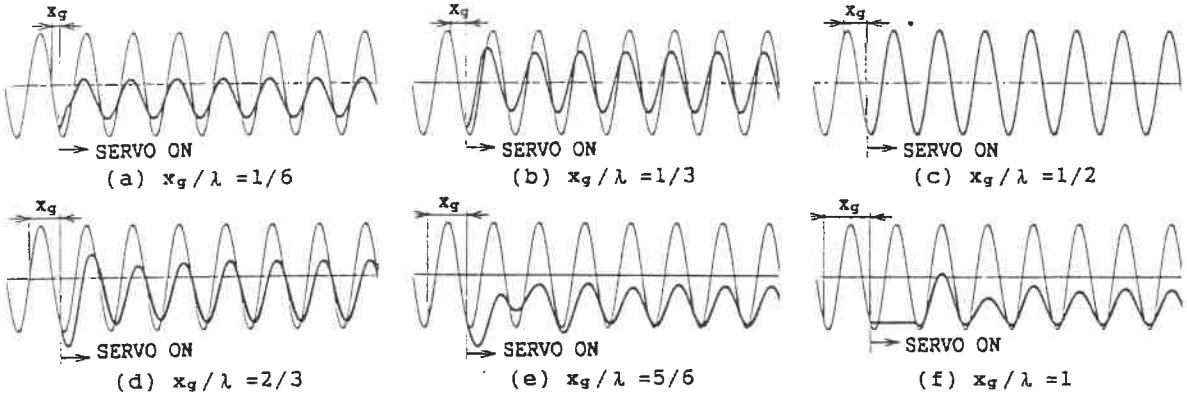

Fig.3 Results of simulation (in the case of m=0.5)

The results of simulation are shown in Fig.3. Figure 4 is a diagram of the relationship between x_g/λ and M, where λ is the wavelength of the slide error motion, and M is the ratio of form error at servo-on to that at servo-off. If $x_g/\lambda = 1/2+n$ (n: positive whole number), M becomes 1 and the form error at servo-on is the same as that at servo-off. For confirming the existence of SP, the experiment of cylindrical turning was carried out using a CNC lathe and a diamond tool. So λ =6mm, then x_g is set 3mm. The form accuracy is measured by a form tester, and the result is shown in Fig.5. The error of 6mm pitch at servo-on is the same amount of amplitude as that at servo-off. But a large slope is changed at the start point of servo-on. The slope

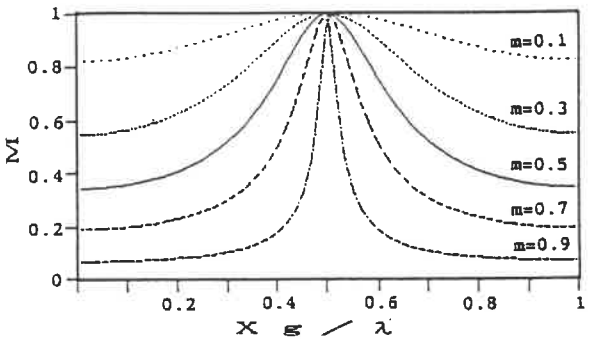

Fig.4 Diagram of relationship between x_g/λ and M

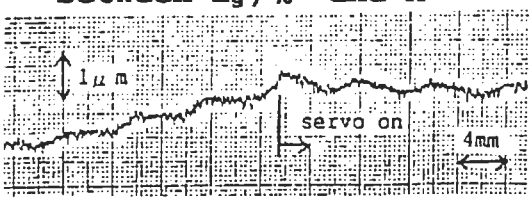

m=0.5 x_g=3mm

Fig.5 Figure accuracy error (x_g/λ =0.5)

can be regarded as a sine wave of which wavelength is almost infinity. If $\lambda \rightarrow \infty$, $x_g/\lambda \rightarrow 0$ and the slope error can be reduced.

4.The Elimination Method and Simulation

At SP, this system is not useful for form accuracy improvement, because the sensing volume is constant. For eliminating SP, another sensor is attached to the same tool post. If the axial distance x_{g2} of the extra sensor can be kept away from SP when that x_{g1} of the original sensor is set at SP, the form accuracy may be improved. One of the solution is $x_{g2}=2*x_{g1}$. In the case of $x_{g1}/\lambda = n+1/2$, $x_{g2}/\lambda = 2n+1$ and x_{g2} can be kept away from SP. If $x_{g2}/\lambda = n+1/2$, $x_{g1}/\lambda = j \pm 1/4$ (j: positive whole number) and x_{g1} is not on the SP.

For simulation of this system, the mechanism is modeled as shown in Fig.6. The sensing volume of two sensors $S_1(x)$ and $S_2(x)$ are written by the equation (1) and (2), where the subscript number are the sensor's number.

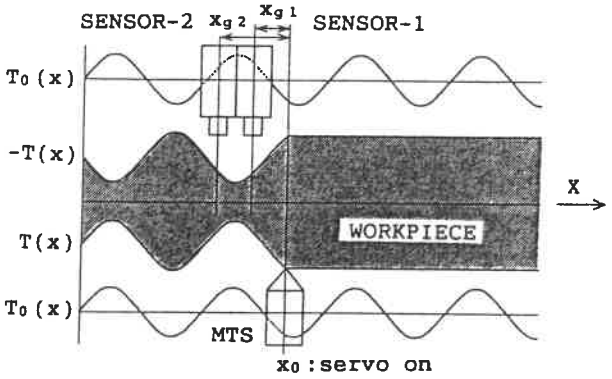

Fig.6 Simulation model of two sensors

$$S_1(x) = T_0(x) + T(x-x_{g1}) + C_1 \quad \cdots\cdots (1)$$

$$S_2(x) = T_0(x) + T(x-x_{g2}) + C_2 \quad \cdots\cdots (2)$$

Where C_1 and C_2 mean the off-set volumes of the sensor in the radial direction and are set so that $S_1(x_0)$ and $S_2(x_0)$ become zero at the starting point x_0 of servo-on turning. Here, the volume of feed-back to MTS is determined that which is $\{S_1(x)+S_2(x)\}/2$ multiplied by the coefficient m. Thus T(x) is expressed by the equation (3).

$$T(x) = T_0(x) - m\{S_1(x)+S_2(x)\}/2 \quad \cdots\cdots (3)$$

The results of simulation are shown in Fig.7. Referring to

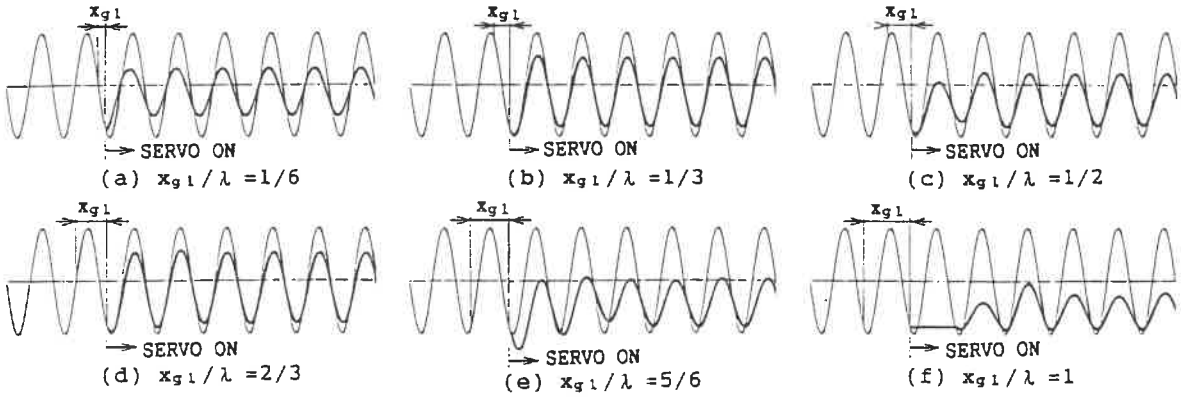

Fig.7 Results of simulation (in the case of two sensors, m=0.5)

Fig.3 and Fig.7, in the case of two sensors, SP is eliminated and the form error at SP is much better than that of one sensor. Figure 8 is a diagram of the relationship between x_{g1}/λ . Though there are two peaks at $x_{g1}=\lambda/3$ and $x_{g1}=2\lambda/3$, the overall form error is improved.

5.Influence of the extra sensor's setting error

A key point of SP's elimination is the setting point of the extra sensor. For investigating the influence of the setting error, x_{g2} change from $2*x_{g1}$ to $(1\pm 0.1)*x_{g1}$. Figure 9 is a diagram of the relationship between x_{g1}/λ and M. If $x_{g2}=1.9*x_{g1}$, the position of both peaks are moved left, M at first peak becomes small, and M at second peak becomes big. In the experiment of Fig.3, the feed rate is 20μ m/rev and the setting accuracy of x_g is achieved less than $\pm$ 2μ m. Therefor $x_{g2}=(1\pm 0.1)*x_{g1}$ is not severe to set the extra sensor.

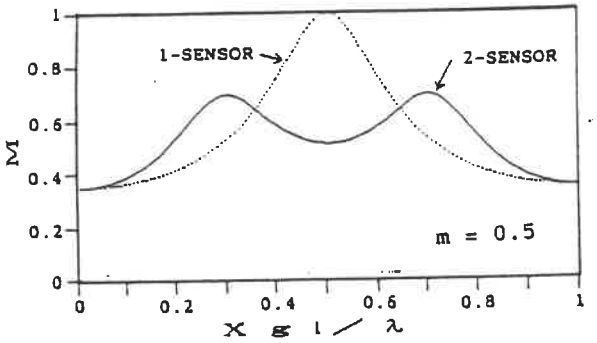

Fig.8 Diagram of relationship between x_{g1}/λ and M

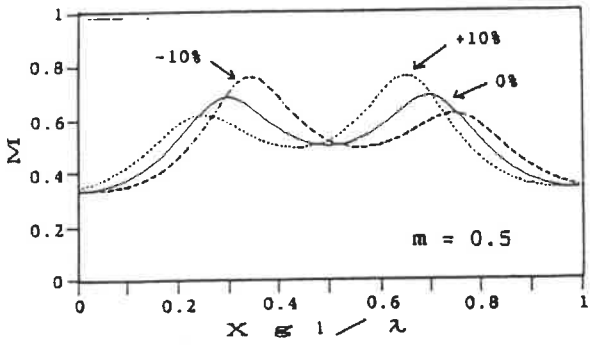

Fig.9 Diagram of relationship between x_{g1}/λ and M (± 10% setting error)

6.Conclusion

Workpiece-referred form accuracy control (WORFAC) is applied an ordinary NC machine tool. In this study, (1)the existence of the special point, (2)the elimination of that, and (3)the influence of the extra sensor's setting error are investigated.

(1)The existence of the special point is confirmed by the experiment of cylindrical turning.

(2)Using another sensor attached to the same tool post, the special point can be eliminated. Though there are two small peaks at $x_{g1}=\lambda/3$ and $x_{g1}=2\lambda/3$, the overall form error is improved.

(3)An influence of the extra sensor's setting error is also simulated by a computer and the setting is found not to be severe practically.

Reference

[1]T.Kohno, et al. Precision Engineering, P.9, Vol.11, No.1, 1989

[2]T.Kohno, et al, Proceedings of ASPE Annual Meeting '92, P.376

[3]Y.Uda, et al, Proceedings of ASPE Annual Meeting '93, P.499

Various Dynamic Micro Tribological Phenomena under SEM Observation Measured by a High-rigid Multi-axis Force Sensor

Hirokuni HACHIUMA, Masayuki NAKAO, and Yotaro HATAMURA
Department of Engineering Synthesis
The University of Tokyo
7-3-1 Bunkyo-ku, Hongo, Tokyo 113, JAPAN

1. INTRODUCTION

Research on micro tribology is drawing much attention in the field of information industry such as computer connector pin or LSI circuit examination probe.

Progress of computer has been increasing the numbers of connector pin in one module. Consequently, friction force has become too high to insert in the module. If the normal force is reduced to avoid the problem, contact resistance becomes high and caused electric trouble. Contact area of present connector is ϕ30μm and it will become smaller for the next computer. However, it is not known how the new connector changes the performance under such a micro contact.

As a new attempt to examine a spontaneous part of a LSI circuit, a probe directly contacts the circuit line of sub-microns width and measures its electrical performances. Basic data of relation between normal force and contact resistance on the present examination pads of ϕ50μm is well studied. However, it is not known if the same relation can apply to the sub-micron contact.

Can micro tribology extrapolate from macro tribology? Most studies on micro tribology cannot answer it. One of the problem is that the physical phenomena are inferred from the results obtained separately. Since the microscopic observation during measurement is difficult, they only measure friction force or observe the measured surface afterward. It is essential for correct understanding of physical phenomena that observation and measurement are made simultaneously. Another problem is a force sensor. They use a AFM/FFM leaf spring for micro force measurement. However, it is easy to twist so that the target system is disturbed by the twist vibration.

Considering the above problems, the authors newly developed "Nano Testing System." In this paper, its function, mechanism, structure, and configuration are explained along the design process, and various micro tribological phenomena analyzed by Nano Testing System are presented.

2. FUNCTIONS AND MECHANISMS OF NANO TESTING SYSTEM

According to the design theory[1], requirements for the Nano Testing System are analyzed into functions shown in Fig.1. In addition to the general functions regardless of test size (Fig.1(a)), special functions in Fig.1(b) are required . They are unconsciously achieved in usual size test but difficult in micro size test; co-localibility, simultaneous and real-time operatability, three dimentionality, etc.

As a mechanism to realize the above functions, SEM observation and multi-axis force sensing are applied.

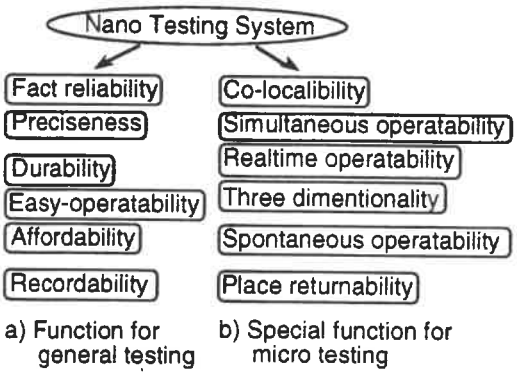

Fig. 1 Functions of Nano Testing System

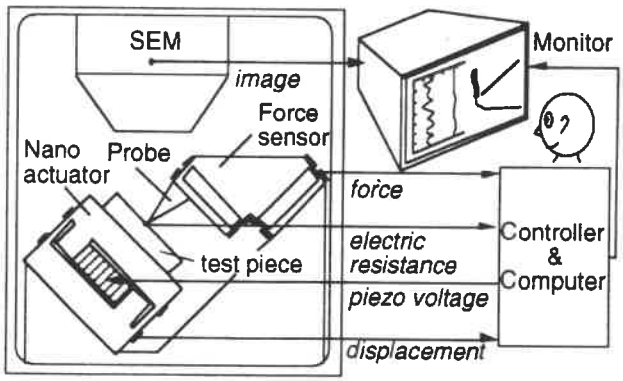

Fig. 2. Configuration of Nano Testing System

3. STRUCTURES AND CONFIGURATION OF NANO TESTING SYSTEM

For the next step, the authors determine structures to satisfy the above mechanism.

For SEM observation, field emission type SEM (Hitachi S4100) is used to obtain high resolution image even in real-time TV mode. Maximum magnification is x300,000. Degree of vacuum in the specimen chamber is under 10^{-3}Pa.

For multi-axis force sensing, a high-rigid two-axis force sensor is newly designed. Its structure is stacked up parallel plate structures[2] with semi-conductor strain gages. By using parallel plate structure, undesired deformation and interference from another axis force are kept within 2%. Resolution of the force sensor is 10^{-6}N, resonance frequency 255 and 163Hz, and rigidity 380 and 1690N/m.

The other structural elements are mentioned below.

A "Nano actuator" makes contact and sliding motion during the testing. It makes two translational movements by piezo electric actuator. Its working range is 10μm and the resolution is under 5nm. Its displacement is measured by strain gages glued on its block and feedback-controls piezo voltage. Force sensor can also control the Nano Actuator in order that the normal or friction force becomes constant. Electric contact resistance is measured by a current-potential method. Probe is made of diamond or WC spattered with Au.

These elements are synthesized to make the configuration of Nano Testing System as shown in Fig.2. Nano Testing System is installed in the vacuum chamber. The probe touches a specimen perpendicularly, and the Nano Actuator and the force sensor are set inclined at 45° with the axis of SEM observation. All the information obtained inside the chamber, such as force, contact resistance, displacement and SEM image, are shown on the TV monitor simultaneously.

4. MICRO TRIBOLOGICAL PHENOMENA ON CONNECTOR PIN

4.1 TESTING METHOD

Tribological progress on computer connector pin is desired as is mentioned above. Using Nano Testing System, a diamond probe (1μm tip diameter) slides on the connector pin at constant normal force. Observing the phenomena by SEM, force and displacement are measured.

The test piece is a Cu alloy/Ni plated/Au plated connector pin for general purpose computer. Its diameter is 0.3mm.

4.2 EXPERIMENTAL RESULTS

Photo.1 shows a TV image after completing the sliding experiment. The surface of the plated Au has much irregularities (0.2-0.6μm_{p-p} measured by scanning laser microscope). Normal and frictional force, and probe displacement are simultaneously superimposed in line graph on the TV image during the experiment. Ploughing-type wear was observed under constant normal force of 0.35mN. The width of the wear was 0.4μm. Making many experiments under various normal force (from 0.2mN to 2mN), ploughing-type wear was observed from 0.2mN to 1.0mN and cutting-type wear was observed over 1.0mN.

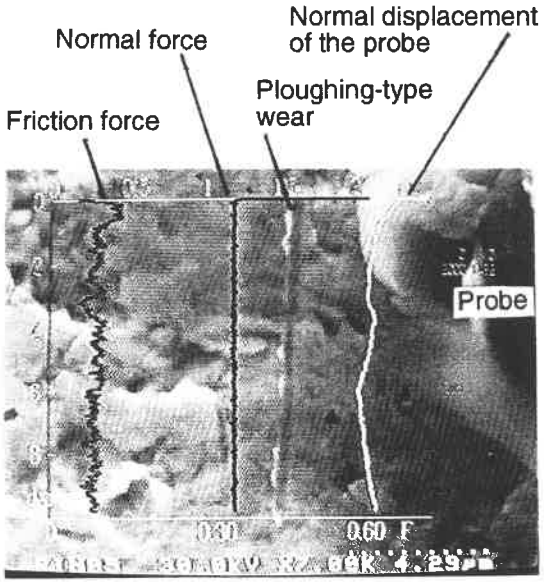

Photo. 1 TV image of the experiment

Figure 3 shows the line graphs in Photo.1. Normal force shown in Fig.3(a) is controlled constant. Frictional coefficient is fluctuated from 0.15 to 0.40. When repetitive sliding experiment is made at the same place under the same condition, friction coefficient at the 100th sliding decreases to 0.1 and still showing the wear growth. Figure 3(b) shows the normal and frictional displacement of the probe. The more the probe is indented to the test piece, the more the normal displacement value decreases. The SEM image and the normal displacement graph tell that the normal displacement follows the surface contours. Moreover, the waveform of friction force is similar to that of differential of normal displacement in Fig.3(c). This means that if the surface is upslope (increasing period of the normal displacement), the friction force increases and vice versa (discuss afterward).

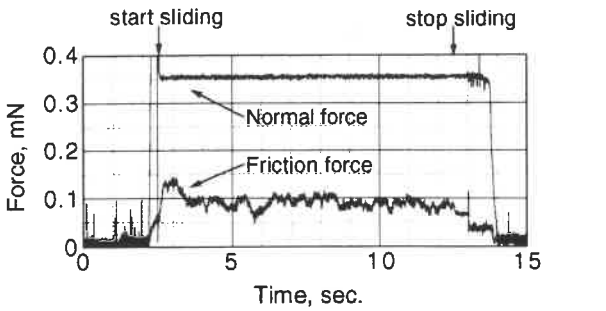

(a) Force

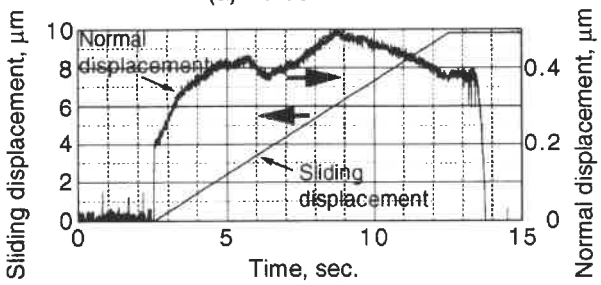

(b) Displacement of the probe

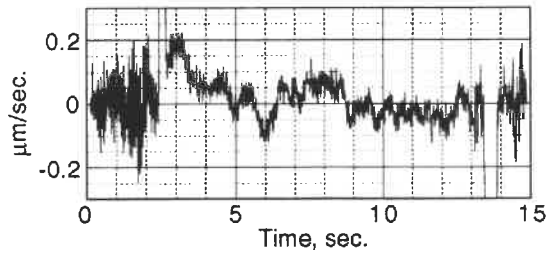

(c) Differential of normal displacement

Fig. 3 Results of micro sliding

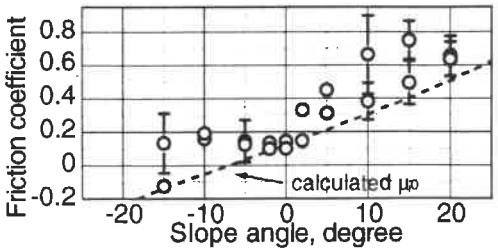

(a) Only a hemisphere glass

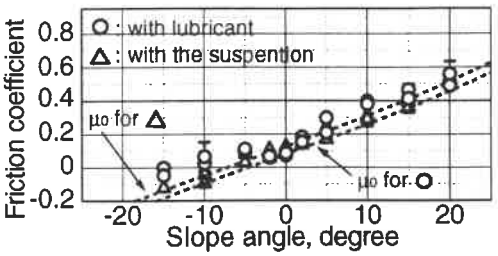

(b) Self-peeling suspention or lubricant oil is added

Fig. 4 Correlation between friction coefficient and slope angle

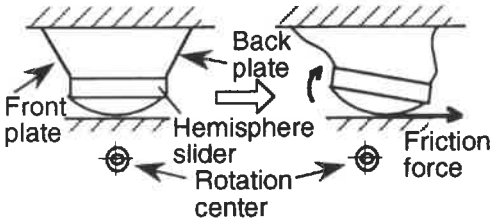

Fig. 5 Structure and deformation of self-peeling suspension

4.3 DISCUSSIONS

Here, we discuss the correlation between the surface slope and friction force.

Apparent friction coefficient μ_0 is calculated by normal force and friction force on the force sensor coordinate. Where the slope angle of the surface is taken θ and actual friction coefficient on the surface is μ, μ_0 is given[3)]

$$\mu_0 = \frac{\mu+\tan\theta}{1-\mu\tan\theta} \qquad (1)$$

Using another system, we made an experiment to verify the correlation: Under the slope angle shifted by goniostage, a R10mm hemisphere glass lens slides on a thin plate that is plated by the same process as the connector pin. Figure 4(a) shows the relation between slope angle and measured μ_0. A dashed line shows the calculated μ_0 of equation(1). When the slope angle ascends, measured μ_0 becomes larger than calculated μ_0, and shows much deviation because of the stick and slip. The phenomena are explained as follows: The probe tip declines forward, squashes a wear chip, and sticks to the test piece. During the sticked probe is drawn, small rigidity part bends and the friction force increases. These phenomena easily occurs if a leaf spring force sensor is used.

A self-peeling suspension[4)] (shown in Fig.5) to avoid the declining of the tip or lubricant between the slider and the test piece to assist the sliding is added. The results are shown in Fig.4(b). Both measured μ_0 correspond with the calculated μ_0 and both deviations are small. These results indicate the sticking should not be occurred.

In consequence, peculiarly high friction force could be generated by its suspension sructure.

5. MICRO TRIBOLOGICAL PHENOMENA ON EXAMINATION PROBE

5.1 TESTING METHOD

In order to assess a part of LSI circuit, a probe should electrically contact the circuit line of sub-microns width directly. Using Nano Testing System, indentation tests on metal surface by several WC probes of different tip radius was performed. While a probe indents and returns, normal force and contact resistance were measured. Test piece is Au plating and probes are WC spattered with Au.

5.2 EXPERIMENTAL RESULTS

Fig.6 shows a relation between the contact resistance and the normal force. Contact resistance is defined zero when a probe comes the bottom point.

While normal force increases, contact resistance decreases in inverse proportion to the normal force. In the force decreasing period, contact resistance is kept smaller than in increasing one. Contact resistance in the force increasing period was smaller in the second indentaion at 20sec. later after the first one. The main cause of these results may be surface contamination removal by electric current.

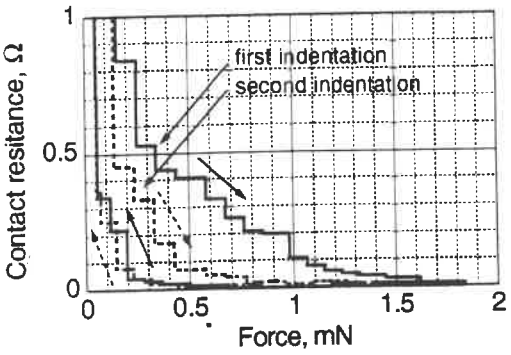

Fig. 6 Force vs. electrcal conductance digaram during the indentation experiment with a 2μm probe on Au plating.

5.3 DISCUSSIONS

In order to check the influence of the apparent contact area. Indentation tests with probes of various tip radius are performed.

Fig. 7 shows the relation between contact resistance and probe tip radius. Regardless of the tip radius, the contact resistance was alomost the same. Under these condition of tip radius and normal force, real contact area must be determined only by normal force. This means the deformation at the contact point is similar regardless of the probe tip radius. With the SEM observation, plastic diformation was not observed on every experiment.

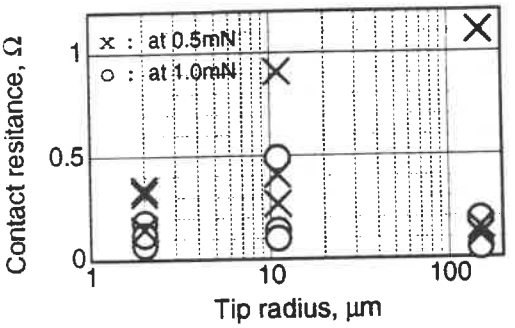

Fig. 7 Contact resistance during the indentation with various probe

6. EVALUATION OF NANO TESTING SYSTEM

Through these experiments, the authors confirmed the effectiveness of the Nano Testing System for micro tribological research. As a structural elements, simultaneous SEM observation and measurement by high-rigid multi-axis force sensor are indispensable for the system.

7. CONCLUSIONS

(1) "Nano Testing System" was developed in order to explain micro tribological phenomena. This system satisfies the functions of three-dimensional, simultaneous, co-localiable, and real-time observation/measurement.

(2) Using Nano Testing System, micro tribological phenomena on computer connector pin that has a contact area of several micrometers diameter and on LSI examination probe that has contact area of sub-micrometers diameter were analyzeded.

References:

1) N. P. Suh: *The Principles of Design*, Oxford Univ. Press (1990)

2) Y. Hatamura: *Multi-Axis Force Sensors and Their Applications*, J. of Advanced Automation Technology Vol. 4 No. 4 (1992), pp180-185

3) F. P. Bowden and D. Tabor: *The Friction and Lubrication of Solids*, Clarendon Press, Oxford (1950)

4) Y. Hatamura, S. Yanabe, N. Ishimaru, T. Shinohara, and M. Ito: *Development of a Self-Peeling Suspension for Non-Crash, Non-Stick and Low Fly-Height*, IEEE Trans. Mag. Vol. 26, No. 5 (1990), pp 2484-2486

Torque Measurement using a Photoelastic Coating Method

Masahiko Hasegawa
Manufacturing Engineering Center, Mitsubishi Electric Corp.,
8-1-1, Tsukaguchi-honmachi, Amagasaki, Hyogo 661, Japan

1. Introduction

It is very useful to measure the torques acting on cutting tools in order to detect tool damage (wear, chipping, breakage, etc.).[1,2] Most torque meters are based on the strain gage method. However it involves a few defects as follows: (1) there is a reduction in stiffness of the machine by placing the torque meter between the motor and the tool, (2) its measuring range is narrow, (3) the machine must be remodelled when mounting the meter or distributing its wiring.

Therefore to solve these defects, we have developed a new torque measuring system using an improved photoelastic coating method (Fig. 1). It is known that a tool shank is deformed elastically during machining. In this system, a photoelastic coat covers the tool. Consequently the coat is strained by the machining torque. This strain is detected by an optical pickup using a laser beam and the machining torque can be measured.

2. Principle of torque measurement

As shown in Fig. 1, when a torque acts on a tool covered with a photoelastic coat, the strain tensor [S] of the coat is equal to that of the tool surface and can be calculated as follows:

$$[S] = \begin{bmatrix} 0 & \dfrac{T}{\pi G \alpha^3} & 0 \\ \dfrac{T}{\pi G \alpha^3} & 0 & 0 \\ 0 & 0 & 0 \end{bmatrix} .$$

In the above equation, T is the torque, G is the shear modulus of the tool and α is the radius of the tool. The index ellipsoid of the coat changes from spherical to elliptical (Fig. 2). The Δn is

$$\Delta n = n_0^3 p_{44} \frac{T}{2\pi G \alpha^3} ,$$

where n_0 is the refractive index of the coat when $T = 0$, and p_{44} is the photoelastic coefficient of the coat. When linearly polarized light is propagated along the z axis, the light wave passing through the strained coat ($T > 0$) is polarized elliptically. By measuring the changes in polarization, the torque can be obtained.

3. Measuring system and calculation

In the conventional photoelastic coating method [3,4], the surface strain is analyzed according to its fringe number by using linearly polarized light or circularly polarized light. But in our improved method, the surface strain of the tool is obtained according to the polarization of light passing through the coat by using elliptically polarized light.

Our measuring system showing the polarization of light (**a**-**e**) is illustrated in Fig. 3. This optical system was developed to have a linear, adjustable sensitivity. The tool has a coat with a high photoelastic coefficient p_{44}. The light wave **a** transmitted by a polarizing beam

splitter(PBS) is linearly polarized light. After passing through a phase plate, this light wave becomes elliptically polarized light **b**. In the coat the light **b** changes into light **c**. After passing back through the phase plate, the light **c** becomes light **d**. It is then bent by a half mirror to become light **d'** and is detected by a photo-diode PDr. The output of PDr is the reference intensity *Ir*. At the same time the signal light **e** which is bent by the polarizing beam splitter is detected by a photo-diode PDs. The output of the PDs gives the signal intensity *Is*. The intensity ratio $R = Is / Ir$ enables us to measure the torque without the influence of reflection on the tool surface.

In this configuration, the intensity ratio R is calculated as follows:

$$R = (Is / Ir)$$
$$= (\sin 2\theta \cos kT - \cos^2 2\theta \sin kT)^2,$$

where

$$k = \frac{2n_0^3 p_{44} d}{\lambda G \alpha^3}.$$

In the above formula, θ is the phase plate orientation as shown in Fig. 3, d is the thickness of the coat and λ is wave length. Some typical examples using this formula are illustrated in Fig. 4. By changing θ the correlation between kT and R is changeable. For example, when $\theta = 20^\circ$ the linearity of R to kT is 0.03%, where $0^\circ < kT < 5^\circ$. And the sensitivity of R to T is adjustable by the parameter k or the orientation θ. Therefore this system has a linear, adjustable sensitivity.

4. Experiment

The theoretical effectiveness of this system was verified experimentally in the following way (Fig. 5). Torque was imparted to a rotating coated pole. The thickness d of the epoxy resin coat was 0.4 mm and the radius α of the pole (SUS303) was 2 mm. The torques were measured by a corrected torque meter and an optical pickup. The pickup contains the optics shown in Fig. 3. Then the two measured values were compared by a computer.

5. Results and discussion

Two sets of the data given by the experiment are shown in Fig. 6 and Fig. 7. These experimental results approximately agree with the theoretical prediction: our torque measuring system has a linear, adjustable sensitivity which is changeable by the phase plate orientation θ and the parameter k.

The resolution realized by the experiment (Fig. 7), defined as the intensity ratio R which gives a S/N of 1, was $\pm 3 \times 10^{-4}$. This resolution is equivalent to $\pm 0.6\%$ of the measuring range under the experimental conditions used. This is as good as that of a torque meter using the strain gage method. It is considered that this experimental resolution depends upon the noise light in the optical pickup and the resolutions of the A/D converters.

6. Conclusions

We have developed a new torque measuring system by using an improved photoelastic coating method. The theoretical prediction (a linear, adjustable sensitivity) was verified experimentally. Also, the resolution realized by the experiment was $\pm 0.6\%$ of the measuring range.

Key words ; torque, measurement, photoelastic coating method, photoelastic effect, wear, chipping, breakage, polarized light, stiffness, shearing strain.

References

1) J. Tlusty and Y. S. Tarng, "Sensing Cutter Breakage in Milling", Ann. CIRP **37/1**, 45-51 (1988).
2) E. J. Armarego and N. P. Deshpande, "Computerized Predictive Cutting Models for Forces in End-Milling Including Eccentricity Effects", Ann. CIRP **38/1**, 45-49 (1989).
3) C. Kitabayashi and T. Kumazawa, "Stress Measurement in a Small Area by on Oblique Incidence Ellipsometry", Journal of the Japanese Society for Non-destructive Inspection **38**, 1094-1100 (1989).
4) K. Ichinose and Y. Niitsu, "Scanning Stress Measurement Method by Laser Photoelasticity", Transactions of the Japan Society of Mechanical Engineers **A 60**, 1114-1119(1994).

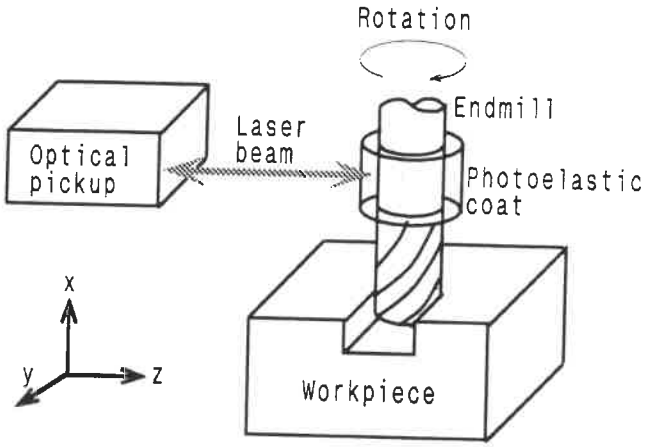

Fig. 1 Machining by photoelastic coated endmill

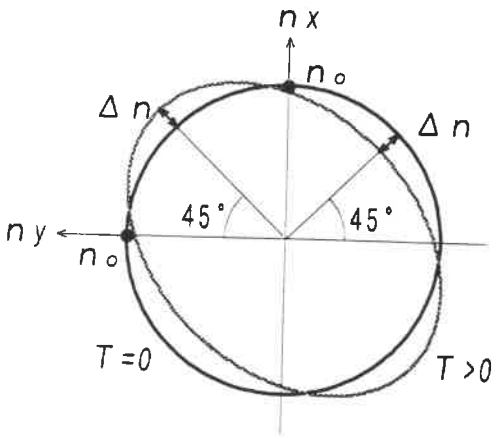

Fig. 2 x-y cross section of index ellipsoid

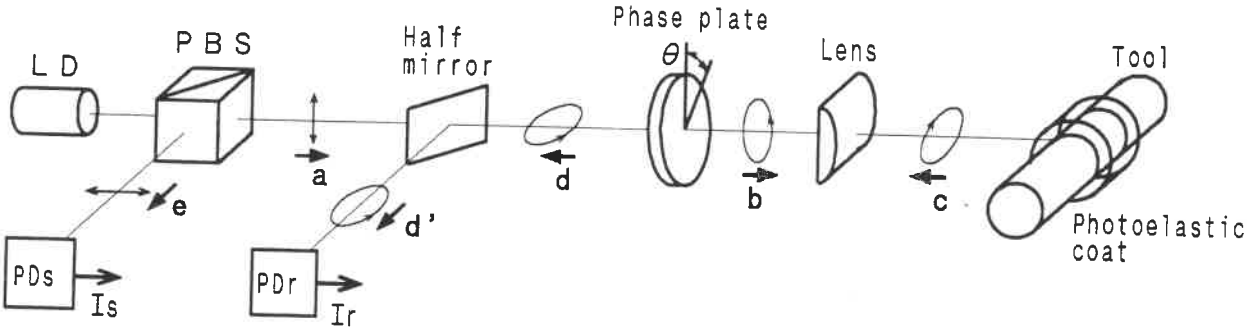

Fig. 3 Diagram of torque measuring system

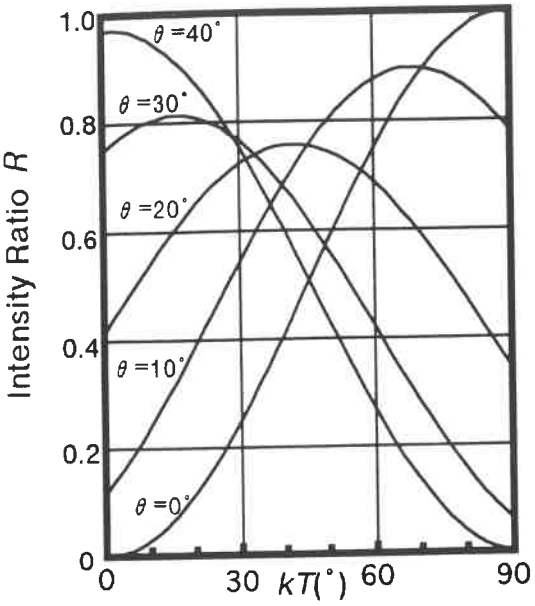

Fig. 4 Static characteristic (calculated value)

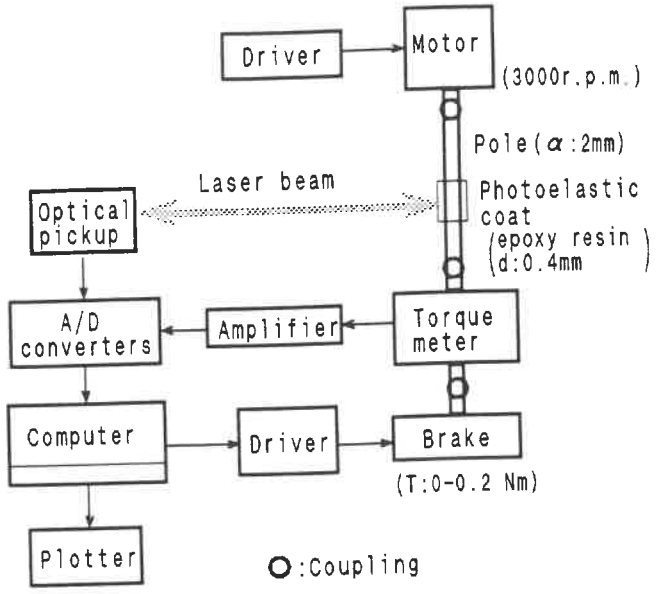

Fig. 5 Diagram of experiment

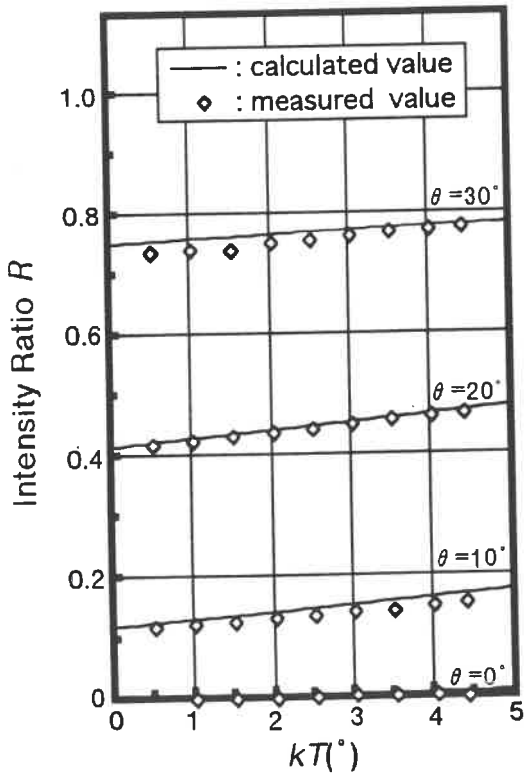

Fig. 6 Static characteristics of narrow range

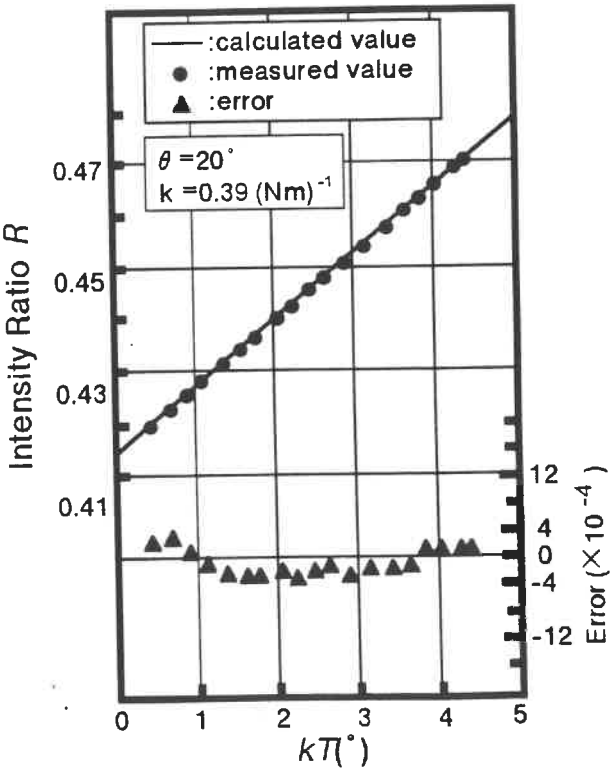

Fig. 7 Characteristics of new torque measuring system

WHAT CAN LASERS DO FOR YOU?

Steven Case, Michael Riddle, Tim Skunes
CyberOptics Corporation - Minneapolis, MN

With the proliferation of the diode package, the laser has become an economical, as well as reliable light source for optical measurement. Because it is bright (a low-power laser is brighter than the sun) and highly directional, a large amount of light can be concentrated on a small, distant point or line. This makes it possible to measure characteristics, such as height or surface contour, that cannot be measured accurately using conventional illumination. Combining this miniature light source with optics and computer intelligence, compact sensors have been developed for gauging in an automated environment.

Types of laser sensors

Laser sensors can be categorized by complexity, ranging from simple to intelligent. A basic sensor incorporates a diode light source, optics, a detector and electrical signal - typically a variation in output voltage or current - to provide raw data. At the opposite end of the spectrum is the intelligent sensor. It uses essentially the same components (in some cases, multiple light sources and detectors), but also incorporates a microprocessor, software and communication to provide the user with specific answers to measurement problems.

Packaging

Laser sensors are packaged to be either transmissive or reflective. A *transmissive* sensor, shown in Figure 1, uses the focusing optics to image the light directly onto the detector. With this technique, an object is passed through the light path creating a shadow on the detector. With the laser focused to a small point, an object larger than the point will block the signal completely as it passes through the light path. The high focal spot intensity, coupled with laser power stabilization, produce a high edge detection signal to noise ratio. This creates a precise limit switch. When combined with motion control and an encoder, the width or diameter of an object can be measured.

Figure 1.

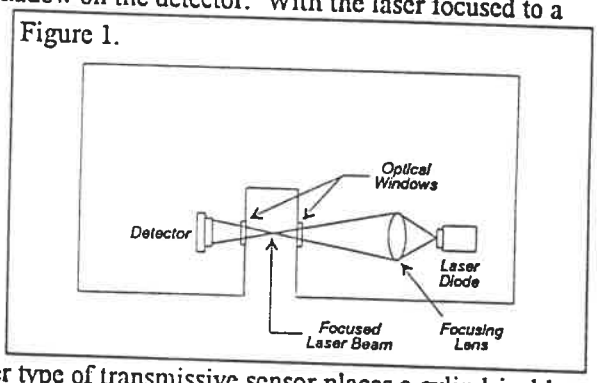

Another type of transmissive sensor places a cylindrical lens in front of the laser source to display a stripe of light. As the object intrudes in the light path, the signal is partially blocked on the detector. By measuring the depreciation of the signal, the amount of the intrusion will be revealed. When a pixelized detector is used, an accurate measurement of the intrusion - or shadow - can be obtained.

Figure 2.

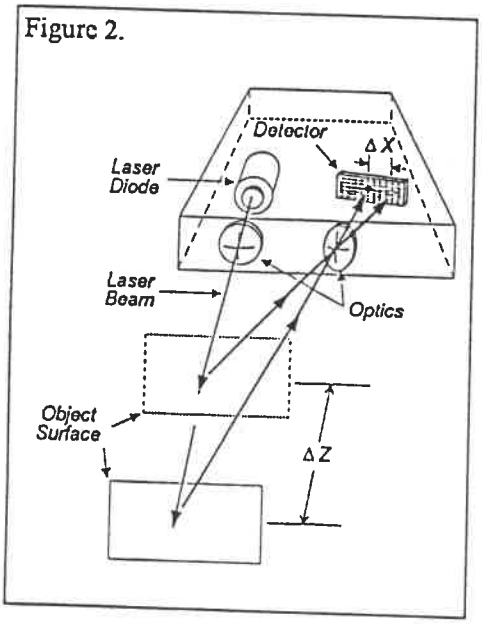

The *reflective* sensor is also known as a triangulation sensor, shown in Figure 2. Using this technique, a the light source is imaged onto the object to be inspected. Light scattered from the object is imaged back to the sensor's detector. If the object's surface were to be moved closer to (or farther from) the sensor by an amount ΔZ, the light reflected from the surface would move to a different position on the detector by the amount ΔX. By reading the detector to find the new position of the spot, the change in the object's distance can be calculated.

As shown in Figure 3, modifying this design with a cylindrical source lens to produce a light stripe, and utilizing a two-dimensional pixelized array detector, a small profile of the object's surface can be realized.

Figure 3.

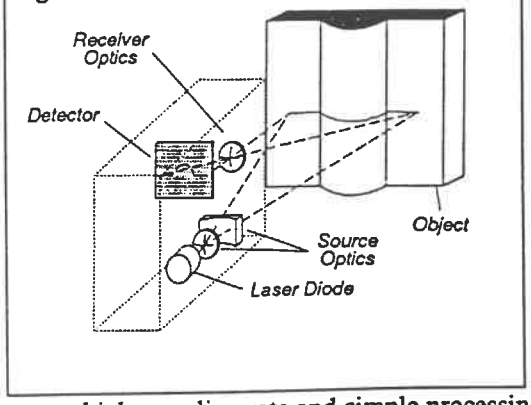

Types of Detectors

For single point transmissive sensors, a light sensitive detector with a high signal to noise ratio will suffice. Many other types of simple laser sensors use a Position Sensitive Device (PSD) known as a Lateral Effect Photodiode or LEP (Figure 4). The LEP measures the position of the laser signal by comparing the ratio of the outputs on each end. Low cost, high sampling rate and simple processing are the major advantages of using this type of detector. On ideal surfaces, where there is little or no variations in color or surface structure, laser sensors using a LEP perform reasonably well. On the other hand, highly contoured objects, or surfaces with a considerable degree of surface microstructure, can cause multiple laser signals to be imaged on the detector. The LEP will simply average these unwanted signals - along with the good one - to produce an erroneous output.

Figure 4. Lateral Effect Photodiode

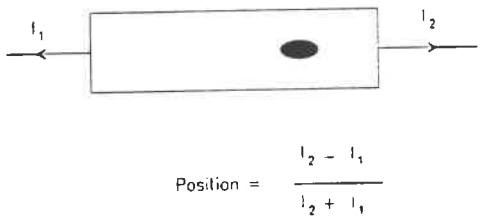

In many real world applications, the measured samples are indeed highly contoured, and vary in surface reflectivity and opacity. For applications where surface variations are common, spatial filtering of the laser signal is often required for an accurate measurement. Here, solid state, pixelized arrays are necessary. An illustration of a such a detector, a video array, is shown in Figure 5. The laser signal can be processed using simple machine vision techniques such as binary thresholding or limited gray-scale analysis.

Figure 5.

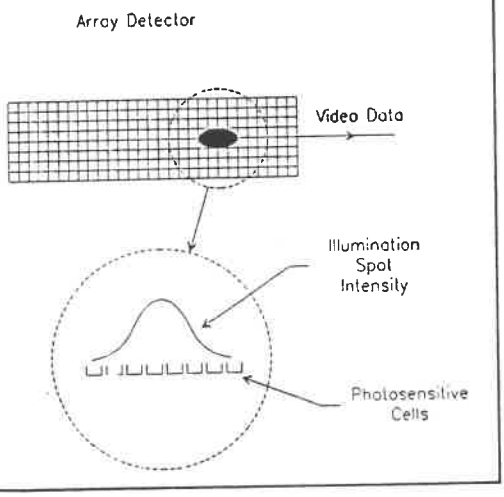

Translucent and transparent surfaces may also cause anomalies in the laser image. Translucent surfaces create a blooming effect in the detector, due to the penetration of the laser light. Simple processing of this signal would indicate that the position of the edge or object is further away than it actually is. By thresholding the video signal, the true surface is revealed.

For transparent materials, multiple images are sometimes obtained: one for the top surface, one for the bottom. Figure 6 illustrates an example of this phenomenon. If the position of only one surface is desired, the pixelized array data can be processed to ignore the unwanted image. If the thickness of the transparency is of interest, calculating the distance between the two and multiplying it by the material's index of refraction will yield the measurement.

Figure 6.

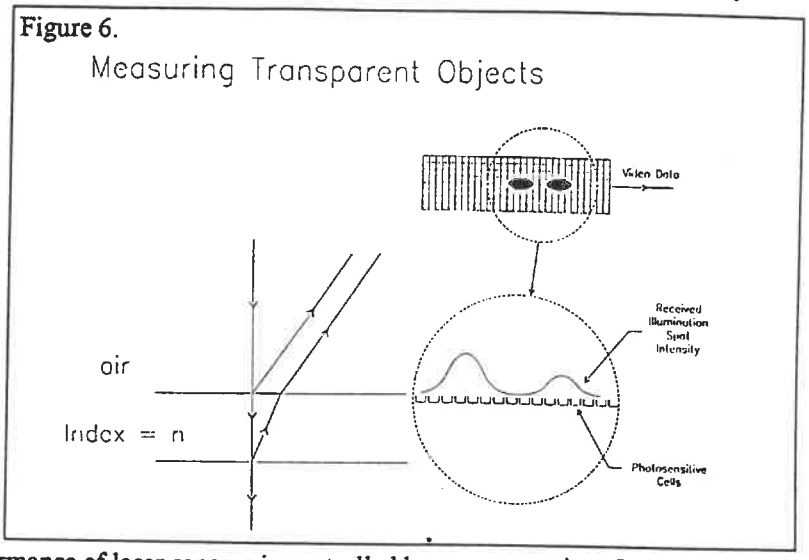

Pixelized arrays require more processing power, adding expense, but they also help to produce a clearer, more precise picture of the object's surface.

Other Design Considerations

In addition to detector choice, the performance of laser sensors is controlled by a compromise of several design aspects including desired **package size, working range,** stand-off and, in the case of reflective sensors, **included angle**. Figure 7 depicts these critical features.

Figure 7.

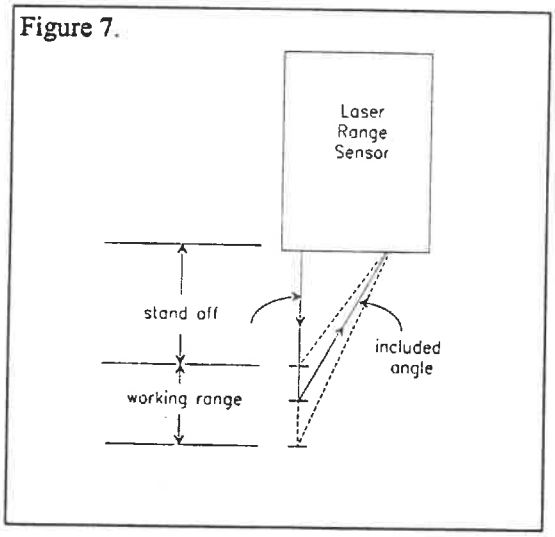

To create the highest precision possible, the laser source must be focused to a very small spot or stripe. A design using a minimum *stand-off*, or working distance from the object, would enable smaller focusing optics to do the job. Thus, the sensor could be contained in a small *package size*. In contrast, a short stand-off may create a problem if the object is highly contoured; taller object features or part fixturing may block the laser signal, or subject the sensor to possible damage should it come in physical contact with the surface.

For reflective sensors, the greater the *included angle* (the angle between the source path and the receive path), the higher the sensor sensitivity or resolution. However, increasing the standoff of a design with a large included angle would proportionally increase the distance between the laser source and receiving apertures, requiring a larger package size.

The sensor depth of field or *working range* also has impact on sensitivity. All detectors have a finite range to resolution ratio. For example, a 1K pixelized linear array used in a sensor with a working range of 1 inch would yield a resolution of 0.001inch. That same detector employed in a sensor with 0.1 inch range would produce a resolution of 0.0001 inch.

These inter-related design constraints must be considered when selecting a sensor for a given application.

Applications: Why would you use a laser?

Laser sensors are not for every measurement application. When considering the universe of sensors, they are expensive and somewhat complex. If presence/absence or simple positioning is all that is required,

laser sensors would not be the most economical choice. The following is a list of questions to review when considering the application of a laser sensor:

- Does the sensor need to be a non-contact measurement device?
- How close can the sensor be mounted to the surface?
- Does the measurement require a small target area (small footprint)?
- How much time is allowed to take the measurement?
- How will the sensor information be processed?
- What will be the operating environment?
- Is there any size and weight restrictions?
- What improvements will this method provide over the present method?

Figure 8 is a matrix the main types of laser sensors and some of their applications.

Figure 8.

SENSOR TYPE	USED FOR:	APPLICATION EXAMPLES
Point Transmissive	Presence/ absence Diameter Measurement TIR/runout; Gap measurement; Edge detection	Diameter of drill bits & Cutting tools; Coplanarity & position of leads on SMT components; Web edge detection
Line Transmissive	Presence/absence; Diameter Measurement; Orientation; Caliper	Diameter measurement of wire, shafts; SMT component orientation on pick & place machines; Sheet thickness in web processing
Point Reflective	Height, displacement; Surface contour; TIR/runout	Thickfilm & solder paste profiling; TAB, Flip Chip inspection; Flat panel display inspection Turbine blade inspection; 3D modeling
Line Reflective	Surface contour; Height, Displacement; Angle; Surface texture measurement Feature detection/position	Component orientation of SMT device in Tape; Weld seam profiling; solder paste, thickfilm profiling

In conclusion, applications for laser sensors can be defined as too complex for simple photoelectric sensors and too specialized and price sensitive for generalized vision systems. Careful attention to all the requirements and constraints of a measurement problem will ensure the proper choice of inspection tools.

First Look at an Angle Multiplying Angle Generator

Steven K. Smith
Air Force Measurement Standards Laboratory
AGMC/MLLP
813 Irvingwick Dr. West
Newark AFB, OH 43055

To facilitate precision angle metrology, the Air Force Measurement Standards Laboratory acquired an angle multiplying angle generator, built by Hunter Metrology, model H200. This system uses an array of stationary mirrors arranged around an optical polygon mounted on a precision turntable. It allows generation of azimuth angles with an accuracy on the order of 0.01 to 0.02 seconds, and generation of 45 degree increments to approximately the same degree of accuracy. Tests of the system using high resolution autocollimators, and phase measuring interferometers are discussed in this report.

The H200 consists of an eight sided polygon attached beneath a precision turntable, surrounded by seven stationary mirrors attached to a base plate. In use, the operator aligns an autocollimator such that its line of sight reflects alternately off each face of the polygon and each of the stationary mirrors in succession, to an outside auxiliary mirror, and then back through the system to the autocollimator. Each time the autocollimator beam reflects off of the polygon, an additional factor of the polygon's rotation angle is added to the beam deviation. Rotations of the turntable, and hence, the polygon, cause an indication on the autocollimator that is sixteen times the turntable rotation angle.

The system's accuracy is independent of the angular accuracy of the polygon and the placement of the stationary mirrors, at first order. Since each mirror is "viewed" twice, once from each direction, deviations caused by mirror placement on the "outgoing" trip tend to be canceled by the same deviation of the mirror on the "return" trip of the autocollimator beam.

Below is a rough sketch of the optical path of the H-200 Optical Angle Generator.

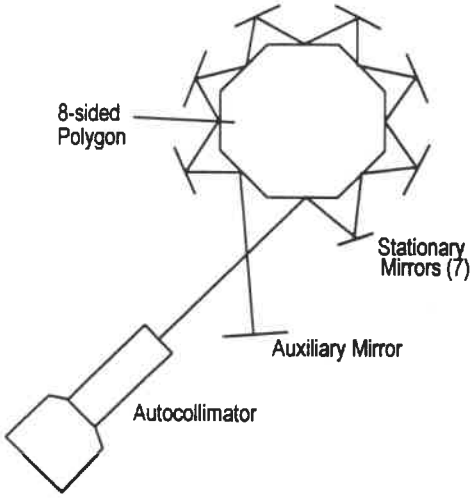

We conducted some tests to establish the accuracy of the multiplication scale factor, and general operation of the system. We placed a mirror on the H200's turntable and aligned it to a Moller Wedel Elcomat HR autocollimator, which has an overall accuracy of about 0.02 seconds. We aligned an Elcomat 2000 autocollimator so that it monitored the angle multiplying optics of the H200. This autocollimator is slightly less accurate than the HR, (about 0.1 seconds) but has a larger range, which would prove to be helpful during these tests.

The test procedure was to record the two autocollimator readings, rotate the H200's turntable (and angle multiplying polygon), and record the two autocollimator readings again. This procedure was repeated until approximately 100 pairs of autocollimator readings were taken. During the course of the test, the air paths of the autocollimators were kept as small as possible and were shielded against stray drafts with a cloth drape. The autocollimators were read by a computer, taking sets of 100 values at a time and averaging them to get the readings used for calculating the scale factor. Each data point on the scale factor plot below contains four autocollimator readings, an initial and final reading for each of the two instruments used in the test. The scale factor is given by:

$S = \frac{R_1 - R_2}{r_1 - r_2}$ Where the R's are the initial and final autocollimator readings of the instrument looking through the optical system, and the r's are the initial and final autocollimator readings of the instrument monitoring the turntable rotation.

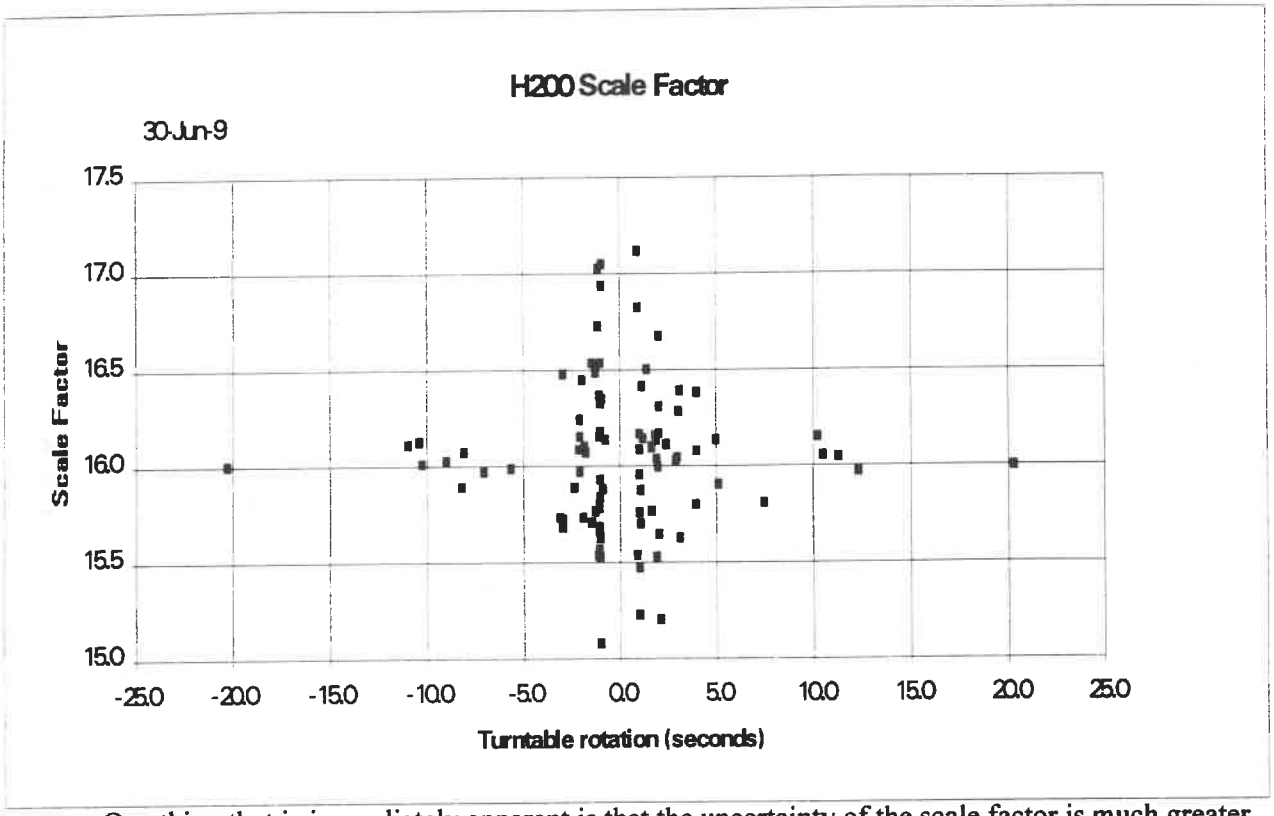

One thing that is immediately apparent is that the uncertainty of the scale factor is much greater for small angles than it is for the larger angles. This is a result of the uncertainty of the autocollimator readings. While the sensitivity of the autocollimators is very high, each one has a certain amount of noise in its output which is dependent on a number of factors, but primarily environmental air currents.

In order to gage the measurement uncertainty caused by autocollimator noise, we set up a test on the two autocollimators used in this experiment. While still in their measurement positions, a series of readings were taken from the autocollimators (actually averages of 100 values sent by the autocollimators) while the system was stationary. Somewhat surprisingly, the Elcomat 2000 had a (slightly) better repeatability and lower noise level than that of the Elcomat HR. The standard deviations of the readings for the Elcomat 2000 and the Elcomat HR were 0.012 and 0.019 seconds, respectively.

Applying the autocollimator uncertainties observed above with the RSS method, the uncertainty of a scale factor determination for a 1 second rotation of the turntable is about 0.5 at one sigma. The scale factor uncertainty decreases as the turntable rotation increases, as discussed above. The data is consistent with a scale factor of exactly 16, which would be predicted from the system's geometric optics.

The design of the H200 is such that it allows accurate measurement of rotations of 45 degree increments of the turntable as well. Rotations of complete segments of the polygon bring the autocollimator back into alignment in exactly 45 degree steps, regardless of the deviations that may exist in the polygon or stationary mirror's position (at first order). This is because the autocollimator beam reflects off every polygon face and mirror in the system regardless of the relative position of the polygon to the stationary mirrors. Thus the autocollimator reading will reflect the sum of the polygon deviations regardless of which 45 degree increment it is aligned to.

To test this assertion, we performed an experiment which amounted to an eight point index position measurement of the H200's turntable. A solid glass polygon with 45° increments was attached to the top of the turntable and the Elcomat HR was aligned to one of its faces. We took a reading, advanced the H200 turntable to the next 45° position, and took another reading on the next polygon face. The turntable position was adjusted such that the Elcomat 2000's reading was within 0.05 seconds of the previous setting. This corresponds (theoretically) to a setting uncertainty of ±0.003 seconds of arc at the turntable. We then rotated the H200's turntable back to it's original position and repeated the process. We took a total of six readings, resulting in five differences between the two positions. Next we loosened the polygon and rotated its original face to align with the next segment of the H200, and repeated the process. In this way we compared each segment of the H200 to a single segment of the polygon. The data taken are summarized below.

H200 segment	Std Dev	Measured Difference	Segment deviation
1 to 2	0.064	0.422	0.006
2 to 3	0.043	0.344	-0.073
3 to 4	0.034	0.356	-0.060
4 to 5	0.028	0.392	-0.025
5 to 6	0.037	0.562	0.145
6 to 7	0.055	0.365	-0.052
7 to 8	0.028	0.499	0.082
8 to 1	0.019	0.394	-0.023
		0.416643 <- AVG	

Each "Measured Difference" in the third column of the table represents the sum of the deviation in that H200 segment and the deviation of the "external" polygon segment. The average of these differences is recorded in the third column of the table. The standard deviation of the five differences is shown in column two. Because of circle closure, the sum of all the segment deviations of the H200 has to add up to zero, and the only remaining deviation is from the deviation in the external polygon. Thus the average of the third column is the actual deviation of the 0 to 45 degree segment of the polygon. If this value is subtracted from each value in the "Measured Difference" column, the result is the deviation in that segment of the H200.

In every case but one, the result is less than three times the standard deviation of the "Measured Difference." The deviation determined for the 5 to 6 segment is about 4 times the standard deviation for that segment, and the 7 to 8 segment deviation is almost 3 times the segment's standard deviation. In no other case is the segment deviation as much as two standard deviations of the difference, and in three of the segments it is less than the standard deviation.

It is worth noting that during the course of these tests, while rotating the turntable back to attain alignment on the angle multiplied autocollimator, differences of less than 0.05 seconds could clearly be seen as the alignment point was approached. This corresponds to rotations of the turntable of about 0.003 seconds of arc, which is less than the measurement resolution of the "high resolution" autocollimator monitoring the turntable rotation.

As a check of the measurement, we measured the polygon with the standard "full closure" method using two automated serrated tooth indexing tables. The measurement was done twice, in the first case the measured deviation of the 0 to 45 degree segment was 0.42 seconds, and in the second, the deviation was 0.46 seconds, which agrees well with the value determined in the test with the H200.

One would expect, from geometric optics, that a rotation of the H200 turntable such that the reading of the angle multiplied autocollimator was repeated before and after the rotation, would result in a rotation of exactly 45°. This is because the autocollimator's path includes every mirror face of the internal eight sided polygon in both cases. Since the sum of the deviations of the eight mirror positions has to be zero because of circle closure, rotations in increments of 45° should be exact. Because of the close agreement of the measured deviation of the 45° segment of the polygon by the two methods, it would seem unlikely that the measurement of the segment deviations of the H200 is seriously in error. It is, however, on the "ragged edge" of measurable. The deviation from an exact 45° is probably due to surface figure errors in the internal mirrors of the system.

We used a Zygo Mark IVxp phase measuring interferometer to measure the surface figure errors of the system. By rotating the internal polygon in front of the aperture window the surface contour of each polygon face could be determined, however the stationary mirrors could not be measured separately. We were able to measure the composite wavefront distortion of the complete optical path, however. The individual mirrors of the internal polygon were quite good, with peak to valley deviations ranging from a high of 0.079 λ to a low of 0.028 λ. Each of these mirrors are concave. The composite wavefront distortion for the entire optical path was about 0.35 λ. While this is not bad, considering that it is a sum of 31 surfaces, it is larger that what is normally desirable for a precision measurement with a high accuracy autocollimator.

An analysis of a similar instrument by Debler at PTB[1] states that the angle uncertainty resulting from the flatness deviation of the mirrors in the system can be estimated by $s_R = \frac{s_r}{R}\sqrt{2}$, where s_R is the uncertainty in the angle output, s_r is the deviation of the beam location on the mirror caused by rotation of the system's polygon, and R is the radius of curvature of the mirrors. For the system under test, $s_r < 0.0002\text{m}$ for rotations of 20 seconds of arc, which correspond to $s_R \approx .003$ seconds, which is much smaller than the value we measured.

There are several assumptions in Debler's analysis that may not be applicable in this case. First, he assumes that the deviation caused by the curvature in any one mirror is randomly distributed. As already noted above, all the mirrors in the internal polygon are concave. We were unable to directly measure the surface figure of the seven stationary mirrors, however, we can infer that they are probably not all concave, since the composite wavefront of the system's optics would have had a higher deviation from planeness if that were the case. In any case, the assumption that the mirror induced deviations are randomly distributed seems suspect.

Second, his analysis is based on a ray deviation where the ray is infinitesimally thin. For these measurements we were constrained to use beams of macroscopic size, so that the measurements represented averages over large areas of the internal mirror surfaces. The possibility still exists that the deviations measured have a large component of autocollimator and environmental noise, as well.

Observations and Conclusions

The H200 is an effective method for generating small angles with a relatively high accuracy, with relatively modest autocollimators. During the course of this study, I was routinely able to see angle rotations on the angle multiplied autocollimator that correspond to about 0.003 arc seconds on the turntable. (0.05 seconds indication of the multiplied angle) While the current state of the art in small angle measurements in air does not permit testing the unit to this level of accuracy, it does seem that the operation of this unit closely agrees with its theoretically predicted performance.

The ability of the unit to generate accurate 45° angles was also demonstrated. The accuracy of the 45° segments is comparable to, or better than high accuracy serrated tooth index tables. (About 0.15 seconds maximum deviation.) Deviations from the theoretical exact angle are most likely due to figure errors of the mirrors in the angle multiplying optics.

Acknowledgments: I'd Like to acknowledge and thank Dwight Oglesby for his work collecting much of the data reported upon here. Without his help I could not have completed this report on time.

[1] Erhard Debler, Winkelmessungen mit Laser-Interferometern, Mehrfachreflexionen und Dreisrosetten-Meßverfahren, Report Me-8, October, 1975 Physikalisch-Technische Bundesanstalt

A Method for the Spatial Calibration of a Commercial Phase Measuring Interferometer - Practical Implementation

by
Paul Sullivan, Christopher Evans
NIST, Gaithersburg, MD 20899

Abstract

This document describes an approach that has been developed to determine the spatial resolution of an existing commercial interferometer. The method also provides a rapid technique to assess distortion in the optical system. Previously we have studied the theoretical capabilities of the calibration using a computer based model. Here we discuss the practical implementation of the method and, in particular, the implementation for the case of a nominally flat test optic and a reference ball. A series of experiments and results are discussed which detail the practical implementation of the method and the achieved capabilities.

1. Introduction

It is becoming increasingly common to specify the figure of elements of advanced optical systems (e.g. COBE, AXAF, and Soft X-ray Projection Lithography optics) in terms of spatial parameters in addition to the amplitude parameters traditionally used in optical fabrication. Thus, characterization of the XY co-ordinate system is important to eliminate errors in the calculation of power spectra etc. Here we consider XY calibration of a phase measuring interferometer (PMI) using a plane wave i.e. for the case of measuring nominally flat surfaces or parabolae in a double pass test configuration.

In a PMI, the interference pattern is focused on a CCD detector array and data points are sampled at the corresponding locations. In most commercially available systems, a zoom lens forms part of the optical configuration to suitably magnify the test optic to fill the detector. Thus, the spatial sampling conditions are variable and determined by the magnification of the optical system and the size and spatial locations of the elements of the CCD.

In order to determine the spatial resolution i.e. the correspondence of the 2-dimensional pixel index location to sample location on the test component, a number of techniques may be used. In particular if an artifact of known dimension is introduced into the OPD, it is possible to relate the co-ordinate system of the artifact with that of the matrix of pixels on the CCD. Features of the artifact that can readily be "measured" include the edge locations. In a PMI the edges may be located using the following techniques.

1 *Intensity Based* Measurements are made directly from intensity data using some sort of threshold value.
2 *Phase Based* Use can be made of the fact that the specimen (or the artifact) can be made to form part of the interference system i.e. the thresholding of the signal is achieved using the modulation value. Thus, the data points from the modulating part of the system form one part of the binary image whilst the unmodulating signal forms the other. When using an artifact, either it can be made to modulate (i.e. when the artifact is sufficiently reflective and with a non reflective background) or it can be set up with a modulating background.

Due to the simplicity of implementation and the inherent robustness, we have adopted the use of the phase based thresholding. Examples of spatial calibration techniques include the following.

1. A common "traditional" technique, utilized in commercial interferometers, for determining the spatial calibration involves the measurement of the maximum detected extent of the test optic in pixels from the video image. This "pixel diameter" can then be used as a scale with the corresponding "true" size of the optic supplied by the operator.
2. A technique that has previously been used at NIST to estimate spatial resolution of interferometers at various zoom positions uses a gage block. The gage is nominally aligned with the co-ordinate system of the CCD i.e. the perpendicular edges are aligned with the rows and columns of the CCD. The extent of the size of the gage block is, typically, determined by inspection. A variant of this technique, used

elsewhere[1], replaces the gauge block with a reticule.

3. A newly developed technique similar to (2) using a gage block. However, in this case the alignment of the gage edges is at an angle with the co-ordinate system of the CCD.
4. A newly developed technique which utilizes a calibrated sphere.

Although the use of technique (1) is common, there are a number of problems associated with its use including: not all components are sub-aperture, the size of the optic is not necessarily accurately known, the measurement is based on information from two pixels and is, thus, integral pixel-resolution limited, and, depending on the type of test optic, edge effects may make location of the diameter difficult. Although technique (2) can be used more generally (i.e. requiring no knowledge of the dimensions of the test optic) the uncertainty of measurement, assuming perfect alignment, is limited to inaccuracies of up to two pixels. We have demonstrated previously[2], using a computer-based model, how technique (3) & (4) may be used to achieve sub-pixel resolution. Although the theoretical capabilities of the gauge block method (3) are superior to the sphere, the practical implementation of the approach is far more demanding; in particular, (i) the need to independently measure the relative angle of the gauge block with reference to the CCD co-ordinate matrix, and, (ii) alignment problems to achieve perpendicularity between the front face of the block and the wave front. Furthermore, from the model we may conclude that when using a sphere, whose projected image diameter covers 100 pixels or more, we may expect to obtain (theoretically) a measurement accuracy of within ±0.1 pixels.

In this extended abstract we describe the practical implementation of technique (4) and illustrate its use with some recent results.

2. Sphere Measurement

The experiments described here have been carried out using a Wyko 6000 PMI using the 44.45mm auxiliary port. All OPDs were measured at 256x240 pixels corresponding to an image area of approximately 61mm x 47mm. High quality reference and test flats have been used along with a set of 3 calibrated steel reference balls (nominally Ball1=15/32", Ball2=3/4", and Ball3=1"). The diameters of the reference balls have a measured uncertainty of 0.1μm.

For the purposes of these experiments, the balls were mounted on a socket head cap screw set in a translation stage with the center of the ball aligned approximately in the center of the CCD. The gage was attached directly to the stage. The Z-direction is defined as perpendicular to the test surface, whilst the X and Y directions are defined by a plane parallel to the test surface with Y being vertical and X horizontal. Using micrometer screws, the ball or gage may be translated in the X, Y and/or Z-directions.

As stated previously, the introduction of the reference ball (or gage) into the OPD prevents the light from the test optic behind the ball from returning to the detector and, thus, interfering with that from the reference optic. Thus, a shadow of the artifact (and its mounting bracket) is formed in the interference image, Fig.1(a). A computer program has been written which interrogates the OPD map and locates the boundary of the reference artifact, Fig.1(b). The corresponding circle boundary pixels co-ordinates are then generated and a least squares circle fit is performed to compute the circle radius and center in fractional pixel co-ordinates, Fig. 1(c).

2.1. Uncertainty in the measurement

The uncertainty with which the sample spacing on the measured test part can be determined, is dependent on many factors including the following: (a) systematic errors due to distortion in the imaging system including the optical system, CCD pixel alignment and variation in pixel sensitivities, (b) distortion of the wavefront due to diffraction effects, (c) variation in the reference ball geometry, (d) de-focus of the test surface and reference ball, (e) position of the reference ball mapping relative to the CCD, and, (f) random errors due to noise (including arising from electrical and vibration sources) in the system.

To assess the extent of these errors and to isolate particular sources several experiments were performed. We summarize the findings here and complete results will be published elsewhere.

1 **Fixed ball position - spread of measurements.** Ball2 was measured at a nominal fixed position in X and Y and, thus, the error in the measurements is random in nature. The SD is approximately 0.2% of the mean (mean=0.2374mm; SD=0.0004mm).

2 **Variation in ball diameter.** The table below shows the results of 10 measurements of pixel spacing (in mm) for the three reference balls. It can be seen that the range of the difference in the mean values of the ball radius varies by only ±0.15% of the mean value. The range of the difference between the individual readings is ±0.50%. The uncertainty of all the measurements is approximately 0.23% as indicated by the standard deviation as a percentage of the mean.

	Ball1	Ball2	Ball3
Mean pixel spacing (mm)	0.2373	0.2366	0.2365
SD ($x10^{-3}$)	0.5614	0.3439	0.5030
Approximate pixel diameter	50	80	107

Measurement statistics for various ball sizes

3 **Variations in tilt.** Clearly, different test parts introduce variations in fringe density (as does variations in alignment). The results indicate that the computed pixel spacing is independent of the fringe density.

4 **Sub pixel X-translation.** For this experiment the position of the Ball2 was translated (starting at the center) in the X-direction in fractions of a pixel up to approximately 1.5 pixel spacings (i.e. 0.35mm). At each location 10 measurements the radius of the ball were computed, and the corresponding pixel spacing computed. The uncertainty in the measurement data, as indicated by the standard deviation, is less than 0.2% of the mean i.e. of the order of the noise level in our system. This implies that the computed pixel spacing is independent of the mapping onto the CCD within a pixel spacing.

5 **Focus**. As we move away from focus (either way) the nominal value of the pixel spacing decreases significantly. Whilst it should be noted that the de-focus positions measured were extreme cases, it is clear that focusing the test part is critical for this and other obvious reasons.

6 **Z-translation**. The 'focus' experiment illustrated the relationship between the focus of the test part and the measured sample spacing. As the center of the calibration ball and the test optic cannot be co-incident it is important that they positioned as closely as possible to minimize the de-focus of the calibration ball. In order to determine the sensitivity of the relative de-focus of the calibration ball to the test surface, the following experiment was performed. Firstly, the test surface is focused and the calibration ball is positioned as close to the surface as possible. The ball is then translated away from the test surface in the Z direction, by increments of 2.5mm for a total of 25mm. At each position 10 measurements of the pixel spacing are made. The results of this experiment indicate that there is no change in the measured pixel spacing for the de-focus of the ball by 25mm.

3. Discussion

An accurate assessment of the spatial resolution is essential in order to (i) determine the existing measurement bandwidth capabilities and (ii) enable accurate assessment of spatial properties of the test surface. We have demonstrated the feasibility of sub-pixel spatial calibration for a commercial PMI. Both the use of the gage block and the ball (summarized here) enable sub-pixel spatial calibration to be achieved. The ball provides a simple straightforward solution to the problem of sub-pixel calibration. Minimal alignment is necessary and redundancies are inherently avoided. Automated software provides readout of computed sample spacing within seconds. It has been demonstrated how uncertainties, indicated by standard deviations, of 0.2% of the mean are achieved under a variety of measurement conditions e.g. slight de-focus, varying fringe densities, various ball diameters, and sub-pixel X-translation.

Due to the small uncertainty inherent in measurements made using the ball approach, the system may be used to investigate distortion in the imaging system. This approach could be developed to use a plate with

holes in it, for example, to enable rapid examination of distortion of the full aperture in a single pass.

References

1. Selberg L., personal communication, 1993.
2. Sullivan, P.J., Evans, C.J., *"A Method for the Spatial Calibration of a Commercial Phase Measuring Interferometer - Theoretical Aspects"*, Proc 6th International Conference on "Metrology and Properties of Engineering Surfaces", University of Birmingham U.K., April 1994.

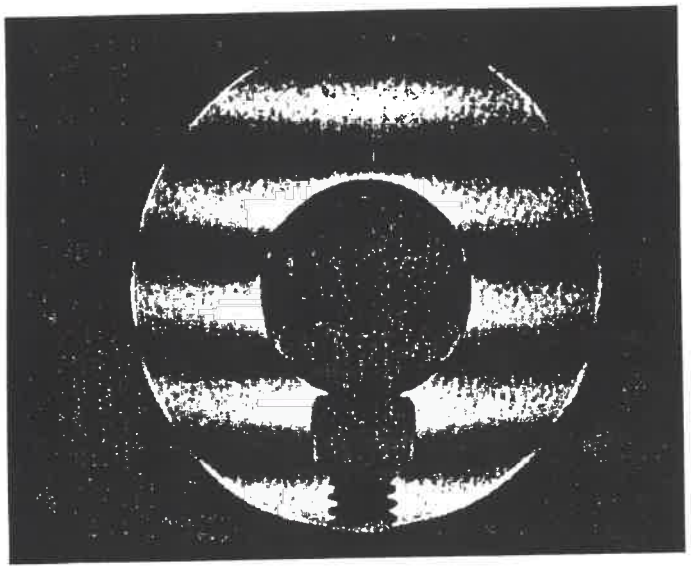

(a)

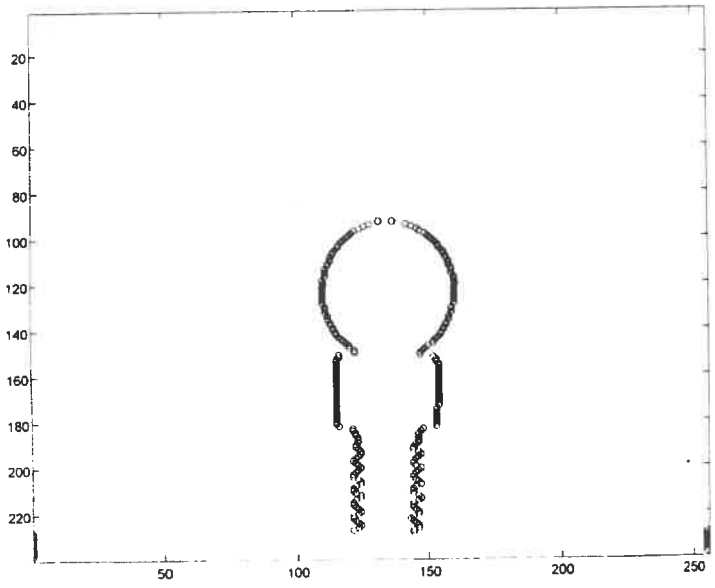

(b)

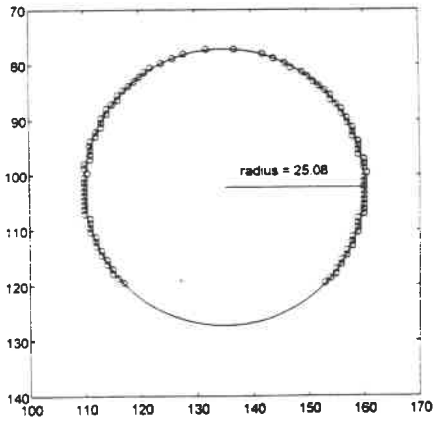

(c)

Fig.1. Illustration of the automated sample spacing computation (a) shadow of artifact masking test surface, (b) tessellation of edge pixels including test stand, and, (c) circular tessellation of edge pixels showing computed circle and radius.

THE AUTOMATION OF MEASUREMENT FOR LENGTH SCALES

W.L. Yang, S.H. Lu, R.H. Hsu, C.J. Chen, H.C. Huang
Dimensional Measurement Laboratory
Center for Measurement Standards, Industrial Technology Research Institute
Hsinchu, Taiwan (R.O.C.)

1. Introduction

A measuring system for calibration of line scales has been developed in the National Measurement Laboratory (NML), Taiwan (R.O.C.). The system is used to calibrate rectangular brass or glass standard scales, which are used frequently in industry. The requirement for calibration of standard scales may range from a few micrometers to a meter. In the calibration, the center of graduations in a test scale must be determined, which is related to the quality of the test scale. Although an electric-photo microscope can be used to decide accurately the center of scale lines, it normally requires the high quality of graduation lines. However, the requirement for the high quality of graduations may not be suitable to the calibration of industry-used rectangular scales.

Due to the consideration above, a photo-microscope with CCD image detection is developed in the determination of line center for industry standard scales. The center-identification device of photo-microscope is the core of an NML-made automation system in calibration of industry scales. The calibration system consists of a motion driver with a servo-control loop, as well as a laser interferometer with environmental correction including air wavelength.

In the paper, the design of a home-made calibration system for length scale is introduced, including the mechanical structure and optical layout. The automatic control diagram is illustrated. In addition, the flow chart of the measurement process and its evaluation of uncertainty is outlined.

2. Design of the system

The calibration system for length scales comprises a line-center identification device and a length measuring system. The graduation identification device includes a motion-control structure and a CCD-based photo-microscope. The motion-control structure contains a main carriage for coarse moving of a test scale and a subcarriage for fine adjustment of the scale. The main carriage is driven by a precision lead screw, and the subcarriage is moved by a PZT. The overall distance of movement of a test scale is measured by a laser interferometer. The detailed specification of the standard scale calibration system is shown in Table 1.

Table 1 Specification of an NML-made calibration system for length scales

Environment temperature	20 ± 0.01 ℃
Environment relative humidity	45 ± 5%
Maxima measurement length	1000 mm
Measurement style	step by step
Resolution of laser interferometer	0.01 μ m
Photo microscope magnification	300×
System uncertainty	0.7 μ m

Fig. 1 is the overall structure of the scale calibration system. The upper part of the structure is the bridge, which is used to support a CCD-based microscope. The lower part of the structure contains a steel bed, based on an air isolator, which can protect the calibration system from the vibration over 1 Hz.

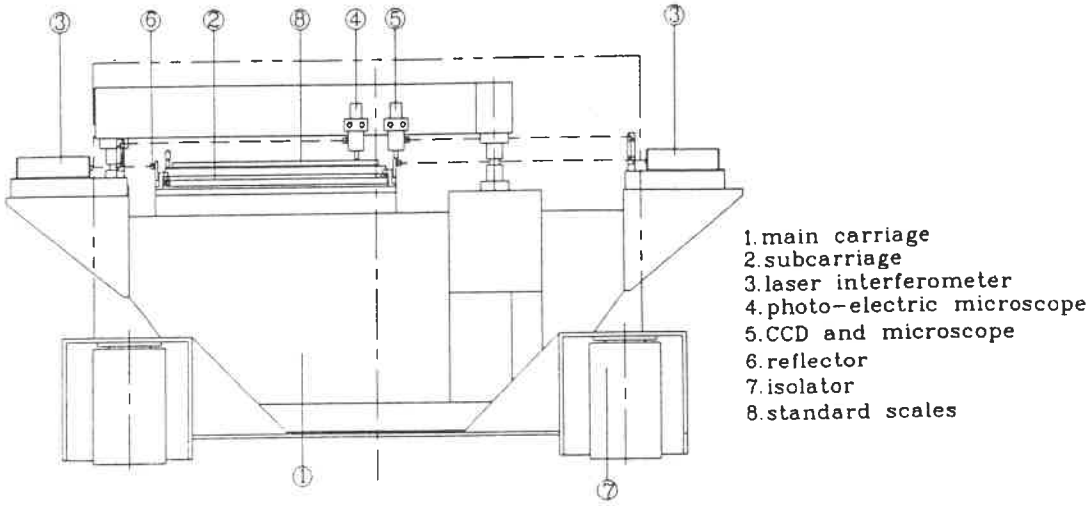

Fig. 1 Overall structure of the scale calibration system

2.1 Mechanical design

(1) Main carriage

In the NML system, line graduations of a test scale are calibrated step by step. This tends to require a main carriage with high positioning accuracy and precision moving straightness. The requirements for the main carriage are as follows: range of moving distance larger than 30 μ m; positioning error less than 2.3 μ m; straightness error less than 1.9 μm; pitch and yaw error less than 0.75 sec.

(2) Subcarriage

The subcarriage of the NML scale system has three functions. The first is to support the test scale standard by Bessel points. The second is to align the scale standard with the optic beam from an interferometer. The last function is for fine positioning control of the test scale. The mechanical structure of the subcarriage is shown in Fig. 2. The subcarriage consists of three parts. The lowest part of the subcarriage is fixed to the main carriage. The middle part is used for micromotion and is fixed to the lowest part with four pieces of spring plates. A PZT and a retroreflector are fixed to the middle part. The upper part, supporting by three steel balls, is used to hold test scale standards and to achieve the function of alignment.

(3) Anti-vibration system

As shown in Fig. 1, the anti-vibration device of the scale calibration system contains 4 air-spring isolators. These isolators can prevent the calibration system from the horizontal frequency of vibration higher than 1.4 Hz and the vertical frequency of vibration over 1.0 Hz.

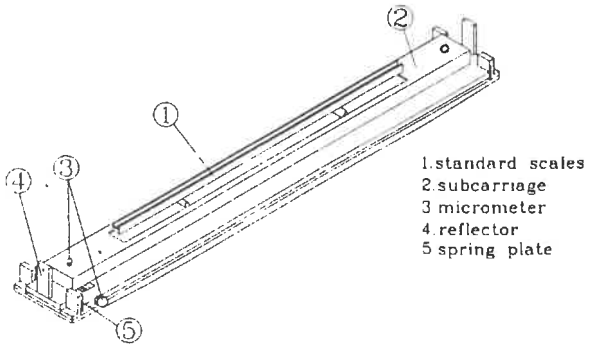

Fig. 2 Mechanical structure of the subcarriage

2.2 Optical design and signal processing

(1) CCD-based photo-microscope

A CCD-based photo-microscope is used in determination of the center of scale graduations. For reducing the thermal effect, an optic fiber is used to direct the white light to the microscope.

(2) Signal processing

As shown in Fig. 3, the measuring system for length scales is controlled by a personal computer and a software program, which is written by the Turbo C++ language. Schematic diagram of control and the flow of signal is shown in Fig. 3. The photo image of a test graduation is converted to an electric signal in digits by the image process card of a CCD camera. The digital data of the graduation image is stored on the RAM of the PC.

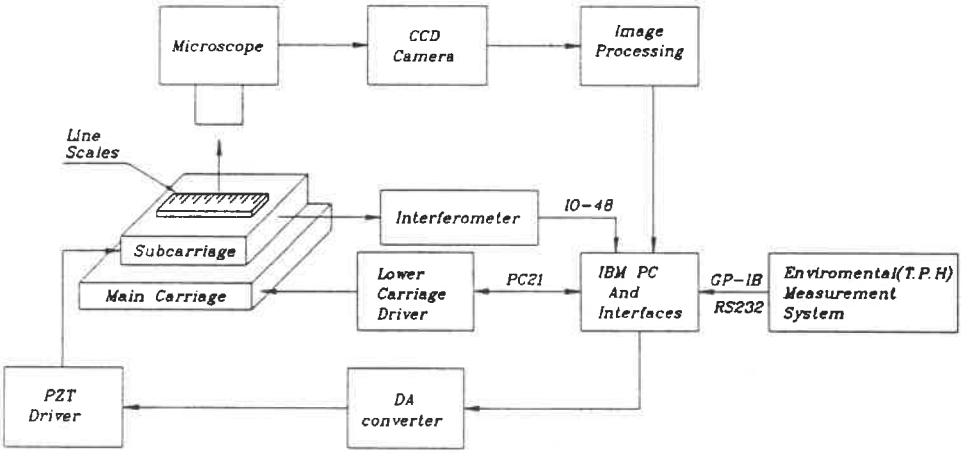

Fig. 3 Schematic diagram of automation control of the system

3. Measurement procedure

Fig. 4 is the outline of the calibration process for length scales. In calibration of line graduations, the main carriage is moved so that the test graduation is shown in the near center of the view field of a CCD-based microscope. Then the fine adjustment of the subcarriage is made to ensure the alignment of

the center of the test graduation with that of the view field of the microscope. The fine adjustment is achieved by the PZT-driven control of the subcarriage. The distance between two scale lines is measured by an iodine-stablised He-Ne laser interferometer. For labour saving and error reduction, the whole measurement process is fully automated.

4. Uncertainty evaluation of the calibration system

The random standard deviation in determination of line center is 0.15 μ m. The measurement uncertainty of the calibration system can be expressed by $U_T = 0.53+0.19L$ (μ m). The evaluation of measurement uncertainty of the system is based on the ISO guide (1992) to the expression of uncertainty in measurement.

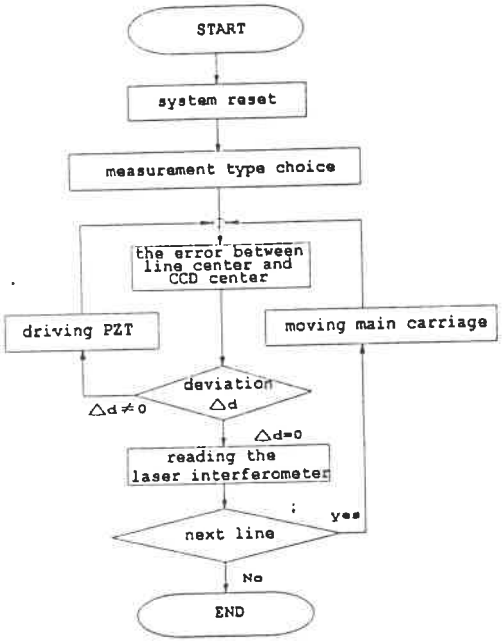

Fig. 4 Flow chart of the calibration process

5. Conclusion

A new measuring system for calibration of industry-used length scales has been developed successfully by the National Measurement Laboratory (Taiwan, R.O.C.). The calibration system employs a graduation identification device in determination of the center of test graduations, which can enhance considerably the accuracy of calibration. The graduation positioning device consists of a servo motion control mechanism and a CCD-based photo-microscope. In consideration of convenience of operation and price of instruments, a CCD photo-microscope may provide a better result in graduation identification (with the aid of digital image technique) than an electric-photo microscope in calibration of industry length scales.

6. References

1. J.S. Beer, "Length Scale Measurement Procedure at the National Bureau of Standards ",NBSIR 87-3625, 1987.
2. ISO/IEC/OIML/BIPM,"Guide to the Expression of Uncertainty in Measurement",ISO, 1992.

EVALUATION OF TOPOGRAPHY OF PRECISION ENGINEERING PART SURFACES WITH THE EMPLOYING OF REPRESENTATIVE METHEMATICAL METHODS

J. Mandak

Foreign Students Institute,MTA - CR
Brno,CR

ABSTRACT: The paper elaborates the representative mathematical methods for quantification of changes in 2D and 3D /two-dimensional and three-dimensional/ roughness characteristics, corresponding to changes in the dynamics of tangential pair in the course of its loading.

KEYWORDS: 2D and 3D roughness characteristics, changes in the characteristics of dynamics of tangential pair, statistic analysis, factor analysis.

INTRODUCTION

Ever growing demands on quality of final machine equipments result in more specified criteria concerning their dimensional, formal and functional accuracy. In order to maximize the output of mentioned equipments it is necessary to know exactly their momentary operationally technical condition /Mandak, 1985/.

It is solved the problem of theoretical and practical evaluation of changes of 2D and 3D roughness characteristics which determine instantaneous topography of contact precision engineering part surfaces, in connection with the changes in dynamics of the pair, in the course of its loading /Mandak et al, 1987/. This problem, here only evaluation of changes of 2D roughness characteristics, is being solved in the paper, with the use of verified experimental and computational techniques /statistic and factor analysis/.

2D ROUGHNESS QUANTIFICATION OF PAIR SURFACES

Number of characteristics /CSN 01 4450, ISO/DIS 4287/1, or others/ are used for quantification of pair surfaces, none of which yields a truthful description of uneven surface /Nakamura, 1959/.

An experimental workplace has been established for quantitative evaluation of microgeometry of three differently worked pair surfaces, before and after fivefold dynamical loading /Mandak et al, 1987/. Profile curves have been scanned by means of a profile indicator, perpendicularly to the movement of the pair. The actual profile in an enlarged scale, together with the set of 2D roughness characteristics /arithmetical mean deviation R_a, arithmetical profile peak height $R_{Z\ DIN}$ - DIN 4768, maximum height of the profile R_m, smoothed height of projections of the

filtered profile R_{pm}, height of the profile from ten points $R_{Z\ ISO}$, average depth of roughness R_{3Z}, maximum depth of roughness R_{3ZM} - Daimler Benz N31 007, root-mean square deviation of the profile R, profile depth p_t, wave depth w_t, maximum double amplitude of uneveness deviation from central arithmetic line, curve of profile bearing length ratio /were first recorded on a memory medium of the experimental device, equiped by 16bit microprocessor. Afterwards they were always evaluated as averaged values x_i out of five successive measurements, together with determination of: - mean square deviation S_i for i-fold 2D roughness characteristics.

STATISTIC ANALYSIS OF DYNAMICAL CHARACTERISTICS

For the analysis of the size of random component of studied extreme values of chosen dynamical characteristics of the pair, i.e. maximum travelled path x_{max}, sliding velocity v_{max}, and resistive force F_{max}, the sets of dynamical characteristics of five successive loadings were statistically processed /validity of normal Gauss law being taken into account/, with the use of following statistical characteristics: selective dissipation S_x^2, selective conclusive deviation S_x, probable selective deviation U_x, selective correlation coefficient r_{ij} /Mandak et al, 1987/.

FACTOR ANALYSIS OF ROUGHNESS AND OTHERS CHARACTERISTICS

For the analysis of mutual relationships between 2D roughness characteristics, pair dynamics or pair vicinity, the factor analysis has been used /Mandak, 1985/. 2D roughness characteristics were used as observed variables; gradually chosen dynamical characteristics $x_{max\ i}$, $v_{max\ i}$, $F_{max\ i}$ and temperature of vicinity T_i, out of which the factors necessary for reproducibility of observed variables were extracted by calculation.

RESULTS

The analysis can be briefly summarized into following results:

- by comparing the results of 2D quantitative evaluation of reliefs of pair surfaces before and after loading it can be deduced that considerable changes in the topography of containing surfaces occur, in the course of pair loading. Among others it confirms a remarkable impact of particular mechanisms of wear which occur in the course of pair loading.

- from the performed factor analysis it followed that the studied variables can be reproduced by two factors. In the framework of the first one, 2D roughness characteristics are represented, except for NR, and partially also w_t and vicinity temperature. In the framework of the second factor, dynamical characteristics are always evaluated gradually, together with 2D roughness

characteristics NR and conceivably w_t and vicinity temperature.

From the above it is obvious that in further experimental studies it is not useful to observe and evaluate 2D roughness characteristics in their complexity /these are mutually e.g. with the use of regression number, mathematically expressible/. Attention will have to be paid to the characteristics NR, conceivably w_t, that explain substantially the studied dynamical characteristics of the pair.

The obtained results, which are original, present a contribution to further development of the representative mathematical methods towards the evaluation of changes in 2D roughness characteristics in connection with the changes in pair dynamics, in the course of its loading. In following step of the solving it will be necessary to realize also these at the paper presented methods to the problem of theoretical and practical evaluation of changes of 3D roughness characteristics /normalised surface height - h, surface bearing area ratio - s_{tp}/h/, material volume ratio - s_{mr}/h/, void volume ratio - s_{vr}/h/, normalised 2-D autocorrelation function - AACF, 2D power spectral density - APSD/ and parameters /root - mean - square deviation of the surface - S_q, ten point height of the surface S_z, skewness of the surface height distribution - S_{sk}, kurtosis of the surface height distribution - S_{ku}, density of summits of the surface - S_{ds}, the fastest decay autocorrelation length - S_{al}, texture aspect ratio - S_{tr}, texture direction of the surface S_{td}, root - mean - square slope of the surface $S_{\Delta q}$, arithmetic mean summit curvature of the surface - S_{sc}, developed interfacial area ratio - S_{dr}, surface bearing index - S_{bi}, core fluid retention index - S_{ci}, valley fluid retention index - S_{vi}/, /Stout et al, 1993/ in connection with the changes in dynamics of the pair, in the sourse of its loading.

BIBLIOGRAPHY: /1/ Wilcock, D. F. et al: Bearing design and application, New York, McGraw-Hill, 1957. /2/ Mandak, J. et al: The influence of roughness of functional leading surface on the dynamics of friction tangential pair, Proc. of 3rd Int. Symp. INTERTRIBO '87, High Tatras, Czech Republic and Slovak Republic, 1987. /3/ Mandak, J.: Use of factor analysis for explaining some principles of object 2A28 dynamics, Part. Report of the ST VVTS Lipt. Mikulas, Slovak Republic, 1985. /4/ Nakamura, T.: Analysis of the surface roughness curves, J. Soc. Proc. Eng., Japan, n. 3-25, 1959. /5/ Ralston, A. et al: Mathematical methods for digital computers, Publ. John Willey and sons, New York, 1962. /6/ Mandak, J.: Evaluation of topography of precision engineering part surfaces, 1991 Annual Meeting ASPE, Santa Fe, New Mexico, U.S.A., 1991. /7/ Mandak, J.: The analysis of mechanical systems with nonlinear hydraulic damper, Proc. Dynamics, Strengh and Elasticity of Mechanical Structures, Institute of Thermomechanics - Czechoslovak Academy of Science, Svratka CSFR, 1992. /8/ Mandak, J.: The analysis of mechanical systems with nonlinear hydraulic damper, ASME Winter Annual Meeting 1993, New Orleans, La, U.S.A.,

1993. /9/ Mandak, J.: Evaluacion de la topografia de las superficies maquinadas, Tribologia, Numero 16, Agosto, 1993, Argentina. /10/ Mandak, J.: Characteristics identification of a mechanical dynamic system, Proc. of the 7th Annual Meeting ASPE, Grenelefe, Florida, U.S.A., 1992. /11/ Stout, K. J. et al: A proposal for standardisation of assessment of three-dimensional microtopography, Univ. Birmingham, U.K., 1993. /12/ Mandak, J.: Tribotechnical Diagnostic with the use of factor analysis, Proc. of the Int. Tribology Symp. INSYCONT - SLOVIANTRIB 94, Krakow - Poland, 1994. /13/ Device working on the light principle for surface roughness measurement. Proc. of the 3rd Int. Conf. on Ultra-Precision in Manufacturing Engineering UME3, Aachen - FRG, 1994.

OPTIMIZING METROLOGY AND CONTROL IN A C.I.M. ENVIRONMENT BY PREDICTION AND DESIGN

Manuel MESTRE and Hisham ABOU-KANDIL

Ecole Normale Supérieure de Cachan - L.U.R.P.A.
61 avenue du Président Wilson - 94 230 Cachan - FRANCE

KEY WORDS: Dimensional metrology, Control, Error of form, C.M.M., Prediction, Confidence intervals, Optimization, Design, C.I.M.

In the field of dimensional metrology of manufactured surfaces, the current method consists of measuring a sample of points on the surface. Then an error of form is estimated from the known data, ignoring the missing data of the surface. This estimation is thus necessarily optimistic, underestimating the actual error. Furthermore, the sample is small, due to the measuring time on a mechanical C.M.M.

The purpose of this paper is to apply to industrial metrology classic methods of linear prediction of a random function Z(x,y). Previous results are first recalled [1]. Considering the data as conditioning values, an expectation and a variance are computed at any point (x,y) of the surface. Z is known by its values on a finite set $S=(S_1,...,S_n)$ of points of the surface. We will denote these values by the set $Z(S)=(Z(S_1),...,Z(S_n))$. The conditional expectation $E(Z(X)\mid Z(S))$ represents the most probable position of Z(X) and stands for its estimated position; the conditional variance $V(Z(X)\mid Z(S))$ represents the uncertainty on the position of the real point Z(X) with respect to the previous expectation. Estimating these conditional moments is known as Bayesian Prediction [2,3,4]; their equations in the Gaussian case are:

$$E(Z(X)\mid Z(S)) = C_{Z(X),Z(S)} \cdot C^{-1}_{Z(S),Z(S)} \cdot Z(S) \qquad (1)$$

$$V(Z(X)\mid Z(S)) = C_{Z(X),Z(X)} - C_{Z(X),Z(S)} \cdot C^{-1}_{Z(S),Z(S)} \cdot C_{Z(S),Z(X)} \qquad (2)$$

where $C_{Z(X),Z(X)}$ is σ^2, the non-conditional variance of Z(X); $C_{Z(X),Z(S)}$ and $C_{Z(S),Z(X)}$ are the vectors of the correlations between Z(X) and Z(S); $C_{Z(S),Z(S)}$ is the covariance matrix of Z(S). The covariances between points depend on the auto-correlation function of the surface, estimated from a 2D dataset acquired on a roughness instrument.

Fig. 1 and 2 illustrate equations (1) and (2): at sites located on a square grid, random values of $Z(S_i)$ have been chosen. The conditional expectation is actually an interpolation, and the data belong to the interpolated surface. The surface is known at the measurement sites, which is expressed by a zero conditional variance; this variance increases with the distance to the closest site. [5]

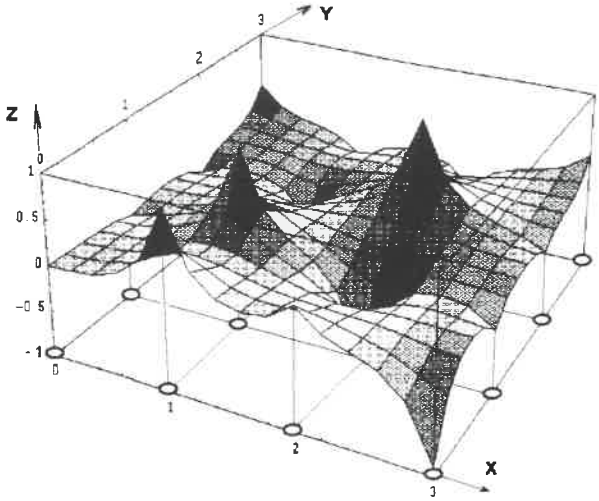

Fig. 1: Conditional expectation

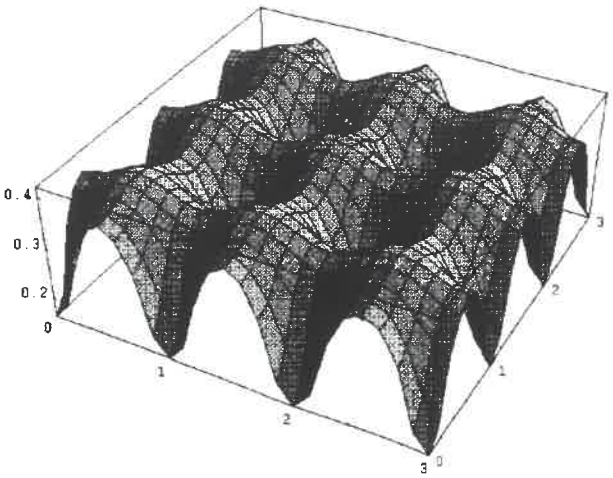

Fig. 2: Conditional variance.

On an industrial surface, the location of the sites (*design* of the experiment) is not straightforward. Various criteria have been defined to maximize information on the form error [2,4,5]; the most suitable criterion for dimensional metrology of industrial surfaces is known as VarMin, which minimizes the largest conditional variance and the estimated error. Fig. 3 is the result of an optimization for 20 sites on a gasket plane, by a gradient algorithm. The same criterion is adaptable for any surface, such as a half sphere (Fig. 4).

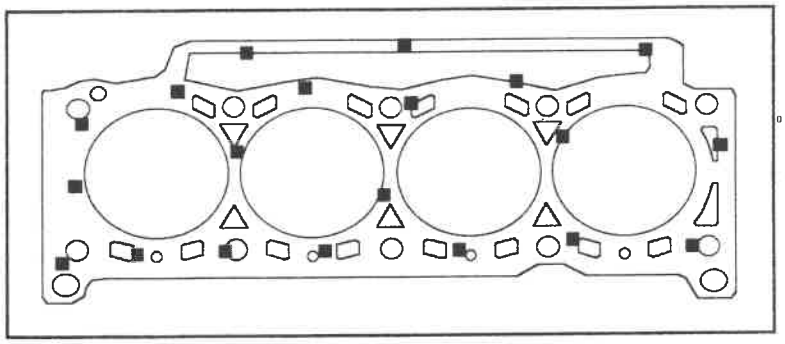

Fig. 3: Optimizing the location of measurement sites

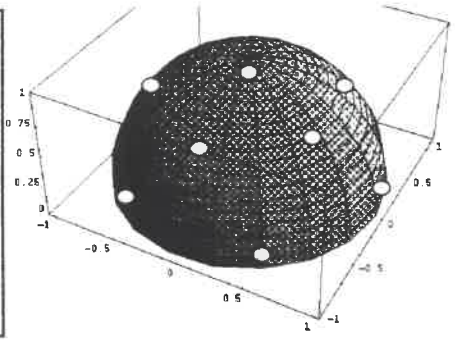

Fig. 4: Optimization on a half sphere

After data acquisition on a C.M.M., a prediction is performed by equations (1) and (2), yielding at each point X=(x,y) confidence intervals. On Fig. 5, the conditional expectation at X is denoted as E(X), the $\pm 3\sqrt{V(X)}$ confidence interval as CI(X), and its bounds as Sup(X) and Inf(X); the actual value Z(X) which is estimated, is unknown to the predictive method; after prediction, this real profile Z(X) is compared to the predictive bounds for validation. In this example, the percentage of values Z(X) out of the predictive bounds is 0.4%, which is close to the theoretical 0.3% that corresponds to the Gaussian probability of 99.7% for $\pm 3\sigma$.

The predictive bounds Sup and Inf are now considered as *the* surface, and two parallel theoretical surfaces, as close as possible, are then adjusted to them. Their distance, FE_3 on Fig.5, is the estimated form error in the sense of ANSI Y14.5M. The form error FE_1 estimated from the data underestimates the actual error FE_2 , which is not acceptable for quality control. On the contrary, the predicted error FE_3 overestimates the actual form error FE_2 and thus can be compared to the tolerance.

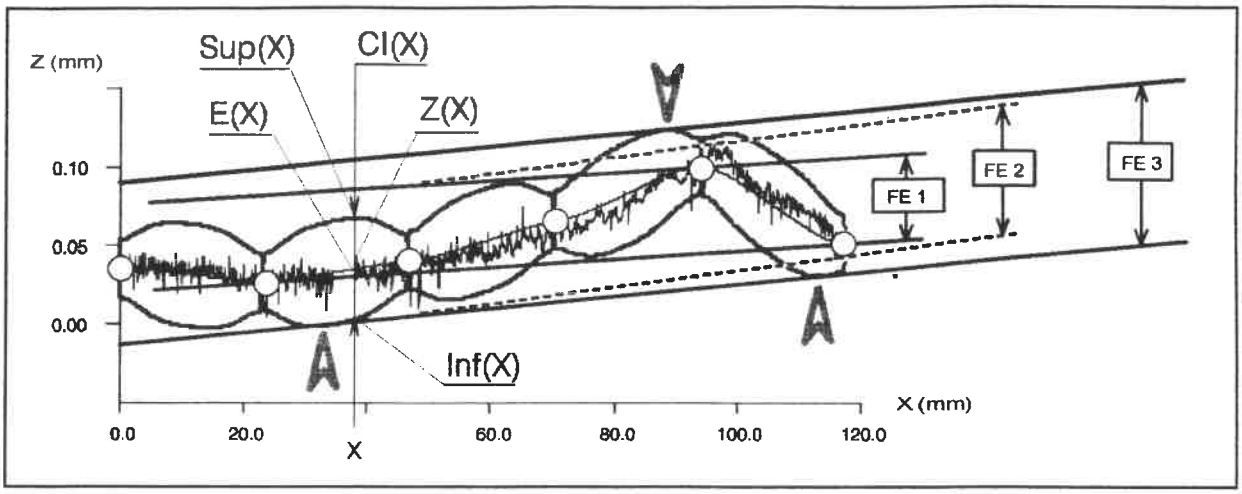

Fig. 5: Prediction of a milled profile

However, this overestimation can be reduced at a minimum cost by an adaptive algorithm based on new data acquisition: at each iteration of the algorithm, predictive bounds are computed from the data and theoretical surfaces are adjusted to them. If their distance is smaller than the tolerance, the algorithm ends. If not, additional data is acquired at sites (plotted as V on Fig. 5) where the theoretical surfaces come close to the predictive bounds. This tends to decrease the conditional variance together with the distance between the adjusted surfaces. In case previous data already exists at such sites, this distance cannot be reduced and the surface is out of tolerance (Fig. 6).

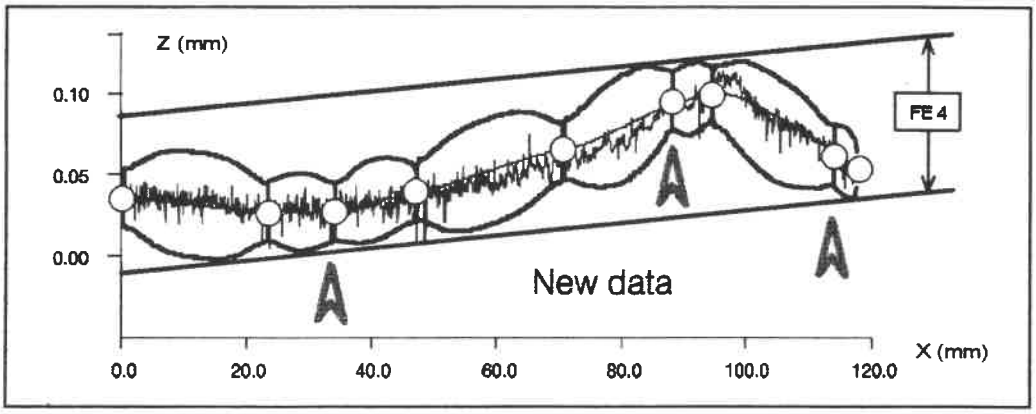

Fig. 6: Reducing the overestimated form error by new data acquisition

This study can be extended in several directions:

- Machined surfaces deviate from the hypothesis of stationarity, demanded by the prediction theorem. This fact can be taken into account by adjusting a low-frequency model to the C.M.M. data and predicting the residual signal considered as random [5]. This method, known as Kriging [5], is used in Geostatistics or Computer Experiments, and can be adapted to engineering surfaces.
- The auto-correlation function may be difficult to estimate in case of non-stationarity. This problem can be solved by predicting the random function of the *increments* of Z, using the structure function (or "variogram") instead of the correlation [1]. The definition of the structure function and discussions of its advantages have been exposed in [6].
- It is possible to take into account the sensor tip radius, measurement errors, as well as the uncertainty on the estimated correlation, to refine the accuracy of the prediction.
- Other applications of linear prediction are possible; for example, an r.m.s. roughness can be computed from the expectation, over all points of the surface. The result is more precise than if computed from the known data. This approach is suitable for optical surfaces for which r.m.s. roughness is significant, whereas interferometers yield few data (sample lag: 10 to 30 mm for a telescope mirror). The variance of the r.m.s. can as well be estimated with prediction, involving higher order moments of the random function Z(X).

As a conclusion, current algorithms can be very sophisticated in the treatment of known data, but blind to unknown data. However, in a C.I.M. environment, a predictive method can be implemented on a C.N.C. coordinate measuring machine with little extra cost. It could decrease dramatically control time, or increase the accuracy of form error estimation.

REFERENCES:

[1] M. Mestre, H. Abou-Kandil, Linear prediction of signals applied to dimensional metrology of industrial surfaces, *Measurement* **11**, 119-134. Elsevier, Amsterdam (1993).

[2] C. Currin, T. Mitchell, M. Morris and D. Ylvisaker. A Bayesian approach to the design and analysis of computer experiment. ORNL-6498, National Technical Information Service, 5285 Port Royal Road, Springfield, VA 22161,USA.

[3] Makhoul. *Linear prediction, a tutorial review*. Proc. IEEE, **63**, 561-580 (April 1975).

[4] D. Ylvisaker. Prediction and design. *Ann. Stat.* **15** 1-19.(1987).

[5] J. Sacks, W. Welch, T. Mitchell and H.P. Wynn, Design and analysis of computer experiment, *Statistical Science* **4-4** (1989) 409-435.

[6] T.R. Thomas, R.S. Sayles et al., *Rough surfaces*, Longman, London (1982).

Some Considerations for a Measurement Strategy for Circular Features

Howard Harary
Precision Engineering Division
National Institute of Standards and Technology
Gaithersburg, MD 20899

and

Celine Buchard, Pascal L'Heritier, J-O Dufraigne and Patrice Chollet
Laboratoire de Mecatronique
Centre d'Etudes Superieures des Techniques Industrielles
Saint Ouen, France 93407

Introduction

The careful study of manufactured parts is a prerequisite for their intelligent inspection. For this study, we conducted a survey of the processes for making holes by manufacturing a set of test parts using ten different machining processes. The holes were measured at high density and high accuracy to produce detailed pictures of the forms of the holes --- characteristic process signatures were found. The full data sets were then sampled with the low numbers of sampling points typical of process control and quality assurance using coordinate measuring machines in industry. The least-squares radii and center position of sampled data sets were compared to those parameters calculated for the full data set. These comparisons will be used to make recommendations to manufacturers for adequate, economical sampling densities to achieve desired inspection tolerances. The present study compliments previous studies because it is based on real measurement data, and not simulations. The processing and use of our data sets as **reference** data sets with well known least-squares radii and center position will also be discussed.

Methods

Part Manufacture

A series of forty 2024 aluminum test parts (152 X 152 X 19 mm) containing 25.4 mm (nominal) thru holes were manufactured by ten different hole-making processes on a Hurco BMC-40 machining center using new high-speed steel tooling. A specially designed fixture was used to kinematically locate the plates and provide even clamping pressure at the plate's corners. We used the tool speeds and feeds recommended by the Machining Data Handbook (Metcut Research Associates, Cincinatti,OH) for maximum production conditions. The ten processes are detailed in Table I.

Part Measurement

The roundness of the holes was measured by a Talyrond 3 (Rank Taylor Hobson, Leicester, England) at 256 equally spaced positions using a 6 mm diameter ruby stylus at a depth of 9.5 mm from the top surface of the plate. Roundness measurements were converted to an absolute measurement of radius (R_i) as a function of angle (θ_i), by assuming a harmonic model for the form of the holes (eq. 1).

$$R_i = A_0 + \sum_{k=1}^{127} A_k . \cos(k.\theta_i + \phi_k), \qquad \theta_i = \frac{2\pi . i}{255}, \qquad i = \{0,1,\ldots,255\}, \qquad \textbf{eq.1}$$

To convert the roundness data sets: (1) we enter the *spatial frequency domain* by taking the discrete Fourier transform; (2) set the zeroth order term A_0 to 12.7 mm, the assumed nominal radius of the hole; (3) set the first order term, A_1, to zero, in order to remove the measurement error due to the mis-centering of the measurement axis with the least squares center of the hole; (4) we then return to the *spatial domain* by taking the inverse discrete Fourier transform. The forms and Fourier transformed data sets for the ten processes are shown in Figures 1 and 2 respectively. It can be mathematically shown that the least-squares radius of the converted data set is A_0. Hence, these data sets can be used a reference data sets to check the least-squares algorithms in coordinate measuring machine (CMM) software. Note that the effect of a mis-centering error of the measurement axis is not completely removed by setting the first order term, A1, equal to zero. However, the remaining effect on higher order terms is less than 0.025 μm and would not be visible in the traces shown in Figure 1.

Sampling Simulation

The converted data sets were sampled at a discrete, small number ($25 \geq n \geq 3$) of locations to simulate a measurement by a CMM. The least-squares radius and center are shown for the hole produced by a counterbore (CB), in Figures 3 and 4 respectively. Note, the abrupt increase in the range of least-squares radius at a sampling density of n=4. At the same sampling density, the error in the center position is a local minimum. These results are unsurprising given the four-fold symmetry visble in the form (fig.1) and the fourth harmonic clearly visible in the Fourier transform of the data set. It is commonly believed that a form must be sampled at greater than *twice* the highest harmonic in its spatial frequency spectrum (the Nyquist criteria) in order to avoid sampling problems when calculating a least-squares radius or center of a form . For the form produced by the counterbore this is clearly not the case -- there is little to be gained by sampling with more than 6 points. Figure 5 the illustrates the comparatively less steep dependence of calculated roundness on the sampling density. In this case we reach a point of diminishing returns at 8 or 9 sampled points, much closer to the 9 points necessary as predicted by the Nyquist criteria.

Conclusion

We have illustrated how a careful study of the form produced by a given manufacturing process can influence the choice of the number of sampled points for the calculation of the least-squares parameters of a hole and its roundness. We have also shown the types of forms that can be produced by a range of other manufacturing processes. Our converted data sets can be used to evaluate the efficacy of other sampling strategies (e.g. stratified) in confidently achieving the required measurement uncertainty to monitor a manufacturing process. These real-world data sets can also be used to verify the accuracy of CMM least-squares algorithms for the circle.

The authors gratefully acknowledge the support of the U.S. Navy ManTech program.

The identification of commercial materials is given only for the sake of clarity. In no instance does such identification imply endorsement by NIST, nor does it imply that the particular material is necessarily the best available for the described purpose.

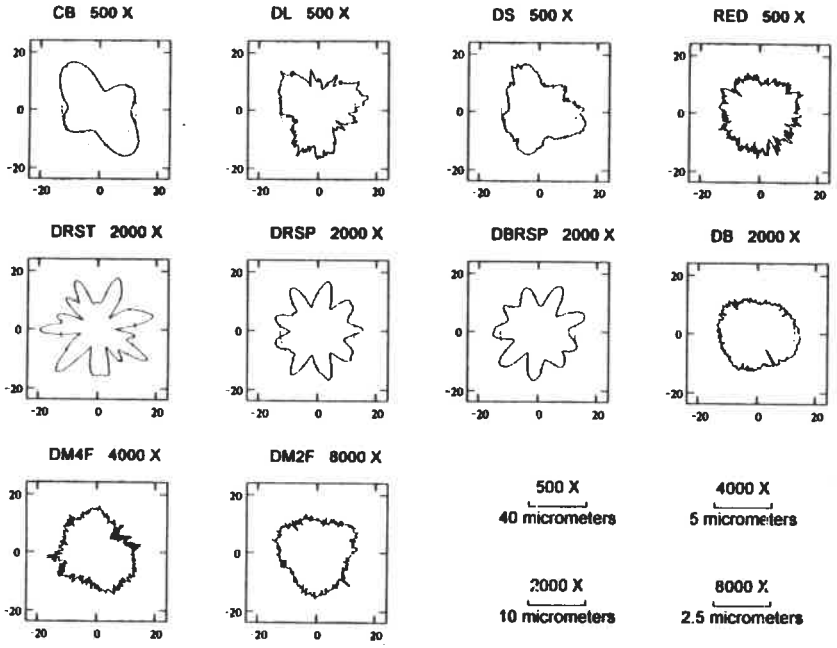

Fig. 1 Amplified forms of the holes made by ten different processes. For the key see Table 1. The forms are amplified with respect to the least-squares circle with various amplification factors.

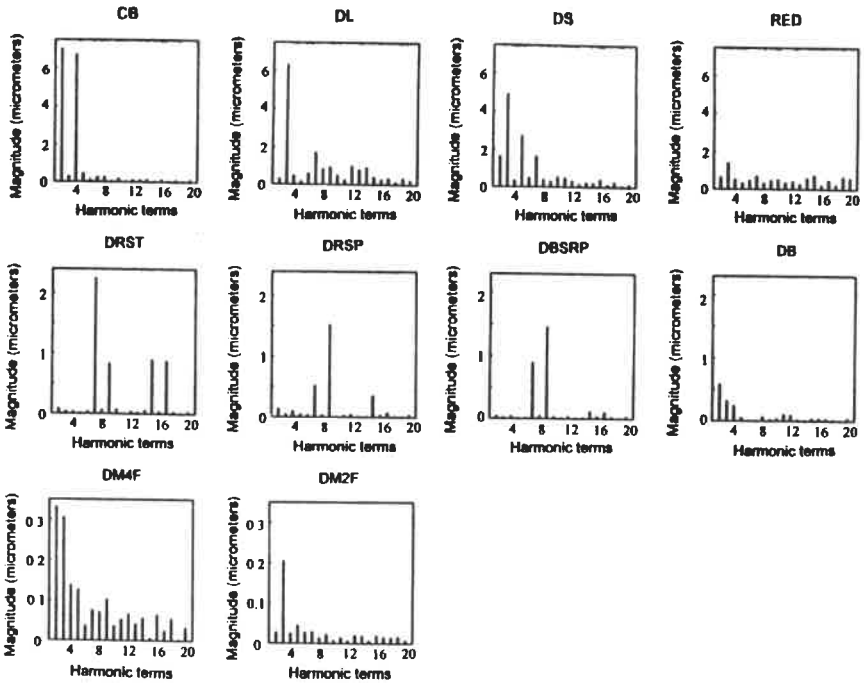

Fig. 2 The magnitude of the Fourier transform (FT) of the forms shown in Fig. 1 as a function of harmonic number (frequency).

Table 1

Process Abbreviation	Process Description	Process Abbreviation	Process Description
CB	Counterbore	DRSP	Drill,Ream(Spiral)
DL	Drill -- Long	DBRSP	Drill,Bore, Ream(Spiral)
DS	Drill -- Short	DB	Drill, Bore
RED	Drill, Re-Drill to Size	DM4F	Drill, Plunge Mill (4 Flutes)
DRST	Drill, Ream(Straight)	DM2F	Drill, Plunge Mill (2 Flutes)

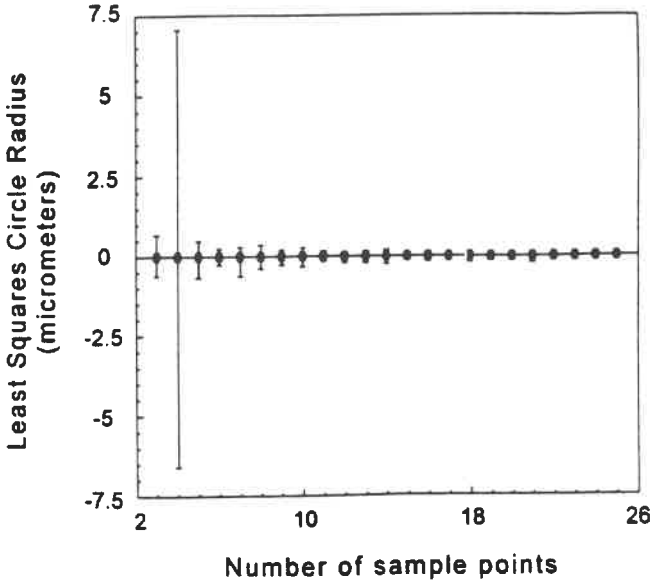

Fig. 3 The least-squares radius of form CB as a function of the number of equally spaced sample points. The mean is shown together with errors bars that show the range for all possible selections of that number of sample points

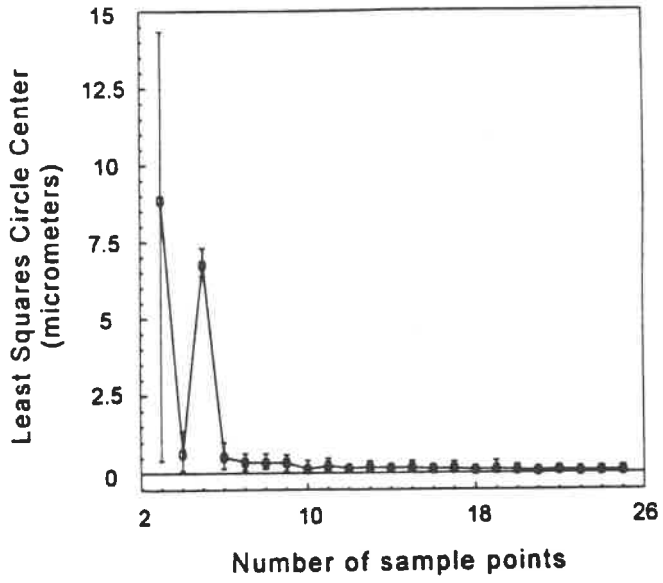

Fig. 4 The least-squares center of the form CB as a function of the number of equally spaced sample points. The mean is shown together with errors bars that show the range for all possible selections of that number of sample points

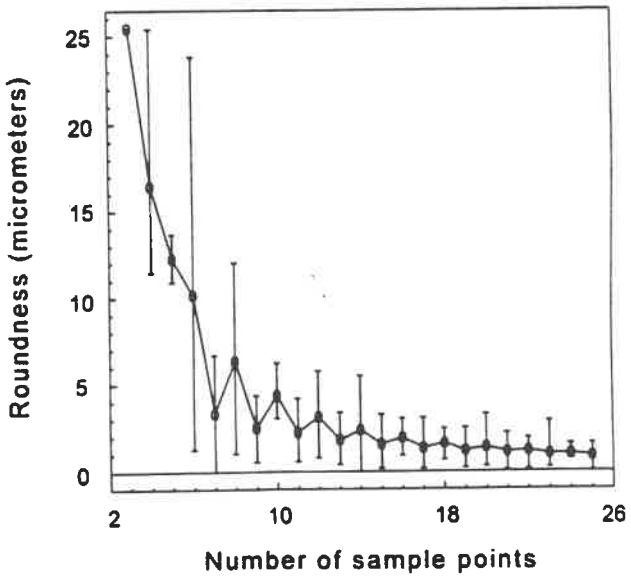

Fig. 5 The roundness error of the form CB as a function of the number of equally spaced sample points. The reference level at zero is the roundness calculated for the entire (256 pts.) data set. The mean is shown together with errors bars that show the range for all possible selections of that number of sample points

Calibration and Real Time Compensation of Errors Introduced by Measurement Probe and Machine Geometry in a Commercial CMM

Heuijae Pahk, Kyoil Lee, Seoul National University, Korea

1.Introduction

Coordinate measuring machines(CMMs) are widely used in manufacturing industry and laboratory. In view of the total measuring accuracy considering a complete chain of measurement link from workpiece to the probe stylus, the probe error calibration/compensation was desired to obtain higher accuracy. Reference sphere balls of known dimension and sphericity were usually recommended([4],[5]) for the probe error assessment. In this paper, practical implementation techniques for the probe error calibration/compensation are shown, using the equi-spaced probing on the hemisphere of a reference ball: definition of probe coordinate system, measurement path generation for hemisphere measurement, probe error calibration, construction of probing error map on the orthogonal nets of probing directions(ϕ,θ), and probe error compensation along the probing direction. Therefore the directional variation in probe performance can be calibrated and compensated efficiently. A computer aided error calibration system using calibrated mechanical artefacts such as ring and step gauges is also shown, which is to assess the geometric errors of the machine in terms of total measuring accuracy. From the ring gauge measurement, the linear positional errors and squareness error are successfully evaluated. High degree of computer aids has been achieved in the measurement path generation, measurement operation, error calibration, and representation.

An interface box and corresponding software driver are developed for data intercepting and correction between the machine controller and machine, thus the volumetric errors can be compensated in real time with minimum interference to the operating software and hardware of the commercial CMM.

2. Calibration and Compensation of Probe Errors

The CMM probe of touch trigger type mainly consists of three parts: stylus tip, probe stylus, and probe body. Measuring forces on the touch probe, though it is expected as small, can cause elastic deflection of the probe stylus in combination with bending effects of the probe body unit. In order to assess and map the probing errors efficiently, the probe coordinate system(x',y',z') is considered. Consider a two axis probe in fig.1, where B, A are roll, and tilt angles, respectively. When the two coordinates have the common origin, the probe coordinate system(x',y',z') and machine coordinate system(x,y,z) can be relatedby a 3X3 transformation matrix, Tp.

$$[x',y',z']^T = Tp\,[x, y, z]^T \qquad (1)$$

where

$$Tp = \begin{bmatrix} \cos A\cos B & \cos A\sin B & \sin A \\ -\sin B & \cos B & 0 \\ -\sin A\cos B & -\sin A\sin B & \cos A \end{bmatrix}$$

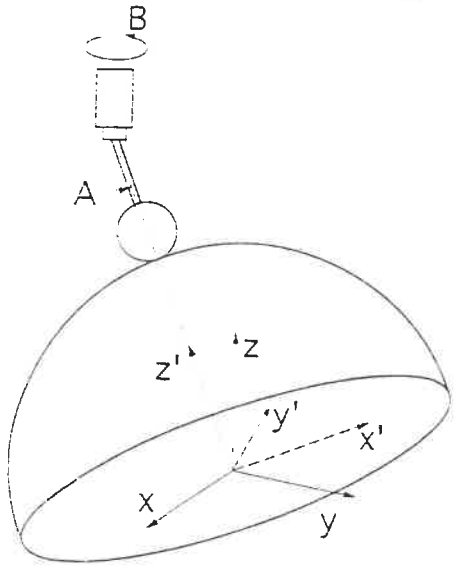

Fig.1 Probe Coordinate System

and B, A are roll and tilt angles of probe, respectively. Eq(1) is useful for the sphere measurement, probing error calibration, and compensation at later stages.

Probe Error Calibration

Once measurement has been performed eui-spaced on the reference sphere, the probing error can be assessed. Let $Rs(\phi_i,\theta_j)$ be the radius at (ϕ_i,θ_j) position of the reference sphere, and $Rm(\phi_i,\theta_j)$ be the measured distance between the centers of the sphere and the stylus.

Assume $Probing(\phi_i,\theta_j)$ as the probing error (positive sense for inward direction) along (ϕ_i,θ_j) direction, and Reff as the effective radius of the probe stylus. The following relationship can be constructed.

$$Ref - Probing(\phi_i,\theta_j) = Rm(\phi_i,\theta_j) - Rs(\phi_i,\theta_j) \quad (2)$$

Thus the effective radius of stylus tip, Reff, and the probing error, $Probing(\phi_i,\theta_j)$, can be obtained. For the probing error representation, two methods are implemented in this paper: (1) 3D representation on the hemisphere and (2) 2D representation on (ϕ,θ) orthogonal nets.

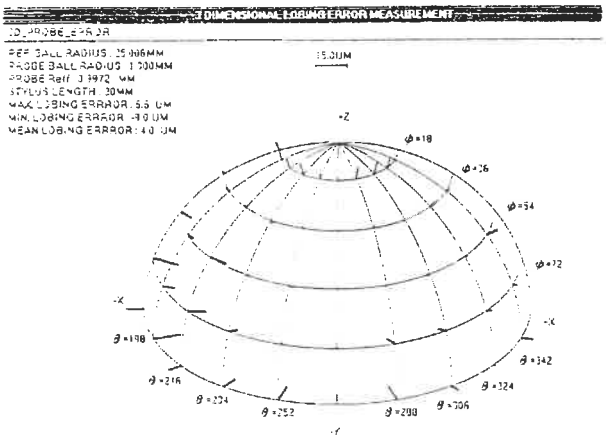

Fig.2 3D probing Error Map

Fig.2 shows a 3D error vector map of the probing error on the hemisphere, where the probing errors are plotted as a bundle of arrows along the normal direction at every (ϕ,θ) directions. Thus alternative representation method has been proposed in this paper, where several concentric circles on (ϕ,θ) orthogonal nets are considered as shown in fig.3. The probing error, $Probing(\phi,\theta)$, can be represented as the radial deviation at every (ϕ,θ) node on the orthogonal nets. The probing error map is unique to a probe setup, and highly repeatable under the same probing conditions such as probing speed, force, stylus length, etc. Thus it can be used for the probing error compensation.

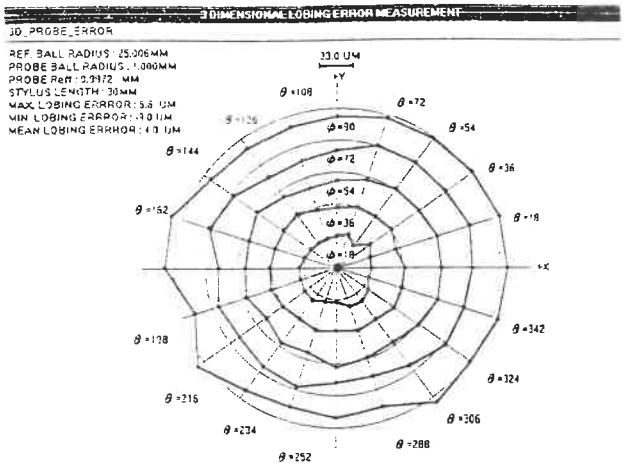

Fig.3 Probing Error map on (ϕ,θ) Orthogonal Nets

Probe Error Compensation

As the probing error is a function of the probing direction, the probe error compensation is be performed for the probing direction. Let (Mx,My,Mz) be the unit vector along the probing direction in the machine coordinate system. The probing direction (Mx',My',Mz') in the probe coordinate system is

$$[Mx',\ My',\ Mz']^T = Tp^{-1}[Mx,\ My,\ Mz]^T \quad (3)$$

where Tp is the transformation matrix between the two coordinate systems. The (ϕ,θ) angles defining Tp are evaluated as follows.

$$\phi = \cos^{-1}(Mz'/\sqrt{Mx'^2+My'^2+Mz'^2}) = \cos^{-1}(Mz') \quad (4)$$

$$\theta = \tan^{-1}(My'/Mx') \quad (5)$$

When the probing direction angles (ϕ,θ) are known, the probing error ,Probing(ϕ,θ) can be obtained from the probe error map as in fig.3.

3. Geometric Error Assessment Using Calibrated Mechanical Artifacts

Mechanical artefacts have been conventionally used for quick acceptance tests. Ring gauges can be very useful tools for the circular error test for CMMs, by which the scale errors and squareness error can be calibrated in the local region. Step gauges have been used for acceptance tests, and high accuracy can be achieved when every step is accurately calibrated and corrected. The advantage of the mechanical artefacts for error assessment is that the geometric errors can be assessed in terms of total measuring accuracy, using the measurement chain from the workpiece to the measurement probe.

4. Error Compensation

4.1 Volumetric Error Equations

When parametric errors are available for a working volume of a machine, volumetric error map can be constructed using the rigid body assumption and kinematic chains[1,2,3]. For a moving horizontal arm type machine is considered, as it was readily accessible, the integrated volumetric error equations are considered, including the probing error and the geometric error. Let [X,Y,Z] be the nominal coordinate values. The compensated coordinate value [Xc,Yc,Zc] can be derived using homogeneous transformation matrices and the probing error map. That is,

$$[Xc,Yc,Zc,1]^T = T(X)T(Z)T(Y)[Xp,Yp,Zp,1]^T - \text{Probing}(\phi,\theta)[Mx,My,Mz,0]^T \quad (6)$$

and the X component of volumetric error , ΔX, is

$$\Delta X = Xc-(X+Xp) = \delta x(x)+\delta x(y)+\delta x(z)-y(Ez(z)+Ez(x))+z(Ey(x)-\beta_1)-Yp(Ez(x)+Ez(y)+Ez(z))+Zp(Ey(x)+Ey(y)+Ey(z)) -Mx\bullet \text{Probing}(\phi,\theta)$$

where (Mx,My,Mz) are the unit vector along the probing direction.

4.2 Error Mapping on the Absolute Scale Coordinate System

The CMM controller usually inputs the absolute coordinates(Xa,Ya,Za) and the probe angles(A,B), and then calculates the corresponding relative coordinate system(Xr,Yr,Zr). In this paper, the absolute scale coordinate system has been used for error calibration/compensation, and this is to overcome the problem of the redundant degree of freedom. Thus, prior to applying the volumetric error equations, the relationship between the two coordinate system is found. For the case of two axis probe, the relationship is,

$$\begin{aligned}(Xr,Yr,Zr) &= (Xa+Xp+Tx,Ya+Yp+Ty,Za+Zp+Tz)\\ &= (Xa+LsinAcosB+Tx,Ya+LsinAsinB+Ty,\\ &\quad Za-LcosA+Tz) \end{aligned} \quad (7)$$

where Tx,Ty,Tz are the offsets between the two coordinates, (Xp,Yp,Zp) are the probe offset, and L is the stylus length. The volumetric error map $(\Delta X,\Delta Y,\Delta Z)$ are calculated according to eq(6), and the absolute coordinates can be compensated. The compensated absolute coordinates(Xa',Ya',Za') are

$$(Xa', Ya', Za') = (Xa, Ya, Za)+(\Delta X, \Delta Y, \Delta Z) \quad (8)$$

The proposed error compensation schemes are practically implemented on the real time basis using a specially designed interface box with software driver as shown in fig.4.

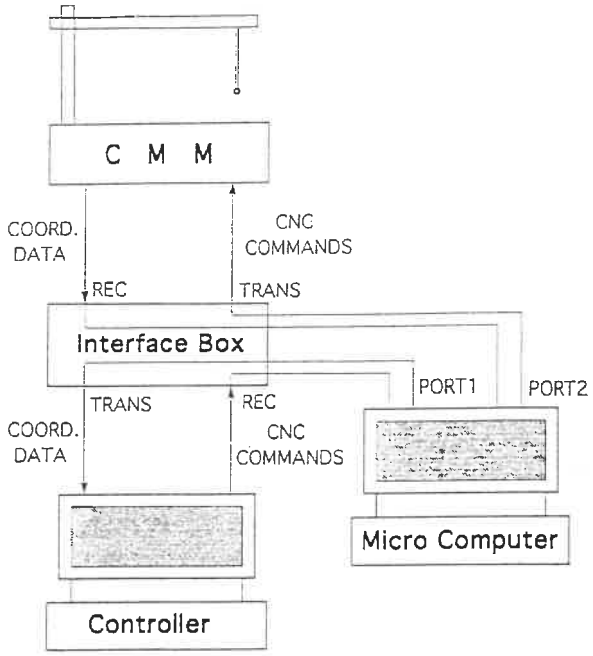

Fig.4 Real Time Compensation System Using an Interface Box

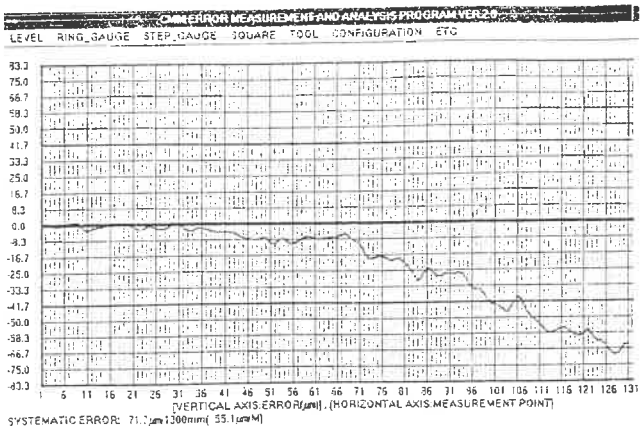
CMM ERROR MEASUREMENT AND ANALYSIS PROGRAM VER2.0
LEVEL RING_GAUGE STEP_GAUGE SQUARE TOOL CONFIGURATION ETC
[VERTICAL AXIS:ERROR(μm)] , [HORIZONTAL AXIS:MEASUREMENT POINT]
SYSTEMATIC ERROR:

Fig.5 Diagonal Measurement before Compensation

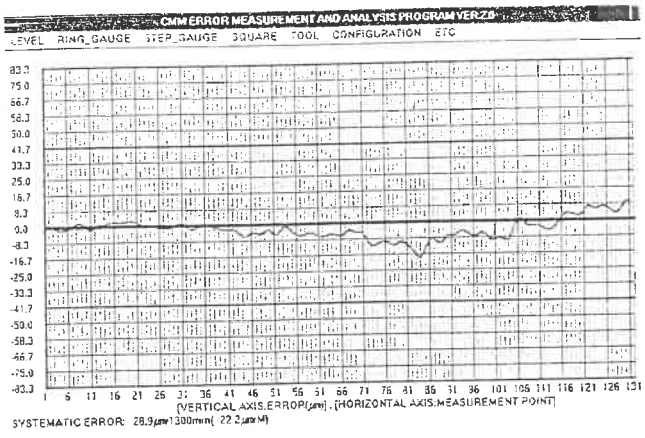
CMM ERROR MEASUREMENT AND ANALYSIS PROGRAM VER2.0
LEVEL RING_GAUGE STEP_GAUGE SQUARE TOOL CONFIGURATION ETC
[VERTICAL AXIS:ERROR(μm)] , [HORIZONTAL AXIS:MEASUREMENT POINT]
SYSTEMATIC ERROR:

Fig.6 Diagonal Measurement after Compensation

5. Discussions and Conclusions

The developed error calibration/compensation systems are practically applied. The machine of consideration was installed on a shop floor, the dimension of the machine was 4500mm X 1500mm X 1200mm. Positional errors, squareness errors, some angular errors, and probe errors were calibrated, and combined to give the integrated volumetric error map. The calculated volumetric errors are then compensated using the developed real time compensation algorithm. In order to check the efficiency of the developed system, a step gauge of 1500mm length has been measured at the time of before and after compensation. Fig.5,6 show the results of the step gauge measurements along a space diagonal,where the error was reduced to about 40% in terms of step gauge measurement after compensation. Therefore the efficiency and validity of the developed system has been demonstrated.

References

1.Zhang,G., Veale,R., Chorlton,T., and Hocken, R., Annals of CIRP, Vol 34/1/1985
2. Busch,K.,Kunzmann,F., and Waldele,F., Vol 7(3) 139-144,1985
3. Hocken,R., Annals of CIRP Vol26/1/1977

THE RESEARCH ON THE HIGH PRECISION MEASUREMENT METHOD AND SYSTEM OF DIAMETER OF LARGE SCALE HOLE

YOU ZHENG
Dept. of precision instruments,Tsinghua University
Beijing 100084, P.R.China

1, INTRODUCE

The diameter accuracy of a large scale workpiece is one of the most important parameters to assure the quality of heavy machine. With the development of manufacture technology,the more precise measuring techniques of large scale workpiece are required, such as, for the diameter measurement of the steam turbine rotor and fixer whose diameter is from 1m to 6m, with uncertainty(4+10 D)um (D--diameter of workpiece measured in meter). Now there is no relatively ideal measurement method and instrument which can satisfy these demands. The traditional measuring method for the large scale workpiece are mechanical measuring caliper or measuring tape. In resent years, the measuring method based on chord and height of the circularity is widely used. But the measuring accuracy of these method is low ,because their measuring accuracy is under the influence of form changing, temperature changing, error of aiming and etc. In the ordinary course of things, the high precision measuring system of diameter of large ~scale hole or axle is developed.

2,~MEASURING SYSTEM

Fig. 1 show the measuring system of diameter of large scale workpiece. the principle of the measuring system is like "optical caliper". It can be described as follows: going through a single pentaprism measuring head, the laser beam which emitted from a laser collimator aims two quardrant silicon photodiodes which are installed on the magnetic positioning cells attached on the two edge of the workpiece measured. The distance between two quardrant silicon photodiodes can be measured by the laser distance measuring interferometer (such as HP5528) or 3.39um multi-wavelength absolute distance measuring interferometer. After calculating, the diameter value of the workpiece measured is got.

2.1 SINGLE MODE FIBER LASER COLLIMATING SYSTEM

In the measuring process, the laser beam is used as the ideal straight line. But under the influence of the environmental factors, the ideal straight line is drifted and the aiming accuracy wouldn't be assured. So the high accuracy laser collimating system must be developed firstly.

As shown in Fig. 2, the laser collimating system incudes a He-Ne laser (8mw, Uniphase Co. U.S.A.), optical fiber coupler(coupling lens, x20, NA0.17), the single mode optical fiber (0.68um, 5um, Newport Co. U.S.A.) and the collimating

~lens (x10, NA0.25). By experience, the measuring result show that the application of the single mode optical fiber is efficient to restrain the drift caused by the laser tube and environmental factors. The accuracy of this collimating system is 0.6x10 L(L is distance in meter) in an hour within the range of 20m.

2.2 POSITION AND AIMING SYSTEM

One of key technique of the measurement of large scale workpiece are positioning and aiming technique. Usually the positioning and aiming method is based on energy variation caused by the action between the laser beam and the surface of workpiece measured. Their measuring accuracy is low because the surface roughness of the workpiece measured have influence on the positioning and aiming energy variation. In this measuring system, the positioning cell is shown in Fig. 3. A magnetics which can be attached to the edge of the diameter measured is installed on the base of the positioning cell.With the coincidence of the incidence laser beam into the positioning cell and the beam reflected from the cell, the correct place of two positioning cell is ensured.

There is a quadrant silicon photodiode which are used as aimed target on the center of the positioning cell. when the positioning cell positioned correctly, the quadrant silicon photodiode ~will the aiming information for corralling the aiming system. So the structure of positioning cell is reliable, convenient and high accuracy.

The aiming system consist of a pentaprism and moving carrier. In the measuring process, the laser beam from the collimator are turned perpendicularly by the pentaprism to aim the quadrant silicon photodiode on the positioning cell, and then moving the pentaprism by moving carrier, the laser beam aim the other quadrant silicon photodiode. The moving distance of the moving carrier is measured by the laser interferometer.

The accuracy of aiming and positioning system is superior to 2 um within the measuring range of 5 meters.

2.3 THE MEASUREMENT OF DIAMETER OF HOLE

As shown in Fig. 1 ,the moved distance (L) of moving carrier is not the measured diameter (D). In order to calculate the diameter, we must obtain the width (S) of groove of the position cell and constant center distance (C) between two quadrant silicon photodiodes firstly (shown in Fig.3).

Now we can obtain the diameter measured (D):

$$D = \sqrt{(L+C)^2 + S^2} \qquad \text{(for Hole)}$$

or

$$D = \sqrt{(L-C)^2 + S^2} \qquad \text{(for axle)}$$

3. RESULTS AND DISCUSSION

After completing this measuring system, a lot of experiments were made by this system. The various error facts of the system

are analysed in detail. The results of experiment and the error analysis are identical. The uncertainty (3σ) within 4 um in measuring the workpiece which be measured by Corrdinate Measuring Machine (D=498.865±6um) is obtained as shown Tab. 1.

Tab. 1 Measuring Results

	Average Value(mm) (10 Times)	Uncertainty(3σ) (um)
1	498.8642	3.2
2	498.8627	3.4
3	498.8630	2.6
4	498.8635	2.1

REFERENCE:

1. M.Shiraishi, Scope of in process measurement, monitoring and control technique in machine processes, Precision Engineering, 1989,Vol.11 No. 1
2. "Precis", Precision Engineering, 1990,Vol.12 No. 2
3. "Precis", Precision Engineering, 1984,Vol.6 No. 2
4. Masaaki Ueki, Bull. Janpan Soc. of Precision Engineering, 1987, Vol.27 No. 2

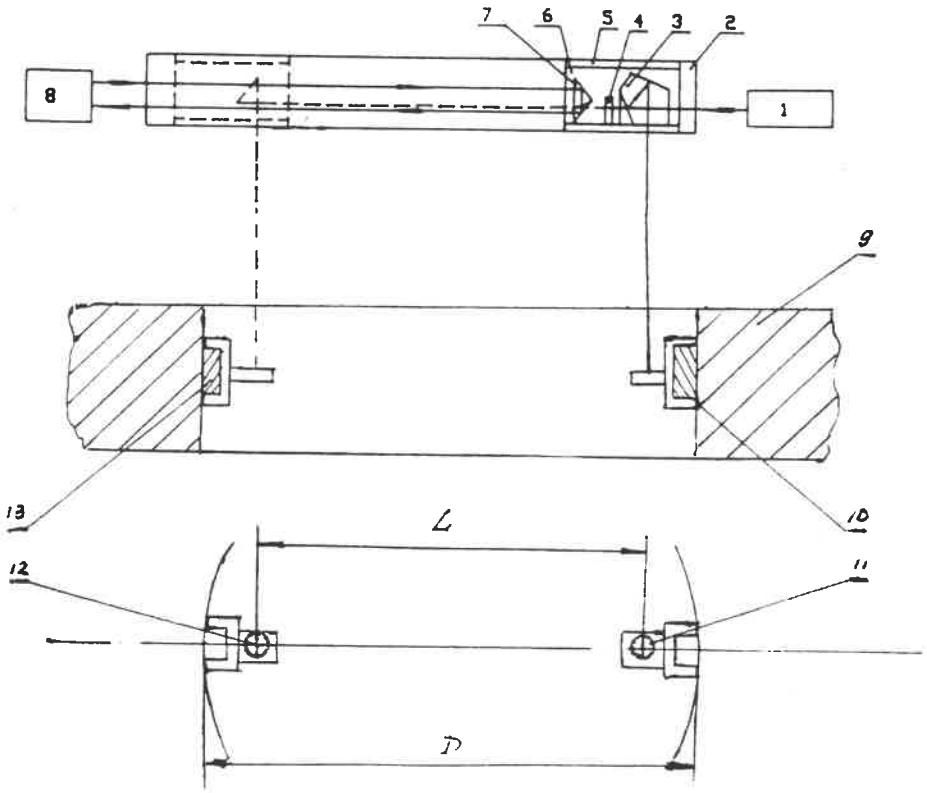

1-Laser collimator, 2-Guideway, 3-Pentaprism, 4,11,12-Quadrant silicon photodiode, 5-Moving carrier, 6-Measuring Head, 7-Cube reflector, 8-Laser distance interferometer(HP5528), 9- Measured hole(axle), 10,13-Magnetics

Fig.1 Measuring system of diameter of large scale workpiece

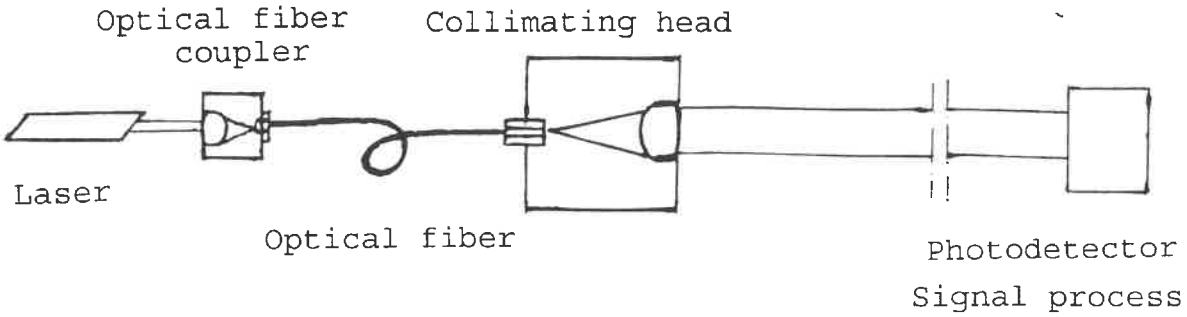

Fig.2 Laser optical fiber collimating system

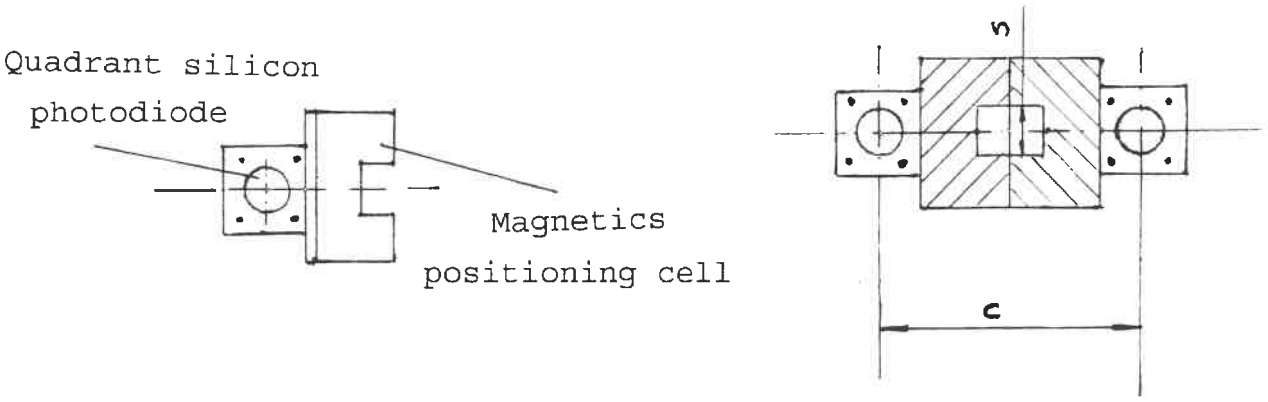

Fig.3 Positioning and aiming cell

DESIGN OF A THREE-DIMENSIONAL SURFACE PROFILER

V.G. BADAMI, S. T. SMITH, J. RAJA, R. J. HOCKEN

DEPARTMENT OF MECHANICAL ENGINEERING AND ENGINEERING SCIENCE

UNIVERSITY OF NORTH CAROLINA AT CHARLOTTE, CHARLOTTE, NC 28223

Introduction

Characteristics of engineering surfaces are often determined using profilometry. The most common method of characterizing such surfaces is by stylus profilometry, where a diamond stylus is drawn across the surface to be measured and the resulting deflection is measured. Such traces are two-dimensional and provide profile data only along the trace line. Real surfaces are three-dimensional in nature and such methods provide profiles that are only representative of the topography given specific characteristics. Surfaces are increasingly being engineered to suit particular applications and an accurate method of obtaining quantitative three-dimensional profile data in the manufacturing environment is necessary. Some examples of engineered surfaces include printing rollers, automotive cylinder liners, internal surfaces of molds and dies, etc.

This paper describes ongoing work in the development of an inexpensive, portable three-dimensional stylus based surface profiler with a scan range of 5 mm by 5 mm and a vertical range and resolution of 150 μm (limited by signal conditioning electronic range) and <1 μm respectively. The instrument occupies a volume having dimensions of approximately 75 by 75 by 40 mm (L x B x H) with scan speeds up to 0.5 mm s^{-1}. The design and construction of the internal datum and the portability of the instrument to facilitate *in situ* measurement of components are emphasized. The adherence to kinematic design principles, compactness and portability will be highlighted. Images illustrating the surface profiling capabilities of the profiler are presented.

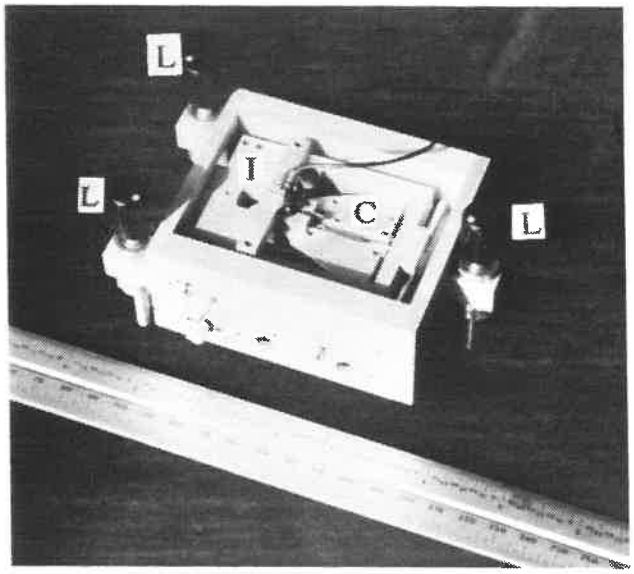

Figure 1: Photograph of profiling instrument; C, carriage, I intermediate stage, P, pulley drive, L leveling screws

Design

A photograph of the three dimensional profiler is shown in figure 1. This consists of a central triangular shaped carriage that rests on an optically flat datum surface via three steel back thin PTFE bearings. The datum surface for the carriage bearings has been replicated from an optical flat using Moglice™ castable polymer. Attached to the underside of the carriage (not visible in figure 1) is the stylus probe which extends through a hole in the center of the reference flat and

makes contact with the specimen surface below the instrument. The stylus transducer consists of a 10 μm radius diamond stylus attached to an aluminum rod that is fixed to the base via a beryllium copper linear flexure. Attached to the top of the stylus rod is a ferromagnetic rod which form the core of the LVDT sensor which converts the mechanical motion to an electrical signal. Simple logarithmic decrement testing of the transducer revealed a natural frequency of 49 Hz and a critical damping ratio of 0.06. Static test also showed that the stiffness of the flexures was 35 N m^{-1} giving an effective mass of approximately 0.37 g. The carriage is constrained by two roller bearings to move along a precision ground steel rod which is referred to as the *x* axis in this paper. There is, however, sufficient freedom in all other axes to permit continuous contact with the datum surface. Translation is accomplished by a pulley/wire drive system which is, in turn, driven by a small DC motor/gearbox combination. An optoelectronic trigger is used to initiate data collection while an encoder on the motor is subsequently used as the trigger for equidistant data collection.

The datum bar for the *x* axis guide is mounted into an intermediate frame that is, in turn, mounted on an orthogonal slideway. This guide consists of two ground steel bars that are fixed to the frame of the instrument. Traverse of the intermediate frame in the *y* axis is again achieved by a DC motor/gearbox pulley drive system with motor shaft encoding for monitoring displacement. Lateral triggering of data in the *x* axis can be obtained every 0.45 μm although, in practice, it is usual only to sample every tenth pulse which is considered adequate for the presently used stylus of 10 μm radius. Lateral triggering in the *y* axis is at 20 μm.

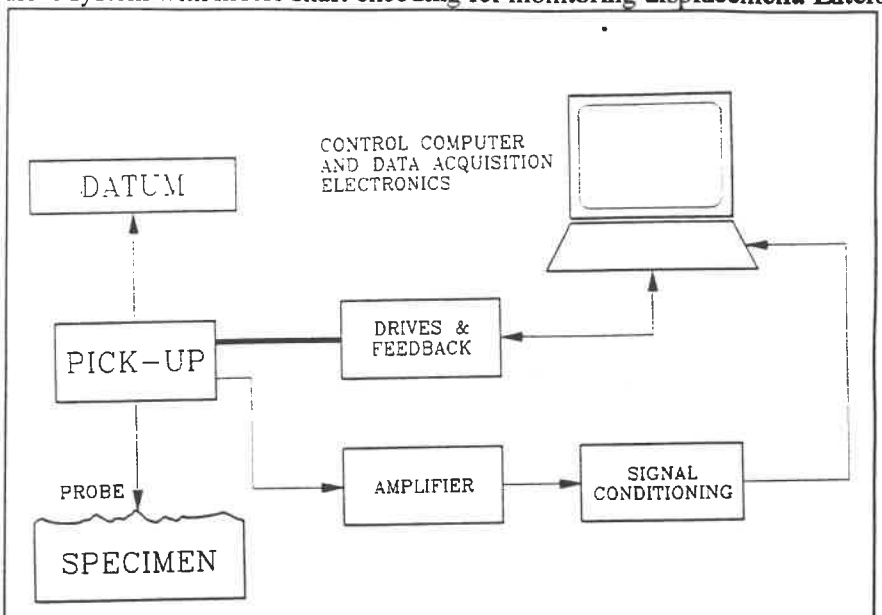

Figure 2: Block diagram of complete instrumentation system

To measure a specimen surface, the stylus is firstly positioned over the sample and then contacted using the three adjustment screws (these can also be used to level the *xy* plane of the instrument datum to that of the specimen). The carriage is then raster scanned over the surface and data collected under full computer control. A block diagram of the complete system is shown in figure 2.

Performance evaluation

Ideally, such an instrument should be capable of scanning the stylus probe in a perfectly planar space while acquiring data. In reality, error sources such as noise, repeatability and drift preclude such a goal.

Calibration

The stylus transducer has been calibrated by placing it on the anvil of a differential micrometer alongside another, calibrated LVDT sensor. The output from both sensors was then recorded for comparative purposes. Based on this, the transducer has a measured sensitivity of approximately 75 mV μm^{-1} from the lock-in amplifier.

Presently the probe range is limited by the signal conditioning electronics with lock-in amplifier saturation corresponding to a displacement of the stylus of 150 μm with data acquisition single converter bit resolution of 66 nm. In principle, it should be possible to monitor stylus output for displacements of up to 1 mm.

Noise

Possible noise sources for this system are those due to air and ground borne mechanical vibrations and electronic. Mechanical noise is invariably present during scanning. Although not fully characterized as yet, observations during many surface measurement have not shown this to introduce significant additional noise with the present transducer discrimination. Electronic noise has been assessed by contacting the stylus with a stationary steel surface and monitoring the output from the signal conditioning amplifier with a digital spectrum analyzer. The subsequent spectra showed a noise characteristic typical of flicker with approximately -95 dBV at 25 Hz and increasing to approximately -60 dBV at low frequency indicating a submicrometer electronically generated noise levels.

Repeatability

To assess repeatability of the complete instrument system. A triangular calibration specimen of wavelength 100 μm and peak to valley height 10 μm was scanned, with the incremental *y* drive disconnected, over nominally the same track. Variations of less than 0.1 μm were observed for over 40 repeat traverses. As a consequence a conservative value of 0.2 μm is chosen as representing the repeatability over the 5 mm traverse.

Thermal stability

Estimating the thermal coefficient of this system is complicated by the different time constant of individual components within the system. However, most of the large mechanical elements have been constructed from aluminum. Because the stylus contacts a flat specimen at a point that is coincident with the plane of contact of the three instrument support legs, under this circumstance there will be an equal length of materials in the upward and downward parts of the measurement loop. Consequently, if all materials were of the same thermal expansivity then the instrument would be fully compensated. In reality we would expect some variations to result in a finite thermal susceptibility. This has been assessed by placing the probe in stationary contact with a steel specimen. The complete system was housed in a temperature and humidity controlled laboratory. For a typical thermal variation of less than 0.1 K, variations of less than 50 nm were observed in the stylus output over a period of 50 minutes. Placing the instrument in an environmental chamber and subjecting it to a rapid step change of 10 K resulted initially in a negative correlation with this then changing to a slow positive response characteristic of a first order system with a time constant of approximately 55 minutes. Assuming a linear relationship between output and temperature this gives a thermal coefficient of approximately 0.27 μm K^{-1} equivalent to approximately a 10 mm length of aluminum.

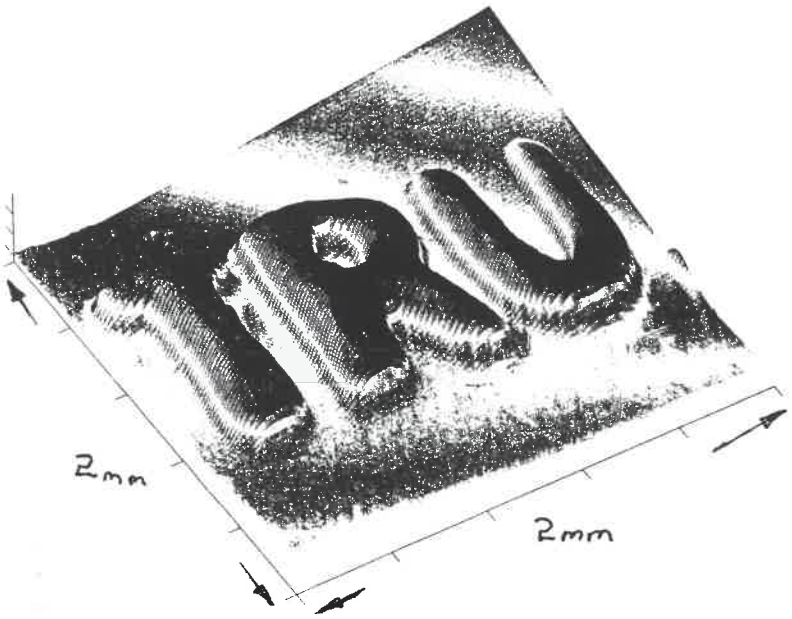

Figure 3: TRU from "IN GOD WE TRUST" on a dime coin.

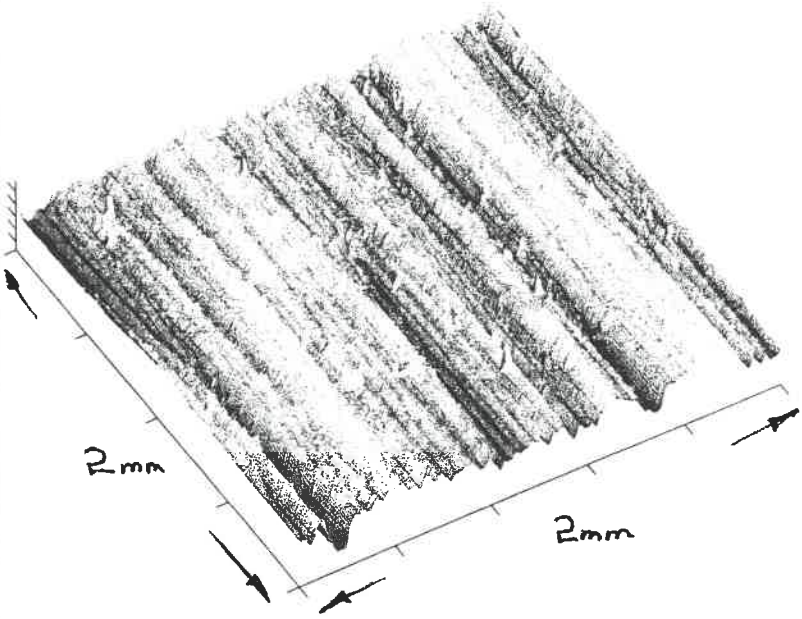

Figure 4: Isometric plot of a ground steel specimen

Results

For illustrative purposes, two topographic images are shown in figures 3 and 4. Figure 3 is a map of the first three letters of "trust" on a dime coin. The raised letters are approximately 45 μm in height and the topograph represents a scan area of approximately 2 mm by 2 mm. The final figure shows an isometric plot of a similar area of a ground steel flat. Using a Rank Taylor Hobson Form Talysurf 120L a typical surface finish value of approximately 1.5 μm was observed. Although originally designed for mapping of relatively coarse print roll surfaces, the sub-micrometer capability of this instrument is clearly demonstarted and it is expected that through relatively simple alterations this might be improved by an order of magnitude or more in future designs.

SURFACE AND SUBSURFACE CHARACTERISTICS OF ULTRAPRECISION GROUND SILICON WAFERS

M. Kerstan, H. Lundt, A. Huber, P.O. Hahn, and M. Brohl
Wacker Chemitronic
P.O. Box 1140, 84489 Burghausen, Germany

1. Introduction

In the 21st century wafer diameters are expected to be larger than current 200mm wafers: 300mm or even 400mm will be the wafer size to come. The increasing number of process steps necessary for advanced chip production together with the increasing chip size ask for a wafer perfection more stringent than ever. The submicron design rules require flatter, purer, and smoother mainstream 200mm wafers, too.

Increasing economical and quality requirements necessitate new wafer preparation techniques. As a prerequisite for geometry improvement the depth of damage at each process step, e.g., slicing, lapping, grinding has to be reduced significantly. In particular recent advances in ultraprecision grinding make this abrasive machining process attractive to be used in silicon wafer manufacturing by reducing the damage to about 1 µm and less after grinding. Ductile mode grinding offers almost damage free surfaces.

Different grinding concepts are currently developed and evaluated: conventional cup-wheel grinding (CWG), horizontal type ultraprecision grinding (HPG), ultrafine abrasive particle grinding (UAPG), and single point diamond turning (SPDT). While in CWG the cup wheel axis is positioned perpendicular to the wafer surface for HPG it is parallel /1,2/. UAPG uses alumina particles with a size of 10-20 nm for grinding /3/. A single diamond tool with a well defined geometry and rake angle was used in SPDT tests /4/.

2. Experimental Method

Scanning Infrared Depolarisation (SIRD) has been applied in order to measure the subsurface damage /5/. The beam of an IR-laser was transmitted through machined silicon wafers to measure the depolarization due to the SSD (stress induced birefringence). The wafers were located between a pair of crossed polarizers. The depolarization of the laser light is a qualitative measure of the SSD. Consequently the damage on the wafer can be mapped by scanning the wafer with the laser beam using computer controlled positioning equipment to move the wafer. In order to investigate a depth of damage SIRD has to be combined with subsequent etching. Measuring the depolarization after each etching step yields a decay curve for the light intensity detected. After removal of all damaged layers the detected light intensity for crossed polarizers decreases to a residual constant level. The depth of damage can be determined from such a decay curve.

An atomic force microscope (AFM), Nanoscope III from Digital Instruments, was used in tapping mode to analyse the surface topography and roughness of the ground wafers. Map sizes were 25x25µm or 100x100µm with lateral resolutions of 50nm or 200nm, respectively. Maps were taken at wafer positions typical for the respective ground textures, in general at half radius. Roughness results are given first as average 2D-RMS-values for the 100x100µm scans at those positions and second as range of RMS roughness results for arbitrarily chosen surface points to take into account roughness inhomogenities.

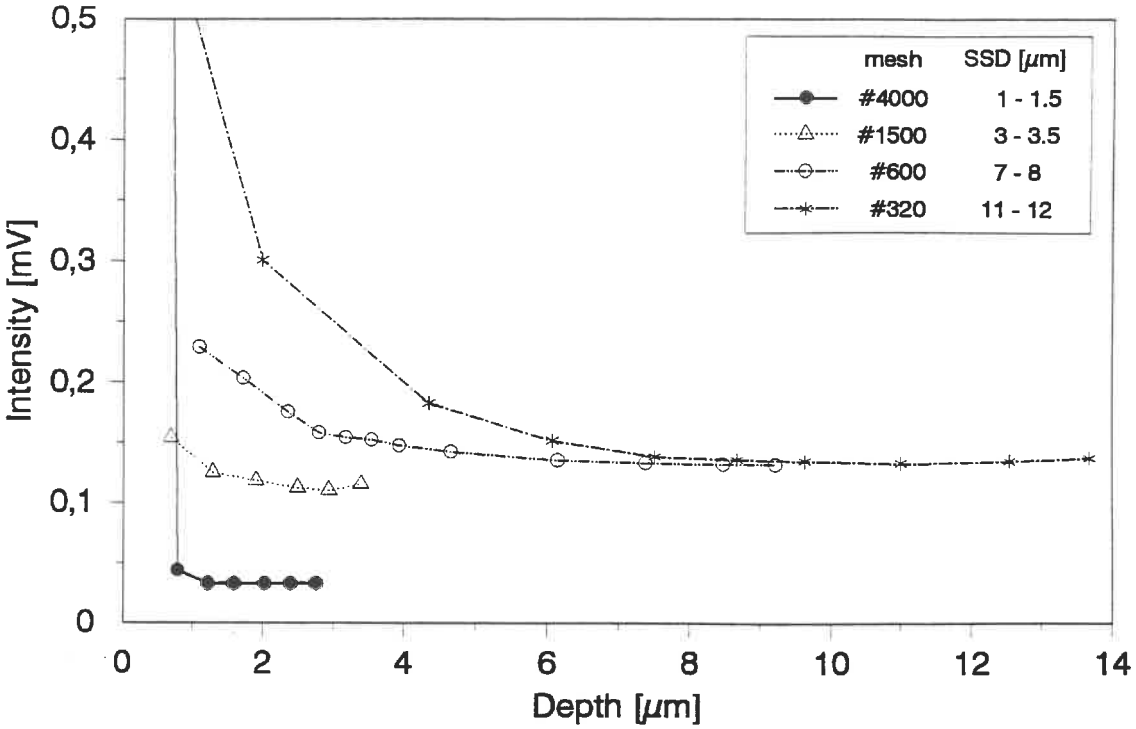

Fig. 1: Depolarization decay curves for CWG ground wafers

3. Results

The subsurface damage of silicon wafers ground with CWG depends strongly on the diamond size on the grinding wheel. The depolarization decay curves reveal that the SSD decreases from 7-8 µm for mesh 600 down to 1-1.5 for mesh 4000 (s. fig. 1). The extremely steep decay curve for wafers ground with mesh 4000 grinding wheels indicates a very shallow strain field due to the machining. The absence of deep reaching strain field components, which are typical for microcracks due to brittle fracture, may indicate that the brittle-ductile mode transition occurs when using mesh 4000 instead of a coarser grit. A very similar transition to the ductile mode depending on grain size of the diamond wheel has been observed when grinding optical glasses /6/.

Ground with mesh 4000 diamonds the wafers had a shiny surface with a typical RMS roughness of 10 nm (range: 7-12 nm). The AFM pictures reveal the typical grind marks due the process kinematics of CWG (s. fig. 2a).

SPDT with a well defined tool geometry leads to a periodically structured surface topography (fig. 2b) characterized by parallel grooves. The depth, shape and the distance of the grooves reflects the tool condition, rotation speed, and feed rate during the turning. The RMS roughness was typically as low as 6 nm with a range of 1-7.5 nm. After removing a 1µm thick top layer of the machined wafer the depolarisation completely decreased to a constant residual level. Thus the depth of damage was below the limit of detection (< 1 µm). The absence of deep reaching strain fields and the smooth grooves due to the diamond turning again indicate that the machining occured in the ductile mode.

UAPG uses bound alumina particles with a size of 10-20 nm for grinding. Due to the extremely small size of the abrasive particles the surface of the machined wafer was shiny without any grind marks. The RMS roughness was typically as low as 1.4 nm with a range of 1-5 nm. This low roughness is

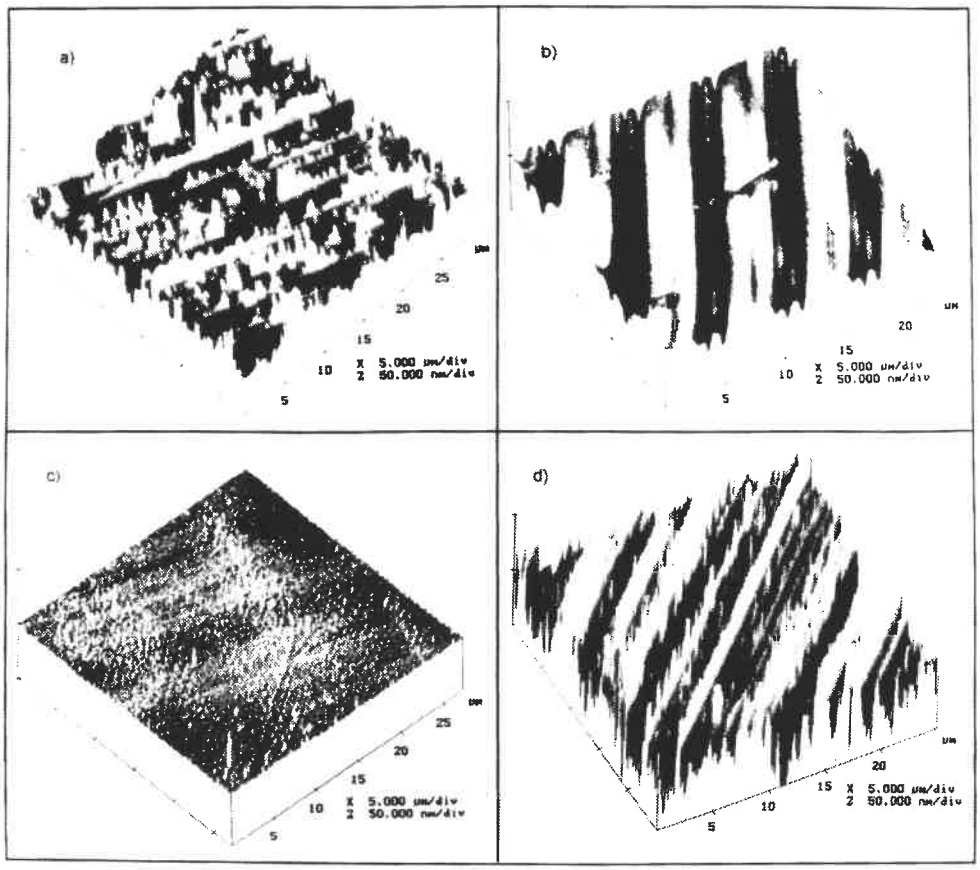

Fig. 2: AFM surface morphology of differently ground wafers:
a) CWG, b) SPDT, c) UAPG, d) HPG

comparable to typical values after a standard first polish step. Again no deep reaching strain fields were detectable (depth of damage: < 1 µm).
HPG offers the advantage of an improved copying accuracy under tight structural stiffness /2/. The HPG ground wafers were machined using a diamond wheel with a mesh 3000 diamond size and two different bonds: ceramic and resin. It was found that wafers ground with resin-bond wheels had a significantly lower roughness (typical RMS roughness: 25 nm, range: 20-60 nm) compared to those ground with ceramic-bond wheels (typical RMS roughness: 40 nm, range: 20-200 nm) and SSD values of about 1 µm and about 1-1.5 µm, respectively (exact SSD measurements were not possible due to the low transmissivity of the silicon material used for these wafers). It was previously reported that bronze-bond wheels in contrast to resin-bond wheels did not produce ductile mode ground surfaces /2/.

4. Discussion

This paper focusses on the surface and subsurface quality of silicon wafers ultraprecision ground using the different techniques mentioned above. Thus a complete evaluation including total wafer geometry and the economic features can not be made at this point.
Concerning CWG ground wafers our results indicate that surface roughness and SSD are strongly depending on the diamond size. For brittle fracture a linear relationship between grain size and SSD was found earlier /7/. Using a conventional CWG machine with a mesh 4000 diamonds it was possible to

reach the brittle-ductile mode transition (BMT) without further optimizing the machine stiffness. It needs to be further examined if the influence of machine stiffness concerning BMT, SSD and roughness has previously been overestimated. A higher stiffness might still be necessary to further improve the wafer flatness.
SPDT offers the possibility to machine silicon wafers with a low surface roughness and SSD. Tool wear and long cycle time (one diamond) are problems of the present machines which still need to be solved to introduce this method as an industrial manufacturing technology.
In UAPG the precondition for BMT can easily be fulfilled because the sizes of the abrasive grain are in the range of only 10-20 nm. Values for the critical depth of cut in silicon have recently been derived from scratching experiments to be 64 nm and 100 nm by Bifano /8/ and Puttik /9/, respectively. Wu and coworkers point out that the critical depth of cut depends on process parameters like temperature and load rate /10/. They expect the critical depth of cut in silicon to be 1 µm at 400°C.
Although HPG utilizes an advanced machine concept with a high stiffness the examined HPG machined wafers showed a higher surface roughness compared to the other wafers. As reported for metal-bond wheels /2/ the ceramic-bond wheels showed disadvantages concerning roughness and SSD. Again this result reveals the importance of the tool quality for ultraprecision grinding of silicon wafers.
Lapped wafers (FO1200) have a typical RMS roughness of 200 nm and a depth of damage of 8-10 µm. Compared to this standard industrial process the new grinding methods offer the opportunity to reduce surface roughness and SSD significantly by at least an order of magnitude.

5. Acknowledgments

We thank Fa. Kugler (Salem, Germany), Nissin Machine Works Ltd. (Hamamatsu, Japan), and Disco Corp. (Tokyo, Japan) for providing wafers ground with SPDT, HPG, and UFPG, respectively. This work has been supported by the Federal Department of Research and Technology under contract No. M2793F. The authors alone are responsible for the contents.

6. References

/1/ Nissin Machine Works Ltd., Hamamatsu, Japan
/2/ T. Abe, Y. Nakazato, M. Daito, A. Kanai, and M. Miyashita, Proc. of the 7th Int. Symposium on Silicon Materials Science and Technology, p. 207, San Francisco 1994
/3/ Disco Corp., Tokyo, Japan
/4/ Fa. Kugler, Salem, Germany
/5/ H. Lundt, M. Kerstan, R. Weiss, Proc. of the Spring Topical Meeting of the American Society of Precision Engineering, p. 42, Tucson 1993
/6/ Y. Namba, M. Abe, Annals of CIRP, Vol. 42, 417, 1993
/7/ H. Lundt, M. Kerstan, A. Huber, P.O. Hahn, Proc. of the 7th Int. Symposium on Silicon Materials Science and Technology, p. 218, San Francisco 1994
/8/ T. Bifano, T.A. Dow, R.O. Scattergood, J. of Engineering for Industry, Vol. 113, 184, 1991
/9/ K. Puttik, Proc. of the Spring Topical Meeting of the American Society of Precision Engineering, p. 14, Tucson 1993
/10/ T. Wu, N. Morita, Y. Yoshida, Proc. of the 7th Annual Meeting of the American Society for Precision Engineering, p. 69, Grenelefe, 1992

Collaborative Precise Operation by Two Miniature Robots -Single Diamond Cutting with Local Position Feedback-

H.Aoyama, H.Nakano, A.Sasaki, J.Fukaya, F.Iwata and T.Kubo

Department of Precision Engineering

Shizuoka University

3-5-1, Johoku, Hamamatsu, Shizuoka 432 Japan

1.Introduction

Small robots which are composed of micro-mechanisms, micro-sensors and micro-manipulators can be also very useful in the field of precision engineering because the lack of mechanical parts should provide higher mechanical stability and great cost-saving benefits when employing them within conventional machines. So as an alternative approach to improve the accuracy of machine tools and measuring machines, several miniaturized robots have been developed and applied to practical precision tasks which need accurate operation over wider working range[1]. Small precise robots, responsible coordinate measuring instruments which can monitor spatial coordinate positions of these robots, and the network of micro-computers should be organized to control all of the system under hierarchical distributed structure[2),3)].

Two miniature robots which have a micro single diamond tool and an optical fiber displacement sensor are designed and constructed to provide precise machining and accurate measuring. These two robots are maneuvered to approach the working area and to take the close formation in a series. Higher accuracy can be achieved with the help of servo techniques though each robot has accurate operation skill. So output signal from the small robot with displacement sensor should be fed back to the actuator which pushes the tool on another robot. This collaboration of two robots can allow both "flexibility" and "precise operation" with temporary closed-loop for fine-machining at any place. In this paper, we describe structures of these small robots, performances and experimental results of fine cutting.

2. Structure of Miniature Robot

2.1 Mini-Robot with Single Diamond Tool

Figure 1 shows the schematics of miniaturized robot which we have developed and **Figure 2** is the photograph. This small robot is composed of piezo elements and electromagnets for clamping and propelling, which are excited synchronously to move like an inchworm walker. A single diamond tool of 0.5μm radius which is mounted on the rotating disk and driven by a micro stepping motor are also actuated by the piezo element on the robot so that scratched grooves perpendicular to moving direction can be given with good positioning resolution. The machining unit is mounted on the lever arm, the opposite end of which is supported by the tiny micrometer screw. So this mechanism can provide easy adjustment of cutting depth to the target. Furthermore a small plane mirror is attached on the frame of the machining unit in order to monitor the tool position by the optical fiber probe on another robot described in 2.2. It is noted that if the lines spacing of a few μm are necessary, cutting action is performed every step of motion while much higher resolution of line spacing is required, the tool position is controlled directly by the piezo element on the machine.

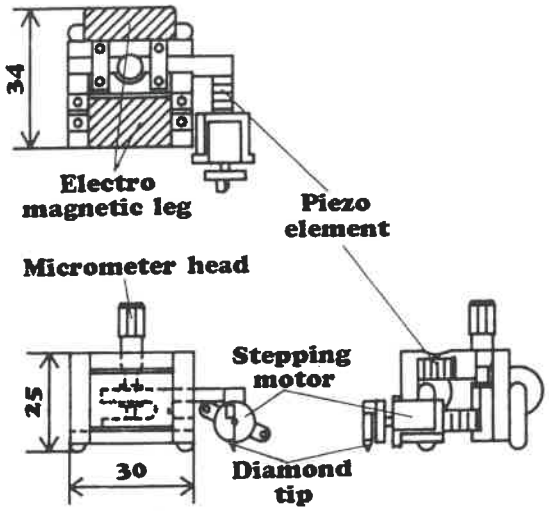

Fig.1 Miniature robot with a single micro diamond tool

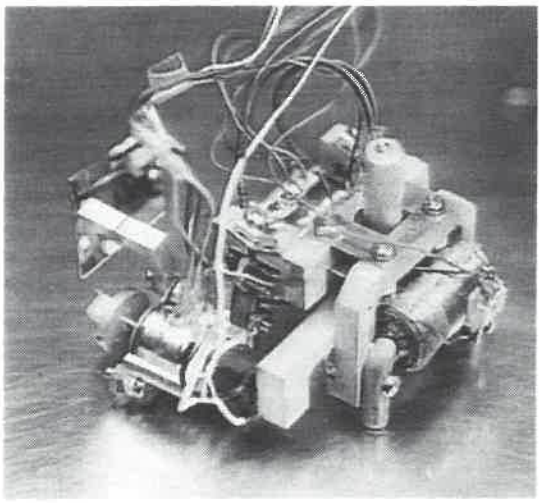

Fig.2 Photograph

2.2 Mini-Robot with Optical Fiber Probe

Figure 3 also gives the schematics of another mini-robot which has an optical-fiber displacement sensor on his head, of which photograph is shown in **Figure 4**. The basic structure is similar to the previous one but optical fibers, one of which is for the light transmitting and the other are for the light receiving, are implemented on this small robot with the optical devices such a light emitted diode and a photo diode. This simple displacement sensor is based on the well-known technique that the reflected light from the target is sensitive relative to the distance between the target and the probe end, and has good robustness to electromagnetic disturbances. Indeed, we obtained the static characteristics which indicated the absolute linear range from 100μm to 1200μm on the test bench. Difference signal between two receiving fibers means the orientation of the robot to the target. Utilizing this signal, he can approach to the target closely in the right angle

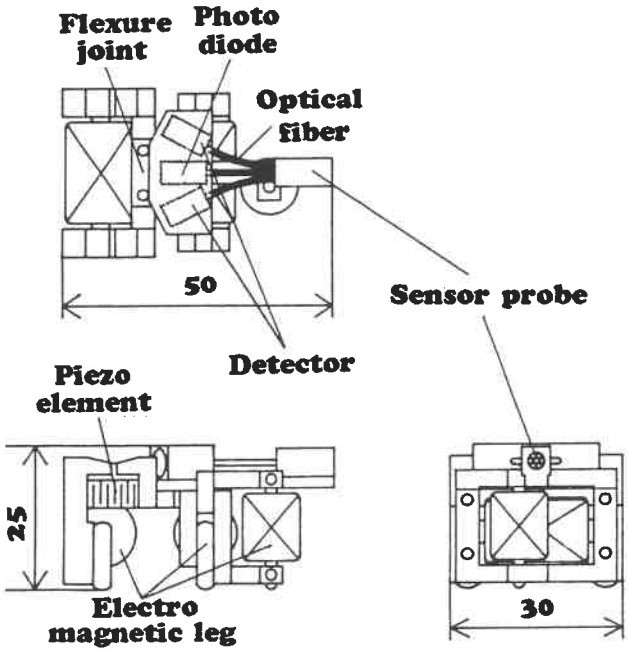

Fig.3 Miniature robot with an optical fiber displacement sensor

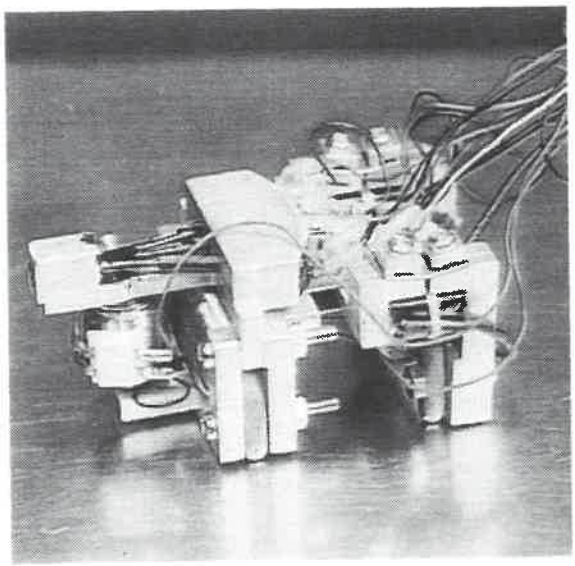

Fig.4 Photograph

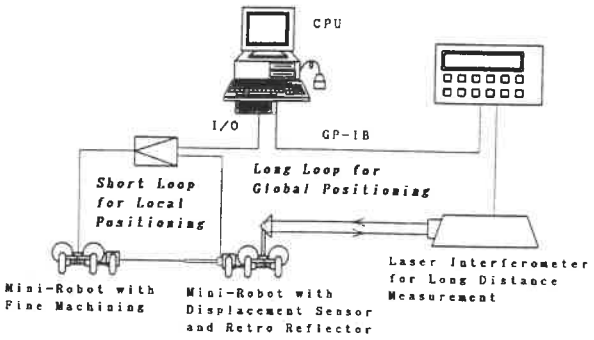

Fig.5 Multi-feedback loops for local and global positionings

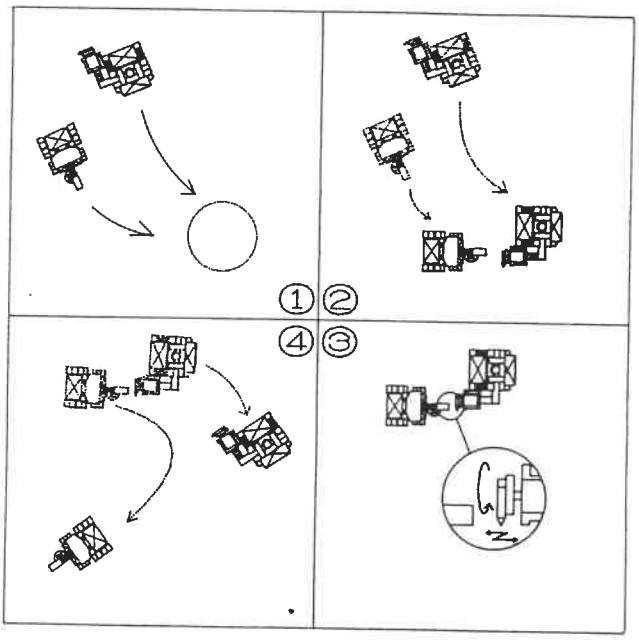

Fig.6 Sequence of collaborative operation

by driving actuators for thrusting with well-controlling manner.

3. Collaborative Precise Operation

3.1 System Concept

We can conceive that precise operation over wide working range by using such miniature robots system should be achieved by multilayered feedback loops with help of precise measuring instruments and micro computers as shown in **Figure 5**. Short feed-back loop between two miniature robots in local area allows higher positioning resolution with good response but poor dynamic range, although the long loop including such a laser interferometer and processor with sufficient low-pass filtering technique provides wide working range for global positioning but poor resolution and response. So we believe that the combination of these loops should give good compatibility of fine operation and wide dynamic range.

3.2 Experimental Result

In order to construct this system mentioned above, we consider the primary setup for experiment so that two miniature robots can approach to the specified working area and there they can collaborate in precision machining performed by the feed-back loop between two robots, which includes a single diamond tool, displacement sensor and tool positioner on the robots. **Figure 6** illustrates the sequence for collaborative operation and **Figure 7** is the photograph of two miniature robots under operation. Each robot is maneuvered into

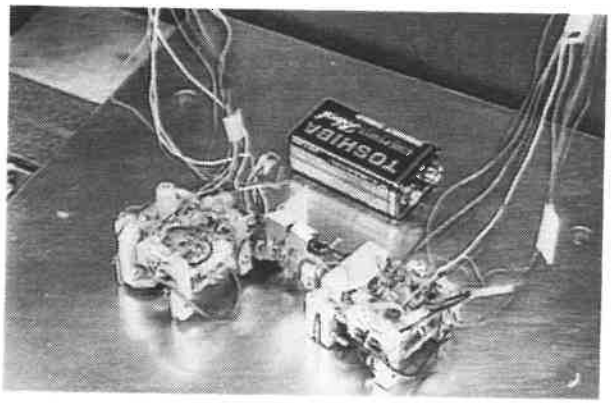

Fig.7 Two mini-robots under operation

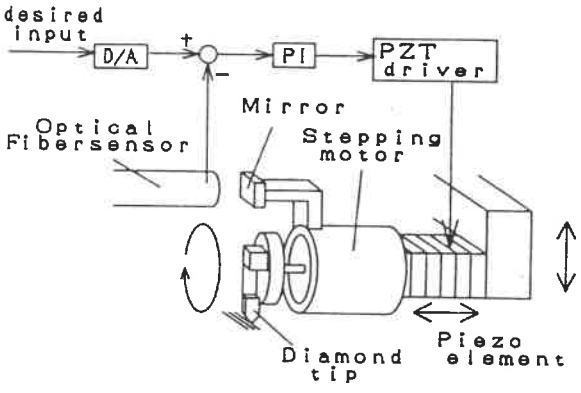

Fig.8 Control diagram between two robots

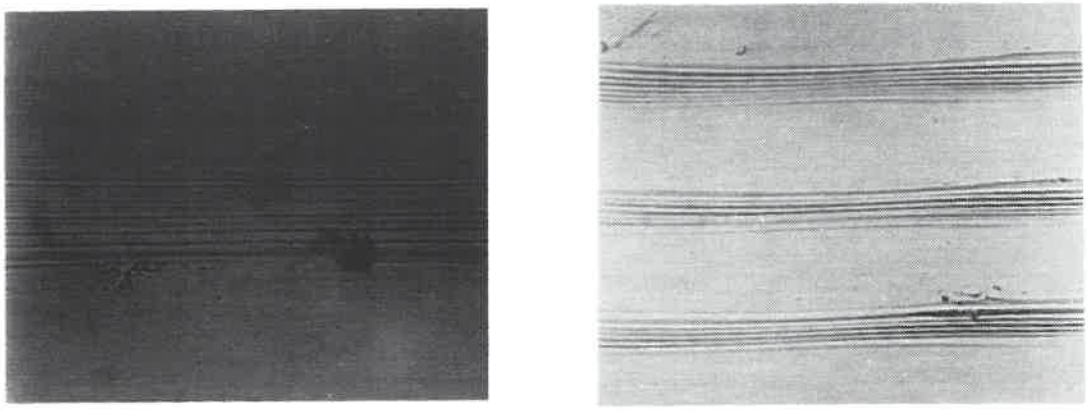

(a) Fine grooves spacing of 0.5μm

(b) Several grooves of 1μm spacing at intervals of 30μm

Fig.9 Experimental results

the working area(1) and they approach to get a close formation(2). Then the mini-robot with a single diamond tool of which position is monitored by another small robot with displacement sensor begins to make several fine grooves such as gratings perpendicular to machine direction(3). The line spacing is controlled accurately by the piezo element through simple PI electronics as illustrated in **Figure 8**. Finally they move away to next working area after finishing the give task(4). (At the present, these machines are remote-controlled by responsible operators yet although automatic controller with the facilities of linked processors are on going development)

Figure 9 demonstrated the result which is machined on the glass sample. We succeeded in fine-cutting by position-controlled single diamond tool. Excellent resolution of line spacing approximately less than 0.5μm have been achieved in the left photograph(a). But unfortunately this picture is poor quality due to the image resolution of an optical microscope. Another unique performance is shown in the right photograph(b). A set of several grooves spacing of 1μm are machined at intervals of 30μm. We believe that this operational performance can be extended from nanometer range to much wider range of a few meter.

4. Current Status and Future Work

In this report, we described the structure of miniature robots which have a single diamond tool and an optical fiber displacement sensor. And the collaboration strategy involving the combination of local and global feed-back techniques for precise operation over wide ranging was proposed. In the experiment, two small machines which were manually controlled succeeded in precise machining of gratings at the sub-micron resolution on a glass sample under collaborative action. We are implementing other components such as spatial coordinate monitoring with task planning and scheduling properties under CPU network structure for "Desktop Precise Flexible Manufacturing System by Miniature Robots". This work is supported financially by Electro-Mechanics Technology Advanced Foundation.

References

1) H.Aoyama et al; "Precision Machining and Measurement Organized by Miniature Robots", Proc. of 8th Annual Meeting of ASPE,(1993)pp.126-129.
2) H.Aoyama et al; "Miniature Robots for Ultra Precision Measurement and Machining", Proc. of 7th International Precision Engineering Seminar,(1993)pp.275-289.
3) H.Aoyama et al; "General Planning of Multiple Movable Workcells for Desktop Flexible Manufacturing", 1994 Japan/USA Symp. on Flexible Automation, Vol.3(1994)pp1347-1350.

MINIATURE LINEAR ACTUATOR USING PIEZOELECTRIC ELEMENTS

Takayuki Goto*, Satoshi Tawara*, Kimiyuki Mitsui**
and Norio Suzuki**

* Advanced Technology Research Center,
Mitsubishi Heavy Industries, Ltd.
Kanazawa-ku, Yokohama, 236 Japan

** Faculty of Science and Technology,
Keio University
Kohoku-ku, Yokohama, 223 Japan

1. Introduction

Micromachine is expected to have future potential applications in a wide range of industrial fields, such as machinery, plant maintenance and medical science. Actuator is one of the most important elements of micromachine technology. Therefore, many works relating the developments of actuator have been done[1][2]. However, at the moment, these actuators are not small enough for using in micromachine. From these points of view, the authors have developed a miniature linear actuator using piezoelectric elements. This paper describes the characteristics of this actuator.

2. Structure of Actuator

The principle of motion of the miniature linear actuator is shown diagrammatically in Fig.1. A slider is moved intermittently by controlling the motion timing of clamp actuators and a feeding actuator. In spite of the extension of piezoelectric elements is very small, the slider can be moved over long distance by repeating this sequence.

Figure 2 shows the structure of the actuator. As shown in Fig.2(a), a clamp actuator comprises a pair of the clamp head consisting of flexure hinges formed by wire cut EDM, and a piezoelectric element (PZT). The displacement of the piezoelectric element is magnified approximately 4 times by the flexure hinge and the tip of the clamp head is moved. In order to convert the force generated by the piezoelectric element into the gripping force effectively, the gap between the tip of the clamp head and the slider is adjusted to nearly

zero. Two piezoelectric elements are used as the feeding actuator and they are joined to the clamp actuators with epoxy resin. The clamp actuator and the slider are made of stainless steel and tungsten carbide respectively. The maximum extension of the piezoelectric elements for the clamp actuator and the feeding actuator are 6.5 μ m/100V and the maximum thrust force of them are are 140N/100V and 870N/100V respectively.

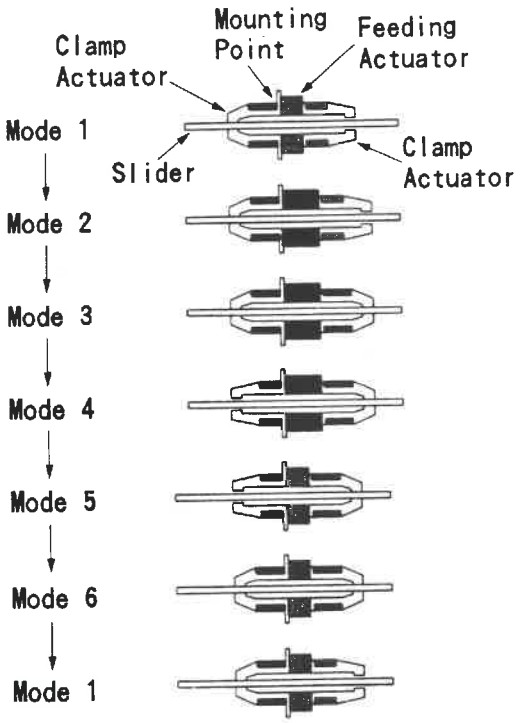

Fig.1 Principle of motion

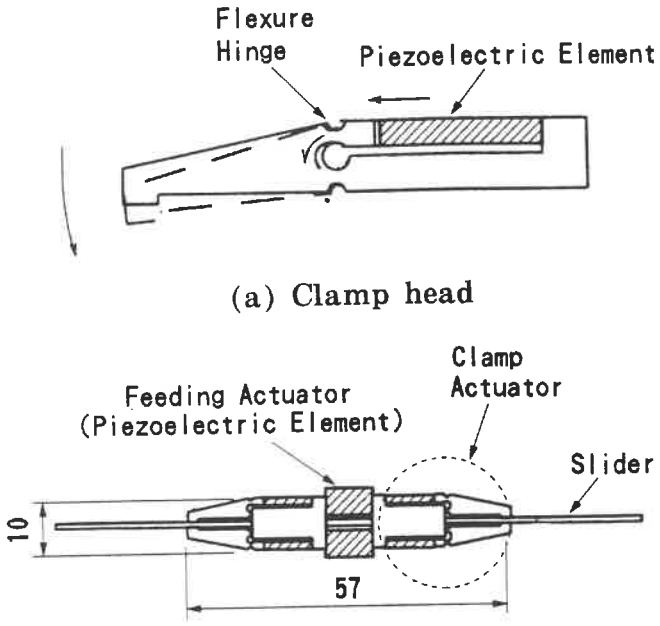

Fig.2 Structurer of miniature linear actuator

3. Characteristics of Actuator

The characteristics of the actuator was investigated experimentally. Figure 3 shows the schematic diagram of experimental setup. The voltage signals were output from a personal computer, and they were amplified by a high voltage amplifier and then supplied to the piezoelectric elements. As shown in Fig.3, the displacement of the slider was measured with a capacitance gage and a axial load was added to the slider by hanging a weight.

The motion of the slider at no load is shown in Fig.4. In this case, the slider was moved rightward and leftward 5 steps each, and a square-wave signal was furnished to each piezoelectric element for the clamp actuator and the feeding actuator. A step stated here is to carry out a sequence which is from mode 1 to mode 6 shown in Fig.1. The motion which the slider moves stepwise can be confirmed from Fig.4. Moreover, the maximum motion speed of the slider at no load was 2mm/sec, and the positioning resolution of the slider was 0.1μm.

Figure 5 indicates the relationship between the motion speed of the slider and the load, when the control frequency of the actuator was changed. One cycle of the control frequency is to move the slider one step; therefore, moving the slider one step for one second, the frequency is 1Hz. As can been

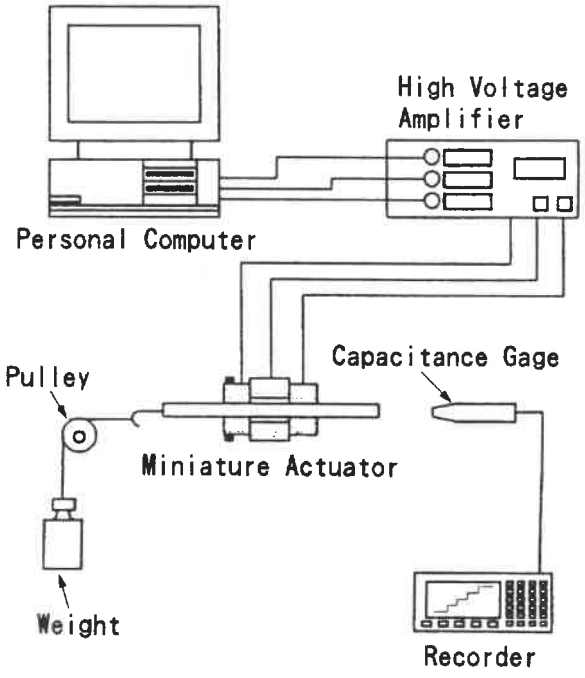

Fig.3 Schematic diagram of experimental setup

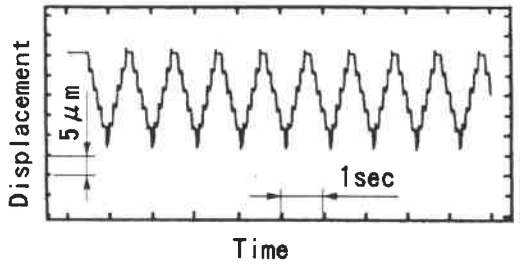

Fig.4 Motion of the slider

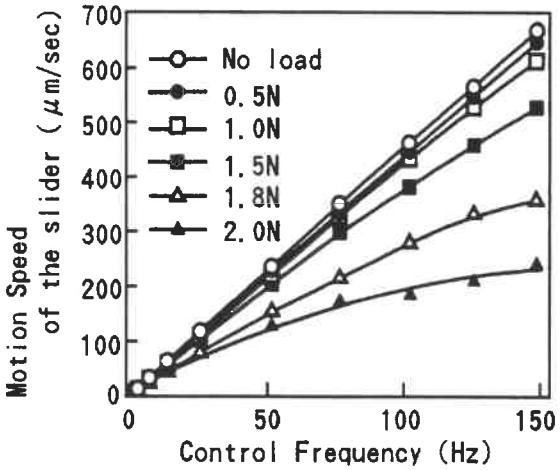

Fig.5 Relationship between motion speed of the slider and load

seen from Fig.5, the motion speeds below a load of 1N linearly rise with increasing frequency and they are nearly equal to the speed at no load. On the other hand, they tend to deviate from linearity with increasing frequency over a load of 1.5N. This decrease of the motion speed with increasing load is due to the slip of the slider by adding a axial force. Furthermore, when the only clamp actuator of one side gripped the slider and a load was made gradually to increase, the axial load at which the slider begun to slip was 4.5N. In this case, this axial load equals the maximum thrust force which this miniature actuator can generate.

4. Conclusions

A miniature actuator using piezoelectric elements was developed. The maximum motion speed of the slider of this actuator is 2mm/sec and the positioning resolution of the slider is 0.1μ m. And also, the maximum thrust force which this actuator can generate is 4.5N. The mechanism of this actuator is suitable for miniaturization, so the development of much smaller one can be expected.

Acknowledgment

The authors would like to thank Mr.Hayashi, Mr.Sanda and Mr.Jinbo of Nanoh Industry Co.,Ltd. for machining and assembling the actuator. We would also like to acknowledge the assistance of Mr.Ishida, Mr.Nakamura and Mr. Sekido who were students of Keio University.

References

[1]K.Ikuta, A.Kawahara and S.Yamazumi: Miniature Cybemetic Actuator Using Piezoelectric Device, Proceedings of IEEE, Micro Electro Mechanical Systems, IEEE Catalog No.91CH2957-9 (1991) 131.

[2]Z.Q.Zhu, B.Zhang and T.D.Howes: Design of Linear Piezomotor Positioning Apparatus for Precision Manufacturing Applications, Proceedings of ASPE Annual Meeting (1993) 472.

Metrology for Characterizing Actuators with Sub-atomic Repeatability

Alson E. Hatheway

Alson E. Hatheway Inc.
Suite 400
595 East Colorado Boulevard
Pasadena, California 91101
(818) 795-0514

The company has developed a line of precision actuators intended to facilitate atomic and sub-atomic research. The actuators are nominally linear and hysteresis free and only very slightly sensitive to temperature. These characteristics would allow the actuators to be operated "open-loop" if they can be verified by suitably rigorous metrology measurements. Since the repeatability of the actuators appears to be beyond the resolving power of optical interferometry, special metrology techniques have had to be developed. The techniques depend upon the application of classical mechanics to the design of position sensors and the use of contemporary precision metrology instruments for the actual measurement.

We have developed a technique and apparatus to demonstrate the repeatability and linearity of the actuators and to be able to study their detailed behavior.

Furthermore, the technique operates successfully under normal industrial conditions of heat, humidity, dust, etc. The metrology techniques will support not only our own research requirements mentioned above but make possible the re-calibration of our products by our customers, if they wish. The techniques may also be used by anyone who wishes to make similar precision measurements, for instance to be able to close a very high precision position control loop.

Our goal is to develop a metrology technique that will be stable to .1 angstrom over a period of ten minutes in a normal industrial environment. This will support solution to the metrology problems stipulated above.

The capacitance transducer technique was selected (over interferometry) because it has the capability of sensing sub-angstrom displacements, it has the potential of being relatively inexpensive and the environmental influences can be mitigated by the design of the capacitance transducer.

High resolution capacitance measurement is provided by an Andeen-Hagerling ultra-precision capacitance bridge, Model 2500A with Option E, (Andeen-Hagerling, Inc., Cleveland, Ohio). A custom-designed parallel plate capacitor transducer (Alson E. Hatheway Inc., Pasadena,

California) is designed to operate in the most effective regime of the bridge (about 40 pf to 80 pf for our purposes). This combination has a resolution of about .01 angstroms in the air gap.

The capacitor transducer is designed to mitigate the environmental influences that interfere with accurate measurement:

Temperature and humidity effects are both mitigated by the design of the capacitor. The thermal influence is less than fifteen angstroms per degree Celsius with a time constant of about seven minutes.

Humidity has two influences on the capacitance transducer. First, a change in the atmospheric composition of the air will cause a change in the permittivity of the air gap. This influence is about two angstroms per point of relative humidity (at 19 degrees Celsius) with a time constant of a few seconds. Second, humidity causes dimensional changes in the adhesives, an effect that has an influence of about six angstroms per point of relative humidity with a time constant of about eight days.

Dust is accommodated by design. The air gap is large enough (about fifty microns) that invisible particulates will not be large enough to interfere with the kinematics of the transducer. Visual inspection is able to assure sufficient cleanliness for operation.

Electromagnetic interference is suppressed by the small air gap and shielding features at the electrical interconnections. The apparatus is enclosed in a small metal enclosure.

We also account for sources of error in the equipment itself, notably the elastic forces from electrical connections to the capacitors and the triboelectric effects in the coaxial cables:

The elastic forces created by the connecting wires are minimized by using #30 AWG wire for the electrical connection and providing a generous service loop for strain relief. The diameter of the wire (.01003 inches) is so small with respect to the proportions of the capacitors and actuators (typically 1.0 inches) that its stiffness is about one millionth of theirs. Over the full range the wire contributes an uncertainty of about .01 angstrom. The metal enclosure shields the wire loops from electromagnetic interference.

The triboelectric effects inside the cables occur when the plastic insulation slides along the electrical conductors. The effect is a maximum just after the cables have been disturbed or bent and may amount to a few hundred angstroms of uncertainty. As the cables relax the triboelectric effect subsides. It appears to have a time constant of several days.

By careful design of the equipment it has been possible to minimize and mitigate both external interferences and internal sources of error in our apparatus. Figure 1 shows a typical twenty-four hour cycle of influences on the metrology equipment readings. The maximum deviation from all sources is about four hundred and seventy-five angstroms, peak-to-valley, and the maximum slope varies from 1.5 to 35 angstroms drift in a ten minute period.

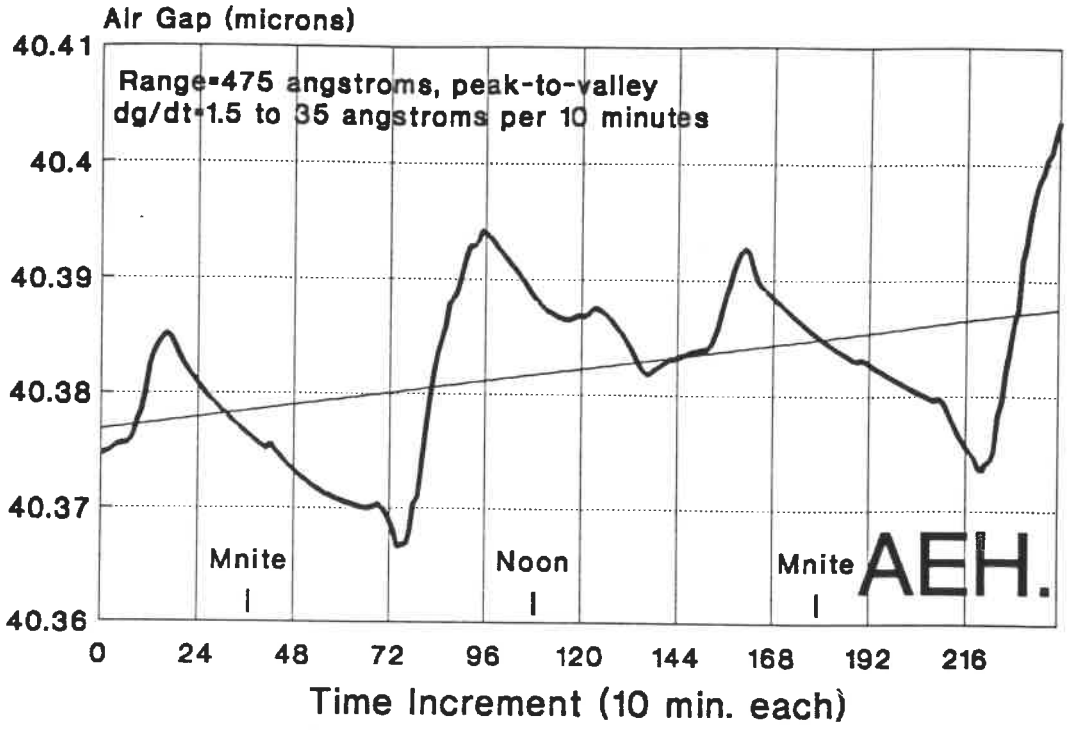

Figure 1. Environmental Influences on the Apparent Air Gap in the Capacitor Transducer.

Performing measurements during the quiet periods of the daily cycle has permitted us to obtain reasonably good behavioral data. A complete hysteresis loop, up and back, is shown in Figure 2. Subtracting from these data a best-fit straight line produces the data presented in Figure 3 which represent the differences between the test data and the straight line (residuals). The 1.073 angstrom amplitude of repeatability is very close to the limit of resolution of the actuator's drive micrometer; direct reading of the micrometer offers a resolution of 1.0 nanometer, but interpolation using the thimble's vernier scale offers another order of magnitude reduction in the practical resolution, to 1.0 angstrom. Therefore it is apparent that the curves displayed in the residuals are characteristics of the actuator that are apparent only at the angstrom level of observation. These data also confirm the excellent open-loop repeatability of this simple actuator system.

We have not yet reached our stability goal of .1 angstrom repeatability over ten minutes but anticipate that as we work with our present apparatus and continue to implement refinements and improvements it will improve by another order of magnitude. Meanwhile we are able to make useful investigations into the detailed characteristics of our actuators.

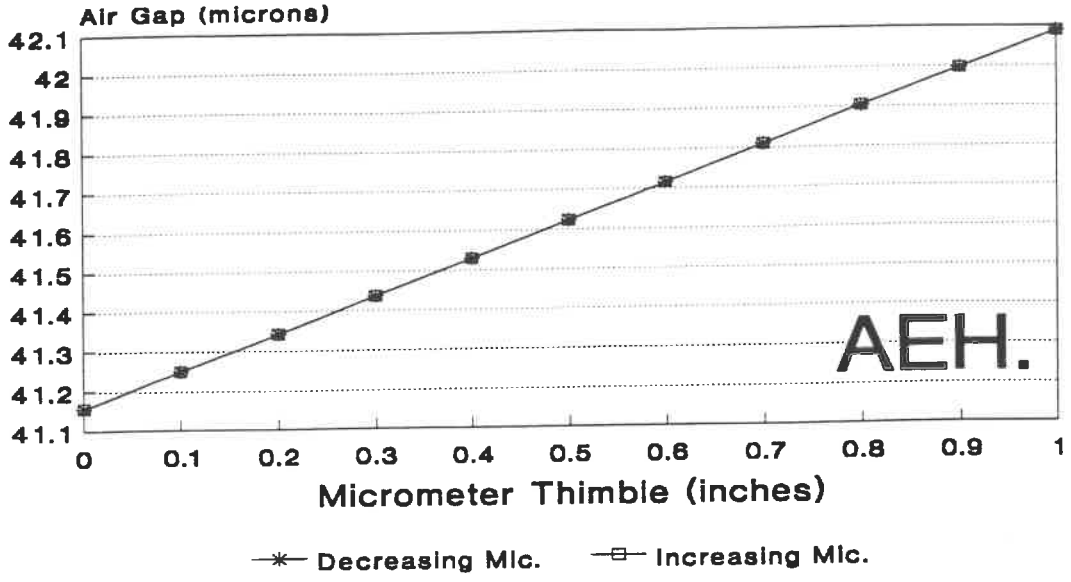

Figure 2. Open-Loop Hysteresis for a Model 1000-1 Angstrom™ Actuator.

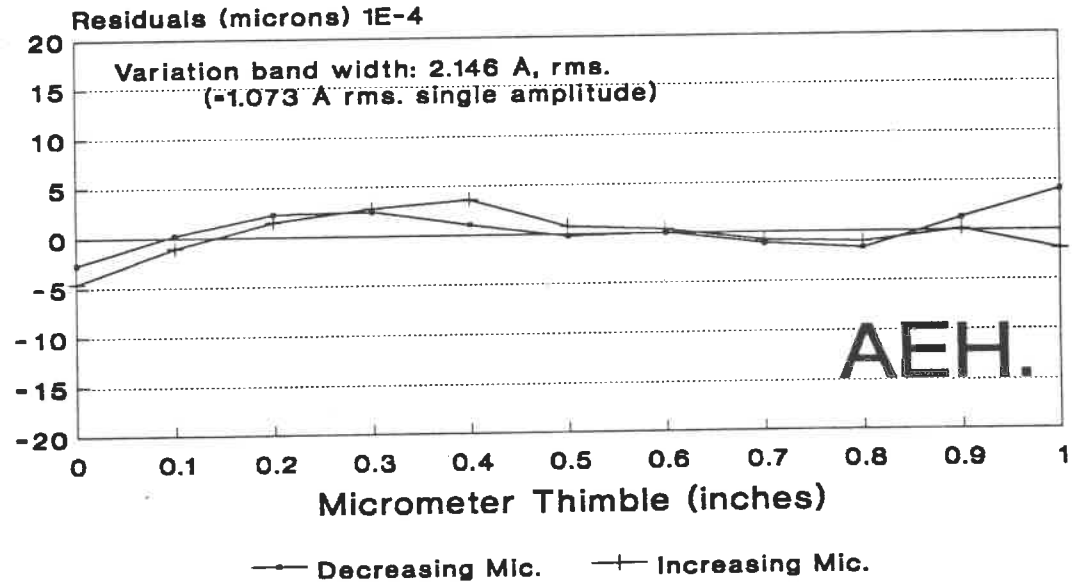

Figure 3. Deviations from Linearity for a Model 1000-1 Angstrom™ Actuator.

DEVELOPMENT OF AN AUTOMATIC FIXTURING DESIGN SYSTEM

Keigo IKEZOE, Tojiro AOYAMA
Faculty of Science and Technology, Department of Mechanical Engineering
Keio University, 3-14-1 Hiyoshi, Kohoku-ku, Yokohama, 223, JAPAN

1. Introduction

Workpiece fixturing process has been automated only in the mass production area. In the usual small-lot production area, workpiece fixturing is carried out by manual operation depending on machine tool operator's skill and experiences. To realize the intelligent manufacturing system in next generation, automating of fixturing process has been demanded. The key factors for automating of fixturing process are fixture design, flexible fixturing devices, fixturing inspection and so on. Among these constituents, fixture design particularly does not lend itself to computerization due to extensive requirements of heuristic knowledge and experience of machine tool operators.

In this research, we developed an automatic fixture design system which infers clamping, locating and supporting points to instruct a method of fixturing to the operators.

2. Principles of Fixturing Design

Fixturing design depends on a large number of factors such as:

(1) Shape and state of the workpiece,
(2) Pre-machined surfaces and tolerances,
(3) Type of operations and the machine tools used,
(4) Safety considerations,
(5) Chip removal

Some of which can be determined logically, but "Safety" for instance may be a delicate area to incorporate completely into the algorithm without the judgment of a skilled tool designer [1]. In this research, a learning system is proposed to solve such intuitive problems.

3. The Components of the Proposed System

The proposed system is consisted of three modules (Fig. 1). First one is a form identifier which identifies the form of a workpiece from a 3D-CAD data. The following module is an inference engine which infers a fixturing method from the output of form identifier, a machining information and datum faces (pre-machined surfaces). The last module provides a learning function which learns the heuristic knowledge of skilled workers in fixturing design process.

4. The Form Identifier

The workpiece form is identified by dividing it into small cubic blocks in an imaginary space (Fig. 2). The cubic blocks are classified into 3 or more types relevant to fixture design (Table. 1). Some blocks are including a corner of workpiece, some are including an edge or a surface of the workpiece and so on. The blocks which are able to be nominated as clamping points are restricted to the blocks including a top surface (block No.11 in Table. 1). The candidates of locating point are

restricted to blocks including a side or a face (block No.12, 14, 15 and 16). The candidates of supporting point are also restricted to blocks including a bottom surface (block No.13). The blocks including a corner or an edge of workpiece provide some useful information for the determination of clamping points. Furthermore, each of the blocks has an information relevant to the geometrical characteristics of the workpiece.

5. The Inference Engine

The fitness as the fixturing point is evaluated for all nominated blocks by the fitness values proposed in this research as follows:

(1) Pmaxc : given to the blocks which locate nearby an edge of the workpiece
(2) Pc : the fitness values of blocks which locate one block away from an edge of the workpiece are reduced by Pc
(3) Pmaxh : given to the blocks which locate near by an datum face
(4) Ph : the fitness values of blocks which locate one block upper than the datum face are reduced by Ph
(5) Pma :the fitness values of blocks which locate near by the machining area are reduced by Pma
(6) Pdat : given to the blocks which locate just over the datum faces
(7) Pdist : given to the blocks according to the average of distances from current clamps

These fitness values are set up on the basis of factors for fixture design expressed in chap.2. For example, the fitness value (5) Pma is set up on the basis of Machining operation and Chip removal, (6) Pdat is arranged from the view point of factor pre-machined surfaces and so on. More than 40 different fitness values are proposed for the determination of clamping points. The decision process of blocks for clamping is summarized in Fig.3. The clamping point is determined on the basis of the sum of the fitness values which are given to each block depending on the situation. According to this manner, the method of fixturing and the locations of clamping devices (i.e., clamps, locaters and supports) are proposed.

6. The Learning System

The locations of clamping devices are proposed according to the above explained manner. However, there is possibility that the system proposes unexpected locations due to the incorrect arrangement of fitness values.

These problems can be solved by implementing the learning function which can revise the fitness values respecting the idea of skilled workers. The structure of proposed learning system is illustrated in Fig.4. If the inference engine proposed unexpected locations by the reasoning as before, a skilled worker indicates the correct locations of fixture devices to the learning system. The system constructs the database which is a file including fixturing rules indicated by skilled workers. Using the database, the learning engine renews the fitness values to correct the arrangement of them.

7. Execution and Evaluation

The geometric information of a workpiece required for this system are extracted from the 3D-CAD data. The other inputs are machining process plans (operation lists) such as the type and

the area of machining on the workpiece and the faces selected for datums. The final output of the proposed system represents an appearance of fixture assembly with computer graphics and cartesian coordinates of clamping, locating and supporting points. The proposed fixture design system indicates the location of fixtures reliably keeping away from the machining area in order to suppress the interfacing with the cutter pass during machining (Fig.5).

8. Conclusion

A new procedure for automating of fixturing design process is proposed. Applying the procedure, an automatic fixturing design system was developed. Proceeding to be applicable to the requirements of industry is the subject for a future study.

Reference

[1] Nee, A. Y. C., N. Bhattacharyya, and A. N., Poo, : *APPLYING AI IN JIGS AND FIXTURES DESIGN*, Robotics and Computer Integrated Manufacturing Vol.3, No,2. pp.195-201, 1987.

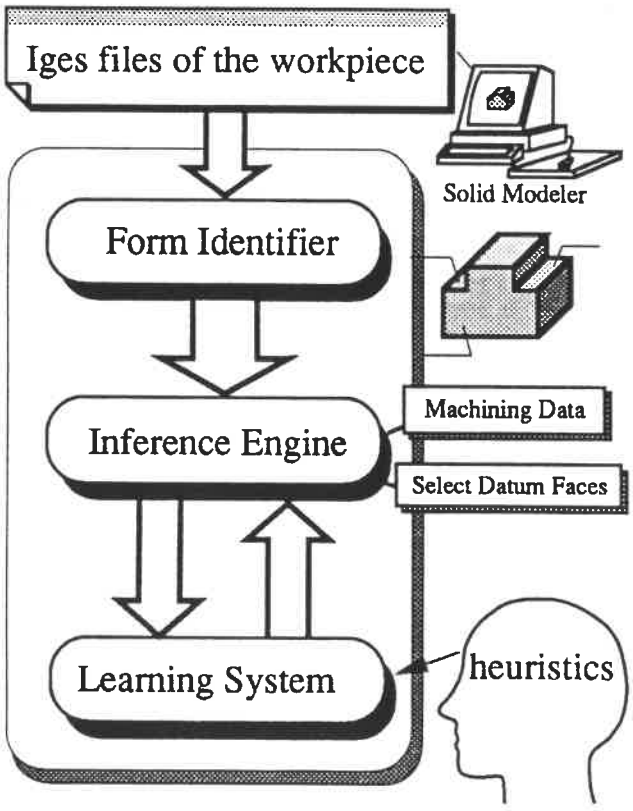

Fig.1 The components of an automatic fixturing design system

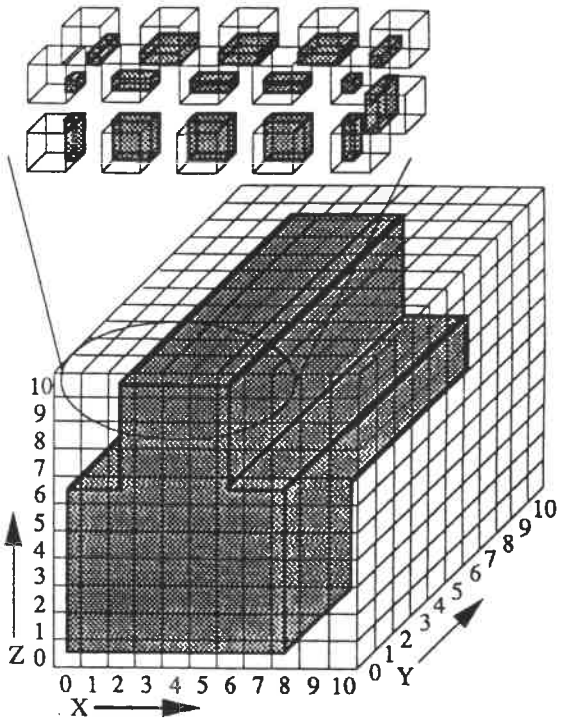

Fig.2 The workpiece divided into cubic blocks

Table.1 Patterns of blocks including part of workpiece

	1	2	3	4	5	6	7	8
10								
20								
30								
40								
50								
	0	1	3	4				

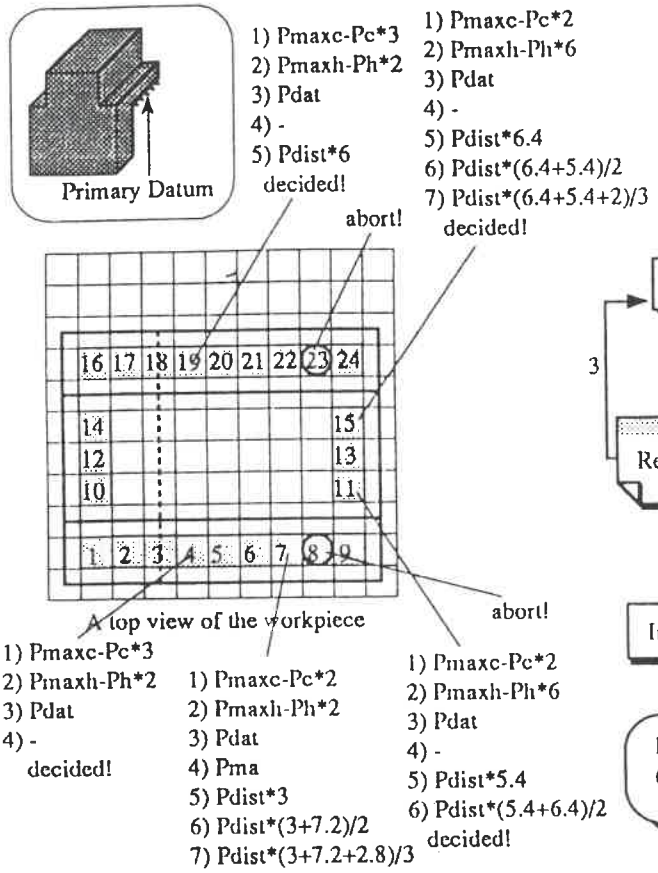

Fig.3 Process of decision of blocks to be clamped

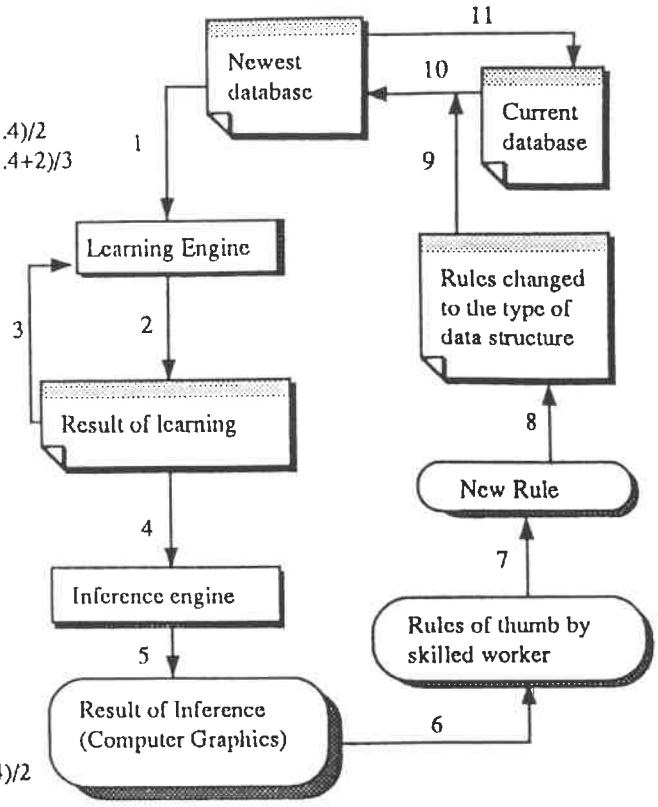

Fig. 4 Structure of learning system

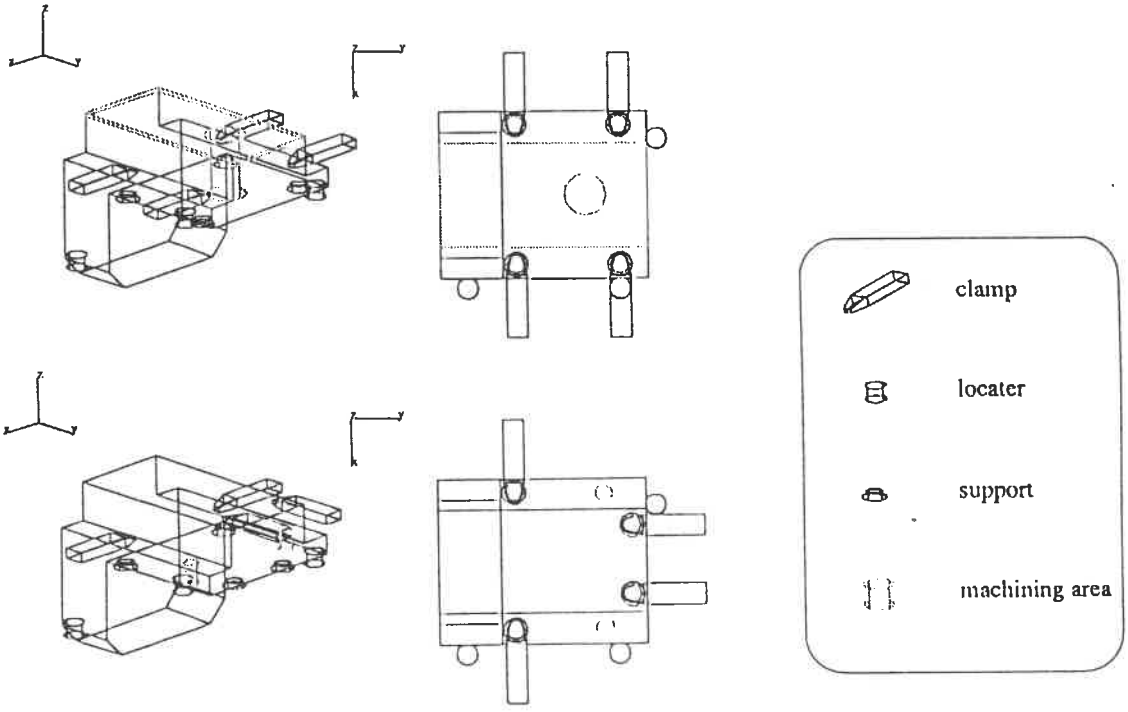

Fig.5 Examples of final outputs of an automatic fixturing design system

An Intelligent Positioner Realizing Precise Positioning and a Wide Working Range through an Internal Monitoring System

Masayuki NAKAO, Yotaro HATAMURA, Shuji TANAKA
The University of Tokyo, Faculty of Engineering, Department of Engineering Synthesis,
Hongo 7-3-1, Bunkyo-ku, Tokyo, 113 Japan
Munemori WATANABE, Kazushi KANEKO
THK Co.,Ltd. Nisi-Gotanda 3-11-6, Shinagawa-ku, Tokyo, 141 Japan

Abstract

In order to simultaneously realize precise positioning, high resolution, and a wide working range, the authors developed an intelligent positioner. Through an intelligent control system and an internal monitoring system, this positioner controls a ball screw and a piezo element that has high position repeatability. Using information from sensors and knowledge about positioning error, the positioner compensates for positioning error caused by external force, thermal deformation, and machining error in real time. The positioner successfully realized precise positioning of 0.3 μm, resolution of 30 nm, infinite rigidity, and temperature insensitivity within a 5 mm working range.

1. Introduction

1.1 The required performances for a precise positioner

Some information devices such as a scanning tunneling microscope (STM) or other ultra-precision machines use a piezo element, which realizes high resolution of the order of 0.1 nm. However, one of its defects is a narrow working range of less than 300 μm even with the structure of levers.

In contrast to this, most manufacturing machines and translation devices use a ball screw or a linear motor, which realizes a wide working range of more than 100 mm, while having the defect of low resolution of the order of 0.1 μm.

Neither of them can realize higher precise positioning than their own resolution. For example, a ball screw of 4 mm in diameter, whose rigidity is no more than 10 N/μm, has positioning error of the order of 1 μm because of large deformation induced by external force. It also has large positioning error of about ± 4 μm because of machining error in grinding.

Thermal deformation of the base block on which a piezo element or a ball screw is mounted often prevents precise positioning. For example, a manufacturing machine has positioning error of its tool of more than 10 μm because of thermal deformation of its column and spindle, although its actuator has high resolution of 0.1 μm.[1]

Thus there is no actuator that simultaneously realize precise positioning, high resolution, and a wide working range. These performances are simultaneously required.

1.2 Proposal of an intelligent positioner

In order to solve the above problems, the authors proposed an "intelligent positioner". This positioner is composed of sensors, a computor, and actuators. This positioner aims at simultaneously realizing the following performances, a wide working range of 100 mm, high resolution of 10 nm, and precise positioning of 100 nm.

The authors designed, produced, and tested a prototype of this positioner. This paper introduce its performances through the design process.

2. Methods for the intelligent positioner

Ordinary positioners measure positioning error directly with a sensor installed outside themselves and are controlled to compensate for positioning error in closed-loop.

However, it is difficult to measure positioning error directly in practical use. In the case of manufacturing machines, for example, a work-piece or coolant often prevents a laser interferometer from measuring the position of a tool. Thermal deformation of the base block on which a laser interferometer or a linear scale is mounted, and deformation between a tool and a scale due to external force also prevent precise positioning measurement.

Thus, the authors adopted two new methods such as "intelligentization" and "internal monitoring" in order to obtain the above performances.

2.1 Intelligentization

The word "intelligentization" means that sensors detect physical quantities, a computer judges the present or future situation through knowledge obtained in prior learning, and actuators are driven using this

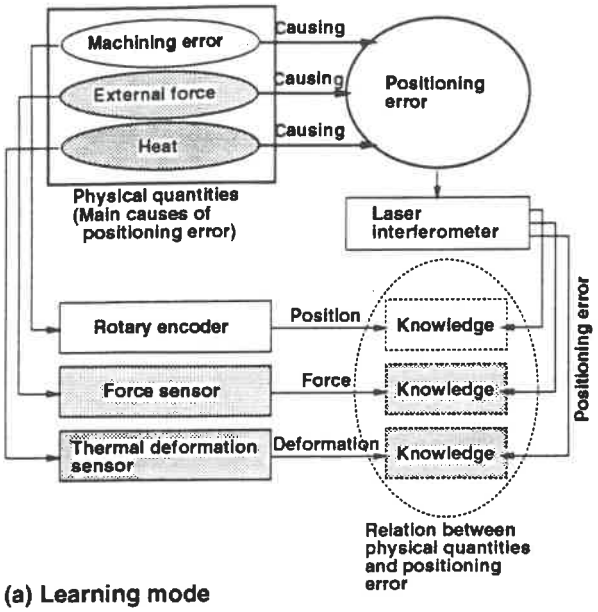

(a) Learning mode

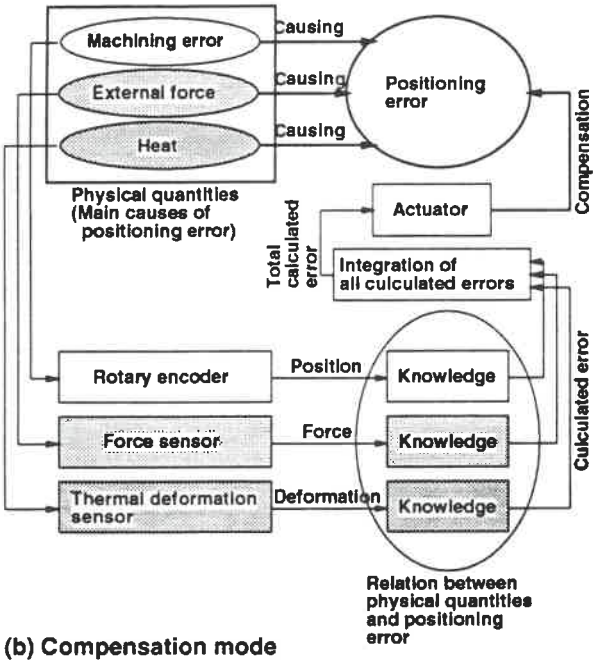

(b) Compensation mode

Fig.1 Fundamental structure of the compensation for positioning error through the intelligentization

judgement.

Figure 1 illustrates the fundamental structure of the compensation for positioning error through the intelligentization. As shown in Fig. 1(a), in a learning mode, the positioner memorizes knowledge about the relation between physical quantities and positioning error. As shown in Fig. 1(b), in a compensation mode, the actuator compensates for positioning error on the basis of the calculation of positioning error

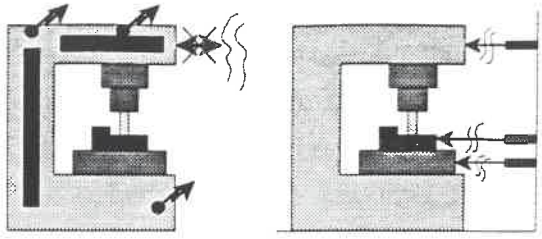

(a)Internal monitoring (b)External monitoring

Fig. 2 Internal monitoring and external monitoring

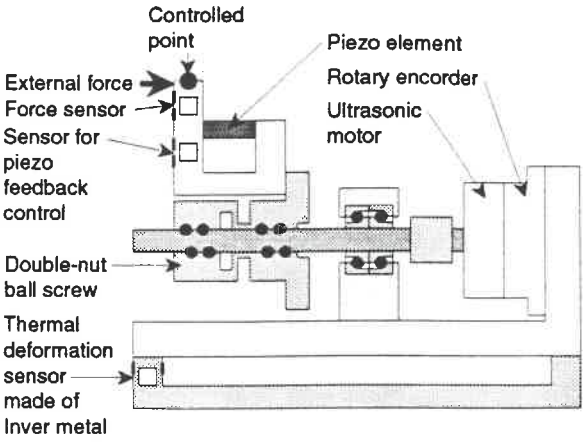

Fig.3 Structure of the intelligent positioner

using the previously learned knowledge. The positioner is controlled in open-loop, and a laser interferometer is used only for learning and evaluation, not for feedback control.

2.2 Internal monitoring

As shown in Fig. 2, internal monitoring is a method of measuring the situation of a device with its own sensors that have internal bench marks. On the other hand, external monitoring is that with sensors installed outside the device. This method is used in ordinary positioners. As discussed previously, it is usually difficult to measure positioning error directly by this method because of thermal deformation and deformation due to external force. Consequently the authors used the internal monitoring system.

3 Mechanism and structure of the intelligent actuator

Functional elements for measuring, judging, and driving are necessary for the intelligent positioner. The intelligent positioner consists of 3 mechanism elements that correspond to the 3 functional elemants: measuring, judging, and driving. The three mechanism elements are sensors, actuators, and a

computer. The sensors measure external force, thermal deformation, and machining error. The actuators are a ballscrew and a piezo element, which are connected with each other in series. The computer previously memorizes knowledge about positioning error and judges the amount to be compensated for.

Figure 3 shows the structure of the intelligent positioner. The force sensor has parallel thin plates and strain gauges. As a result, it has small hysteresis and non-linearity of less than 2 %. The rated load is 5 N, and the rigidity is 1.4 N/μm.

The thermal deformation sensor has the same structure as that of the force sensor, and is made of Inver metal in order to measure the thermal deformation of the stainless base block of the positioner in a 105 mm span.

The rotary encoder has a limiting resolving angle of 0.025 degrees, which corresponds to the positional deviation of 70 nm at the controlled point.

The ballscrew has two nuts (THK Co.,Ltd. BNK-040, 4 mm in diameter, 1 mm in lead) connected with each other by thin plate springs to prevent backlash. As a result, the repeatability of positioning becomes less than 100 nm.

The piezo element (TOKIN Co.,Ltd. NLA 5 × 5 × 9) is feedback controlled with a displacement sensor placed parallel to the piezo element to eliminate non-linearity and hysteresis between input voltage and output displacement. As a result, the non-linearity and hysteresis become less than 1 %, and the repeatability of the displacement decreases to about 5 nm.[2]

4 Evaluation of the intelligent actuator

4.1 The method of evaluation

A laser interferometer (ZYGO Co. AXIOM2/20, 2.5 nm in the maximum resolution) was used to measure the position of the positioner for learning and evaluation. Weights were used to give external force of up to 1.2 N in the feed direction, and a constant temperature oven was used to uniformly apply heat up to 35 °C. The vibration at the place where the positioner was located was about 50 nm p-p.

4.2 Result of the evaluation

Figure 4 shows the positioning error under the condition that the actuator moved a total of 5 mm at 1,389 nm intervals without external force or heat. The horizontal axis represents the nominal position culculated from the value of the rotary encoder. The vertical axis represents the positional deviation between the nominal position and the position measured with the laser interferometer. The two curves indicate the controlled result and the uncontrolled result. The computer memorized the uncontrolled result as knowledge, and then used this knowledge to drive the piezo element in order to compensate for positioning error.

The large fluctuation of the uncontrolled curve was caused by the machining error of the ballscrew. The deflection was about ± 3 μm, and the cycle was 1 mm, which is equal to the lead of the ballscrew. The impulse of the controlled curve of about 0.3 μm was caused by the shock which occurred when the balls return from the returner to the nut groove. The control cancelled the machining error and reduced the positioning error of ± 3 μm to ± 0.3 μ m.

Figure 5 shows the relation between external force and positional deviation under the conditions of no motor rotation, no heat, and external force change in the feed direction.

The two straight lines indicate the controlled result and the uncontrolled result. Through compensational control of external force, the rigidity of the actuator increased from

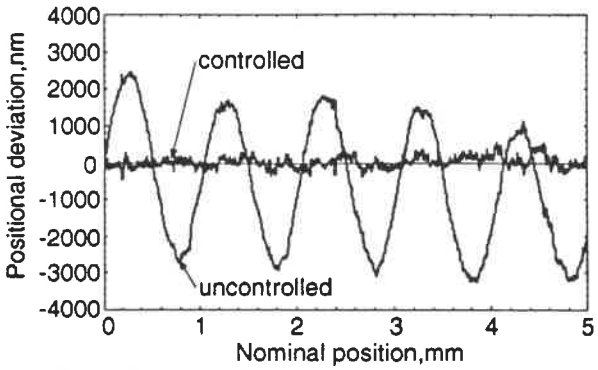

Fig. 4 Relation between nominal position and positional deviation

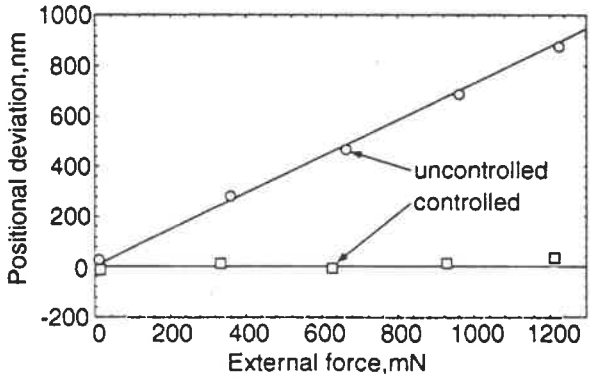

Fig. 5 Relation between external force and positional deviation

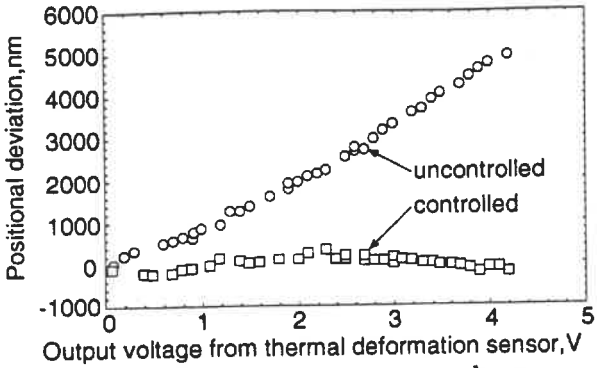

Fig. 6 Relation between output voltage from thermal deformation sensor and positional deviation

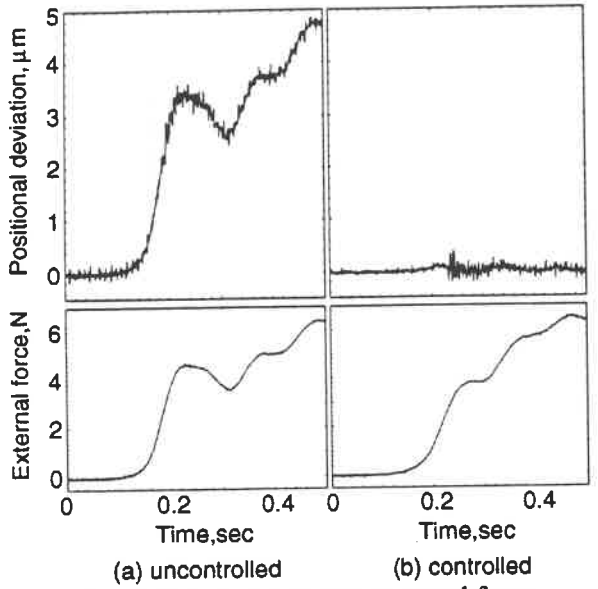

Fig. 7 Relation between external force and positional deviation

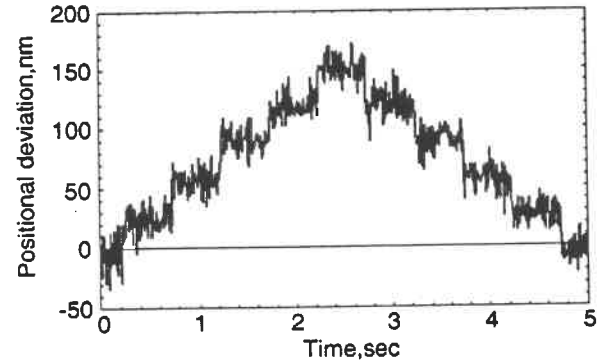

Fig. 8 Relation between time and positional deviation

1.4 N/μm (equal to the rigidity of the force sensor) to almost infinite.

Figure 6 shows the relation between output voltage from the thermal deformation sensor and positional deviation under the conditions of no motor rotation, no external force, and 4 degrees temperature change. The square symbols indicate the controlled result, and the circle ones indicate the uncontrolled result. Although positioning error of about 5 μm appeared in the uncontrolled mode, little positioning error appeared in the controlled mode. Through compensational control of thermal deformation, the sensitibity to temperature decreased from 1.3 μm/K to almost infinite.

Figure 7 shows dynamic positioning error under the conditions of no motor rotation, no heat, and external force change in the feed direction. Without control, the positioning error was proportional to external force, and became about 5 μm. However, with control, external force similar to the uncontrolled one caused vibration only as small as 0.3 μm p-p.

Figure 8 shows the resolution of the positioner. The maximum resolution was more than 30 nm. Because of the vibration of the place where the actuator was located, resolution of less than 30 nm was not observed clearly. The actuator returned to the same position as the start position after movement of 10 steps.

4.3 Evaluation of the total system

As a result of the above evaluation, the validity of the intelligentization and the internal monitoring, and the usefulness of the mechanism of the positioner were confirmed. If these 3 positioners are assembled, a 3-axis precise positioner can be realized.

5 Conclusion

The authors designed, produced, and tested the intelligent positioner that compensates external force, thermal deformation, and machining error through the intelligent control system and the internal monitoring system. The positioner successfully realized precise positioning of 0.3 μm, resolution of 30 nm, infinite rigidity, and temperature insensitivity within a 5 mm working range.

References

[1] Yotaro Hatamura et al., Development of an Intelligent Machining Center Incorporating Active Compensation for Thermal Distortion, Annals of the CIRP, vol 42/1/1993 pp549-552

[2] Yotaro Hatamura et al., Direct Coupling System between Nano-meter World and Human World, Proc. of MEMS 90, pp203-208

Application of Flexure-Hinges to Displacement Amplifiers for Piezo-Actuators

Wei Xu and Tim King
School of Manufacturing and Mechanical Engineering The University of Birmingham, Edgbaston, Birmingham, B15 2TT, UK

1 Introduction

The use of piezoelectric actuators can have many advantages over other actuator types, (e.g. electromagnetic or hydraulic) in many different areas such as clutching devices [1], high accuracy alignment devices for optical fibres [2], precision X-Y stages [3] and accurate mechanism drives. Although piezoelectric devices can provide large output forces, the typical 15 μm displacement of a stack type of actuator is not sufficient for the majority of general engineering applications, for which much larger movement ranges (0.05 to 0.5 mm or more) are typically required. As the flexure hinge has numerous advantages, such as smoothness of movement, no need of lubrication, zero backlash and high precision, in most cases the use of a flexure-hinged mechanical displacement amplifier is the most appropriate approach to enlarging the output displacement of the piezo-actuators.

Flexure-hinged displacement amplifiers are divided, for the purposes of this paper, into two groups; precision oriented and displacement oriented, according to their application. Three basic topologies of flexure-hinged structure are introduced which provide the elemental components of the majority of compound amplifiers and the performance of different flexure hinge profiles is studied, by using finite element methods, in terms of *flexibility* and *accuracy*. Finally, a brief summary is presented on the selection of hinge profiles for the two groups of applications.

2 Topologies of Hinged Displacement Amplifier

A variety of flexure-hinged displacement amplifier topologies have been studied for micro movement in the range up to approximately 50 μm [2, 3]. Fundamentally, they are compound amplifier topologies which combine three basic amplifying elements; *simple lever, bridge* and *four-bar linkage* amplifiers [4]. Assuming a *right-angle* hinge profile is used, a PC based designer program has been developed [5], which covers design of all three basic elements and facilitates the design and selection of amplifier topologies. The program accepts the geometrical and material parameters of both the piezo-actuator and the amplifier and generates a good approximation for the output displacement and force, and maximum stress data to assist in selecting an amplifier topology. To obtain more accurate performance predictions for precision oriented applications or when the hinge profile has to be considered, the use of FE methods is required.

Study of simple lever flexure-hinged displacement amplifiers shows that they can produce large output displacements. Since the movement is arcuate it may not, however, be suitable for some high precision applications requiring linear motion. The simple lever topology shows the highest efficiency because it uses less hinges than the other two topologies. Benefiting from a symmetrical structure, a bridge displacement amplifier has a higher gain and linear output motion which can be used for precision oriented applications. The four-bar linkage flexure-hinged amplifier can provide some special output movement for both precision and high-displacement oriented applications.

3 Geometrical Profile of the Hinge

Currently, the *right circular hinge* is the most common profile used in flexure-hinged displacement amplifiers, since analytical methods were developed to design circular and right circular hinges about

thirty years ago [6]. However, there is no analytical method available for other profiles, such as *elliptical* and *corner-filleted* ones. Therefore, finite element analysis methods have been employed here for these profiles.

In order to investigate the deflection and accuracy aspects of different hinge profiles, two groups of FE model have been created for analysis. The difference between the two groups is that one has elliptical hinge profiles (with varying minor axes) and the other has circular corner (fillets of varying radius). The right angle and right circular profiles may be regarded as limiting cases of both groups as illustrated in figure 1.

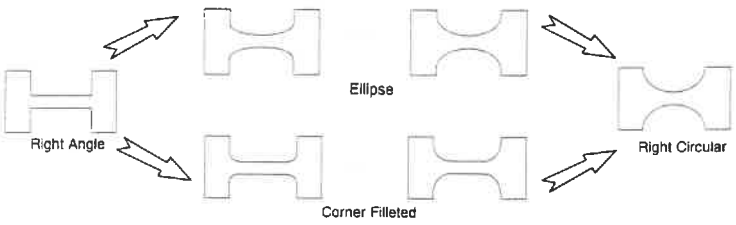

Figure 1 Two Groups of Hinge Profiles

The geometric configurations of the two groups of FE models are given in Table 1. Figure 2 shows a typical finite element meshed hinge model. Displacement restrictions are applied on the left edge of the model in all directions, but rotation movements are allowed. A 10 N force is applied on the centre node of the right edge.

Table 1 Geometric Configurations of FE Models

Hinge/Model Number	1	2	3	4	5	6
Ellipse (minor axis mm)	0	1	2	3	4	-
Corner-Filleted (radius mm)	0.5	1	2	-	4	5

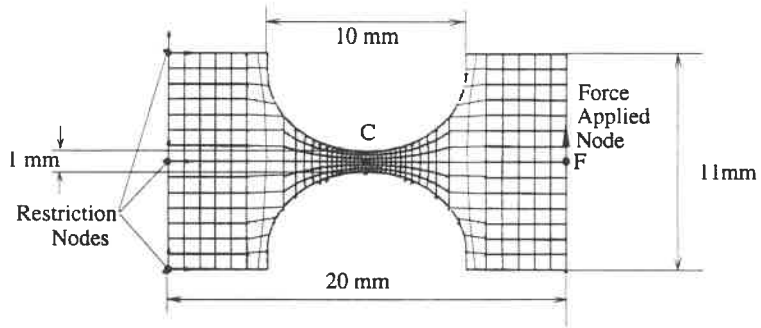

Figure 2 A Meshed FE Hinge Model Showing Boundary Conditions

FE analysis results are given in Tables 2 and 3, in the form of node displacements, for the two groups of hinge profiles. The displacement of two specially defined nodes (shown as *C* and *F* in fig. 2) are used to present two important performance characteristics of the hinges; their flexibility and their accuracy. The geometrical location of the special nodes is constant for all of the models. Node *C* is in the centre of the hinge. Node *F* is where the deflecting force is applied.

Table 2 FE Results of Elliptical Hinge Models

Hinge/Model Number	1	2	3	4	5	6
Centre Displacement (mm)	22.63×10^{-3}	6.77×10^{-3}	4.01×10^{-3}	2.88×10^{-3}	2.27×10^{-3}	-
Deflection (mm)	13.59×10^{-2}	6.50×10^{-2}	4.85×10^{-2}	4.07×10^{-2}	3.60×10^{-2}	-

Table 3 FE Results of Corner-filleted Hinge Models

Hinge/Model Number	1	2	3	4	5	6
Centre Displacement (mm)	19.40×10^{-3}	16.73×10^{-3}	11.58×10^{-3}	-	3.95×10^{-3}	1.87×10^{-3}
Deflection (mm)	12.52×10^{-2}	11.58×10^{-2}	9.54×10^{-2}	-	5.30×10^{-2}	3.25×10^{-2}

An ideal hinge should be able to move freely around its central point, but for a real flexure hinge, a force is required to deflect it. Obviously, a flexure hinge which needs less deflecting force has a higher flexibility. But however small a force is used to deflect a flexure hinge, it will offsets the centre of the hinge from its geometrical centre, as shown in Figure 3. This offset will affect the accuracy performance of the flexure hinge and have an effect on the displacement amplifier (of particular importance for precision oriented displacement amplifiers).

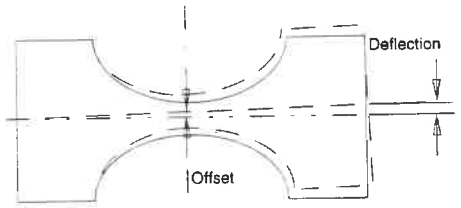

Figure 3 Offset and Deflection of a flexure hinge

In order to study the flexibility quantitatively, the deflection of the node at which the force is applied (Node *F*) is taken to characterise the flexibility of the hinge. The offset of the centre node *C* is used to characterise its accuracy. Figures 4a and 4b show the flexibility and accuracy of the two groups of hinges. They indicate that corner-filleted hinges have a higher flexibility than the elliptical ones when the minor axis of the ellipse is equal to the corner-fillet radius, but a lower accuracy. The general trend of the two groups are similar in that the flexibility increases with decreasing ellipse minor axis and corner-fillet radius, while the accuracy decreases.

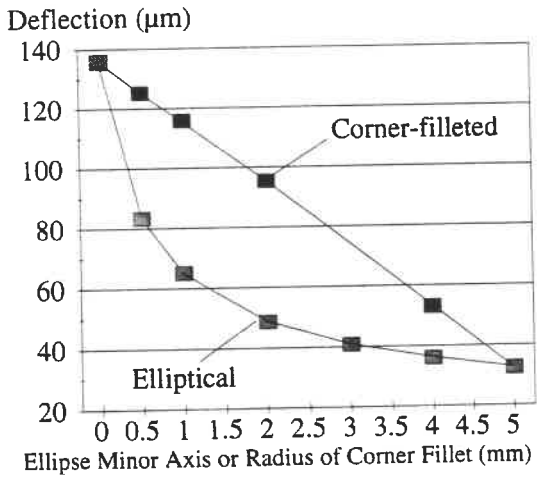

Figure 4a Flexibility of Elliptical and Corner-filleted Hinge Shapes

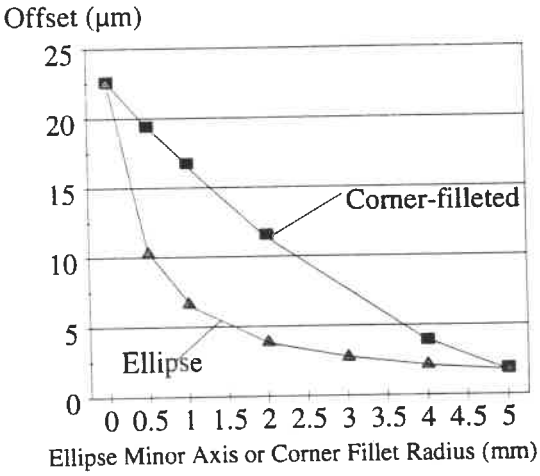

4b Accuracy of Elliptical and Corner-filleted Hinge Shapes

To compare the performance of the two groups of models, a *relative accuracy* is defined as the difference in offset between the two models when their deflections are equal. It can be achieved by finding the ellipse minor axis and the corner fillet radius which give the same deflection from fig. 4a and then reading the corresponding offset values from fig. 4b. Figure 5 shows the relative accuracy of two groups.

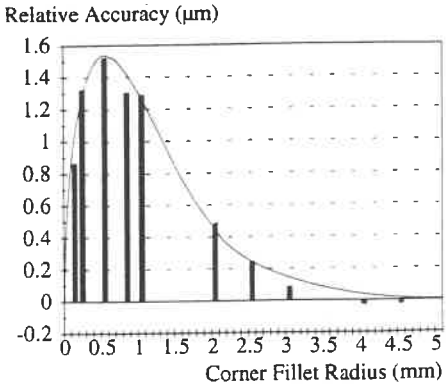

Figure 5 Relative Accuracy of Elliptical Hinge vs Corner-filleted Hinge

The relative accuracy in figure 5 shows a maximum point. It indicates that the corner-filleted hinge has its best relative accuracy compared with the elliptical hinge when the fillet radius is around 0.5 mm for the model dimensions used, i.e. around 5% of the hinge length. Since the relative accuracy values in fig. 5 are almost all positive it also indicates that corner filleted hinges may generally be considered superior to elliptical ones when compared in this way. It is, however, interesting to note the scale of this effect. The maximum point of the curve in fig. 5 represents a difference in offset of around 1.5μm. The absolute offset of either hinge type is around 13 times larger than this figure.

4 Summary

In summary, FE analysis of elliptical profile flexure hinges shows that, compared with the corner-filleted designs, they have a lower relative accuracy. Two special cases of corner-filleted hinge, the right circular and right angle types, have their own features. The right circular hinge profile has a high stiffness. It should be avoided for use in amplifiers for high displacement oriented applications, since it could reduce the achievable displacement of the amplifier very significantly. The right angle hinge, the other extreme case of the corner-filleted profile, has the lowest stiffness. It therefore appears attractive for high displacement oriented applications. However, from the points of view both of fatigue and manufacture, right angle hinges are not a practical possibility. Since the highest relative accuracy of corner-filleted hinge is obtained when the fillet radius approaches 5% of the hinge length, this may be a suitable starting point for further design optimisation.

References

[1] J Thornley, M Preston and T King, A Fast Electro-Mechanical Clutch Element Using a Piezoelectric Multilayer Actuator, Colloquium on Robot Actuators, Dig. Ref. 199/146, pp. 1-4.

[2] J Galvagni, Electrostrictive Actuators and Their Use in Optical Applications, Optical Engineering, Vol. 29, No. 11, 1389-1391, November, 1990.

[3] S Moriyama, T Harada and A Takanashi, Precision X-Y Stage with a Piezo-driven Fine-Table, Bull. Japan Society of Precision Engineering, Vol. 22, No. 1, pp. 13-14. March 1988.

[4] T King, W Xu and J Thornley, A Piezoelectric Harmonic Motor, Joint Hungarian-British Mechatronics Conference, September 21-23, 1994.

[5] W Xu, Piezoelectric Harmonic Motors: Construction Possibilities and Performance Characteristics, MPhil Thesis, School of Manufacturing and Mechanical Engineering, The University of Birmingham, May 1994.

[6] J M Paros and L Weisbord, How to Design Flexure Hinges, Machine Design, Vol. 37, pp. 151-156, November 25, 1965.

DESIGN AND MANUFACTURE OF A HYDROSTATIC BEARING FOR PRODUCTION PRECISION MACHINING

Vincent Delbrugge and William Hockenberger, *Precision Grinding and Manufacturing Corporation*, Rochester, NY 14606

Forrest Titcomb, *DevTek, Ltd.*, Suite 206, 304 S. 8th St., Colorado Springs, CO 80905

Selection of a bearing for machining precision components usually means exchanging load capacity for minimal error in the bearing. Maximum load capacity can be obtained with fluid lubricated hydrostatic bearings, which are not accurate in the micro inch range. Gas lubricated bearings, more commonly known as air bearings, have accuracy measured in fractions of a micro inch. However, air bearings do not have load capacities that are required for conventional finish machining operations.

A high stiffness hydrostatic fluid bearing is being designed and built for ultra precision production machining applications. The novelty of this design is the retention of stiffness and precision when machining conditions include the higher loads, speeds, and feeds typical in production environments. Loads that result from turning hardened tool steel were modelled for the hydrostatic bearing design. Successful design and manufacture of a precision hydrostatic bearing will increase productivity as a result of higher material removal rates, without sacrificing precision.

One of the major obstacles preventing liquid bearings from being as accurate as air bearings is due to the heat that is evolved during use. This heat, which is a function of the rotation speed of the bearing and the viscosity of the lubricating fluid, results in elastic deflections in the spindle. A cooling scheme that will maintain the thermal stability of the unit is still in the modelling stage.

The bearing is designed for application with commercially available tooling and machines. The presence of some of the tooling has significant effects on bearing loading conditions. For example, an air chuck mounted on the bearing face effectively increases the load that must be resolved by the bearing. This air chuck increases the length of the moment arm of the cutting force.

Flexibility with different types of drive systems is also part of the design. Drive mechanisms also contribute to the thermal effects on the system.

Work is presented that describes the methods used to design and build an ultra precision hydrostatic bearing that performs in the production environment previously described. Modelling variables include machining parameters, bearing materials and lubricants, coolant, and additional tooling. All available results will be summarized in the paper.

Application of the hydrostatic lubrication principle will also be extended to the design of a precision slide for use in machining centers.

Analyses of the Rotating Accuracy of Externally Pressurized Air Bearings Considering the Roundness Errors of Spindle and Bearing

Dong-Chul Han , Professor
Sang-Shin Park , Graduate Student

Institute of Advanced Machinery and Design
Seoul National University
San 56-1, Shilim-Dong, Kwanak-Ku, Seoul, KOREA

1. Introduction

The recent successful applications of externally pressurized gas-lubricated bearings for the high-precision spindles adapted for measuring instruments or machine tools are based on their excellent characteristics of running accuracy. The clearance of an air bearing is about 5 to 20 μm, but the roundness errors of shaft is 1 to 2 μm and that of bearing bore is 2 to 5 μm. So the machining error ratio to the bearing clearance can be about 10 to 20 percentage. As to the running accuracy of a rotor supported by a gas bearing, so-called "averaging effect" is well known, which means that the rotating accuracy is much better than the magnitude of machining errors of the rotor and the bearing. However, the theoretical studies on the relation between machining errors and running accuracy characteristics have scarcely been reported in the literature. Though Yabe[1] reported the relation between rotating accuracy and machining errors, he did not consider the hydrodynamic effects. Due to the lack of information on the run-out characteristics of the bearing, the manufacturing tolerances at the bearing design are usually determined primarily in view of the manufacturing level and cost. It is neccessary to calculate the effect of the machining errors on the running accuracy of the externally pressurized air bearings which includes the hydrodynamic effects.

In this paper, the run-out characteristics of a rotor supported by an externally pressurized air journal bearings are investigated theoretically about the relation between the orbit and the manufacturing errors such as roundness errors in rotor and bearing bore, in order to obtain a fundamental information for the precision design of a gas lubricated journal bearing.

2. Theoretical Model

Fig.1 shows schematics of externally pressurized air bearing system. In order to calculate the characteristics of the air bearing system, the Reynolds' equation must be solved. The Reynolds' equation for compressible fluid is as follows.[2]

$$\frac{\partial}{\partial X}\left(PH^3\frac{\partial P}{\partial X}\right)+\frac{\partial}{\partial Z}\left(PH^3\frac{\partial P}{\partial Z}\right)=\Lambda\frac{\partial(PH)}{\partial X}+2\Lambda\frac{\partial(PH)}{\partial \tau} \tag{1}$$

Assuming that the motion of the center of rotor shaft is very small in the vicinity of the steady state point, the perturbed Reynolds' equation is derived by perturbing the film thickness and the film pressure.

$$\nabla\cdot\left[\ P_oH_o^3\nabla P_o-\Lambda(P_oH_o)\right]\ =0 \tag{2}$$

$$\nabla\cdot\left[\ P_oH_o^3\nabla P_k+3P_oH_o^2H_k\nabla P_o+H_o^3P_k\nabla P_o-\Lambda(P_oH_k+P_kH_o)\right]\ =i2\Lambda(P_oH_k+P_kH_o) \tag{3}$$

where $k = x, y$ and $H_o = 1 - \cos(\theta - \phi)$, $H_x = -\cos\theta$, $H_y = -\sin\theta$.

Integrating the equation (2) and (3) along the lubricated surface which encompass the arbitrary point (i,j), then Gauss' divergence theorem is applied to obtain the line integral equation. The pressure and film thickness functions are assumed to be linear in the finite difference domain. Then by using a central difference method, the algebraic equation is obtained for each mesh point,. The dimensionless mass flow rate through the inherently compensated air supply restrictor is obraitned assuming the isentropic process for compressible fluid.[3] The perturbed mass flow rate equation can be obtained as in the perturbed Reynolds' equation. The authors have already published the detailed equations.[4]

The stiffness and damping coefficients can be obtained by integrating the solved P_k's over the bearing surface.

$$K_{ij} = \frac{k_{ij} \cdot C}{p_a \cdot B \cdot D} \tag{4}$$

$$D_{ij} = \frac{d_{ij} \cdot C \cdot \omega}{p_a \cdot B \cdot D} \quad , \quad i = x, y \ , j = x, y \tag{5}$$

Fig.2 is a schematic diagram considering the machining errors such as roundness errors. For a rotor supported by the air bearings, we supposed that it has no straightness error, but has only roundness error as shown in the figure. The roundness error functions are assumed to be sinusoidal. This function should be added to the air film height function in oreder to calculate the effect of the shape error on the characteristics of the bearings.

$$H = 1 - \cos(\theta - \phi) - H_s(\omega t) + H_b \tag{6}$$

where, $H_s(\omega t)$ is the roundness error of shaft and H_b is that of bearing.

After the film force, stiffness and damping coefficients are calculated, the equation of motion of rotor shaft center should be calculated in order to obtain the orbit of shaft center.

$$\begin{bmatrix} m & 0 \\ 0 & m \end{bmatrix} \{\ddot{u}\} + \begin{bmatrix} C_{XX} & C_{XY} \\ C_{YX} & C_{YY} \end{bmatrix} \{\dot{u}\} + \begin{bmatrix} K_{XX} & K_{XY} \\ K_{YX} & K_{YY} \end{bmatrix} \{u\} = \begin{Bmatrix} mu\omega^2 \sin(\omega t + \phi) - F_X \\ mu\omega^2 \cos(\omega t + \phi) + F_{st} - F_Y \end{Bmatrix} \tag{7}$$

The equation (7) can be solved applying Runge-Kutta method with initial conditions for x_o and y_o obtained at each static equilibrium point, and those for $\dot{x_o}$ and $\dot{y_o}$ are assumed to be zeroes. The dimensionless time interval $\Delta(\omega t)$ is set 750 per one revolution, i.e. $2\pi/750$. After the orbit of shaft center is obtained, the radius of orbit is set to be the radius of the circumscribed circle as in Fig.3.

3. Calculated results

The prescribed analytical methods are applied to an air bearing with its major dimensions, bearing width ratio to diameter $B/D = 80/100$, clearance $C = 20\mu m$, diameter of a feeding hole $d_s = 0.25\ mm$, and the mass of shaft $5\ Kg$. The supply restrictors are assumed to be located equidistantly with each other along the circumference.

Fig.4 and Fig.5 show the fluctuation of stiffness and damping coefficients during two revolutions. The fluctuation frequency is coincident with the geometric frequency of shaft. That means the fluctuated stiffness and damping coefficients can change the orbit of shaft center.

Fig.6 shows the orbit of the shaft whose roundness shapes are 3 lobe and 4 lobe when

the bearing has 4 supply holes. The diameter is larger than the ideal circular shaft. Fig.7 shows the orbit when the number of supply holes is 12. In this case, the upper orbit is when the shaft is elliptic and the bottom is when the bearing is elliptic. The diameter of the orbit when only the shaft has roundness errors is larger than when only the bearing has roundness errors. So the precision of shaft is more important than the precision of bearing.

Fig.7 shows the orbit radius according to the feeding parameters. The stiffness coefficients are maximized when the feeding parameter[4] is in 1 to 2. As you can see, the orbit radius is minimized at that region, about 10 nm. In this case, the roundness error is 2 μm, but the orbit radius is about 10 nm. So the avereging effect is verified theoretically.

4. Conclusion

In this paper, theoretical run-out characteristics of a rotor supported by an externally pressurized air journal bearing are discussed with relation to the machining errors of roundness in rotor and in bearing bore considering hydrodynamic effect. The stiffness and damping coefficents are fluctuated by the roundness and the orbit of shaft center is changed by the roundness errors. The precision of shaft is more important than the precision of bearing. And the averaging effect is verified theoretically.

Referece

1. Hiroshi Yabe, "Theoretical Investigation of Run-Out Characteristics of Externally Pressurized Gas Journal Bearing", Proc. 6th Int. Congress on Tribology, Vol. 4, Eurotrib'93, 1993.
2. Gross, W.A., ***Fluid Film Lubrication***, John Wiley & Sons, New York, 1980.
3. Sharpiro, A.H., ***The Dynamics and the Thermodynamics of Compressibility Fluid Flow***, Vol.1, the Ronald Press Company, New York, 1953.
4. Dong-Chul Han, Sang-Shin Park, Woo-Jung Kim, Jongwon Kim, "A Study on the Static and Dynamic Characteristics of Externally Pressurized Air Bearings", Proc. of ASPE 1992 Annual Meeting, pp.336-339.

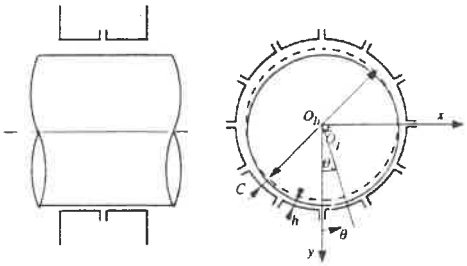

Fig.1 Shematics of bearing system

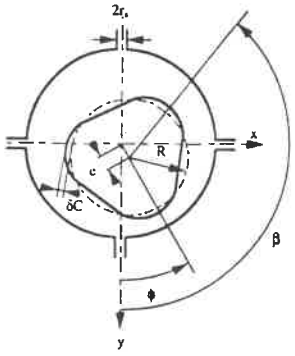

Fig.2 Shape error modelling

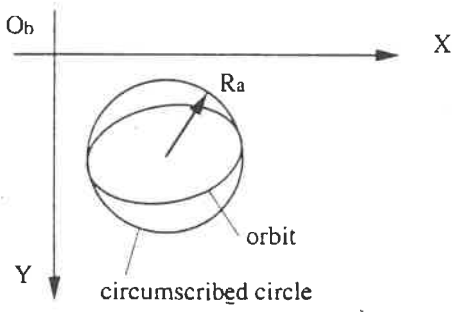

Fig.3 Definition of orbit radius

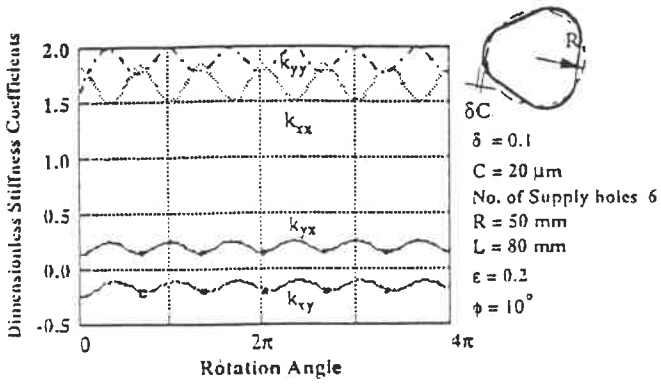

Fig.4 Fluctuation of stiffness

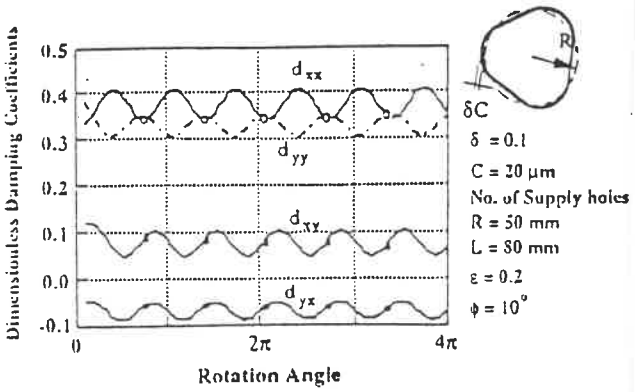

Fig.5 Fluctuation of damping

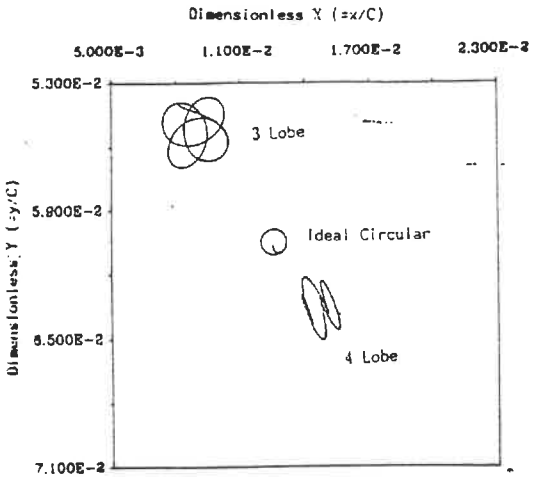

Fig.6 Rotational Orbit(Supply holes 4)

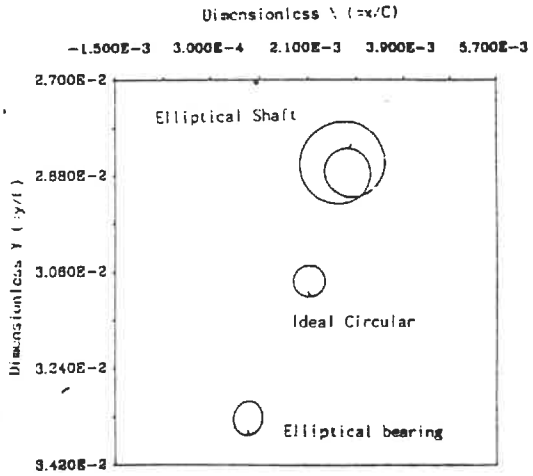

Fig.7 Rotational Orbit (supply holes 12)

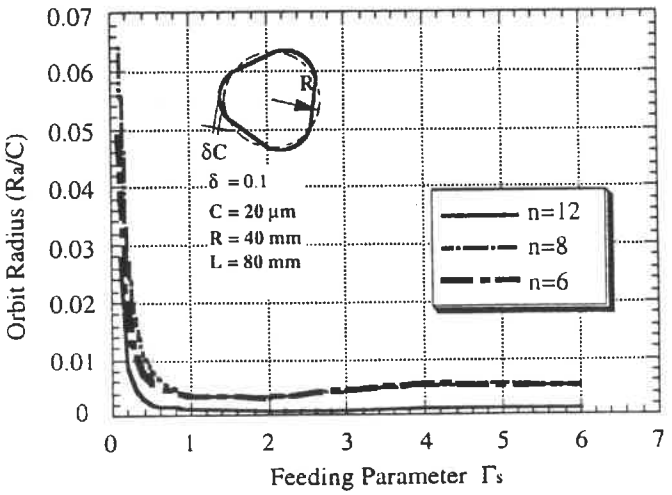

Fig.8 Orbit radius according to the feeding parameter

Experimental Analysis of Force-operated Feed Mechanism of Slide on Plain Bearing Guideways for Long Travel Range

J.Hisada*,A.Kanai**,and M.Miyashita**
*Niihama Research Laboratory,Sumitomo Heavy Industries,Ltd.
**Ashikaga Institute of Technology,268 Omae Ashikaga,Tochigi 326,Japan

1.Abstract

Forced-operated positioning servo mechanism has been assured to be characteristic of high feed resolution and high static and dynamic stiffness under frictional load of plain bearing guideways[1][2][3]. However, a feedback sensor applied to the servo system was a capacitive one and travel range of the test rig was limited up to 4 μm.
We made a new experimental test rig applied the proposed ultra-precision feed mechanism to confirm the positioning characteristics for longer travel range(100mm). This paper reports the following experimental results;
(1) stepwise positioning characteristics, (2) positioning accuracy, (3) pitching and yawing,
(4) static stiffness .

Keywords:positioning accuracy,ultraprecsion,feed mechanism,plain bearing guideways,linear actuator

2.Introduction

Dimensions of Si wafer, glass for liquid crystal,etc. recently become bigger and bigger and also their manufacturing tolerances are asked to be much more tight. For the demand of higher accuracy ductile mode processing based on motion copying principles instead of pressure copying principles like lapping or polishing has been presented. Processing based on motion copying is the one that directly controls the feed less than ductile-brittle transition value (d_c) of material and processes by the high accuracy motion of a machine. The d_c value of brittle material like Si, glass, etc. is known such as being less than submicron meter. Therefore it is required that the minimum step feed is to be 10nm to 1nm. Some methods which reduce the friction force have been design to achieve the positioning accuracy of submicron meter and air bearing has been adopted in many cases. But the positioning system is easily affected by the processing force or other disturbances due to low friction. As a method to solve the problem the high rigid drive system using plain bearing and force-operated hydraulic linear actuator has been developed.[1],[2],[3] We designed a 1(one)-axis fine positioning test rig which consists of force operated hydraulic linear actuator, slide with plain bearing, laser interferometer as a feedback sensor, and carried the experiments on positioning characteristics and static stiffness of the drive system. The testing is designed to give the slide's travel range of 100mm for application to the grinding wheel head slide mechanism.

3.Test rig

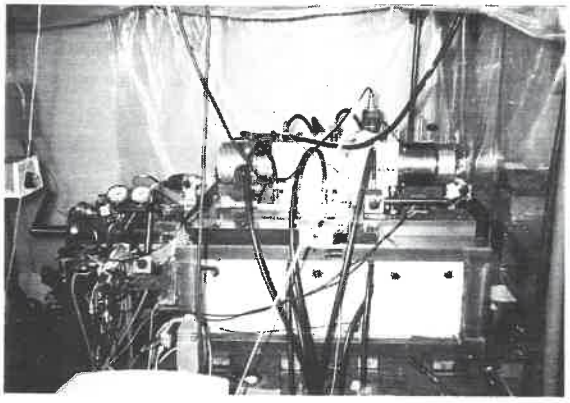

Fig.1 Photograph of Test Rig

Fig.1 shows Test Rig and Table 1 shows specification of the Test Rig.

Table 1 Specification of Test Rig

Slide Dimension	300×475 mm
Mass	abt. 180 kg
Guideways	Plain bearing (V-V type) applied antifriction coating
Travel range	100 mm
Feed speed	0～20 mm
Loading mass	95 kg
Servo valve & Actuator	Pressure control servo valve & Force-operted hydraulic linear actuator (C.D.100×R.D.40 mm)
Feedback sensor	He-Ne laser interferometer with 2.5 nm resolution

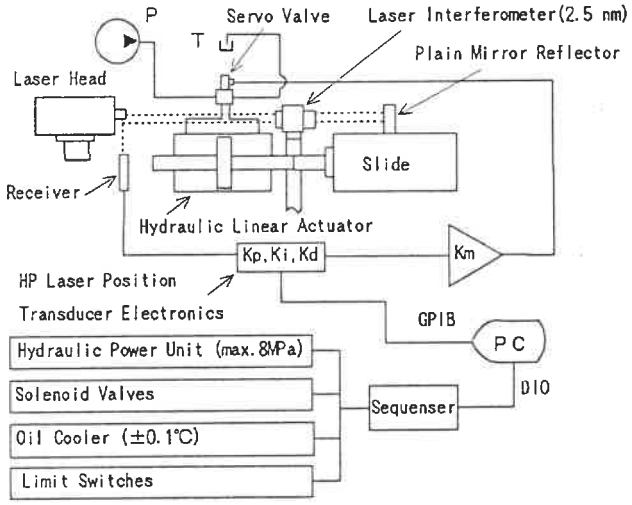

Fig.2 Control System of the Test Rig

As shown in Fig.2 the error signal between command signal from the computer and feedback signal from the laser position transducer of the laser system is fed back the hydraulic linear actuator through the servo valve, which positions the slide.

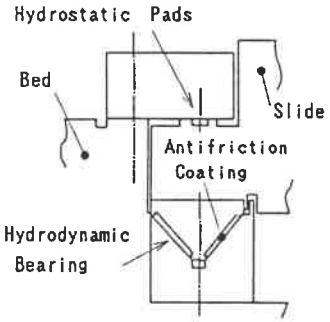

Fig.3 Guideways

Fig.3 shows the construction of the guideways. The contact pressure of the hydrodynamic bearing is kept at about 64 kPa by controlling the pressure of the hydrostatic pads placed independently against the bearings.

4.Experimental results

4.1 Fine Positioning

Fig. 4 and 5 show respectively the responses to the stepwise feed of 2.5 and 10nm. Fig.6 shows statistic analysis of each step's position data from laser position detect system. It is found that the test rig can feed well to even 2.5nm step at feedback sensor and deviation of position after settling is less than 9 nm in 3 σ and mean value is 1 nm to −3 nm. It is concluded that the positioning system is very stable in such a fine positioning.

4.2 Positioning Accuracy in Long Travel Range

Measurement was made at 5 target positions according to the test cycle shown in Fig. 7 based on ISO 230−2. Each target position was attained five times in each direction. 100 points of position data from the laser measuring system at each step where sampling time was about 10 msec are recorded and the positioning accuracy in mean value and deviation of 3σ is estimated. The Mean Unidirectional deviation was 2.5nm from Fig.8, the Mean reversal value (Lost motion) was 0.5nm from Fig.9, and the Accuracy was 6.3nm and the Repeatability was 4.9nm from Fig.10. It is concluded that the drive system has high stiffness because of no the Lost motion.

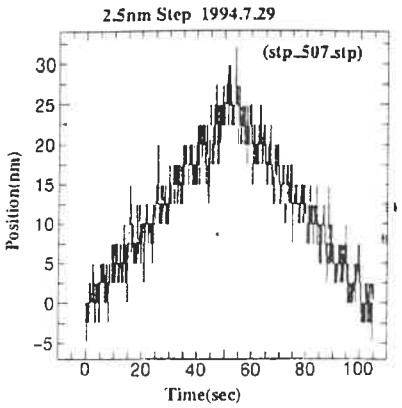

Fig.4 2.5nm Step Response

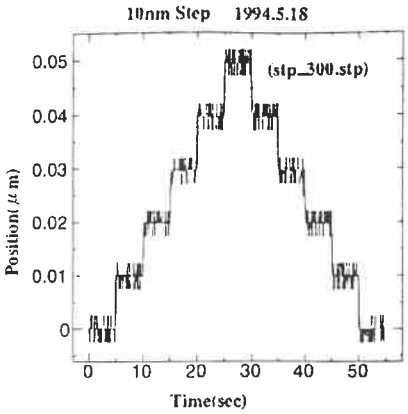

Fig.5 10nm Step Response

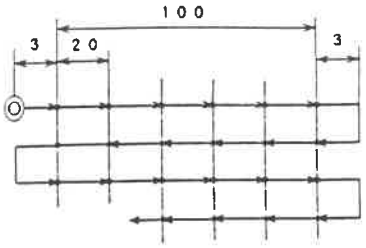

Fig. 7 Linear Cycle

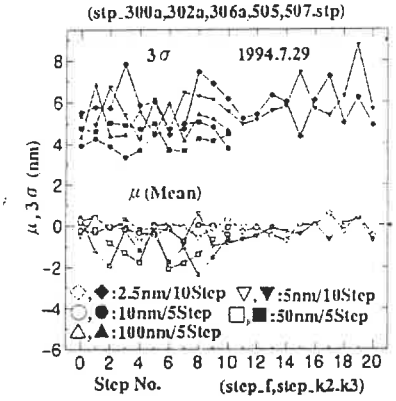

Fig.6 Statistic Analysis of Step Response

Fig.11 or 12 shows that the deviation is within about 14nm and the pitch error (average value) is within several nm even after five times reciprocating motion, and it is found the positioning is stable within uniform deviation in the + – direction. It took over 1 hour to measure the positioning accuracy. Those results shows test rig wasn't strongly affected by heat from hydraulic oil or environment due to oil cooler, material of slide,simple cover and air conditioning of the room. The hydraulic linear actuator and the plain bearings can be applicable to ultraprecision processing machine if proper countermeasurements will be considered for heat effects.

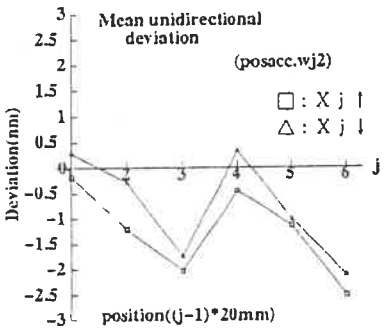

Fig.8 Mean Unidirectional Deviation

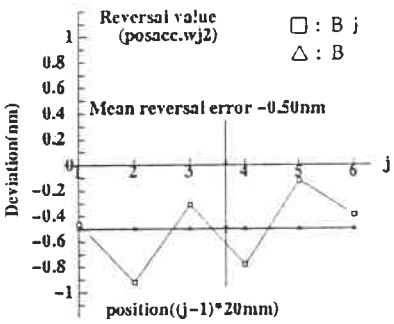

Fig.9 Reversal Value

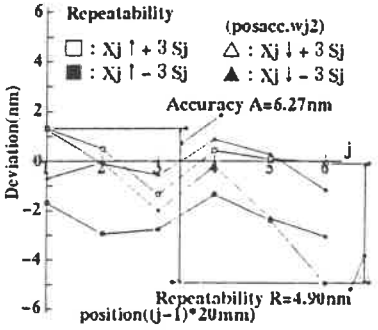

Fig.10 Repeatability

4.3 Motion Accuracy

Fig.13,14 shows respectively Pitching & Yawing Error in the + and – direction. The twist error of the V–V slideways measured with TALYVEL 4 (R.T.H.) indicated that the slide tends to go up twisting against the linear hydraulic actuator. Fig.13 and 14 also show the same tendency and the slide moves following the surface geometry of the slideways. The reason why the trace between + direction and – one is different is presumed the posture of motion changes because of the clearance or deformation by drive force of the slideways. Nevertheless, it is concluded that the high motion accuracy is achievable using the slideways shown in Fig.3.

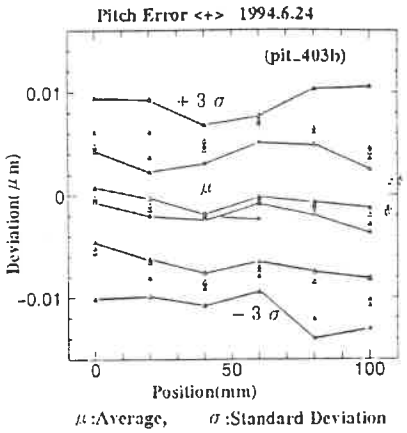

Fig.11 Statistic Analysis of Pitch Error (+)Direction

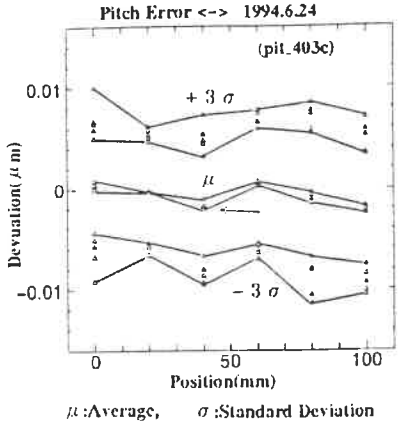

Fig.12 Statistic Analysis of Pitch Error (−)Direction

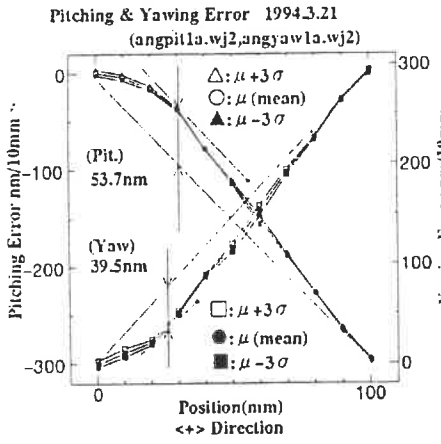

Fig.13 Pitching & Yawing Error (+) Direction

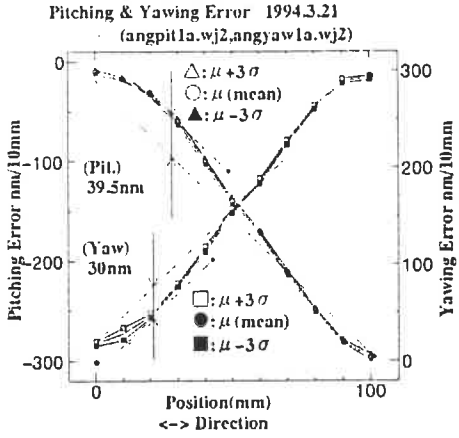

Fig.14 Pitching & Yawing (−) Direction

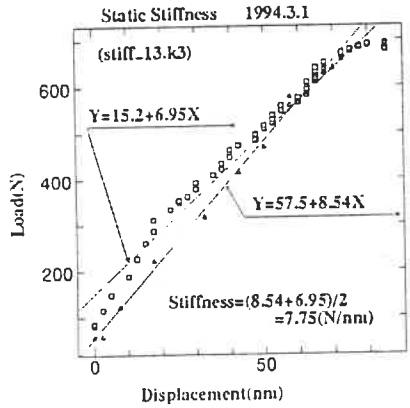

Fig.15 Static Stiffness

4.4 Static Stiffness of Drive System

The static stiffness is measured with the load cell and the capacitive sensor to plot the displacement to load curve. The capacitive sensor is located near to the base of the laser interferometer. Fig.15 shows the stiffness of 7.75 N/nm. The drive servo system involving the force-operated hydraulic actuator has a high stiffness against the plain bearing friction load and is applicable to ultra-precision processing machines.

5.Summary

(1)Positioning accuracy of the slide on the plain bearing guideways is achieved within several nanometers for relatively long travel of 100 mm by use of the force-operated hydraulic linear actuator by introducing the laser interferometer system.

(2)Pitching and yawing error kept within the geometrical datum error of the plain bearing guideways by controlling the contact pressure distribution with the by hydrostatic pads.

(3)High static stiffness of the drive system is achieved by the high power hydraulic actuator with the high pressure resolution in spite of its compactness.

6. References

(1)A.Kanai, S.Sano, M.Miyashita, J.Yoshioka, Ultraprecision Positioning System of the Order of 1nm, Proceedings of The 2nd Annual Meeting of ASPE(1987)

(2)A.Kanai, S.Sano, M.Miyashita, Nanotechnology No.2, 43(1991)

(3)A.Kanai, M.Miyashita, Y.Kishimoto, Experimental Analysis of Grinding Wheel Head Feed Mechanism on Plain Bearing Guideways with Force-operated Linear Actuator, Proceedings of 1994 Spring Topical Meeting of ASPE(1994)

Step Response Characteristics of Air-lubricated Slideways for Ultraprecision Machine Tools

Shigeo Kato
Nippon Institute of Technology
Miyashiro, Saitama 345, Japan

1. Introduction

Air-lubricated slideways have extremely precise straightness, because the movement of their wide sliding surface averages the precise guideway. Properly designed, these slideway can be produced with a high stiffness. They have thus used for the slideways of light cutting ultraprecision machine tools such as the diamond turning lathes.

However, the damping characteristics of air-lubricated slideways is poor, because the viscosity of the air is lower than the viscosity of spindle oil by a factor of about 10^{-3}. Indeed, for damping characteristics based on the viscosity of air alone, the damping ratio may be on the order of 10^{-3}. This small damping ratio is inappropriate for the slideways of the machine tools.

This study analyzes the damping characteristics of the air-lubricated slideway related to the damping force caused by the squeezing effect. The results are applied to the slideway of an ultraprecision machine tool, whose table has a mass of 1500 kg and static stiffness of 0.795 kN/μm.

It has been demonstrated by reverse Laplace transformation that a damping ratio is 0.078, the over-shoot by a step input is 71% and the vibration of the slideway can be damped to 48 ms according to the step response.

2. Dynamic stiffness of the air-lubricated slideway

A cross-section of the air-lubricated slideway is shown in Fig. 1. A table is suspended by some sliders. Air pressure, P_s is supplied to the slider. Clearance between the slider and the guide is H. Width and length of the slider are B and L, respectively. The slider has some orifice restrictors and recesses. Diameter of the orifices is d. Diameter and depth of the recesses are D and H_r, respectively. The pressure at the recesses is P_r. An effective area of the sliders is represented by A_e.

The dynamic stiffness of the slideway is shown as Eq. (1)[1]. In Eq. (1), ΔW and ΔH represent changes from equilibrium of weight and clearance of the slideway, respectively.

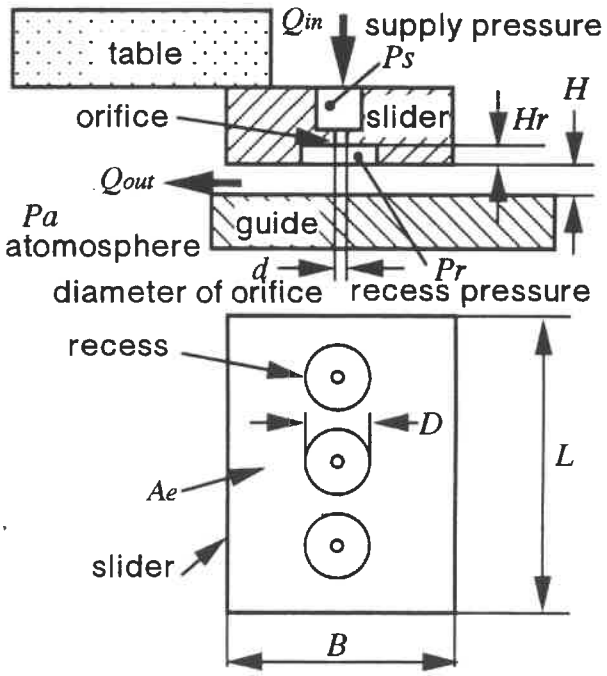

Fig. 1 Air-lubricated slideway

$$Kd = -\frac{\Delta W}{\Delta H} = Ae\left(\frac{Ps}{H}\right)\left(\frac{Pr}{Ps}\right)$$

$$\times \frac{\{\frac{\rho}{Q} vc \frac{(1+\frac{D}{B})}{2} s + (b_2 - b_1)\}}{[\frac{\rho}{nQ}\{vr + vc \frac{(1+\frac{D}{B})}{2}\}s + (a_2 - a_1)]} \quad (1)$$

This is based on the following conditions that ρ is air density at the recess, Q is mass flow rate in a state of equilibrium, vc $(=BLH)$ is the clearance volume, $vr\{=(\pi/4)D^2Hr\}$ is the recess volume, s is the Laplace variable, n is the polytropic exponent of air and is equal to 1.4.

Parameters of b_2, b_1, a_2 and a_1 of the air-lubricated slideway are shown in Eq. (2).

$$\left.\begin{array}{l} b_1 = 0,\ b_2 = 3, \\ a_1 = \left(\frac{Pr}{Ps}\right)\left\{\left(\frac{2}{\kappa}\right)\left(\frac{Pr}{Ps}\right)^{\frac{2-\kappa}{\kappa}} - \left(\frac{\kappa+1}{\kappa}\right)\left(\frac{Pr}{Ps}\right)^{\frac{1}{\kappa}}\right\} \quad \left(\frac{Pr}{Ps} > 0.528\right) \\ \quad = 0 \qquad\qquad \left(\frac{Pr}{Ps} \le 0.528\right) \\ a_2 = \frac{2\left(\frac{Ps}{Pa}\right)^2\left(\frac{Pr}{Ps}\right)^2}{\left\{\left(\frac{Ps}{Pa}\right)^2\left(\frac{Pr}{Ps}\right)^2 - 1\right\}} \end{array}\right\} \quad (2)$$

Now Kc which represents stiffness and $C2$ which represents damping coefficient are introduced.

$$Kc = Ae\left(\frac{Ps}{H}\right)\left(\frac{Pr}{Ps}\right)\frac{\{n\ vc \frac{(1+\frac{D}{B})}{2}\}}{\{vr + vc \frac{(1+\frac{D}{B})}{2}\}} \quad (3)$$

$$C2 = Ae\left(\frac{Ps}{H}\right)\left(\frac{Pr}{Ps}\right)\frac{\{\frac{\rho}{Q} vc \frac{(1+\frac{D}{B})}{2}\}}{(a_2 - a_1)} \quad (4)$$

We call Kc the compressible stiffness and $C2$ the damping coefficient due to the squeezing effect at the recess.

From Eqs. (1), (3), and (4), the dynamic stiffness Kd is represented as

$$Kd = Ks\frac{(\frac{C2}{Ks}s + 1)}{(\frac{C2}{Kc}s + 1)} = Ks + \frac{(1 - \frac{Ks}{Kc})}{(\frac{1}{Kc} + \frac{1}{C2\,s})} \quad (5)$$

The dynamic stiffnes Kd is shown in Fig. 2. In the Fig. 2, the lever ratio $l1:l2$ is the ratio of $Ks:Kc$.

3. Equation of motion of air-lubricated slideway

An equation of motion of the air-lubricated slideway is

$$m\ddot{x}(t) + Kd\ x(t) = f(t) \quad (6)$$

where m is the mass of a table which includes sliders of the slideway, $x(t)$ is the upward displacement of the table, and $f(t)$ is the outer force.

Next, two time constants are introduced.

$$T1 = \frac{C2}{Ks}, \quad T2 = \frac{C2}{Kc} \quad (7)$$

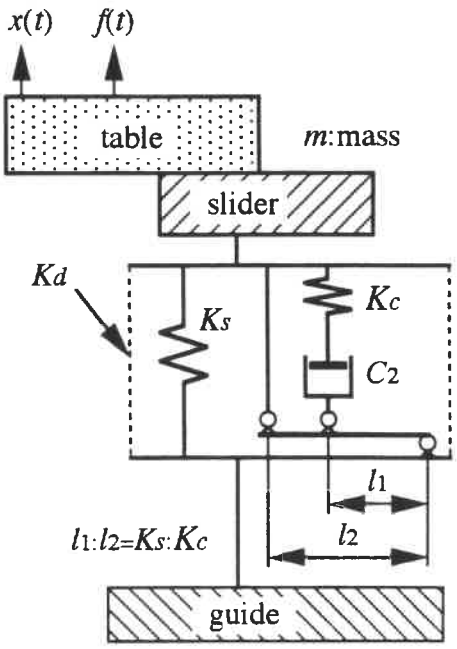

Fig. 2 The air-lubricated slideway suspended by the dynamic stiffness : Kd

Substituting Eq. (7) into Eq. (5) and Laplace-transforming of Eq. (6) gives

$$X(s)=\{\frac{F(s)}{Ks}\}\frac{1}{(\frac{s^2}{\omega_n^2}+\frac{T_1 s+1}{T_2 s+1})}=\{\frac{F(s)}{Ks}\}G(s) \quad (8)$$

where $X(s)$, $F(s)$ are Laplace transformation of $x(t)$, $f(t)$, respectively, and $\omega_n^2=Ks/m$.

$G(s)$ is a transfer function which shows the dynamic characteristics of the slideway. From Eq. (8), $G(s)$ is represented as

$$G(s)=\frac{(s+\frac{1}{T_2})\,\omega_n^2}{s^3+\frac{1}{T_2}s^2+\frac{T_1}{T_2}\omega_n^2 s+\frac{1}{T_2}\omega_n^2} \quad (9)$$

The transfer function has a formula of the first order in numorator and a formula of the third order of Laplace variables in the denominator.

4. Step response of an air-lubricated slideway

A step response of an air-lubricated slideway for an ultraprecision machine tool is calculated. Data of dynamic characteristics shown in Table 1 are applied.

The transfer function $G(s)$ is represented by the data as

$$G(s)=\frac{0.53\times10^6\,(s+0.84\times10^3)}{s^3+0.84\times10^3\,s^2+0.709\times10^6 s+0.445\times10^9} \quad (10)$$

The denominator of Eq. (10) is resolved to factors as

$$G(s)=\frac{0.53\times10^6\,(s+0.84\times10^3)}{(s+0.717\times10^3)\times(s^2+0.123\times10^3 s+0.621\times10^6)} \quad (11)$$

It is known that the transfer function $G(s)$ is shown by the first order lag and delay system, and the second order vibration system. The second order vibration system is

Table 1 Data for calculating the dynamic characteristics of the air-lubricated slideway

supply pressure	$Ps/Pa=6(Ps=0.588\text{MN/m}^2)$
recess prssure	$Pr/Ps=0.75$
difference of parameters	$b_2-b_1=3$, $a_2-a_1=3$
density of air	$\rho=5.4225\ \text{kg/m}^3$
flow rate	$Q=2.33\times10^{-3}\ \text{kg/s}$
ratio of D/B	3/100
clearance volume	$v_c=3980\times10^{-9}\ \text{m}^3$
recess volume	$v_r=94.2\times10^{-9}\ \text{m}^3$
static stiffness	$Ks=795\ \text{MN/m}$
mass of table	$m=1500\ \text{kg}$
effective area	$Ae=3.064\times10^{-2}\ \text{m}^2$
compressible stiffness	$Kc=1064\ \text{MM/m}$
damping coefficient	$C_2=1.267\ \text{MNs/m}$
time contants	$T_1=1.592\times10^{-3}\text{s}$
	$T_2=1.189\times10^{-3}\text{s}$
ratio of time constants	$T_1:T_2=l_1:l_2=Kc:Ks=1.338$

rewritten as

$$\frac{1}{(s^2+0.123\times10^3 s+0.621\times10^6)}=\frac{1}{(s^2+2\zeta_0\omega_0 s+\omega_0^2)} \quad (12)$$

Therefore, the resonant frequency ω_0 and the damping ratio ζ_0 are shown as

$\omega_0=0.788\times10^3$ rad/s

$\zeta_0=0.078$.

Next, the outer force $f(t)$ of step function shown in Eq. (13) is input to the table.

$$f(t)=Ks\ u(t) \quad (13)$$

Laplace transformation of $f(t)$ is represented as

$$F(s)=\frac{Ks}{s} \quad (14)$$

Therefore the Laplace transformation of the upward displacement of $x(t)$ is represented as

$$X(s) = \frac{F(s)}{Ks} G(s)$$

$$= \frac{0.53\times10^{6}\,(s+0.84\times10^{3})}{s\,(s+0.717\times10^{3})\times (s^{2}+0.123\times10^{3}s+0.621\times10^{6})}$$

$$= \frac{1}{s} - \frac{0.087}{s+0.717\times10^{3}} - \frac{0.913\,s+0.175\times10^{3}}{(s^{2}+0.123\times10^{3}s+0.621\times10^{6})} \quad (15)$$

Reverse Laplace transformation of Eq. (15) gives

$$x(t) = 1 - 0.087\, e^{-0.717\times10^{3}t} - 0.913\, e^{-0.0616\times10^{3}t}\{\cos(0.785\times10^{3}t) + 0.165\sin(0.785\times10^{3}t)\} \quad (16)$$

Eq. (16) has the first order delay part with fast decay and the second order vibration part. The resonant frequency and the damping ratio are $\omega_0=0.788\times10^3$ rad/s and $\zeta_0=0.078$ as already shown. The ratio of the resonant frequency ω_0 and the natural frequency ω_n which is obtained by the static stiffness of the slideway and the mass of the table gives 1.08. This value is coincident to the value that has been obtained by the frequency response.[2] The step response is shown in Fig. 3. It is known that the response is damped to 48 mS. The damping ratio obtained by logarithmic decrement is 0.078 and is coincident to ζ_0. However, the over-shoot is 71%. This value is obtained by a pure second order vibration system whose damping ratio is 0.108. Thus the actual damping ratio of the slideway is higher than 0.078. This is coincident to the damping ratio of 0.085 that has been obtained by the frequency response.[2]

5. Conclusions

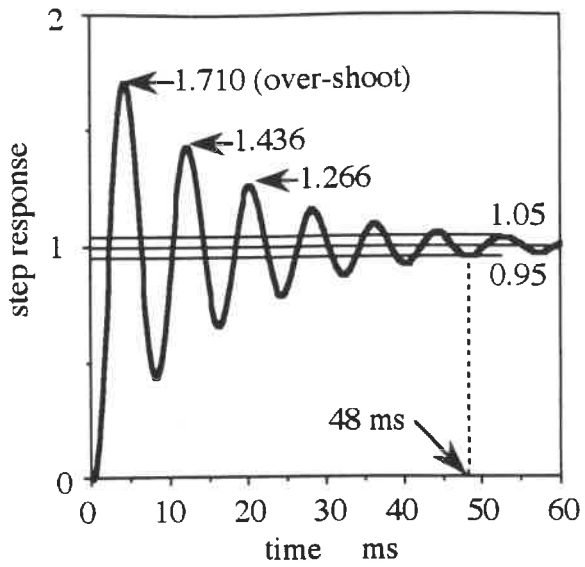

Fig. 3 Step response of the air-lubricated slideway by a unit input (calculated).

The step characteristics of the air-lubricated slideway related to the damping force caused by the squeezing effect is analyzed. The results are applied to the slideway of an ultraprecision machine tool, whose table has a mass of 1500 kg and static stiffness of 0.795 kN/μm. A transfer function, which is represented by an equation of motion of the slideway, has a formula of the first order in the numorator and a formula of the third order in the denominator. As a result of the reverse Laplace transformation, the damping ratio of 0.078 is obtained. However, the over-shoot is 71%. This value is obtained by a pure second order vibration system whose damping ratio is 0.108. Thus the actual damping ratio of the air-lubricated slideway may be higher than 0.078.

6. References

1) Richardson, H.H., Static and Dynamic Characteristics of Compensated gas Bearings, Trans. of ASME, Vol. 80, No. 7 (1958) 1503.

2) Kato, S., Damping Characteristics of Air-lubricated Slideways for Ultraprecision Machine Tools, Proc. of ASPE Spring Topical Meeting, April (1994) 63.

LOW NOISE FLUID CIRCUIT DESIGN METHOD FOR HYDROSTATIC BEARING SYSTEMS

PAUL SCAGNETTI, ALEXANDER SLOCUM, NATHAN KANE
PRECISION ENGINEERING RESEARCH GROUP
DEPARTMENT OF MECHANICAL ENGINEERING
MASSACHUSETTS INSTITUTE OF TECHNOLOGY

Hydrostatic bearings are frequently the bearing of choice for precision machine applications. When properly designed, they offer high motion resolution, low friction, high transverse stiffness, and excellent damping [1]. They are promising for machine tool applications such as ceramic grinding machines where high stiffness, high damping, and durability are important. However, such bearings have the potential to introduce pressure induced vibrations [2] and thermal errors (due to fluid shearing) into machine tools.

Since the stiffness of a hydrostatic bearing system is directly proportional to the supply pressure, high supply pressure is usually beneficial (300psi. is a typical supply pressure). However, in supplying high pressure from a pump, pressure fluctuations will be present. Usually, either piston pumps or diaphragm pumps are used for hydrostatic bearing systems. Such pumps typically produce large fluctuations in pressure, up to 20% of the nominal pressure.

Therefore, a fluid circuit for supplying fluid to the bearings must remove pressure fluctuations which are caused by the pump so that the fluid system does not introduce vibrations into the machine tool [3]. Supplying pressure to the bearings without pressure fluctuations requires careful modeling. Typically, the pressure fluctuations are suppressed by placing gas charged accumulators in the transmission line. A simplified schematic of a hydrostatic bearing system and fluid supply system is shown in figure 1.

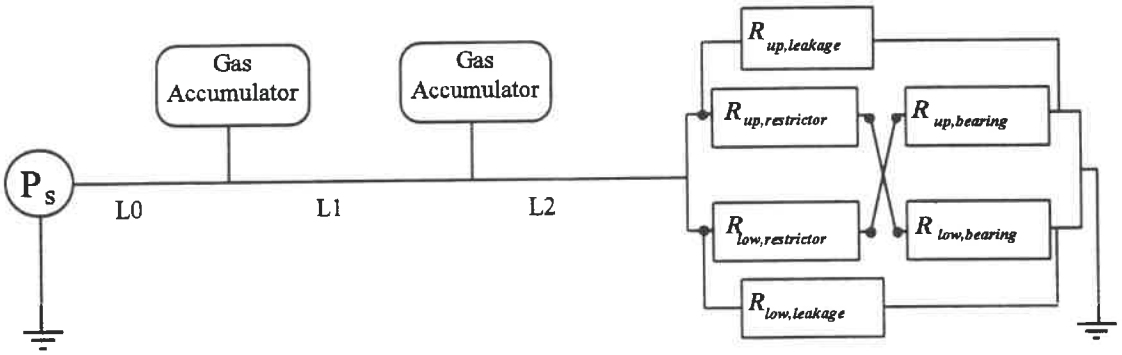

Figure 1: Block diagram of the fluid path of a self-compensated, hydrostatic bearing system. The restrictors and bearing lands are represented as fluid resistances.

The main variables which enter into the circuit design are (1) the diameters (D1, D2, and D3) of the transmission lines, (2) the lengths (L1, L2, and L3) of the transmission lines, which will determine the frequency of the peaks, (3) the location of the accumulators, which will determine what frequencies they are able to filter, (4) the size of the accumulator which effects the natural frequency of the accumulator, and (5) the charge pressure of the accumulators which effects the natural frequency of the accumulators.

BOND GRAPH DIAGRAMS [4] OF HYDROSTATIC BEARING SYSTEMS

Developing a dynamic model of a hydrostatic bearing system is difficult because the system has multiple energy domains. The fluid energy supplied by the pump is transformed into mechanical energy on the carriage. For this reason, bond graphing is a useful method of obtaining the dynamic equations of motion for the system. Although not widely known, bond graphs are a useful technique for deriving the dynamic equations for multiple energy domain systems. Figure 2 is a bond graph of an opposed pad hydrostatic bearing system with a supply line that includes two accumulators. The fluid supply line can have as many degrees of freedom as necessary.

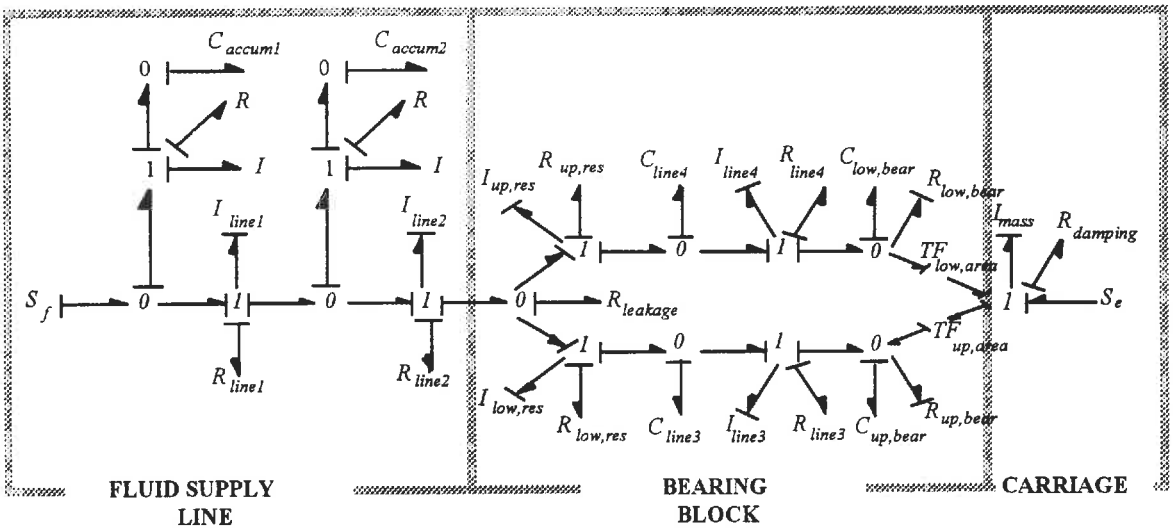

Figure 2: Bond graph of a self-compensated, opposed pad hydrostatic bearing system. The model includes one opposed bearing pad and one mass. The model also includes the effect of an external force acting on the carriage, such as a grinding force.

The model is a developed as a series of lumped capacitances C, resistances R, and interia I elements. For the fluid domain, these elements can be calculated as:

$$C_{line} = \frac{V_{line}}{B_{fluid}} \qquad R_{line} = \frac{128\mu_{fluid} l_{line}}{\pi d_{line}^4} \qquad I_{line} = \frac{\rho_{fluid} l_{line}}{A_{line}}$$

SIMULATION RESULTS OF HYDROSTATIC BEARING SYSTEM NOISE

Differential equations relating the supply pressure to the bearing pocket pressure can be systematically derived from the bond graph. In the actual bearing system, the resistances of the restrictors and the bearing pads are functions of the position of the carriage. For such a case, the equations are nonlinear, and it is not possible to derive a transfer function between the supply pressure and the bearing pocket pressure, However, since the resistances of the restrictor and the bearing pad are not likely to vary by more than 3% under normal operating conditions, they can be modeled as constant parameters, Then the transfer function between the supply pressure and the bearing pressure can be expressed in closed form.

Table 1: Simulation plots of the transfer function between bearing pressure and supply pressure for a hydrostatic bearing systems with and without accumulators.

Figure 3: Transfer function for a system with no inline accumulators.	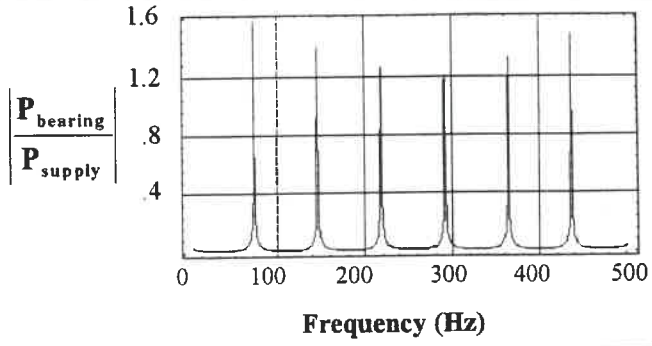
Figure 4: Transfer function for a system with one accumulator. The accumulator is placed near the hydrostatic bearing with volume of 1/8 gallon and is charged to 60% of the supply pressure.	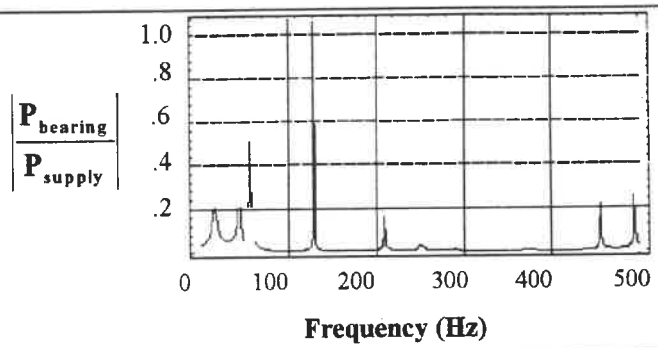
Figure 5: Transfer function for a system with two accumulators. The first accumulator (1/8 gallon) is placed near the hydrostatic bearing. The second accumulator (1 gallon) is placed near the pump. Both are charged to 60% of the supply pressure.	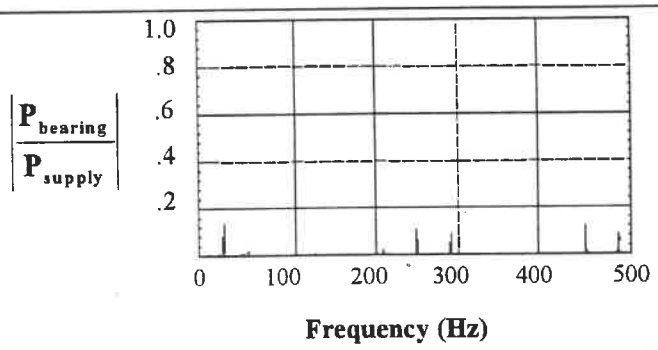

EXPERIMENTAL RESULTS OF HYDROSTATIC BEARING SYSTEM NOISE

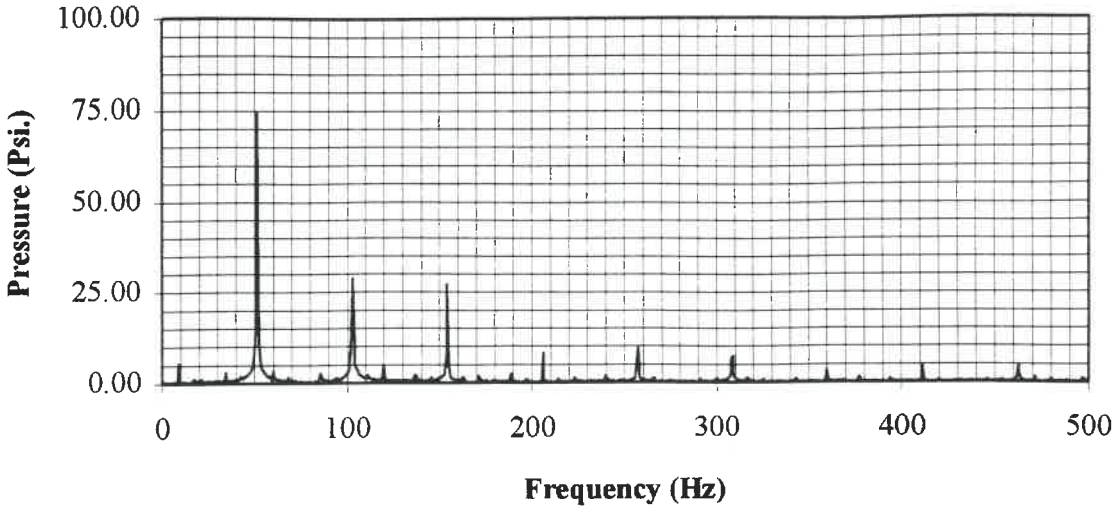

Figure 6: Power spectrum of the pressure from a piston pump (three pistons). The nominal supply pressure is 400psi.. Note that the pressure fluctuations are nearly 20% of the nominal supply pressure.

Table 2: Experimental power spectrum for the bearing pocket pressure for an opposed pad, self-compensated, water-hydrostatic bearing system with and without accumulators.

Figure 7: Power spectrum of the bearing pocket pressure for a system with no accumulators.	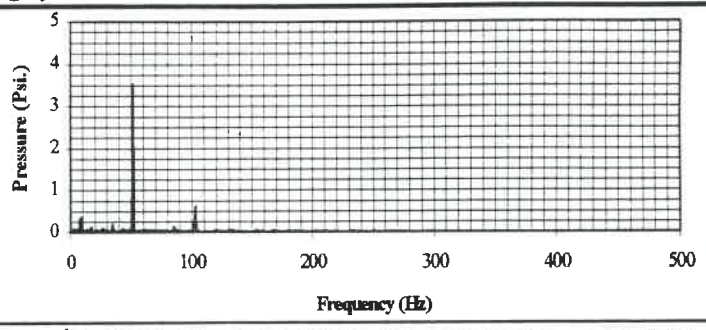
Figure 8: Power spectrum of the bearing pocket pressure for a system with one accumulator. The accumulator has a volume of 1/8 gallon and is placed near the hydrostatic bearing.	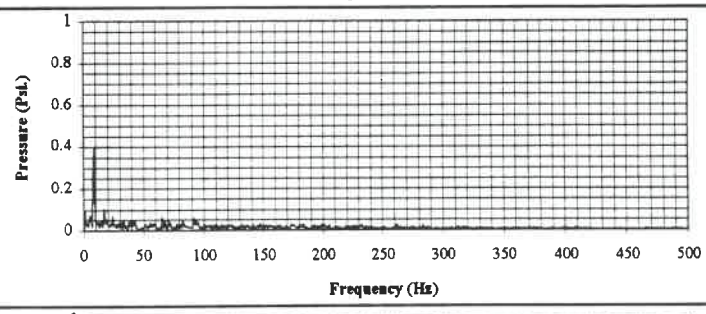
Figure 9: Power spectrum of the bearing pocket pressure for a system with two accumulators. The first accumulator (1/8 gallon) is placed near the hydrostatic bearing. The second (1 gallon) is placed near the pump.	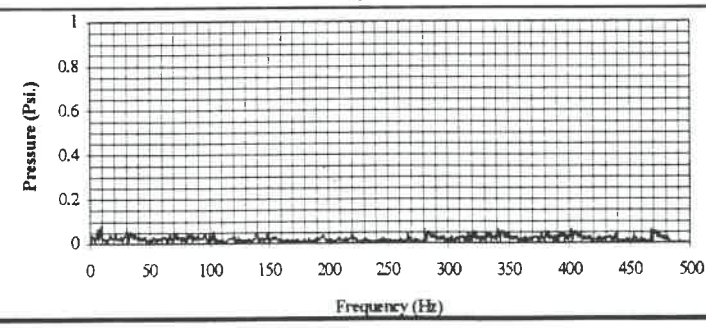

RESULTS AND CONCLUSIONS

The simulations and experiments run in this study have shown good agreement. Therefore, simulations have proven an effective method of designing hydrostatic bearing fluid systems. The experimental results shown in figures 7, 8, and 9 demonstrate that the conventional strategy of placing one accumulator in the fluid circuit is not sufficient for precision machine applications. This strategy however is the usual method of filtering out pressure fluctuations in industrial machine tools.

Experiments on the linear guide prototype at M.I.T. have shown that proprt selection and placement of accumulators can reduce the vertical error motions of the carriage by more than .1μm. Prior to simulations, the following general rules are useful for choosing the size and location of accumulators:

- Generally two accumulators are required for filtering out supply pressure noise in the 0 Hz to 500 Hz frequency range.
- One accumulator (usually about 1 gallon volume) should be placed as near to the pump as possible and the charge pressure should be set in order to match the natural frequency of the accumulator with the pump.
- The second accumulator (usually about 1/8 gallon volume) should be placed as close to the hydrostatic bearing system as possible. The charge pressure can be set at approximately 60% of the supply pressure.
- The accumulators should be placed off of the supply line with a T fitting. Experimentally, the results were better when the accumulator is in line with the transmission line as shown in figure 10. This behavior is not demonstrated in the simulations.

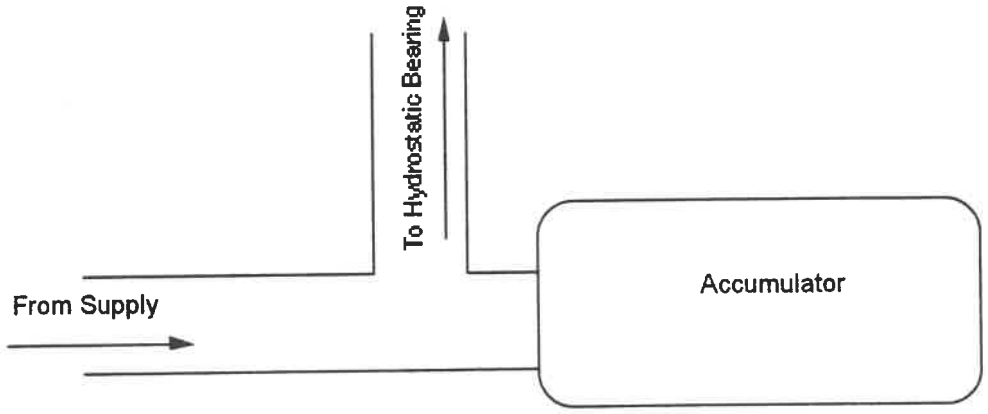

Figure 10: Diagram of accumulator positioning within the fluid circuit. Notice that the accumulator is in line with the supply rather than the line to the hydrostatic bearings.

REFERENCES

[1] For general information about hydrostatic bearings see, A. Slocum, Precision Machine Design, Prentice Hall, Englewood Cliffs, New Jersey 07632, 1992. Also, F. Stansfield, Hydrostatic Bearings for Machine Tools, Machinery Publishing Co., Ltd., London 1970.

[2] For an example of this problem see, "Chatter Marks due to Pulsation of Hydraulic Oil Pressure in Surface Grinding and its Suppression", Nakano, Y., Kato, H., Low, S., Bulletin of the Japan Society for Precision Engineering, Vol. 20, No. 1 (March 1986), p. 43-44.

[3] For general references of noise suppression in hydraulic circuits see, S. Skaistis, Noise Control of Hydraulic Machinery, Marcel Dekker, Inc. New York, 1988. Also see, T. Viersma, Analysis, Synthesis, and Design of Hydraulic Servosystems and Pipelines, Elsevier Publishing Co., New York, 1980.

[4] For an introduction and description of bond graphing techniques, see Rosenburg, R.C., Karnopp, D. Introduction to Physical System Dynamics, McGraw-Hill Publishing Co., New York, NY 1983.

Characteristics of Aerostatic, Hydrostatic and Rolling Element Spindles and Slide Systems and Their Influence on the Machining Accuracy

M. Weck, J. Luderich, A. Wieners, M. Vos
Fraunhofer Institut für Produktionstechnologie, Aachen, Germany

Summary

The characteristics of different types of spindles and linear slide systems and their influence on the workpiece accuracy are discussed. Aerostatic, hydrostatic and rolling element bearing systems are evaluated and compared. Taking the static, dynamic, geometric and thermal behaviour into account every bearing and guideway type has its advantages and disadvantages that define its optimum application. Based on measurement results of the component behaviour and analysed workpiece surfaces correlations are made to help the machine designer to choose the optimum bearing type for different applications.

Introduction

The manufacturing process and the accuracy of the machine tool together with the workpiece material are the factors that define the achievable roughness, dimensional and form accuracy. Manufacturing processes like diamond turning, grinding of brittle materials like glass or ceramics and high precision turning of hardened steel have the potential to create accuracies in the sub-micrometer range and roughness values of a few nanometer. But only if the machine tool as well as its components achieve a good performance high precision parts become available. Analyzing both, commercially available and experimental machine tools, aerostatic, hydrostatic and rolling element bearing systems can be found in various ways for high precision machines. To analyze the characteristics of spindle and slideway systems which work with different principles three spindles and three cross slides were realised and tested under the same conditions. Additionally the influences of the different components on the workpiece quality were analysed.

Spindle systems

In high precision applications aerostatic spindles are used widely. During the project a double-sphere, orifice restricted aerostatic spindle was used as a reference spindle. The design of this commercially available spindle is shown in fig.1. The ball bearing and the hydrostatic spindle are special developments that were designed for highest accuracy and stiffness by the companies SKF (Schweinfurt) and Zollern (Herbertingen). Both spindles can be seen in fig. 1. In addition to the spindles' construction a plot of the radial error motions in x-direction at low speed (100 rev./min) is shown. The error motions of every spindle type have their own characteristics. Whereas the aerostatic system runs very repeatably, the error motions of the ball bearing spindle are strongly non-repeatable. The values for the asynchronous motions are 50 nm for the aerostatic and 300 nm for the ball bearing spindle. With a value of about 100 nm the synchronous error motion of both spindles are in in the same order. Depending mainly on the manufacturing accuracy of the spindle shaft the synchronous error motion dominates the behaviour of the hydrostatic spindle. The asynchronous error motions reach a value of about 100 nm.

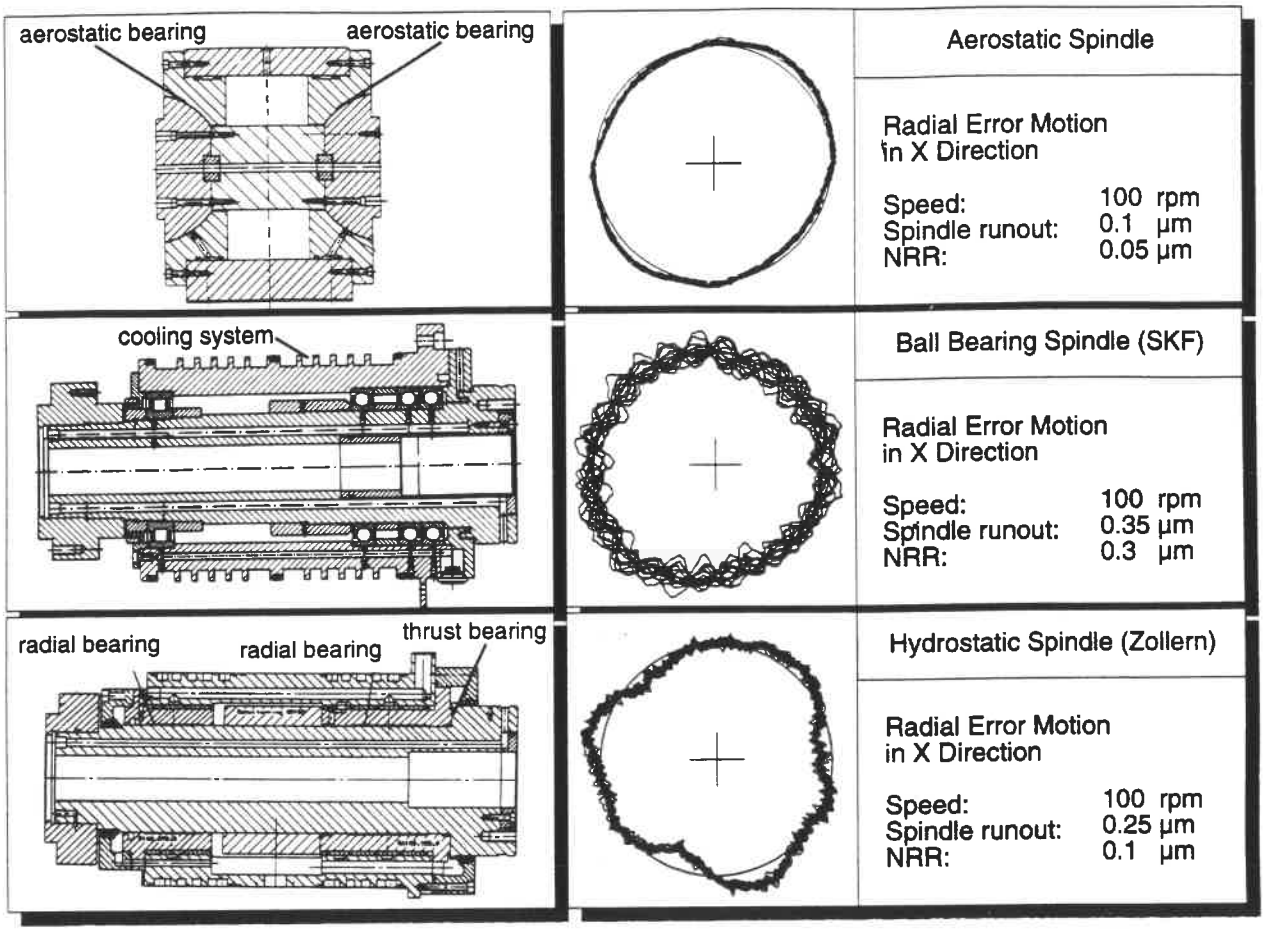

Figure 1: High Precision Spindle Systems

Guideways

To compare the characteristics of aerostatic, hydrostatic and rolling element guideways three slide systems were designed under the same restrictions. Fig. 2 shows the rolling element guideway, designed and manufactured by SKF Linearsysteme, Schweinfurt, and IPT as an example. The hydrostatic system (by Zollern, Herbertingen) and the aerostatic system (Fig. 2) (by IPT) have approximately the same dimensions. To realize maximum comparability the same drive system can be used for all three guideways.To characterise the different linear guiding systems and their influence on the manufacturing quality the static, dynamic, thermal and geometric behaviour were examined. Beside a number of other parameters the straightness of the slideways especially in the directions that are sensitive for turning operations was measured, Fig.3. With deviations of 0,1 to 0,4 µm the aerostatic cross slide reached the best results. Because of the integrating effect of the gap there are only long period errors. The deviation of the needle bearing slide is dominated by an error with a 100 mm period, which is precisely the distance between two fixing bolts. In spite of that, results between 0,3 and 0,7 µm are absolutely good for needle bearings.

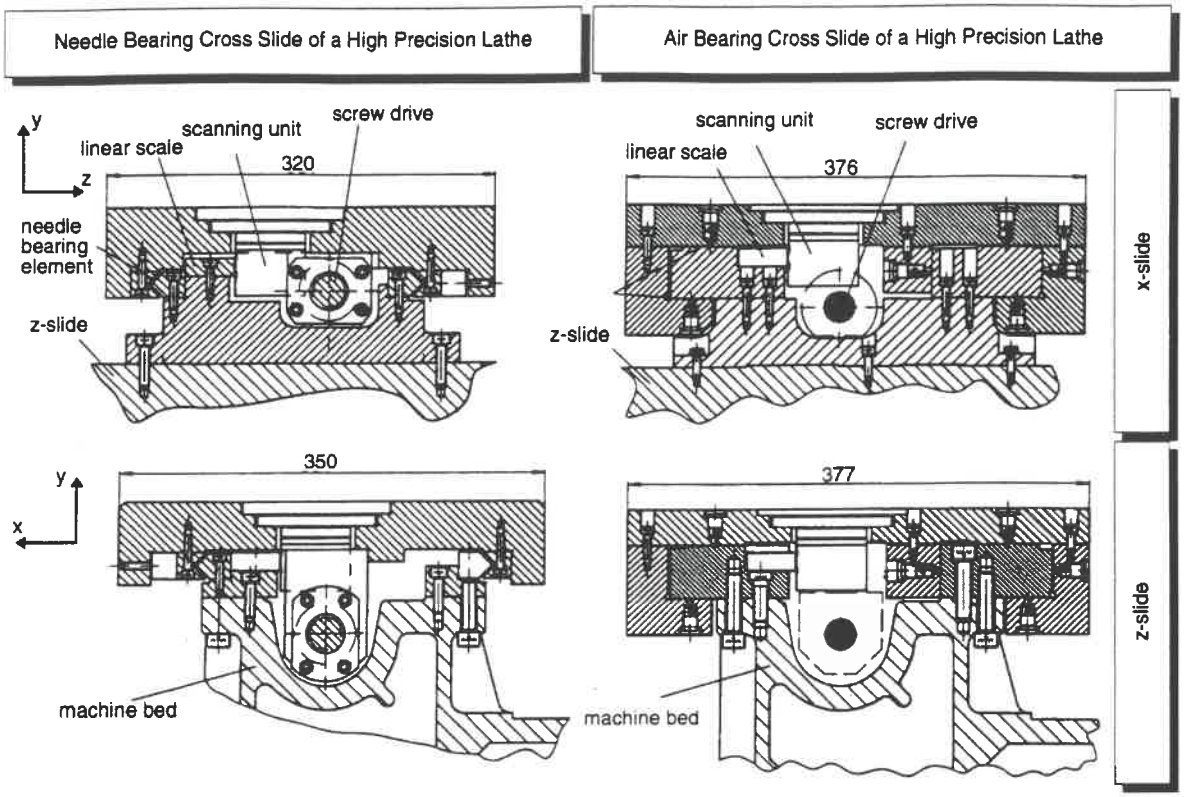

Figure 2: Needle Bearing and Air Bearing Cross Slide System

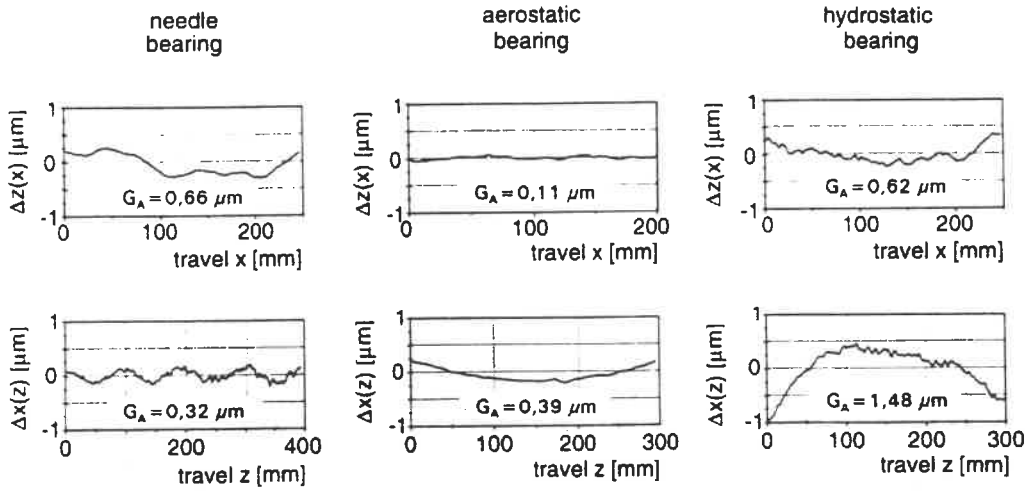

Figure 3: Straightness Deviation of Three Different Slide Systems in the sensitive Directions

For optimization the slideways themselves had been lapped manually. By that the deviations could be reduced to about 40 %, the friction to about 50 % at similar preloading. The hydrostatic cross slide reaches values of only 0,6 to 1,5 µm. Especially the deviation Δx of the z-axis is out of the ordinary. Reason for this is that the guideway for the hydrostatic z-slide was finish machined before assembling. Because of inner stress in the material the guideway's form accuracy after machining cannot be transferred to the machine base. It is obvious, that the guideways have got to be machined in an assebled state to guarantee highest straightness accuracies.

Correlation between the component behaviour and the workpiece accuracy

Not all characteristics of a spindle or a guideway have a perceptible influence on the workpiece accuracy. The influences depend strongly on the process technology, the machining time and parameters, like feed and infeed. Additionally the frequency and direction of the statically, dynamically, thermally and geometrically generated error motions between workpiece and tool are very important. It is essential to understand that the assessement of the component behaviour is a direct function of the aspects of a machining process that were mentioned above. Although the correlation between the machine characteristic and the workpiece accuracy is often very complex, in some cases this correlation can be shown easily. Fig. 5 shows for example the roughness of a brass workpiece which was turned twice under the same conditions. The only difference was the used spindle system. The surface on the left side was turned with a standard rolling element spindle, the surface on the right side by using the same lathe with an aerostatic spindle. The difference in roughness is significant and can be directly correlated to the asynchronuos error motions of the spindle system.

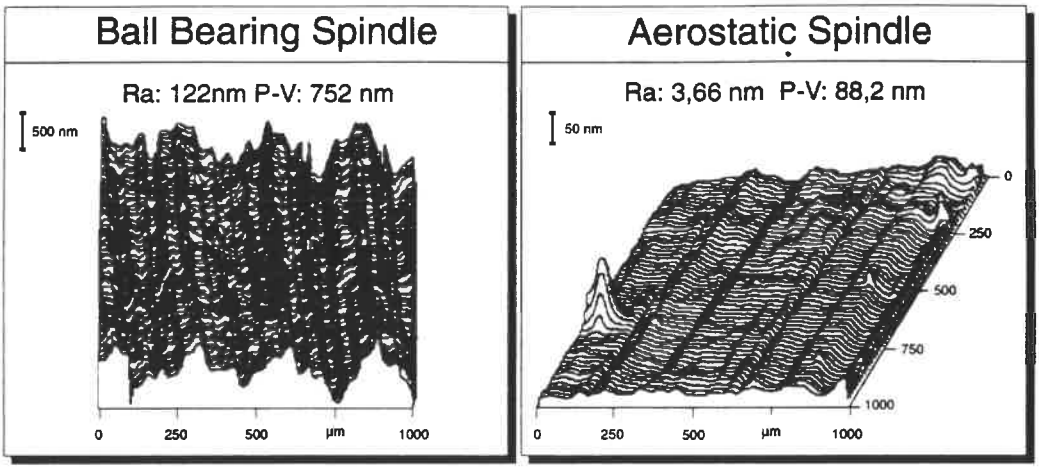

Figure 5: Achieved Roughness with Ball Bearing and Aerostatic Spindle

Conclusion

The geometric qualities of all analyzed bearing systems are mainly influenced by the bearing principle and manufacturing accuracy. Typical for rolling element bearings are higher asynchronous error motions, that have to be taken into account more for main spindles than for slide systems because of higher speed. The asynchronous errors are responsible for worse roughness values. In spite of that all bearing principles are able to reach excellent geometric accuracies with a suitable construction and layout so that the selection of the best spindle in correspondence to the desired maching process is a question of other qualities like stiffness or thermal behaviour.

Literature

Autorenkollektiv: Hochpräzisionsdrehen mit geometrisch bestimmter Schneide. Band I: Drehen. Beuth Verlag Berlin, 1994. ISBN 3-410-32846-7

J. Luderich: Hochgenaue Spindelsysteme: Untersuchungen über die Laufgenauigkeit und deren Einfluß auf das Bearbeitungsergebnis. Shaker Verlag Aachen 1994. ISBN 3-86111-824-6

DEVELOPMENT OF APPROACH AND REAL PRESSURE IN MULTIPLE CONTACT LOADING PROCESS

A. Polijaniuk

Institute of Fundamental Technological Research
Polish Academy of Sciences
ul.Swietokrzyska 21, 00-049 Warsaw, Poland

Introduction

Contact joints constitute an indispensable part of nearly every machine. Their design is based on particular requirements depending on , among other factors, the state of the technological surface layer of contacting parts. The state of the surface layer combines the physical features of the material and the geometrical features of the surface. The presence of surface roughness causes contact to take place on discrete areas, the sum of these determines the real contact area. Load usually aplied to matting elements causes an elastic-plastic deformation of surface layer. An effect of loading is a simultaneous approach variation between surfaces (**a**) as well as variation of real contact area (**RCA**), fig.1.

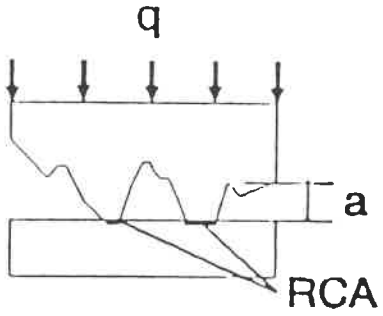

Fig.1: The configuration used in measuring contact characteristcs **a(q)** and **RCA(q)**

As is well known a real contact pressure (**qr=q/RCA**, where **q**-nominal pressure), which takes place during machine part work substantially influences part reliability. Real contact pressure development which takes place during work of rough part surfaces has an influence on part wear, growth of backlash, changing of stiffness characteristics, vibratons, widely understood conductivity and many other parameters that influence of a machine performance.

The subject of the work is to show simultaneous development of a real contact pressure and a contact approach by allowing for multiple increasing nominal pressures. The results refer to the initial phase of cycled load applied to a stationary joint consisting of: nominally flat element and counter - surface ideally rigid and smooth. This basic configuration is usually employed in the studies of contact mechanics [1-4]. Contact process takes place within the surface layer area, which state depends on physical properties of material and on surface roughness. Both features are the result of technological process applied to the material and may have different roles in contact. Elements with various surface texture obtained with different technology were analyzed.

In experimental research a method was used for simultaneous measurement of the real contact area (**RCA**) variations and the contact approach (**a**) of surfaces, taking place during loading of

joint [3,4]. The completion of measurement of **RCA(q)** characteristics with **a(q)** characteristics gave a possibility of an analysis of real pressure **qr(q)** and approach **a(q)** development under multiplied load.

2. Method and Scope of Work

In this paper, we are going to pay particular attention to the formation of contact properties of elements remaining in a stationary contact and subjected to quasi-static load. Such evaluation will be based on an analysis of simultaneously recorded variations in "**qr**" (RCA) and approach "**a**" resulting from an increase, within 10 load cycles, in the rated pressure "q" - from zero up to q_{max}=400 MPa.

The results preseted and analyzed in the paper were made with the use of an measurement stage for studing contact phenomenon [3,4]. Measurement methods used on stage are: (1) echo method and ultrasonic technique for RCA measuremet, (2) measurement basis localizaton in the contact plane (Demkin method) and inductive displacement technique, (3) electric resistance strain gauge method together with force transducer for determine the nominal pressure.

Certain errors occurred when quantities were measured during this experimental work. Here, 3rd standard deviation of the mean value is as follows: ± 3.25 MPa for "q" measurement, ± 0.5 μm for "a" measurement and ± 2% for "RCA" measurement.

The elements examined were made of structural steel containing 0.45% carbon. The experiments were limited to ground elements (SR_a=0,1 μm), which were then subjected to impact burnishing:

- Bead blasting with the use of 0.8 mm dia. glass beads - samples marked with **"K"**,
- Bead blasting with the use of 0.8 mm dia. x 0.8 mm wire pieces - samples marked with **"D"**.

Also, to • an abrasive blasting with the use of No. 30 aloxite grain - samples marked with **"E"**. Compressed air nozzle operating at a pressure of 0.55 MPa, and positioned perpendicularly 50 mm away from the surface was used in each case.

Smooth elements featuring hardened (rough) surface layer were nominally obtained as a result of the treatment described above. Three-dimensional parameters of the examined surface - recorded by means of a scanning profile measurement - are shown in the Table 1.

Table 1

Element	SRa [μm]	SRq [μm]	SRp [μm]	SRv [μm]	SRku[μm]	SRsk[μm]
"K"	1.17	1.66	16.00	36.60	16.91	-0.58
"D"	4.63	5.99	29.20	101.60	5.91	-0.55
"E"	5.00	6.44	28.00	59.00	3.51	0.01

No attempt was made to relieve stresses resulting from the surface treatment. This means that we have here an actual complex physical geometric condition of a surface layer.

3. Experimental Results

As regards the results, the first and the tenth load cycles received particular attention. As from the third cycle, no substantial differences in a(q) and qr(q) characteristic curves were recorded. Figs 2, 3, and 4 show the results of simultaneous measurements of both functions relating to the "K", "D", and "E" elements.

If we compare measurements of an approach (see Figs 2A, 3A, and 4A) leads us to the following conclusions:

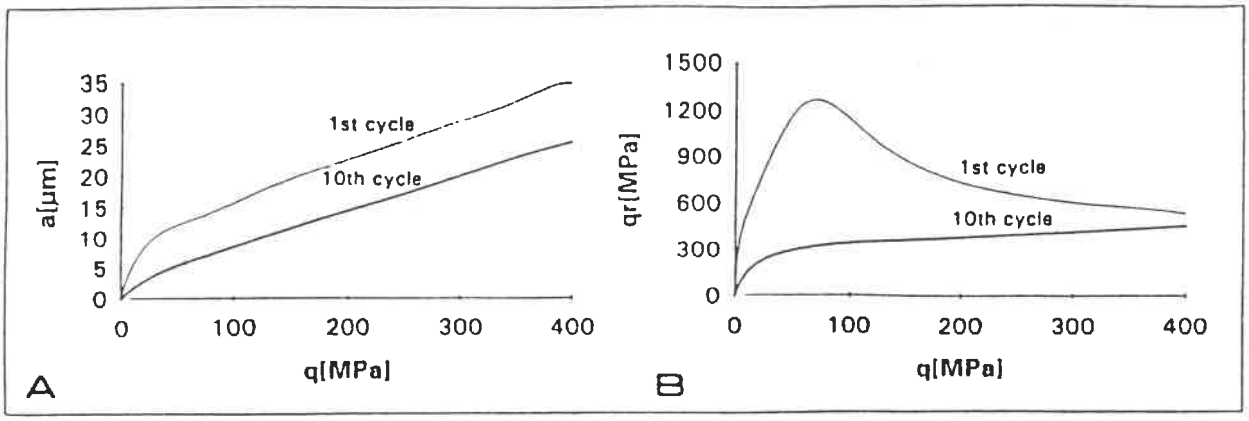

Fig. 2: Contact characteristic curves for the "**K**" element: a(q), qr(q)

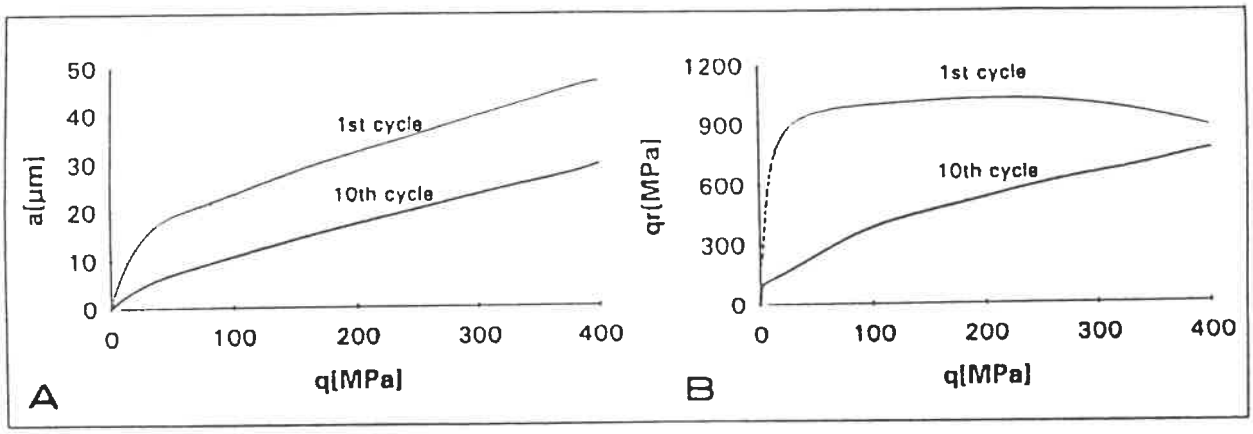

Fig.3: Contact characteristic curves for the "**D**" element: a(q) and qr(q)

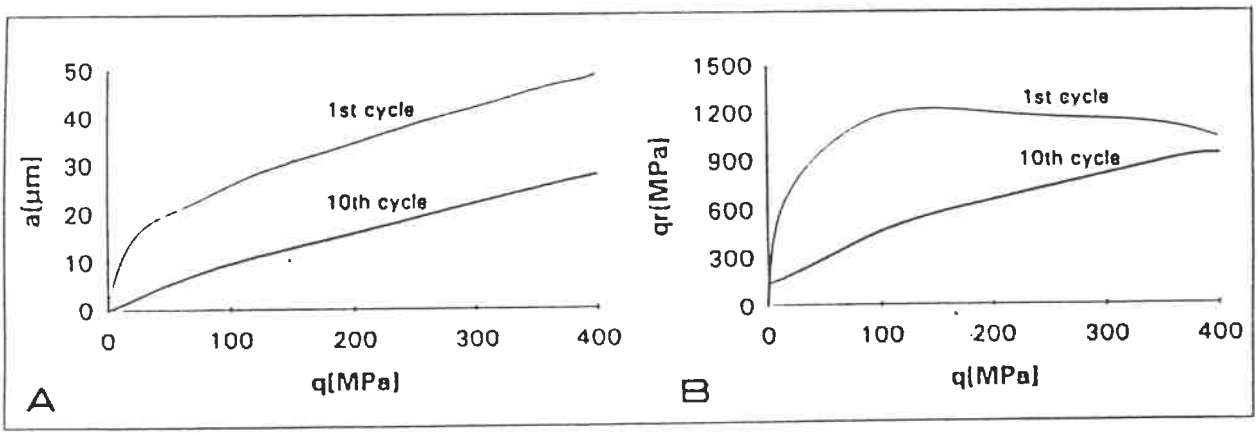

Fig.4: Contact characteristic curves for the "**E**" element: a(q) and qr(q)

• Characteristic curves for a(q) are similar in shape, however, the approach values achieved for the same q - are different.
• Load carrying capacity of the "E" element was the least of all, while that of the "K" element was maximum. Relative increase in an approach for q=400 MPa was 24.3%, 36.9%, and 42.2% for the "K", "D", and the"E" elements respectively.
• In case of relatively stable cycles, the "K" element was found more rigid during the tenth cycle, followed by the "E" and "D" elements.
• Non linearity of the characteristic curves within the 0 - 50 MPa range in the tenth load cycle is most likely an evidence of micro roughness non-uniform relaxation.

Basing on Figs 2B, 3B, and 4B presenting the qr(q) dependence, further conclusions may be drawn:
• The qr(q) characteristic curves are different as regards their shape and values reached.
• Minimum actual pressure was found in the case of the "K" element, while that for the "E" element reached maximum. For example, for q=400 MPa in the tenth cycle, the following pressures were attained: 461.5 MPa for the "K", 763.3 MPa for the "D", and 935.2 MPa for the "E".
RCA relative increase of 17.5% for the "K", 15% for the "D", and 11% for the "E" resulted from ten loadings.
• Distinctive qr peak values were found in the first load cycle: 1277 MPa for the "K" element at q=72 MPa, 1022 MPa for the "D" in the range of 194 - 225 MPa, and 1227 MPa for the "E" in the range of 144 - 147 MPa.

4. Conclusions

Basing on, naturally simplified analysis of the results, it may be said that the "K" element has shown the best contact properties, at the same time producing minimum increase of an approach and minimum actual pressure. Practically, this may mean minimum design clearance and minimum wear. In this respect, performance of the "E" element was the worst of all. A possibility of occurrence of peak values in the first cycle of the qr(q) characteristic curve was proved. Their presence that is related to the loads within the range of their occurrence, may become important for the development of a contact process.The results presented prove that the process is of a complicated character and its analysis is both possible and desirable.

Key words: multiple load, real contact area, real contact pressure, contact approach.

Acknowledgments

This work was supported by the State Research Committee under Grant KBN No.3 P402 071 04. I am indepted to dr. Z. Handzel-Powierża for her kindness in making voluable comments.

References

[1] McCool J.I.,Wear, 107 (1986),37-60
[2] O'Callaghan P.W., Probert S.D.,Wear,120 (1987).29-49.
[3] Polijaniuk A.,Kaczmarek J., J.of Testig and Eval. 21(3) (1993), 174-177.
[4] Polijaniuk et al., Proc.of the 7th Int. Prec. Eng. Sem., Kobe, Japan, (1993), 429-440.

Design and analysis of a new type multi-functional machine tool

N. Sugimura[1], S. Ueno[2], N. Mishima[3], and S. Hachiga[4]

1) College of Engineering, University of Osaka Prefecture
Gakuencho, Sakai, Osaka 593, Japan
2) Technical Research Institute of JSPMI
3) Mechanical Engineering Laboratory, AIST, MITI
4) Japan Machine Tool Builders' Association

1. INTRODUCTION

In the last decade, particular emphasis has been given to automation and integration of manufacturing processes of mechanical products in order to cope with large-variety small batch production with high accuracy and quality of products. In particular, one of the important problems to be solved is to develop a flexible and multi-functional machine tool which can adopt to various types of mechanical products in very small batch productions.

Some researches have been carried out dealing with analysis of functions and configurations of machine tools and proposals of new types of machine tools [1-5]. However, main objective of these multi-functional machine tools is to integrate the machining process and the grinding process of the mechanical products. A few special purpose machine tool has been developed, which include such processes as inspection and assembly processes.

The objective of the present research is to develop a new type flexible and multi-functional machine tool which is applicable to integration of such manufacturing processes as machining, grinding, inspection and heat treatment processes of mechanical products in the very small machine factories. The design of the machine tools is carried out through a cooperative research among JMTBA (Japan Machine Tool Builders' Association), machine tool builders in Japan and academic researchers.

2. ANALYSIS OF REQUIREMENTS

The functional requirements of the multi-functional machine tools to be designed are analyzed based on the questionnaire to both the users and the builders of machine tools. The manufacturing processes and their sequences of typical mechanical products are also investigated in order to clarify the types of manufacturing processes to be integrated.

Machining functions and basic configurations of commercially available multi-functional machine tools are firstly analyzed referring to their catalogues and specifications. Table 1 summarizes the machining functions and the control axes of typical conventional machine tools. They are basically classified into three types; they are, machining centers, turning centers and grinding centers. The maximum control axes of feed motions of the machine tools are in the range from three to five axes. One turning center has the shaping function to generate non-rotational shapes by applying single point tools and three axis simultaneous control of C, Z, and X-axes. The grinding centers are equipped with a high speed tool spindle unit to carry out the grinding process.

Table 1 Machining functions and basic configurations of machine tools

Machining Functions	Control Axes
Machining Center (Milling, Boring, Drilling, Tapping, Reaming)	X, Y, Z B, X, Y, Z (Rotation of Workpiece) C, B, X, Y, Z (Rotation of Worktable) X, Y, Z, C, A (Rotation of Tool) B, X, Y, Z, A (Rotation of Worktable and Tool)
Turning Center (Turing, Milling, Boring, Drilling, Tapping Reaming)	C, X, Y(Rotation of Worktable) C, Z, X, Y (Rotation of Worktable) C, B, Z, X, Y (Rotation of Worktable)
Turing Center (Turning, Milling, Boring, Drilling, Tapping, Reaming, Shaping)	C, Z, X (Rotation of Workpiece)
Grinding Center (Milling, Boring, Drilling, Tapping, Reaming, Grinding)	X, Y, Z

Secondly, the manufacturing processes of

typical mechanical products to be manufactured by the multi-functional machine tool are investigated on the basis of the drawings and the process sheets presented by the machine tool builders and their subsidiary companies. The products presented are classified according to the GT. (Group Technology) code called KK-1 [6], and the characteristics of their manufacturing processes are analyzed for individual product classes. Table 2 summarizes the characteristics features of the grinding process and the heat treatment process of the products. The numbers of the table gives the number of parts which require the grinding and the heat treatment processes.

Table 2 Grinding and heat treatment processes of mechanical products

				Grinding			Heat treatment	
				Cylindrical Grinding	Surface Grinding	Internal Grinding	Hardening	Others
Rotational parts	Large size parts		24	19		10	13	8
	Small-medium size parts	Plate type	51	16	10	18	15	13
		Cylindrical type	33	22	6	17	27	14
		Shaft type	17	12	4	1	12	4
Prismatic parts	Large size parts		38	1	19	1	5	24
	Small-medium size parts	Bar type	17	2	9		5	8
		Plate type	18		8		4	2
		Block type	36	2	10	2	3	10
Total			234	74	66	49	74	83

The functional requirements of the multi-functional machine tools are finally obtained through the questionnaire to the users of the machine tools. The questionnaire have been sent to more than 900 factories, and 410 factories have returned the answers. The answers give the requirements on such items as types, dimensions and weights of products, machining accuracy, total number of control axes, manufacturing processes to be integrated, lead time and lot size.

The important functional requirements obtained through the investigations above mentioned are summarized as follows;

(1) Manufacturing processes to be integrated are machining, grinding, inspection, set-up and heat treatment processes.
(2) Products to be manufactured include both the rotational products and the box-type products.
(3) Total number of control axes is more than five.
(4) Accuracy of products is less than 5 mm.
(5) Lot sizes of products are less than 100.

3. BASIC STRUCTURE OF MULTI-FUNCTIONAL MACHINE TOOL

Basic configuration of the multi-functional machine tool is discussed aimed at realizing the functional requirements. A combination of spindles and feed axes of machine tool is designed based on a mathematical model representing the shape generation processes of machine tools [7].

Figure 1 shows a schematic illustration of the designed configuration of the multi-functional machine tool. The machine tool has two main spindles shown by 11 and 29. The workpieces and the tools are fixed on the work spindle (11) and the tool spindle (29), individually, in order to carry out the various machining processes, such as the milling, the turning and the grinding processes. The tool turret is also fixed on the tool spindle. One additional sub-spindle is equipped in the tail stock (32) for the internal grinding process.

The number of feed axis of the machine tool is 8; they are, Cw, Bw, Xw, Xt, Zt1, Yt, Zt2 and Za in the figure. The combinations of the main motion and the feed motions used in the machining processes are summarized in Table 3. All the machining processes of the turning, the milling, the 5-axis machining of sculptured surfaces, and the grinding are carried out without manual set-ups with use of the spindles and the feed axes.

Special equipment is also designed to realize the additional processes. A laser head (50) is equipped to carry out the on-machine heat treatment. A moving table shown by 46 is used for the automatic change of workpieces, tools and tool turrets.

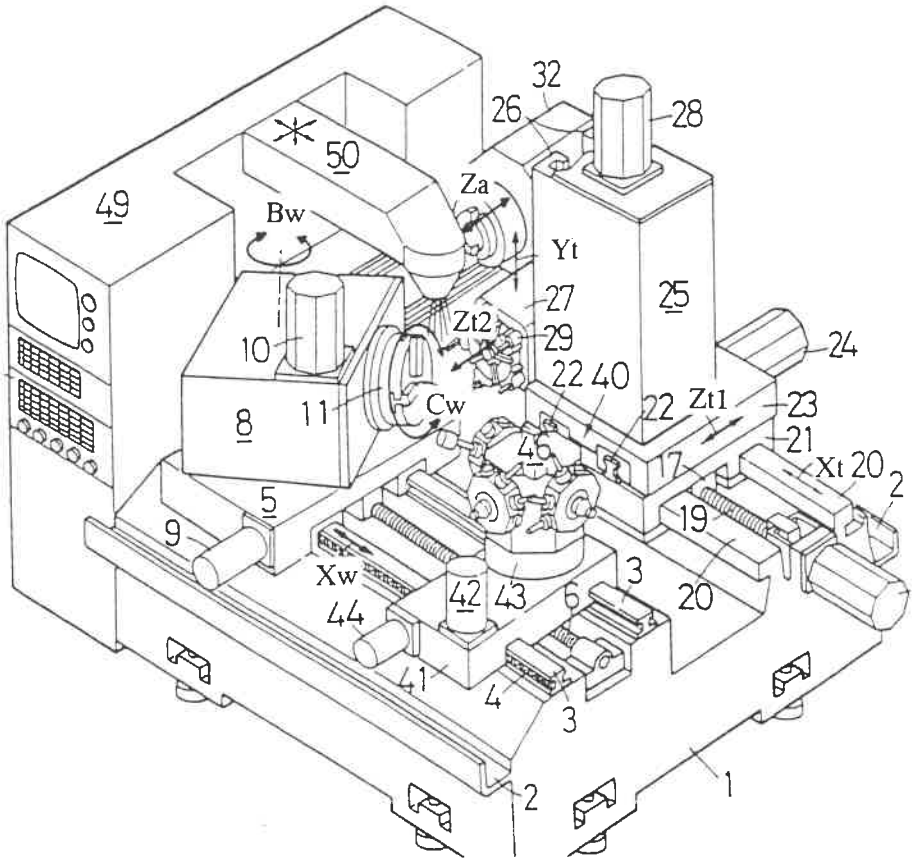

Fig. 1 Basic configuration of multi-functional machine tool

Table 3 Combinations of main motion and feed motions for various machining process

Machining Process	Main Motion	Feed Motions
Milling, Drilling, Boring, Tapping, Reaming	Tool Spindle	Cw, Bw, Xw(Xt), Zt1(Zt2), Yt
Turning, Drilling, Boring	Work Spindle	Xt, Zt1(Zt2)
Surface Grinding	Tool Spindle	Cw, Bw, Xw(Xt), Zt1(Zt2), Yt
Cylindrical Grinding	Tool Spindle	Cw, Zt1(Zt2)
Internal Grinding	Sub-Spindle	Cw, Za

4. COMPUTER AIDED ANALYSIS OF MACHINE TOOL

A mathematical model has been developed for the kinematic analysis system ADAMS in order to simulate the manufacturing processes and the set-up processes of the designed machine tool. The model describes the relative motion between the components, the dynamic characteristics of the individual components, and the dynamic characteristics of the joints between the components. The ADAMS system carries out the kinematic and dynamic analysis based on the model data, and displays the motions of the components in the machining and set-up processes.

An example to the results of the kinematic simulation is presented in Fig. 2. This figure shows the configurations of the machine tool in 5 axis machining of a sculptured surface. The input data of the simulation are the relative motion between the tool and the workpiece, and the ADAMS system calculates the positions and the orientations of

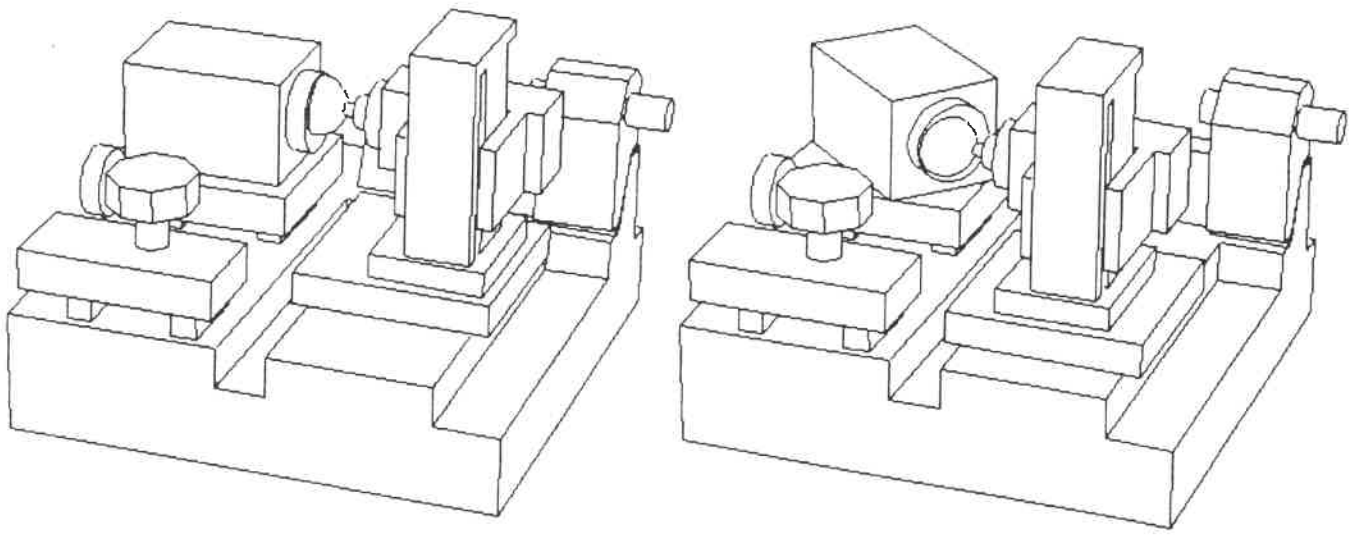

Fig. 2 Results of kinamatic simulation of multi-functional machine tool

individual components and displays the configurations of the machine tool.

The dynamic characteristics of the components, such as the linear feed mechanism and the work spindle has been also carried out based on the dynamic characteristics of both the components and the joints.

5. CONCLUSIONS

The functional requirements of the multi-functional machine tools were analyzed based on the questionnaire to both the users and the designers of machine tools. Basic configuration of a new type multi-functional machine tool was proposed based on the functional requirements. The designed configuration has two main spindles for both the tool and the workpiece, one sub-spindle for the internal grinding tool, and eight feed axes. A mathematical model was developed for the kinematic analysis system ADAMS in order to carry out the kinematic and the dynamic analysis of the designed machine tool. It was shown, through the simulation, that the machine tool designed here is applicable to the various manufacturing processes of mechanical products.

REFERENCES

[1] E. Salje and W. Redeker, Design of machine tools (cutting machines) by means of Computer Aided Design, Proc. of the 4th ICPE (1980), pp.386-393

[2] V. T. Portman, Synthesis of machine tool configurations based on an analysis of the form generation process, Soviet Eng. Research, 2-7 (1982), pp.65-69

[3] R. Schultschik, Requirements for structures of automated machine tools, Annals of the CIRP, 32-1 (1983), pp.433-437

[4] Powerful 5-axis software drive unique vertical 5 axis CNC machines, CNC/WEST, June 1987 pp.11-14.

[5] T. J. Lindem, Development of the Ingersol octahedral-hexapod machine tool for five-axis metal cutting, Proc. of the 7th IPES (1993), pp.149-152.

[6] JSPMI, Guidebook for introduction of group technology, JSPMI (1979).

[7[N. Sugimura et. al., Formulation of shape generation process of machine tools, Proc. of the IFAC 81 (1981), pp.XIV158-153.

THE BULGING EFFECTS OF BOLTED MACHINE TOOL GUIDEWAYS

Zhen Q. Zhu and Bi Zhang
Precision Manufacturing Center, University of Connecticut, Storrs, CT 06269

Introduction

The performance of precision machine tools is closely related to the performance of bolted joints. To increase machine tool performance, a great deal of work has been carried out towards the investigation of the behavior of bolted joints, e.g. the stiffness of bolted joints and their contribution to the overall stiffness of machine tools,[1-4] the interface pressure distribution of a bolted machine tool guideway with different distance between bolts,[2,5] the dynamic behavior of bonded, machined joint surfaces,[6] the surface roughness of bolted joint members on the frictional behavior of the joint,[7] and the finite element analysis and experimental study of stresses in bolts and nuts.[8-9] However, little work has been carried out to investigate the deformation or bulging of bolted guideways and other bolted members, and further, the effects of bulging on machine tool performance.

For high precision machine tool designers, it is important to know the geometric change or deformation of bolted members after bolting torque is applied. If such deformation is not tolerated for any reason, either new bolted joint configurations are to be designed or an additional machining process will be carried out on bolted members assembled with the torque to be used in service. For a high precision machine tool guideway, wave-like bulging will occur both on the top and two sides of the guideway after a certain torque is applied to bolts. This wave-like bulging will become high in amplitude as a large torque is usually applied to machine tool guideways to ensure high joint stiffness in both vertical and horizontal directions. Possible problems resulting from the wave-like bulging guideway will be the uneven preload of bearing members along the guideway, which in turn, results in an uneven resistance to the motion of a table top and large straightness error in the horizontal direction.

Theoretically, bulging of a bolted guideway is classified as a problem of a thick plate with mixed boundary conditions. Although analytical solutions of a thick plate of infinite radius are available,[10-12] the mixed boundary conditions of a bolted guideway are so complex that analytical solutions are difficult to get,[13] thus for certain purposes, e.g. calculating joint stiffness and axial deformation of bolted members, equivalent cones, cylinders and spheres are used.[4,14] However, these equivalent shapes have not been used for calculating the bulging of bolted members because the surrounding materials of the equivalent solids will tend to constrain the center solids and play an important part in horizontal deformation of the bolted members. To partially count the effect of the surrounding materials, a two dimensional physical model was proposed based on an inclusion embedded in a matrix.[15] This model will give an estimation of average horizontal deformation of bolted members if the inclusion and matrix are cylindrical in shape. In this investigation, the finite element method is employed to analyze the bulging problem. High resolution capacitance sensors are used to detect bulging when torque is applied to the bolts.

FEM analysis

The basic assumptions about two bolted plates are that these two plates can be represented by a single plate of the same thickness as the combined thickness of the two plates under symmetric bolting torque, and there is no z-displacement at the interface of two bolted members shown in *figure 1*. This is not true for a real case and also ignores any effect brought by two contact bodies with different dimensions, however, these effects are small at the vicinity of the bolt[10] where the three dimensional deformation of the bolt occurs. Further, it is assumed that there is no friction force between the plate and nuts and bolted members have isotropic linear elastic material behavior. *Figure 1a and 1b* show the cross sections of two guideways of a linear piezomotor and are used in both FEM analysis and experimental investigation. Side walls are designed as bearing area. *Figure 1c* is the configuration of many commercial guideways and is investigated by using FEM. For the commercial guideway, bearing balls or rollers can be arranged both at the top and the middle parts of the guideway to transmit external load from a table to the guideway.

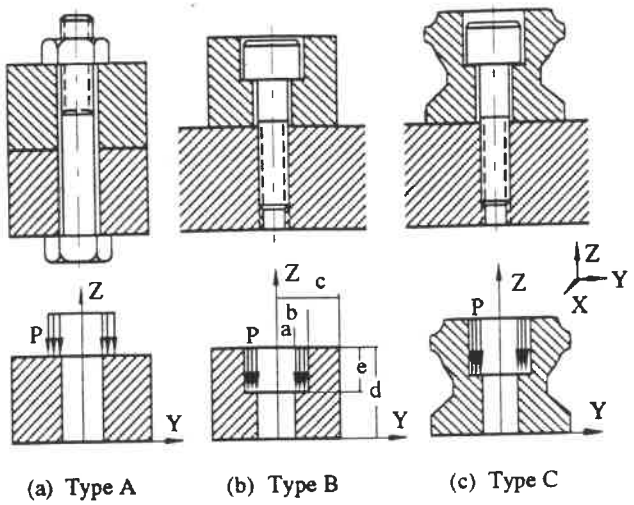

(a) Type A (b) Type B (c) Type C

Figure 1 Different configurations of bolted guideways and models for FEM analysis

Due to the symmetric geometry, loading conditions of bolted guideways, and homogeneous and isotropic properties of the materials used, deformation will occur symmetrically to the middle cross section plane between two bolts resulting in zero x-displacement of this plane, the cross section plane through the axis of a bolt also resulting in zero x-displacement, the XZ plane of the guideway resulting in zero y-displacement. Thus only a short quarter block around a bolt hole is needed for the FEM analysis which was carried out on the Mentat II/MARC finite element program from MARC Analysis Research Corporation.

Experiment

Guideways of tool steel were ground to 25 mm high and 38 mm wide with bolt holes of 12 mm (7/16) in diameter. The guideway shown in *figure 1a* is 200 mm long with 4 holes and *1b* is 400 mm long with 8 holes which have shoulders 12.5 mm in depth. A torque wrench was used to apply bolting torque. Three capacitance sensors of 9.5 mm in diameter were used for measuring the deformation of the guideway walls in the y-direction. Two of them were placed at both sides of the guideway symmetric to the middle XZ plane to pick up the total deformation from the two walls so any small shifting and rolling of the test guideway during tightening the bolt will be filed out. The third sensor could not be used in a pair and was used for collecting some information not used in this paper. Since the capacitance sensors from Lion Precision were initially calibrated for measuring master balls of one inch in diameter, calibration for measuring a flat surface was conducted first by using a laser interferometer from Zygo Corporation. A small flat surface was positioned by the nanometer resolution linear piezomotor developed at the Center, and part of the measured results is shown in *figure 2* .

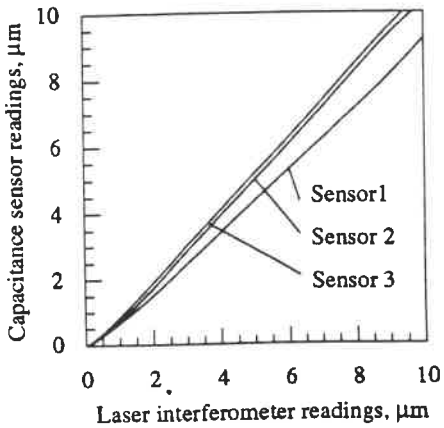

Figure 2 Capacitance sensors readings vs. laser interferometer readings

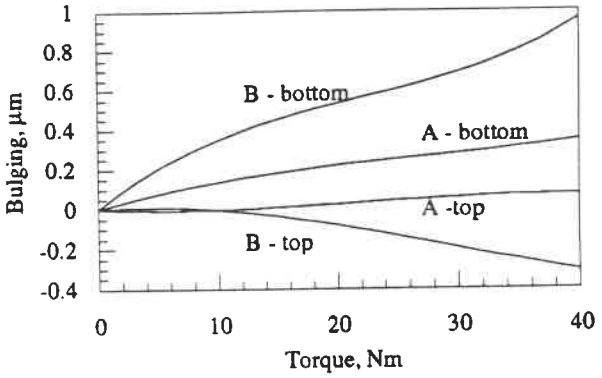

Figure 3 Bulging of guideway A and B in the y-direction measured with capacitance sensors

Results

Y-direction deformation

The y-direction deformations of guideways A and B were measured with tightening torque of 13.7 Nm (10 ft-lb), 27.4 Nm (20 ft-lb), and 41.1 Nm (30 ft-lb) as shown in *figure 3* . As the diameter of the sensor is 9.5 mm, the center of the sensor head is 4 mm below the top edge of the guideway, and 5 mm above the bottom edge for the y-deformation measurment. For the largest torque used, the experimental results show that the lower part of the guideway expands in the y-direction and the upper part shrinks very little or expands very little, i.e.,

0.66 μm and 0.07 for guideway A, and 0.97 μm and -0.3 μm for guideway B. These results agree with those of the FEM analysis as shown in *figure 4 and 5.* Instead of a tightening torque of 41.1 Nm (30 ft-lb), axial load of 20 kN was used in FEM analysis. The near bottom and near top y-deformation are 0.81 μm and -0.1 μm for guideway A, and 1 μm and -0.34 μm for guideway B.

For guideway C, which is 39 mm high, 45 mm long with bolt hole diameter of 14 mm and bolt shoulder of 18 mm deep, a 60 kN axial load is applied to each bolt hole, which are 102 mm away from each other. The FEM result in *figure 6* shows that the bottom part also expands, but maximum shrink occurs at about two thirds of the height of the guideway. For guideways with bearing balls arranged at the middle part, 2.3 μm expandsion and -2.1 μm shrinkage in y-direction are right on the paths of these balls.

Z-direction deformation

Due to the special geometry of guideway C, the z-deformation becomes significant as shown in *figure 7.* The side wall downward

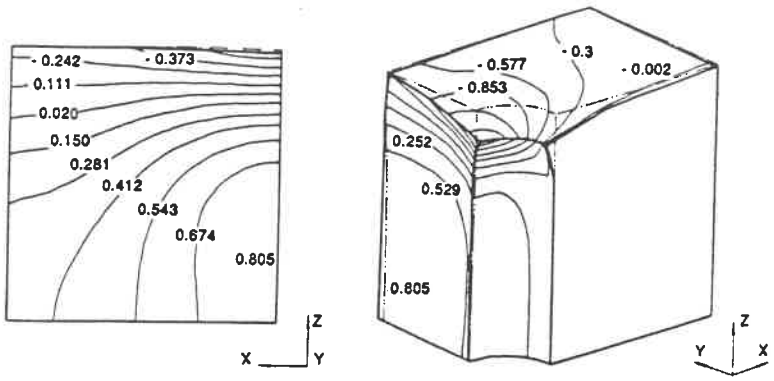

Figure 4 Bulging of guideway A in the y-direction obtained by FEM (in μm)

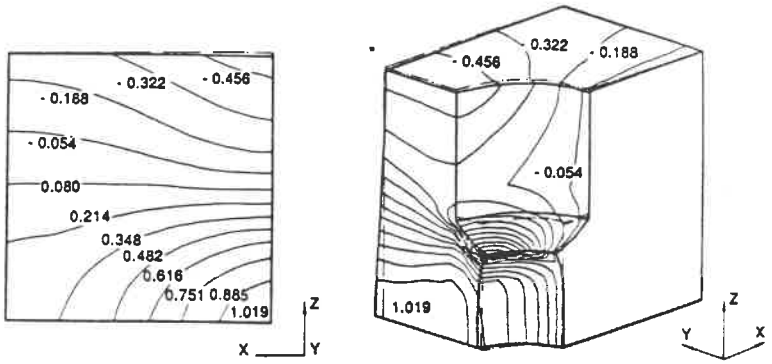

Figure 5 Bulging of guideway B in the y-direction obtained by FEM (in μm)

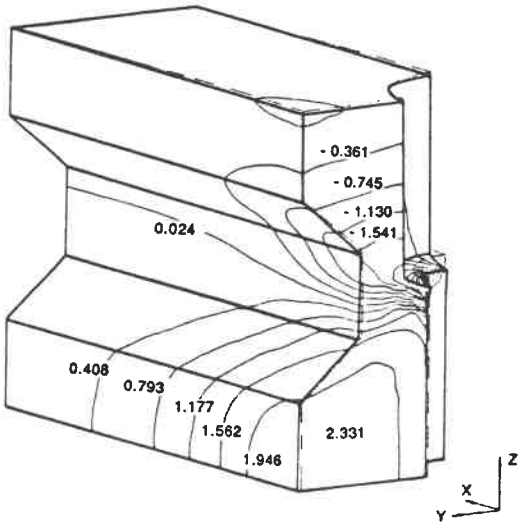

Figure 6 Bulging of guideway C in the y-direction obtained by FEM (in μm)

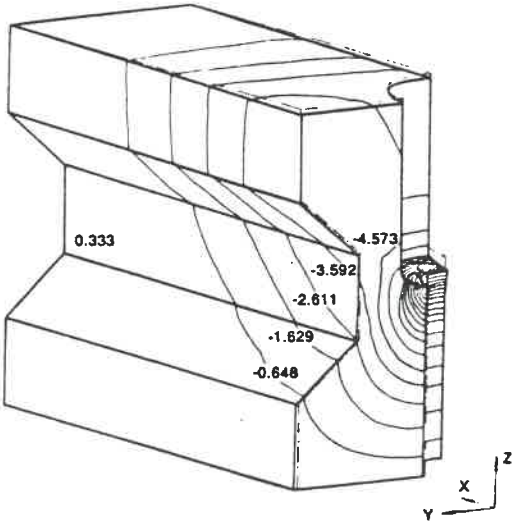

Figure 7 Bulging of guideway C in the z-direction obtained by FEM (in μm)

deformation of the top part is up to 5.2 μm. For the guideways with bearing balls arranged at their tops, this downward deformation is located right on the paths and will cause uneven loads on a group of bearing balls, which may result in a series of problems to a precision machine tool positioning system. Even for the lower bearing arrangement, the z-deformation is still in such an effect. If both y-deformation and z-deformation are considered, the lower bearing arrangement may result in more distortion and stress concentration of bearing components and carriages, which increases wear of these components and decreases the motion accuracy of a positioning table.

Conclusions

As an original research based on the increasing accuracy requirement from a bolted precision machine tool guideways, the bulging of such guideways is investigated by using both capacitance sensors for measurement and FEM analysis and the results coming from these two methods agree for the two guideways used. FEM analysis is also carried out on a typical commercial precision guideway. The above results show that the bottom part of a guideway expands, and the top part of guideway A and B shrinks, while the upper middle part of guideway C shrinks in the y-direction. For the commercial guideways with higher bearing arrangement, the z-direction deformation at the top part is found to be relatively high in amplitude and may cause uneven loading of groups of bearing balls, while for guideways with bearings arranged in the middle, the combination of the y-deformation and z-deformation may cause more distortion of the bearing components. As a practical correcting method, the bulging of a guideway could be eliminated by finish grinding the guideway with all bolts tightened with the specific torque used in service and a surface profiler could be used for checking the deformation caused by these bolts.

References

1 Connoly, R.and Thornley, R. H. "The significance of joints on the overall deflection of machine tool structures," in *Proceedings of the 8th MTDR*, 1967

2 Levina, Z. M. "Research on the static stiffness of joints in machine tools," in *Proceedings of the 8th MTDR*, 1967

3 Kobayashi, T. and Matsubayashi, T. "Considerations on the improvement of the stiffness of bolted joints in machine tools," *Bulletin of JSME* 1986, **29**, 3934-3937

4 Motosh, N. "Determination of joint stiffness in bolted connections," *Trans. of ASME J Eng Ind* 1976, 858-861

5 Ito, Y., Toyoda, J. and Nagata, S. "Interface pressure distribution in a bolt-flange assembly," *Trans ASME J Mech Design* 1979, 330-337

6 Thornley, R. H. and Lees, K. "Some static and Dynamic characteristics of bonded machined joint faces," in *Proceedings of the 8th MTDR*, 1972

7 Karamis, M. B. and Selcuk, B. "Analysis of the friction behaviour of bolted joints," *Wear*, 1993, **166**, 73-83

8 Fukuoka, T. and Yamasaki, N. "Stresses in bolt and nut," *Bulletin of JSME* 1986, **29**, 3275-3279

9 Patterson, E. A. and Kenny, B. "Stress analysis of some nut-bolt connetions with modifications to the external of the nut," *J. Strain Analysis* 1987, **22**, 187-193

10 Sneddon, I. N. "The elastic stresses produced in a thick plate by the applications of pressure to its free surfaces," in *Preceedings of the Camb Phil Soc* 1946, **42**, 260-271

11 Lardner, T. J. "Stresses in a thick plate with axially symmetric loading," *Trans ASME J Appl Mech* 1965, 458-459

12 Nelson, C. W. "Further consideration of the thick-plate problem with axially symmetric loading," *Trans ASME J Appl Mech* 1962, 91-98

13 Gould, H. H. and Mikic, B. B."Areas of contact and pressure distribution in bolted joints,"*Trans ASME J Eng Ind* 1972, 864-870

14 Bickford, J. H. *An introduction to the design and behavior of bolted joints.* Marcel Dekker, Inc., 1990

15 Li, Y. Y., Bailey, G., Kim, J. and Liang, S. "Thermal, phase transformation and residual stresses estimation of multi-phase materials for cylindrical or plate shape," 1994 (to be submmitted to *Trans ASME J Eng Mat & Tech*)

MEASURING METHOD TO DETERMINE DIMENSIONAL CHANGES ON ION NITRIDED STEELS

G. Ascanio, R. Nava, R. Trejo*, J. Rickards*
Centro de Instrumentos, Universidad Nacional Autonoma de Mexico
Apartado Postal 70-186, 04510 México, D.F.
*Instituto de Física, Universidad Nacional Autonoma de México
Apartado Postal 20-364, 04510 México, D.F.

ABSTRACT

Protocols developed and employed to determine dimensional changes on ion nitrided specimens are presented. Since the distortions measured are small, of the order of a few micrometers, the surface finishing of the specimens is very important. Specimen surfaces must be rectified to decrease the roughness and then small probes can be used in the coordinate measuring machine. The geometry of the sample is also important, because grooves are hard to measure, generally when using large diameter probes. The mounting of the samples on the measuring table is also considered. Other features of the method are mentioned, considering the design of a reliable, accurate and highly reproducible method.

INTRODUCTION

To improve the nitriding of iron and alloy elements, it is desiderable that the steels be quenched and tempered before the surface hardening process. During heating, distortion occurs as result of temperature difference in regions with small and large cross sections. Sometimes the resulting change in size or shape cannot be corrected by a subsequent machining in high precision parts.

A solution to this problem is the ion nitriding process, that is usually carried out at low temperatures, between 120°C and 300°C; therefore the distortion risk is minimum. The purpose of ion nitriding is to increase the amount of nitrogen on steel surfaces, producing a higher resistance to fatigue, corrosion and softening due to tempering.

Ion nitriding is a process that has been used extensively for improving surface properties of steels. It consists of placing the sample to be treated as the cathode in a glow discharge that contains nitrogen. One simplistic explanation for the observed effects is that positive ions from the discharge are accelerated towards the cathode and acquire energies up to a few thousand electron-volts. These high energies contribute to implant the nitrogen ions into the steel to a certain depth, which depends on the applied voltage. The heating induced by the ion bombardment of the cathode produces a thermal diffusion of the nitrogen deeper into the steel. In the process several nitrides of iron and other alloying elements are formed, that modify the hardness of the material.

EXPERIMENTAL DEVELOPMENT

In this work we present the method developed and employed to determine dimensional changes on ion nitrided samples. Samples used were Navy "C" specimens approved by the American Society for Metals (ASM). Three commercial grade steels were chosen: AISI 4140, 8620 and 9840. Two 4140 samples, one 8620 and two 9840 were used to determine the dimensional changes. Before nitriding, one 4140 sample and one 9840 were quenched and tempered.

The samples were heat treated under the following conditions: Austenitized at 850°C, quenched in fast oil, tempering temperature 200°C, during 45 minutes.
The ion nitriding was carried out under the following conditions:

Temperature*	300°C
Time	5 hours
Cathode voltage	2000 V
Pressure	$6{,}0 \times 10^{-2}$ mm Hg
Atmosphere	20% N_2 - 80 H_2

* The temperature was monitored at the base of the sample holder and stabilized around 300°C

Broadly, the method consists of measuring the dimensions of the samples both before and after ion nitriding; then comparing measurements and evaluating the dimensional changes. The shape and the dimensions of the samples used are shown on figure 1.

The measurements were carried out on a Karl Zeiss MC 850 coordinate measuring machine, by means of a computer control program. The MC has the following features:

Measurement range:	850 mm x 240 mm x 600 mm
Precision:	0,2 µm
Antivibration system:	air bearings, rigid structure
Air pressure:	7 kg/cm²
Probe:	five points (3 mm diameter)

For most reliable comparisons, measurement protocols have been developed taking into account all the parameters, controlled or not, for reducing to a minimum the uncertainty due to the instrument and the method. In this way, it was neccesary to determine the sources of errors, to evaluate their effects on the repeatability of the results, and to define criteria for improving the accuracy. Therefore, a strict process control was carried out as well as eliminating of sources of errors as follows:

1) The repeatability of the instrument was evaluated under different humidity and temperature conditions in the laboratory, measuring the same sample without removing from the MC. The measuremets were carried out with the same measuring protocol on different dates. In this case the average of the differences was 0.2 µm.

2) The repeatability of the mounting protocol of the samples on the MC was evaluated. It consisted of measuring a sample, remove it from the MC, place it and measure it once again. A block was used for placing the sample and the probe in the correct orientation of the sample on the MC. The average of the differences in this case was 10 μm.

3) The numeric control program was evaluated considering the measuring sequence and the selection criteria of reference surfaces, traslations and rotations around the axes. Although the program is 100% repeatable, small changes in the placing of the sample can generate big repeatability deviations.

4) Sample surfaces were rectified in order to decrease the roughness and small probes were used in the MC.

The last step was to assure the total repeatability of the method as well as the MC by means of two test samples, which were not heat treated nor ion nitrided. These test samples were measured using the same protocols of the dimensional change samples.

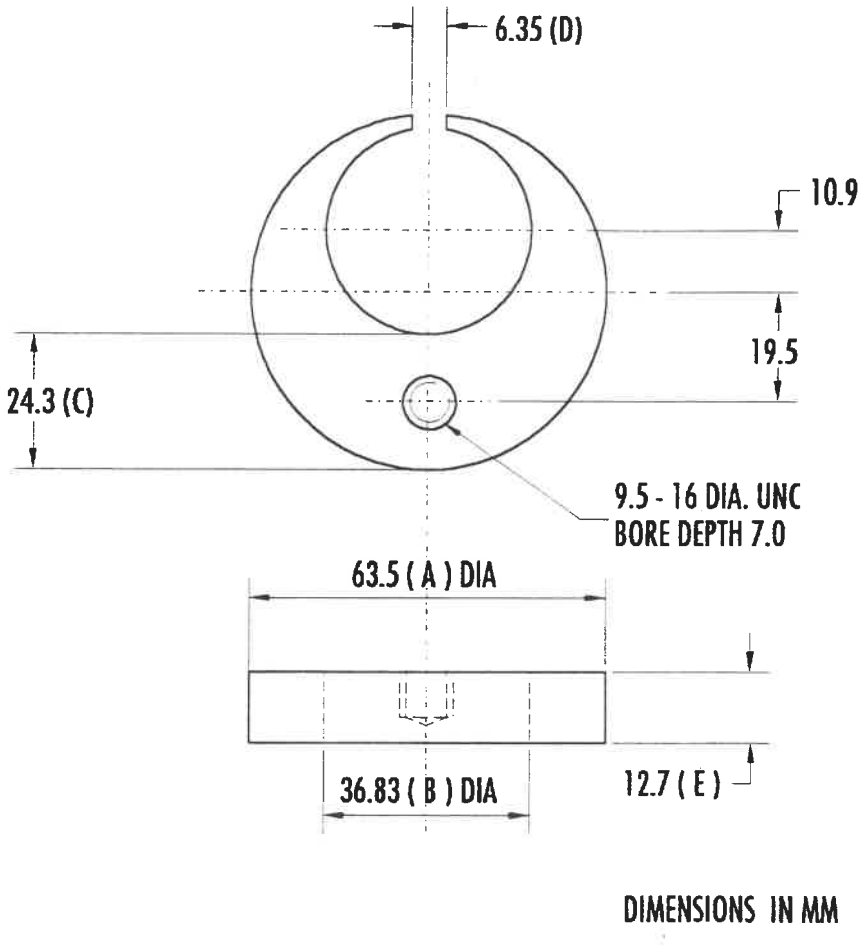

Figure 1. Dimensions of the Navy "C" Specimens

RESULTS AND DISCUSSION

The results obtained are shown on table 1.

STEEL	A	B	C (micrometers)	D	E
test sample 1	-0.2	-0.1	-0.1	0.2	0.1
test sample 2	0.2	0.2	0.0	0.1	-0.2
4140	3.7	4.6	3.4	2.2	1.3
4140T*	-70.8	-243.7	53.8	-532.5	62.3
8620	3.5	7.0	7.5	-2.0	0.7
9840	-1.6	-6.6	2.8	-0.8	0.7
9840T*	4.0	-96.5	38.9	-261.2	4.4

*T indicate that the steel has been heat treated before ion nitriding

Table 1 Difference between measurements before and after ion nitriding.

Referring to table 1, we can observe the influence of the quenching and tempering on the dimensions of the samples. The 4140T sample presents the biggest changes, while the 9840 sample the smallest.

It´s important to mention the results of the method on the test samples. The variations are so small that we can consider that the method is reliable in this application. They are an indication of the limits of the method.

CONCLUSIONS

A method for determining the dimensional changes in ion nitrided steels was developed. By comparing with test samples, the method employed is shown to be reliable, accurate and highly reproducible.

REFERENCES

R. Nava, G. Ascanio, R. Trejo-Luna and J. Rickards, Cuantificación de las Deformaciones Causadas por la Nitruración Iónica de Aceros, II Seminario Internacional de Metrología, (1994).

R. Trejo-Luna, E. Zironi, J. Rickards and G. Romero, Some Features of Low- Temperature Ion Nitriding of Steels, Scripta Metall. 23, 1493-1496 (1989).

T. Spalvins, Ion Nitriding, ASM International (1987).

Scratch Test of Glass Slides

Kangjie Li Yelena Shapiro and J.C.M. Li

Materials Science Program, Department of Mechanical Engineering
University of Rochester, Rochester, NY 14627

Introduction

Grinding and polishing of brittle materials like ceramics and glasses are necessary for precision instrumentation. Recently, it has been demonstrated that brittle materials like glasses can be ground without inducing fracture damage. This process is called ductile-regime grinding in which cutting depths of less than 50nm are generally required [1]. As we know, scratch tests [2] are fundamental to the understanding of grinding, polishing and wear with respect to material transport and removal [3,4]. A series of single point scratch tests were made on the soda-lime glass slides to shed some light on the deformation and brittle fracture of glass during grinding.

Experiment

A dead load scratch tester was designed and built in our laboratory to simultaneously record the normal load and horizontal force during the test (details to be published elsewhere). Fig.1 shows a typical experimental plot in which the normal load and horizontal force are shown as a function of time. The normal load was almost constant during the test while the horizontal force increased from zero and then stabilized at some value. The effects of normal load, driving speed and the shape of indenter were examined as well as the influence of liquid environments. In our study scratches were made at lower speeds (1 to 200 μm/sec) than those used in grinding so as to avoid the heating effect. High speed situations will be studied later.

1. Indenter Shape Effect:

Four different diamond indenters were used in the tests, i.e. a 76μm radius spherical indenter and three conical indenters with 60°, 90° and 136° included angles (2θ). The force ratio (horizontal force to normal load) increased with the sharpness of the indenter. The damage mechanism changed from plastic deformation (spherical and 136° indenter) to cracking (60° and 90° indenter) when the scratches were made under 10g normal load and at 10 μm/sec speed. For example, Fig.2 is an atomic force microscope trace of the cross section of the groove made by the 136° indenter showing pileups on the two sides, No cracks were seen in the optical microscope around the scratch made by this indenter. However there were chevron cracks along the sides of the scratch made by the 90° indenter. Fig.3 shows that the force ratio increases linearly with cot(θ), where θ=90° is taken for the spherical indenter.

The damage mechanism changes from plastic deformation to cracking with the increase of the sharpness of the indenter or normal load, i.e. with the increase of scratch depth. Therefore when the cutting depth is sufficiently small cracking damage may be avoided.

When the scratches were made with the spherical indenter surrounded by a drop of liquid stick-slip phenomenon was observed. However it was absent for conical indenters. So during grinding with a liquid, stick-slip motion may occur which may induce the vibration of the system when the depth of cut is small. The understanding of stick-slip phenomenon in scratching will be published elsewhere.

Acknowledgment

The work was supported by NSF through DMR 9221326 monitored by Dr. Bruce MacDonald. We thank Beta Ni of Kodak for the use of her indenters and Suresh Kudallur and Edward Li for helping build the equipment.

References

[1] T. G. Bifano, T. A. Dow and R. O. Scattergood, Ductile-regime grinding: a new technology for machining brittle materials, *ASME J Eng Industry*, **113**, 184-189 (1991).

[2] S. Jacobsson, M. Olsson, P. Hedenqvist and O. Vingsbo, Scratching Testing, *ASM Handbook*, Vol. **18**, 430-437 (1992).

[3] A. Broese van Groenou, N. Maan and J. D. B. Veldkamp, Scratching experiments on various ceramic materials, *Phillips Res. Repts.*, **30**, 320-359 (1975).

[4] A. Broese van Groenou, N. Maan and J. D. B. Veldkamp, Single-point scratches as a basis for understanding grinding and lapping, *The Science of Ceramic Machining and Surface Finishing II*. 43-60 (1979).

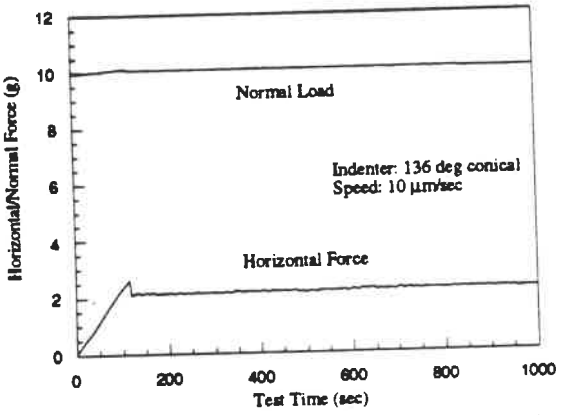

Fig.1 Typical experimental plot of normal and horizontal forces versus time.

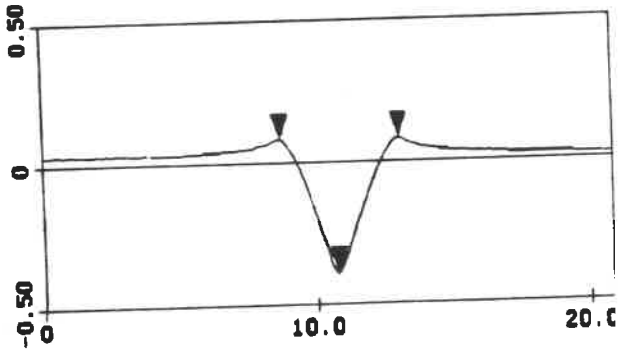

Fig.2 Cross section of a scratch made by the 136 deg indenter.

2. Normal Load Effect:

Normal load effects were studied with 90° and 136° conical indenters and the spherical indenter at a speed of 10 μm/sec. The normal loads used were 5, 10, 15, 20 and 25g for the conical indenters and 20, 30 and 50g for the spherical one. Fig.4 shows that the square of the scratch width increases proportionally with the normal load for different indenters. Although the force ratio is nearly independent of the normal load (Fig.5), the morphology of the scratches changed drastically with the normal load. For 90° indenter, more cracking occurred along the scratch with the increase of normal load, while for 136° indenter cracks appeared only when the normal load was more than 15g.

3. Speed Effect:

Speed tests were done with 90° and 136° conical indenters under a normal load of 10g. The speeds used were 2, 5, 10, 20, 40, 100 and 200 μm/sec. For 136° indenter, the depth and width (measured by atomic force microscopy) of the scratch grooves decreased with the increase of speed. For the 90° indenter, the crack density (defined as the fraction of the scratch covered by cracks) decreased with increasing speed. However, the force ratio didn't depend on the speed.

4. Liquid Environment Effect:

Scratches were made also in a liquid environment by surrounding the diamond indenter with a droplet of liquid. Water, sodium hydroxide, paraffin oil and glycerin were used. The horizontal force exhibited a saw-teeth wave form characteristic of a stick-slip behavior when the scratches were made with the spherical indenter (Fig.6). However when the conical indenters were used no stick-slip phenomena were observed (Fig.7). The horizontal force was higher when the scratches were made in water and NaOH, while paraffin and glycerin didn't have noticeable effects.

Discussions & Conclusions

The force ratio is independent of the normal load or the driving speed. However it is a function of the indenter shape. The relationship between the square of the scratch width and the normal load follows a single line for different indenters (Fig.4), indicating that the normal load is proportional to the vertical projected area. Since the force ratio increased linearly with $\cot(\theta)$, the horizontal force should be proportional to the horizontal projected area, i.e. $F \propto w^2\cot(\theta)$, where w is the scratch width. Since w^2 is proportional to the normal load, i.e. $N \propto w^2$, the force ratio F/N is only a function of $\cot\theta$ (Fig.3).

The depth and width of the scratch, as well as the crack density tends to decrease with the increase in driving speed. Since cracking needs time, the relationship of crack density (f_c is fraction of scratch covered by cracks) and speed can be derived based on the first order kinetics, namely, the probability of crack formation is proportional to the available uncracked portion of the scratch: $1-f_c = \exp(-k/v)$, where k is the rate constant. This equation is shown in Fig.8.

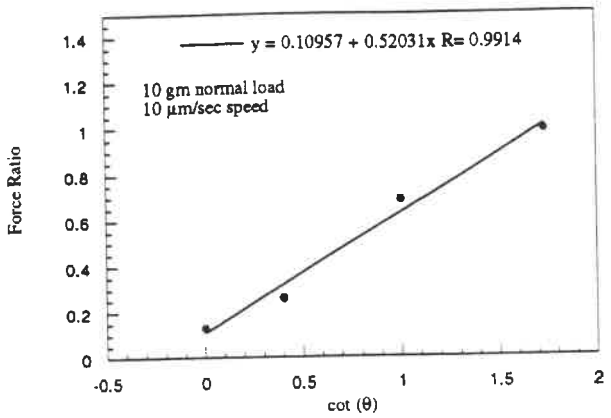

Fig.3 Force ratio as a function of cot(θ)

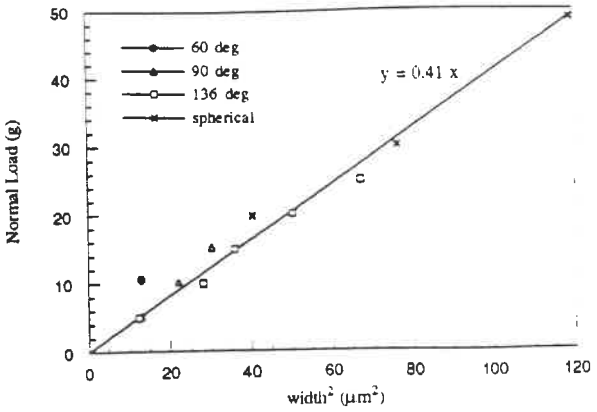

Fig.4 Effect of normal load on the scratch width

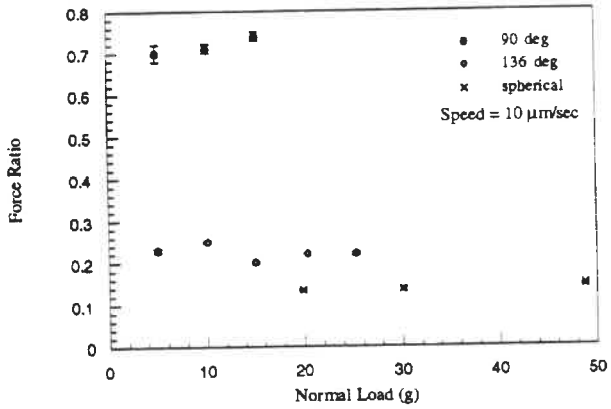

Fig.5 Normal load effect on the force ratio

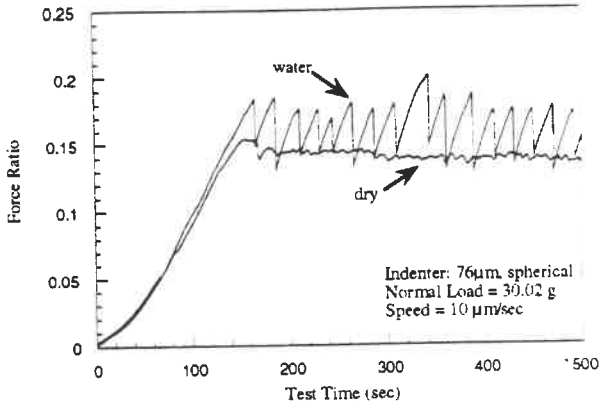

Fig.6 Effect of water for scratches made with the spherical indenter

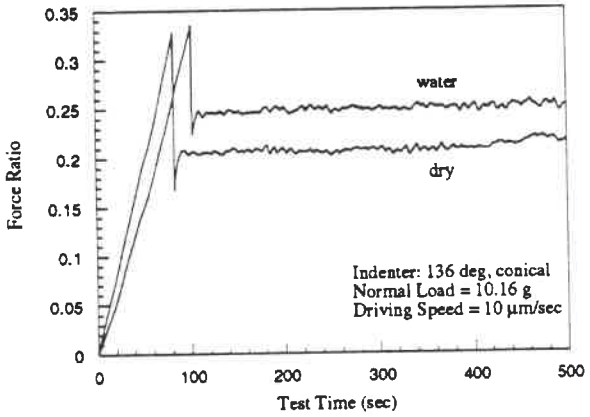

Fig.7 Effect of water for scratches made with the 136 deg conical indenter

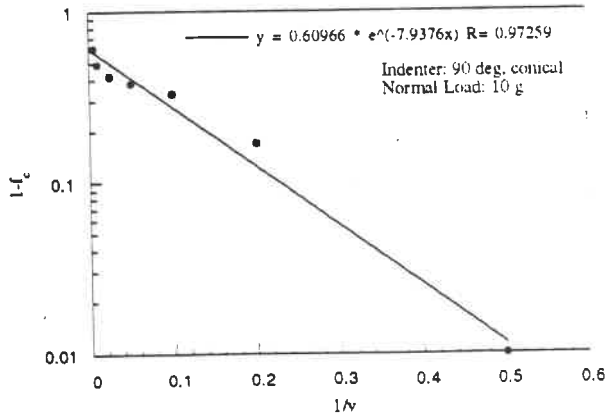

Fig.8 Relationship between crack density (f_c) and scratch speed (v)

Effect of Temperature and Load Rate on Brittle-Ductile Transition of Silicon Single Crystal

Noboru MORITA and Yoshitaro YOSHIDA
Faculty of Engineering, Chiba University
1-33, Yayoi-cho, Inage-ku, Chiba, 263, Japan

Introduction

It is well known that during the machining process of hard and brittle materials such as ceramics, the transition of the machining mode from the ductile mode to the brittle one, is related to the machining conditions and the tool shapes besides material properties. On the other hand, the micro-mechanism and primary factor dominating the transition has not been totally understood yet. In order to basically investigate the mechanism of brittle-ductile transition (BDT), the indentation experiments using silicon single crystal were carried out at various temperatures, loads and indenting speeds.

Experiments

The specimen and diamond indenter were heated up to 1473 K in a vacuum of 1×10^{-5} torr for the prevention of their oxidation and kept at the same temperatures by PID control method. The sapphire indenter was also used at temperatures above 1073 K. The load was applied to the plane (100) of silicon single crystal. Silicon single crystal is an ideal material as the experimental one because of crack-free and defect-free. The relations among crack length, temperature, load and indenting speed were discussed.

Results

Figure 1 shows the temperature dependence on the Vickers hardness at an indenting speed of 0.2 mm/s and an applied load of 1000 gf. The Vickers hardness HV decreases by a temperature rise. The logHV-T plots are divided in three segments of different gradient in three temperature regions and have two inflection points, which characterize a covalent bond-material. This behavior is independent of the indenting speed and applied load, and can be explained well by the transition of bonding system from covalent bonding to metallic one at high temperature. The following relationship can be established between the Vickers hardness HV and the

temperature T. Table 1 gives α and β in the three regions of temperature in Fig.1.

$$HV = \alpha \exp(-\beta T) \qquad (1)$$

Figure 2 shows the temperature dependence on crack length at an indenting speed of 0.2 mm/s and an applied load of 1000 gf. The crack length increases by a temperature increase at temperatures under 853 K before quickly decreasing in the temperature region between 853 K and 883 K. No crack propagates at temperatures above 883 K while appling load of 1000 gf at an indenting speed of 0.2 mm/s. BDT occurs in a very narrow region of temperature and is completed at 883 K under this experimental condition. This behavior is independent of the applied load [1].

Figure 3 shows the indentation features, cracks and slip lines being observed on the specimen surface at three temperatures. The largest cracks with slip lines is grown around the indented part at 853 K. On the other hand, slip lines and no crack are observed at 883 K. The square slip lines are characteristic of material with diamond crystal structure and results from the dislocation movement being much more active at high temperature. From these results, it is obvious that BDT is dominated by temperature in itself, and that the micro-mechanism of BDT is directly affected by the dislocation movement at BDT temperature because the dislocation velocity depends on temperature [2].

Figure 4 shows the temperature dependence on the critical indenting speed Vc, which means a maximum indenting speed required to cause brittle fracture at certain temperature. The critical indenting speed increases by a temperature rise. The linear relationship between logVc and 1/T can be established as follows:

$$Vc = f(\sigma)\exp\{-E/(kT)\} \qquad (2)$$

where, $f(\sigma)$ is a stress function, E is an activation energy and k is Boltzmann constant. The critical indenting speed up to the neighborhood of a melting point of the specimen can be estimated by outerpolation of the linear relationship illustrated in Fig.4. For example, the material temperatures above 1453K are required to indent in crack-free at a speed of 1000mm/s in the case of a load of 500gf. This mean that the material surface temperature during cutting process can be estimated to rise up to BDT temperature Tc under the ductile-mode cutting condition. In the actual machining, it seems that the temperature rise for the BDT is brought about by the friction heat between the tool edge and the material surface.

Conclusions

According to the results of the indentation experiments at high temperature with a silicon single crystal, the critical indenting speed depends on the material temperature

and applied load which have to do with the dislocation movement. We inferrer that the temperature and load rate are the controlling factors to BDT behavior, and that the brittle fracture occurs when the load rate is larger than the dislocation velocity at certain temperature. Deductively, in the actual machining, cutting load and cutting speed have strong connection with BDT behavior and the critical depth of cut.

References

1. T.C.WU, N.MORITA and Y.YOSHIDA, "Study on the Ductile Mode Grinding of Silicon Single Crystal", Proceedings of ASPE 7th Annual Meeting, 1992, 69-72.
2. M.Imai and K.Sumino, "In situ X-ray topographic study of the dislocation mobility in high-purity and impurity-doped silicon crystals, Philosophical Magazine A,Vol.47,No.4(1983)559.
3. N.MORITA, T.C.WU and Y.YOSHIDA, "The Effect of the Interaction of Abrasive Grains on the Deformation and Fracture Behavior of Brittle Materials", Proceedings of ASPE 7th Annual Meeting, 1992, 390-393.

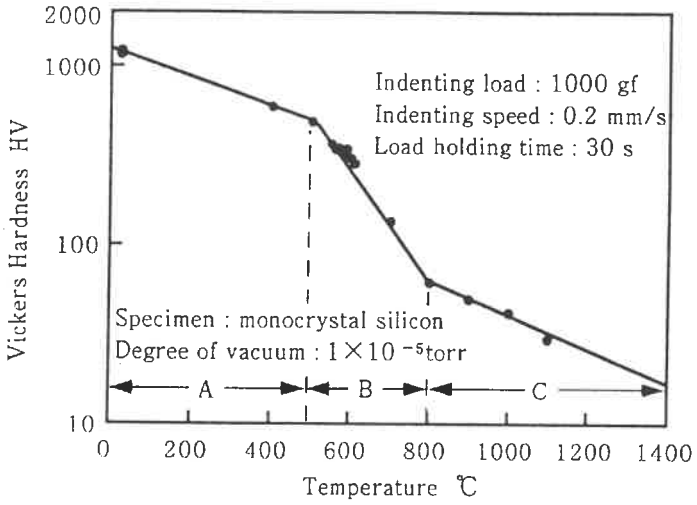

Fig.1 The temperature dependence on the Vickers hardness

Table 1 α and β in the three regions of temperature in Fig.1

Indenting load	Region	α	$\beta(\times 10^{-3})$
500gf	A	1570	1.327
	B	105900	6.952
	C	872	2.479
1000gf	A	2180	1.927
	B	66077	6.245
	C	790	2.357

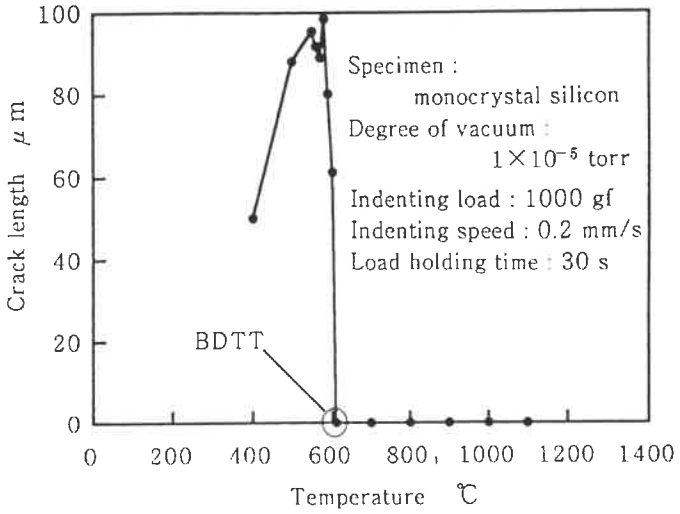

Fig.2 The temperature dependence on the crack length

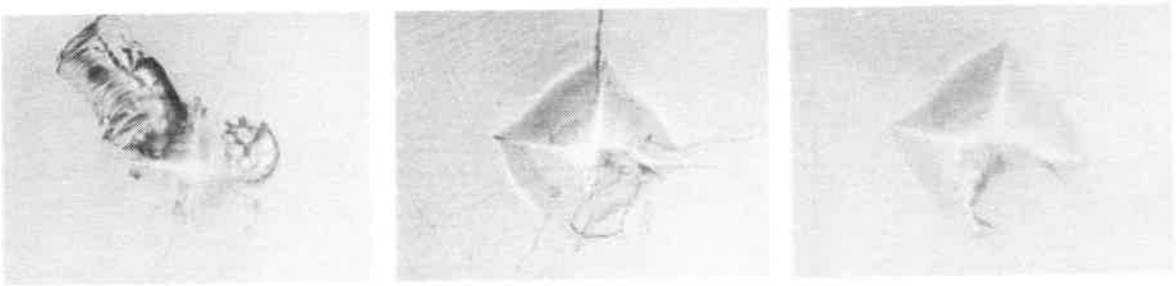

(a)673 K (b)853 K (c)883 K

Fig.3 The indentation features, cracks and slip lines observed on the specimen surface at three temperatures

50 μm

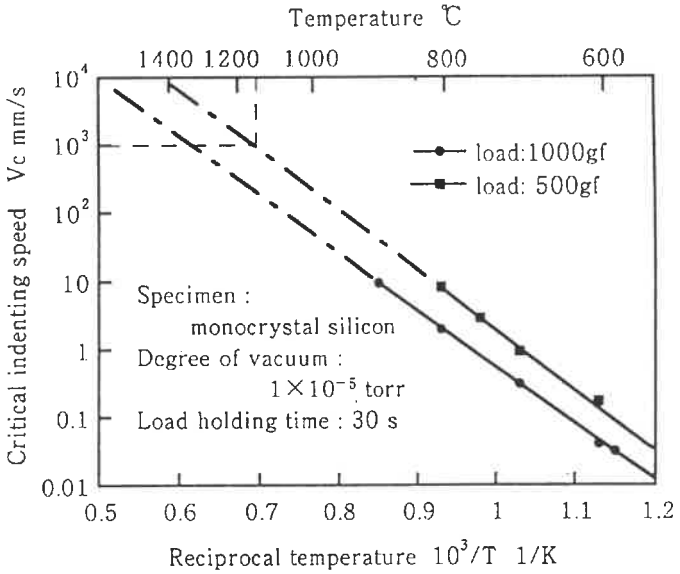

Fig.4 The temperature dependence on the critical indenting speed

A MODEL FOR PREDICTING GRINDING DAMAGE IN CERAMICS

Bi Zhang
Department of Mechanical Engineering
Precision Manufacturing Center
University of Connecticut
Storrs, CT 06269

I. INTRODUCTION

Grinding introduces damage in a surface layer of ceramics. To predict the grinding induced damage is extremely difficult because a grinding process is usually very complicated. Numerous research papers have been published towards predicting grinding induced damage, and understanding the underneath mechanisms. These include applications of the quasi-static indentation tests using a hardness tester to assess surface and subsurface damage, single-point scratching tests [1-2], and grinding tests [3-5].

Subsurface damage can be affected by numerous factors including (a) material properties, such as hardness, fracture toughness, and Young's modulus, (b) grinding conditions, such as depth of grinding, grinding wheel and workpiece speeds, (c) grinding wheel parameters, such as wheel diameter, grit size, grit type, concentration and hardness, and (d) grinding wheel truing and dressing conditions. To describe surface and subsurface damage nucleation and development requires a systematic investigation on the effects of all these factors. However, it is nearly impossible to do so because of many uncertainties involved in a grinding process. These uncertainties can be non-uniform distribution and extrusion of abrasive grits on a wheel surface, surface variations of a grinding wheel due to wear, pulling off, fracture, and loading of abrasive grits, as well as coolant application. For simplicity, many researchers evaluated grinding induced damage using models purely based on workpiece material properties.

Brittleness, which has been defined as the ratio of hardness to fracture toughness H/K_c [6], is a governing factor affecting the penetration depth of subsurface damage. Very little work has been done as to what role the brittleness plays and how much influence the brittleness gives towards damage initiation and propagation. In 1977, Lawn and Evans established a critical condition for the initiation of subsurface flaws based on an assumption that subsurface "fortuitous" flaws of the right critical dimensions exist in the vicinity of the elastic-plastic boundary of the highest indentation tensile stresses. They showed that the critical flaw size is inversely proportional to the square of the brittleness:

$$C_{\min} = \zeta\left(\frac{K_c}{H}\right)^2 \tag{1}$$

This was then modified by Hagan with a lower value of the constant ζ in 1979. In investigating surface damage generated in soda-lime glass by a Vickers hardness tester, Hagan identified that the median, radial and lateral cracks formed around Vickers indentations. These cracks arose from the inhomogeneous nature of the subsurface deformation [7]. Based on Stroh's hypothesis about dislocation pile-up, Hagan assumed that indentation cracks formed by collapsing and coalescing dislocation pile-ups to decrease the overall energy level.

The concept of Lawn and Evans' critical flaw size was further developed and extended to a grinding situation by Bifano *et al.* in 1991. They advanced a model to correlate the critical grit depth of cut with the material properties. The model was described by a simple power-law equation [4]:

$$d_c = 0.15\left(\frac{E}{H}\right)\left(\frac{K_c}{H}\right)^2 \tag{2}$$

Equation (2) indicates that brittleness plays a predominant role in determining the critical grit depth of cut. It has been, therefore, obvious that the critical flaw size and the critical grit depth of cut are inevitably determined by the brittleness of a workpiece material.

From the above review, we understand that under a given test condition, subsurface damage is solely a function of material properties, with brittleness being the predominant factor. No models, however, have been proposed for predicting subsurface damage in different grinding conditions. This paper presents analytical results on subsurface damage induced by grinding. A model is proposed for the prediction of subsurface damage. This model correlates subsurface damage with both grinding conditions and material properties.

II. DAMAGE PREDICTION MODEL

The normal grinding force on a single grit is proportional to the mean chip cross sectional area a_m which can be expressed as follows [8]:

$$F_n = \chi K_s a_m \tag{3}$$

where χ is the ratio of the normal to tangential grinding forces, and is a constant for a given grinding condition; K_s is the grinding force per unit chip cross sectional area, also called specific grinding force. K_s and a_m are given by the following equations:

$$K_s = K_o a_m^{-\varepsilon} \tag{4}$$

and

$$a_m = \frac{v}{VC}\sqrt{\frac{h_w}{D}} \tag{5}$$

where h_w, D, v, and V are wheel depth of cut, wheel diameter, workpiece speed, and wheel peripheral speed; C is the grit surface density which is defined as the number of active points per unit area of the wheel periphery. On the other hand, Lawn and Swain [9] developed a model that correlates median/radial crack size with the indentation load :

$$F_n \propto K_c Z_o \xi^{1/2} \tag{6}$$

where ξ is the radial crack depth; K_c is the critical stress intensity factor; Z_o is the depth of the irreversibly deformed zone under the diamond indenter. This model was modified by Kirchner [10]:

$$F_n \propto \xi \tag{7}$$

based on the assumptions that the irreversibly deformed zone remains geometrically self-similar as a function of load, and that the interfacial pressure is constant as a function of contact area. Kirchner further assumed that the cracks are propagating in the far field so that the characteristics of the contact do not influence the extent of crack propagation. This assumption resulted in the relation

$$F_n \propto \xi^{3/2} \tag{8}$$

In discussing the initiation and propagation of median and lateral cracks, Inasaki [3] obtained the relation

$$F_n \propto \xi^m \tag{9}$$

The exponent in equation (9) is given in the range of $1/2 \le m \le 3/2$ for different indentation conditions. By substituting the equations (4), (5) and (9) into (3), we then obtain

$$\xi = \left(\Psi \frac{4v}{VrC}\sqrt{\frac{h_w}{D}}\right)^{\psi/2} \tag{10}$$

In which ψ and Ψ are factors to be determined by material properties and machining conditions, and r is the ratio of chip width to average undeformed chip thickness. It is assumed that ψ is predominantly a function of material properties, and Ψ a function of machining parameters, i.e., $\psi = f(H/K_c)$, and $\Psi = f(\theta_1, \theta_2, \theta_3)$. Where H/K_c is the brittleness of the workpiece material, θ_1, θ_2, and θ_3 are related to grinding conditions, wheel conditions, and dressing and truing conditions.

Equation (10) directly relates subsurface damage size with the brittleness of a workpiece material H/K_c, the wheel depth of cut h_w; wheel diameter D; workpiece speed v; wheel peripheral speed V; the grit surface density C, and the ratio of chip width to average undeformed chip thickness r. This equation presents that the penetration of subsurface damage is enhanced by increasing the workpiece speed and wheel depth of cut, and is inhibited by increasing the wheel speed, the grit surface density of the grinding wheel, the wheel diameter, and the ratio of chip width to average undeformed chip thickness. Equation (10) can be simplified in terms of the maximum grit depth of cut:

$$\xi = \left(\Psi h_g\right)^{\psi} \tag{11}$$

This equation combines the grinding force models with the indentation induced crack model. The model proposed in the form of equation (11) needs to be verified by grinding experiments. It is noted that the factors ψ and Ψ are to be determined by experiments.

III. RESULTS AND DISCUSSION

Three ceramic materials were used in the study, including silicon nitride, alumina, and silicon carbide. These polycrystalline ceramics were tested and measured for the hardness and fracture toughness values using a micro-Vickers hardness tester. Table 1 lists the results of the test and measurement for brittleness values of these ceramics. For the comparison purpose, Table 1 also provides the values of brittleness of other selected materials. Table 2 lists the values of the mean grit size and grit surface density of three diamond wheels, and the corresponding grit depths of cut.

Figures 1&2 show experimental results on variations of subsurface damage depth with the brittleness and grit depth of cut for three types of ceramics. It was found that damage depth increased with the increase of grit depth of cut, but decreased with the decrease of brittleness of workpiece materials. However, the growth rates

of the damage penetration into surface were different among these materials. The growth rate for silicon nitride was the highest which was then followed by alumina and silicon carbide. As the grit depth of cut increased from 0.38 to 0.91 μm, the increase of the damage depth was only 10% for silicon carbide as compared to that of 100% for silicon nitride. These results strongly suggest that the brittleness of these materials play an important role in control of the damage penetration depth. This interprets that for a material with a large brittleness value, surface chipping or crushing is readily to occur, inhibiting a profound penetration of subsurface damage. The results also suggest that the increase of damage depth with the grit depth of cut do not follow a simple linear relationship, instead, it follow a relationship of an exponential function.

Table 1 Brittleness of Selected Materials [10-11]

Materials	H/K_c $\times 10^2$ /m$^{1/2}$
Diamond (single crystal)	225
Silicon (single crystal)	143
silicon carbide (pressureless -sintered)	83
Silica glass	75
Alumina (hot-pressed)	34
Silicon nitride (hot-pressed)	27
Silicon carbide (reaction-bonded)	17
Zirconia	16
Tungsten carbide	15

Table 2 Diamond Wheels Parameters

Diamond Wheel	Mean Grit Size μm	Grit Surf. Density grit/mm^2	Grit Depth of Cut μm
SD80-N50M	230	3.1	0.91
SD140-N75M	100	6.3	0.64
SD400-N75M	40	17.4	0.38

It should be noted that two factors ψ and Ψ are correlated with material properties, grinding wheel parameters, grinding, truing, and dressing conditions. The influences of variations in grinding, truing and dressing conditions are not considered in this experiment.

Based on the experimental results in Figures 1&2, two factors for the proposed model can be determined as

$$\psi = \frac{1}{\log\left(\frac{H}{\lambda K_c}\right)} \quad \text{and} \quad \Psi = 200$$

where $\lambda = 10^2 / \sqrt{m}$ is a constant. By substituting the factors ψ and Ψ into equation (11), the proposed model then become

$$\xi = \left(200 h_g\right)^{1/\log\left(\frac{H}{\lambda K_c}\right)} \qquad (12)$$

It can be shown that ψ is inversely related to brittleness H / K_c. Therefore, damage depth ξ is also inversely related to H / K_c.

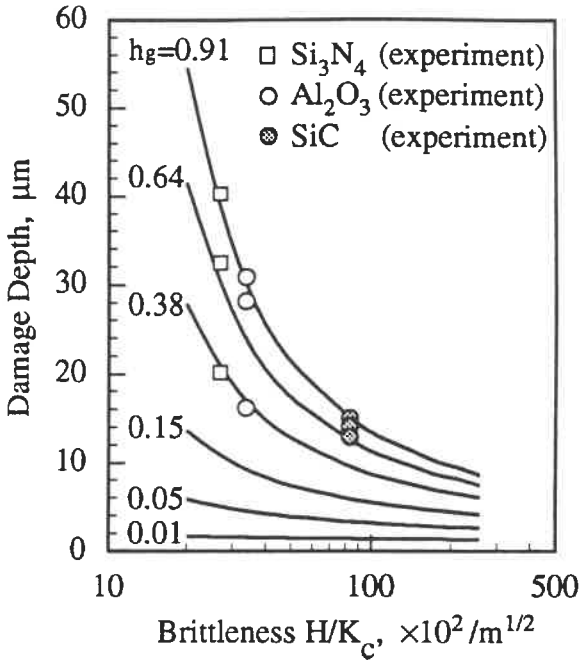

Figure 1 Variations of damage depth with brittleness of various materials at different grit depth of cut. Solid lines are plotted based on equation (12)

Based on equation (12), variations of predicted damage depth are plotted against brittleness of workpiece materials in Figure 1, and against grit depth of cut in Figure 2. As it can be seen from these figures, the predicted damage depths have a good agreement with the experimental data for these ceramic materials. According to Figures 1&2, several points need to be addressed: (a) The penetration depth of subsurface damage exponentially increases with increasing grit depth of cut; (b) A material with a large brittleness value receives subsurface damage with a small penetration depth, however,

a material with a low brittleness value will receive subsurface damage with a large penetration depth; (c) As the grit depth of cut decreases (e.g. < 0.1 μm), the difference in penetration depth among these materials tends to be smaller and smaller, suggesting that in a precision grinding process, the predominant subsurface damage be powder regime and scattered voids because of the decreased grit depth of cut; (d) As the grit depth of cut increases, the difference in damage depth among these materials becomes larger and larger. This interprets that for a material with a large brittleness value, surface chipping or crushing is readily to occur, inhibiting a profound penetration of subsurface damage.

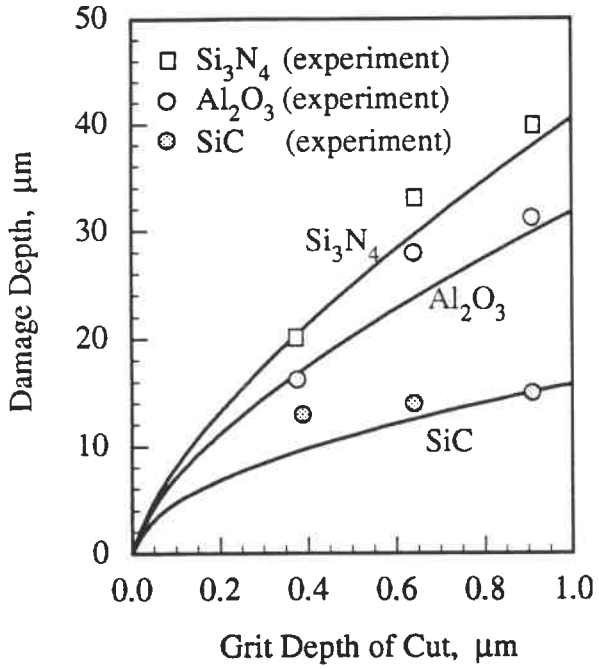

Figure 2 Variations of damage depth with grit depth of cut for various materials. Solid lines are plotted based on equation (12)

IV. CONCLUSIONS

This investgation presents a model for the prediction of grinding induced damage in ceramics. The following is a summary of the results obtained from this study:

- An analytical model is proposed for the prediction of grinding induced damage in ceramics. This model is presented in a simple form as

$$\xi = \left(200 h_g\right)^{1/\log\left(\frac{H}{\lambda K_c}\right)}$$

The model correlates subsurface damage with brittleness of workpiece and grit depth of cut of a grinding wheel.
- The damage depth predicted by the proposed model has a good agreement with the experimental results.
- The correlation of subsurface damage depth with grit depth of cut does not follow a simple linear relationship. Instead, it follows a relationship of an exponential function with the exponent being related to the brittleness of a workpiece material.

REFERENCES

1. Xu, H.K., and S. Jahanmir, "Microfracture and Material Removal in Scratching of Alumina," submitted to Journal of Materials Science, 1994.
2. Zhang, B., H. Tokura, and M. Yoshikawa, "Study on Surface Cracking of Alumina Scratched by Single-Point Diamonds," Journal of Materials Science, 23 1988, pp. 3214-3224.
3. Inasaki, I., "Grinding of Hard and Brittle Materials," Annals of the CIRP, Vol. 36, 1987, pp.1-9.
4. Bifano, T., T.A. Dow, and R.O. Scattergood, "Ductile-Regime Grinding: A new Technology for Machining Brittle Materials," Journal of Engineering for Industry, Vol. 113, 1991, pp 184-189.
5. Yin, L., R.Y. Chen, Z. Liu, and Y.T. Fu, "Study of Chip Formation Mechanisms in Engineering Ceramics Grinding," Proceedings of 3rd International Conference on High Technology, Chiba, 1992, pp 403-407.
6. Lawn, B.R., "Fracture of Brittle Solids - Second Edition," Cambridge University Press, 1993, pp. 314-319.
7. Hagan, J.T., "Micromechanics of Crack Nucleation during Indentations," Journal of Materials Science, Vol. 14, 1979, pp. 2975-2980.
8. Kawamura, S., A. Yano, M. Higuchi, and T. Sugita, "Grinding and Abrasive Machining," Kyoritsu Shuppan Ltd., Tokyo, 1984, pp. 38-46.
9. Lawn, B.R., and M.V. Swain, "Microfracture Beneath Point Indentations in Brittle Solids," Journal of Materials Science, Vol. 10, 1975, pp 113-122.
10. Kirchner, H.P., "Damage Penetration at Elongated Machining Grooves in Hot-Pressed Si_3N_4," Journal of American Ceramic Society, Vol.67, 1984, pp 127-132.
11. Zhang, B., "Study on Surface Integrity of Advanced Ceramics Ground by Diamonds," *Ph.D. dissertation*, Tokyo Institute of Technology, Tokyo, Japan, March 1988.

The Implementation of Visual Sensory Data in a Closed Loop Video Feedback Manufacturing Environment

Bruce R. Mackie
DI/MAC Technologies
2160 Premier Row
Orlando, FL 32811

Introduction

The quest for ever increasing productivity, in a modern manufacturing environment, has spurred the advancement in the application of computer technology at an increasing pace. Due, in part, to the desire to have these applications perform in a real-time closed loop control environment, many applications dictated the incorporation of dedicated embedded hardwired processors for high data rate applications. Relegating the general computational capabilities of a host processor (typically PC based) to supervisory and/or low data rate acquisition and analysis tasks

Manufacturer's are fast approaching the natural limits of these traditional architectures (driven more by cost issues than technological barriers) and are seeking alternatives which will increase the scope of applicability of these technologies. Thus, providing increased flexibility in applying their manufacturing resources to a wider array of tasks. In this regard a truly precise and independent, yet tightly coupled, multi-processing architecture offers the greatest potential for reducing the barriers to high data rate acquisition (digital image processing) enabled closed loop manufacturing systems.

This paper presents one such alternative architecture applied in a Video Feedback Closed Loop (**VFCL™**) manufacturing environment. The underlying theoretical basis for such systems, the benefits realized in addition to a real-world example of such an implementation of a **VFCL** system are discussed herein.

VFCL Architectural Implementation Example

A successful blow molded bottle manufacturing process is highly dependent upon a wide array of variables, that if well controlled, will yield a consistently precise output. Critical factors monitored during this multi-step manufacturing process include; mold thermal characteristics, plastic shot material volume, plastic shot material thermal characteristics, shot pressure, post molding cooling characteristics, post molding flaming to seal the bottle surfaces, etc. If all of these variables are maintained within process minimum/maximum values, a highly efficient production process is the end result.

The collection, collation, storing and analysis of such a large database of information is both human and resource intensive. Further, due to the human in the loop variable, the accuracy and repeatability of the data collection function is often factored into the analysis equation as an assumed constant. Thereby, degrading the impact of the data collected; often leading to a skew (or bias) in the results derived. Finally, the cost of the data collection and database maintenance function quite frequently leads manufacturers to sample production runs (to reduce costs) rather than perform 100% real-time inspection. In doing so the results derived are further degraded by large gaps in the data stream collected.

Although these statistical analysis techniques have proven to be "good enough" to date, leading to fairly well defined and reasonably well controlled processes; the days of "good enough" are fast coming to a close. The globalization of the economic system has applied new pressures on manufacturers to transform their manufacturing operations into world class, high quality and lowest cost of production environments. World class typically is dictated by the adoption of products and standards that apply to a wider market community. In general these are well defined and easily achievable at low to moderate cost to the manufacturer.

However, the interrelated (and often conflicting) goals of quality and efficiency are less altruistic and more deterministic. Currently, quality control and assurance is more of an end game (post-production analysis and feedback) and efficiency is a province of the process control engineering community (in process control and feedback). These differing perspectives typically establish an adversarial relationship between the two groups. It is now possible, via **VFCL** technology, to create a real-time quality control function, that enhances the efficiency of existing closed loop process control systems.

Figure 1 illustrates a traditional architecture relating quality control and process control. Figure 2 illustrates a **VFCL** enhanced relationship between these two functions.

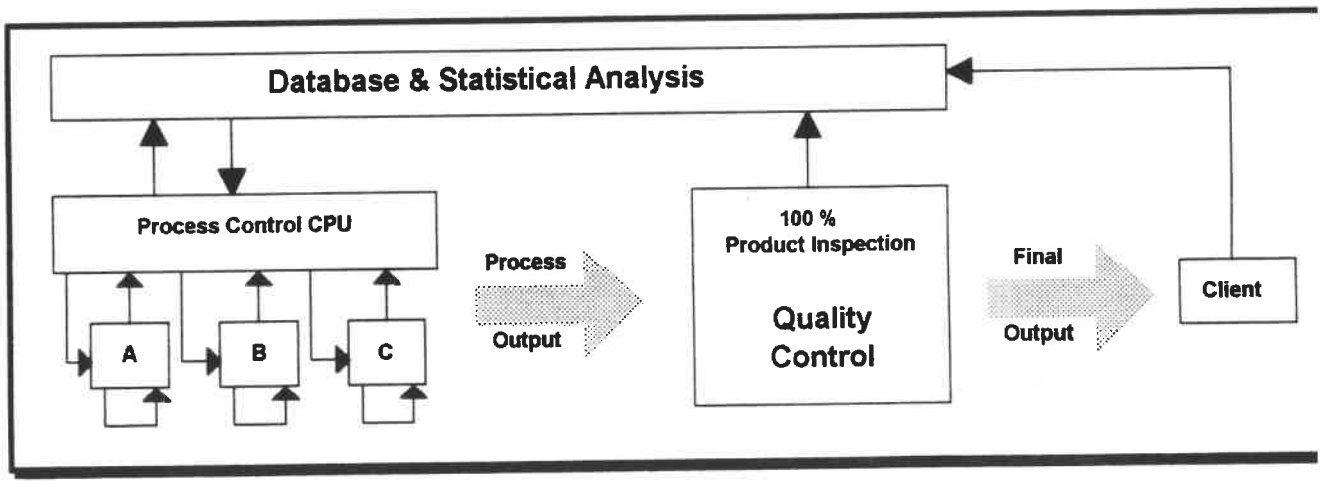

Figure 1 Traditional Interrelationship of Quality and Process Control Functions

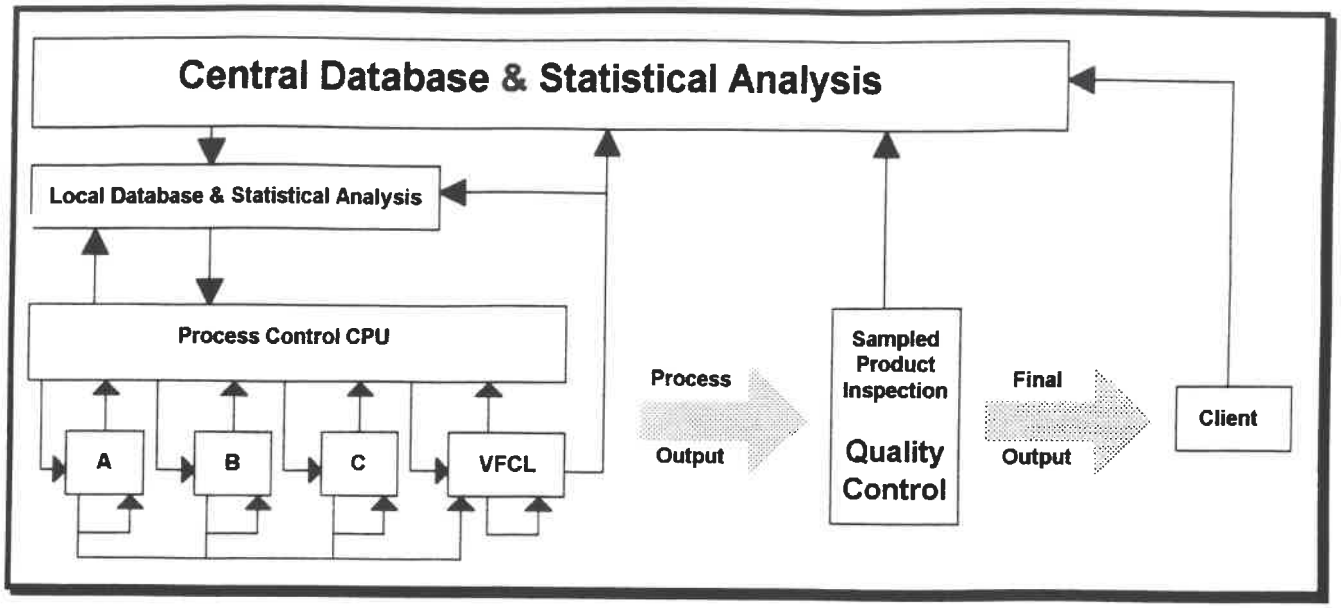

Figure 2 VFCL Enhanced Interrelationship of Quality and Process Control Functions

As is clearly illustrated in Figure 1, the long feedback loop that exists within a traditional manufacturing process allows only for long term systemic changes within the manufacturing loop. Although this allows a process to be fairly predictable over time, the benefits achieved through conversion to this form of feedback control topology are primarily realized when such a system is initially implemented. However, due to the loop feedback cycle, it is virtually impossible to realize any efficiency improvements whose significant contributing factor is short term and locally (within the process) based.

Within the **VFCL** implementation both forms of benefit are realized with the initial establishment of the system and significant long term benefits can be extended due to the direct connection between the quality control function and the process outputting product. Further, as is illustrated the output of the VFCL element can be archived centrally for long term statistical analysis and feedback thereby providing both short term and long term statistical perspectives of any manufacturing process adaptable to visual inspection/metrology technologies.

Results and Benefits

Utilizing our sample application of blow molded bottle manufacturing as an example, how can a VFCL enhanced process be beneficially deployed? Utilizing both metrological methods and gray scale image analysis, it would be possible to establish a closed loop environment that improves process efficiency, improves the quality of process product fed forward to subsequent processes and reduces waste of material, human resources and capital investments. Each is detailed herein.

Through a metrological examination of the structure of the blow molded bottle (in comparison to industry established standards) it is possible to immediately determine the structural integrity of the bottle. All out of tolerance bottles are reprocessed, immediately, to recapture the material for incorporation into the current process. All structurally sound bottles are then subjected to a gray scale analysis to determine the wall thickness of the bottle last produced. Again, all bottles not meeting industry standards is reprocessed, immediately, to capture the material content and all known good bottles pass on to the next manufacturing step. Thus only known good bottles are produced at the primary blow molding stage. Thereby, satisfying a critical quality control requirement.

However, through a statistical analysis (both physical and time based) trends can be isolated, detected, analyzed and acted upon. Certain classes of defect or trends toward the industry standard minimum/maximum values for either metrological of gray scale analysis values can be statistically correlated to specific process variables. These correlated values can initiate corrective actions within the process, in real-time, to insure that a process operates as closely as possible to centerline norms, established for the process.

For example, thinner than normal sidewalls can be an indication of a shortage of raw material injected into the mold. A variable thickness sidewall can be an indicator of low air pressure within the molding environment. Neck feature metrology variations may be an indicator of improper mold thermal control. The detection of contaminates with the bottles surface are indicators of source material contamination.

Conclusions

As can be seen, the incorporation of digital imaging within a manufacturing process can be both financially and productivity enhancing. However, since imaging tends to be compute intensive it is not readily adaptive to existing and future processes due to the demands of other process elements for the limited local computing power. Through the implementation of **VFCL** capable industrial imaging technology, little if any additional computational burden is placed upon the process CPU, significant amounts of data can be capture and analyzed to further enhance the localized manufacturing process, as well as all subsequent down stream processes.

From a corporate perspective, an investment in **VFCL** industrial technologies will greatly enhance the quality of output from any discrete manufacturing stage. Thus insuring that each subsequent manufacturing stage's resources are applied to a maximized benefit. Further, due to the immediate feedback (with integral analysis capabilities) into the current process, the **VFCL** industrial imaging system significantly enhances the efficiency of any process that it is incorporated within.

Significant return on invested capital (**ROIC**) can be anticipated, well beyond the expenditure for the **VFCL** technology itself. This is a direct result of the **VFCL** system's ability to minimize wasted process throughput. Thereby, fully utilizing investments in material, human and capital equipment.

Finally, the public and customer relationship of a manufacturer is greatly enhanced. A less wasteful process translates into lower cost of production. This is a client enhancement or a profit enhancement dependent upon market needs. Less waste focuses attention on the manufacturer as an environmentally aware corporate citizen. A manufacture that is capable of doing more with less. Overall **VFCL** enhanced manufacturing processes are truly **WIN-WIN** situations.

MANUFACTURING ERROR FLOW AND ITS MODELING

*Z. Luo, †Y. Rong and ‡Y. Zhu
*Department of Precision Instruments, Tsinghua University, Beijing, China
†Manufacturing Systems Program, Southern Illinois University at Carbondale, USA
‡Dept. of Mechanical Engineering, Beijing Institute of Machinery Industry, Beijing, China

In modern industry, quality of products has become a key factor that determine competitive capability of a company. In order to improve the production quality, increase the productivity, and reduce the cost and reject/scrap rate, research on real-time monitoring, control, and quality assurance technologies in manufacturing processes has attracted more and more attention.

One of the purposes in manufacturing is to change the geometry of workpieces by removing unnecessary volumes of material or other methods, from a blank form to a finished product with a certain accuracy. A manufacturing process could be actually a process of changing the initial geometric error (blank error) into an allowable manufacturing error desired in the product design. In production, the stabilization of manufacturing errors is a pre-requisite for effectively processing workpieces with manufacturing equipment. In order to deeply investigate on the variation and transferring of machining errors, the concept of Manufacturing Error Flow (MEF) is introduced in this paper. In fact, the monitoring, control and quality assurance in manufacturing processes is the process of MEF detection, signal processing and recognition, as well as decision making and control, to satisfy the quality requirement of product designs and to meet the need of customers. Therefore this study may provide a new observation of the manufacturing error control.

In this paper, the MEF concept is introduced first, which describes the relationship of input and output manufacturing errors in a specific operation. An iterated model is established to characterize the dynamic features of MEF. A catastrophe model of manufacturing errors is constructed to discuss the stability of MEF. On the basis of analysis of the two methods above, the stabilization conditions of MEF are presented, which provides a basis of manufacturing error controls. A neural network (NN) simulation method is developed to predict the MEF, which is compared with the results from a least square regression (LSR) model. Production data from measuring manufacturing errors are utilized to verify the results from these models.

Manufacturing Error Flow (MEF) and its Iterated Mapping Model

The term "flow" mentioned in this paper can be described as "the status and changes of a system". In a manufacturing system, there are different kinds of flows, i.e., material flow, energy flow, information flow, finance flow, error flow, etc. With the progress of sequential operations in production, the input blank errors of machining system is transferred into the output workpiece/part errors.

Manufacturing error flow (MEF) presents a process of the variation and transferring of manufacturing errors where the blank errors is entered into a manufacturing system and regularly transferred to the finished product errors within a certain allowable range. It characterizes the variation process of workpiece error in the manufacturing system. In a certain process sequence consisting of n operations, for any specific operation, the relationship between the output dimension y and the input dimension x can be expressed as:

$$y = f(x) + d \tag{1}$$

where d is an inherent error which is a natural manufacturing error generated by the manufacturing system itself and related to factors such as the manufacturing method, the dynamic precision of machine tools, cutters, fixtures, and measuring equipment/devices, as well as the thermal and forcing effects in the manufacturing process. f(x) is the "inherited" (transferring) function which transfers a dimension from x to y.

If y_0 and x_0 represent the nominal values of y and x respectively, the Taylor's series of f(x) at $x = x_0$ is:

$$f(x) = f(x_0) + \frac{f'(x_0)}{1!}(x - x_0) + \frac{f''(x_0)}{2!}(x - x_0)^2 + \ldots + \frac{f^{(k)}(x_0)}{k!}(x - x_0)^k + \ldots \tag{2}$$

where k = 1, 2, ... K, ...

When $|(x - x_0) / x_0| << 1$, the first truncation of Eq. 2 becomes:

$$y = f(x_0) + f'(x_0)(x - x_0) + d. \tag{3}$$

Considering operation i, let $y_i = y - f(x_0)$; $x_i = x - x_0$; $a_i = f'(x_0)$; and $d_i = d$. i = 0, 1, 2, ... n. it is the ordinal number of operations. Then we obtain:

$$y_i = a_i x_i + d_i \tag{4}$$

where a_i is the inherited coefficient; $a_i x_i$ is the inherited error which is partial error that is transferred from input error x_i to the output error y_i; and d_i is the inherent error.

The a_i and d_i in Eq. 4 are variable coefficients which may be obtained from a regression of dimension data of sample workpiece/parts, if the manufacturing process is stable. For those operations that improve the precision of workpieces, $0 < a_i < 1$, and $d_i < d_{i-1}$. For the operations that enlarge manufacturing errors, $a_i > 1$ and $d_i > d_{i-1}$ (e.g., in a heat treatment process). Reference [1] gave out measuring data from seven different operations of producing piston rings. Through regression calculations, it is obtained that a_i = 0.280 - 0.615, d_i = 0.0142-0.054 mm, which verifies the validation of Eq. 4.

The nature of Eq. 4 is to divide the manufacturing errors into two parts: inherited errors, $a_i x_i$, and inherent errors, d_i. However, this is just a static description of manufacturing errors [2]. In order to study the dynamic characteristics, a dynamic model of manufacturing errors can be constructed by using a one-dimension (single variable) iterated mapping F [3]. With the generality, the relationship between x and y can be expressed as:

$$y = F(x) \tag{5}$$

After the first truncation of Taylor series, it is obtained:

$$y_i = \Phi(x_i) \tag{6}$$

where $\Phi(x_i) = F'(x_0)\, x_i$, i = 1, 2, ... n. If output error of previous operation y_{i-1} is regarded as input error of current operation, it becomes:

$$y_i = \Phi(y_{i-1}) \tag{7}$$

Eq. 7 is the one-dimension iterated model of manufacturing error. It is a dynamic description of MEF.

Catastrophe Model of MEF and its Analysis

Catastrophe theory has been developed to study non-linear stability problems [4] and was applied to the study of chip formation in machining processes [5]. Because the iterated model of MEF could be non-linear (a_i is a variable), the catastrophe theory may be used to characterize MEF. The core issue of constructing a catastrophe model is to build a potential function with system parameters [6].

The Catastrophe Model of MEF

The catastrophe model of MEF can be constructed according to the topological mapping of differential manifold [6]. The pre-requisite of Eq. 3 and 4 is $|(x - x_0) / x| << 1$. In fact, the order of truncation in Taylor series depends on the truncation error and should be determined according to the "1/10 rule" in the accuracy theory [2], i.e., mean error $\bar{y}_i$ and allowance $\delta\bar{y}_i$ shall satisfy the condition $\bar{y}_i \le (1/3 - 1/10)\, \delta\bar{y}_i$. Therefore, the order of truncation should be determined according to specific manufacturing conditions. In this research, on the basis of the measured data of piston ring samples given in reference [1], the fourth order truncation is used (details are described in Section 3). After the truncation of Taylor series, Eq. 5 becomes:

$$y = F(x_0) + \frac{F'(x_0)}{1!}(x - x_0) + \frac{F''(x_0)}{2!}(x - x_0)^2 + \frac{F^{(3)}(x_0)}{3!}(x - x_0)^3 + \frac{F^{(4)}(x_0)}{4!}(x - x_0)^4 \tag{8}$$

Let: $y_2 = y - F(x_0)$, $x_2 = x - x_0$, $a = F^{(4)}(x_0)$, $b = F^{(3)}(x_0)$, $c = F''(x_0)$, and $d = F'(x_0)$. Eq. 8 becomes:

$$y_2 = \frac{a}{24} x_2^4 + \frac{b}{6} x_2^3 + \frac{c}{2} x_2^2 + d\, x_2 \tag{9}$$

Let: $x = x_2 + b/a$, then

$$y_2 = A x^4 + B x^3 + C x + D \tag{10}$$

where $A = \frac{a}{24}$; $B = \frac{2ac - b^2}{4a}$; $C = \frac{6a^2 d - 6abc + 2b^3}{2a^2}$; and $D = \frac{12ab^2 c - 24a^2 bd - 3b^4}{24a^3}$.

Let: $V(x) = \frac{5}{A}\int (Ax^4 + Bx^3 + Cx + D)\, dx$, and $u = \frac{5B}{3A}$, $v = \frac{5C}{2A}$, $w = \frac{5D}{A}$, then, we have:

$$V(x) = x^5 + u x^3 + v x^2 + w x \tag{11}$$

where the integral constant can be eliminated through a coordinate transformation.

According to the Thom's Theorem of Classification, Eq. 11 is the standard form of the potential function in swallowtail catastrophes. V(x) is an elementary catastrophe function of single state variable x and three control

variables, u, v, and w. If it is considered as an iterated mapping, Eq. 11 may not only be expressed as the change of manufacturing errors in a single operation, but also be used as the model of manufacturing errors in multiple operations.

Characteristics Analyses of the Iterated Mapping Model and Catastrophe Model

As mentioned above, from the view of point that manufacturing errors can be divided into two parts: inherited and inherent errors, the static model of manufacturing errors is constructed in Eq. 4. From the overall features of the errors, the one dimension iterated model (Eq. 7) and catastrophe model (Eq. 11) are developed, which characterize the MEF. Once the 1/10 rule is satisfied, the fold-catastrophe and cusp-catastrophe models could be established from second order and third order truncations of Taylor series (Eq. 5) [6]. In our research, dynamic characteristics of Eq. 7 and 11 are analyzed to understand more about the dynamic characteristics of MEF.

In Eq. 7, what we are interested in is that how the changes of Φ influence on the stability of MEF. The stability of the iterating result depends on its previous value and eventually depends on the original value y_0, i.e., the blank error. According to a chaos analysis, stable solutions of Eq. 7 may take the form [3]:

$$y_i = \mu y_{i-1} (1 - y_{i-1}) \tag{12}$$

It is found that only when the coefficient μ in Eq. 12 is in the range of $1 < \mu \leq 3$, y_i will keep stable while if $\mu > 3$, y_i become unstable.

In Eq. 11, the equilibrium surface, M in Figure 1 (a), satisfies the condition of that the first-differentiation is zero, i.e.,

$$DV(x) = V'(x) = 5x^4 + 3ux^2 + 2vx + w = 0 \tag{13}$$

The bifurcation set B is a subset of M, which satisfies the zero second-differentiation, i.e.,

$$D^2V(x) = V''(x) = 20x^3 + 6ux + 2v = 0 \tag{14}$$

Transversals of the bifurcation set B are shows in Figure 1 (b) and (c) in terms of different u values. The stability of Eq. 10 can be discussed through the characteristic analysis of Eq. 11. The results are shown as:

1) When $u \geq 0$, the minimum point exists only at $x = 0$ and $v = 0$, and at these points there is not a catastrophe of morpho-characteristics, i.e., y_i changes gradually. This situation corresponds to the upper portion of the curvature in Figure 1(a) and the transversals in Figure 1(b).

2) When $u < 0$, there are three cases: a. If $w > \frac{9u^2}{20}$, neither the equilibrium position nor catastrophe point exists; b. If $0 < w < \frac{9u^2}{20}$, there are two stable equilibrium positions, I and II, and two unstable positions, III and IV. Position I and II correspond to $x = \pm\sqrt{-0.3u}$ and $x = 0$, and position III and IV are catastrophe points which correspond to $x = \sqrt{-0.1u}$ and $x = -\sqrt{-0.1u}$, respectively; c. If $w < 0$, there are also two equilibrium positions and only one is stable.

Therefore Once the condition, $u \geq 0$, is kept, there will be no catastrophe appearing at MEF output error y_i. In another word, y_i will only change gradually.

Control and Neural Network Prediction of MEF

The Control of MEF

According to the analyses mentioned above, the dynamic models of MEF can be used to control the manufacturing errors. In the one-dimension iterated model, μ is the control coefficient. In the catastrophe model, u, w and x are the control variables. The control strategy of MEF can be expressed as:

1) Keep $1 < \mu \leq 3$ or $u \geq 0$ so that the one-dimension iterated model or catastrophe model remains in the non-catastrophe zone, which will keep the MEF stable. Under this condition, once a proper error limit is set up, output error y_i will fulfill the design requirement.

2) When $\mu > 3$ or $u < 0$, it is necessary to further control the u, w and x in order to prevent a possible catastrophe of MEF. Otherwise the MEF will become unstable and the output error of manufacturing errors will become uncontrollable.

3) The pre-requisite of keeping MEF stable is to strictly control the input (initial) error of a manufacturing system.

Least Square Regression (LSR) of Manufacturing Errors

Manufacturing errors can be represented by a high-order polynomial function which may be obtained through a regression operation on the measured data [7]. In a workshop, the thickness of a certain type of car pistons are measured as samples. The data of input errors x and output errors y in multiple operations (from the blank casting to final precision turning operation) have been used to estimate model parameters of high-order polynomial functions with a least square regression program [8]. The results are shown in Figure 2 and Table 1.

From Figure 2 and Table 1, it can be found that when $r \geq 4$, i.e., the order of the polynomial function is greater or equal to four, the standard deviation of residual errors, σ, becomes identical as the order continuously increases. Therefore, it is concluded that the manufacturing errors of the piston thickness can be described by a fourth-order polynomial function with the variable of input error x. These LSR models are built up from the measured data of manufacturing errors and can be used in presenting the relationship of input and output manufacturing errors in production operations.

Neural Network (NN) prediction of MEF

From the theoretic analysis and experimental results shown above, it can be seen that the dynamic characteristics of MEF is non-linear. The MEF can be modeled (simulated) and predicted through NN.

In our research, a backward propagation NN model is applied where the model structure is chosen as 1-5-1, i.e., there is one node in the input layer and the output layer, and five nodes in the hidden layer (Figure 3). The self-learning (training) processes are carried out under a supervision algorithm. The weights obtained are shown in Table 2. After training, the model residuals of manufacturing errors are less than 0.0045. This NN model can be used to predict the manufacturing errors. Figure 4 shows a comparison between the results from the fourth order polynomial function model and the NN model prediction, which are identical.

Summary and Conclusion

1. The concept of manufacturing error flow (MEF) is introduced in order to study the characteristics of manufacturing errors in production systems. Based on the accuracy theory, iterated mapping in chaos theory, catastrophe theory, and neural network (NN) principle, three dynamic MEF models are developed, i.e., one-dimension iterated mapping model (Eq. 7), catastrophe model (Eq. 11), and NN model (Figure 3 and Table 2).

2. The investigation of the one-dimension iterated mapping model and catastrophe model of MEF have shown that the MEF will remain stable, non-bifurcation and non-catastrophic when the coefficients μ and u, w, x are kept with in certain limits, i.e., $1 < \mu \leq 3$ and $u \geq 0$, etc. Beyond these limits, the bifurcation and catastrophic points will appear, which may result in an instability of MEF. Therefore, one crucial point of the control strategy of MEF is to avoid the unstable or catastrophic zones.

3. The analysis of experimental data in this paper shown that the pre-requisite of stabilizing MEF refers to the stability of the whole machining system (machine tool, cutting tool, workpiece, and fixture). It is also suggested that the initial input error, i.e., the error of blanks, has a significant influence on the stability of MEF and should be limited in a reasonable range.

4. Experimental data based simulation has shown that the NN is a useful tool in the research of MEF. The NN model, BP-1-5-1, can be constructed through a self-learning process under supervision. The prediction of MEF through the NN model provides an identical results with the regression modeling of experimental data.

References

1. Y. D. Kolker, *Analysis on Accuracy of Manufactured Parts,* Techniques, Moscow, Russia, 1976 (in Russian).
2. Y. Zhu, Z. Chen and Z. Luo, *Ultra-precision Machining and Micro-fabrication Techniques,* Mechanical Engineer University press, Beijing, China 1990 (in Chinese).
3. R. S. Neil, *Chaotic Dynamics of Non-linear Systems,* John Willey and Sons, New York, 1990.
4. R. Gilmore, *Catastrophe Theory for Science and Engineers,* Willey-Interscience, New York, 1981.
5. B. E. Klamecki, "Catastrophe Theory Models of Chip Formation," J of Eng for Ind, Vol. 104, 1982, p. 369-374.
6. P. T. Saunders, *An Introduction to Catastrophe Theory,* Cambridge University press, London, 1980.
7. Z. Luo, et al, "Study on Monitoring of Wear/Fracture using a Regression Model," *Manufacturing Science and Engineering,* ASME WAM, New Orleans, LA, Nov. 28-Dec. 3, 1993, PED-Vol. 64, p. 241-244.
8. Z. Luo, et al, "Application of High-order Polynomial Functions with Variable Coefficients (HPVC) to Investigation on Tool Wear and Fracture Fusion Model in Monitoring Turning and End-milling Processes," *Int. Sym. of Manuf. Tech. in Industry,* Wuhan, China, 1993.

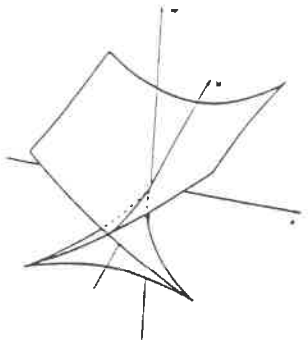

(a) Equilibrium surface

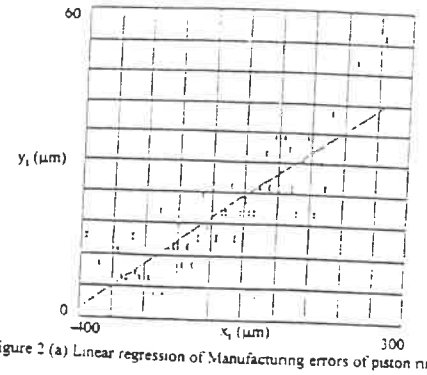

Figure 2 (a) Linear regression of Manufacturing errors of piston rings

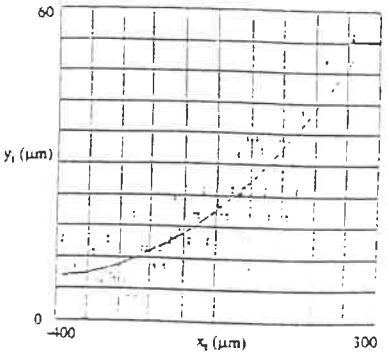

Figure 2 (b) Second-order regression of manufacturing errors of piston rings

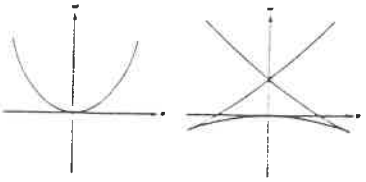

Bifurcation when u ≥ 0 (c) Bifurcation when u < 0

igure 1 Characteristics analysis of catastrophe model

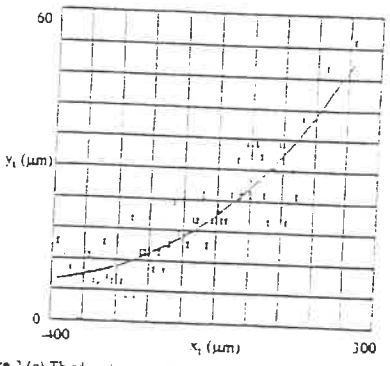

Figure 2 (c) Third-order regression of manufacturing errors of piston rings

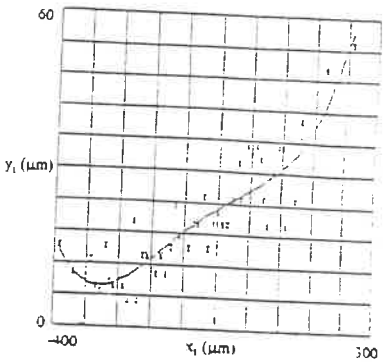

Figure 2 (d) Fourth-order regression of manufacturing errors of piston rings

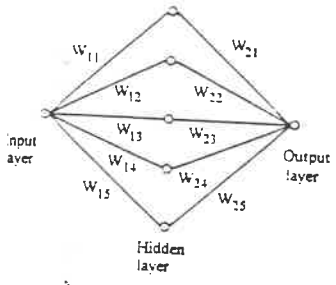

Figure 3 BP-1-5-1 Neural Network Structure

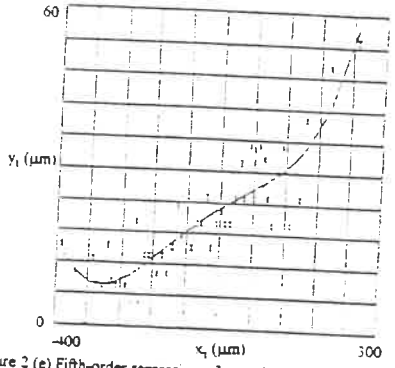

Figure 2 (e) Fifth-order regression of manufacturing errors of piston rings.

Table 2 Weights of BP-1-5-1 NN

Layers	Weight matrix
Input layer to hidden layer	$W_1 = [1.005864,\ 2.836416,\ -7.010451,\ -10.939390,\ 10.801795]^T$
Hidden layer to output layer	$W_2 = [62.253468,\ -37.293190,\ -25.739981,\ 8.307792,\ -8.573314]^T$

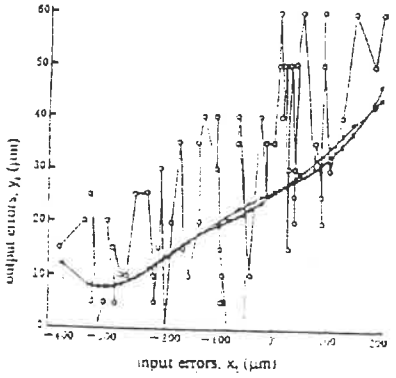

* — measuring data
x — regression results
• — NN prediction values

Figure 4 Comparison of polynomial regression and NN prediction

Table 1 Regression modeling on manufacturing errors in piston production

Order	Regression model	Coefficient matrix	Residual variance
1	$y = b_0 - b_1 x$	$B = [b_0, b_1]^T = [-25.537,\ 0.0622]^T$	35.9307
2	$y = b_0 - b_1 x - b_2 x^2$	$B = [b_0, b_1, b_2]^T = [25.015,\ -0.0815,\ 1.0036\times10^{-4}]^T$	29.4644
3	$y = b_0 - b_1 x - b_2 x^2 - b_3 x^3$	$B = [b_0, b_1, b_2, b_3]^T = [-24.883,\ 0.0804,\ -1.0980\times10^{-4},\ 3.7735\times10^{-8}]^T$	29.4351
4	$y = b_0 - b_1 x - b_2 x^2 - b_3 x^3 - b_4 x^4$	$B = [b_0, b_1, b_2, b_3, b_4]^T = [25.933,\ -0.0517,\ -1.2196\times10^{-5},\ -8.1554\times10^{-7},\ 2.5555\times10^{-9}]^T$	25.4834
5	$y = b_0 - b_1 x - b_2 x^2 - b_3 x^3 - b_4 x^4 - b_5 x^5$	$B = [b_0, b_1, b_2, b_3, b_4, b_5]^T = [25.872,\ -0.0518,\ -1.9192\times10^{-5},\ 8.2014\times10^{-7},\ 2.8753\times10^{-9},\ -3.2524\times10^{-12}]^T$	25.482

Integration of Tolerances and Process Capability for Concurrent Engineering

Robert Wilhelm
Precision Engineering Laboratory
Department of Mechanical Engineering and Engineering Science
University of North Carolina at Charlotte, Charlotte, NC 28223

Introduction

In this paper we describe a method by which tolerance specifications and process capability can be integrated for concurrent engineering. Concurrent product and process design requires knowledge of the relationships between product function and process capability. In previous work [1, 2], we have focused on product function and shown how a tolerance synthesis framework can be used to describe variations that are acceptable during manufacture. The same approach can also be used to relate the process capabilities found in manufacturing processes to shape and performance variations specified in design.

Recent advances in testing standards [3] describe procedures that can be used to characterize, in a gross sense, the accuracy that can be expected from particular machine tools. By reapplying the framework that we developed for tolerance synthesis, the process cability of machining centers can be taken into account when specifying the design tolerances for product features.

This integration of tolerances and process capability can be used to support early make or buy decisions. In comparing the tolerance specifications and the machine performance measures, four types of conclusions can be drawn : machines available in the enterprise are not capable of meeting the tolerance specification, the tolerance specification can be satisfied if process capability is improved by a particular amount, the process capability can be accommodated if tolerances are relaxed by a particular amount, or it is most cost effective to buy the part.

Several related research efforts have touched on this type of integration. The NextCut system [4, 5] provides several ways to use process planning results and machining simulation to determine relationships between design specifications and process capability. Earlier work by Srinivasan [6]demonstrated how encoded design features could be related to manufacturing process descriptions. Theoretical results by Etesami [7] show a method for product modeling that includes manufacturing imperfections. More recent work by Wood [8] suggests that fractel-based representations may be useful to describe expected performance from manufacturing processes.

As introduction, we first briefly review the role of tolerance specifications in a concurrent engineering enterprise and describe the performance measures available in the new B5.54 standard. Extensions to the tolerance synthesis framework are then presented along with the parametric models we employ for design features and machine errors. To demonstrate our approach for linking tolerance specifications and process capability, we discuss an example where tolerance specifications for a design are compared to B5.54 machine performance measures.

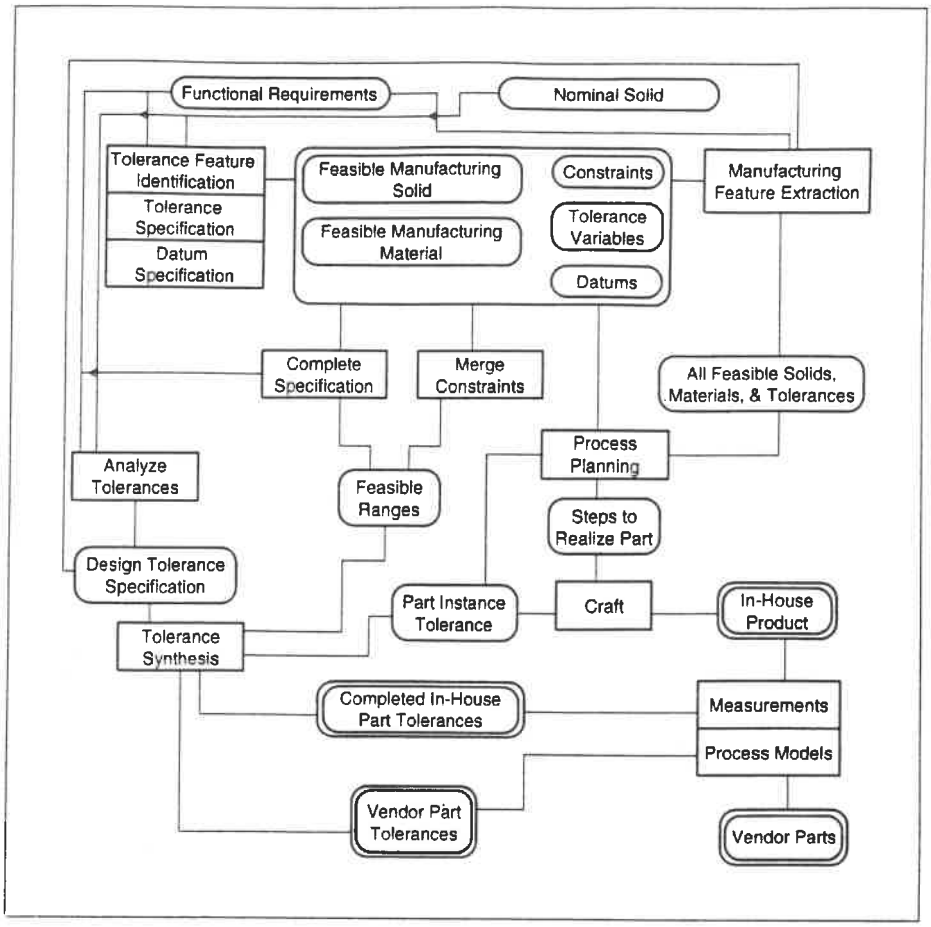

Figure 1: Geometric Tolerances in the Enterprise

Tolerance Specifications

Tolerances place bounds on the uncertainty found in engineering practice. In a concurrent engineering environment, tolerances also serve as an interface between product function and process capability. Just as demanding design requirements may drive a new process design, limitations on process capability may restrict a new product design. Figure 1 illustrates [1] the many ways that tolerances are considered during design and manufacturing. Functional requirements drive tolerance ranges and tolerances determine the steps and parameters of a particular process plan. Metrology results quantify the manufacturing performance and establish bounds for future design specifications. Note that the current figure neglects machining performance.

Performance Measures in the B5.54 Standard

Machine tool performance testing standards such as ANSI B5.54 measure the effectiveness of particular machine tools in a variety of ways as shown in Table 1. While each test tells something about the tolerances that a machine tool can achieve, the machine performance, geometric accuracy, and volumetric tests provide the most direct measures for predicting geometric tolerances.

[1] See [2] for a thorough discussion of this figure.

Table 1: ANSI B5.54 Testing Procedures by Category

Environmental Effects	Thermal, Axes at rest
	Vibration
Machine Performance	Compliance and Hysteresis
	Linear and Angular Displacement
	Axis of Rotation (Spindle)
Geometric Accuracy	Straightness
	Angular Error
	Squareness
	Parallelism
Volumetric Performance	Diagonal displacement
	Contouring
Cutting Performance	Cutting
Machining Test Parts	Test Parts
Multi-Function	Thermal, Axes in motion

Linking Tolerances and Process Capability

Tolerances specify a point space relative to one or a collection of coordinate reference frames. A finished part satisfies the tolerance if it can be positioned within the point space. Machine tool performance measures usually describe variation with respect to a fixed coordinate system that is related to how a part is positioned on the machine tool. If the reference frame(s) for a tolerance specification can be related to the coordinate system of a particular machine tool, machine tool errors can be used to restrict or grow the point space of the tolerance specification.

Most geometric tolerance specifications can be described with parametric models. The Virtual Boundary Requirements (VBR) approach [9, 10] is a particular parameterization that lends well to inspection. Geometric surfaces and relationships between surfaces are defined to describe each geometric tolerance and then parameterized and converted to conditional tolerances. The conditional tolerance relations serve as the mathematical equivalent of a functional gauge. For example, a cylindrical feature can be described with 7 parameters. The diameter, s_1, refers to the diameter of a perfect form cylinder fitted to a part instance. On the xy plane, c_1 and c_2 specify the intersection point for the axis of the fitted cylinder. The attitude of the axis, specified by c_3, is the angle between the axis and the z axis. The azimuth, specified by c_4, describes rotation about the z axis. The length of the cylinder is specified by l_1. The location of the midpoint of the fitted cylinder, with respect to the z axis, is specified by l_2.

The conditional tolerances for a maximum or least material condition tolerance on a cylindrical hole are given by equations 1 and 2.

$$Z = \left\{ z \;\middle|\; \begin{array}{l} (s_1 > 0) \wedge (l_1 > 0) \wedge (0 \leq c_3 < \frac{\pi}{2}) \wedge \\ (2o + s_1 \sec c_3 + l_1 \tan c_3 - s_{N1} - 2|a_1| \leq 0) \end{array} \right\} \tag{1}$$

$$\text{where } o = \sqrt{(c_1 + l_2 \sin c_3 \cos c_4 - c_{N1})^2 + (c_2 + l_2 \sin c_3 \sin c_4 - c_{N2})^2} \tag{2}$$

The coordinate reference frame for this parameterized cylinder varies according to the values of c_1, c_2, c_3, and c_4. This coordinate reference frame is the frame that must be associated with the machine tool errors. Linear displacement errors will influence c_1 and c_2, the position parameters of the frame. Straightness, angular errors and volumetric performance will influence c_3, and c_4, the orientation parameters of the frame.

As the machine tool errors increase, c_1, c_2, c_3, and c_4 will take on larger values indicating departure from the nominal geometry. These large c_i values will either drive a reduction in nominal size or an increase in the specified tolerance. In either case, a calculation and comparison will suggest whether or not a particular part and tolerance can be achieved on a particular machine.

To employ this approach within the tolerance framework suggested in Figure 1, additional data and computing elements must be added for machine testing and data synthesis. Just as design specifications and static manufacturing capabilities are merged to yield feasible tolerance ranges, machine performance data which changes over time must be considered as a constraint on the tolerances.

Conclusions

Concurrent product and process design are successfully implemented when accurate relationships can be identified between product function and process capability. In this paper we described a method by which tolerance specifications and process capability can be integrated to accurately describe these relationships. The results of machine tool performance tests are coupled with a parametric representation of geometric tolerances. The effects of particular machine tool errors can be evaluated with respect to the tolerances specified for geometric features.

References

[1] S. C-Y. Lu and R.G. Wilhelm. "Automating Tolerance Synthesis : A Framework and Tools", *Journal of Manufacturing Systems*. 10(4):279–296, 1991.

[2] R.G. Wilhelm and S. C-Y. Lu, *Computer Methods for Tolerance Design*, World Scientific Publishing Co., 1992.

[3] ANSI/ASME B5.54, *Methods for Performance Evaluation of Computer Numerically Controlled Machining Centers*, American Society of Mechanical Engineering, 1993.

[4] M.R. Cutkosky, J.M. Tenenbaum, and D. Muller, "Features in Process-Based Design", in *ASME Computers in Engineering Conference*, San Francisco, July 1988.

[5] Mark R. Cutkosky and Jay M. Tenenbaum, "A methodology and computational framework for concurrent product and process design.", *Mechanism and machine theory.*, 25(3):365, 1990.

[6] R. Srinivasan and C.R. Liu, "Generative Process Planning Using Syntactic Pattern Recognition", *Computers in Mechanical Engineering*, 1984.

[7] Faryar Etesami, "Tolerance Verification through Manufactured Part Modeling", *Journal of Manufacturing Systems*, 7(3):223–232, 1988.

[8] Kristin L. Wood and R.S. Srinivasan, "Fractel-based tolerance representations in design and manufacturing", in *Proceedings of the 1992 Design and Manufacturing Systems Conference*, SME, 1992.

[9] R. Jayaraman and V. Srinivasan, "Geometric Tolerancing : I, Virtual Boundery Requirements", *IBM Journal of Research and Development*, 33(2):90–104, March 1989.

[10] V. Srinivasan and R. Jayaraman, "Geometric Tolerancing : II, Conditional Tolerances", *IBM Journal of Research and Development*, 33(2):105–125, March 1989.

NONLINEAR EFFECTS IN BALL SCREW ACTUATORS

James F. Cuttino and Thomas A. Dow
Precision Engineering Center
North Carolina State University
Raleigh, NC 27695-7918

INTRODUCTION

Ball screw actuators are commonly used for accurate positioning in precision mechanisms such as diamond turning machines (DTM) and precision grinders. At levels of several hundred nanometers, ball screws behave nonlinearly, contrary to traditional assumptions that output displacement is directly proportional to the input screw rotation. Torque in the nut results in windup of the screw which manifests itself in the form of hysteresis, representing a variable gain in the system.

In this work, the dynamic response of a ball screw driven slideway on the Rank Pneumo ASG 2500 DTM is studied. Hysteresis in the system results in a 33 db or 98% drop in the response of the slide to a 1.7 mm/min open loop input signal at 50 Hz. This hysteresis represents a variable gain which can vary by several orders of magnitude, making it difficult for the control system to operate efficiently.

A compensation scheme is proposed to *linearize* the system by inverting the ball screw hysteretic effect and adjusting the controller output signal accordingly. The results of this compensation technique are presented.

BALL SCREW HYSTERESIS

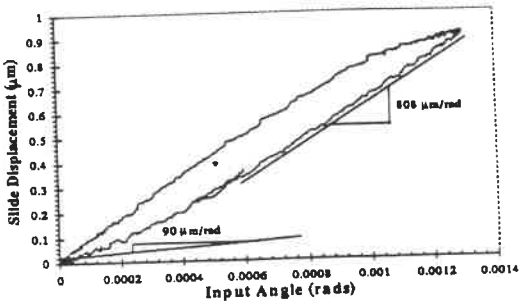

Figure 1: Experimental Ball Screw Hysteresis

Figure 1 shows the experimental hysteresis exhibited by the ball screw on the DTM. The curve was obtained by measuring the input angular displacement of the ball screw and the output displacement of the slide at very slow feed rates. The widest point of the hysteresis curve represents 0.24 milliradians, or 0.014 µm. The initial slope of the hysteresis is around 90 µm/rad rather than the specified ball screw pitch of 808 µm/rad. The hysteresis is evident in the first milliradian of motion following direction reversals, after which the pitch of the screw is realized.

OPEN LOOP DYNAMICS

Open loop transfer functions were obtained for the ball screw mechanism using the commanded input voltage to the

motor (in Digital to Analogue Counts, DACs) and the slide displacement as measured by a laser interferometer. The range of inputs varied from 8000 DACs (approximately 140 mm/min) to 30 DACs (approximately 0.5 mm/min) to incorporate a full range of velocities that might be used on the DTM. The input signal is sinusoidal and proportional to rotational velocity. Integration yields rotational displacement for a linear system and is represented by

$$\Theta = -A/\omega \cos(\omega t),$$

where A is the amplitude in DACs, ω is frequency, and t is time. Referring to the ball screw hysteresis in Figure 1, it is apparent that the nonlinearity has a greater influence for small displacements ranges (on the order of 1 mrad) than for large; thus at low amplitudes and high frequencies. At amplitudes much higher than 1 mrad, the nonlinear range becomes less significant compared to the linear motion.

Figure 2 shows the open loop amplitude ratio (AR) of the ball screw / slide system. Since the input is a commanded rotational velocity (in DACs), and the output is a displacement (in laser counts), the amplitude ratio shows an initial -20 db/decade slope. As the input velocity becomes large enough that the system remains mostly in the linear region of motion, the ratios converge to the curve representing the 8000 DAC case. The amplitude ratio for one laser count of displacement (= 2.54 nm) is defined as

AR = 20 log (1 laser count / Input DAC).

The amplitude of the output displacement for the 30 DAC case falls below the noise range for AR < -29.5 db; ie., near 10 Hz. If the system were linear (following the 8000 DAC curve), the 30 DAC displacement would be 0.137 μm.

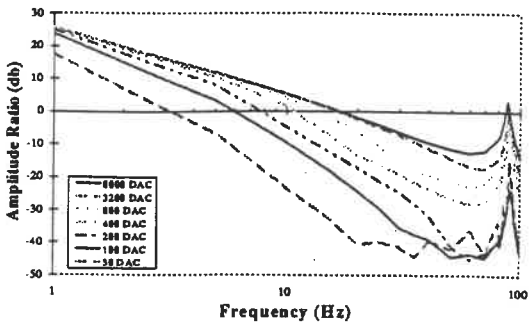

Figure 2: Open Loop Amplitude Ratio of Ball Screw / Slide System

CLOSED LOOP DYNAMICS

Figure 3 represents the closed loop amplitude ratio of the slide system under proportional control, where input and output signals are displacements in nanometers. A number of advanced controllers have been developed and tested on the DTM including zero/pole placement, directional damping, and others. These controllers have met with limited success because they are subject to nonlinearities similar to those evident in Figure 3, and optimal controller coefficients are dependent on amplitude and frequency of operation.

The amplitude ratio in Figure 3 shows that the controller is very inefficient at low amplitude and high frequency inputs. For 200 nm amplitude displacements the bandwidth of the system is less than 5 Hz and is less than half of the bandwidth for an amplitude of 3.2 μm. There is also a spread of 32 db at 20 Hz between the 3.2 μm case and the 50 nm case.

The effect of hysteresis on following error is shown in Figure 4 for a 0.9 μm input signal at 5 Hz. The theoretical following error for a perfectly linear system with phase resembles a sinusoidal curve. In Figure 4, the error resembles a sine wave with a sharp peak superimposed following reversal of the reference signal. Examination of the position curve shows that, following reversal, the slide "overshoots" the input, resulting in the peak error. Error is maximized following reversal since reversal marks the beginning of the hysteresis and subsequently the lowest system gain.

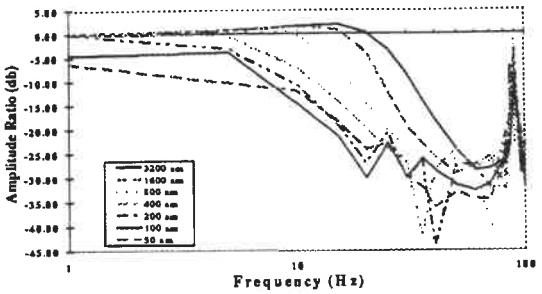

Figure 3: Closed Loop Amplitude Ratio of Ball Screw / Slide System

COMPENSATOR THEORY

The system hysteresis was modeled with a geometric curve fit which defined the relationship between output displacement and input command. Differentiating the curve, the instantaneous gain of the system can be predicted. Dividing this gain into the pitch of the screw yields a compensation ratio, K_{comp}, defined as

$$K_{comp} = \frac{\sqrt{C_1^2 + (\Theta + C_2)^2}}{\Theta + C_2},$$

where Θ is the input command, and C_1 and C_2 are curve fit parameters. In the case of the ball screw hysteresis, Θ is the input screw angle. This compensation ratio is used to "linearize" the system by amplifying the controller signal when the system nonlinearity attenuates the motion.

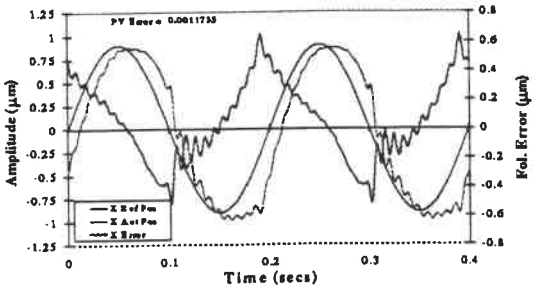

Figure 4: Following Error for Uncompensated System, 100 DAC (0.9μm) Amplitude Input at 5 Hz.

IMPLEMENTATION

Using the theory described above, several compensators were tested on the DTM by varying the curve fit parameters. Performance was based on: a) The ability to linearize the open loop amplitude ratio, and b) the ability to improve the following error.

Curve fit parameters for the compensator were varied to represent several cases including; a) the assumption that the ball screw is the sole source of hysteresis (C_1 and C_2 were chosen to fit the curve in Figure 2); b) a much wider hysteresis curve with a very small initial slope, meaning that the ball screw represents only *part* of the system nonlinearities, and c) a wide hysteresis curve with a larger initial slope.

RESULTS

Test 1: The test modeling the ball screw as the sole source of nonlinearities reduced

the open loop transfer function nonlinearity, and the closed loop following error was reduced by 16%. Excitation of the system natural frequency limited improvement, however, and the closed loop results were not tested.

Test 2: A wider hysteresis curve was also tested and resulted in the excellent open loop results shown in Figure 5. These results seem to indicate that other nonlinearities may exist besides the ball screw, such as the amplifier, motor, or other component. Unfortunately, this curve fit resulted in very high compensation factors which caused unstable following error, and the closed loop tests were not conducted.

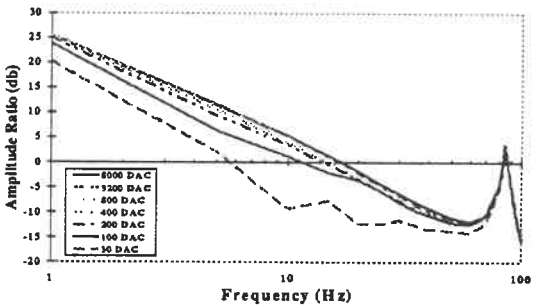

Figure 5: Test 2 Compensation - Open Loop System Amplitude Ratio

Test 3: A third test was conducted with slightly different parameters to reduce the compensation upon reversal. Figure 6 shows the improvement in the open loop amplitude ratio linearity. At 10 Hz, the 30 DAC displacement amplitude is 0.028 μm which is 10 times greater than when uncompensated. The following error was improved by approximately 55% as shown in Figure 7. The error more closely resembles a sinusoidal curve than does Figure 4, meaning the system is acting more like a linear system with a phase lag. The following error was reduced from 1.17 μm in Figure 4 to 0.53 μm peak to valley.

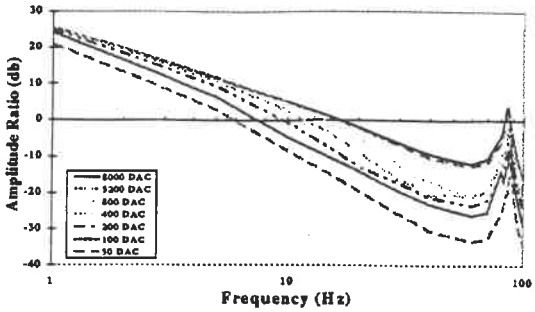

Figure 6: Test 3 Compensation -Open Loop System Amplitude Ratio

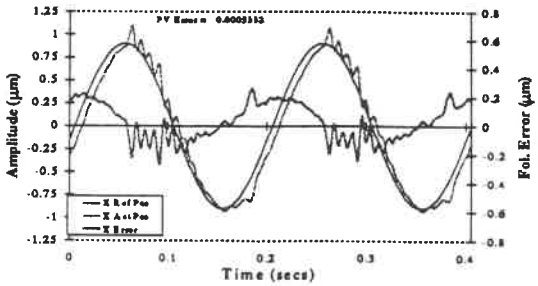

Figure 7: Compensated Following Error for Test 3, 100 DAC (0.9μm) Amplitude Input at 5 Hz.

CONCLUSION

The effect of system nonlinearities on performance of a ball screw driven slideway have been examined using open loop transfer functions and following error curves. Nonlinearities in the ball screw have been identified to be significant, but it is still uncertain if they are the sole source of hysteresis in the system.

A compensation technique has been developed to effectively "linearize" the system, resulting in an improved open loop transfer function and a reduction in following error of 55%.

Control Method for Thermal Displacement of a Hydrostatic Air Spindle

Nozomu Mishima, Kiyoshi Mizuhara, Yuichi Okazaki

Mechanical Engineering Laboratory, AIST, MITI

1-2 Namiki, Tsukuba, Ibaraki, JAPAN

1.Introduction

Hydrostatic air spindles are often applied to main spindles of ultra precision machine tools because of their low heat generation and high rotating accuracy. But even an hydrostatic spindle is not free from a certain quantity of thermal displacement. According to our measurements, the displacement amounts more than 6 microns under some conditions, and that displacement is not negligible for ultra precision machining. To achieve higher accuracy, a countermeasure against this displacement is necessary. In our former research, it was able to improve thermal properties of the spindle by controlling precisely the temperature of the air to be supplied to the hydrostatic spindle. Since that method was adaptable just for a constant rotating speed, an improved experimental set-up having a closed-loop temperature control capability has been developed. The improved system can control the temperature of the air so that the appropriate constant value of the thermal displacement in the spindle can be always maintained. In this report, system description of the improved set-up and results of experiments are mentioned.

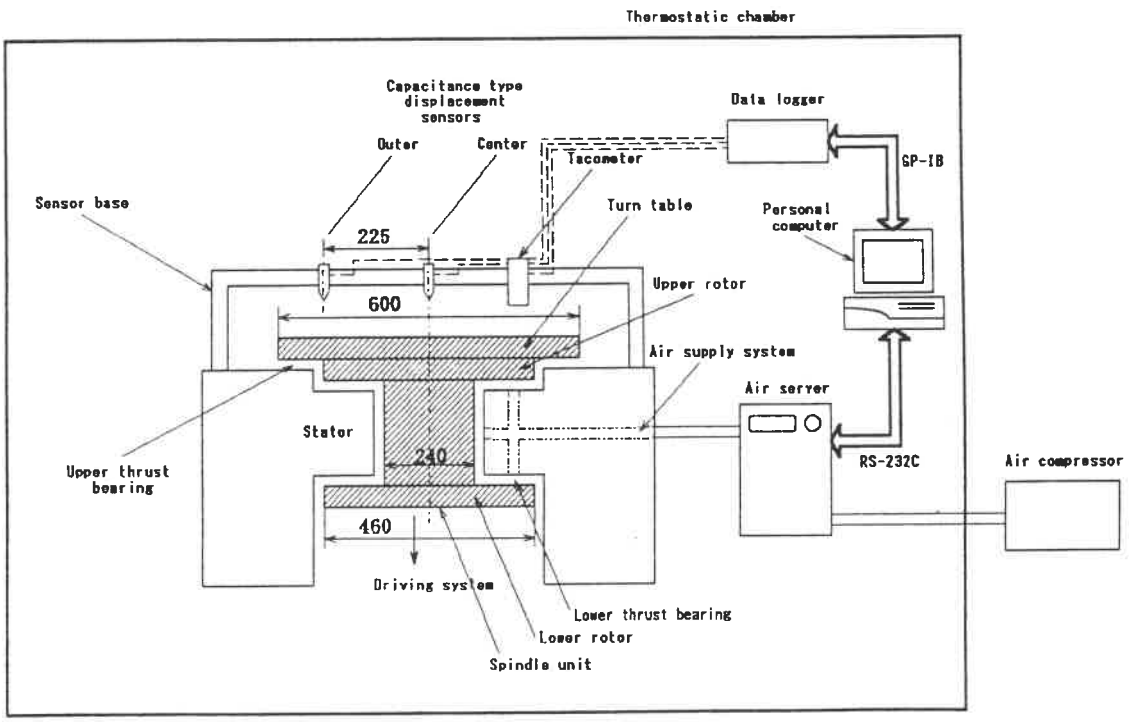

Fig.1 Experimental Set-up

2.Experimental set-up

The over view of the experimental set-up is shown in fig.1. Thermal displacement of the spindle is measured by static capacitance displacement sensors, as an expansion of the turn table to the vertical direction. Compressed air is supplied in any temperature through the "air server", and air pressure is set to 0.49MPa. The thermal displacement is measured by the "data logger" and sent to the personal computer through GP-IB. The temperature of the supplied air is input manually by a operator or set automatically by PC through RS-232C. The spindle is driven by AC servo motor. Fig.2 shows the results of the preliminary experiments. The figure make two problems clear, one is that the quantity of the displacement is not negligible for a ultra precision machining and the other is that it costs long time to its stabilization, which amounts more than 6 or 7 hours.

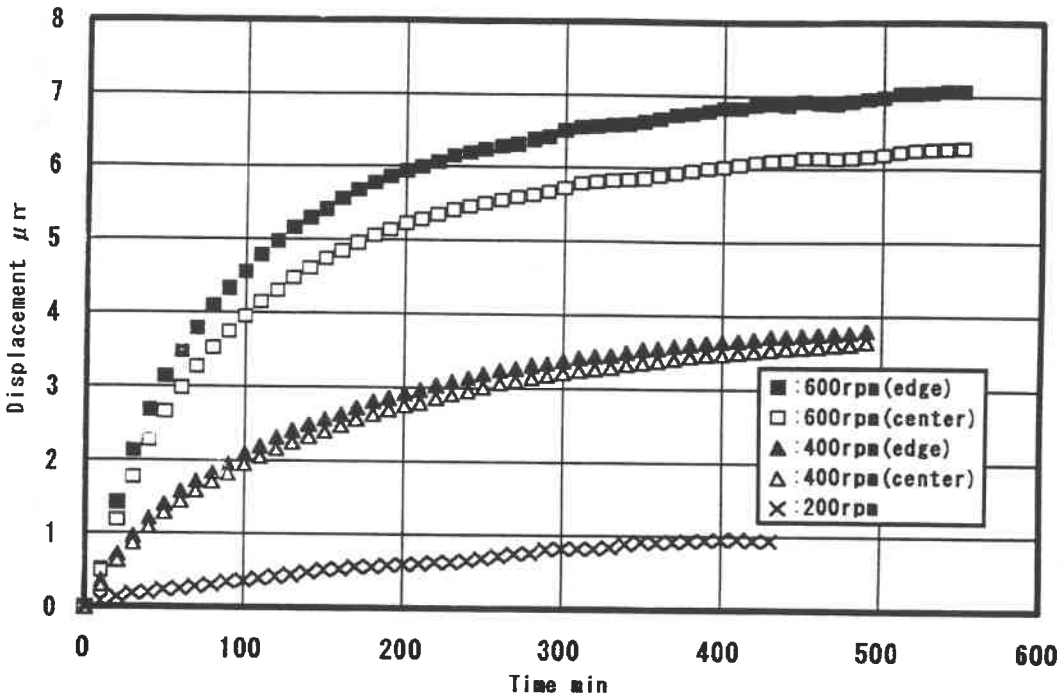

Fig.2 Thermal displacement of the spindle

3.Control method of thermal displacement

(1) Open-loop control

An ultra precision machine tool is ordinary settled in a thermo-static chamber and air is supplied with the same temperature as the chamber. However, there must be a local heat generation in the bearing, it is not enough to cool whole the machine. Against such an inner heat generation, it is said that the direct cooling of the heat source is effective. We also tried a simple method to decrease the displacement and to shorten the time to its stabilization, which is to control the temperature of supplied air precisely. In the experiment, the spindle was warmed up by heated air

from the beginning of the rotation, and then, cooled by chilled air. The temperature of the air was decided from some approximations before the experiment, and preset manually. We call this type of control "open-loop control". Fig.3 shows the result of the experiment under a constant rotating speed, 400rpm. The figure shows that the displacement increased rapidly and then kept stable. The time to stabilization was shortened from 7 hours to one and half hour, and the deviation of the displacement in the stable state was also suppressed to ±0.2 microns. Another advantage of this method is that any additional equipment or rebuild of the spindle is not necessary.

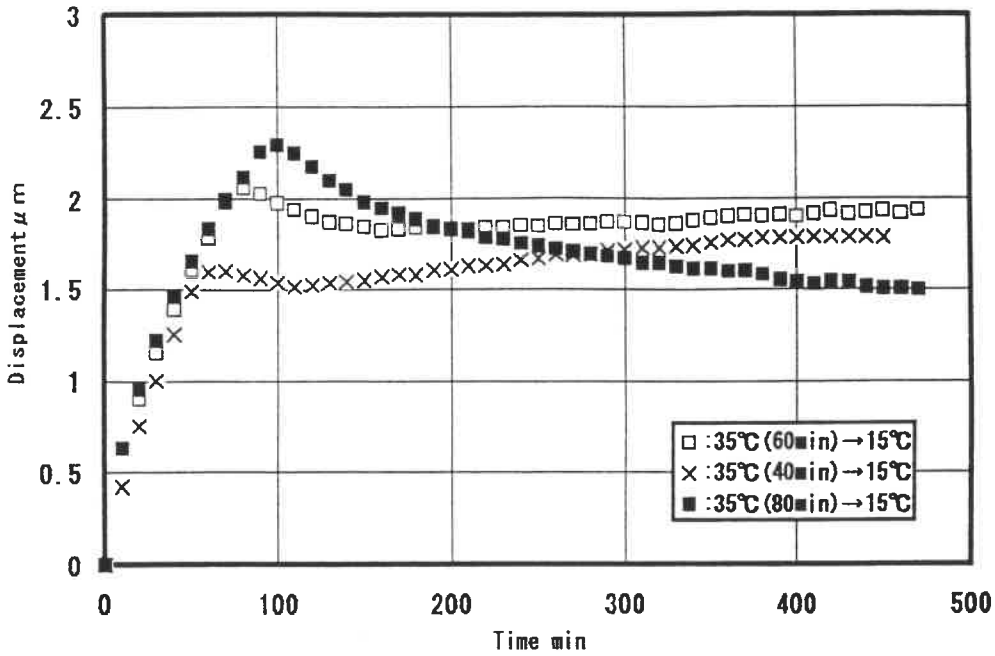

Fig.3 Open -loop control of thermal displacement

(2) Closed-loop control

As it was mentioned above, under a constant rotating speed, it is enough to control the thermal displacement using two levels of air temperature. But in actual machining, rotations of spindles are often changed to various speeds. In these cases, more advanced method is necessary. For the purpose, we tried another experiment. In this experiment, the temperature of the air was changed successively to maintain the appropriate constant value of the displacement. The temperature was calculated by personal computer according to the measured value of displacement. The principle of the control is proportional feed-back control. We call this control method "closed-loop control". Fig.4 and fig.5 show the results. In fig.4 rotating speed was 400rpm and in fig.5 rotating speed was changed step-like from 200rpm to 400rpm. According to fig.4, it was able to shorten the time to stabilization to one hour and the deviation of the displacement was less than ± 0.1 microns. Also fig.5 shows that it was able to maintain the thermal displacement to the target value under the various rotating speed and the error was less than ±0.3 microns.

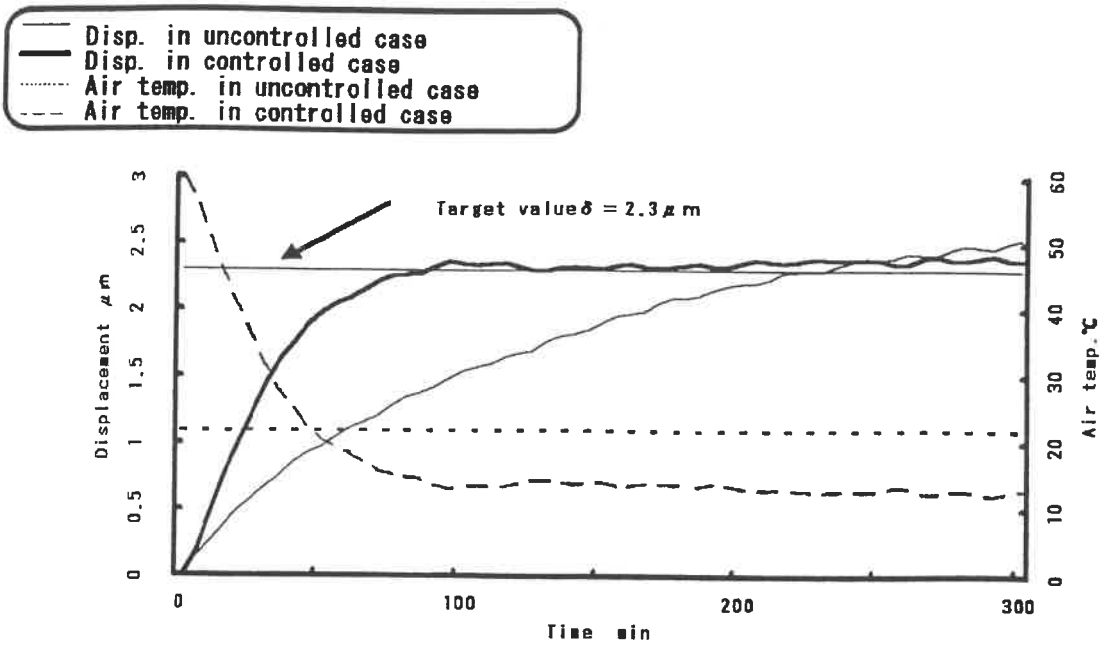

Fig.4 Closed-loop control of thermal displacement (constant speed)

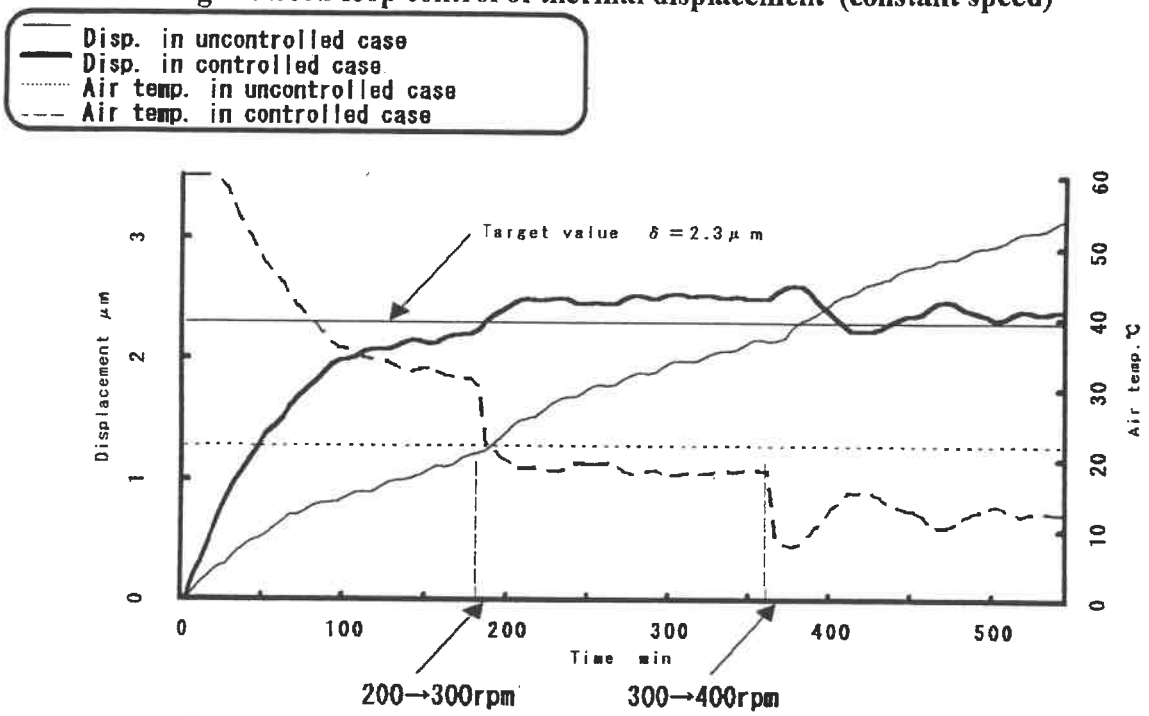

Fig.5 Closed-loop control of thermal displacement (various speed)

4.Conclusions

In this report, it was proved that precise temperature control of supplied air is effective to reduce thermal displacement and to shorten the time to stabilization. Even when the driving pattern of the spindle is complicated, feed-back control of the supplied air temperature was adaptable to keep the displacement low and stable. This control method was useful and easy to realize.

Accuracy improvement of machine tools by computer real-time control

Chengrui Zhang, Frank Margrave and Alan Bradshaw
Engineering Department
Lancaster University
United Kingdom

Abstract.

This paper proposes an adaptation of the least-mean-square (LMS) algorithm to estimate the parameters of an auto-regressive model adaptively. The algorithm was implemented on a MCS-8098 microcomputer system to model and control kinematic errors of a gear hobbing machine, these include long and adjacent periodical errors. These errors were detected using a rotary inductosyn and a capacitor encoder as a high precision measuring system. The statistical model of the error forming process was then determined and used to forecast errors and hence control them. The method overcomes the effect of time lag of the mechanical system by forecasting the long and adjacent periodical errors and providing compensation signals to the machine. The experiments indicated that 65% of the combined errors can be eliminated by this method.

Keywords: Real-time control, LMS algorithm, Machine tool accuracy, Error correction, Forecasting.

Introduction.

Since the late 1960's manufacturing technology has undergone great changes with the development of microcomputer technology, these are found mostly in two major areas of application, high efficiency and high precision.[1] In many nations precision machining is often used as a benchmark of the technological advancement of manufacturing engineering into the next century. A practical and cost-effective way to obtain high machine precision is by implementation of computer control and software compensation techniques rather than the use of highly accurate but expensive machines. The aim of this research is to achieve high accuracy gear production utilising a relatively low accuracy gear hobbing machine by the adoption of a micro-computer to implement precise measurement, and control through the use of sensors and control technology.

It is important in real time modelling and control to adopt an algorithm with the properties of simplicity in computation, good convergence, and robustness. Based on a LMS algorithm, which was developed by Widrow[2] and has been widely used in various applications[3], a modified variable step adaptive LMS algorithm is proposed. A MCS-8098 based microcomputer system is used to implement the real-time measurement, modelling, forecasting and compensatory control of the kinematic transmission errors of a machine tool. The experimental results show that 65% of the combined kinematic errors of the hobbing machine can be compensated for.

1. A modified LMS algorithm.

The LMS algorithm was developed by Widrow-Hoff in 1959, because of its simplicity, small computation requirement and easy realisation, it has been widely used in various areas. The parameters of the auto-regressive model (AR) at time $j+1$ can be expressed in the form

$$\overline{W}_{j+1} = \overline{W}_j + 2\mu E_{fj} \overline{X}_j \qquad (1)$$

where the calculation is based upon the last parameter at time j and the forward prediction error is given by $E_{fj} = x_{j+1} - \overline{W}_j^T \overline{X}_j$ (2)

where, $\overline{W}_j^T = (w_{1j}, w_{2j}, \ldots, w_{pj})$, $\overline{X}_j^T = (x_j, x_{j-1}, \ldots, x_{j-p+1})$, p is the order of the AR model and μ is a constant step size.

This constant step size in the LMS algorithm controls not only the convergence rate of the weights but also determines the Mean Square Error (MSE). A large μ will give fast convergence, however, it also results in a higher MSE, and therefore μ must be carefully selected to achieve a trade-off between these. It is found that the step size μ affects the relaxation time constant (τ_i) before convergence, and MSE (M) after convergence. The relaxation time constants τ_i and mean-square error M of LMS algorithm are given by

$$\tau_i = \frac{1}{2\mu\lambda_i} \quad (i = 1,2,\ldots,p) \quad \text{and} \quad M = \mu\sum_{i=1}^{p}\lambda_i = \tfrac{1}{2}\sum_{i=1}^{p}\frac{1}{\tau_i} \tag{3}$$

where, the λ_i are the eigenvalues of the autocorrelation matrix R_X of the stationary time series X.

If a variable step size μ_j which decreases corresponding to the convergence rate can be found, the algorithm will obtain fast convergence and a small steady-state MSE. The proposed modification of the LMS formula is to incorporate auto-regressive parameters, which is achieved through the use of a variable step size. The basic idea of the new algorithm is to let the step size change with the amplitude of prediction error E_{fj} according to the formula.

$$\mu_j = \mu_{j-1}F + E_{fj}^2 K = K\sum_{i=1}^{j} E_{fj}^2 F^{j-1} + \mu_0 F^j \tag{4}$$

where, F is a forgetting factor, $0<F<1$; μ_0 is the initial step size; K is the step size coefficient, which limits the size of μ_j and assures the convergence of the algorithm. Fig. 1 shows a comparison of results for the modified LMS and the conventional LMS algorithms.

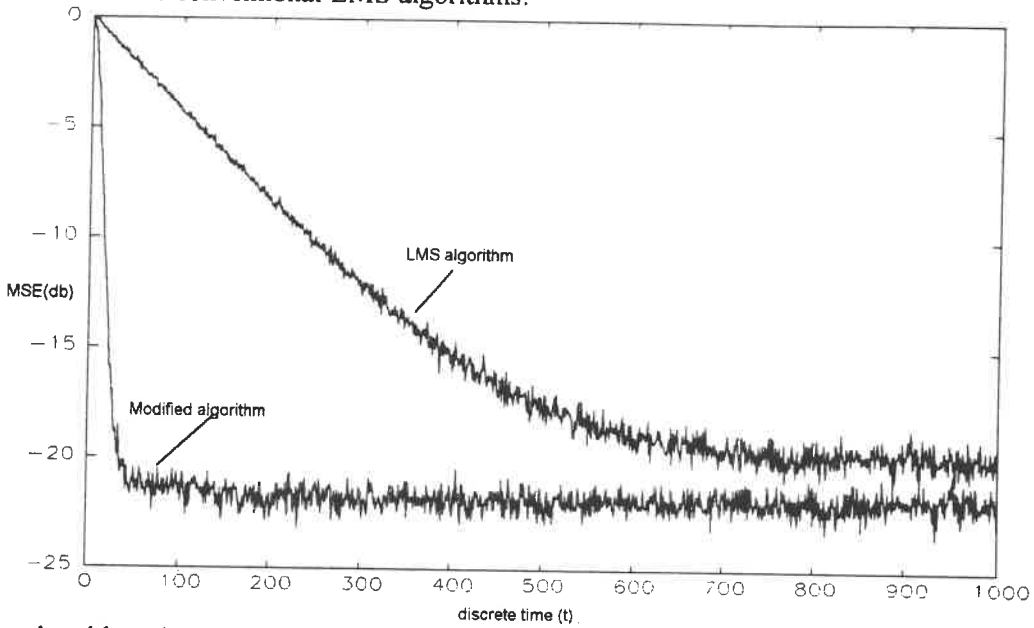

Fig. 1. Simulated learning curves (200runs) of LMS and modified LMS algorithms with $X(t)=\sin(0.2\pi\cdot t)+a_t$ (a_t ~NID(0,σ^2)), where Signal to Noise Ratio=10db, p=8, $\mu=\mu_0=0.003$, k=0.015 and F=0.99

It can be seen that the modified LMS algorithm obtains a faster convergence rate and a lower MSE, and that the results verify that the properties of the new algorithm outperform those of the conventional LMS algorithm.

2. Development of the Control Scheme.

The kinematic error of the indexing mechanism of a gear hobbing machine is generated by the driven elements in the train. This error can be divided into long and adjacent periodical errors[4], the

former refers to that part of the error with relatively low frequencies and deterministic properties, which are generated by machining and installation errors of the worm gear; the latter with relatively high frequencies and stochastic properties, are formed by the worm gear pair and other drive elements in the transmission train.

To achieve high accuracy in manufacturing requires precise positional and dimensional measurements, we have developed a high accuracy measuring system with an inductosyn and a capacitor transducer to detect the kinematic error of the transmission train of gear hob machine[4]. A rapid response electromagnetic device is utilised as a control actuator to exert the control action on the gear hobbing machine through a differential shaft. The non-linearity of the actuator caused by magnetic hysteresis is remedied by look-up table software. A MCS-8098 microcomputer-based system was developed to implement the real time detection, modelling and control of kinematic error. The control system schematic diagram is shown in Fig. 2.

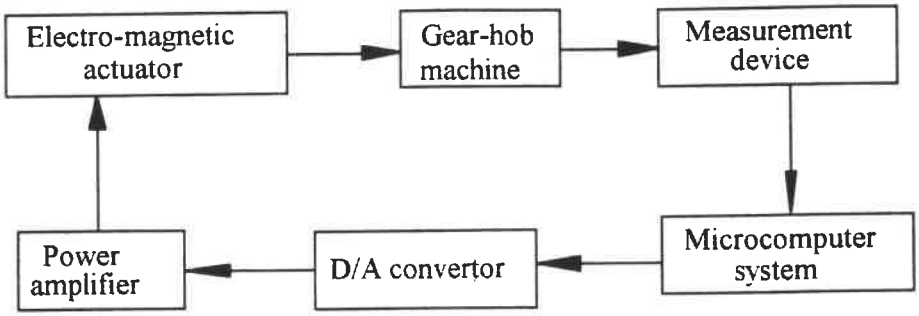

Fig. 2 Control system schematic diagram

The steps implemented in the process of real-time detection, modelling and control are as follows:

(1) the kinematic error, which includes the long and adjacent periodical errors, of the transmission chain is detected on-line,

(2) an auto-regressive model is used to fit the error adaptively with the proposed algorithm.

(3) the forecast method is employed to obtain the next step error thus eliminating the time lag of the system between the compensating action and occurrence of error, and

(4) the compensation action, according to the proportional control law, is taken through an actuator to maintain the correct movement relationship of the two ends of the transmission chain.

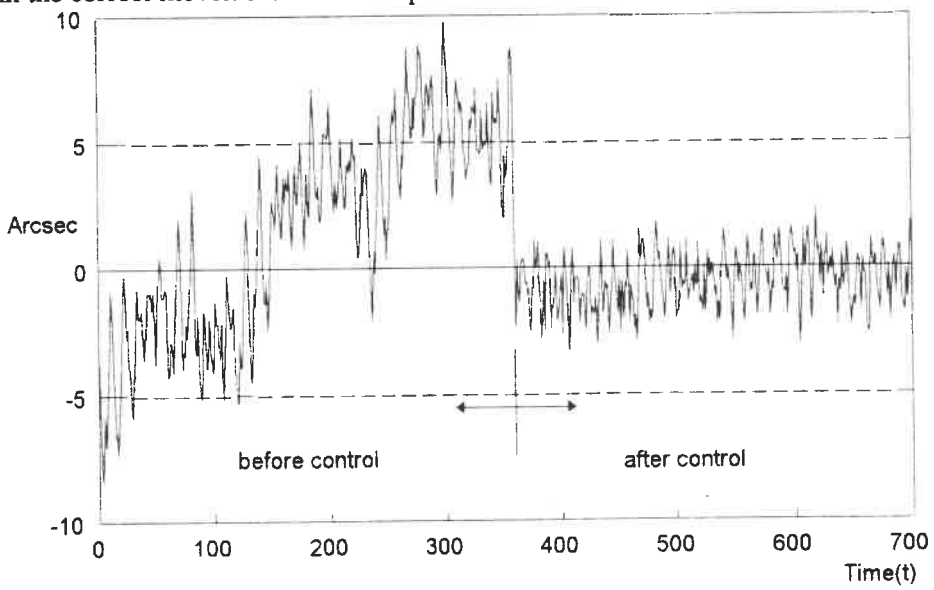

Fig 3. Kinematic error of the gear hobbing machine before and after the control scheme.

3. Experimental results.

The experiment was conducted on a model Y38 (800mm) gear-hobbing machine operating with a hob shaft rotation speed of 47 rpm, and machined gear of 72 teeth. Fig. 3 shows the kinematic error of the indexing transmission train of the hobbing machine before and after implementation of the control scheme. The peak-peak value of kinematic error before the control is about 18 arcsec, whilst after application of the control scheme it is reduced to within 6 arcsec. Thus it has been shown that more than 65% of the kinematic errors can be compensated. Spectral analysis of the kinematic errors are shown in Fig. 4 (a) and (b) showing before and after implementation of the proposed control scheme. The results indicated that the amplitude of error components under a frequency of 2 Hz. are greatly reduced.

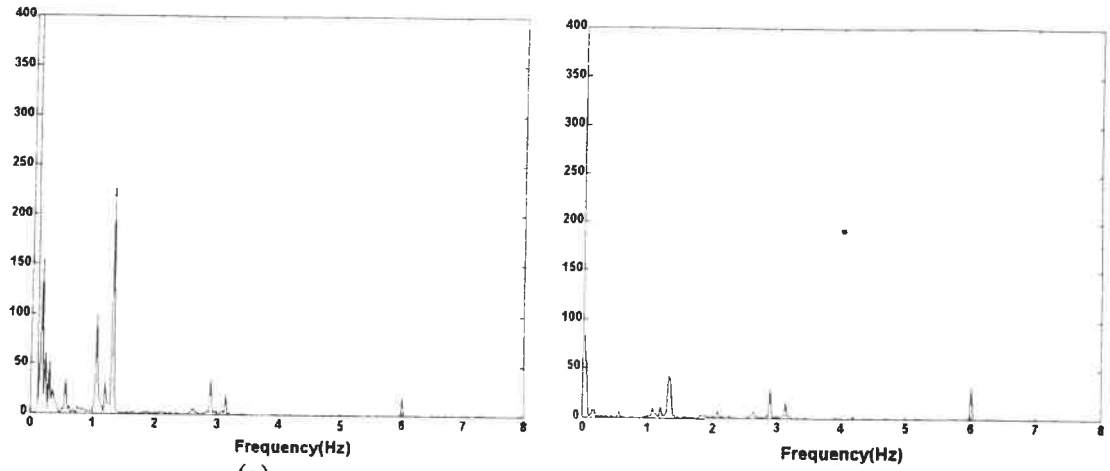

Fig. 4 Power Spectral Density of kinematic error before(a) and after(b) implementation of control scheme.

4. Summary

(1) The modified LMS algorithm outperforms the conventional LMS algorithm. Its simplicity and high computational efficiency make it easy to implement in the real time case.

(2) It has been shown that 65% of the kinematic error (long and adjacent periodical errors) of the transmission train can be eliminated and the accuracy of machine tool can therefore be greatly improved.

References

[1] Mekeown P.A., High Precision Engineering in the 1990's. Proceedings of CIRP conference on PE & MS, Tianjin China, Sept. 1991.

[2] Widrow B. and Stearns S.D., Adaptive Signal Processing. Englewood Cliffs, NJ: Prentice-Hall, 1985.

[3] McCool J.M.and Widrow B., Principle and Applications of Adaptive Filters: A Tutorial Review, 1980 IEEE ISCAS pp1143-1157

[4] Zhang C. and Margrave F., High-precision Measurement System for a Rotary Table, ASPE 1994 Spring Topical Meeting Tucson April 1994 pp110-115

Automatic Acquisition of Machining Conditions: Towards a Self-Evolving Machining Center

Mamoru MITSUISHI, Shin'ichi WARISAWA, Takashi OHTA and Takaaki NAGAO
Department of Engineering Synthesis, Faculty of Engineering
The University of Tokyo
Hongo 7-3-1, Bunkyo-ku, Tokyo 113, Japan

1. Introduction

In many cases of single piece or prototype production, the machining conditions are not well determined in advance. Under these situations, it is helpful to have a system which has the ability to judge the machining state in real-time and to feedback the system state information to a machining condition determination component.

In this paper, the machining knowledge is stored in a map called a "stability lobe diagram" and the machining conditions are modified by referring to the force information and an experimentally obtained stability lobe diagram. The stability lobe diagram is obtained by a real-time machining state detection method using the information from a multi-axis force sensor and is continuously updated during machining through the use of a learning function. Therefore, machining conditions such as depth of cut and main axis rotational speed can be dynamically changed according to considerations of machining efficiency.

2. Related work

Many researchers have developed physical models of end-milling, for example in references [1, 2, 3, 4]. Tlusty [1] has proposed an NC data generation method that considers not only the geometrical model of a mechanical part but also the occurrence of chatter as a machining state, and has applied it to pocket milling. Minis [2] has proposed a model considering every element necessary for the analysis of end-milling. Armarego [3] has addressed an end-milling model, and the average and the fluctuating cutting force is calculated considering the eccentricity and cutter deflections. The calculated result is quite similar to the experimental result. Altintas [4] has discussed a simulation system for endmilling to generate the tool path based on a solid model. The problem of monitoring tool wear or breakage has been approached through the use of acoustic emission sensing [5, 6], video image analysis, accelerometers, pulse generators or heat flux measurement. Neural networks have been tried recently for sensing signal processing [5, 6, 8]. Smith and Tlusty [9] have presented a method for machining state detection and the modification of the machining conditions, however, it has the problem that it takes several seconds to judge the machining state using FFT. The "stability lobe diagrams," which plot the boundaries separating stable and unstable machining under constant machining conditions, are discussed in, for example, reference [10]. Generally, the diagram is obtained from a static machining condition model. In this paper, in contrast, the stability lobe diagram is experimentally obtained. Furthermore, this paper discusses a system which can deal with varying machining conditions. This is important, since conditions change frequently in real parts, due to changes in the geometrical model of the mechanical part. Such adaptation is possible using our real-time machining state detection method because the method is fast enough to use force data during a single tool rotation.

3. Real-time machining state detection

It is essential to monitor the multi-axis force information produced by machining to judge the machining state. Therefore, a six-axis force sensing table has been installed on a machining center. The machining state is judged from the sensed force data plotted in a single or in multiple dimensions, using time as a parameter (Fig.1). We have called the method the "force vector locus" method. The center of gravity of the area bounded by the closed force locus is calculated for each tool rotation, as is the center of gravity including each subsequent sample point. Then, the variance of these distances is calculated. The machining state is judged to be normal if the variance is small and chatter is deemed to have occurred if the variance is large (Fig.2,

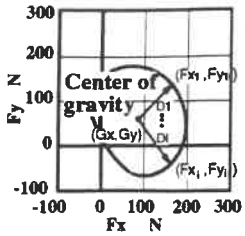

Fig.1 Variance of distance

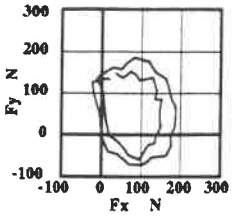

Fig.2 Force vector locus in normal cutting

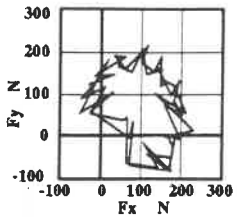

Fig.3 Force vector locus in chatter cutting

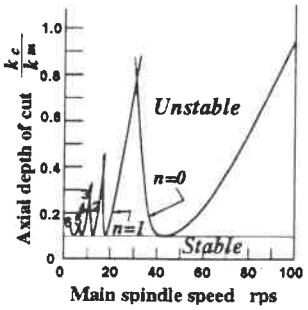

Fig.4 Stability lobe diagram of the system

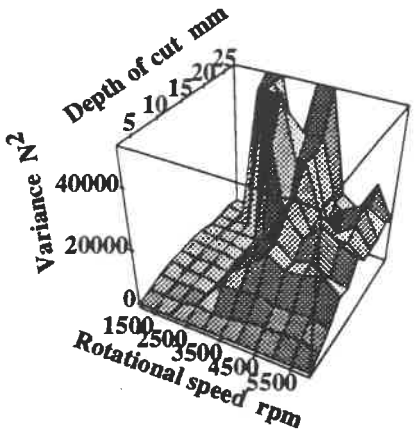

Fig.5 3-dimensional experimentally obtained stability lobe diagram

Table 1 Cutting conditions

Tool	: Square Endmill (helix angle=40deg., 2-edge, ϕ15)
Workpiece	: Aluminum alloy (A2017)
Cutting type	: Full immersion
Feed per edge	: 0.025 mm/edge
Sampling rate	: 5000 Hz
Coolant	: on

Fig.3). However, since the variance varies with the cutting conditions, as well as with the machining state, a threshold variance is determined for each cutting condition using a physical model of the cutting process [11].

4. Experimental acquisition of the stability lobe diagram

The stability lobe diagram represents stable and unstable machining conditions using the methods of control theory, considering the dynamics of the structure, which consists of the tool, workpiece and machine tool (Fig.4), and the cutting mechanism. To obtain the stability lobe diagram, the dynamics of the structural loop which consists of tool, workpiece and machine tool has to be analyzed. In general, the dynamics of the structure is experimentally obtained by methods such as (i) excitation by tapping, (ii) the impulse response method, and (iii) oscillation tests. To apply method (i), it is difficult to realize the same conditions such as excitation point, time duration and direction. Method (ii) is still being researched. Consequently, method (iii) is most commonly used, although it is very time-consuming. For practical use it is important that the stability lobe diagram be obtained. Therefore, a cutting operation is actually executed by a machine tool and the stability lobe diagram is automatically obtained by judging the machining state in real-time using force information. In the case of endmill cutting, the horizontal and vertical axes of the stability lobe diagram are the rotational speed of the main axis and depth of cut, respectively.

The cutting force was measured with varying depth of cut and main axis rotational speed while keeping the feed speed constant. Fig.5 shows the 3-dimensional stability lobe diagram based on variance of distance in the force vector locus. The other cutting conditions are shown in Table 1. In Fig.5 the z-axis shows the variance of distance in the force vector locus. Therefore, a lower value indicates a more stable state.

5. Dynamic tool path planning using stability lobe diagram

Fig.6 and Fig.7 show stability lobe diagrams under the same machining conditions. In these figures the sign ● and × show stable and unstable state, respectively. The difference in both experiments is the usage time of the cutter. In Fig.6 a completely new cutter was used and in Fig.7 the cut length was approximately 510 m. In these experiments, the effect of "initial tool wear" is obvious. The boundary of the stability lobe diagram varies because the cutting dynamics change depending on tool wear. It is difficult to trace the tool wear in the case of one-piece

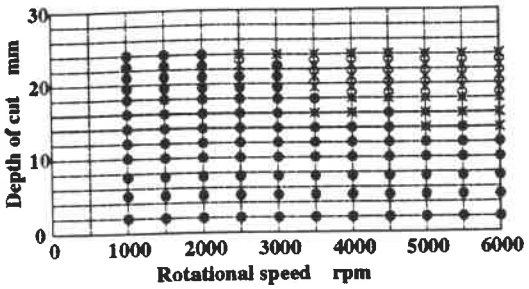

Fig.6 Stability lobe diagram (sharp tool)

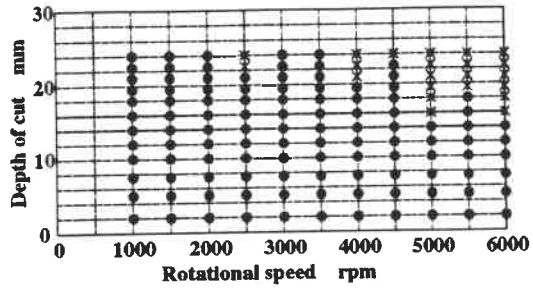

Fig.7 Stability lobe diagram (significant tool wear)

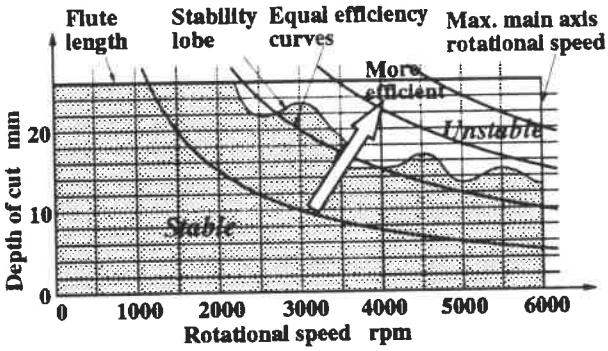

Fig.8 Tool path planning using machining efficiency evaluation

production because generally the shape of the workpiece is complicated. It is difficult to specify the optimum cutting conditions such as depth of cut and main axis rotational speed. Therefore, machining conditions must be modified by judging the machining state in real time. Concerning the main axis rotational speed change, it is presented in reference [12]. The dynamic change of the depth of cut is also necessary and the method is described in this paper. Furthermore, the data-base concerning stability is continuously updated during cutting.

6. Evaluation of machining efficiency

To generate a tool path with the capability of high efficiency cutting, a machining efficiency evaluation function for the generated tool path should be introduced. The following features are required for the evaluation function. (i) The value should reflect the machining efficiency. (ii) The evaluation function should be described with the parameters of a stability lobe diagram. Generally, high efficiency machining is accomplished by reducing the machining time while keeping the machining accuracy within a threshold value. In this paper, it is assumed that the machining accuracy is maintained while the distance of variance in force vector locus is kept below a predefined value. In the stability lobe diagram for end-milling, the horizontal axis is the main axis rotational speed and the vertical axis is the depth of cut. To calculate the machining efficiency, the feed speed of the cutter is needed. According to the analysis of endmilling, feed speed change does not contribute to system stability. In this system, the feed speed is controlled to be proportional to the main axis rotational speed to keep the feed per tooth constant. If there are several stable points in main axis rotational speed for the same depth of cut, the higher one is adopted. Finally in this system, the machining efficiency evaluation function G is determined as follows:

$$G = bV_f$$

where b and V_f are depth of cut and feed speed, respectively. With the assumption mentioned above, it is possible to determine the high efficiency machining conditions using an experimentally obtained stability lobe diagram (Fig.8), remembering that there is an upper limit for the depth of cut because of the flute length of an endmill. Furthermore, there is an upper limit for the main axis rotational speed of a machine tool which is controlled as proportional to the feed speed in this paper. The constant machining efficiency curves are hyperbolas as presented in Fig.8. At the right upper position the machining efficiency is high and, on the contrary, at the left lower position it is low. By moving the constant efficiency curve from right upper position to the left lower position, highest efficiency can be realized while maintaining the system stability where the stable-unstable boarder and a constant efficiency curve contact each other.

7. System implementation

Fig.9 shows the schematic diagram of a system realizing the functions described above. The geometry of a workpiece is input at the "3-dimensional modeller" which is located in CAD system. The "3-dimensional modeller" used in this paper has a feature that the generation

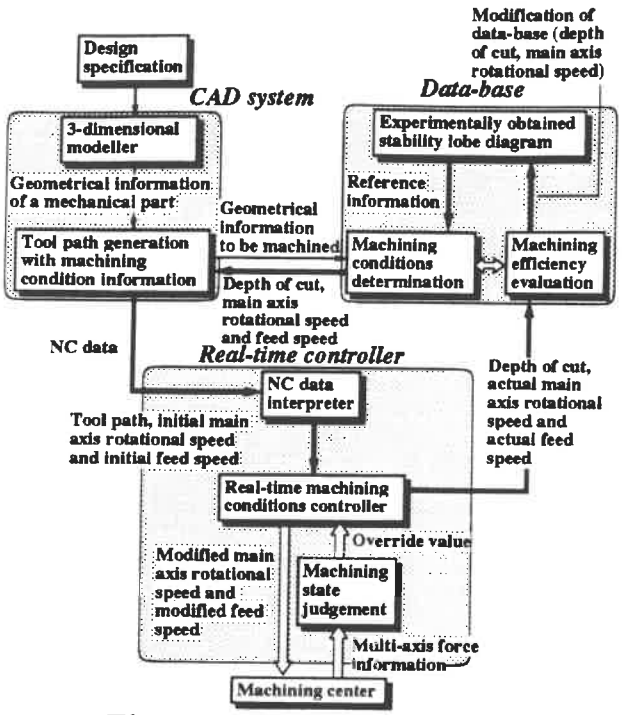
Design specification
CAD system
3-dimensional modeller
Geometrical information of a mechanical part
Tool path generation with machining condition information
Geometrical information to be machined
Depth of cut, main axis rotational speed and feed speed
NC data
Real-time controller
NC data interpreter
Tool path, initial main axis rotational speed and initial feed speed
Real-time machining conditions controller
Override value
Modified main axis rotational speed and modified feed speed
Machining state judgement
Multi-axis force information
Machining center
Modification of data-base (depth of cut, main axis rotational speed)
Data-base
Experimentally obtained stability lobe diagram
Reference information
Machining conditions determination
Machining efficiency evaluation
Depth of cut, actual main axis rotational speed and actual feed speed

Fig.9 System construction

and logical operation can be executed by previously made programs. "Tool path generation task" calculates the 3-dimensional cut area and sends depth of cut information to "machining conditions determination task." The "machining conditions determination task" determines main axis rotational speed, feed speed and division pattern for depth of cut. Tool path with machining conditions has an extended APT format and is sent to "NC data interpreter." The "NC data interpreter" interprets each step of NC data file and sends its information to "real-time machining conditions controller." The "real-time machining conditions controller" modifies the main axis rotational speed and feed speed in real time based on machining state acquired by "machining state judgement task" and drives a machining center. "Machining efficiency evaluation task" calculates cut efficiency using the actual adopted main axis rotational speed, feed speed and depth of cut. Furthermore, the data-base described as a stability lobe diagram is updated. The machining conditions to realize adequate machining efficiency are renewed using the modified data-base. In case it is judged that the depth of cut should be changed as a result of the data-base modification, the recommended depth of cut is adopted in the next tool path generation procedure.

As has described in this paper, programs in the CAD system and data-base are executed as dynamic tasks during the machining operation and tool path, depth of cut and data-base can be dynamically modified. This is one of the best features of the proposed system.

8. Conclusions

A machining system which has a capability to determine the machining conditions including depth of cut and, furthermore, to modify the tool path dynamically during machining was proposed. In the proposed system, the tasks in the CAD system, real-time controller and data-base are varied dynamically by communicating with eachother.

References

[1] Tlusty,J., et al., "New NC Routines for Quality in Milling," *Annals of the CIRP*, 39/1, pp.517-521, 1990.

[2] Minis,L., et al., "Analysis of Linear and Nonlinear Chatter in Milling," *Annals of the CIRP*, 39/1, pp.459-462, 1990.

[3] Armarego,E.J.A. et al., "Computerized End-Milling Force Predictions with Cutting Models Allowing for Eccentricity and Cutter Deflections," *Annals of the CIRP*, 40/1, pp.25-29, 1991.

[4] Altintas,Y. et al., "End Milling Force Algorithms for CAD Systems," *Annals of the CIRP*, 40/1, pp.31-34, 1990.

[5] Moriwaki,T. et al., "Application of Neural Network to AE Signal Processing for Automatic Detection of Cutting Tool Life," *Journal of JSPE*, vol.57, no.7, pp.1259-1264, 1991.

[6] Dornfeld,D.A., "Neural Network Sensor Fusion for Tool Condition Monitoring," *Annals of the CIRP*, 39/1, pp.101-105, 1990.

[7] Lundholm,T., et al., "Advanced process monitoring — A major step towards adaptive control," *Robotics and Computer-Integrated Manufacturing*, vol.4, no.3, pp.413-421, 1988.

[8] Moriwaki,T. et al., "Recognition of Cutting State Based on Neural Network Sensor Fusion," *Journal of JSPE*, vol.59, no.5, pp.779-784, 1993.

[9] Smith,S. et al., "Stabilizing Chatter by Automatic Spindle Speed Regulation," *Annals of the CIRP*, 41/1, pp.433-436, 1992.

[10] Merritt,H.E., "Theory of Self-Excited Machine Tool Chatter," *ASME J. Eng. for Industry*, pp.447-454, Nov. 1965.

[11] Mitsuishi,M., et al., "Real-time Machining State Detection Using Multi-axis Force Sensing," *Annals of the CIRP*, 41/1, pp.505-508, 1992.

[12] Mitsuishi,M., et al., "Development of a Rapid Manufacturing System Using Real-Time Machining State Detection," *Proc. of the 8th Annual Meeting of the American Society for Precision Eng.* , pp.531-534, Seattle, U.S.A., 1993.

Non-circle Cutting by an NC Lathe Using DNC System

Yoshitaka MORIMOTO*
Takeshi YASUI**
Toyokazu TSUBONO**
Kenichi HIROSAKI*
*Industrial Research Institute of Ishikawa
Ro-1 Tomizu-machi Kanazawa 920-02, JAPAN
** Kanazawa University

1. Introduction

NC lathe plays an important role in FA(Factory Automation). It has been equipped various functions with progress of computer. But the machined cross sectional profile is limited to circle as it was in spite of composite milling or drilling tool.

Therefore, the new application of NC lathe is expected from the point of flexible productivity. The non-circle cutting is one of the representatives and is machined by the copying machine which is suitable for mass production. But in the case of trial design, it is useful to machine the non-circle cutting by NC lathe.[1)]

This paper reports that the application method of the repetitive control that enables to cut the work piece with the non-circle cross section by using a conventional NC lathe, and that the experimental results showed remarkable improvement of both the tool trajectory and the profile error.

2. Application Method

2.1 Repetitive Control[2)]

The target value of the depth of cut during the non-circle cutting is almost periodic data which consist of a few frequency spectra. Thus, the dynamic characteristics of the tool post is required as constant. But it is impossible to constant value about conventional NC lathes and it depends on feed velocity, friction loss, depth of cut and so on, at each cutting.

In this study, we look at the periodicity of target value and try to apply the repetitive control method as shown in Fig.1. This method is enough effective to control the periodic trajectory of the depth of cut with the desired motion. The ith

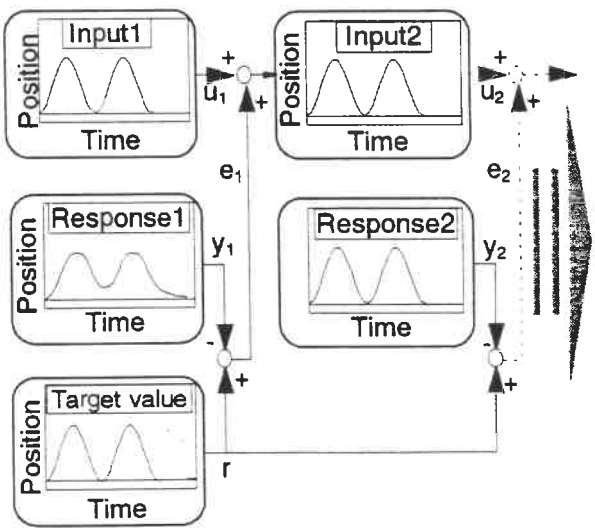

Fig. 1 Repetitive control

control command is described as follows.

$$U_i(j\omega) = U_{i-1}(j\omega) + aE_{i-1}(j\omega) \quad \cdots(1)$$

$$E_{i-1}(j\omega) = R(j\omega) - Y_i(j\omega) \quad \cdots(2)$$

Where,

$Y(j\omega)$:response of the tool base
$U_i(j\omega)$:ith control input
$E_i(j\omega)$:deviation between the target value and the measured motion
$R(j\omega)$:target value
a :positive coefficient factor (a<1)

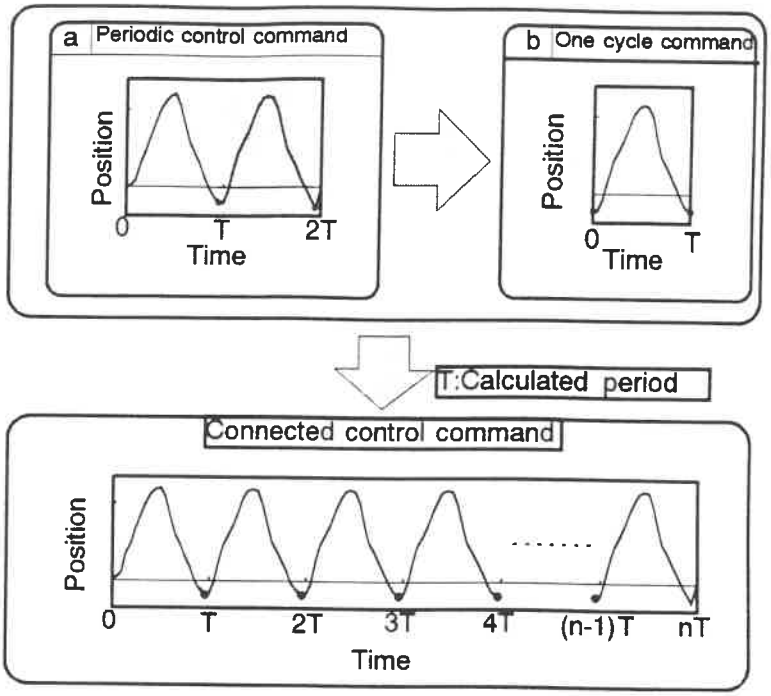

Fig.2 Calculation method of control command

Assuming that the dynamic characteristics of the tool base $G(j\omega)$ is constant, several control methods can be applied and could be effective. The repetitive control is more effective than other methods when $G(j\omega)$ is not constant.

2.2 Calculation Method

When the control command is calculated by using the repetitive control method, it must be calculated from the deviation between the control command and the present motion of the tool trajectory throughout the whole tool path. But in the case of the periodic target value, only one cycle tool trajectory is needed in calculating the control command with the repetitive control. The result obtained from this operation is connected from the first cycle to the final one as shown in Fig 2.

3 Experimental

3.1 DNC system

The conventional NC lathe does not have the function which enables to realize the non-circle cutting. Then, a DNC (direct numerical control) has been developed as shown in Fig.3. The control command calculated at the personal computer is fed to the

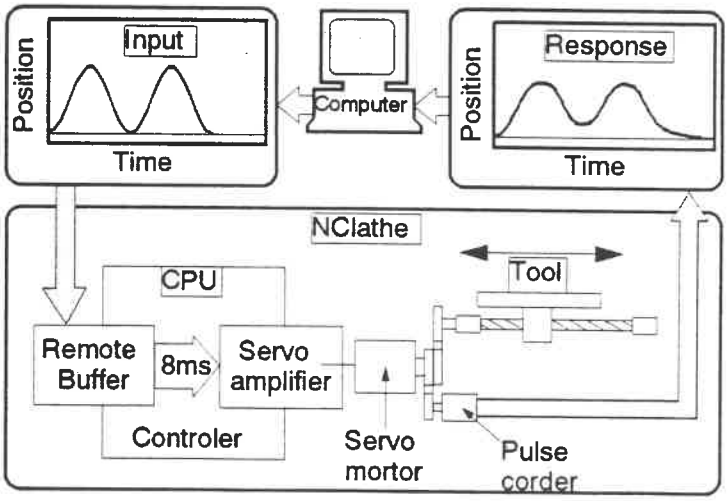

Fig.3 Schematic diagram of DNC system

servo amplifier of the NC lathe directly. It is possible to move the X and Z axes' tables by 8ms.

Figure 4 shows that the dynamic characteristics of this table between the step input and the tool motion in the frequency domain are different and depend on the each depth of cut. But each result is constant at each measurement. Thus, the repetitive control is suitable for this kind of system. Because the positioning deviation approaches to the target value.

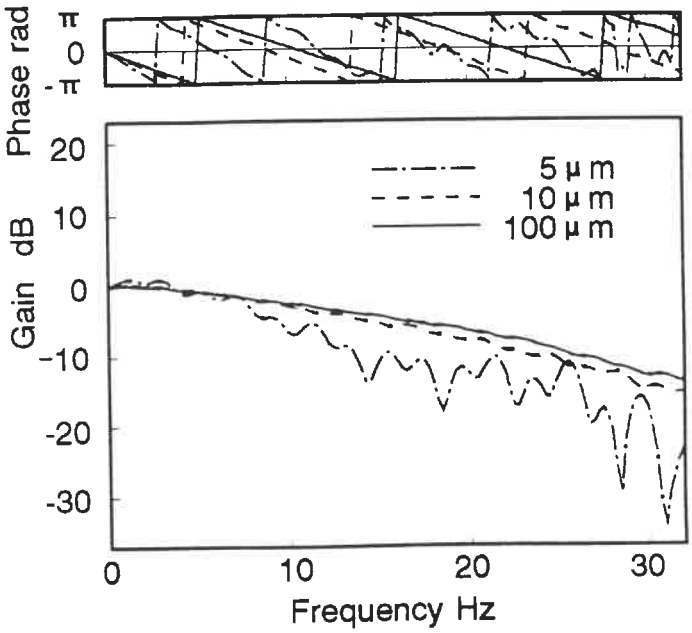

Fig.4 Dynamic characteristics of X-axis table

3.2 Positioning of tool base

By using this system, the experimental procedure has been done in the case of two periods' positioning without cutting. The amplitude of this motion was 200 μm. First, the repetitive control by using only the deviation of positioning between the target value and the measured one was used to calculate the control command. In this case, the accuracy of positioning was ±5μm as shown in Fig.5.

Then, the velocity compensation by the repetitive control in addition to the positioning

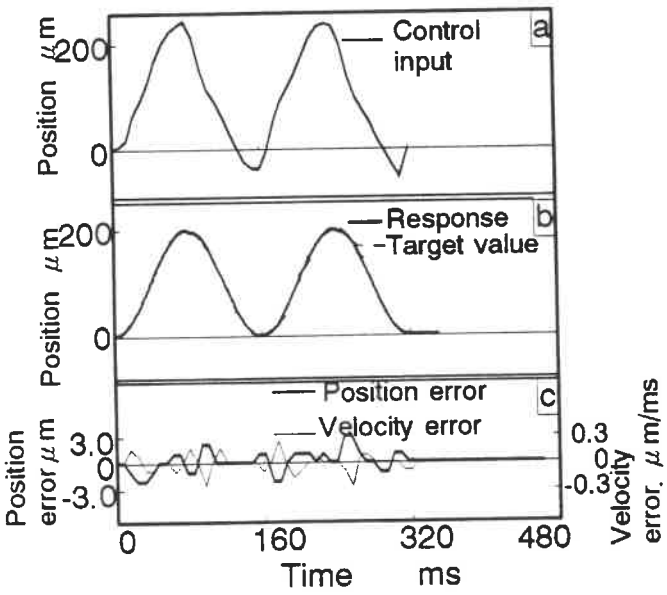

Fig.5 Control result using position feed back

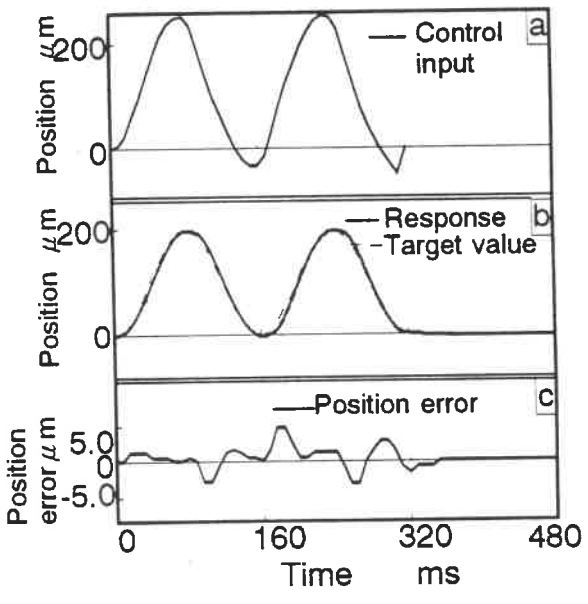

Fig.6 Control result using position feed back and velocity feedback (4th compensated result)

feedback was applied to improve the rapid response of the tool base. The accuracy of the tool base motion was reduced positioning from over ± 50μm to within ± 3μm by the 4th repetitive compensation of input as shown in Fig.7.

3.3 Non-circle cutting

The experimental cutting has been done with brass in the case of the profile consisted of two periodic sin wave as shown in Fig.7. The maximum amplitude of this depth of cut was 200 μm. In this case, the control command is calculated by connecting the repetitive compensated input obtained by the previous experiment. Figure 8 shows that the profile error of the work piece has been achieved within ± 3μm as same as the positioning without cutting.

4. Conclusions

(1) A DNC system was developed to realize the non-circle cutting by using a conventional NC lathe.

(2) The application method is proposed by using the repetitive control method.

(3) The profile error was converged with in ± 3μm by the proposed method.

References

1) T.Higuchi, T.Yamaguti: Non-circular Machining (1st Report), JSPE,(1988)145.

2) S.Hara, T.Omata and M.Nakano: Synthesis of Repetitive Control Systems and Its Application, Proc.CDC,(1985)1384.

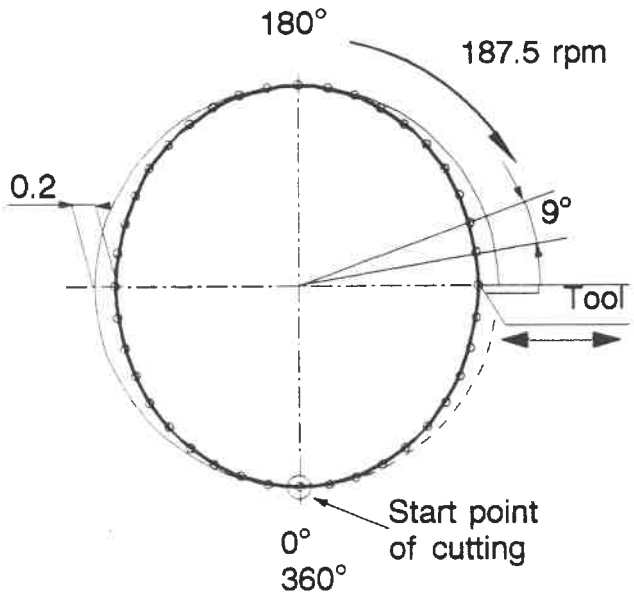

Fig.7 Cutting condition

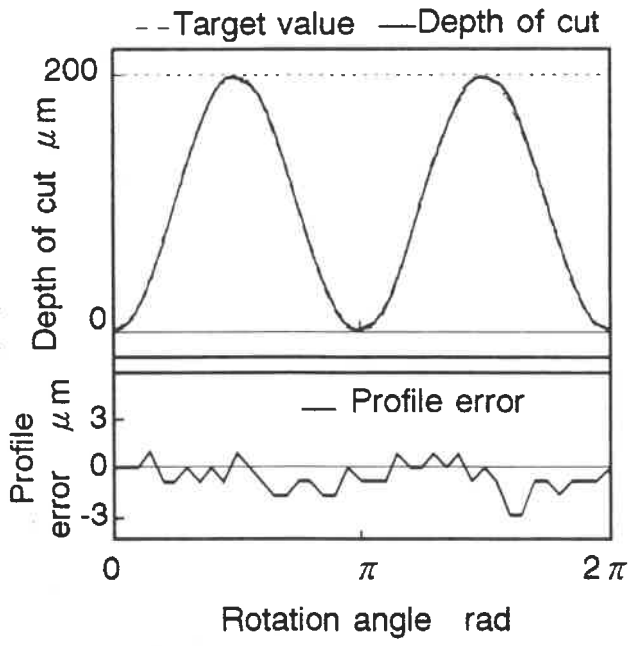

Fig.8 Profile error of machined cross section.

Development of Thermally Stabilized Aluminum Mirrors for the Composite Infrared Spectrometer

Steven C. Fawcett
Optical Fabrication Branch, EB53
National Aeronautics and Space Administration
Marshall Space Flight Center, AL 35812

Thermally stabilized aluminum mirrors are being developed for the Composite InfraRed Spectrometer (CIRS) instrument which will be one of twelve science instruments aboard the Cassini probe to Saturn scheduled for launch in 1997. The instrument is a combined Mid-IR and Far-IR Fourier transform spectrometer. The mirrors are being built and qualified at Marshall Space Flight Center for both the engineering test and flight units. The group of mirrors consist of the beam splitting mirror, two collimating mirrors, a fold flat and a focus mirror. The collimating optics are off-axis parabolas and the focus mirror is an on-axis parabola. The beam splitter consists of a spherical and toroidal surface and serves to divide the incoming energy for the mid and far infrared spectrums. The mirrors are made from 6061 aluminum that has been stress relieved so that the mirrors will perform adequately at the operating temperature of 170 degrees Kelvin. The spectral range of interest includes wavelengths ranging from 7 to 1000 micrometers. These mirrors are rough machined, diamond turned, electroless nickel plated and subsequently polished. Each component receives stress relieve heat treatment processes to ensure thermal stability. After completion, the mirrors are qualified at their cryogenic operating temperatures at Goddard Space Flight Center where they will be integrated into the instrument. The key components of the fabrication process will be presented with the appropriate testing results.

The mirror development process began with a set of drawings provided by Goddard Space Flight Center (GSFC). These mirrors were designed to prevent substrate deformations when the mirrors are cooled to the operating temperature of 170° Kelvin. The mirror substrates are machined 6061-T6511 aluminum. The mirrors are rough machined from extruded rod stock and stress relieved prior to final finishing. The optical surface is diamond turned and the entire optic is electroless nickel plated. After plating the surfaces are polished to the required surface finish and final metrology is performed. The key aspects of the fabrication process are as follows: 1) The mirror surfaces are designed to allow for plating both the mirror face and the back surfaces to minimize the bi-metallic deformations at the operating temperature. 2) The entire mirror substrate (including mounting flanges and through holes) will be nickel plated. This makes mounting the substrate back into the surround for polishing quite difficult. 3) The stress relieve process needs to minimize the residual stresses to a level where the optical performance can be maintained at the operating temperature. 4) One mirror has both a spherical surface and a toroidal surface on the same substrate. These four issues are the significant

complications in an otherwise simple project. The solutions to the problems will be briefly presented in the following sections.

The mirrors were designed to maximize the surface area behind the reflective surface so as to minimize the bi-metallic deformations that occur when the component is cooled from ambient to the operating temperature of 170° K. This design was provided by GSFC and could not be significantly altered. Figure 1 shows the mirror layout for one of the off-axis parabolas. The mirror is approximately 3.5" diameter, 0.4 " thick supported by a 0.75" square post from the mounting flange. These off axis parts are supported in a surround during the turning and polishing operations. The mounting flange is mated flush with the back of the surround and creates a problem when the top of the flange is plated with electroless nickel. To position the mirror surface flush with the surround after plating, the back surface of the surround is diamond turned an amount equal to the plating thickness. The lack of a uniform support under the mirror surface created a problem during the turning operation. The centrifugal forces on the mirror were transmitted to the flange through the post and caused a distortion in the flange. This resulted in a tilt of the optic with respect to the surround after turning. Originally, the tilt was approximately 0.01 degrees and was minimized by placing a wedge between the mirror and the flange and reducing the turning speed.

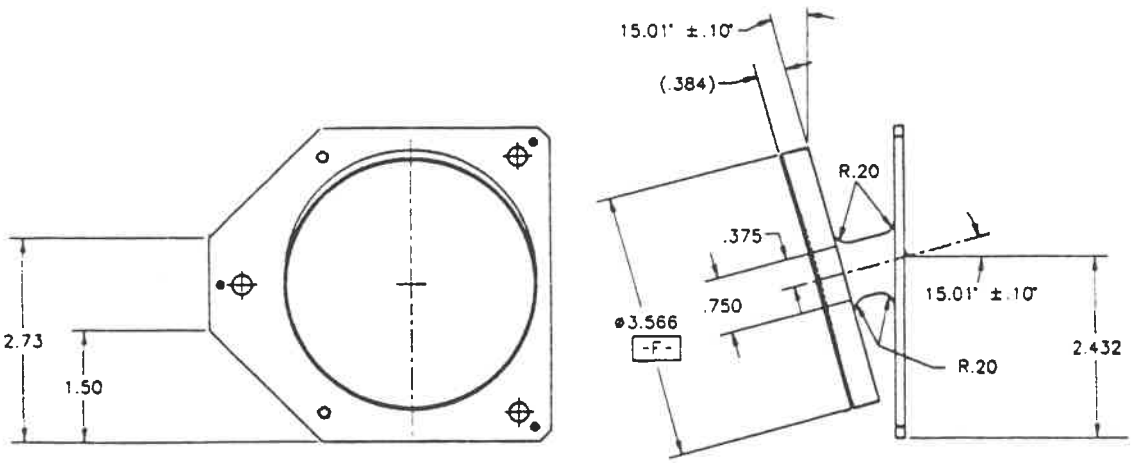

Figure 1 Sketch of off axis parabolic mirror.

The other mirror that created a problem with it's geometry was the beam splitter. The part is shown in Figure 2. The component has two distinct mirror surfaces. Surface 1 (S1) is convex spherical and surface 2 (S2) is convex toroidal. The geometry of the part required the turning of S2 with the part rotating at the longer radius (33.46") while the shorter radius (16.14") is programmed axes movements. A holding fixture was designed to mount the part to the M-40 diamond turning machine at the required radius. Several attempts at test cuts failed to give adequate surface finish quality. The average surface finish was approximately 600 Å RMS. This poor surface quality coupled with the difficulties in measuring the toroidal figure led to a re-design of the

optical profile. The new design incorporates a spherical surface of 24.8" radius for S2 and can be turned on axis.

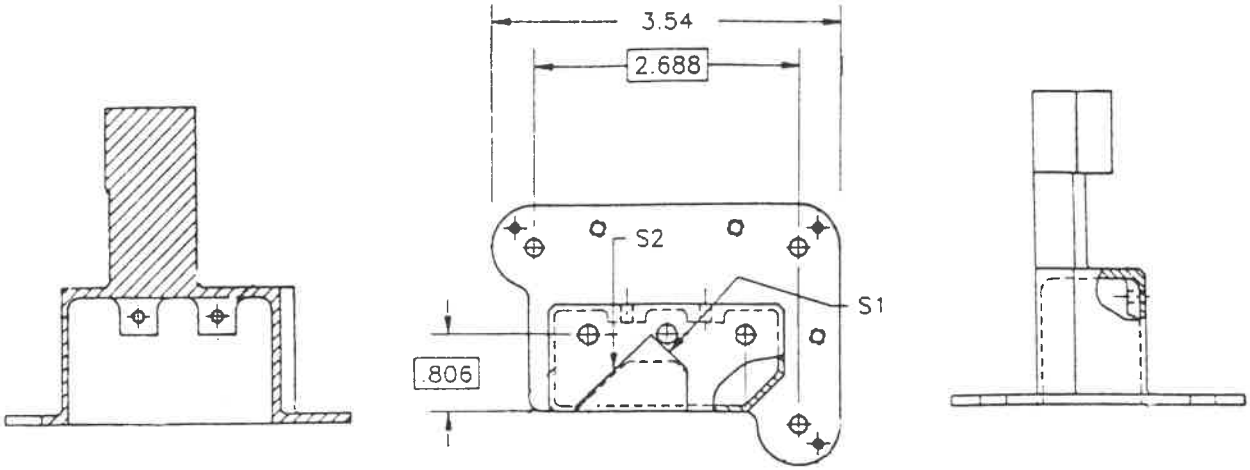

Figure 2 Beam splitting mirror.

The stress relieve heat treatment process evolved through various phases during the project. The initial process was derived from previous mirror programs at GSFC and included 5 heat treatment steps of 325° F for 12 hours. The process also dictated the use of a vacuum environment during the procedure. This technique was time consuming and left questions as to whether the residual stresses were minimized to an acceptable level (defined as where the optics maintained figure at operating temperature). The stress relieve process was simplified to utilize a higher temperature for a shorter duration. This procedure is given below and uses an uphill quench (liquid nitrogen to boiling water) to assist the process. Initially the mirrors are rough machined leaving 0.005" of material on the mirror surface and the critical mounting areas. Then step 1 is performed followed by machining the last 0.005" of material from the mirror and mount. Step 2 is then performed followed by diamond turning. This process results in decrease in the yield strength from a nominal value of 40 ksi to about 26 ksi. The hardness also decreased from B48 to B17 as a result of the processing. The project team evaluated the resulting mechanical properties and deemed them satisfactory.

1.1. Heat parts to 500 degree Fahrenheit for two (2) hours.
1.2 Allow to cool to 150° F at 125°/Hr. Air cool to room temperature.
1.3 Suspend parts 2 to 5 inches above the surface of liquid N_2 and allow to cool for 15 minutes. Slowly immerse part in liquid N_2 and allow to stabilize. Remain submerged for an additional 5 minutes.
1.4 Immerse parts in boiling water within 7 seconds of removal from liquid N_2 for ten (10) minutes minimum. Air cool to ambient.
2.1 Heat parts to 325 degree Fahrenheit for twelve (12) hours.
2.2 Allow to cool to 150° F at 125°/Hr. Air cool to room temperature.
2.3 Cool parts to -170° F at 50° F/Hr maximum rate. Soak for 1.0 hour.
2.4 Warm parts to room temperature at 50 degree F/Hr maximum rate.

Stress Relieve Heat Treatment Process (6061-T6511)

The mirror fabrication program for the engineering unit continues and the flight optics development will soon be initiated. The initial testing of the thermally stabilized mirrors has only been performed on the flat substrates. This testing proved that these mirrors maintained their figure tolerance at the 170° K operating temperature. The testing of the curved components is still incomplete.

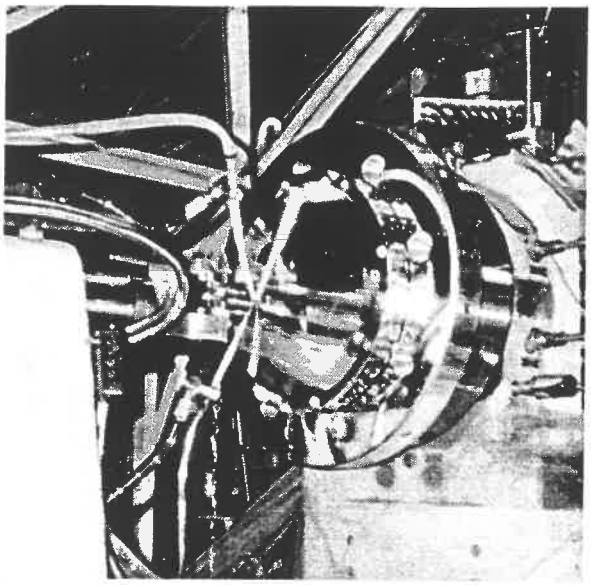

Diamond turning of surround.

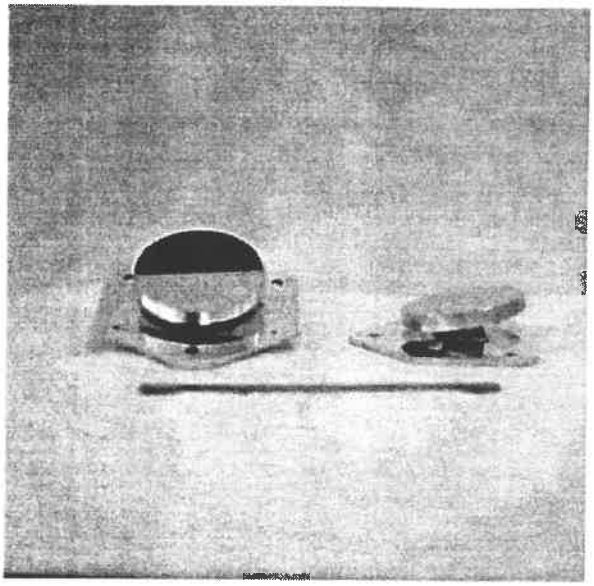

Off axis parabolic mirrors.

On axis parabolic mirror.

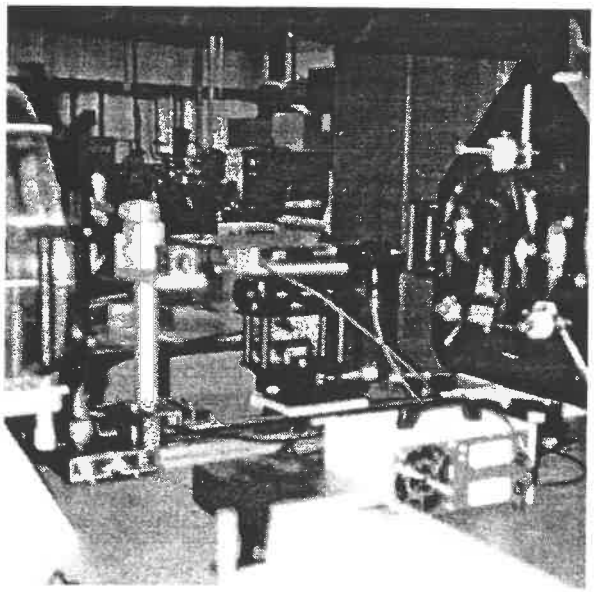

Radius measurement setup.

Study of Process Parameters in Diamond Tool Manufacturing —Influence of Scaife Material—

Ken'ichiro HORIO, Toshio KASAI, Hiroyuki TAKEI
Department of Mechanical Engineering, Saitama University
255 Shimo-okubo, Urawa 338, Japan

1.Introduction

Ultraprecision cutting, single point diamond turning, critically depends on highly developed machine tool, metrology and control, cutting tool, environmental control, and machining strategies and software. Though enormous numbers of works have been performed to develop the technique, there are few, almost no, scientific works concerning with manufacturing diamond tools. With the present techniques making the diamond tool totally depends on skills of individual manufacturers. In our paper, rather systematic approach on the manufacturing process is discussed. As very sharp edge in the diamond tool is mandatory for obtaining good machining surfaces, finishing process which is creating the sharp edge is the most important technology in manufacturing the good quality diamond tools. Therefore we took up this stage. The problem is also lead to re-sharpening process.

2.Process of Diamond Tool Fabrication

2.1.Thorough Process

Flow of the diamond tool fabrication process is as follows.

Inspection of original gem stone $\Longrightarrow$Cleaving, Sawing and Grinding (cutting a piece from a gemstone) $\Longrightarrow$Brazing the tip to the shank $\Longrightarrow$Rough finishing (form generation) $\Longrightarrow$Fine finishing (edge preparing and sharpening).

2.2.Finishing Process

The final process is polishing rake and flank surfaces. The diamond tool polishing technique came from that for jewelry which is 'diamond cut diamond' process. Fine diamond powders mixed with olive oil are applied on a disc (polishing tool), which is called scaife, and the diamond tool is polished by being pressed to the rotating scaife. Cast iron disc have been traditionally and widely used material as the polishing tool (scaife). We tried to use hardened steel in stead of the cast iron. Even by using the hardened steel scaife, we could get sharp edge diamond tool without chipping on the edge line.

3.Experimental Procedure

3.1.Apparatus

Fig.1 shows the conceptual figure of our apparatus. The apparatus is made of scaife, its driving equipment, and tool holder. We used dead weight method in order to make polishing pressure constant. The scaife is supported with a static air bearing. Moreover we adjusted vertical deviation

Table 1 Experimental conditions

workpiece	natural monocrystalline diamond tool rake surface ; (110)plane
polishing direction	< 001 > *easily polished direction*
scaife	cast iron ϕ160mm hardened tool steel
polishing pressure	500kPa
polishing speed	800m/min (scaife rotation:1800rpm)
time unit of machining	30min
abrasive	polycrastalline diamond powder
polishing fluid	olive oil

Table 2 Diameter distribution of diamond powders

	nominal value from supplier		actual value by microscope	
symbol	range(μm)	central(μm)	range(μm)	average(μm)
No.1	0~0.2	0.1	0.18~0.28	0.21
No.2	0.25~0.75	0.5	0.61~1.33	0.86
No.3	0.75~1.25	1.0	0.91~1.63	1.28
No.4	1.0~3.0	2.0	1.56~2.88	2.03
No.5	2.0~4.0	3.0	2.03~4.44	3.0

of the rotating scaife to less than 0.5μm. The tool holder includes an attitude control mechanism for the tool to the scaife.

Machining amount of diamond is so small that we measure it by weight change of the tool between before and after experiment by means of a micro-gram balance (sensitivity 2μg).

Table 1 shows our experimental conditions. The conditions are same as our finishing (edge sharpening) process.

3.2.Scaife

Disc of 160mm diameter which is made of hardened tool steel or cast iron was used as the scaife. In order to make machining condition constant, fine polishing by felt with #4000 white corundum after rough polishing by stainless lap with #2000 white corundum was performed before each experiment.

3.3.Diamond powders

In our study in order to examine the influence of diamond abrasive's diameter distribution, we used five step classified powders between diameter 0 to 4μm, whose distributions have narrower width than usual. Table 2 shows those five ranges of powders. In each column both nominal diameter from the supplier and actual size with a photo magnifying method done by us are given. The average diameter of the actual size is calculated on a assumption that the distribution is a normal distribution in the logarithmic scale.

The powders were synthetic polycrystalline diamond made by impact compression. The diamond powders dispersed into olive oil and the kneaded paste was supplied onto the scaife.

4.Experimental results

4.1.Influence of scaife material

It has been common knowledge that the scaife material for diamond machining (both jewelry and tool) is the cast iron. In our laboratory, however the attempt of applying the hardened (tool) steel instead of the cast iron has been succeeded. We have got the same level quality (edge sharpness, chippingless) between them. As the hardened steel is much harder than the cast iron, it has the advantage of avoiding easily unnecessary digging of the tool onto the scaife if it is set at a slight inclination from the scaife. So the two materials were compared quantitatively, that is machining rate, in consideration of the abrasive distribution.

In Fig.2, diamond tool stock removal by both the hardened tool steel scaife and the cast iron scaife with the five ranges of powders are shown. In the case of the cast iron scaife, machining amount is almost in proportion to the mean size of the abrasives. On the contrary, by the hardened tool steel scaife the machining amount has a peak around 1μm and decreases with the size of the abrasives.

In order to investigate the reason of that we performed observation of the used scaife with light microscope. Though on the hardened steel only a lot of scratches supposed to be made during machining process were observed, we found several abrasives stacked on soft part of the cast iron scaife.

As we concluded the phenomena in Fig.1 depended on the each scaife's holding ability of abrasives, we decided to make three steps of surface roughness of the hardened tool steel scaife. The scaifes were roughened with #1000 green silicon carbide grain, #320 of that and #100 black silicon carbide grain. The surface roughness of each scaife was 0.6μm (peak to valley), 2.1μm and 4.6μm, respectively. Experimental results by three scaifes are shown in Fig.3. Though in large size grain, machining amount by the rough (4.6μm) hardened steel scaife is less than that by the cast iron, those with No.1 to No.4 abrasives are more than the cast iron scaife. We supposed that abrasive holding ability of the roughed steel scaife is sufficient as the cast iron scaife especially with fine powders.

We evaluate the cutting performance of the tool finished by the roughest steel scaife with No.3 abrasive. Surface roughness of 6nm could be derived on aluminum alloy cut with our fly cutting method. The value is ranked with that with commercially available tools.

As the result we think we can propose an effective way of combining the rough polishing with the cast iron scaife as a first step and the smooth polishing with steel scaife as a second step.

4.2.Influence of powder distribution

In order to investigate the influence of powder distribution to machinability, we mixed two ranges of diamond powder abrasives. We selected No.1 and No.3 abrasive in Table 1. The diameter distributions of those two are not overlapped. We mixed those two abrasives in ratio of 1:3, 1:1 and 3:1. Including pure No.1 or No.3, we got five kinds of the abrasives. The mixed three have the same total diameter range, that is from 0 to 1.63 μm in the actual value.

By the usual common knowledge of loose abrasive grinding (lapping) or polishing, machining ability, especially stock removal rate depends on the upper limit of the supplied abrasive's size distribution. In this case three mixed abrasive and pure No.3 has the same upper limit. As shown in Fig.4, however, there is a strong linear relation between stock removal rate and weighted average. It is supposed that this peculiarity is due to 'diamond cut diamond' process. It is also suggested that you should take care of minute distribution of abrasives in using broad distributed abrasives.

5.Conclusions

(1) The hardened tool steel can be satisfactorily applicable instead of the cast iron on the diamond tool finishing process.

(2) Combining the rough polishing with the cast iron scaife as a first step and the final polishing with steel scaife as a second step can be proposed.

(3) The stock removal rate is affected not by existing maximum size of abrasives but by the weighted average size of that.

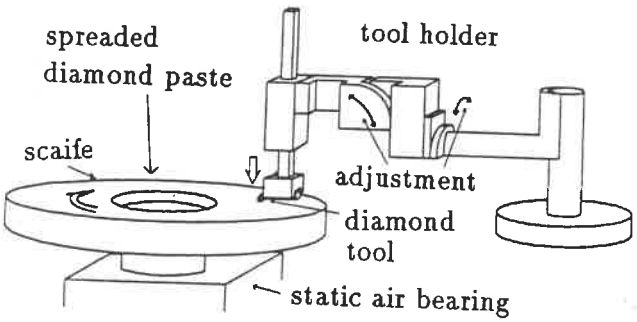

Fig.1 Diamond tool finishing apparatus

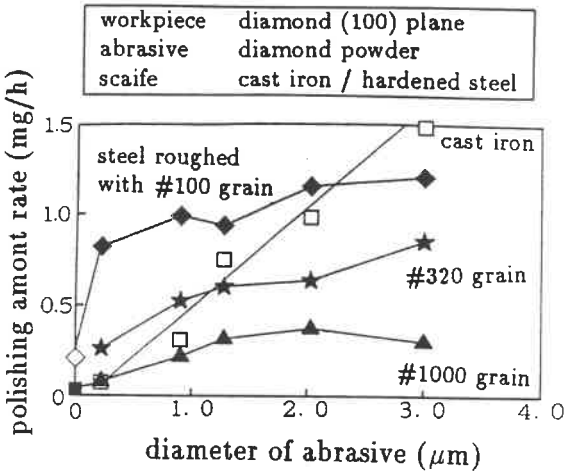

Fig.3 Polishing amount rate by roughed hardened steel scaife

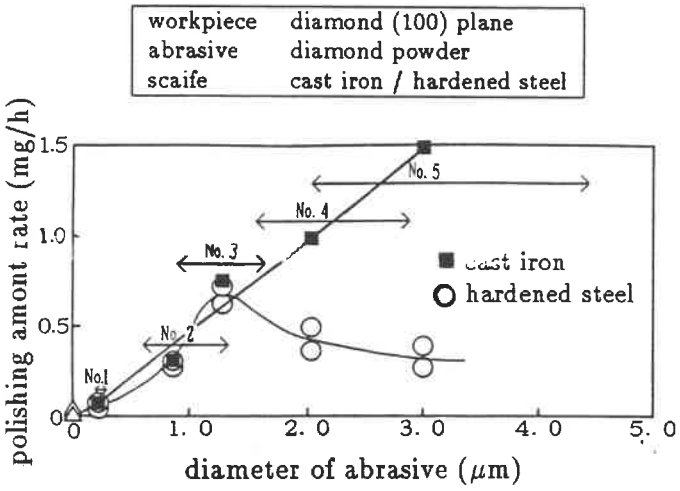

Fig.2 Polishing amount rate by cast iron and hardened steel scaife with five ranges of powders

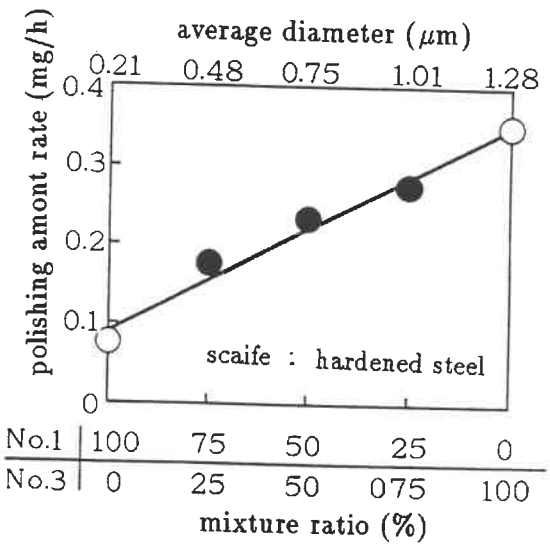
average diameter (μm)
0.21 0.48 0.75 1.01 1.28
scaife : hardened steel
polishing amont rate (mg/h)
No.1 100 75 50 25 0
No.3 0 25 50 075 100
mixture ratio (%)

Fig.4 Influence of mixture ratio of abrasives to polishing rate

A MICRO FEEDING TOOL POST (MFTP) WITH OPTICAL FIBER DISPLACEMENT FEEDBACK FOR DIAMOND TURNING MACHINES

*+ X. M. Lu, * W. B. Lee, * T. P. Leung and + Z. J. Yuan
* Faculty of Engineering, Hong Kong Polytechnic, Kowloon, Hong Kong
+ Harbin Institute of Technology, Harbin, China

1. Introduction

With the advance of science and technology, the requirements for precision machined workpieces in industries become more demanding, and the technology of single point diamond turning is significant importance in ultraprecision manufacture. To obtain sufficient surface and form accuracy, tool position control at nanometer resolution and high accuracy are required. There are two approaches in high precision manufacturing. One depends on high precision machine tools, and the other relies on on-line compensation of machine error. For both of the above methods, it is necessary to maintain the positioning and velocity accuracy of the relative movement between the tool and the workpiece. Therefore, a high resolution accurate, stable and reliable micro feeding tool post (MFTP) is indispensable for a diamond turning machine.

There are two types of control used in micro feeding tool posts. they are : (a) open-loop control, and (b) closed-loop control type. Due to its flexibility and robustness in compensation for modeling errors and rejecting external disturbances, the closed-loop control of a micro feeding tool post is preferred for ultraprecision machines. Considering the need of high measuring accuracy and high frequency response, the displacement sensor must be non-contact. The choice of displacement sensor is very limited. So far only two types of sensor, the capacitance displacement sensor and the LVDT displacement sensor, have been used in MFTP. In this paper, a new MFTP with optical fiber displacement feedback is introduced.

2. Mechanical Design

The MFTP consists of a pair of elastic diaphragm, an electrostrictive actuator, an optical fiber displacement sensor and a diamond tool. A schematic drawing of the MFTP is shown in Fig.1 The MFTP is connected by screw joint. It has small size and is easy to install.

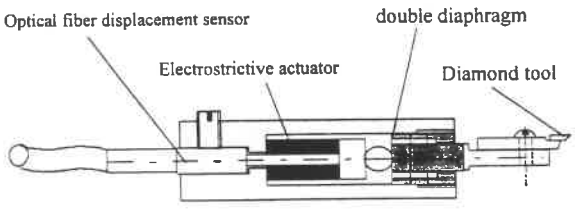

Fig.1 Micro Feeding Tool Post (MFTP)

The MFTP is designed by using a double diaphragm structure which is arranged in parallel, so that the tool base(diamond tool), which connected the center part of the diaphragm may move exactly in a horizontal direction. The double diaphragms can be dissembled. Each diaphragm is fabricated

separately and assembled together to form the double structure. The machining accuracy is then guaranteed. To allow the control system to have a bandwidth of 100 Hz, it is desirable that the first natural resonance of the MFTP be above 1 kHz. Fig.2 shows the measured resonance curve of the mechanics of the MFTP.

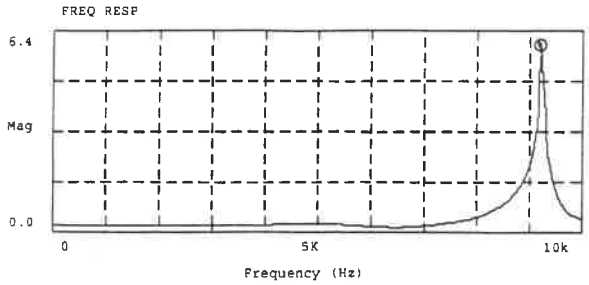

Fig.2 Measured resonance of the mechanism of the MFTP

Among many types of actuators, the piezoelectric element and electrostrictive element makes use of the control signal given to the actuators which can be easily controlled and possess high response and high resolution features. The difference between piezoelectric element and electrostrictive element is that for piezoelectric actuator, the direction of the strain is sensitive to the polarity of the field in a linear relationship, whereas in the electrostrictive material, the second order effect insures unidirectional displacement. In comparing the typical characteristics of the two material types, it is obvious that the electrostrictive effect is a better choice when repeatable, exact movement is required. An electrostrictive actuator with high stiffness and resolution is need to drive the tool and to provide the small infeeding for cutting.

3. Optical fiber displacement sensor

The displacement measuring-loop of the MFTP is made by optical fiber displacement sensor. The sensor consists of a light source, a detector and a optical fiber as a probe. The operation principle of the displacement optical fiber sensor is shown in Fig.3(a). The light emitted from one bundle is backreflected by the object to be measured and collected by another bundle (receiving fiber). As a result, the returned light at the detector is intensity-modulated to a degree dependent on the distance between the end of the bundle fiber ands the object. The intensity of the returned light as a function of distance is shown in Fig.3(b). As shown in this figure, the intensities increase with distance and reach a peak at a certain discrete distance. After that, the intensities fall off very slowly.

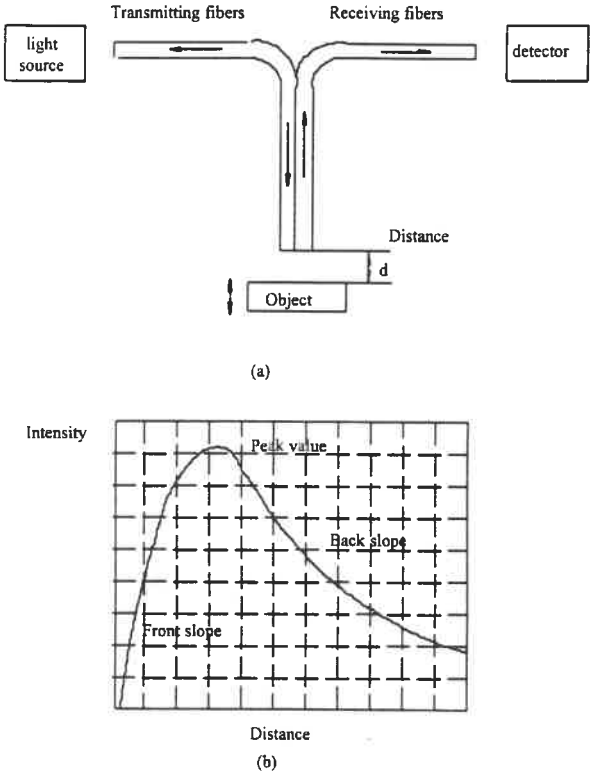

Fig.3 The principle of the optical fiber sensor

In the curve, the front slope is the high-sensitive regions. To obtain a high sensitivity and a high signal-to noise ratio, a special set-up which can compensate for the dc component is employed. In this design, through the specially formed optical fiber bundle, the object and reference surfaces are illuminated by the same light source, and the reflected light from both surfaces is transmitted to their equivalent detectors (A1) and (A2) respectively as shown in Fig.4. The difference between the detectors obtained from detectors (A1) and (A2) is converted to an output voltage by the differential amplifier as shown in Fig.4 Thus, the amplifier gives a signal corresponding to displacement only.

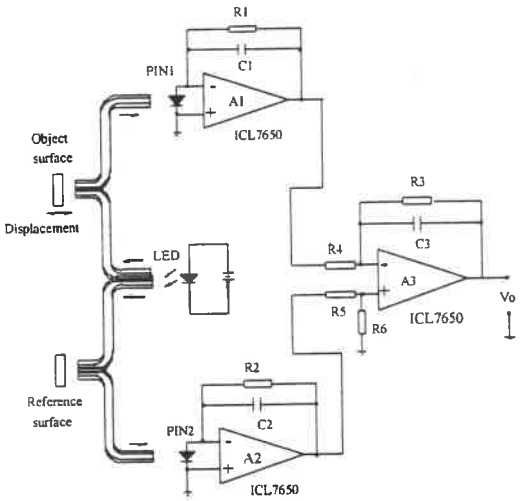

Fig.4 Schematic diagram of the optical fiber displacement sensor

The displacement resolution of the optical sensor can be measured by an open-loop MFTP driven by electrostrictive actuator. Firstly, the open-loop MFTP is calibrated by an capacitance displacement sensor, and then input an appropriate voltage signal to the MFTP, the MFTP will generate a corresponding displacement. From the testing results, the resolution of the sensor is considered to be greater than 0.005 micron.

Theoretically, the frequency response of the sensor is determined by the characteristics of the detector and the amplifier. The cut-off frequency of the amplifier in the present design is set at about 1 kHz which is much lower than that of the detector, so the sensor's frequency response is enough to meet the demand of the MFTP.

In the working range, the linearity of the optical fiber displacement sensor is measured by a capacitance sensor, and Fig.5 shows the linearity of the sensor. When the distance between the sensor probe and the object surface is .from 15 micron to 25 micron, which is within the range of 10 micron, the linearity is about 1 %.

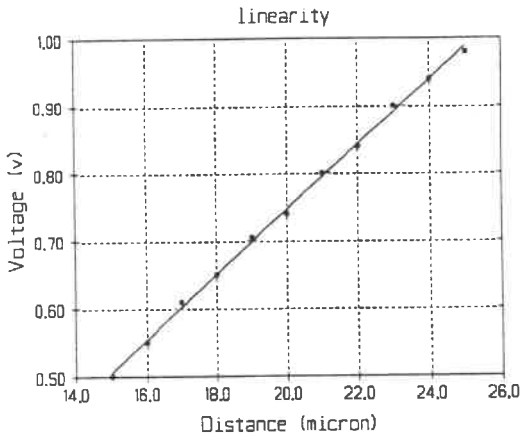

Fig.5 The linearity of the optical fiber displacement sensor

4. Results

To determine the linearity and frequency response of the MFTP with the optical fiber displacement sensor, the static and dynamic behaviors of the MFTP has been tested using a capacitance gauge provided by Beijing Machine Tool research Institute and a FFT Analyzer provided by Analog Co.. Fig.6 shows the result of the static test without feedback and with the optical fiber

displacement sensor feedback. The curve gave the average of results of three tests, and fitted by a least square method. As shown in the Fig.6, the linearity without feedback is about 3%, and the linearity with the optical fiber displacement sensor is within 1%.

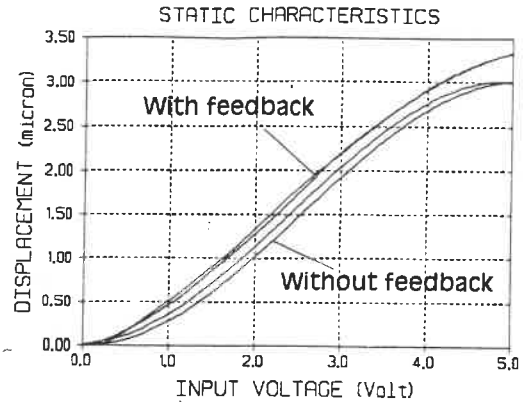

Fig.6 Static characteristics of the MFTP

Fig.7 shows the response of the MFTP without feedback for a sinusoidal input.

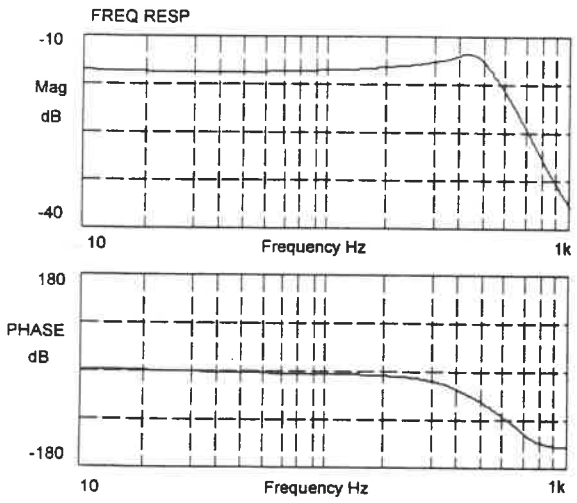

Fig.7 Frequency response of the MFTP

The response is good in a wide amplitude range without any gain change or stick-slip behavior. Because the control algorithm is not completed yet, the other testing results and control algorithm will be presented in another paper.

5. Conclusions and future work

For the purpose of improving the machining accuracy and compensating the error motions of the diamond turning machines, a MFTP with optical fiber displacement was designed.

A part of the test results indicate that the infeed resolution of the MFTP is smaller than 0.01 micron. With the feedback of optical fiber displacement sensor, the deviation from linearity of the static displacement over a range of 5 micron is better than 1%, which is 3 times better than that of a MFTP without feedback. Further work is being planed to complete the control algorithm, and use the MFTP in ultraprecision machining.

6. References

1. X. M. Lu, T. P. Leung, W. B. Lee and Z. J. Yuan, "A Study of an Open-loop Micro Feeding System Used for Ultra-precision Machining", Proceeding of the 5th Sino-Japan Joint Seminar on Ultra-precision Machining. 1994. Harbin.

2. Lu Xiao Ming and Ren Xin, "reflective Optical Fiber displacement Sensor", Proceeding of SPIE, Volume 1572, October, 1991.

3. Uoshihiro Hara, Suguru Motonishi, Koji Yoshida, "A New Micro-cutting Device with High Stiffness and Resolution", Annals of the CIRP, Vol. 39/1/1990.

4. S.R. Patterson and E.B. Magrab, "Design and Testing of a Fast Tool Servo for Diamond Turning", PRECISION ENGINEERING, July 1985 Vol. 7 No.3.

"The Development of a Non-contact Diamond Tool Alignment and Measuring System"

by John Schaefer, Steve Kaiser, and Tom Carrington

Texas Instruments, Inc.
Dallas, Texas

Introduction

Cost effective fabrication of diamond point turned components requires efficient, accurate positioning of the tool to the spindle axis of rotation to better than 40 microinches both the X-axis and tool height directions. Characterization of the tool edge waviness to less than 4 microinches also required to reduce surface profile errors and the actual tool edge radius must be known to better than 200 microinches to turn accurate aspheric base radii. Most conventional tool centering methods rely on LVDT contact probe methods. Although contact methods are quite effective with zero rake angle tools with zero set-up rotation, their effectiveness becomes limited in a production environment where multiple variations of aspheric crystalline lenses are machined for infrared applications. Contact probe methods have a particularly difficult time accurately determining the cutting edge height of negative rake angle tools and they loose accuracy in the X-axis direction on rotated tools due to the tilted cylindrical clearance. There is also a high risk of chipping the diamond tool cutting edge when using contact probing. A method that avoids the pitfalls of contact probing for diamond tool centering is a vision based, non-contact Diamond Tool Alignment and Measuring System (DTAMS). All three production diamond point turning lathes at Texas Instruments, two Rank-Pneumo MSG325 and one Moore M18-AG, are using DTAMS for tool centering. The Moore M18-AG version includes a tool normalization routine for positioning the tool to the B-axis center of rotation.

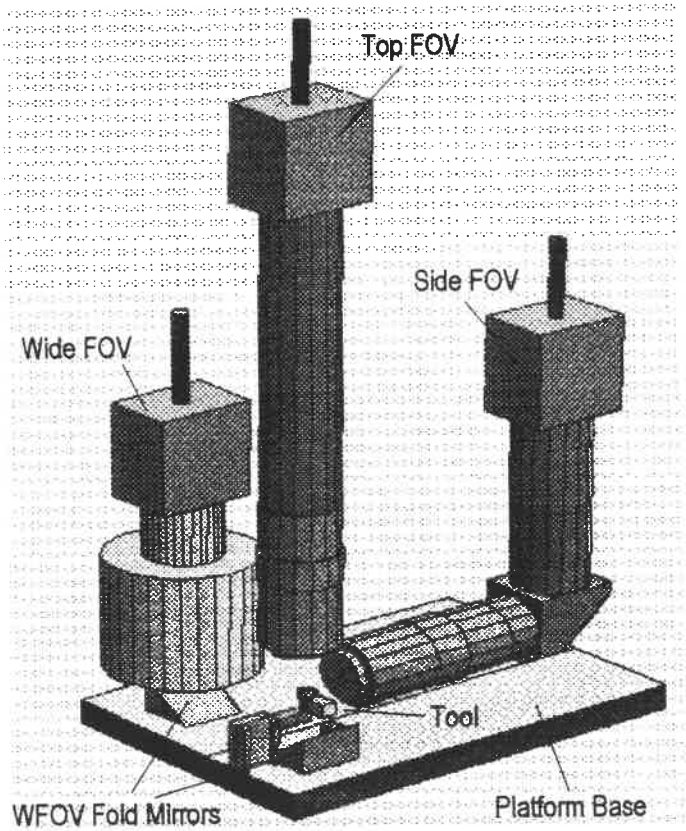

Fig. 1 DTAMS Camera/Objective Layout

System Configuration

DTAMS is a PC based controller that incorporates machine vision, digital input/output, and temperature monitoring to identify diamond tools and calibrate their location. The PC based vision system collects measurements of a tool using three different remote head cameras. The camera and optics assembly are mounted on a specially constructed platform that is fixed to the spindle housing of the diamond turning lathe. A standard CCD camera lens and two microscope objectives are used on the cameras to image the

tool. Each camera has its own light source to provide proper illumination of the tool tip. Thermal probes are mounted on the spindle head and key structural members of the platform to collect temperature profile data. The PC accesses the lathe controls and monitors the optical platform through special interface cards. DTAMS takes control of the movement of the diamond tool through a unique method of emulating the jog box of the Allen Bradley 8200 controller. The software instructs the operator through the tool centering procedure and regains control of the jog box once DTAMS completes the tool centering procedure.

System Operation

The DTAMS PC has its own custom designed program to control the lathe and interact with the operator. An interactive system of menus and graphics screens guides the operator through each step of the tool measurement and alignment operation. The operator positions the diamond tool in the field of the first camera of the optics platform. The DTAMS machine vision camera locates the tool in a 0.4 inch field of view (FOV) and asks the operator to verify the identification of the tool. The computer positions the tool in the center of the camera's FOV and the operator makes a course adjustment to the tool height using graphic feedback from the vision system. The computer then moves the tool to the next camera that uses a microscope objective to image the tool. This camera has 0.005 inch FOV and looks at the top of the tool. At this point, DTAMS collects and archives tool radius, waviness and tip location information. Next the computer switches to the 3rd camera that is mounted perpendicular to the Top FOV camera. The Side camera also has 0.005 inch FOV but it looks at the profile of the tool tip. The tool clearance angle is measured and the computer graphics instruct the operator to adjust the tool tip to the calibrated tool height position. Using axis position information entered by the operator the computer then calculates the distance from the tool tip to the spindle center. The computer then removes the tool from the optics enclosure, displays the tool measurements and distance to the spindle center. The tool is now centered within 40 microinches and the calculated tool radius is used to generate an accurate asphere CNC program.

Thermal Issues

The initial calibration procedure establishes the distance from camera boresight to spindle centerline to less than 40 microinches at a specific temperature. To maintain this specification over time and temperature changes, the optical platform is constructed of 410 stainless steel which closely matches the thermal expansion coefficient of the cast iron spindle housing of the DPT lathe. Given that the temperature gradient within the lathe enclosure can vary by as much as 0.5 deg F, a dynamic temperature compensation system was incorporated into DTAMS. Three surface, and one ambient temperature probes, capable of resolving .001 deg F, record the temperature delta from the calibration temperature. Expansion movement of the optical platform and boresight is given by the following equations;

$$\Delta X = L_x * a' * \Delta T$$
$$\Delta Z = L_y * a' * \Delta T$$

The computer then calculates the dimensional changes of the optics platform due to the temperature delta, calculates the required offset value from the thermal expansion growth equations, and offsets the boresight distance displayed to the operator.

Mechanical Issues

Since DTAMS is mounted to the spindle housing that moves on the axis perpendicular to the spindle centerline, special consideration was given to the dynamic characteristics of the platform. Damping and natural frequencies were estimated to avoid potential interaction during motion and to minimize settling time. Stiffeners were added in the direction of motion to minimize settling time and reduce harmonic vibrations. Mounting to the spindle was facilitated by tapped holes already present at suitable locations. The basic attachment was through four bolts arranged in a rectangular pattern. An additional mounting point was added near the top of the platform to increase stiffness in the direction of motion.

The mounting location is critical to allow the Top and Side FOV's to focus simultaneously on a calibrated tool. The overall placement of the platform was adjusted to the required .006 inches during initial installation. The lighting system employed required less than .002 inches offset between the two cameras at final positioning in order to maintain an acceptable lighting level with minimal edge shadowing. Therefore, the optical systems on the platform were designed to be adjustable within a range to meet the required .002 inches camera-to-camera boresight.

Design Features

DTAMS was designed using off-the-shelf equipment whenever possible to allow easy repair and replacement of components. A 386DX computer is used as the DTAMS controller. A PC vision card along with custom designed hardware and software interacts with the Allen Bradley controller using optically isolated interfaces. Interlocks are tied into the Allen Bradley system to allow standard or emergency stopping of the controller. The optical platform is totally enclosed and is maintained at a positive pressure to help keep the optics from being contaminated during the cutting operations. Special impact switches are mounted inside the enclosure to monitor if the platform has been accidentally bumped hard enough to shift its calibrated position. The main custom electrical component of the system was an electrical interface board designed to plug into the back of the Allen Bradley control panel so the computer could control each axis of the lathe. Even though the PC to Allen Bradley control system is open loop, extensive testing has shown 100% reliability in the motion controller circuits. The use of optically isolated interfaces ensures that the PC and Allen Bradley controller do not damage each other during operations. The DTAMS interface is also designed to allow upgrade work and limited testing of the hardware without interfering with normal operation of the lathe controller.

Software Menu System

The DTAMS menu system is a multilevel, custom software package created in the C language. The primary components of the program are the Tool Input Menu (Fig. 2) and Results Screen (Fig. 3). The remaining components include the execution, utilities, and hardware diagnostic modules. The execution module includes initial calibration, tool alignment, radius and temperature collection routines. Utility functions include a live video mode and a screen capture mode. Within the hardware diagnostics module there are vision, computer, temperature, digital I/O and motion control software diagnostic routines. All data collected during these software routines is automatically archived into data files.

Fig 2. DTAMS Input Menu

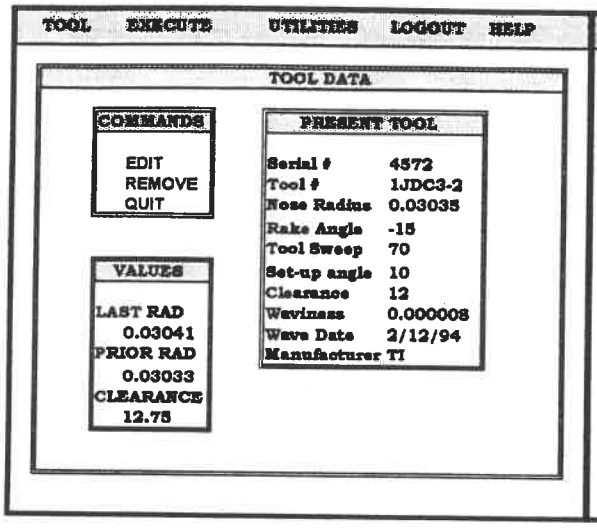

Fig 3. DTAMS Output Menu

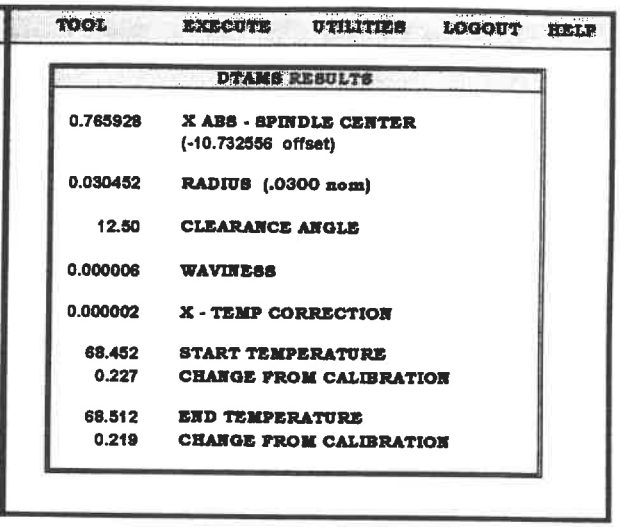

System Resolution

The machine vision system uses a PC based vision board made by Matrox Corp. This board is connected to 3 cameras to image the tool from different angles and varying resolutions. The vision board captures images at a resolution of 512x480 pixels. The cameras are remote head units built by Pulnix Corp. The CCD imager has a 768x492 pixel array mounted in a small (1.6 x 1.2 x 1.4 inch) head that allowed us to keep the size of the enclosure smaller and removed most of the heat generating components from the enclosure to prevent temperature problems. The coarse vision resolution for the large FOV camera is about 700 microinches/pixel. The other 2 cameras use microscope objectives with special C-mount adapters to give a top and side image of the tool tip at a coarse resolution of 10 microinches/pixel. All images are captured and analyzed at 256 gray scales. Software developed allows gray scale edge detection to sub-pixel accuracy. This in addition to the positioning resolution of 0.4 microinch for each lathe axis has allowed detection of the tool tip in the X-axis direction to within 5 microinches.

Conclusion

A vision based tool setting system has been developed and implemented onto two Rank-Pneumo MSG325 and one Moore M18-AG production lathes. The accuracy and repeatability of DTAMS has eliminated the non-value added operation of cutting center plugs and best fit radii to verify centering, tool height, and radius. Total tool change out time is less than 10 minutes. With DTAMS, the operator is able to make more accurate programs and more informed process decisions because of the precise tool radius, waviness, and clearance angle information provided. Future work includes utilizing the tool waviness mapping capability to offset the CNC programs to remove residual form errors and using the PC to archive and analyze tool life information as related to on-machine tool force measurement data.

Evaluation and Application of Precision Contour Grinding for a RBSiC Off-Axis Spherical Mirror

W.K. Kahl
Oak Ridge National Laboratory
Oak Ridge, Tennessee 37831-8039 *

Introduction

Reaction-bonded silicon carbide (RBSiC) offers very stiff and lightweight opportunities for aerospace mirror designs. However, the optical figuring of the front surface to general aspheric shape presents problems to conventional superabrasive grinding and single point diamond turning. This difficulty arises largely due to the hard, brittle nature of this ceramic and is complicated by it's multi-phase composition (SiC in a matrix of silicon). Vapor-deposited silicon or SiC claddings are often applied to provide a more machinable, reflective surface; but ideally the uncoated substrate would be finishable to polish quality [1-3]. Previous work on optimized grinding of silicon-infiltrated SiC has addressed conditions of production surface grinding for high removal rate and improved strength [4]. This paper describes a cooperative effort with United Technologies Optical Systems to utilize ductile regime grinding to generate a 200mm by 72mm rectangular off-axis mirror manufactured from bare RBSiC.

Test Equipment and Procedures

This effort consisted of a statistically-designed study which focused on machining parameters such as feedrate, depth of cut, grinding wheel velocity, and abrasive wheel grit size and bond type. Test specimens were 40mm diameter flat coupons of as-ground RBSiC. Grinding coolant was a water/oil emulsion. The results of the individual tests were measured as surface roughness values obtained from a Chapman laser profilometer (50μm filter). The specimen testing and the contour grinding of the rectangular off-axis mirror were conducted on a Moore M-3 platform retrofitted with a two-axis PC-based controller and servomotors. The figure was a best-fit sphere. The mirror was ground in sequentially finer steps from an as-cast condition and final finishing passes were performed.

Designed Experiment for RBSiC Grindability

In order to properly assess the influence of known critical machining parameters upon the material response, a statistically-designed experiment was formed and executed. The experiment consisted of sixteen unique combination runs which spanned four variables and multiple levels within those variables. Additionally, four test replicates were included. Table 1 contains details of the experiment. The tests were conducted in two randomized blocks of ten runs. The design was constructed to reveal the linear effects of the considered variables and to measure two-way interactions among factors.

Specimens were prepared uniformly using a 30 μm grit metal bond wheel. Preparation of each specimen surface was performed using 5 μm depth of cut per pass and 0.254 cm/min feedrate. The intent was to machine away (in a low damage-inducing mode) the residual subsurface damage from rough sawing of samples. In general, approximately 25.4 μm of material were removed prior to the test run.

Keywords: Ductile Grinding, Silicon carbide, Off-axis mirrors

** Research sponsored by the Ballistic Missile Defense Organization under Interagency Agreement No. 1855-1562-A1 under Martin Marietta Energy Systems, Inc. contract DE-AC05-84OR21400 with the U.S. Department of Energy.*

Table 1. Experimental Factors and Levels for RBSiC Grinding

Factor	Type	No. of Levels	Levels
Wheel bond	Qualitative	2	Metal, Resin
Wheel grit size	Quantitative	2	9, 30 μm
Cross feedrate	Quantitative	2	0.0508, 0.254 cm/min
Contact velocity	Quantitative	2	1067 , 1524 m/min
Depth of cut	Quantitative	2	0.250 , 2.5018 μm

Results

Statistical analyses of the data concluded that the RMS and P-V surface roughness could be minimized by using a resin bond wheel with 9 μm grit size and a slow surface velocity at contact. There appeared to be a significant interaction between feedrate and depth of cut. Succinctly, when using a lower feedrate, a deeper cut is better. However, when using a higher feedrate, a more shallow depth of cut is better. Hence, the following two combinations appear to yield the best results:

Combination Number	Wheel Bond Type	Grit Size (μm)	Feed Rate (cm/min)	Surface Velocity (m/min)	Depth of Cut (μm)
1	Resin	9	0.254	1067	0.250
2	Resin	9	0.0508	1067	2.5018

It should be noted that neither of the two combinations were explicitly performed in the experiment; but because a statistical design was utilized, results could be predicted for the above combinations. Predicted results for these two selected combinations are given in Table 2. Error bounds are for 95% confidence.

One test run out of the twenty was identified as a statistical outlier and was discarded.

Table 2. Results of Statistical Evaluation of Data

Selected Operating Conditions					*RMS Finish (Å)*			
Wheel bond type	Grit size (μm)	Feed rate (cm/min)	Surface velocity (m/min)	Depth of cut (μm)	Predicted process avg.	Error Bounds for proc. avg.	Error Bounds for indiv. runs	R^2
Resin	9	0.254	1067	0.250	257	± 42	± 75	0.84
Resin	9	0.0508	1067	2.5018	266	± 41	± 75	0.84

One principal result of the study was the application of the knowledge of grinding factors and their influence upon the figure of merit in this material (i.e. surface finish) towards the fabrication of a challenging prototype aerospace mirror. The shape of the demonstration mirror was a 200mm x 72mm rectangular mirror placed 68.5 mm off-axis (Fig.1). The figure of the mirror was a 600mm radius of curvature sphere. The mirror was constructed using lightweighting technology which introduced a closed-cell backstructure with a thick facesheet for the mirror surface. The mirror blank was received as-cast and required preliminary machining. A special fixture was employed in machining that mounted the mirror off-axis from the rotational center and tilted forward. This demonstration mirror was machined using the recommended parameters from the analysis.

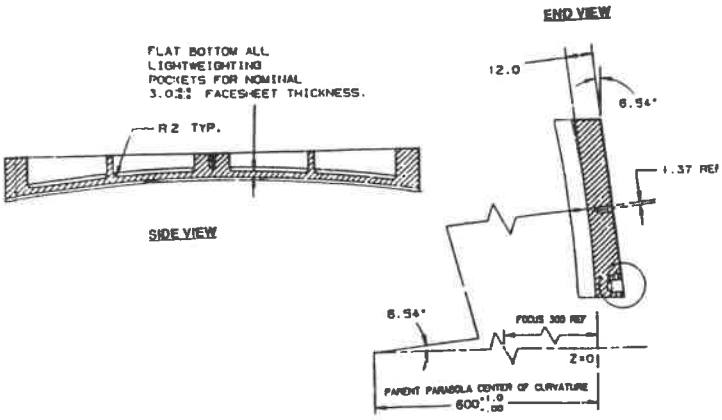

Figure 1. Schematic of off-axis mirror design

Machining results for this figured mirror were encouraging. The surface finish was measured at 257 Å RMS using a laser profilometer and 0.050mm filter at 20x . The mirror figure was sufficiently poor to defeat optical interferometry efforts at quantifying the errors. Qualitatively, the mirror exhibited concentric bands of varying accuracy which had the overall effect of degrading the figure beyond acceptable limits for use beyond the visible waveband. These were assessed to be inherent problems in the machining platform's stiffness and control.

A photograph (Fig.2) reveals the reflectivity of the mirror that was deemed significant for this bare material.

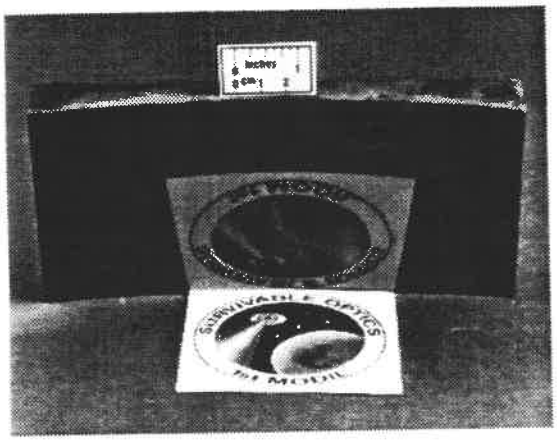

Figure 2. Photograph of as-ground RBSiC off-axis sphere

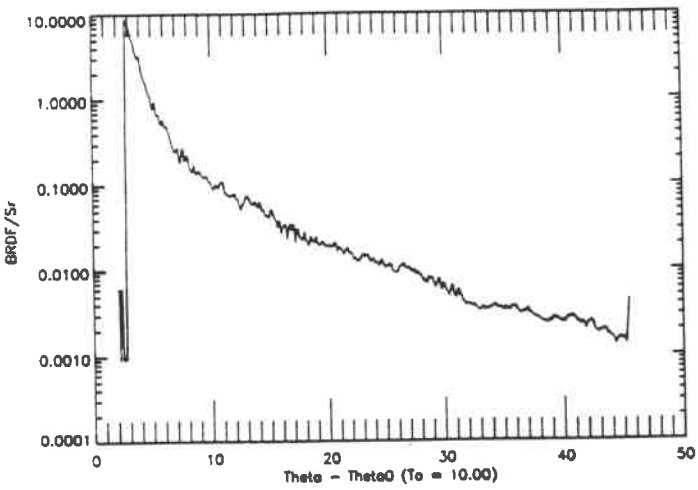

Figure 3. BRDF Plot for 200mm x 72mm mirror

Figure 3 provides a measure of the optical scatter which was measured off of the 200mm x 72mm mirror. The wavelength was 0.833nm and the incident beam was tracked tangentially to the grinding path. There are clearly mid- to high-spatial frequency features on the part which induce scattering that adversely affect the scatter. Values for the measured bireflectional distribution function (BRDF) are presented in Table 3.

Table 3. 200mm x 72mm mirror BRDF values (tangential) as function of angle

	Angle			
	5°	10°	25°	45°
BRDF	1.62	1.45E-01	1.94E-02	3.11E-03

For comparison, two 40mm diameter specimens of RBSiC were lapped for approximately 4 hours using 3 μm diamond grit on a Lapmaster 12C. The resulting surface finish was ~175 Å RMS using the Chapman settings. In practice, the surface finish limits on this material appear to be driven by differential removal rates in the separate phases of Si and SiC [1]. Additionally, it has been noted that the relief which emerges between phases illustrates the effects of material grain sizes (on roughness) which are employed in the sintering of this material. Grain size distributions are approximately 50% in the 25-40 μm range and 50% in the 1-10μm range. Aggregation of smaller grains around larger ones during sintering is observed. Porosity also accounts for some measure of the intergranular crack propagation in grinding, which contributes to poor finish.

Summary

Previous work in SiC polishing has concluded that the limit to optical performance of a SiC-based system is not figure control, but rather is surface quality. This experiment sought to determine optimal grinding conditions for achieving best surface quality in bare two-phase reaction-bonded silicon carbide. The predicted machining parameters were consistent with expectations which drive ductile removal in brittle materials through reduced scale of machining. A demonstration mirror was precision contour ground to a best-fit sphere using process knowledge gained in the statistically-designed experiment. The results suggest that there material limits to surface quality which might best be overcome with post-polishing.

Acknowledgement

The author expresses his gratitude to T.L. Marlar for his patience and efforts in executing the rigorous testing requirements and ensuring the integrity of the results through his diligence.

References

[1] Kahl, W.K., "Ductile Grinding of Silicon Carbide as a Production Method for Reflective Optics", SPIE Vol. 1994-05 Advanced Optical Manufacturing and Testing, 15-16 July 1993, pp. 31-38.

[2] Johnson, S., "SiC Coatings on RBSiC Mirrors for Ultra-Smooth Surfaces", SPIE Vol. 2018 Passive Materials for Optical Elements II, July 1993, pp. 237-247.

[3] Bender, J.W. and Ewing, D.G., "Manufacture and Testing of Lightweight Silicon Carbide Mirrors", SPIE Vol. 2018 Passive Materials for Optical Elements II, July 1993, pp. 248-254.

[4] König, W. and Wemhöner,J., "Optimizing Grinding of SiSiC", Ceramic Bulletin, Vol. 48, No. 3, 1989, pp.545-548.

Design Strategies of an Ultraprecision Surface Grinding Machine for Ductile Mode Surface Finishing of Brittle Materials

M. Daito*, A. Kanai** and M. Miyashita**
*Nissin Machine Works, Co., Ltd., Aritamanishi-machi 300, Hamamatsu, Shizuoka 431-31, Japan
**Ashikaga Institute of Technology, 268 Omae, Ashikaga, Tochigi 326 ,Japan

1. Introduction

Ductile mode grinding (DMG) process, which can provide geometrical accuracy of the order of 100 nm without cracks on the surface, is highly expected as a next stage machining process of brittle materials such as in semiconductor or memory disk industry. It is indispensable to develop an ultraprecision grinding machine which has high motion accuracy and high stiffness in order to industrially apply DMG process. Two type of grinding machine has been designed and built. A vertical type ultraprecision grinder (VPG) equipped with a diamond cup wheel [1] and a recently developed horizontal type ultraprecision grinder (HPG) in which workpieces are chucked on rotary work spindle and ground with the outer periphery of straight diamond wheel. Grinding layout on VPG and HPG is shown in Fig. 1. The present paper deals with the HPG for DMG of brittle materials based on the improved design concept derived from research work on the VPG.

VPG has several disadvantages compared to the HPG. For example,

(1) to obtain parallelism between working surface of cup wheel and rotary table chucked with silicon wafer; so called face-to-face contact is difficult to achieve,

(2) a distortion of wheel takes place due to Abbe's offset between wheel axis and grinding load,

(3) the accuracy of motion copying is degraded due to increase in heavy grinding load by face to face contact.

In case of the HPG, on the other hand, this offset is very small. The contact between working surface of the wheel and workpiece is simple line contact and promises less grinding load.

2. Design basis of HPG

The other design features of the HPG are;

(1) T shaped layout of work slide, equipped with work head and truer, and wheel slide both supported on plain bearing guideways with double vee configuration which can minimize offset between a drive point and guideway and yield high stiffness and damping in feed direction,

(2) to overcome the problems of positioning resolution, a positioning system based on the principle of differential force actuator[2],

(3) coupled with a linear scale with 10 nm resolution as feedback sensor, and

(4) low thermal expansion material for principal machine components to reduce thermal deformation.

The drive point of the slide is located at the center of double vee guideways as shown in Fig. 3. Hydrostatic pad can give adjustable preload on plain guideway lubricated by VG68 oil. X and Z slides weigh 600 and 310 kg respectively. Output sensitivity of NC is 122 mV/μm and positioning force actuator can yield maximum thrust force gain of nearly 5 kN'/μm under the power supply of 3 MPa. Fig. 4 shows a record chart how the wheel slide moves when command signals of 50 nm/step × 20 are given each every 5 seconds to forward and backward directions. Slide moves at both points in accordance with every command single without lost motion even at the reversing point of feed direction. Yawing of wheel slide there is less than 50 nm/300 mm. Detailed chart shows response of slide to the stepwise command of 10 nm/step. Slide makes displacement of some 10 nm/step equal to one feedback pulse of the scale.

Fig. 5 shows (a) generator profile and (b) thrust run-out at two points 21 and 74 mm from the center of self ground surface of vacuum chuck, alumina, 150 mm OD. SD800M diamond wheel is used after truing and dressing / GC slurry operations. Profile error is 0.1 to 0.2 μm and run-out is 0.05 to 0.1 μm. It must be

noted that these errors indicated on the record chart include all the error sources such as motion accuracy of each machine element, truing and dressing accuracy of diamond wheel, surface texture of finished wheel, and environmental disturbance of vibration and temperature.
Fig. 6 shows an example of generator profile and radial run-out of SD3000B diamond wheel trued for traverse grinding. Wheels can be trued to any profile by interpolation control of X and Z axis.

3. Grinding experiments.
Silicon wafers (as etched surface, 150 mm diameter) are ground with a vitrified diamond wheel SD3000V, and stock removal 2~4 μm, traverse rate 60 mm/min. Typical geometrical accuracy, 3D image (interval 0.1 μm) and local thickness variation (LTV) for 15 × 15 mm cells is shown in Fig. 7. Flatness and LTV is near 0.2 and 0.1 μm except edge. Surface roughness 10 nm RMS. Subsurface damage measured by Scanning Infrared Depolarization is 1 to 1.5 μm. Though it is possible to provide a small quantity of sample wafers by DMG process, enormous volume of research work, especially that concerned with diamond wheel itself, truing and dressing technology is required to apply DMG to the industry. 3D surface images, Fig. 8. shows one of these problems, that is different surface texture of the workpiece at the enter (a). Cutting grooves are observed at a point of half radius of the workpiece (b). Irregularity in (a) is caused by the variation of grit height, because every higher grits pass through the center. Fig. 9. shows Nomarski micrograph and 3D roughness image of turned silicon wafer. Groove geometry is different from geometrical locus of diamond tool, nose radius of 50 mm and feed of 35 μm per revolution. No subsurface damage is found by X ray topograph inspection on some wafers turned by a new diamond tool.
Metal bond wheel is preferable for DMG because the stiffness to hold grains is higher compared with resin or vitrified bond. Electrolytic dressing which gives no damage to the grain or cutting edge can applied in this case. Fig. 10. shows an example of DMG of carbon ceramics using SD12000M wheel after slight electrolytic dressing. The feature of roughness is small Rsk value, and this means good cutting ability of dressed wheel.

4. Conclusions
From a series of experiments achieved performances are summarized as follows;
(1) Linear movement of both wheel and work slide is controlled in 10 nm/step with no lost motion
(2) Thrust run-out of self trued work spindle surface is less than 100 nm and radial run-out of self-trued diamond wheel is less than 200 nm.
(3) Flatness of wafer on the chuck less than 200 nm, LTV (local thickness variation) for 15 × 15 mm cells around 100 nm, and crack free surface are achieved for 150 nm silicon wafer ground with 3000 grit wheels .

Keywords : ductile mode grinding, ultraprecision grinding machine, straight diamond wheel, silicon wafer
References
1. Abe, K., Yasunaga, N., Miyashita, M.,Yoshioka, J., Daito, M., Proc. 7th IPES, 53(1993)
2. Kanai, A., Sano, H., Yoshioka, J., Miyashita, M., Nanotecnology No.2, 43(1991)

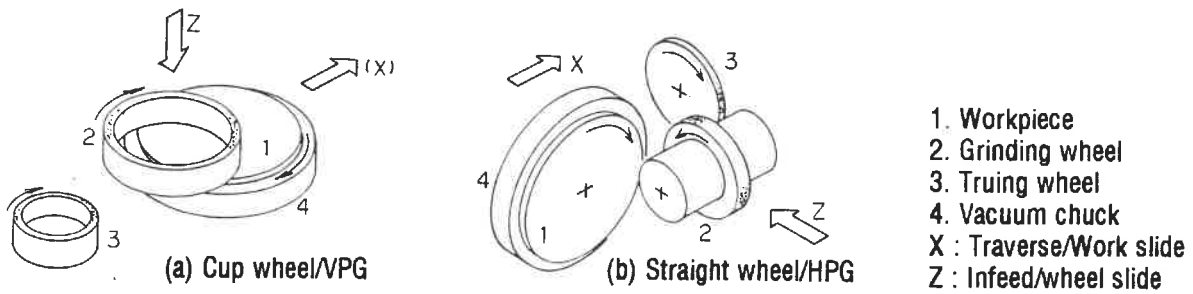

Fig. 1. Grinding layout

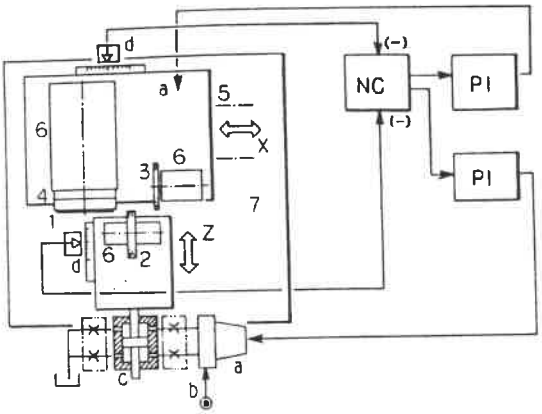

Fig. 2. Design concept of HPG
1. Workpiece
2. Grinding wheel ; ø175 × (40)
3. Truing wheel ; ø175 × (2)
4. chuck ; ø200 max.
5. Double vee plain bearing guideways
6. Spindles/hydrostatic oil bearings
7. Low thermal expansion material

NC: Numerical controller
PI: PI controller
a. Hydraulic power
b. Hydraulic actuator
c. Laser scale, resolution;1nm

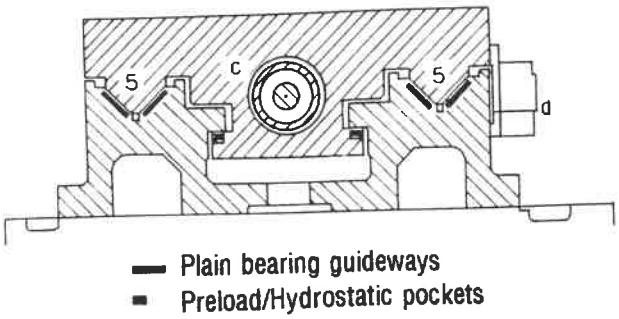

Fig. 3 Structure of work slide

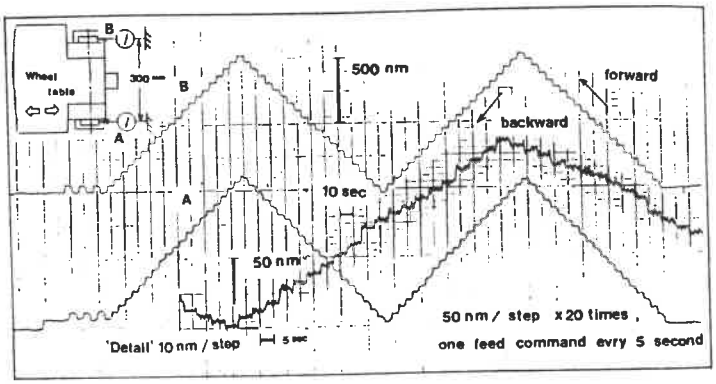

Fig. 4 Linear movement of wheel slide
(command signal ; 50 nm/step, 10 nm/step x 20 times)

(a) generator profile

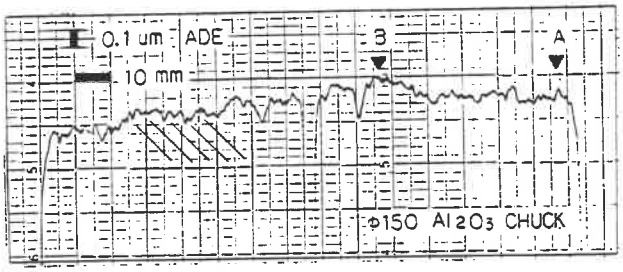

(b) thrust run-out

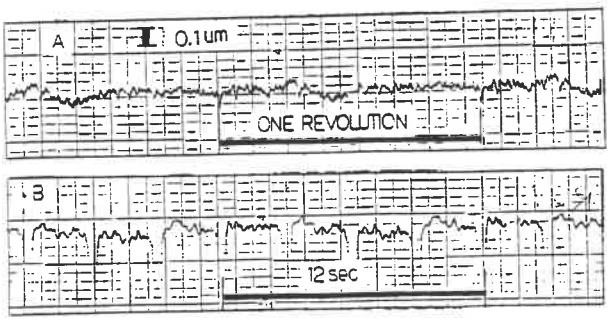

Fig. 5 Self ground vacuum chuck surface
grinding wheel ; SD800M
material ; Alumina, ϕ150

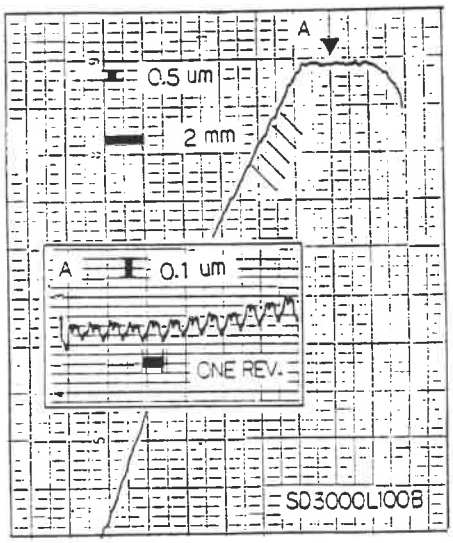

Fig. 6 Accuracy of trued diamond wheel
wheel ; SD3000L100B, ϕ175 x 20
truer ; SD200B

(a) 3D surface image / Flatness
(interval ; 0.1 μm)

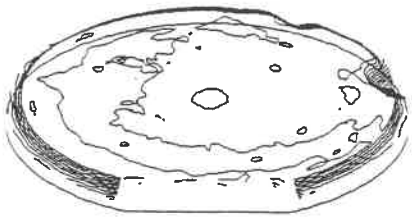

(b) Local Thickness Variation
for 15 x 15 mm cell

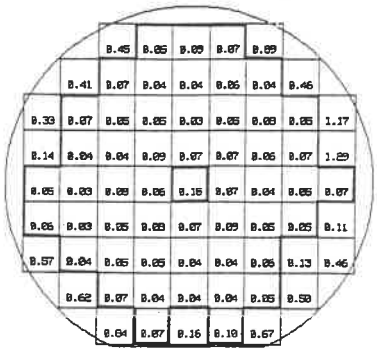

Fig. 7 Geometrical accuracy of ground Si wafer
grinding wheel ; SD3000V
stock removal ; 2-4 μm
feed ; 60 mm/min.

(a) micrograph

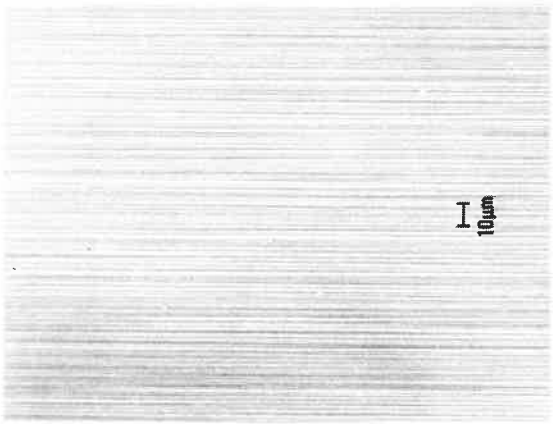

(b) Talysurf record
Ra 3.8 nm, Rsk -0.54

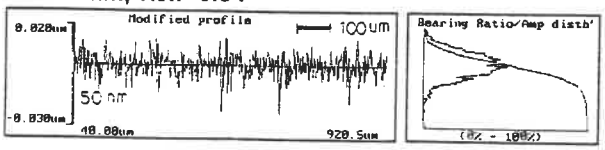

Fig. 10 Nomarski micrograph
and Talysurf record of ground carbon ceramics wheel ; SD12000(0/2)M
truer ; SD200M, dress ; electrolytic dressing

(a) center, Ra 13.3 nm

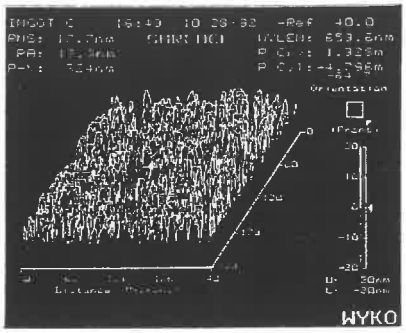

(b) R/2 position, Ra 9.40 nm

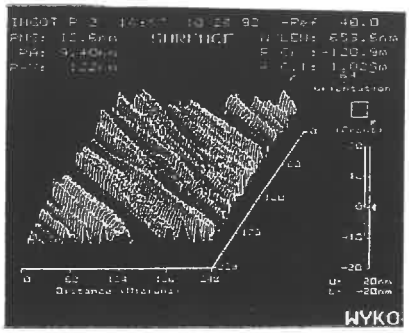

Fig. 8 3D roughness image of ground Si wafer
(measuring area ; 240 x 240 mm)

(a) Nomarski micrograph

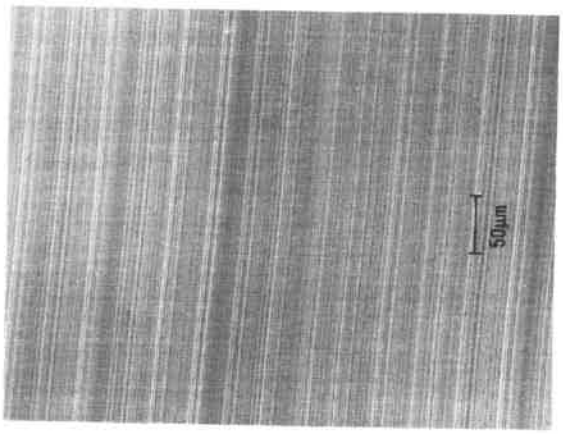

(b) 3D roughness image
measured area : 240x 240 mm
Ra 2.33 nm

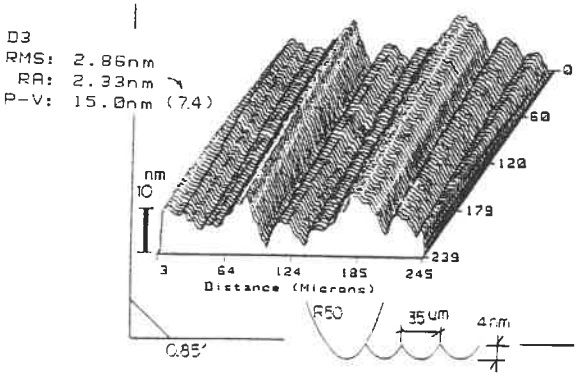

Fig. 9 Nomarski micrograph
and 3D roughness image of turned Si wafer
nose radius of diamond tool ; 50 mm
feed ; 35 μm/rev
depth of cut ; 2 μm

MECHANICS AND MATERIALS ISSUES IN OPTICS MANUFACTURING

J. C. Lambropoulos, P. D. Funkenbusch, D. J. Quesnel, S. M. Gracewski, and R. F. Gans

Department of Mechanical Engineering & Center for Optics Manufacturing (COM)

University of Rochester, Rochester, NY 14627

ABSTRACT: We summarize the recent work of faculty and students in the Mechanical Engineering Department on some mechanics and materials issues concerning the deterministic microgrinding of optical glasses and crystals using bound abrasive grinding tools in the Center for Optics Manufacturing at the University of Rochester. Deterministic microgrinding of spherical surfaces has been shown to lead to surface roughness better than 20 nm, and subsurface damage less than 2 μm.

Further details of the various projects described in this summary can be found in the monthly proceedings of the Manufacturing Sciences Group at the Center for Optics Manufacturing at the University of Rochester.

I. STRUCTURE/COMPONENT LEVEL

At the structure/component level (where relevant length scales are in the range from 1 mm to 1 m) we have used numerical techniques to examine the static and dynamic response of components and systems used in deterministic microgrinding.

I.1 *RING TOOLS*: Our numerical analyses of ring tools used in deterministic microgrinding, based on commercially available finite element and graphics pre- and post-processor software, show that for optimizing the structural response of a tool both axial (i.e. longitudinal) and bending (i.e. transverse) stiffness must be optimized, and that localized forces, arising, for example, from contact between abrasive particles and the work surface lead to higher structural deflections than distributed loads. Another manifestation of the enhanced bending type of tool elastic deformation is the fact that the lowest normal modes correspond to bending oscillations.

In order to facilitate and expedite the preliminary design of ring tools used in deterministic microgrinding, we have developed approximate analytical expressions that describe the stiffness of the ring and stem portions of the tool. Such analytical expressions, which can be implemented on a desk-top computer or a usual spreadsheet, are based on the description of the ring as an elastic shell, and of the stem as an elastic beam. This approach may be used in quickly estimating the stiffness of tools whose dimensions are required to be much smaller or larger than the tools currently used.

For uniformly applied grinding loads (expressed as a uniform force per unit arc length along the line of contact between the tool and the workpiece) on the rim of the ring tool, the estimated stiffness depends strongly on the dimensionless length ratios T_{ring}/R_{ring}, and $H_{ring}/\sqrt{(T_{ring}\, R_{ring})}$, with T denoting the thickness, H the height, and R the radius of the ring, on the elastic properties of the ring, and, less sensitively, on whether cutting occurs along the inner (producing convex surfaces) or outer surface of the ring. Due to the bending deformation of the ring, the elastic stiffness is quite sensitive on the thickness of the ring. For example, the radial stiffness per unit of contact arc length can be enhanced by a factor of 100, and the axial stiffness by a factor of about 5 as the ring thickness increases from 0.25 to 2 mm.

I.2 *SYSTEMS*: In addition to the structural analysis of individual components used in deterministic microgrinding facilities, we have performed extensive finite element analyses at the system level. Such analyses include the tool and tool spindle, and the axes describing the motion of the spindle in several directions. The objective of such work has been to understand the detailed dynamics of the grinding facility at the system level, and to improve on future designs by identifying and improving components of reduced stiffness.

I.3 *NONLINEAR DYNAMICS*: The dynamic nonlinear structural interaction between the tool and the workpiece is expressed in terms of the grinding force per unit of contact arc length. Such forces must take into account the nonlinear grinding process (either plastic plowing or brittle microcracking). The nonlinear interaction is significant since it couples the structural response of the tool to that of the work. Such structural vibration interactions may cause mid-spatial frequency errors (often referred to as cutter marks).

It is interesting to observe that the nonlinear force of interaction between elastically supported tools and workpieces may lead to chaotic vibrations [Tlusty and Ismail, 1981; Scott, 1989]. Such chaotic patterns have been previously analyzed in terms of simple 2-D elastic oscillators. Recent work in our group has examined in detail a model developed single-point cutting of metals [Grabec, 1987], and shown that an important process parameter is the ratio of work of cutting to the kinetic energy of the tool. For low or high values of this parameter, the tool executes periodic oscillations, whereas for intermediate values the periodicity is lost, resulting in chaotic oscillations.

I.4 *MISALIGNMENTS*: In addition to mid-spatial frequency errors resulting from dynamic interactions, we also have developed geometrical models which account for the misalignment of the tool with respect to the work surface, and how the resulting figure error may be used in estimating the extent of misalignment. Such models can easily be implemented in desk-top computers using software such as MATHCAD.

II. MATERIALS/PROCESS LEVEL

At the materials/process level (length scales in the range from 1 nm to 1 mm) we have measured the mechanical properties of glasses and crystals which are relevant in deterministic microgrinding, the mechanical properties of tools, the effects of mechanical properties and process parameters on the resulting quality of the optical surface, and we have modeled the interaction of ring tools and abrasive grains with optical glasses.

II.1 *NEAR-SURFACE MECHANICAL PROPERTIES OF OPTICAL GLASSES AND CRYSTALS*: We have concentrated on near-surface mechanical properties, rather than bulk properties. We have used microindentation techniques to measure hardness and fracture toughness.

The measurement of the hardness H by Vickers microindentation exhibits three regions describing the dependence on the permanent depth of penetration L_p (or, more traditionally, on indentation diagonal D or applied load P) of the hardness, defined as the applied load divided by the contact area based on the size of the residual impression and assuming similar shapes for the contact area and the indenter profile. At large penetrations (region I), the hardness is constant and independent of L_p. At intermediate depths (region II), the hardness usually increases as the penetration diminishes according to the indentation size effect (ISE), although we have also measured hardness significantly diminishing with diminishing L_p for glasses known to absorb large amounts of water. At very low depths (region III), the glasses and crystals exhibiting the ISE show a hardness that significantly decreases with decreasing L_p. Thus, the overall dependence of the measured hardness on plastic penetration L_p exhibits a maximum.

We have developed a simple model to explain the behavior in region III. This model accounts for the presence of a junction offset in the Vickers indenting diamond. The junction offset has been observed by Atomic Force Microscopy on shallow permanent indentations. AFM has allowed us to completely characterize the profile of the indenting diamond from the residual impressions, and account for the H-L_p relation in region III.

We have extracted the fracture toughness K_c by measuring the surface trace (2c) of cracks emanating from the Vickers microindentation. It is interesting to note that a plot of $Pc^{-3/2}$ vs. c increases at low c, a manifestation of the fact that shallow cracks, which scale as c ~ P, are not similar to radial cracks which scale like $c^{3/2}$ ~ P [Sakai and Bradt, 1993].

Various models from the literature model have been used to extract the fracture toughness K_c from the measured c(P) relationship [For reviews, see McColm, 1990; Cook and Pharr, 1990]. The model by Evans [1979] is especially attractive for such purposes. This model predicts the dimensionless dependence of the fracture toughness $K_c(H/E)^{0.4}/[H\sqrt{(D/2)}]$ on the dimensionless crack size c/(D/2). Evans [1979] used dimensional analysis to correlate K_c and c, and further curve fitting over a range of c/(D/2) from 1.5 to 7 for many ceramic materials to completely determine the relation of K_c and c. Our data typically have c/(D/2) in the range 2.5 to 6, and show that the fracture toughness is essentially independent of the crack size.

To verify the fracture toughness determinations from microindentatioon measurements, we are also performing bulk measurements which require more careful sample preparation.

In addition to experimental measurements, we have performed numerical simulations of indentation in elastic-plastic solids. Such finite element computations show that the load-penetration curve strongly depends on the shape of the indenter, and that for typical optical glass material data, the elastic spring-back at complete load removal is a significant fraction of the total penetration at maximum load. We have simulated indentation using a conical tip with a tip radius of curvature of 1 μm. The computed hardness was essentially independent of the load at which the hardness was determined.

II.2 *MECHANICAL PROPERTIES OF BOUND ABRASIVE TOOLS*: Typical tools consist of abrasive particles (typically diamonds in the size range of 0.5-1 μm to 10-20 μm), a binder, and a metallic matrix. We have modeled the dependence of the elastic moduli and uniaxial yield stress on the diamond volume fraction of such composites.

We have also measured the elastic moduli by using ultrasonic techniques to determine the longitudinal and shear wave speeds, and the hardness by microindentation. These properties scale very roughly with the measured sample density. The measured porosity is a strong function of the type of diamond powder (diamond size and state: single crystal or polycrystalline) used in manufacturing the bound abrasive tools. Thus, different diamonds require different processing conditions. In effect, both the diamond volume fraction and the precise processing conditions are required in order to characterize fully the mechanical properties of bound abrasive tools.

The friability of various diamond powders has been measured by using a milling experiment. The friability, defined as the time constant describing the temporal evolution of the diamond particle size during milling, is a strong function of diamond type and size.

II.3 *THE EFFECT OF FRICTION*: In addition to normal loads, tangential loads, related to normal loads via an apparent coefficient of friction, also develop during microgrinding

We have used elastic contact theory [Johnson, 1985] to examine the effect of the coefficient of friction on the state of stress near a bound abrasive grain embedded within a metallic matrix, and on the surface of glass during grinding: Friction enhances both the normal and shear stresses transmitted across the particle/matrix interface, thus enhancing the tendency of an abrasive grain to be removed from the surrounding matrix. Friction also leads to large tensile stresses in a thin layer near the surface of the glass, as well as to large hydrostatic tension. Such hydrostatic tension enhances the rate of water diffusion [Nogami and Tomozawa, 1984; Tomozawa and Tomozawa, 1989], which, in turn, may be affected by the rate at which the material is removed from the surface. For example, large infeed rates suppress the contribution of diffusion when water diffuses into the glass surface while the glass surface is being removed [Lambropoulos, 1994].

Friction plays an important role in the interaction between a cutting edge and the optical surface during microgrinding with ring tools. Elastic stress distributions have been determined to model such interaction for the cases of sharp, worn, or curved ring tools. Friction leads to significant tensile stresses behind the trailing edge of the ring tool, which are singular for the cases of sharp and worn tools, but bounded for curved tools. The pressure underneath the contact region is also affected by the shape of the contact region. It is singular for the sharp tool, low with high

localized singularities for the worn tool, and high but bounded for the curved tool. Such stress distribution behind the trailing edge, and pressure distribution underneath the contact region, may be related to the formation of subsurface damage and to the tool wear rate, respectively.

II.4 *MECHANICAL MEASURES OF SURFACE QUALITY IN MICROGRINDING*: Following microgrinding, the surface roughness (SR) and subsurface damage (SSD) is measured. Can the measured roughness and damage be correlated with mechanical length scales describing the interaction between a sharp abrasive grain and an elastic-plastic-cracking surface? The interaction leads to the depth a and extent (ma) of elastic-plastic penetration, where m is a factor related to the geometrical shape of the indenting abrasive particle, as well as of the size b of the boundary between the permanently deformed and elastic regions (b>a, ma). The lengths a and b are primarily dictated by the elastic and plastic properties of the material.

The presence of such a boundary is associated with high localized tensile stresses occurring after completely removing the indenting load. Once plastic flow has occurred, the residual tensile stresses scale with the flow stress or hardness H (assumed constant), and lead to the nucleation and growth of subsurface cracks which eventually become radial or lateral cracks with extents dictated primarily by the fracture toughness of the material (Chiang et al, 1982 a-b). Assuming that the elastic spring-back can be ignored during load removal, it is tempting to correlate the surface roughness with the indentation size a, and the extent of the subsurface damage region with the largest of b and c, c being the size of any cracks resulting from the indentation event of the abrasive grain on the optical surface. This correlation is further discussed in another presentation in this conference (Lambropoulos, 1994).

ACKNOWLEDGEMENTS: We acknowledge the support and encouragement of the Manufacturing Sciences Group at the Center for Optics Manufacturing.

REFERENCES

S.S. Chiang, D.B. Marshall, and A.G. Evans, 1982a, The response of solids to elastic/plastic indentation, I. Stresses and residual stresses, J. Appl. Phys. 53, 298-311.

S.S. Chiang, D.B. Marshall, and A.G. Evans, 1982b, The response of solids to elastic/plastic indentation, II. Fracture initiation, J. Appl. Phys. 53, 312-317.

R. F. Cook and G. M. Pharr, 1990, Direct observation and analysis of indentation cracking in glasses and ceramics, J. Am. Ceram. Soc. 73, 787-817.

A.G. Evans, 1979, Fracture toughness: the role of indentation techniques, in *Fracture Mechanics Applied to Brittle Materials*, ASTM STP 678, S.W. Freiman, ed., American Society for Testing and Materials, 112-135.

I. Grabec, 1988, Chaotic dynamics in the cutting process, Int. J. Mach. Tools Manufact. 28, 19-32.

K.L. Johnson, 1985, *Contact Mechanics*, Cambridge University Press.

J.C. Lambropoulos, 1994, Mechanical, thermal, chemical, and geometrical length scales in polishing and grinding, 1994 ASPE Annual meeting, Cincinatti (these proceedings).

I.J. McColm, 1990, *Ceramic Hardness*, Plenum Press, New York.

M. Nogami and M. Tomozawa, 1984, Effect of stress on water diffusion in silica glass, J. Amer. Ceram. Soc. 67, 151-154.

M. Sakai and R.C. Bradt, 1993, Fracture toughness testing of brittle materials, Int. Mat. Rev. 38, 53-78.

P.J. Scott, 1989, Nonlinear dynamic systems in surface metrology, Surface Topography 2, 345-366.

J. Tlusty and F. Ismail, 1981, Basic non-linearity in machining chatter, Annals of the CIRP 30, 299-304.

H. Tomozawa and M. Tomozawa, 1989, Diffusion of water into a borosilicate glass, J. Non-Crystall. Solids 109, 311-317.

EFFECT OF GRINDING ENERGY ON WHEEL SPEED AND SURFACE FINISH

Michele H. Miller, Gene E. Storz, Thomas A. Dow, Ronald O. Scattergood
Precision Engineering Center, North Carolina State University
Raleigh, NC 27695-7918

1 Introduction

In grinding operations, wheel speed has a significant effect on surface finish and chip thickness. For a grinding geometry in which the grinding wheel and workpiece both rotate but at different frequencies, the theoretical surface finish may vary with grinding wheel speed as shown in Figure 1[1].

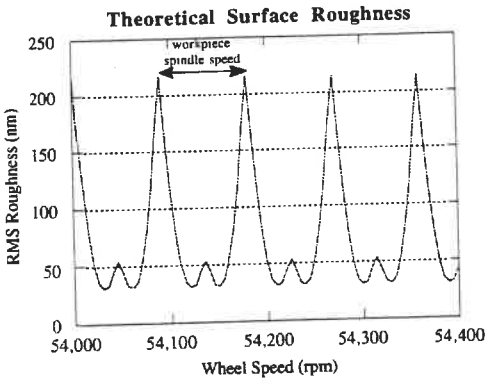

Figure 1: Dependence of theoretical surface finish on wheel speed

Variations in phase between cusps lead to the periodicity in this plot. The local maximums correspond to in-phase cusps, and the period between local maximums is the workpiece rotational frequency ω_{wp}. As this figure shows, small changes in wheel speed can cause large changes in theoretical surface roughness. Likewise, small changes in wheel speed can cause significant changes in chip size and grinding force. Because changes in grinding force can in turn cause changes in wheel speed, an interactive relationship exists between wheel speed and chip size. Predicting wheel speed and ultimately surface finish therefore requires an examination of energy relationships in the grinding process and in motor operation.

2 Equation of Motion for Grinding Spindle

A sum of moments on the grinding spindle produces the following equation of motion:

$$T_{int}(\dot{\theta}) - R_{int}(\dot{\theta}) - R_{ext}(\dot{\theta},\theta) = I_m\ddot{\theta} \qquad (1)$$

$$\ddot{\theta} + \frac{R_{int}(\dot{\theta}) - T_{int}(\dot{\theta})}{I_m} + \frac{R_{ext}(\dot{\theta},\theta)}{I_m} = 0 \qquad (2)$$

where,

T_{int} = torque generated by motor
R_{int} = resistance torques in motor (friction, bearing windage, eddy current loads, etc.)
R_{ext} = grinding load
I_m = moment of inertia of spindle

In general, this equation is non-linear and can be solved numerically. However, for the special case where T_{int} - R_{int}, and R_{ext} are linear functions of $\dot{\theta}$, the differential equation can be solved analytically. Determination of R_{ext} and T_{int} - R_{int} is described below.

Model of Grinding Energy The geometric chip model developed by Storz[1] was extended to predict the energy to remove one chip. Grinding energy as a function of chip thickness was determined from force data collected during plunge grinding experiments[2]. Because the thickness of a contour grinding chip is not constant, the modeled chip was divided into square elements of different thicknesses. After

1 Storz, G. E., "Theoretical Modeling of Contour Grinding," *Master's Thesis*, N. C. State Univ., 1994.

2 Fawcett, S. C., "Development and Implementation of a Grinding Technique for Precision Finishing of Brittle Materials," *PhD Dissertation*, N. C. State Univ., 1991.

the energy of each element was calculated based on its thickness, the elemental energies were summed to yield the energy for removing the entire chip.

The geometric chip model shows that chip volume varies with phase. In the ductile regime, where material deforms plastically, removal energy is approximately proportional to volume. In the brittle regime, however, the energy is related to crack area, and the energy per volume (specific grinding energy, μ) decreases as chip thickness increases. The portion of material removed by brittle fracture affects how much the energy versus phase relationship deviates from the volume versus phase relationship. Figure 2 shows an example of how energy varies with phase.

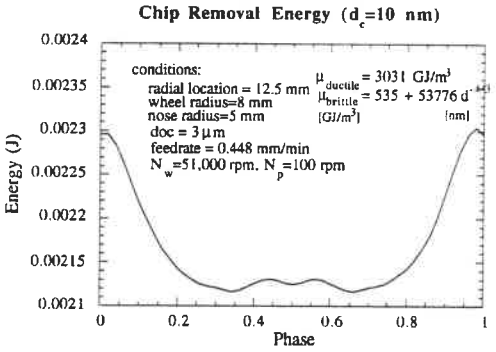

Figure 2: Energy to remove one chip

Similar to surface roughness (Figure 1), chip removal energy is periodic with wheel speed. A phase repeats when grinding wheel frequency is increased or decreased by the workpiece frequency.

Dynamic Model of Grinding Spindle A Westwind D1090 air turbine spindle capable of speeds up to 60,000 rpm was characterized to determine how T_{int}-R_{int} varies with wheel speed ω. The torque applied by the air approximately follows the form:

$$T_{int} = C_1' - C_2'\omega \tag{3}$$

The losses in this type of spindle are primarily due to shearing forces in the air bearings, and therefore follow the form:

$$R_{int} = C_3'\omega \tag{4}$$

Subtracting Equation (4) from (3) yields:

$$T_{int}\text{-}R_{int} = C_1 - C_2\omega \tag{5}$$

The intercept C_1 is the maximum torque capability of the motor. The slope C_2 indicates the sensitivity of the wheel speed to changes in load. When C_2 is small, minor changes in load produce significant changes in wheel speed.

The constants C_1 and C_2 were determined experimentally for three different input air pressures--0.364, 0.271, and 0.129 MPa. With the grinding spindle spinning at its no-load speed, an approximately constant grinding torque was applied. Wheel speed and grinding force were measured simultaneously. The average torque (the cutting force times the radius of the wheel) and the steady-state speed for these tests are plotted in Figure 3.

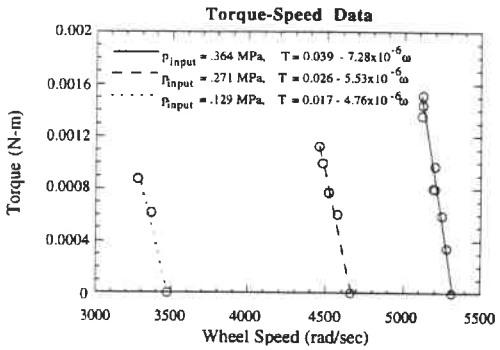

Figure 3 Torque-speed data for air turbine spindle at three different input pressures

3 Theoretical System Response

When T_{int} - R_{int} is linear as in Equation (5), the equation of motion becomes:

$$\ddot{\theta} + \frac{C_2}{I_m}\dot{\theta} + \frac{R_{ext}(\dot{\theta},\theta)}{I_m} - \frac{C_1}{I_m} = 0 \tag{6}$$

When the grinding torque R_{ext} is constant, Equation (6) has a first order exponential solution for θ or ω.

Because chip removal energy varies with phase, grinding loads are not linear with wheel speed. Approximating grinding torque with a sinusoidal function shows how a non-linear but periodic grinding load might affect wheel speed. Figure 4 shows the theoretical time response of a grinding spindle subject to the following grinding loads where A ranges from a to $2a$:

$$\frac{R_g}{I_m} = A\left(1 + 0.25sin\,\frac{2\pi}{\omega_{wp}}\omega\right) \qquad (7)$$

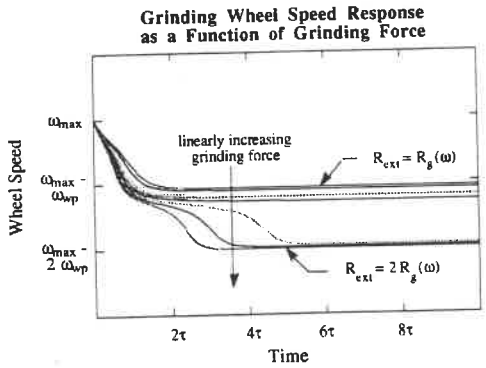

Figure 4: Numerical solutions to nonlinear equation of motion

A linear torque-speed relationship was assumed for the spindle. However, the non-linearity in grinding torque causes a deviation from the exponential first order response. The figure shows that there are loci of possible steady-state speeds. The loci would become narrower as the variation in grinding torque increased or as C_2 decreased.

Equilibrium Speed When the wheel speed reaches a steady-state, the phasing between cusps remains constant. Therefore, predicting steady-state speed is useful for determining phase and theoretical surface roughness. Equilibrium occurs when the moments on the grinding spindle sum to zero.

$$T_{int}(\omega) - R_{int}(\omega) - R_{ext}(\omega) = 0 \qquad (8)$$

From an energy perspective, equilibrium occurs when the system's power is at a minimum or when $dP/d\omega = 0$.

The moments in Equation (8) can be represented as in Figure 5. These curves are based on qualitative representations of T_{int}, R_{int}, and R_{ext}. R_{ext} was defined as Equation (7). Equilibrium occurs where the curves intersect (or where the net torque T_{int} - R_{int} - R_{ext} is zero). This plot shows that when ω is less than ω_{ss}, the net torque is positive which causes the spindle to accelerate. An energy approach yields the same ω_{ss}.

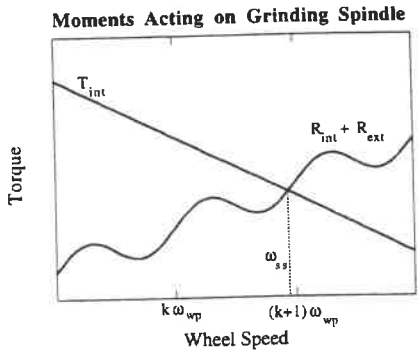

Figure 5: Balance of moments on grinding spindle

Figure 5 helps to explain the behavior in Figure 4 by illustrating how the wheel speeds which correspond to positive slopes on the R_{int}+R_{ext} curve are the most likely intersection points. For this example, the greatest positive slopes occur at multiples of the workpiece rotational frequency ω_{wp}. Note that the steady-state speeds of Figure 4 are also clustered around multiples of ω_{wp}. Figure 5 indicates that wheel speed lock-in (or a narrow locus of possible equilibrium wheel speeds) is most likely when T_{int} has a shallow slope (small C_2) and R_{int}+R_{ext} has large periodic variations.

With a model of grinding energy and motor torque-speed behavior, equilibrium speed can be predicted. Figure 6 shows calculated values of R_{ext} (for a prescribed set of silicon carbide grinding conditions) at three radial workpiece

locations and T_{int}-R_{int} for the air turbine spindle. The intersection of T_{int}-R_{int} and one of the R_{ext} curves predicts the speed ratio for that radial location. Although there is some variability in both the motor and grinding energy models, Figure 6 suggests that ratios with fractional parts between 0.5 and 0.9 are likely because R_{ext} has the largest positive slope at those phases.

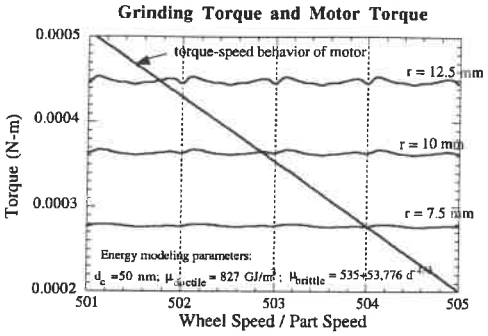

Figure 6: Estimated grinding torque at three radial locations superimposed onto motor torque

4 Experimental Verification

Experiments were conducted to determine what speeds, if any, are preferred during grinding. Figure 7 shows wheel to part speed ratio data taken while grinding under the same conditions used to generate Figure 6. The fractional portion of the speed ratio value is equivalent to *one minus phase*. This figure shows that the speed ratio locks in between 509.8 and 509.9 for several minutes early in the test and then later at 508.6.

Evidence of the constant speed ratio was also seen on the finished surface. Figure 8 shows the surface between $r = 9$ and $r = 11$ mm. The upfeed direction is up while the crossfeed direction is to the right. The phase appears to be about 0.14 or 1/7 (seven crossfeeds must be traversed to arrive at another cusp on the same vertical level). A speed ratio between 509.8 and 509.9 would cause feature phases between 0.1 and 0.2.

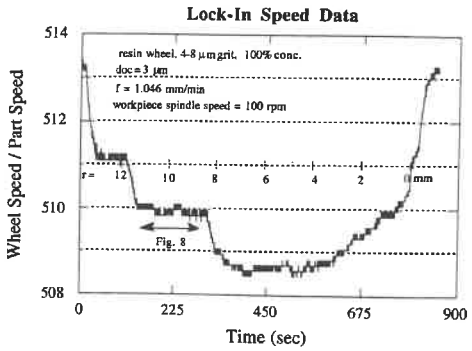

Figure 7: Speed ratio during grinding of SiC

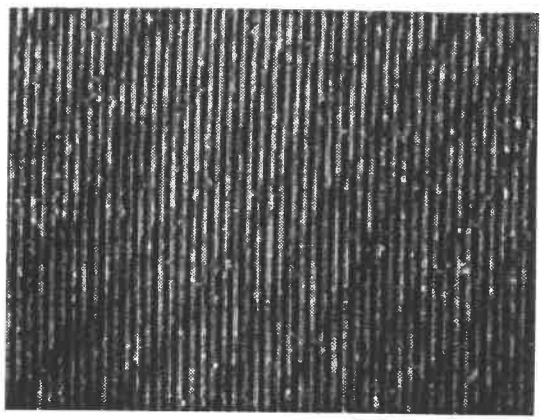

Figure 8 Nomarski micrograph of ground silicon carbide (picture width ≅ 500 μm)

5 Conclusions

The wheel speed lock-in concept, demonstrated and explained above, has some important implications. The variation of roughness with phase means that surface finish is dependent not only on geometric parameters (wheel and nose radius, wheel and part speed, part diameter, feedrate, and depth of cut) but also on specific grinding energy (which depends on work material, chip thickness, and the grinding wheel characteristics).

Effect of Elevated Wheel Surface Speed in the Internal Grinding Process

Kunihiro YASUI*, Ichiro INASAKI* and Minoru HATAKEYAMA**

Faculty of Science and Technology, Department of Mechanical Engineering, KEIO University*
3-14-1 Hiyoshi, Kohoku-ku, Yokohama, 223, JAPAN
and
Okamoto Machine Tool Works, LTD. **

1. Introduction

The increase of using CBN wheels has made the study of high speed grinding a center of interest. The special structure of the wheel, which consists of an abrasive rim and a metal hub, makes it possible to increase the rotational speed of the wheel significantly. Improvements in accuracy as well as productivity are potential advantages of high speed grinding. However, the influence of elevated wheel surface speed on the wheel life has not been investigated in detail so far. Beside, most studies and research has been performed on the cylindrical or surface grinding which uses a wheel with a large diameter.

In this study, therefore, the influence of wheel surface speed on the wheel life in the internal grinding process using a CBN wheel was experimentally investigated for two different cases: constant workpiece speed and constant speed ratio between the wheel and the workpiece.

2. Effect of elevated wheel surface speed

The effect of increasing wheel surface speed on the process can be estimated by introducing the parameter "average cross sectional area of chips a_m" given by the following equation:

$$a_m = \frac{V_w}{CV_s}\sqrt{h\left(\frac{1}{D_s} \pm \frac{1}{D_w}\right)} \qquad (1)$$

+ : Cylindrical grinding
− : Internal grinding
$D_w \to \infty$: Surface grinding

Where, V_w is workpiece speed : V_s is wheel surface speed : h is depth of cut : D_s is wheel diameter : D_w is workpiece diameter : and C is number of cutting edges per unit area of wheel surface.

If only the wheel surface speed is increased, the parameter a_m decreases and thus the grinding force and the surface roughness will decrease. The decrease in grinding force will consequently result in an improvement of the machining accuracy. In contrast, when the workpiece speed is increased in proportion to the increase of the wheel surface speed, the parameter a_m remains constant. Therefore, the grinding force will remain constant and the material removal rate will increase in proportion to the increase in the workpiece speed. High speed grinding provides those opportunities[1].

3. Experimental procedure

Some parts of the internal grinding machine, that is, the spindle and the chuck, were improved for achieving high speed grinding. In this study, the vitrified bonded CBN wheel with diameter of 40mm was used . The wheel surface speed V_s was increased from 45 to 90m/s. Experiments were performed under the conditions shown in Table 1. In the first case, workpiece speed V_w was kept constant at 1.05m/s. In the second case, surface speed ratio between the wheel and the workpiece was kept constant, therefore, workpiece speed V_w was changed in proportion to V_s.

Figure 1 shows the schematic illustration of the procedure. In the first place, dressing was carried out with a column shaped diamond dresser, the cross section of which was 0.2mm ×0.2mm. During the grinding process, the grinding power was monitored so that the tangential grinding force can be obtained. After grinding, the surface roughness, out-of-roundness and cylindrical error of the workpiece were measured. This procedure was repeated until the wheel reached the life. The wheel life is defined by the time when one of these four parameters start to increase rapidly.

Table 1. Experimental Conditions

Wheel	CBN Wheel (B170J100V) Diameter : 40mm Width : 5mm
Workpiece	SK3 Inner Diameter : 100mm Width : 10mm
Grinding Conditions	Exp.1 V_w=const. Wheel Surface Speed : 45, 60, 90m/s Workpiece Surface Speed : 1.05m/s Speed Ratio (V_w/V_s): 2.33×10^{-2}, 1.75×10^{-2}, 1.17×10^{-2} Exp.2 V_w/V_s=const. Wheel Surface Speed : 45, 60, 90m/s Workpiece Surface Speed : 0.79, 1.05, 1.57m/s Speed Ratio (V_w/V_s): 1.75×10^{-2} Oscillation Grinding Without Spark-out Grinding
Derssing	0.2mm Square Column Diamond Dresser
Lubricant	SA-02 20times diluted Solution (NORITAKE)

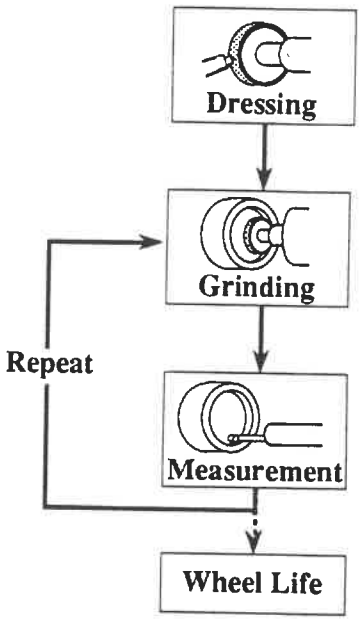

Fig. 1 Experimental Procedure

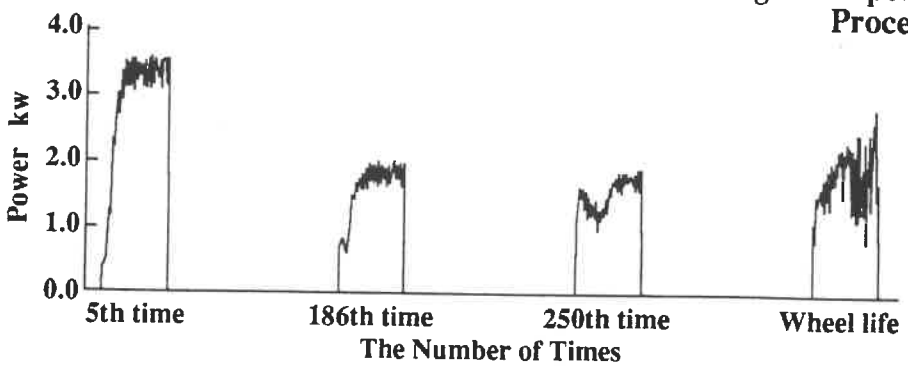

Fig. 2 Changes in the Grinding Power (V_s=90m/s, V_w=1.57m/s)

4. Experimental results

All experiments were performed in monitoring the grinding power in process. In all five experiments, according to the increase of grinding number of times, the pattern of grinding power changed as shown in Figure 2. At first, the power was rather high and depending on the increase of the number of grinding, it became lower and remained constant. Further grinding resulted in the excessive attritious wear of the grain cutting edges and made them difficult to penetrate into the workpiece. Eventually, grinding power started to increase rapidly and reached the life.

4.1. Constant workpiece speed

When the workpiece speed was constant, tangential grinding force decreased with increasing grinding speed as shown in Figure 3. The decrease in grinding force resulted in an improvement of the machining accuracy as shown in Figure 4 and Figure 5. The surface roughness decreased with the elevated wheel surface speed as shown in Figure 6. The wheel life was extended according to the elevated wheel surface speed.

4.2. Constant speed ratio

On the other hand, when the workpiece speed was increased in proportion to the elevated wheel surface speed, the grinding force remained constant as shown in Figure 7. The machining accuracy as well as the surface roughness remained constant as shown in Figure 8, 9 and 10 . A significant difference could not seen in the surface roughness at first, however, the difference become marked as grinding time elapsed. The roughness is lower when the grinding speed is high. The material removal rate increased in proportion to the increase in the workpiece speed. The wheel life was also extended by elevated wheel surface speed.

5. Conclusions

The results obtained in this study are summarized as follows;

(1) When the wheel surface speed was increased keeping the workpiece speed constant, grinding force reduced significantly and consequently machining accuracy was improved.

(2) When the workpiece speed was also increased with the increase of wheel surface speed, the material removal rate could be increased in proportion to the workpiece speed, under the constant machining accuracy.

(3) The wheel life could be extended by increasing the wheel speed for both cases.

Reference

1. I. Inasaki, S. An, T. Yosida, M. Wakuda and M. Itagaki, The basic study of high speed grinding, Journal of the Japan Society of Grinding Engineers, Vol.37, No.6, (1993), P.38

Vw=constant

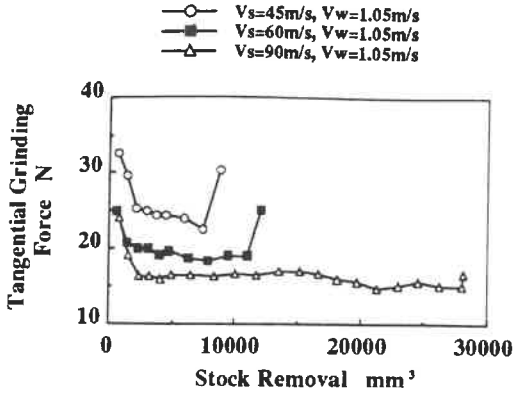

Fig 3. Influence of Wheel Surface Speed on Tangential Grinding Force

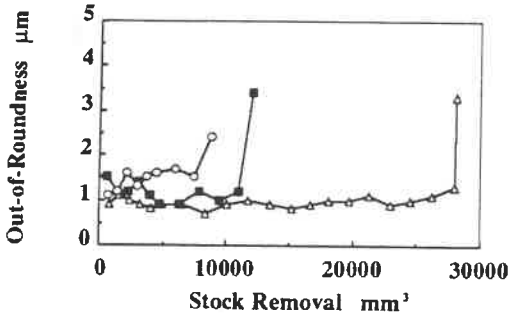

Fig 4. Influence of Wheel Surface Speed on Out-of-Roundness

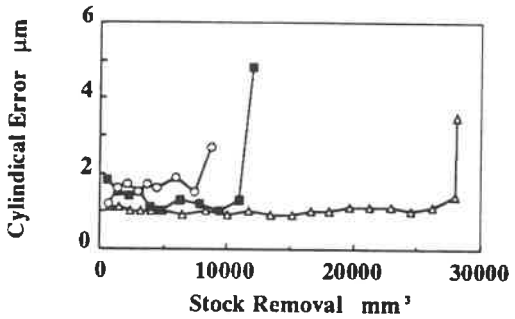

Fig 5. Influence of Wheel Surface Speed on Cylindrical Error

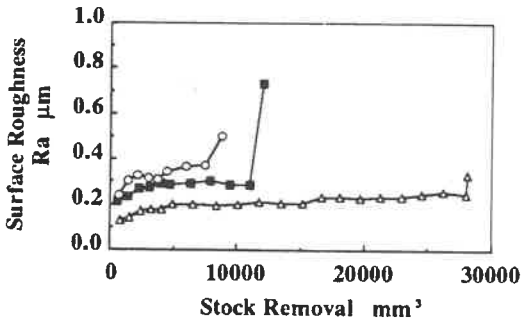

Fig 6. Influence of Wheel Surface Speed on Surface Roughness Ra

Vw/Vs=constant

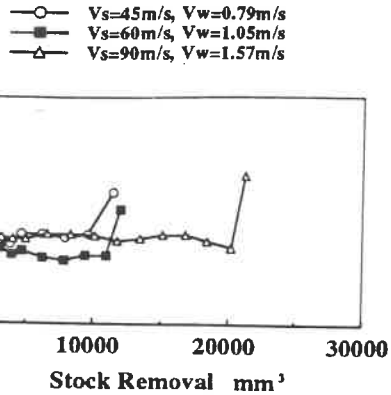

Fig 7. Influence of Wheel Surface Speed on Tangential Grinding Force

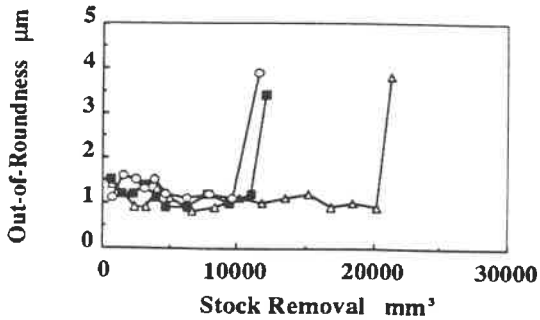

Fig 8. Influence of Wheel Surface Speed on Out-of-Roundness

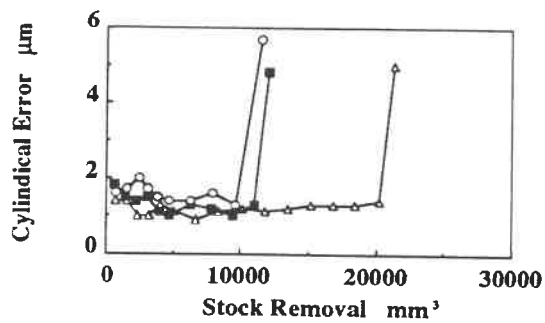

Fig 9. Influence of Wheel Surface Speed on Cylindrical Error

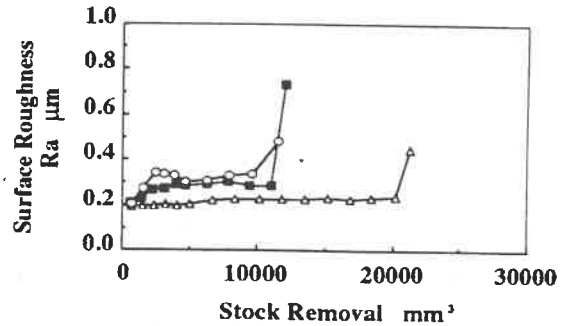

Fig 10. Influence of Wheel Surface Speed on Surface Roughness Ra

GRINDING INDUCED DAMAGE IN CERAMICS

Bi Zhang
Department of Mechanical Engineering
Precision Manufacturing Center
University of Connecticut
Storrs, CT 06269

I. INTRODUCTION

Grinding technique has been used as the most efficient and effective way to finish ceramic workpiece in industry. As the quality of advanced ceramics has been dramatically improved by the modern manufacturing techniques, the bulk defects are significantly reduced in terms of their sizes and numbers. The primary source to introduce damage into ceramic workpiece is grinding or other machining processes. The residual surface and subsurface damage may seriously alter the surface properties, and cause a strength degradation or even a catastrophic failure of a ceramic component. The exact nature, the manner and the penetration depth of grinding induced damage are, however, still not clear, leaving many uncertainties and sometimes danger in using ceramics as structural materials. Damage assessment and prediction thus become a critical issue in grinding of ceramics.

Three destructive inspection techniques are used in this study to assess subsurface damage in grinding of ceramics. This paper presents results of assessment of subsurface damage of four types of ceramics ground by three metal bonded diamond wheels. The results provide valuable insights into the dependence of grinding induced damage on the properties of workpiece materials, and grit sizes of diamond wheels. Furthermore, nucleation and development of subsurface damage are investigated and discussed.

II. EXPERIMENTAL PROCEDURE

Polycrystalline silicon nitride, alumina, zirconia, and silicon carbide were used as workpiece materials for this investigation. The slip-cast zirconia was a partially stabilized material containing certain amount of the metastable tetragonal modification which could transform into the monoclinic form at an elevated temperature or under a high level stress field. Table 1 lists the properties of these ceramic materials.

Table 1 Properties of Ceramic Materials

	Si_3N_4	Al_2O_3	ZrO_2	SiC
Density, g/cm^3	.3.28	3.94	6.05	3.15
Grain size, μm	2-3	2-3	5	5
Vickers hardness GPa	17.9	18.3	12.3	31.0
Flexure strength MPa	800	500	1,100	490
Fracture toughness MN/m$^{3/2}$	6.6	5.3	7.7	3.6
Brittleness, /m$^{1/2}$	2,700	3,400	1,600	8,300

The ceramic specimens were sliced into bars with dimensions of 5×5×30 mm. The grinding wheels were metal bonded SD80-N50M, SD140-N75M, and SD400-N75M diamond wheels of grit mesh sizes of #60-80, #140-170, and #325-400. The experiments were carried out at a grinding speed of 1,600 m/min, a table speed of 1.4 m/min, a wheel depth of cut of 15 μm, and a grinding width of 5 mm on a precision surface grinding machine. The grinding coolant was soluble type (JIS W-2-2) 2% dilution. Truing of the wheels was performed by a cup type diamond wheel SD140-P100M-30, and dressing by an alumina stick WA150G10V.

Subsurface damage inspection was conducted by SEM and TEM. Lapping technique was used for removing surface layers to expose grinding induced subsurface damage. Inspection of subsurface damage using TEM followed the following procedures. A ground sample was sliced to a thickness of about 1 mm. The sliced sample was then coated with SiO_2 to reserve the damage information in the ground layer. Two sliced pieces were bonded

by Araldite adhesive with ground surfaces facing each other. The bonded sample was lapped by diamond abrasives from the two sides to a thickness of about 20 μm. The sample was further thinned by ion sputtering. A sample thickness of less than a couple of hundred Å was obtained with an accelerating voltage of 4-5 kV and an ion sputtering angle of 10-15° in 10 minutes.

III. RESULTS AND DISCUSSION

Pulverization was observed on the superficial layers of the ground ceramics. Pulverization is a consequence of intergranular and/or transgranular microcracking due to a localized stress field of shear stresses superimposed by hydrostatic compressive stresses induced by abrasive grits in grinding. Ceramic grains tend to be fractured into finer ones by a pulverization process. Figure 1 shows an observation example of a superficial layer of a silicon nitride sample ground by the SD80-N50M diamond wheel. The TEM micrograph reveals a variation of grain sizes. A cluster of finer grains with an average grain size of 0.3 μm are observed in the micrograph. The grains, mostly hexagonal crystals, have appreciable gaps between each other, suggesting a loose bonding condition. These submicron-sized grains are randomly oriented with some of them marked by slip bands. A tortuous crack is observed on a one-micron-sized grain, which tends to cleave the grain into several smaller ones. This crack arrests at the grain boundary, which hinders the further propagation of cracks into the surrounding grains. The crack arrests by grain boundaries confine microcracking at a local level. This result explains that pulverization causes micron-sized grains to fracture into finer grains along their cleavage planes. The TEM examination established an experimental fact that the superficial layer is pulverized into a powder regime layer in which grains are loosely connected. Due to a hydrostatic compressive stress field underneath the cutting edge of an abrasive grit, the powder regime layer could be compacted and consolidated.

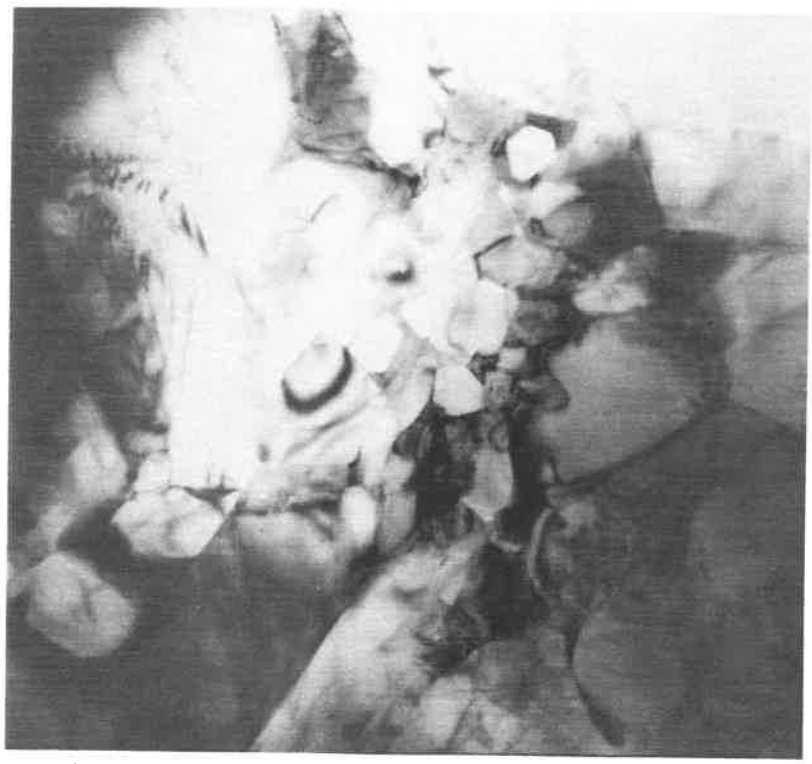

Figure 1 Observation of a superficial layer of ground silicon nitride by TEM. A cluster of fine grains of approximately 0.3 μm, transgranular microcracks causing gaps around the fine grains. A tortuous intergranular microcrack running across a one-micron-sized grain, tending to cleave the grain into several smaller pieces.

Figure 2 shows the thickness variations of the powder regime layers on various ceramics ground by metal bonded diamond wheels of different grit sizes. For silicon nitride and alumina, the thicknesses of powder regime layers were the largest in using the SD80-N50M diamond wheel, and followed by that in using the SD140-N75M diamond wheel. The results revealed that a grinding wheel of a larger grit size generates more amount of powder regime than does that of a smaller grit size. The powder regime generated by the diamond wheel with a mesh size of #60-80 was three times more than that by the diamond wheel with a mesh size of #325-400.

When a diamond wheel was used on different ceramic workpiece, the amount of powder regime generated on the silicon nitride

sample was the largest, and then followed by the alumina and zirconia samples. Silicon carbide had the least amount of powder regime. This suggests that hardness and fracture toughness play a significant role on pulverization of ceramic grains, and retention of the pulverized grains. Due to the high hardness and the low toughness, silicon carbide exhibited chipping on its ground surfaces. The chipping level increased with the grit size of the diamond wheels. It was chipping that carried away most part of the powder regime generated. In contrast to silicon carbide, silicon nitride and alumina had reasonably low hardness, and high toughness. The chipping levels on these materials were not as high as that in silicon carbide. The powder regime, once generated, were mostly retained on the ground surface.

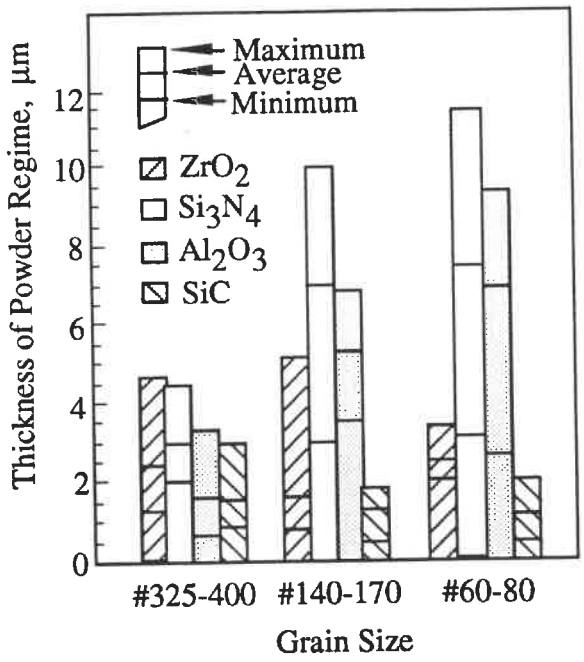

Figure 2 Thickness variations of powder regime layers of various ceramics with grit size of metal bonded diamond wheels.

Although the zirconia sample had the lowest hardness and the largest toughness among these ceramics, no significant amount of powder regime was generated on the ground surface of this material. This might be addressed to the fact that the partially stabilized zirconia contained certain amount of the metastable tetragonal modification which could transform into the monoclinic form. The phase transformation would result in a high fracture toughness, and bestows an excellent resistance to pulverization and crack initiation.

To quantitatively evaluate the effect of grit size on the subsurface void formation, the ground ceramics were inspected using SEM in aid of the etching technique. Figure 3 shows the micrographs of subsurface voids in the ceramic samples ground by the SD80-N50M diamond wheel. Figure 3a reveals a subsurface of a ground zirconia sample. This sample was lapped parallel to the ground surface to unveil subsurface damage. The clustered voids were found in the subsurface of 12 μm down from the ground surface. These clustered voids aligned themselves in the grinding direction. The void density decreases with an increase of the depth of subsurface layer, with the densest distribution adjacent to the powder regime layer of the ground surface. Besides the clustered voids, scattered voids were also identified surrounding the clustered voids. The size of the voids were about 1-3 μm in diameter. Figure 3b shows the subsurface of a silicon carbide sample after a lapping of 12 μm from the ground surface. Only scattered voids were found in this sample.

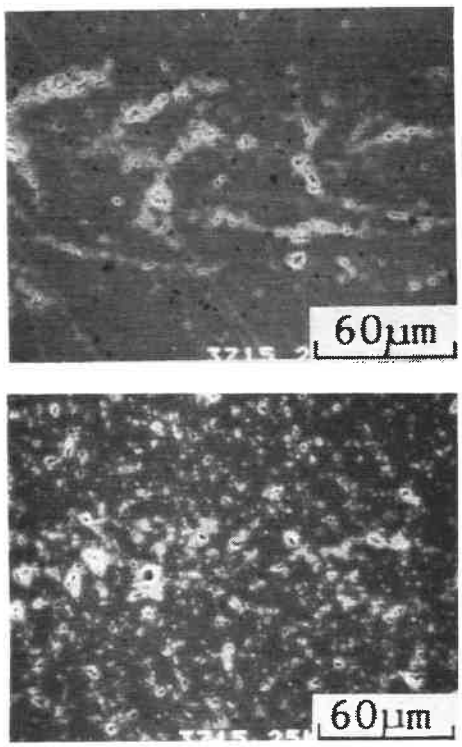

Figure 3 Voids generated in (a) zirconia; and (b) silicon carbide by the SD80-N50M diamond wheel in various ceramics

The SEM observations strongly indicate that whether clustered voids or scattered voids form depends on the properties of the workpiece materials, specifically, hardness and fracture toughness. A material with a large hardness and a low toughness, e.g. silicon carbide, tends to have more amount of scattered voids than clustered ones, while on the other hand, a material having a low hardness and a large toughness, e.g. silicon nitride, tends to have more amount of clustered voids than scattered ones.

The maximum depth of voids has been quantitatively measured with respect to the grit size of the diamond wheels used. Figure 4 gives results of the measurement on void depth. The maximum depth of voids were examined across an area of 500×500 μm of a lapped subsurface. In using the SD80-N50M diamond wheel, silicon nitride showed the largest depth of voids which was as large as 40 μm. This was then followed by alumina, zirconia and silicon carbide. The same trend was observed in using the SD140-N75M diamond wheel. However, silicon carbide formed larger depth than zirconia did in using the SD400-N75M diamond wheel. On the other hand, as the grit size decreased, the maximum void depth decreased, but the rate of decrease was different among these materials. There were two categories of materials in terms of void penetration depth, with silicon nitride and alumina being the first category, zirconia and silicon carbide the second category. The maximum void depth of the materials in the first category showed a larger rate of decrease than that showed by the ones in the second category. There was little decrease of the maximum void depth for the materials in the second category as the grit size decreased. This was especially true for silicon carbide. Hardness and fracture toughness might be the major factors of material properties controlling the penetration depth of voids. The results also indicate that a relatively coarse wheel induces almost the same level of subsurface damage as a fine wheel does in a material with a relatively large value of brittleness, whereas, a relatively coarse wheel induces higher level of subsurface damage than a fine wheel does in a material with a relatively low value of brittleness. In other words, it does not make a large difference on a workpiece surface integrity whether a rough or a fine grinding conditions are used on a relatively brittle material; however, it makes a large difference on a relatively less brittle material.

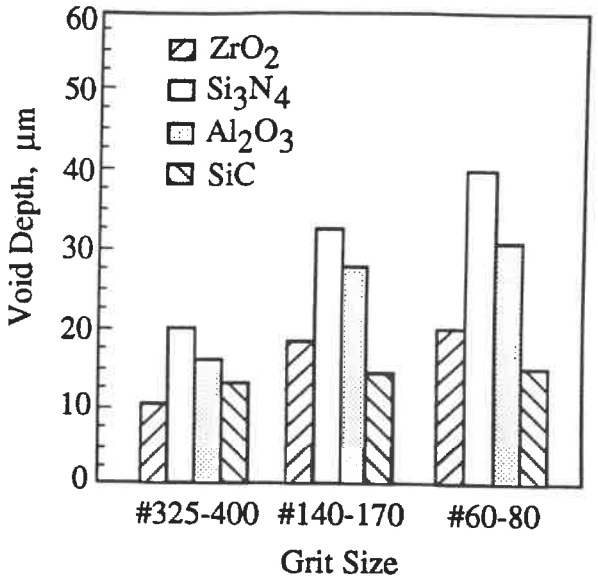

Figure 4 Variations of the maximum depth of voids with grit size of metal bonded diamond wheels in grinding of various ceramics

IV. CONCLUSIONS

- Two types of subsurface damage were identified: powder regime in the superficial layer, and voids in the subsurface of a ground ceramic material.
- The penetration depth of the subsurface damage was related to the properties of ceramic materials, specifically hardness and fracture toughness. The penetration depth was found to be smaller for ceramics with a lower hardness and a larger toughness, and larger for those with a higher hardness and lower toughness.
- The penetration depth of the subsurface damage varied with the grit size of diamond wheels. The larger penetration depth was found in a workpiece ground with a larger grit size of a diamond wheel, and vice versa.
- Two types of grinding induced voids were found: clustered voids, and scattered voids. Clustered voids formed void clusters in a ground workpiece, while scattered voids did not.
- The diamond wheel with the smallest grit size did not generate any clustered voids in any of the ceramic materials.

AN EXPERIMENTAL STUDY OF THERMAL ASPECTS OF CYLINDRICAL GRINDING

Shihui Zhou, John Webster
The Center for Grinding Research and Development
The University of Connecticut
Storrs, Connecticut

INTRODUCTION

The grinding process, one of the most utilized precision machining processes, is widely used to manufacture components requiring higher accuracy and a smooth surface profile. However, in the grinding process, the thermal damage often limits the productivity and quality of the ground components. Much reported research has been done to study and to prevent thermal damage in the grinding process. However, while cylindrical grinding have been widely used in industry, especially in the bearing industry, there has been limited reported research on the thermal behaviors in the cylindrical grinding process, mainly due to the difficulty in instrumentation. Therefore, thermal damage in cylindrical grinding has not been fully understood, since the research conducted and the thermal theories developed that are based on the surface grinding process may not be applied to cylindrical grinding process. This paper presents the instrumentation and experimentation of a research project in the Center for Grinding Research and Development, located at the University of Connecticut, as a effort to understand the thermal behaviors in the cylindrical grinding process, as well as for developing a thermal model for the cylindrical grinding.

Another purpose of this research is also to provide a comprehensive experimental study of thermal behaviors in the cylindrical grinding process with CBN superabrasive wheels. CBN grinding wheels are increasingly being used recently, since they have longer lifespan, require less frequent truing and dressing, and produce more consistent quality, compared with conventional abrasive wheels, such as aluminum oxide wheels. The results of this research will also provide information regarding usage of CBN wheels and their thermal effects on the workpiece.

EXPERIMENTATION

To detect the temperature field during the grinding process, a cylindrical workpiece, which consists of two halves with perfectly machined surfaces, was made. One of the halves has 12 small slots (0.032 inch width) milled into it, in to which are fitted small thermocouples (0.005 inch in dia.), as shown on the top of Figure 1. These two halves are coupled together by screws, after the interface is filled with a very thin layer of high thermal conductivity, high strength, and high electric resistant cement. FEM results show that this design can produce a temperature field very similar to a whole workpiece during grinding processes. Since in the cylindrical grinding process, the workpiece is a rotating component, the signals from these 12 thermocouples in the workpiece are connected to the non-rotating parts of the machine using a slip-ring device (Figure 1). The workpiece is supported at two ends by centers, one of which has been machined with 4 flats. Two

pairs of strain gages have been installed on the machined center to monitor the normal and tangential forces during grinding. The temperature and forces signals are conditioned and recorded by a Keithley data acquisition system, controlled by a 486 IBM personal computer.

RESULTS

This rig has been carefully designed and built onto a Landis external cylindrical grinder. Calibration and grinding tests have shown that this device performs well. Figures 2 and 3 show the calibration results of the force transducer. The results show that the strain gage force transducer responds linearly and give a correlation coefficient above 0.98 under the required loading range, and exhibit 3-5 % of crosstalk between channels. These cross errors can be further reduced by applying a transfer matrix obtained from the calibration results to acquisited forces data.

Figure 4 shows a typical grinding test result. The result shows that the grinding forces quickly increase and reach a stable value under a constant infeed rate, while the temperature field is built slowly and gradually reaches its own stable value. Each variation in the temperature responds to the workpiece revolution period, since each thermocouple is close to the grinding wheel only once per revolution. The result indicates that the workpiece background temperature at the given point increases during grinding, and will reach a steady temperature after a certain time. The once per revolution peak temperature variation is superposed onto the background temperature. This suggests that in the cylindrical grinding, the temperature will be accumulated in the workpiece, and a thermal model for cylindrical grinding may also consider this cumulated background temperature as well as peak temperature variation in the grinding zone for better predictions. A cumulative thermal model is under development based on this observation.

Other results about grinding temperature and related grinding forces have also been obtained under various grinding infeed rates, workpiece speeds, etc., which allow in-depth understanding of the thermal behaviors with CBN wheels, and enable a comparison with conventional wheels.

DISCUSSIONS

The instrumentation and experimentation presented here have provided much needed first-hand information to better understand the cylindrical grinding process, and enabled us to further development of a thermal model for the cylindrical grinding process. The results present show the unique temperature fields in cylindrical grinding, due to the continuous moving heat source, generated by the wheel cutting actions, along the workpiece. This research suggests that it is important to look at the workpiece as a whole object to study its temperature field, although only the cutting zone temperature is responsible for thermal damage, since the background temperature accumulated in the workpiece during grinding is superposed onto the once per revolution peak temperature variation, and may cause the cutting zone temperature increase to critical values, such as film boiling point, and cause thermal damage. This research also provides an alternative methods to estimate the grinding energy into the workpiece, as well as to verify any thermal models developed for the cylindrical grinding process.

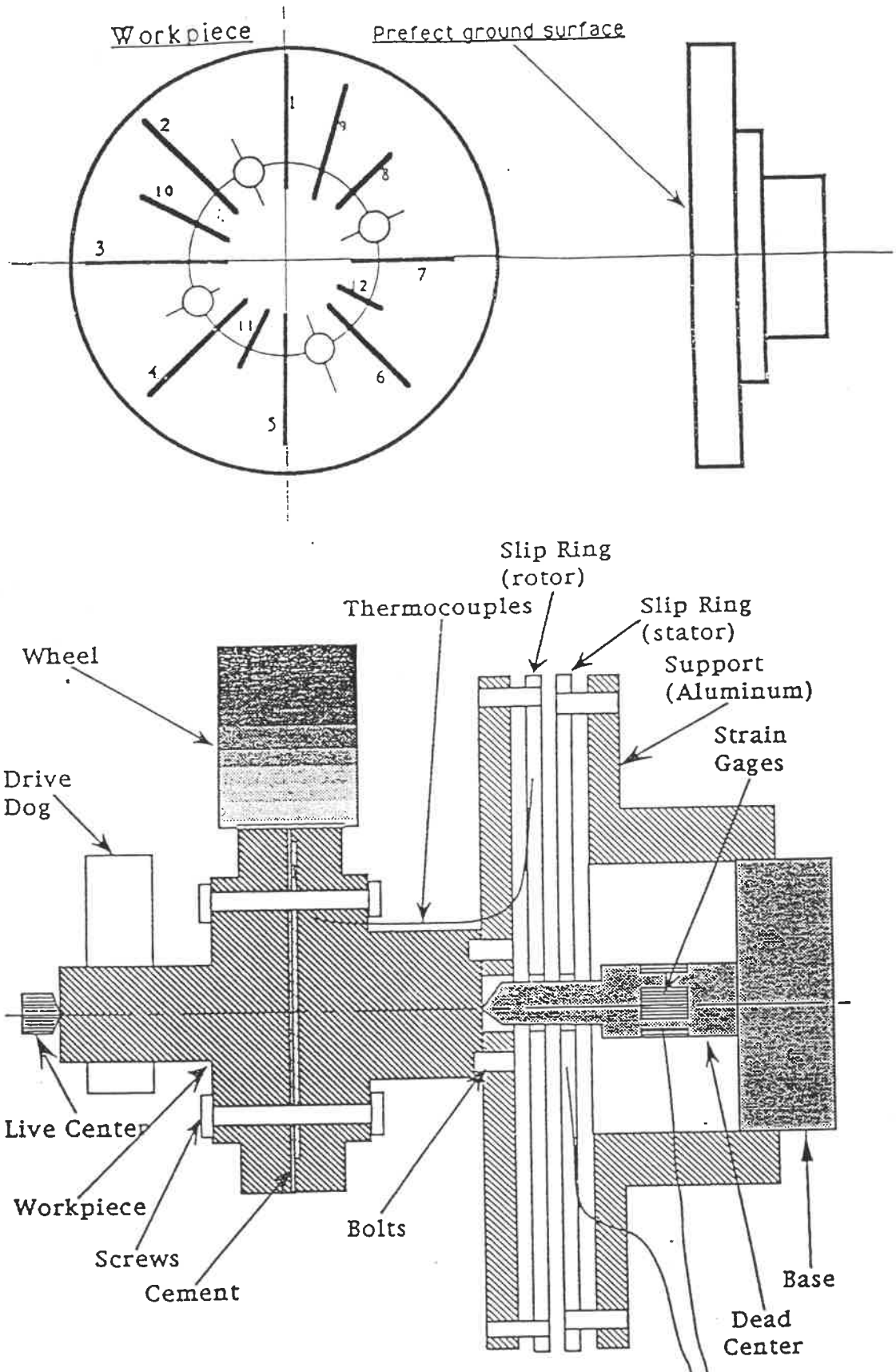

Fig. 1 TEST RIG ASSEMBLY

Fig. 2 Horizonal Force Calibration

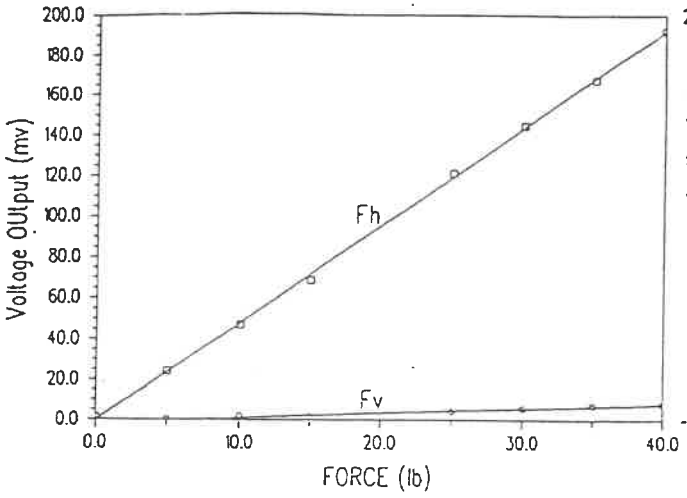

Fig. 3 Vertical Force Calibration

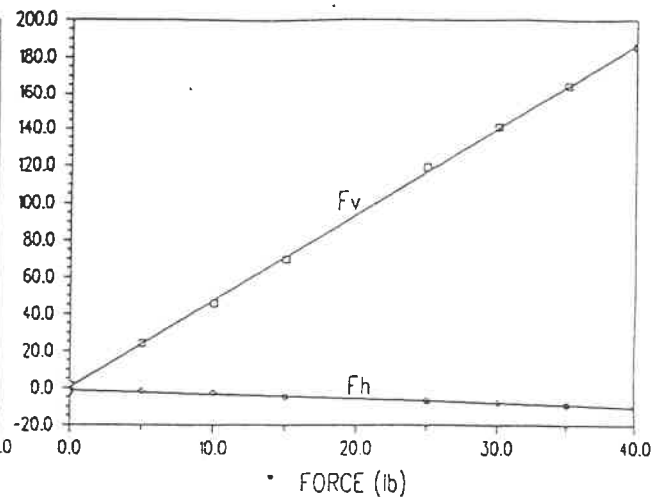

Fig. 4 CYLINDRICAL GRINDING TEST

Dw=1.7 in,Vw=70 rpm,infeed 0.005 in/min

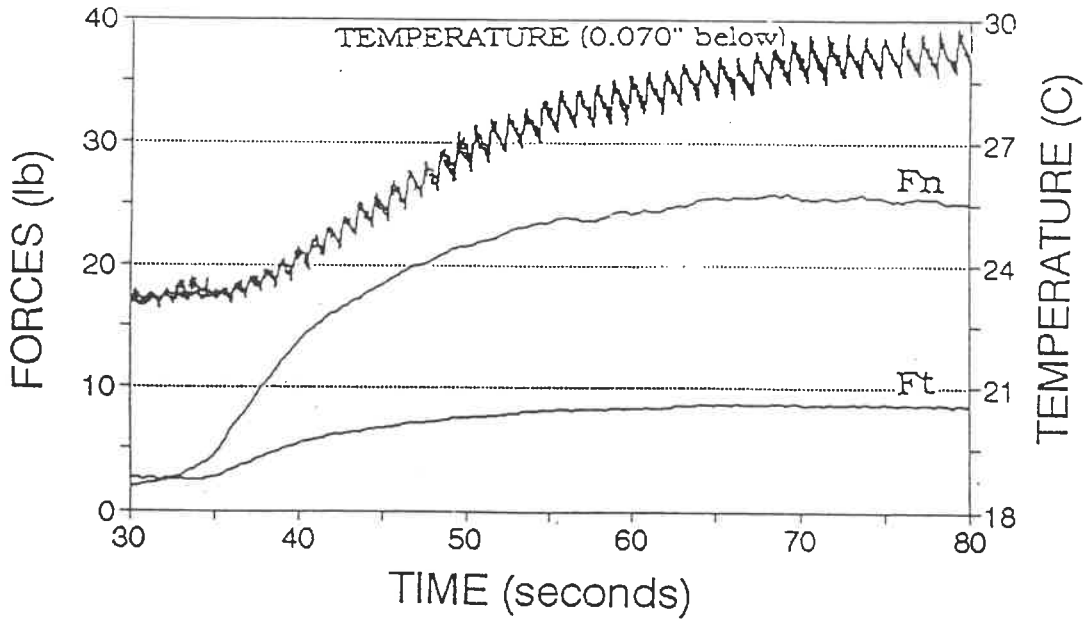

An Experimental Investigation of Workpiece Out-of-roundness in Centerless Grinding

S. Steven Zhou and Joseph R. Gartner
Center for Grinding Research and Development
University of Connecticut, Storrs, CT 06269

1. Introduction

Improving workpiece roundness in centerless grinding can be quite challenging due to the large number of process parameters and grinding disturbances involved in the process. Previous research on the subject [1,2] has focused on stability analysis of the grinding process along with recommendations for improving the workpiece roundness by selecting stable centerless work setups. Fig 1 shows a centerless work setup which is most often characterized by the two setup angles α and β. However, this approach is not always effective in improving the workpiece roundness in centerless grinding practice. An experimental study presented in this paper showed that wave interference condition on the workpiece can have a significant effect on workpiece roundness, leading to the conclusion that the wave interference condition and centerless work setup must both be considered in order to control the workpiece roundness effectively.

2. Experimental Design and Setup

An experimental investigation of workpiece out-of-roundness was conducted on a Cincinnati Milacron Twin-Grip 230-12 centerless grinder. The grinder was equipped with a programmable controller, and an automatic grinding wheel spindle balancer. The machine was instrumented to measure the grinding wheel spindle power, grinding and regulating wheel speeds, machine structural vibration, and component forces on the support blade during the grinding process.

In order to concentrate only those parameters having significant effect on the workpiece roundness, the process parameters listed in Table 1 were kept constant for all grinding tests. A batch of heat-treated AISI 52100 bearing steel workpieces was used for the tests. The workpieces were 1.5" in diameter and 6" in length, and hardened to Rc 60-62. For all grinding tests, the grinding wheel spindle was balanced within 40 microinches, and a grinding cycle with constant infeed rate and no spark-out was utilized.

Initial grinding tests were conducted by varying the setup angles, infeed rate, and workpiece rotational speed. It was found that the setup angle adjustment alone was not always effective in suppressing the workpiece surface waves that cause the out-of-roundness. Further study revealed that the interference between the existing workpiece surface waves and the grinding disturbances generating new surface waves had a profound effect on the resulting workpiece roundness. This wave interference can generate two different types of surface waves on the workpiece, namely standing waves and precessing waves. A standing wave refers to the surface wave that appears to be stationary with regard to the workpiece during grinding; while a precessing wave refers to the surface wave that appears to precess on the workpiece. A grinding experiment designed to specifically investigate the effect of wave interference to workpiece roundness is described in the following paragraph.

Fig 2 shows a measured spectrum of the component force acting on the support blade along the infeed direction. The spectrum clearly shows that the grinding disturbance associated with the grinding wheel rotational speed and its higher harmonics was dominant during grinding. Since the grinding wheel spindle had already been balanced within 40 microinches, the disturbance caused by the grinding wheel spindle unbalance was identified as the main source of grinding disturbance, and therefore, the wave interference condition on the workpiece could be controlled by properly adjusting the speed ratio of the grinding wheel rotational speed over the workpiece rotational speed. The value of the speed ratio represents the number of lobes to be generated on the workpiece per work revolution (also referred to as lobe frequency). When the speed ratio is an integer, a standing wave will be generated on the workpiece surface, which has minimum wave interference. When the ratio is a noninteger, a precessing wave will be developed that interferences with the existing waves, leading to lower workpiece surface waviness. In the experiment, the speed ratio was adjusted by changing the workpiece rotational speed. This was realized by controlling the regulating wheel surface speed. The ground workpieces were then placed on a Federal Products Formscan 3200 measurement system for roundness measurement.

3. Results and Discussion

3.1 Theoretical Background

Lobing behavior in centerless grinding can be described by a lobing system model, called lobing loop [3]. The transfer function of the lobing loop for such a grinding process is given as

$$\frac{R}{X}(n) = \frac{1}{\frac{K_w}{K_c}(1 - e^{-j2n\pi}) + 1 - K_1 e^{-jn\alpha} + K_2 e^{-jn(\pi - \beta)}}$$

where:

$$K_1 = \frac{Sin\beta}{Sin(\alpha+\beta)} \quad ; \quad K_2 = \frac{Sin\alpha}{Sin(\alpha+\beta)}$$

R-- workpiece surface waviness; X-- grinding disturbance; K_w-- cutting stiffness; K_C-- contact stiffness; n-- lobe frequency given as number of lobes per revolution.

For stable grinding operation, the magnitude of the lobing loop transfer function at any given lobe frequency is proportional to the magnitude of the corresponding workpiece surface wave, therefore, a magnitude plot of the transfer function can be utilized to qualitatively represent the workpiece surface waviness. Fig 3 shows a magnitude plot for a work setup of: $\alpha=57.1°;\beta=7.6°$. As the plot shows, the magnitudes of standing waves, corresponding to integer lobe frequencies, are significantly higher than those of precessing waves; the magnitude decreases as the wave interference increases and reaches a minimum between two consecutive integer lobe frequencies. One shall also note that the magnitudes at odd integer lobe frequencies are higher than those at even integer lobe frequencies for the lobe frequency bandwidth of interest. This is mainly caused by the centerless work setup and is beyond the scope of this paper.

3.2 Experimental Results and Discussion

Two sets of centerless grinding tests with different work setups were conducted in this experiment. The first set of tests was carried out with a machine setup of: $\alpha=57.1°;\beta=7.6°$ and an infeed rate of 20 mil/min. The grinding tests were conducted with a speed ratio ranging from 2.5 to 8 in increments of 0.5. This was realized by varying the regulating wheel surface speed from 60 ft/min to 210 ft/min for a given grinding wheel rotational speed of 1312 RPM. Five workpieces were ground at each speed ratio and then measured on the Federal measurement system. Fig 3 plots the measured roundness verses speed ratio. As the plot shows, the measured roundness at integer speed ratios are significantly higher than that at noninteger ones as a result of workpiece surface wave interference. The plot further shows that the measured roundness at odd integer ratios are higher than that at even integer ones. This relates to the work setup configuration. Comparing these results with the corresponding magnitude plot of the lobing loop (also see Fig 3), it can be seen that the experimental results correlate well with the magnitude plot. This leads to the conclusion that the wave interference condition and the work setup configuration both have significant effects on the workpiece roundness.

The second set of tests was conducted with a work setup of: $\alpha=58.2°;\beta=5.2°$ and an infeed rate of 10 mil/min. The speed ratio varied from 2.5 to 3.5 in increments of 0.1. Five workpieces were ground at each speed ratio and the measured results were plotted in Fig 4. It is evident that the measured roundness depends on the wave interference condition. When the phase shift between the existing wave and the new wave being generated is in close approximity of 180 degrees, a maximum wave interference occurs that leads to a minimum workpiece out-of-roundness. The experimental results are again supported by the magnitude plot of the lobing loop. Therefore, it is preferable to setup a centerless grinding operation such that the wave interference for all dominant grinding disturbances is maximum.

4. Conclusions

The experimental study shows that the surface wave interference condition, as well as the work setup configuration, has a significant effect on the workpiece roundness. This experimental observation is reaffirmed by the magnitude plot obtained from the lobing loop transfer function. It is, therefore, suggested that both the wave interference condition and work setup configuration shall be considered in order to effectively control the workpiece roundness in centerless grinding.

References

[1] Reeka, D., 1967, Ph.D. Thesis, Technical University of Aachen.
[2] Miyashita,M., F.Hashimoto, A.Kanai, 1982, Annals of CIRP, 31/1, pp 221-223.
[3] Zhou, S.S., Z.Gan, J.R.Gartner, 1993, SME Paper No. MR93-359-6.

TABLE 1

Grinding Wheel	97A801-J6-VFM; diameter:24"; Width:12"; speed:1312 RPM; dressing lead: 3.7 mil/rev.
Regulating Wheel	A80-R2-R; diameter:14"; Width:8"; dressing lead: 13.3 mil/rev.

FIGURE 1

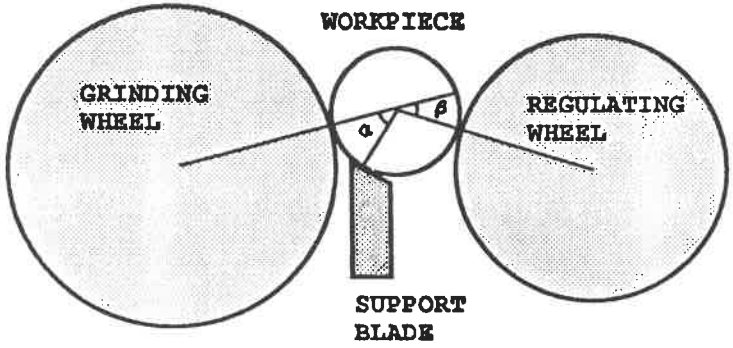

FIGURE 2

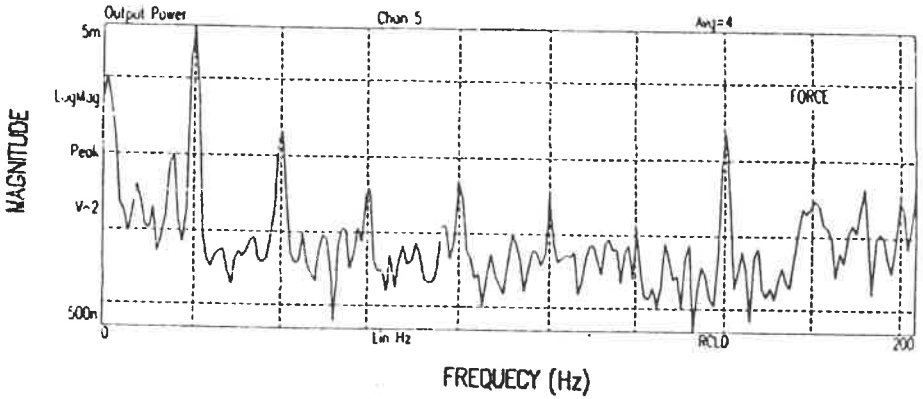

FIGURE 3

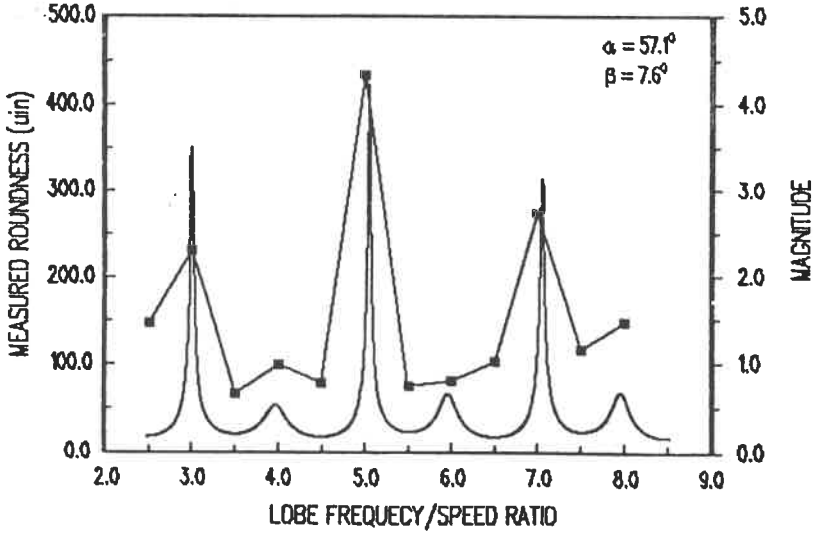

FIGURE 4

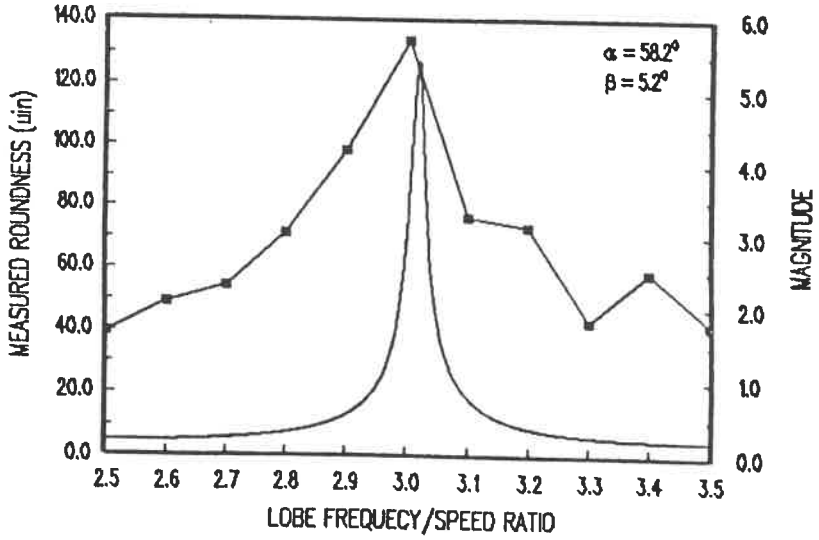

THE INFLUENCE OF POLISH PARTICLE SIZE DISTRIBUTION ON SPEED AND SURFACE QUALITY IN THE PRECISION POLISHING OF GLASS

D. J. Bell

Optical Surface Technologies
(A Division of London & Scandinavian Metallurgical Co. Ltd.)
Fullerton Road, Rotherham, South Yorkshire, S60 1DL, England

Introduction

Precision polishing of glass components for use in precision optics and optoelectronics applications using cerium oxide based polishes is an established process. The components for these applications need to be polished to a high degree of surface conformity and surface finish. Earlier work [1] investigated the effect of the polish particle size on the finish and sub-surface damage of LCD glass and on the speed of polishing. It concluded that the smaller the average particle size of the polishing powder, the finer was the surface finish. Fine powders also led to a reduction in sub-surface damage. Finer powders however impose a speed penalty and the polishing times may be unacceptably slow. The work also showed that faster overall polishing speeds could be achieved for a specific surface quality by using a two stage polishing regime. This however detracts from the convenience of the process and can add to the capital costs by the duplication of polishing equipment.

The present work has followed on from these investigations and has further explored the relationship between particle size distribution, polishing speed and surface quality. One of the limiting factors in the surface quality achievable in a polishing operation using cerium oxide is the size of the largest particles present in the size distribution. In a conventional polishing powder it may be necessary to reduce the overall size distribution more than is desirable in order to ensure that the proportion of large particles is reduced to an acceptable level for the surface quality required. This then reduces the speed of polishing and also leads to a larger proportion of very fine material being present in the polishing powder. This very fine, high surface area material contributes little to the overall polishing speed but can be difficult to remove from the polished substrates because of the high attractive forces between the glass and the fines. The effect of narrowing the particle size distribution on the polishing speed, surface quality and surface contamination of LCD glasses is investigated and the results have been used to design improved products for precision glass polishing which are both faster and cleaner in use.

Experimental

The powders chosen for this study were derived from cerium oxide concentrates normally used in the manufacture of glass polishing powders. Powders of different particle size distribution were prepared from the same base material and all have the same chemical composition. The

three polishes chosen illustrate the effects of both breadth of distribution and average particle size. The particle size distributions plotted by the Sedigraph® X-ray sedimentometer are shown in figure 1

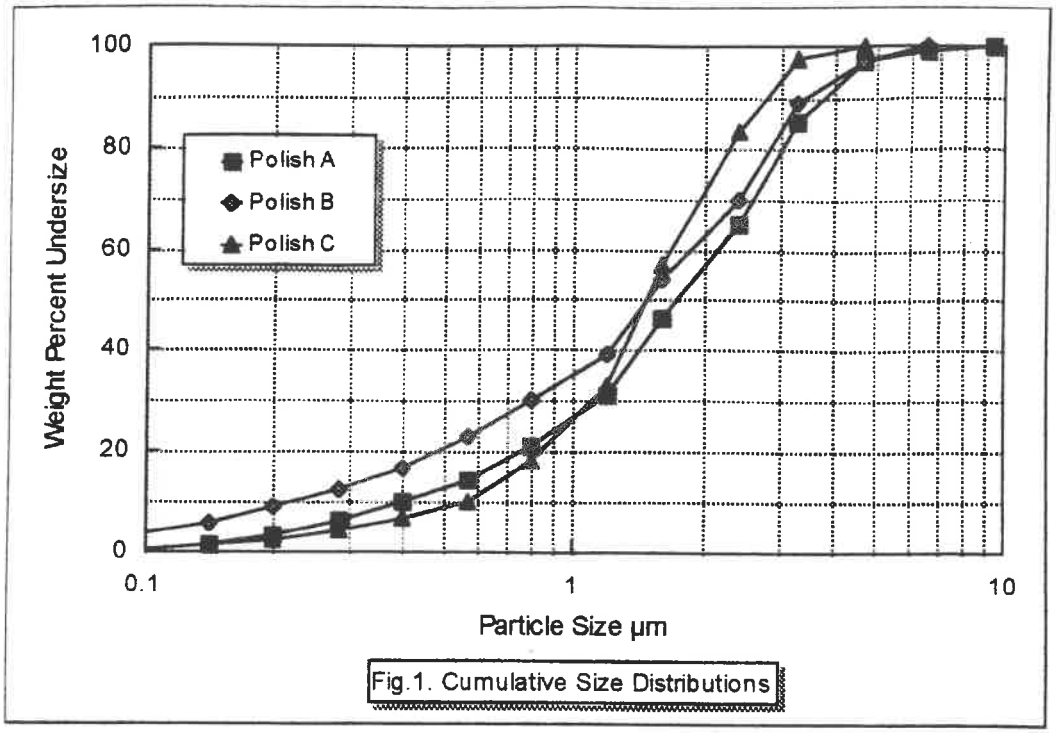

Fig.1. Cumulative Size Distributions

Polishing tests were carried out on a Speedfam 12B single-sided precision polishing machine using soda-lime float glass of a type used for LCD display screens. Polishing was carried out on a foamed polyurethane pad at an overall pressure of 125 g/cm^2 using predispersed slurries of the polishing powders in deionised water at a concentration of 100 g/l. The polish was drip fed onto to the pad at a rate of 400 ml/hr. Polishing speed was assessed by measuring the glass removal rate by weighing the test pieces at intervals during the test and the surface quality of the polished surfaces was measured using a Topometrix® TMX 2000 Atomic Force Microscope. The particle size data and the polishing rates of the samples tested are given in table 1.

Table 1. Comparative Polishing Speeds of Test Polishes

Polish	APS µm	Spread d_{90}-d_{10} µm	Speed mg/hr	Speed Index
Polish A	2.2	3.7	193	1
Polish B	1.8	3.7	180	0.93
Polish C	1.8	2.5	201	1.04

The spread of the particle size distribution given in column 3 is the difference between the d_{90} and d_{10} percentages in the particle size distribution.

The initial assessment of the surface quality of LCD glasses polished by the test powders showed that Polish C achieved the best overall surface finish. Polishing and assessment of the surface quality is still continuing and a comprehensive set of data and surface micrographs is being prepared.

Discussion

The polishing tests clearly showed that the fastest overall polish was achieved by Polish C which had the tighter particle size distribution but the lowest average particle size. Both Polish A and Polish B which had particle size distributions of similar breadth, wider than Polish C, gave inferior polishing speeds. The surface finish achieved with both of these polishes was also inferior to Polish C. The latter also showed a distinct advantage in the way in which the polish could be washed off the glass, giving a cleaner surface with less effort.

Polished glass surfaces with R_a values of below 1 nm are possible with polishes prepared in this way. This has been achieved using a polish with an average particle size (d_{50}) of 1.8μm. Previous work [1] indicated that it was necessary to mill the polish to below 1μm to produce surfaces of this quality. The speed advantage over the finer polishes allows this finish to be achieved in a single polishing operation rather than a two stage process as previously employed. In addition, the polishes are much cleaner in use and wash off the glass surface easily when compared with polishes with a preponderance of superfines which tend to adhere strongly to the glass.

Conclusions

The object of this programme of work has been to improve the precision polishing of glass without sacrificing the polishing speed. The conventional way of achieving finer surface finishes is to produce finer polishes by progressively milling the base material to finer particle sizes so that the proportion of coarse particles is reduced. This has the disadvantage of generating superfines which contribute little to the polishing performance, and cause problems in the cleaning of the polished surfaces. Polishes produced by methods which control both coarse and superfine material have proved to be much faster in operation than the conventional fine polishes, to give comparable surface finishes and to be much cleaner in use. They represent a significant step forward in the polishing of precision glass surfaces.

Work is continuing on this programme to elucidate further the role of the different size fractions in cerium oxide polishing powders and to explain the polishing process in terms of the chemical and physical interactions between the polish, polishing pad and substrate.

Acknowledgement

The author is indebted to Adam Kelsall of Nottingham University Department of Materials Science and Materials Engineering for his valuable assistance with the atomic force microscope measurements.

Reference

1. C. M. Lee and D. J. Bell, "The Effect of Polishing Particle Size on the Surface Finish and Subsurface Damage of Glass". American Society for Precision Engineering, Proceedings of the Seventh Annual Meeting, Grenelefe, Florida, October 1992, pp 240-242.

SUB-SURFACE DAMAGE IN ULE FROM LOOSE ABRASIVE GRINDING AND POLISHING

Louis Lombardo, John Nemechek
TROPEL Corporation
Fairport, New York

Arne Lindquist
Center for Optics Manufacturing
University of Rochester
Rochester, New York

Abstract

Tropel prepared ULE^{tm} substrates for ion beam figuring with an emphasis on achieving minimal sub-surface damage (SSD). This paper presents our findings of SSD in ULE, for different loose abrasives used in various grinding and polishing operations. Median particle size was found to be a good predictor of SSD depth.

Introduction

Ion beam figuring is a relatively new process being applied to the fabrication of precision optical components(1). This process technology may augment more conventional processes presently used in the production of projection lithography systems. It has promise as a likely process for fabrication of ultra-precise optical components, for demanding applications such as soft x-ray based imaging systems.

The Experiment

Tropel sought to prepare ULE substrates with minimal SSD. Stringent process definition and control was undertaken, due to the concern that the SSD from loose abrasive processing would limit the performance of ion figured components(2).

ULE blanks were first generated with a bound abrasive to arrive at the nominal starting thickness of 0.7 inches and diameter of 2 inches. The SSD from the 150 grit diamond cutting tool was measured and found to be 75 microns in depth. The methodology for this experiment was to then remove a minimum of twice the measured damage depth from the subsequent process.

The preparation of the substrates followed this pattern, with the depth of SSD measured at each successively finer grade of loose abrasive. In total, 5 "grinding" and 3 "polishing" abrasives were evaluated.

Data Collection

The primary data is the SSD measurements. These measurements were performed by personnel at the Center for Optics Manufacturing (COM) at the University of Rochester.

The SSD measurement process has been previously described(3). Briefly, the modified ball technique consists of first etching the sample in 5% HF for 30 seconds. A steel ball bearing of known radius is then used to produce a small spherical dimple (~1 millimeter diameter) in the sample, with 0.5 micron diamond polishing compound. The sample is then observed with an optical microscope over an area which includes the damage free diameter and the dimple diameter, with both diameters determined with a digital indicator. The difference in the two calculated sag values is the measure of the depth of SSD.

The loose abrasives were evaluated at COM using a Horiba particle measurement instrument; prior to ULE processing. Particle size was measured in solution immediately following a 3 minute ultrasonic excitation.

Results/Analysis

A total of 14 paired measurements of median particle size and SSD were completed. The three polished samples were found to have SSD below the estimated 1 micron measurement accuracy of the modified ball technique. Therefore, the analysis was performed with and without these three data points.

We expected SSD depth to be related to abrasive particle size. Therefore, the data was subjected to a bivariate regression, with SSD as the dependent variable. In the instance of the 14 data samples, the slope of the ordinary least squares (OLS) fit was calculated to be 0.86, with 0.070 standard error. That is, for a 1 micron change in abrasive particle size, the SSD was predicted to change 0.86 microns. Further, with 95% confidence, the slope of the OLS fit is predicted to lie within the range of 0.72 and 1.00.

The 14 data samples included an estimate of 1 micron SSD for each of the three polished samples. Removing these three data points provides essentially the same results. With 11 data points, the slope of the OLS was found to be 0.84 with 0.095 standard error. The R-squared values for the OLS applied to the 14 and 11 data samples were 92.7% and 89.7%, respectively.

Summary
SSD depth and loose abrasive particle size have been measured for several samples over the range of ~1 to ~20 microns. Median particle size has been found to be a good predictor of SSD depth; when coupled with the rule of removing material at least twice the amount of the previous process SSD depth.

Future Work
Perhaps the most glaring assumption made in this experiment is that median particle size remains constant during processing. This is a subject of future work. Secondly, with the modified ball technique presently limited to SSD depth of approximately 1 micron; we hope to measure all the samples using an alternate technique such as scatter.

References:

1 L.N.Allen and H.W.Romig, "Demonstration of an ion figuring process," Advanced Optical Manufacturing and Testing, SPIE, Vol.1333, pp. 22-23, July 1990

2 J.R.McNeil, "Ion Etching of Optical Glass," contract research per GCA PO#54467, July 1991.

3 A.Lindquist, S.D.Jacobs and A.Feltz, " Surface Preparation Technique for Rapid Measurement of Sub-Surface Damage Depth," OSA Topical Meeting on Science of Optical Finishing, Monterey, CA, June 1990.

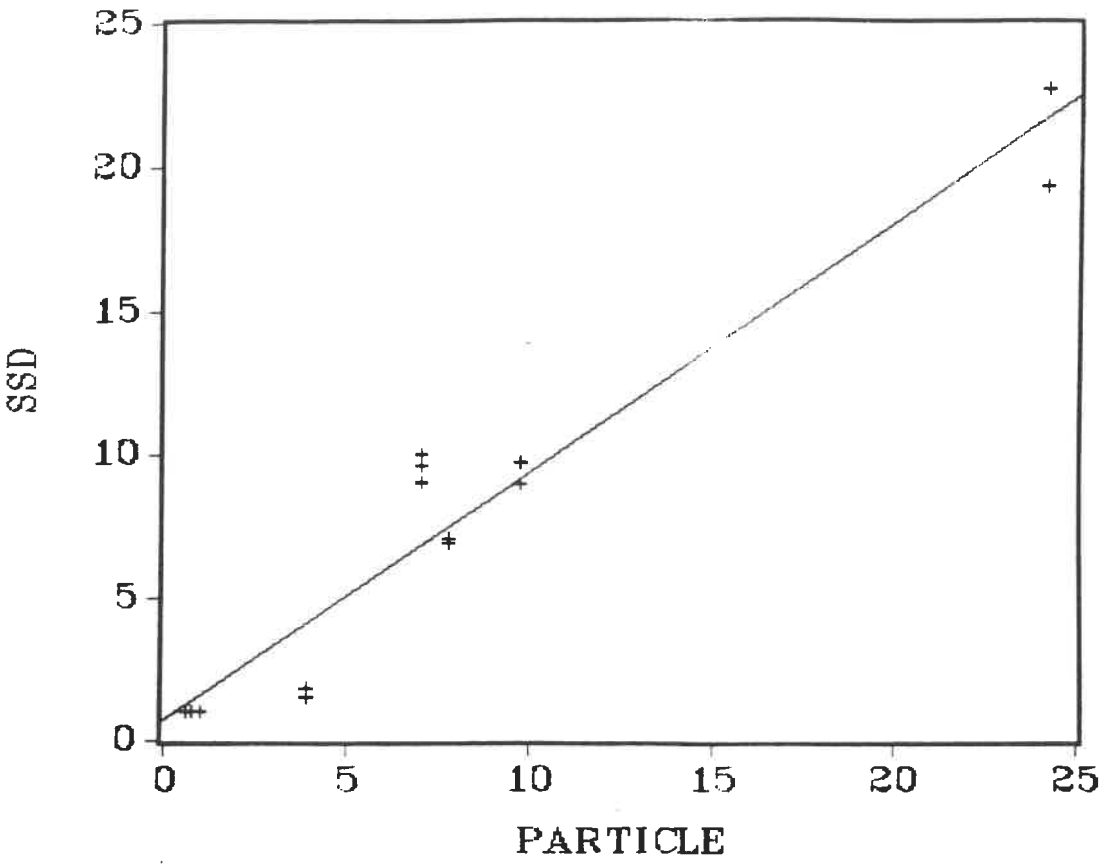

Figure 1. OLS Fit of SSD and Particle Size (microns)

==========

LS // Dependent Variable is SSD
Date: 4-06-1994 / Time: 14:12
SMPL range: 1 - 14
Number of observations: 14

VARIABLE	COEFFICIENT	STD. ERROR	T-STAT.	2-TAIL SIG.
C	0.7349294	0.7635100	0.9625667	0.3548
PARTICLE	0.8647549	0.0700118	12.351553	0.0000

R-squared	0.927079	Mean of dependent var	7.830429
Adjusted R-squared	0.921002	S.D. of dependent var	6.695224
S.E. of regression	1.881800	Sum of squared resid	42.49407
Log likelihood	-27.63729	F-statistic	152.5609
Durbin-Watson stat	1.027139	Prob(F-statistic)	0.000000

Table 1. Descriptive Statistics of OLS Fit

TWIN SURFACE LAPPING AND SINGLE SURFACE POLISHING OF SILICON WAFERS FOR THE ELECTRONICS INDUSTRY

Peter Wright
Speedfam Limited, Europe

Kathy Leaf
Speedfam S.G., USA

This paper describes the principles involved for the mass manufacture of silicon wafers to the extremely tight tolerances specified and demanded by the electronics industry. The industry requires wafers, in disc form, with one surface polished and the opposite face smooth ground to a "light gray" uniform surface texture. The textured surface assists in the further processing of the wafers.

Pre-sliced and edge rounded discs, 150mm diameter in single crystal material are twin surfaced lapped flat and parallel with a surface finish of better than 0.35 microns Ra or 0.16 microns Ra, using loose abrasives in a fluid medium.

It is revealed that the lapping process is conducted in relatively complex machines in which both surfaces of the silicon discs are machined simultaneously and whilst removing the same amount of material from both sides of each individual disc.

The motion of the discs within the machine is epicyclic, sometimes referred to as "planetary" motion around the central vertical axis of the machines, or more precisely, the sun/ring gear drives the multi-element carriers around the central vertical axis. The silicon discs freely rotate in their individual pockets within the multi-element carrier whilst the surface of the discs are lapped between the upper and lower rotating lapping plates.

The carriers rotate in a controlled manner between the lapping plates around the sun gear drive. By using relatively large lapping plates 1400mm - 1600mm diameter in the machines and continuously controlling their shape relative to each other and better than 5

microns in the described way, the tolerances demanded of the industry can be achieved at high yields, high throughputs and cosmetically void of scratches and chips.

One surface of the lapped silicon discs is polished in a described manner in a multi spindle, multi element single surface polishing machine using hard and flat polyurethane/polyester felt pads using controlled pH silica gels. The flatness of the polished surface achieved in TTV terms is better than 2 microns with a surface roughness of better than 0.5 nm Ra without haze or scratches.

The mass production of silicon wafers is in the domain of nanotechnology.

DEVELOPMENT OF A TOOL FORCE/SURFACE FINISH MODEL FOR DIAMOND TURNING

Thomas A. Dow, Professor
Chris Arcona, Graduate Student
Precision Engineering Center
North Carolina State University
Raleigh, NC 27695-7918

1 INTRODUCTION

In diamond turning, the steady state and dynamic tool forces contain information on both the condition of the tool and the cutting process. The relationships between these forces, the geometry of the diamond tool, the instantaneous cutting parameters and material properties are not known for the conditions typical of precision diamond turning. Machining experiments involving various materials and cutting parameters have been conducted. A model relating the measured steady state force components to chip area, tool geometry and material characteristics is being developed. This model will allow the forces to be used as a measure of the quality of the tool as well as the machined surface.

2 DEVELOPMENT OF TOOL FORCE MODEL

2.1 Description of Cutting Experiments

Diamond turning experiments involving various materials and cutting parameters have been performed. Electroless nickel, plated copper, 6061-T6 aluminum and annealed 6061 aluminum were machined simultaneously at a cutting speed of about 1.5 m/s. The tests were performed at feed rates of 5, 10, 20 and 40 μm/rev for 3 and 10 μm depths of cut. Each set of eight tests was conducted with two tools: Tool #1 has a 5.08 mm nose radius, 0° rake and 8° clearance while Tool #2 has a 1.52 mm nose radius, 0° rake and 10° clearance. The forces parallel (cutting force) and perpendicular (thrust force) to the surface of the workpiece were measured using a Kistler 9251A three axis load cell and a MASSCOMP data acquisition system. The effect of tool wear was studied by cutting 6061-T6 aluminum, measuring the tool edge radius and flank wear in a scanning electron microscope [1] and repeating the sixteen tests.

The diamond turning experiments were designed to provide insight into the influences of chip parameters, tool geometry and material properties on the tool forces. A tool force model previously developed at the PEC for diamond turning with a straight-edged tool [2] is being investigated. This model is based on the hypotheses that 1) the cutting force is linearly dependent upon the uncut chip area and 2) the thrust force is linearly related to the combined areas of the

cutting edge and flank wear of the tool projected into the plane of the workpiece. The cutting and thrust forces are also influenced by friction on the flank and rake faces, respectively.

2.2 Results of Cutting Experiments

Cutting Forces. The cutting forces have been found to be linearly related to the undeformed chip area. This result is not unexpected, as several researchers have found a linear dependence of cutting force on uncut chip thickness in the orthogonal machining of steel, brass and aluminum alloys [3-6]. Figure 1 shows the cutting forces generated from 3 and 10 μm depths of cut as a function of chip area for the new Tool #1 (~50 nm edge radius, no flank wear). For each of the four materials tested, the force data lies on a line when plotted against chip area. The effect of tool wear on this relationship is shown in Figure 2. Figure 2 is a graph of cutting force associated with electroless nickel vs. chip area for Tool #1 after cutting 3 km in 6061-T6. The forces from cutting at a depth of 3 μm have a different dependence on chip area than those resulting from a 10 μm depth of cut. The separation of the lines shown in Figure 2 has been found to vary with material and could be due to an increase in friction along the flank land of the tool. A comparison of Figures 1 and 2 shows that the forces for machining the electroless nickel at small chip areas increase with tool wear, as predicted by the model, but the forces measured at large feed rates decrease with tool wear. This latter observation is currently not understood.

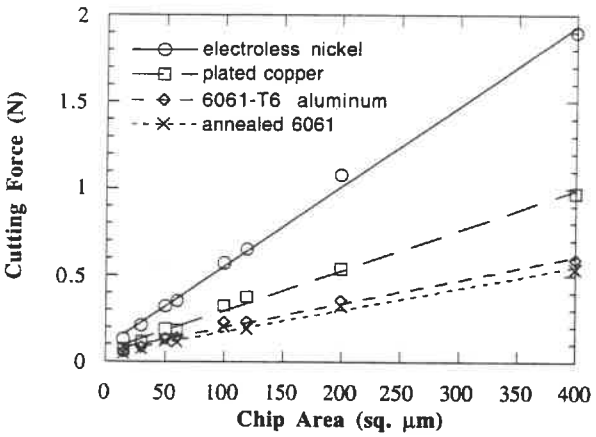

Figure 1. Cutting force vs. chip area for sharp Tool #1; 3 and 10 μm depths of cut.

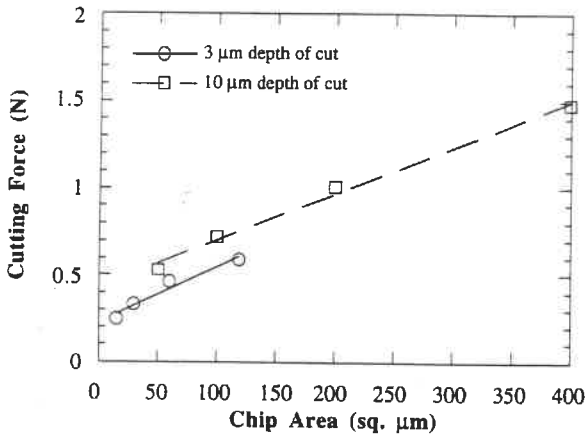

Figure 2. Force vs. chip area for electroless Ni and dull Tool #1; 3, 10 μm depths of cut.

The undeformed chip area has been found to be very nearly equal to the product of the depth of cut and feed rate for the round nosed tools. Thus, if the cutting forces are proportional to area, the forces recorded for Tool #1 should be nearly equal to those obtained with Tool #2 at the same depth of cut and feed. This statement is true for machining with new tools having similar edge radii (~ 50 nm) and no flank wear, as shown by Figure 3. Note that the force data lies on a line for the sharp tools (see Figure 3). However, this is not true for the data collected with worn tools, as demonstrated by Figure 4. This figure depicts the cutting forces as a function of uncut chip area

for the two tools after cutting 7 km in 6061-T6. The best fit line from Figure 3 is included in Figure 4 for comparison. The scatter in the data between the tools prevents a correlation of force with chip area and is probably due to differences in the geometries of the worn tools (0.22 μm edge radius, 1.3 μm wear land for Tool #1 and 0.35 μm edge radius, 1.0 μm wear land for Tool #2). For the other materials, the relationship between force and chip area is linear for sharp tools and is hidden by scatter in the force data for the worn tools. Figures 3 and 4 reinforce the conclusion drawn from Figures 1 and 2, that is, as each tool wears, the cutting forces associated with small chip areas increase, but the forces decrease slightly for large chips.

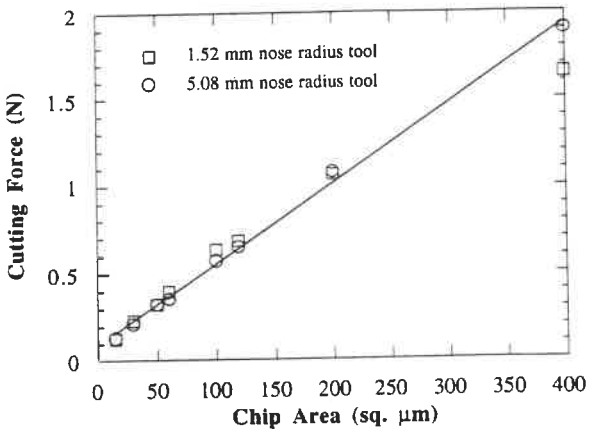

Figure 3. Comparison of cutting forces in electroless nickel for sharp tools.

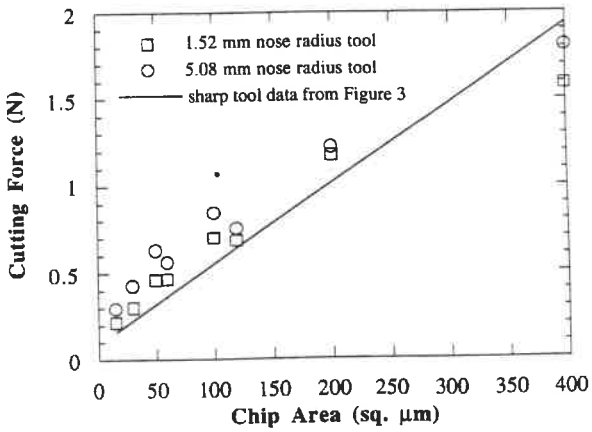

Figure 4. Comparison of cutting forces after cutting for 7 km in 6061-T6.

Thrust Forces. Contrary to the hypothesis in the tool force model [2], the thrust forces are not linearly related to the area of tool/workpiece contact projected into the plane of the workpiece. An illustration of this lack of linearity is shown in Figure 5, where the thrust forces obtained with Tool #1 are plotted as a function of the combined areas of the tool edge and flank wear projected into the plane of the workpiece for 3 μm depths of cut and 40 μm feeds. For the aluminum, the thrust forces and the variation in these forces are small. The results for the plated copper and the electroless nickel, however, are not linear functions of the projected contact area. Other experiments showed this same non-linear relation between thrust force and flank contact area. Figure 6 demonstrates that the thrust forces depend on the length of tool/work contact, which, in turn, is affected by the nose radius of the tool. In Figure 6, the thrust forces obtained with sharp tools (~50 nm edge radii, no flank wear) for 3 μm depths of cut and 5, 10, 20 and 40 μm feeds are plotted against the projections of the tools' cutting edges in the plane of the workpiece. If the thrust force was linearly related to projected contact area, then the data for each material would lie on a single line. For example, given the thrust forces for electroless nickel cut with Tool #2, a linear relationship between thrust force and projected contact area would require the forces for Tool #1 to be greater than 2 N. Figures 5 and 6 suggest that the thrust forces are non-linear functions of cutting parameters, tool geometry and properties of the workpiece.

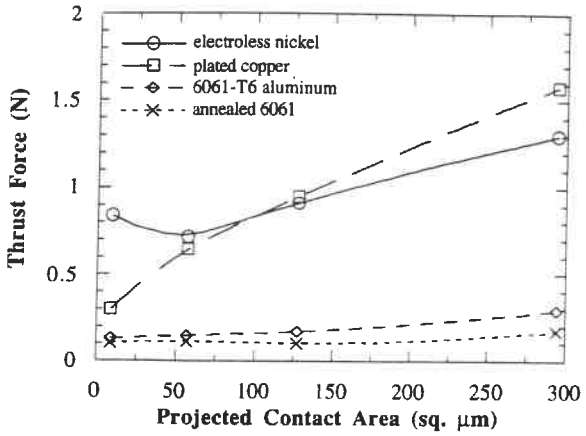

Figure 5. Thrust force vs. projected area for Tool #1; 3 μm depth of cut, 40 μm feed.

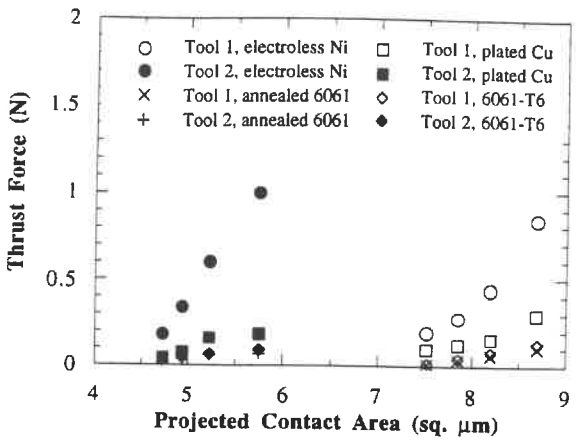

Figure 6. Thrust force vs. projected area for sharp tools, 3 μm depth of cut.

3 CONCLUSION

Diamond turning tests have been conducted to determine the effects of cutting conditions, tool geometry and material properties on the measured tool forces. A linear dependence of the cutting force on the uncut area of the chip has been observed for sharp tools. The variation in force vs. chip area curves due to tool wear and material properties has not yet been quantified. The thrust forces have been found to vary with the workpiece material and depend upon parameters that affect chip geometry, such as tool nose radius and feed, in a non-linear manner. Quantitative explanations for the variations in cutting and thrust forces with tool and chip geometries and with the properties of the workpiece are being developed.

REFERENCES

[1] Drescher, J.D. "Scanning Electron Microscope Technique for Imaging a Diamond Tool Edge." *Precision Engineering*, v. 15, Jan. 1993: 112 - 114.

[2] Drescher, J.D. "Tool Force, Tool-Edge, and Surface Finish Relationships in Diamond Turning." PhD Thesis, North Carolina State University, May 1992.

[3] Kobayashi, S. and Thomsen, E.G. "Some Observations on the Shearing Process in Metal Cutting." *Trans. of ASME, Journal of Engineering for Industry*. v.81, Aug. 1959: 251-262.

[4] Wallace, P.W. and Boothroyd, G. "Tool Forces and Tool-Chip Friction in Orthogonal Machining." *Journal of Mechanical Engineering Science*. v. 6, no. 1, 1964: 74-87.

[5] Lucca, D.A.; Seo, Y.W. and Rhorer, R.L. "Energy Dissipation in Ultra-Precision Machining." *Proceedings of the 1993 NSF Design and Manufacturing Systems Engineering Conference*, UNC Charlotte, 1993: 225-229.

[6] Nakayama, K. and Tamura, K. "Size Effect in Metal-Cutting Force." *Trans. of ASME, Journal of Engineering for Industry*. v. 90, Feb. 1968: 119-126.

VALIDATION OF A DYNAMIC GRINDING MODEL

Thomas R. Kurfess
Georgia Institute of Technology
The George W. Woodruff School
of Mechanical Engineering
Atlanta, GA 30332-0405

Hodge E. Jenkins
Georgia Institute of Technology
The George W. Woodruff School
of Mechanical Engineering
Atlanta, GA 30332-0405

Stephen J. Ludwick
Carnegie Mellon Univ.
Dept. of Mechanical Eng.
Pittsburgh, PA 15213

Abstract

In precision grinding it is important to create a smooth and consistent surface finish on a ground part. Variations in the material removal rate can cause unwanted surface defects and damage. (This is especially critical in ductile grinding of optic lenses.) As the material removal rate cannot always be measured or controlled directly, a related metric is desired. The normal force is such a metric. Thus it is important to establish the relationship between the normal contact force and the material removal rate, for effective grinding control in achieving a desired surface finish.

With such a relationship established, controlling the normal force during grinding will allow the machine tool deflections and material removal rates to be repeated more accurately from part to part, improving the repeatability of the resulting part shape and finish. Additionally, accumulation of the ground material in the grinding wheel (wheel loading) may be detected using the model, indicating a need for wheel dressing and modification in machining parameters.

The Preston equation has been used to establish such a relationship between the normal grinding force and the material removal rate (MRR) without the need of accounting for friction and specific energy. The Preston equation (1) serves as a model of the grinding process to predict the MRR from the wheel contact speed and normal force. This relationship is expressed below.

$$Q = K_P F_N V \tag{1}$$

The variable (Q) represents the material removal rate, and is given in units of volume per time. (K_P) is the experimentally derived Preston coefficient. It compensates for the different removal rates expected with varying part and wheel materials, and is given in terms of area per unit of force. (F_N) is the normal force between the part and the grinding wheel. Finally, (V) represents the relative velocity between the surfaces of the grinding wheel and the part. One of the goals of this study is to verify this model and establish the

Preston coefficient to be used in an adaptive force-controlled grinding system in the future. However, a limitation in the use of the Preston equation is the stability of the coefficient. Variation in Preston's coefficient is seen as a decreasing function with grinding.

Using the Preston grinding model, simplified grinding relationships have yielded reasonably good results for determination of the Preston coefficient and a grinding model. The grinding model based on the Preston coefficient is more expeditiously found than that of the Hahn and Lindsay. The dynamic grinding model links the grinding rate to the measured force. The Preston's coefficient of the grinding model must be determined empirically. In this research, experimental data has been gathered and is used to identify parameters and validate a Preston-type grinding model, while gaining insight into model improvement. The parameters were determined from experimental data using a least squares parameter estimation technique.

Experimental Servo Grinding System Description

To validate the dynamic grinding model a force controlled grinding system is developed and used to test grind position as a function of normal force. The grinding system used in this experiment consists of a three-axis prismatic servo stage shown in Figure 1. For this research, only one axis is used, the Z axis, although this work is extendible to three dimensional grinding. The servo stage is controlled by a programmable multi-axis controller (PMAC) motion controller at a sample rate of 2.26 kHz (the maximum sampling rate of the PMAC system). The power amplifier for the PMAC has output limits of 48V and 150W. An Assurance Technology 6-axis analog force sensor is used to measure force in all three axial direction. A 100-count, optical encoder is connected to the grinding shaft for use as a tachometer. An eddy current probe is used to measure actual displacement between the grinder and the workpiece. Both the encoder and eddy current sensor are connected to the PMAC controller and sampled at 2.26 kHz.

Typical grinding experiments that one might run include constant force grinding and the execution of a variety of other force trajectories. In this research constant grinding force regulation experiments were performed, at various force levels. System identification techniques are also used to estimate a first order transfer function between commanded position and the force output. Accelerations were limited to reduce the order of the system dynamics, without significantly compromising the effective servo update rate. Proportional and integral control are used in the feedback loop to regulate the Z axis force. Considerations on the gains were minimal overshoot and a 1-second rise time. The integral term is necessary to eliminate any steady state force errors. As the effective sample time of the PMAC-based force controller is ~22 msec, a digital control design is implemented for

determining system gains. Test runs on force servoing were performed on the system without grinding to verify design gains and modify them as necessary to limit mean force overshoot.

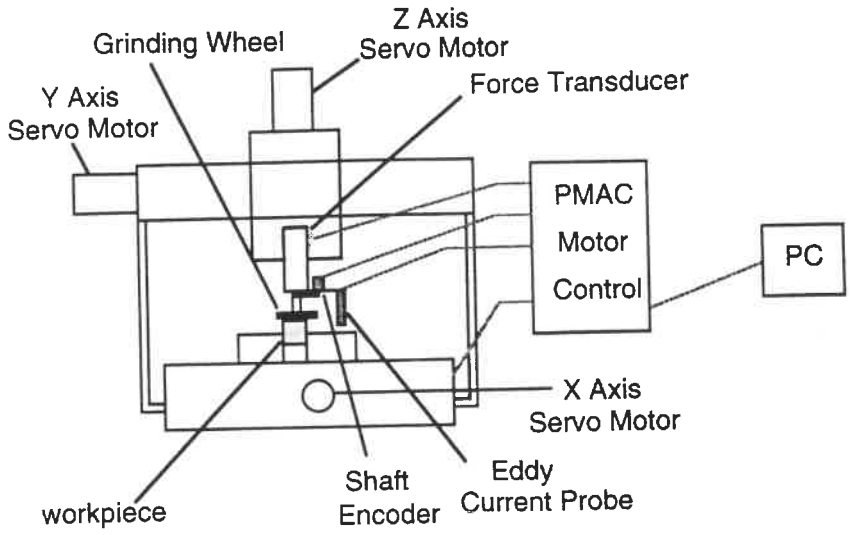

Figure 1. System Schematic.

The experiments were performed using the 3-axis servo table equipped with a rotary grinder and cup-shaped grinding wheel attached to the Z-axis of the table. The grinder is servoed downward making contact with a steel part. Normal grinding force is then maintained by the Z-axis servo stage. A diagram of the resulting contact area is shown in Figure 2. The grinding wheel consists of vitrified bonded aluminum oxide, while the ground part is made of low carbon steel.

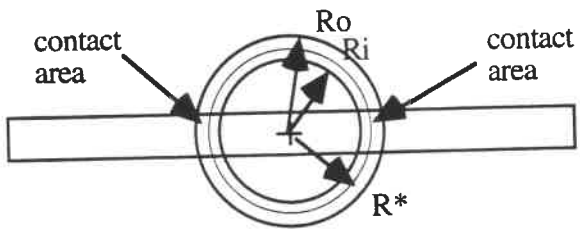

Figure 2. Diagram of the Contact Area Between the Part and Wheel.

Figure 3 shows a typical PI force controlled plunge grind in terms of the normal force and the material removal rate (MRR). Figure 4 plots the Preston coefficient versus normal grinding force, using several wheels. Initial findings show a fairly strong linear relationship between the Preston coefficient and the normal grinding force, although the

coefficient varies. This variation may be dependent on the higher order system dynamics, wheel loading, wheel wear, normal force characteristics and can be specific to a particular grinding wheel. Also indicated in Figure 4 is that a minimum force or threshold is needed for appreciable grinding to take place. This agrees well with Hahn and Lindsay. Clearly the Preston type model has validity as a basis for grinding, however modification to the model should improve the correlation to grinding experiments.

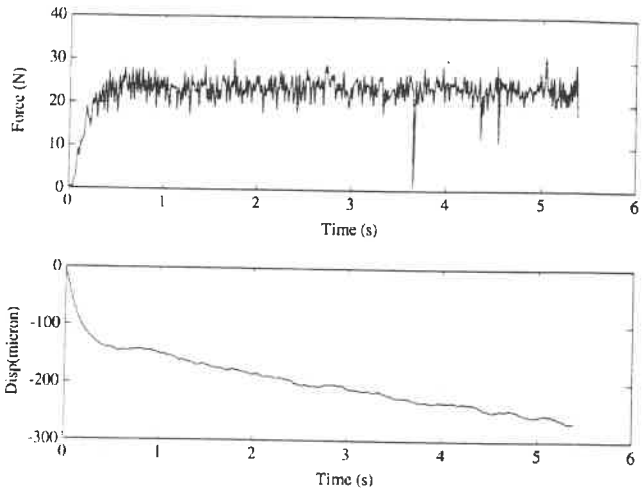

Figure 3. Controlled Normal Grinding Force and Resulting MRR

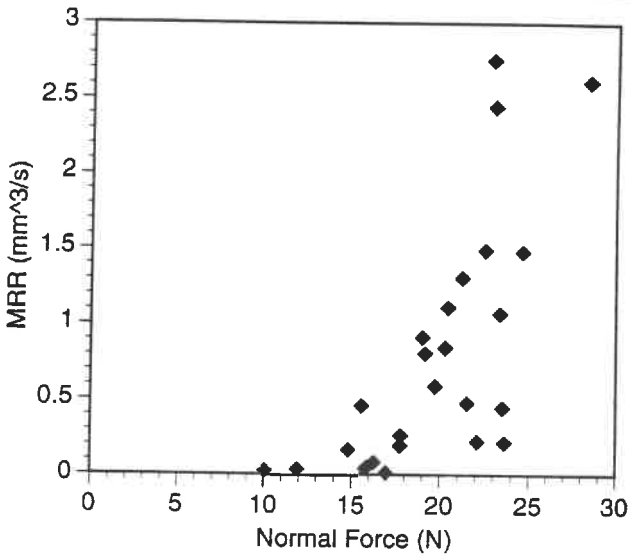

Figure 4. Preston Coefficient versus Normal Grinding Force.

COMPUTER SIMULATION OF TRANSMISSION AND SIDE SPUTTERINGS BY MONTE CARLO METHOD

Iwao Miyamoto, Akio Kuroda, and Kazuhiro Yoshimura

Department of Applied Electronics,
Science University of Tokyo, Noda, Chiba, 278 Japan

1. Introduction

When the ion beam machining is applied to fabricate ultra-fine and ultra-precision devices such as micro-machines, and ULSI self-standing ultra-thin foils will be used in the future. In such fabrication processes, one must take into account of transmission sputtering which is defined as the sputtering atoms from the rear surface of the target foil or the side surface of the ultra-fine pattern. Considerable experiments works, however, have been done on backward sputtering but little has been done on transmission sputtering, because experiments on transmission sputtering is very difficult. In this study, therefore, some characteristics of transmission sputtering have been investigated using Monte Carlo simulation method.

2. Monte Carlo simulation

2.1 Simulation model

For this Monte Carlo simulation or calculation, the following assumptions are introduced:

(a) Amorphous or polycrystalline thin foil materials,
(b) Elastic collision of two bodies,
(c) Inelastic collision among an ion and atoms of thin foil,
(d) Single scattering,
(e) Geometrical flat thin foil surfaces.

The behaviour of primary impinging ion (incident ion) and target atoms in the target can be affected or governed by various factors such as the atomic properties of ions and target atoms, bulk binding energy Eb or displacement energy Ed and surface binding energy Es in the target, and interatomic potentials. Recently, the Ziegler-Biersack-Littmark(Z-B-L) potentials [1] has been used frequently in the modeling of atomic collision processes. However, in the study a Thomas-Fermi (T-F) potential field is used for higher energy of impinging ions than E*, where E* is the critical energy of impinging ions at the boundary of the range of the Born-Mayer (B-M) potential field. At the energy E*, nuclear stopping power calculated with a T-F potential becomes equal to that with a B-M potential.

When an ion moves in a target at high velocities, the ion losses his energy due to ineleastic collision between the ion and atoms of target. Then, in this study energy loss of the ion was calculated from the same equation used by Kang et al [2].

Other important factors in modeling atomic collision processes are Eb (=Ed) and Es. If the struck or bombarded target atoms received kinetic energy in excess of a displacement (threshold) energy Ed, the atom would be knocked-out from its lattice site with a loss of binding energy Eb, selected as equal to the Ed. Without the loss of this binding energy energy Eb the number of recoil atoms set into motion, which in turn results in excessive sputtering yield values. Displacement energy Ed of various materials have been obtained from experiments and culculation by Wehner [3] and Yamamura et al [4].

In this study, the equation deceloped by Yamamura et al was used, because calculated values coincide very well with experimetal values. Usually, the value Eb of the target was set equal to half of the value of Ed or equal to the value of Us. In this study, the Eb was set equal to the sublimation energy Us of the target.

If the least scattering angle ϕ_{min} is set at a constant value of 2°, the total scattering cross section σ_T happens to be larger than the mean cross sectional area of the target atom $\pi(\ell/2)^2$, where ℓ is the mean distance between target atoms randomly located. Therefore, by controlling the value of the ϕ_{min}, and σ_T must be determined not to exceed the value of $\pi(\ell/2)^2$.

2.2 Computer programing procedure

In this study, trajectories of the ion and target atoms during collision cascades in a semi-infinite plane were stored in main or auxiliary memory. Then the backward sputtering yield S, the forward sputtering yield (transmission sputtering yield) St and sideward sputtering yield Ss at an ion incidence angle and a target thickness can be obtained by searching the trajectry of the ion and struck target atoms, which are stored in merories.

3. Results and discussion

The dependence of the transmission sputtering yield St obtained with our code on foil tickness Tfis shown in Fig.1 along with results obtained experimentally by Robison [5]. As shown in the figure, the St depend upon the Tf and increase with decrease of the Tf. Above the Tf of 100 nm, the yield data obtained with simulation lie below the experimental data. However, both data are well fitted to each other at the Tf ranging from 50 nm to 100 nm. From the results it can be said that the code may be useful in fundamental studies of transmission or

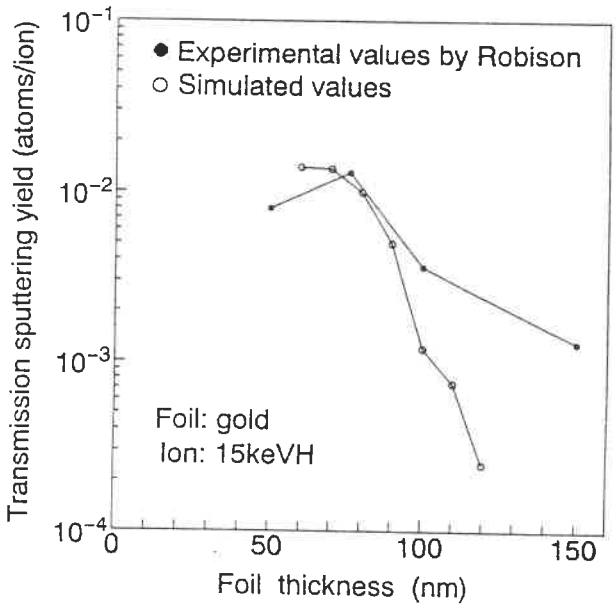

Fig.1 Foil thickness dependence of the St of gold foil bombarded with 15keV H ion

backward sputteing.

Fig.2 shows the simulation results of backward sputtering yields for gold foils bombarded with 60 keV silicon ion at various ion incidence angles. As shown in the figure, transmission sput-tering can be observed when the foil thickness becomes thinner than about 40 nm. The S of gold foil of a thickness under 40 nm increase with decreasing the Tf of gold foil. The backward sputtering yields increase as the ion incidence angle increases and approches a maximum value at an ion incidence angle of about 70°. Then the backward yield decreases as the ion incidenca angle increases. The angular dependence curves of the backward yields have the same general tendency regardless the thickness of the gold foil.

Fig.3 shows the simulation results of forward sputtering or transmission sputtering yields St for gold foils bombarded with 60 keV silicon ions at various ion incidence angles. As shown in the figure, when gold foils were bombarded at a normal ion incidence angle, the St of gold foils of thickness ranging from 40 nm to 6 nm increase with decreasing thickness of gold foil and the St value of gold foil of thickness under 4 nm decrese with decreasing the thickness of gold foil. When the thickness of a gold foil is thicker than 10 nm, the St decrease monotonically as the ion incidence angle increases. However, when the thickness of the gold foil becomes thinner

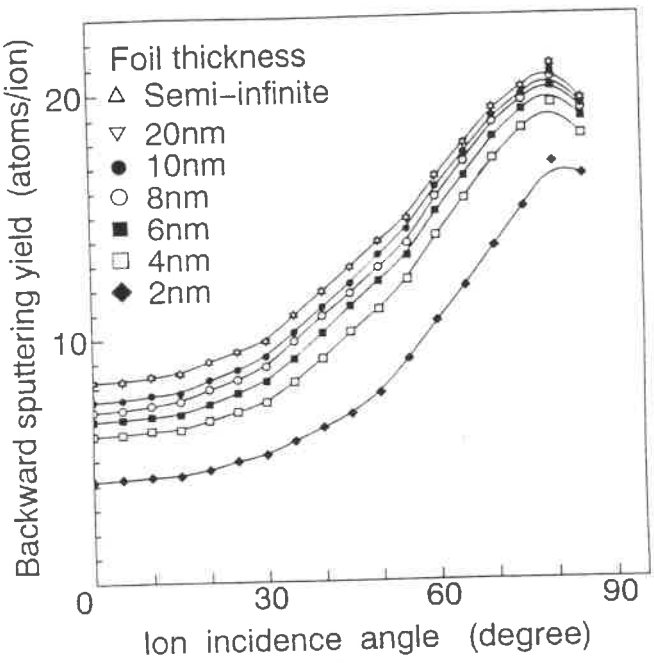

Fig.2 Angular dependence of S of gold foil bombarded with 60 keV Si ion

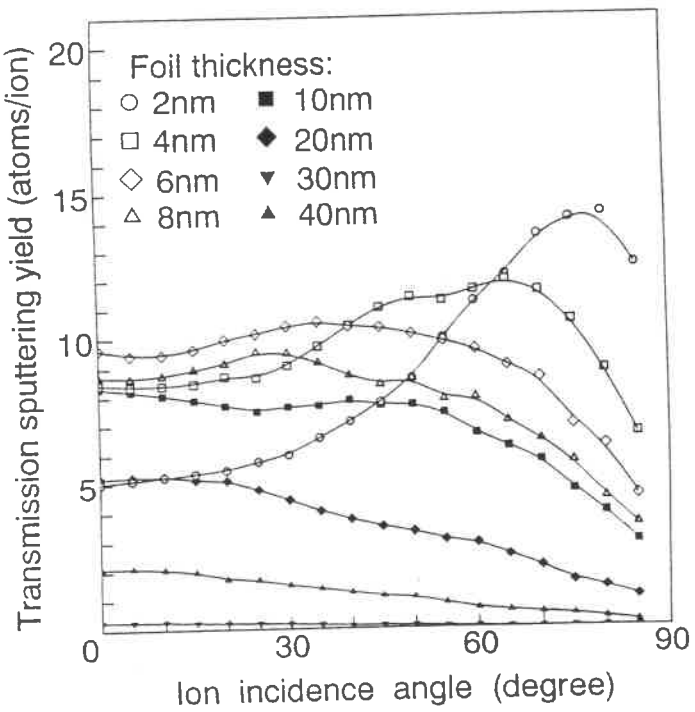

Fig.3 Angular dependence of St of gold foil with 60 keV Si ion

than 8 nm, the St increases as the ion incidence angle increases and approches a maximum value. The ion incidence angle at which the St becomes a maximum shifts to the higher ion incidence side with decreasing foil thickness. the reason why the trans-mission yield of gold foil of 2 nm thickness increases as ion incidence angle increases seems to be due to the increase of the effective range (cascade length) of ion in the gold target.

Fig.4 shows the dependence of the side sputtering yields of the silicon pattern on the distance D which is defined as the interval between the pattern edge and impinging point of ion. As shown in the figure, the yield Ys has a maximum at the D of 1 nm and decreases with increasing the D. The results indicates the possibility of rounding of the sharp edge of the pattern due to side sputtering.

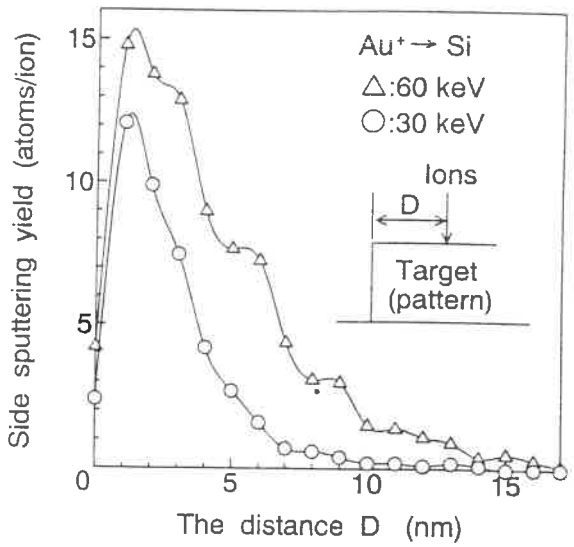

Fig.4 Dependence of the Ss upon the distance D

5. Conclusion

When a gold thin foil was bombarded with 15 keV H ions, the transmission sputtering yields obtained by the Monte Carlo Simulation method coincide with the experimental results by Robinson et al.. When the gold thin film was bombarded with 60 keV Si ions, results obtained by the Monte Carlo method shows that sputtering yields and transmission sputtering yields depend on the thickness of the thin foil and the transmission sputtering yields also depend on the ion incidence angle. Namely, when thickness of the thin gold foil becomes thiner than 10 nm, the sputtering yield decreases with decreasing the foil thickness and when foil thickness becomes thiner than 50 nm, the transmission sputtering yields incerases with foil thickness to a maximum at 6 nm, and then decreases with foil thickness. When the silicon pattern was bombarded with 60 keV Au ions, the side sputtering yield Ys has a maximum at the distence D of 1 nm and decreases with increasing the D.

References

1) J. F. Ziegler et al., in T. Takagi (ed.), Proc. Int. Ion Engg. Cong. (ISIAT '83 & IPAT '83), Kyoto (1983) 1861.
2) H. J. Kang et al., Jpn. J. Appl. Phys., 24 (1985) 1409.
3) G. Wehner, Phys. Rev., 93 (1954) 633.
4) Y. Yamamura et al., Rad. Effect, 55 (1981) 49.
5) C. H. Robison, J. Appl. Phys., 39 (1968) 3441.

FINITE ELEMENT MODELING OF ULTRA PRECISION MACHINING OF COPPER

B.C. Rao and R.X. Gao
Institute of Micromanufacturing
Louisiana Tech University
Ruston, LA 71272

I. INTRODUCTION

In recent years, the ultra precision cutting technique has been used extensively for the machining of small and delicate non ferrous workpieces to a high degree of surface finish and close tolerances. This is mainly due to the significant advances in machine tools and controls technology that make the technique less tedious. Despite its widespread utilization, the physics of micro machining at very small depths of cut is not well established due to the complexities of the deformation process. Unlike conventional machining, micro machining involves extra expenditure of energy that is not responsible for metal cutting [1]. As a result, the stress and temperature variation around the tool edge is different from conventional machining. Although closed formed solutions have been obtained for the forces and temperatures in micro domain [2], their use is limited by the assumptions made. The efficiency of the ultra precision machining process may be greatly improved by incorporating real time features in a general predictive model. With the advent of numerical tools like the Finite Element Method, it is possible to overcome the computational difficulties and model limitations associated with analyses for micro machining.

This paper presents the FE analysis of ultra precision machining of a 101 oxygen free copper workpiece to evaluate the distribution of the von Mises stress in the workpiece and the chip. For simplicity, plain strain conditions have been assumed by selecting an orthogonal diamond tool with a 0^0 rake and flank clearance of 6^0. The tool used has a edge radius of 0.3 μm and a flank workpiece contact length of 0.3 μm. The workpiece was fed at a speed of 7.2 m/min. against the diamond tool. Modeling was carried out by splitting the tool–chip interface into two regions to account for plowing. Emphasis has been given to the existence of low sliding friction conditions at all the tool–workpiece contact regions. The flow results obtained were elucidating and give a good insight as to the improvements required in the tool control system and design of precision machine tool elements.

II. THEORETICAL BACKGROUND

As shown in Fig. 1, when the depth of cut is of the order of the cylindrical cutting edge, the tool tends to plow through the workpiece material and there is marked rubbing at the flank–workpiece interface. Hence the forces acting on the cylindrical cutting edge and flank–workpiece area can no longer be neglected. This in turn increases the radial force, making it greater than the tangential cutting force. Thus the specific energy has to account for plowing and flank–work interaction in addition to shearing along the shear plane and friction on the rake face. It should also be noted that in micro machining the force acting on the tool–chip interface is very

small when compared to conventional metal cutting and with decreasing depths of cut, it reduces to zero.

With the depth of cut approaching the edge radius, the definition of a shear plane is somewhat different. It tends to extend from one end of the cylindrical cutting edge to the point on the chip intersecting with the workpiece. Hence the chip starts from one end of the cylindrical edge, and departs some where near to the other end of the cylindrical edge.

As far as the heat transfer problem is concerned, the distribution of thermal energy is different from conventional machining. This is due to the presence of a third heat source at the flank–workpiece interface and the splitting of the tool–chip interface into two distinct regions. Therefore there is some amount of heat transfer between the individual regions of the tool–chip interface in addition to the heat transfer taking place between the tool–chip interface as a whole and the flank–workpiece interface. With the primary shear zone, the secondary shear zone, and the flank–work interface being very near to each other, the temperatures encountered at the tool–workpiece contact zones may be high.

III. FINITE ELEMENT MODELING

To model the mechanics of micro machining, a depth of cut of 0.3 μm was selected. The depth of cut along with the pre estimated chip thickness were incorporated in the initial or undeformed finite element mesh as shown in Figs. 2 and 3. The workpiece material is 101 oxygen free copper and the tool is a diamond bit brazed to a steel shank. For simplicity, plane strain two dimensional condition was assumed with the width of cut being sufficiently larger than the depth of cut. The cylindrical cutting edge was approximated to a negative rake tool. The undeformed workpiece, shear zone, and the chip were meshed separately and later merged. Due to the low friction conditions (μ =0.03) existing between the tool and the workpiece, there is no possibility of a built up edge formation in diamond machining of copper. However a certain amount of the workpiece material is assumed to adhere to tool tip to facilitate motion of deformed mesh. Based on the procedures outlined in [3–5], the mesh consists of 500 isoparametric 4 node 2D PLANE elements and 33 1 node GAP elements defined within the COSMOS package [6]. It can be seen that the upper portion of workpiece is displaced horizontally to account for the intense compression the elements will experience on moving towards the tool. Note that the upper portion of the workpiece is also refined to obtain better deformation plots.

After defining the initial mesh, boundary conditions were specified to model diamond machining of copper. The tool as a surface was constrained to move in the horizontal direction. Both, upper and lower portions of the workpiece were merged at points away from the cylindrical edge. The tool was represented as a rigid surface due to the fact that diamond is extremely hard when compared to copper. As far as the constitutive deformation laws of the workpiece are concerned, a linear law was assumed. independent of the temperature. To simulate the formation of a chip, a few nodes ahead of the tool tip were unconstrained in an attempt to allow the chip flow up the rake face and the new workpiece to move horizontally. After all the boundary and material definitions, the modeling was performed by subjecting the initial mesh to a quasi static finite element analysis. Here the whole of workpiece was moved incrementally in the horizontal direction against the rigid tool surface at a speed of 7.2 m/min.

V. RESULTS AND DISCUSSION

Quasi static FEA was performed by moving the undeformed workpiece incrementally against the cylindrical cutting edge a total distance of 150 nm. The parting of the chip and workpiece at the tool tip depends on the ease of chip formation and not on any particular governing law as given in [3–5]. The deformation and stress plots for the time step of 1.2×10^{-6} sec. are shown in Figs. 4 and 5. As seen from the deformation plot, the geometry of the chip has not changed much, but it has displaced slightly in the vertical direction. This is due to the fact that the undeformed mesh has to slide on the cylindrical edge before sliding on the rake face. The distribution of the von Mises stress (in N/nm^2), as shown in Fig. 5, illustrates the presence of relatively higher stresses in the primary shear zone and some distance ahead of tool tip. Also note the development of residual stresses in the lower portions of the newly generated workpiece. The portion of the chip on the rake face has lower stress values excepting areas near to the primary shear zone. The analysis was performed with smaller time steps to avoid convergence related problems. In fact, work is in progress to achieve larger deformations with smaller increments.

V. CONCLUSION

A quasi static finite element analysis of the orthogonal ultra precision machining of copper has been conducted. An initial chip geometry was incorporated in the initial finite element configuration and the cylindrical edge was approximated to a negative rake tool. Machining was simulated by incrementally displacing the workpiece against the tool and allowing the deformed and undeformed portions of the workpiece to seperate near to the cutting edge. All material properties were assumed to be linear and independent of temperature. Due to convergence problems associated with GAP elements, a comparatively lower total displacement value was provided. Both the von Mises stress distribution and deformed mesh plot were obtained and discussed for the second time step. It was seen that the areas near to the primary shear zone and cylindrical cutting edge were highly stressed. Also there was no appreciable change in the chip geometry except a slight vertical displacement. Efforts are in progress to expand and modify the above model. This in turn will be helpful in achieving a better control over the ultra precision cutting process.

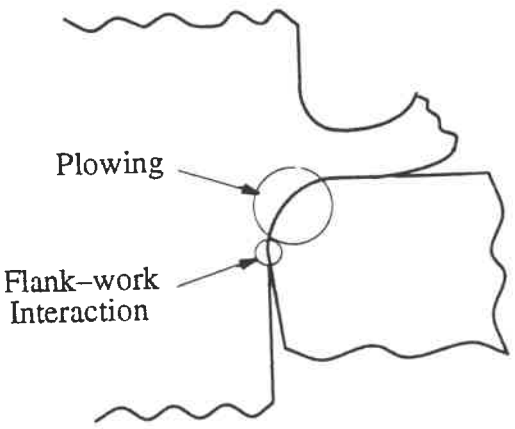

Figure 1: Micro machining.

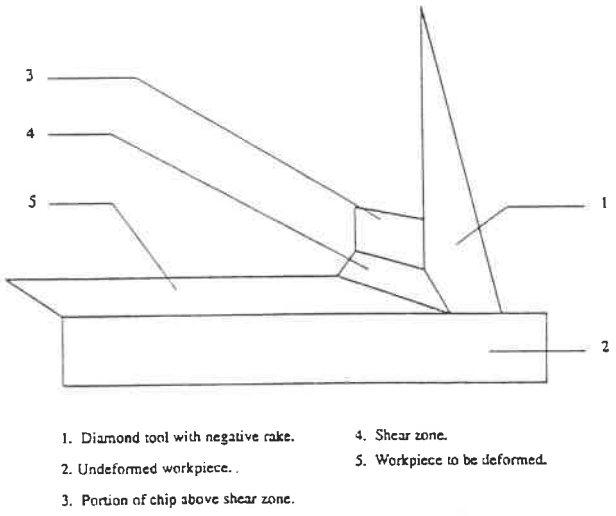

Figure 2: Outline of finite element model.

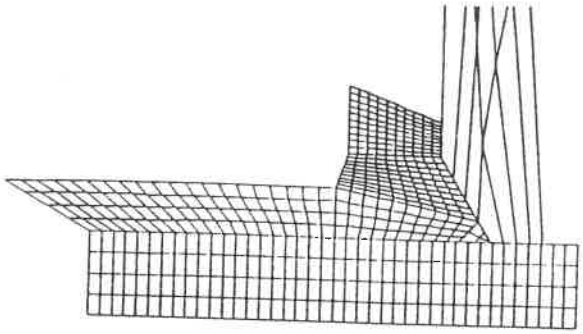

Figure 3: FEM of micro machining.

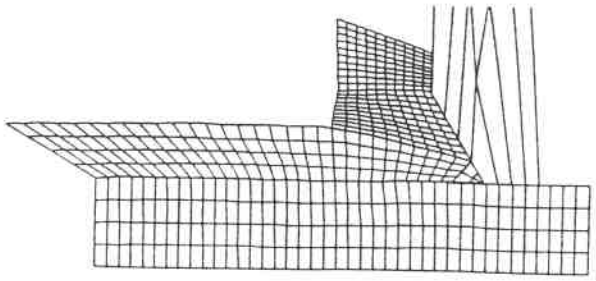

Figure 4: Deformation plot.

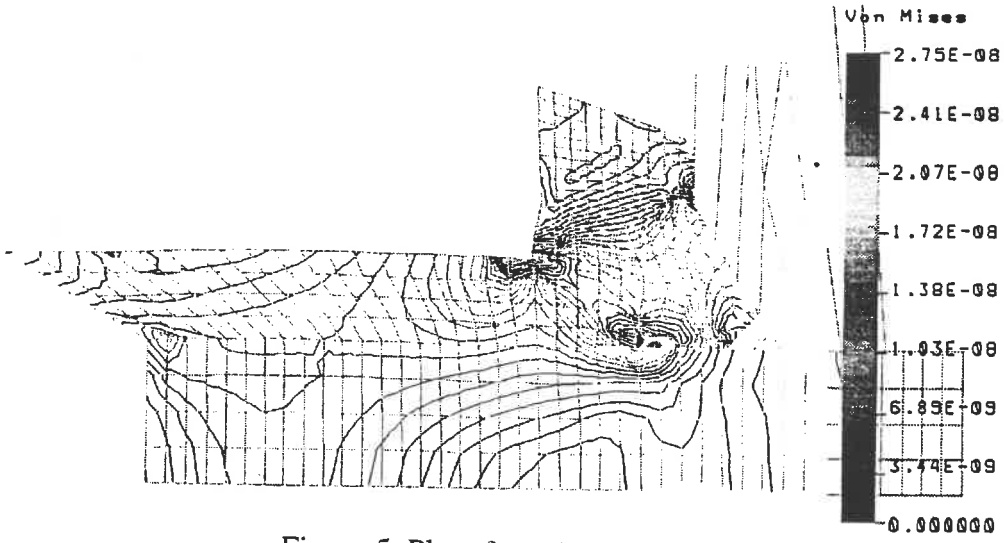

Figure 5: Plot of von Mises stress.

VI. REFERENCES

[1] D.C. Lucca, R.L. Rhorer, and R. Komanduri, "Energy Dissipation in the Ultra Precision Ma chining of Copper," Annals of the CIRP, Vol. 40, pp. 69–72, 1991.

[2] B.C. Rao, R.X. Gao, C.R. Friedrich, and R.O. Warrington, "A Mathematical Model for On–line Measurement of Micro Channel Geometry in Diamond Machining Technique," *Proc. ASPE 8th Annual Meeting*, pp. 507–510, Nov. 1993.

[3] K. Komvopoulos and S.A. Erpenbeck, "Finite Element Modeling of Orthogonal Metal Cut ting," *ASME Journal of Engineering for Industry*, Vol. 113, pp. 253–67, Aug. 1991.

[4] J.S. Strenkowski and J.T. Carroll, "A Finite Element Model of Orthogonal Metal Cutting," *ASME Journal of Engineering for Industry*, Vol. 107, pp. 349–54, Nov. 1985.

[5] K. Iwata, K. Osakada, and Y. Terasaka, "Process Modeling of Orthogonal Cutting by the Rig id–Plastic Finite Element Method," *ASME Journal of Engineering Materials and Technology*, Vol. 106, pp. 132–138, 1984.

[6] COSMOS/M User Guide, Structural Research and Analysis Corporation, Santa Monica, California, May 1993.

A Practical Guide To Theoretical Modeling Of Contour Grinding

Gene E. Storz II, Thomas A. Dow
Precision Engineering Center
North Carolina State University, Raleigh, NC

Introduction

As the demand for precision components increases, manufacturers must develop newer and faster methods to fabricate materials with improved performance. Of these, precision contour grinding has come to the forefront as a method to combine the speed and form accuracy of grinding techniques with the nondamaging material removal of polishing.

To optimize the precision grinding process, an understanding of the process parameters and their effect on surface quality must be developed. Extensive development has led to methods for obtaining high quality surfaces on specific materials. But until recently, a model to examine the process and visualize the creation of a chip for different grinding conditions was not available. If the formation process of the chip can be formalized, predictions for surface roughness and surface damage can be made as well as optimizations for desired part characteristics. The program developed at the Precision Engineering Center (PEC) to perform these tasks is called the Virtual Chip Model [1] and is the basis for the following formulations.

Several models related to contour grinding are described in this paper. These include a generalized 3D model of the chip geometry for different contour grinding layouts, and a simplified means of determining the theoretical surface roughness and the theoretical maximum chip thickness over the finished surface. A short explanation will be given for each of these methods. An example combining these theories in a practical application is also shown.

Contour Grinding Geometry

Two different grinding layouts exist for precision contour grinding: rotary and raster. In rotary grinding, the grinding wheel and part are rotating and the wheel feeds towards the center of the part. In raster scan grinding, the grinding wheel is located on a moving bridge that raster scans across the part. The grinding parameters used for the rotary and raster grinding layouts are shown in Table 1.

Parameter / Symbol		Rotary	Raster
Wheel Radius	R	mm	mm
Nose Radius	A	mm	mm
Wheel Speed	Nw	RPM	RPM
Part Diameter	D	mm	mm
Part Speed	Np	RPM	
Crossfeed Rate	cf	mm/min	
Crossfeed Dist.	xf		mm
Upfeed Velocity	uv		mm/sec
Depth of Cut	dc	µm	µm

Table 1: Standard operating conditions for rotary and raster type grinders

The geometries shown in Table 1 can be simplified in a single generalized geometry shown in Table 2 for use in theoretical calculations. Equations (1) through (3) are

used for rotary grinding and Equation (4) for raster grinding. These equations simplify the geometries by changing the rates at which the wheel and part move into distances the wheel moves relative to the part in the upfeed and crossfeed directions. The relative speeds are also normalized into a speed ratio called the phase.

$$uf = \frac{\pi * N_p * D}{N_w} \quad (1) \qquad xf = \frac{cf}{Np} \quad (2)$$

$$ph = \frac{N_w}{N_p} - INT\frac{N_w}{N_p} \quad (3) \qquad uf = \frac{uv}{Np} \quad (4)$$

Parameter	Description	Units
R	Wheel Radius	mm
A	Nose Radius	mm
uf	Upfeed	mm
xf	Crossfeed	mm
ph	Phase	radians
d_c	Depth of Cut	μm

Table 2: Grinding parameters for simplified geometry

Theoretical Surface Roughness Curves

The Virtual Chip Model [1] was used to calculate the surface roughness for a wide variety of grinding conditions. These results were then normalized using the maximum surface roughness from Equation (5) and plotted as a function of phase in Figure 1. A Pattern Index ,C, defined in Equation (6) was created to correlate the shape of the curves to the geometric grinding parameters. To use Figure 1, the maximum surface roughness is multiplied by the point on the characteristic curve at the appropriate phase to yield an estimate of the geometric surface roughness. Equation (7) provides an estimate of the minimum surface roughness as a function of the pattern index.

$$RMS_{max} = \sqrt{\frac{uf^4}{720 * R^2} + \frac{xf^4}{720 * A^2}} \quad (5)$$

$$C = \log\frac{R}{A} - 2 * \log\frac{uf}{xf} \quad (6)$$

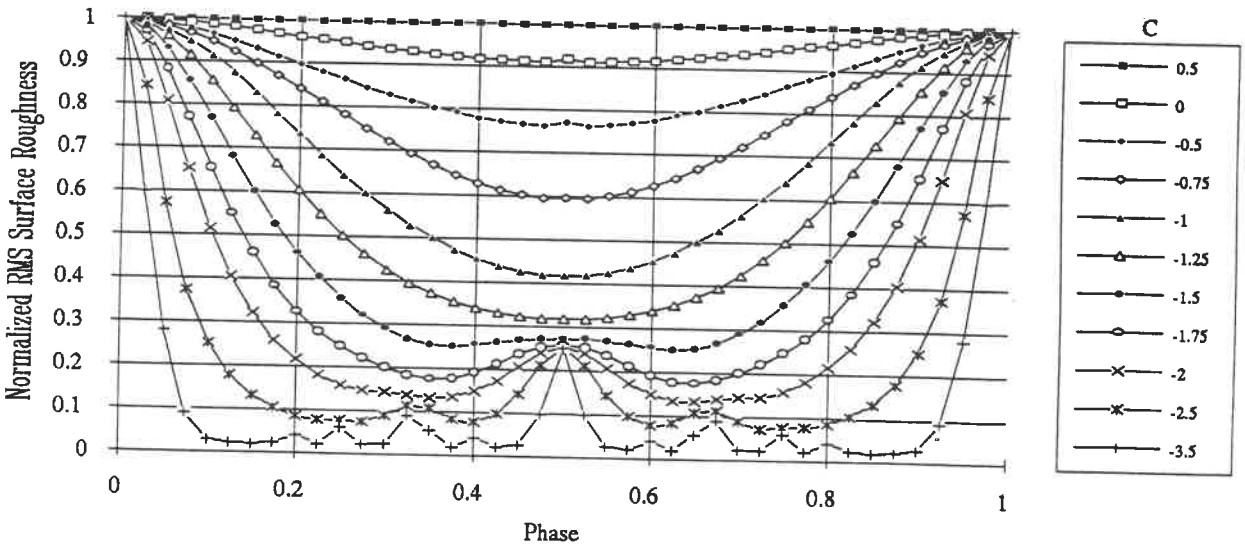

Figure 1: Theoretical surface roughness curves (Storz Curves) for contour grinding

$$\log RMS_{norm_{min}} = -0.0348 + .17855 * C - 0.165 * C^2 - 0.02374 * C^3 \quad (7)$$

Theoretical Surface Chip Thickness Curves

The maximum chip thickness over the finished surface (surface chip thickness) is the maximum thickness over the region of the chip.that defines the edge of the finished surface. This region will remain untouched by future passes of the grinding wheel. If the thickness at this location exceeds the critical chip thickness of a material, damage will be visible in the final surface. Therefore, to predict the onset of damage, it is necessary to gain a more complete understanding of the surface chip shape and the effect of different grinding conditions on the local thickness. The Virtual Chip Model was used to determine the chip shape and the magnitude and location of the maximum thickness. A set of curves similar to Figure 1 was created and equations developed to predict the maximum and minimum thickness.

Equations (8)-(10) show the maximum and minimum surface chip thickness. Equation (8) returns the maximum surface chip thickness as a function of the grinding conditions using the offset value from Equation (9). The offset changes with the ratios of the upfeed to crossfeed and wheel radius to nose radius. The offset shown in Equation (9) are valid for conditions where the ratios of upfeed to crossfeed and wheel radius to nose radius are greater than 1. A minimum surface chip thickness shown in Equation (10) is a function of the pattern index and is good for all grinding conditions.

$$\log t_{s_{max}} = 2 * \log \frac{uf^2}{xf} - \log \frac{R^2}{A} + \text{offset} \quad (8)$$

$$\text{offset} = 1.4851 * \log \frac{R}{A} - 2.9723 * \log \frac{uf}{xf} + 2.9574 \quad (9)$$

$$\log t_{norm_{min}} = -0.0649 + 0.27538 * C - 0.08794 * C^2 \quad (10)$$

Application Of Models

The surface roughness and chip thickness models can be applied individually to predict the geometry of a particular grinding operation. Such information is useful but when these models are combined, greater insight into the details of the process are obtained. As an example these models will be applied to the small form grinder (SFG) used at the PEC.

Figure 2 shows how the maximum surface roughness and maximum surface chip thickness varies with different grinding conditions on the SFG. Each curve was generated by varying the upfeed at a specific value for the crossfeed and wheel size. The maximum upfeed is 0.043 mm located at the far right of each curve and decreases by 0.002 mm at the left. To apply the model, the critical chip thickness of the material and a desired surface roughness must be known. If a material had a critical chip thickness of 20 nm and a required surface roughness of 2 nm, then the bounding box in Figure 2 would give the range of possible grinding conditions. A crossfeed of 0.01, 0.007, or 0.005 mm could be used with a range of upfeeds depending on time requirements and available speeds.

In addition to the usefulness of these models to select appropriate grinding conditions, they may also be used to transfer similar grinding conditions from one machine to another.

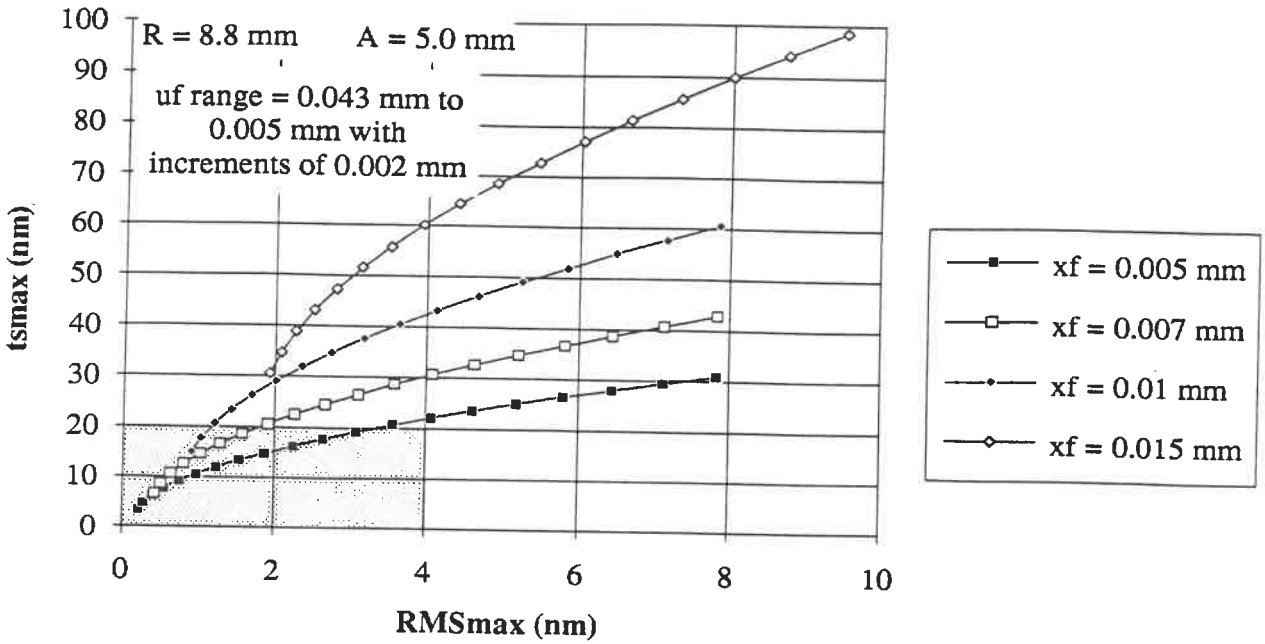

Figure 2: Maximum surface chip thickness versus maximum surface roughness for the SFG at varying upfeed and crossfeed distances

Table 5 shows the geometry of the SFG and the large form grinder (LFG) used at the PEC.

Grinder	R (mm)	A (mm)	uf (mm)	xf (mm)
SFG	8.8	5	0.0616	0.0105
LFG	38.1	21.65	0.1282	0.0218

uf / xf	R / A	C	RMS_{max} (nm)	t_{smax} (nm)
5.9	1.76	-1.30	16.103	92.0
5.9	1.76	-1.30	16.103	92.0

Table 5: Change of parameters on LFG to simulate grinding conditions on the SFG

Conditions on the SFG can be simulated on the LFG if the conditions are chosen such that the pattern index, RMS_{max}, and t_{smax} have the same value. These conditions will produce the same variation in shape with phase and therefore the same resulting surface.

Conclusions

Several new theories have been proposed to predict the surface roughness and fracture in a grinding operation. Conditions can be selected to optimize the grinding process given a critical chip thickness and a required surface roughness. To make an exact prediction as to the nature of these quantities, a phase "lock-in" value will be required. Although a method for determining this value has not been developed, it is unnecessary for applying the procedures related to the maximum surface roughness and surface chip thickness shown here.

References

1. Storz, G.E., *"Theoretical Modeling Of Contour Grinding,"* MS Thesis, North Carolina State University, 1994.

ION FIGURING OF SMALL OPTICS

Thomas W. Drueding, Thomas G. Bifano
Aerospace and Mechanical Department
College of Engineering, Boston University
Boston, MA 02215

Steven C. Fawcett
Optical Fabrication Branch, EB53
National Aeronautics and Space Administration
Marshall Space Flight Center, AL 35812

An important step in the fabrication of an optical component involves the imparting of a precise contour on the optic, which can be expensive and time consuming. Ion beam figuring is the imparting of a contour on an optical component by removing material through the impingement of a broad beam of accelerated neutral particles. This technique provides a highly deterministic method for the final precision figuring (or correcting) of optical components with advantages over conventional methods. The high predictability allows for rapid convergence in figuring, resulting in significant time and cost savings. And unlike grinding, polishing and lapping, ion figuring is non-contacting and so avoids several problems including: edge roll off effects, tool wear, and loading of the work piece. It has previously been demonstrated that ion figuring is effective for the correcting of large optical components [1][2]. These implementations typically use the process for final figure correction on meter class optical components. The work discussed here is the development of the Precision Ion Machining System (PIMS) at NASA's Marshall Space Flight Center, designed for the processing of smaller (less then 10 cm diameter) optics. The facility has recently been completed and initial experiments were successful in using a Kaufman type ion source to figure 8 cm diameter fused silica and silicon carbide samples. The experiments involved correcting flat samples, and imparting shallow spherical and aspherical contours. The process has a wide variety of commercial application in the areas of optics manufacturing as well as other potential uses in fields where components are required with precision figure and surface tolerances.

In the figuring process, a surface contour map of the sample is measured using a ZYGO Mark IVxp interferometer. The desired surface contour is then subtracted from the map to give a map of the material to be removed. The ion beam removal is assumed spatially and temporally invariant, with a Gaussian removal distribution. Specific figures are achieved by rastering the beam over the workpiece at varying velocities. The removal is used to determine the velocities by a unique deconvolution algorithm developed for this application[3]. Using a series expansion to represent the removal map, the algorithm provides a series expansion for the velocities by relating the expansions and the statistical moments of the static removal rate. In the PIMS, the beam is rastered over the sample in concentric circle paths, and angular velocities are varied within each annulus to account for non-axial symmetric removal. In the actual system the beam is held fixed and the workpiece is moved under the beam. Immediately available translational motors are not capable of the necessary velocities but the rotation motor can achieve the required tangential velocities. Using the circular path configuration also allows for figuring larger components

Case	Target Profile	Part #	Initial rms	Final rms	Convergence
	Fused Silica (3 cm Beam Width)				
1	Parabola (radius: 100,000 mm)	FS2	1138 nm	80 nm	14.20
2	Parabola (radius: -100,000 mm)	FS8B	1071 nm	434 nm	2.47
3		FS8	1170 nm	380 nm	3.08
4		FS8	858 nm	359 nm	2.39
5	Spehere (radius: 100,000 mm)	FS6B	2279 nm	419 nm	5.44
6		FS6B	817 nm	256 nm	3.19
7	Saddle (radius: 160,000 mm)	FS7B	933 nm	638 nm	1.46
8		FS9	934 nm	456 nm	2.05
9	Saddle (radius: 140,000 mm)	FS10	934 nm	261 nm	3.58
			Average		4.21
	Silicon Carbide (3 cm Beam Width)				
10	Saddle	SC2	982 nm	324 nm	3.03
	Fused Silica (1cm Beam Width)				
11	Flat	FS2B	59 nm	24 nm	2.44

Table 1. Results of ion beam figuring 8 cm fused silica and silicon carbide samples. An Ion Tech 3 cm beam created parabolic, spherical, and saddle figures. In addition, a 1 cm aperture on the beam was used to correct a flat fused silica sample. The initial and final rms deviation from the desired figure is shown for each case. The convergence ratio represents the effectiveness of the process and is the inital over final rms deviation.

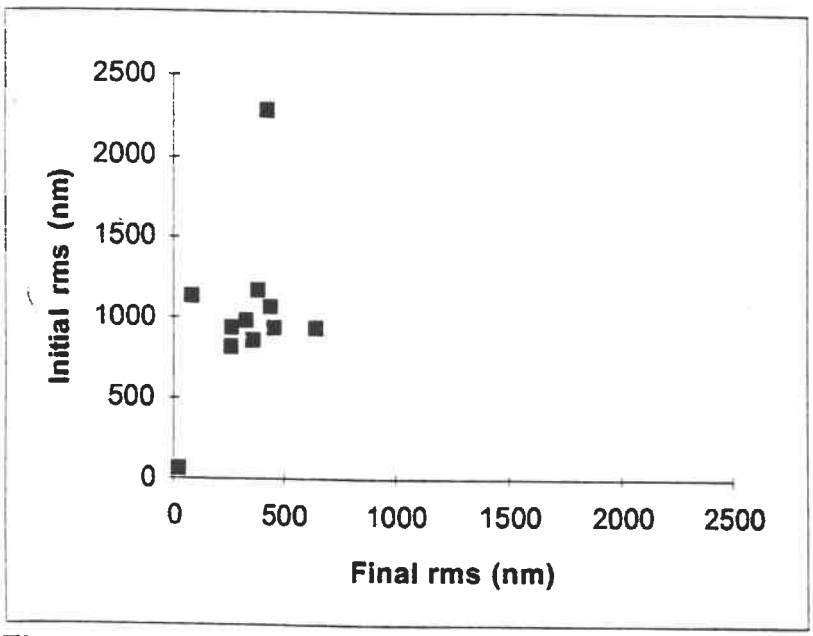

Figure 1. Results of ion figuring, displaying final rms figure error vs initial rms figure error for all eleven cases. The slope from the origin is the convergence ratio of each case.

because the workpiece is rotated under the beam, requiring the workpiece to be translated only half the diameter.

The static removal rate and distribution of the ion beam is determined by positioning the beam over the center of a flat sample for a known amount of time. The resulting removed shape is measured on the interferometer and the rate is calculated by dividing by the duration of the beam operation. Several methods of linear curve fitting can be used to match a Gaussian function to the resulting shape, but manual tweaking of the Gaussian parameters produces the most useful results. The statistical moments of the function are required to perform the deconvolution in determining the raster velocities. The function distribution is constant for a set of ion source parameters but a removal rate must be determined for each material.

Initial experiments were conducted involving pre-polished 8 cm diameter fused silica and chemical vapor deposited silicon carbide samples. The results of the process for eleven cases are shown in Table 1 and Figure 1. Using a 3 cm diameter Ion Tech ion source, nine fused silica samples were figured to spherical, parabolic (concave and convex), and saddle shapes. The saddle shapes demonstrated non-axial symmetric corrections. Initial deviations from the desired figures ranged from 1000 to 2000 nm rms and the ion figuring process corrected the figures to an average of 365 nm rms error. The average convergence ratio over nine cases was 4.21. For comparison, some polishing methods only provide convergence ratios below 2. None of the samples experienced significant increases in surface roughness. The samples were expected to contain little subsurface damage that would be exposed and exacerbated during matching [4]. The best case involved imparting a shallow sphere(4 μm of sag) on a flat sample that had an initial surface error of 1138 nm rms error from the sphere reduced to 80 nm rms. The final shape is shown in Figure 2. The process took a total of 121 minutes of beam operation and the surface roughness before and after machining was 10 angstroms rms. A saddle figured on a CVD silicon carbide sample resulted in improving the figure error from 982 to 324 nm rms.

In addition, a small 1 cm aperture was installed in the ion source to obtain higher frequency corrections. A simple non-magnetic stainless steel annulus was used as for the aperture. It was necessary to reduce the beam current, therefore the peak removal rate, in order to achieve a stable beam with the aperture in place. The resulting beam removal was still Gaussian shape but it had greatly reduced volumetric removal rates both because the overall width (footprint) was smaller and the peak removal was reduced. This reduced removal rate makes the aperture source only useful for small (less than 100 nm rms) corrections. The process reduced an initial surface error of 59 nm rms to 24 nm rms on a flat fused silica sample.

The results demonstrate the feasibility of using the PIMS for final figuring of small optics with no appreciable increase in surface roughness. Ion figuring can not currently be utilized to improve the finish of optical components, and will uncover and open up subsurface damage. The technique is used to complement standard polishing and grinding methods that provide contour accuracy of the component to within 4 μm of the final specification, and the component is finished to final surface roughness specifications. Subsequent ion figuring is used to improve the contour accuracy while maintain angstrom-level roughness. Finer corrections can be made with various apertured beam widths. The system currently uses concentric circle paths but other raster patterns will be tested. Specifically the PIMS provides reliable, rapid contouring or correcting of optical components.

References

[1] L. N. Allen and R. E. Keim. *Current Developments in Optical Engineering*, SPIE, 1168 (1989).
[2] S. R. Wilson and J. R. McNeil. *Current Developments in Optical Engineering*, SPIE, 818 (1987).
[3] T. W. Drueding, T. G. Bifano, and S. C. Fawcett, *Contouring Algorithm for Ion Figuring*, Submitted to Precision Engineering (1994).
[4] S. C. Fawcett, T. W. Drueding, and T. G. Bifano, *Neutral Ion Figuring of Chemical Vapor Deposited SiC*, Optical Engineering, March 1994.

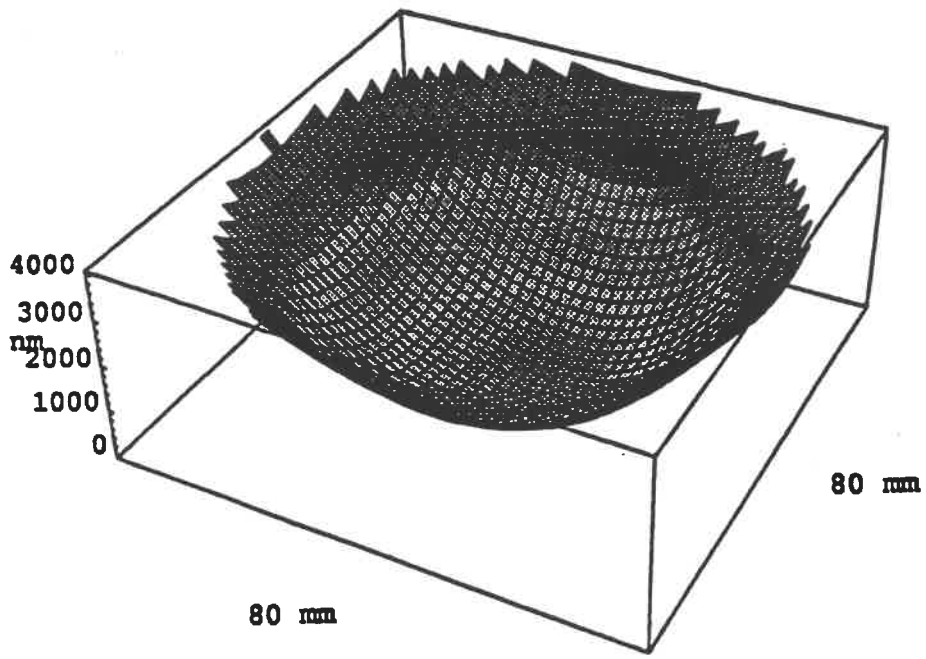

Figure 2. Final parabolic contour imparted on flat fused silica sample with 4 um sag.

Biochemical Machining of Plastics

Toshiaki Kaneeda*, Seiichi Yokomizo**, Akio Miwa**, Kazuta Mitsuishi**,
Yoshiyuki Uno***, and Hiroyuki Morioka*

* Okayama University of Science, 1-1 Ridai-cho, Okayama 700, Japan
** Industrial Technology Center of Okayama Prefecture, Imabo, Okayama 701-01, Japan
*** Okayama University, Tsushima-naka, Okayama 700, Japan

Key words: Biochemical machining, biodegradable plastics, removal process, micromachining, lipase, enzyme, filamentous fungus

1. Introduction

Plastics have many advantages compared with the metals on specific strength, specific weight, high corrosion resistance and so on, thereby a number of products are made from plastics. Plastic products and parts have spread all over the world, however, plastic home and industrial waste can hardly be degraded. Hence, disposals of the plastic waste have recently become an annoying problem in order to maintain clean environment of the earth. Some biodegradable plastics[1] have been developed corresponding to demands of waste-free plastic products. Biodegradable plastics can be degraded by microorganism or enzyme by means of cutting down the molecular chains. From machining point of view, this degradation action appears to be a kind of micro removal process at molecular chain size, therefore, biodegradable plastics could be biochemically micromachined by microorganisms or enzyme. A new removal process of biodegradable plastics has been developed here. This paper deals with biochemical machining of biodegradable plastics using neutral lipase and enzyme. A typical commercial biodegradable plastic "biopol"[2] was used as the workmaterial.

2. Experimental Procedures

2.1 Biodegradable Plastic "Biopol"

The biodegradable plastic served in this experiment was "biopol" (Zeneca Co.). This commercial biodegradable plastic is thermoplastic resin, as shown in Fig.1, being composed of 3-polyhydroxybutyrate (PHB) and 3-polyhydroxyvalerate (PHV). Mechanical properties of biopol depend upon the rate of PHV mol %. The biopol employed in this experiment involves 8 mol% PHV. Tensile tests were conducted in order to examine mechanical properties of the biopol at a crosshead speed v=50mm/min. The experimental results offered 24.3 MPa tensile strength and 10% fracture strain. Biopol is a type of normal chain polyester and produced by sugar fermentation of bacteria "Alcaligenes Eutrophus".

2.2 Preparation of Crude Enzyme Solution

To begin with the micromachining experiment, it is inevitable to find appropriate microorganisms or enzyme which have high performance of biodegradation ability. It is not elucidated what kind of microorganisms or enzyme is able to biodegrade biopol. At first, neutral lipase was tried to micromachine biopol cylindrical specimen as the tool. The biochemical machining

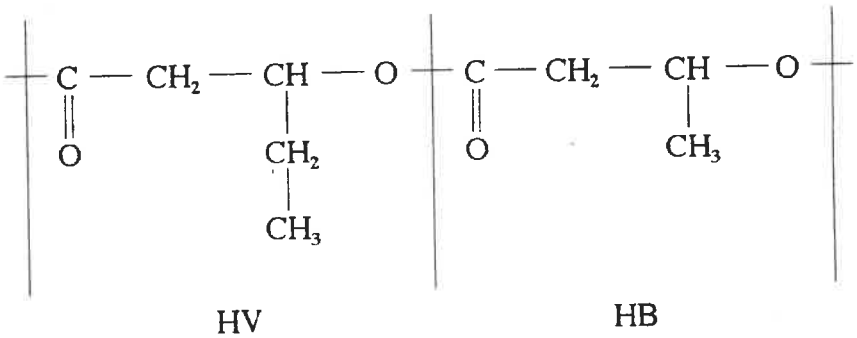

Fig.1 Structural formula of biopol

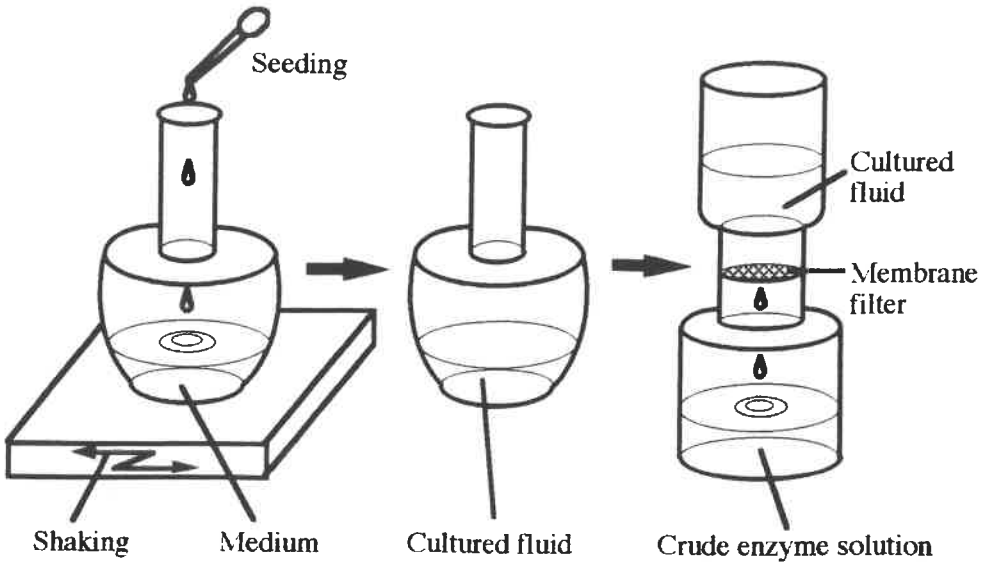

Fig.2 Preparation of crude enzyme solution

test results indicated that neutral lipase can biodegrade the biopol, however the removal volume for 24 machining hours was too small to detect. Hence, filamentous fungus, a typical mold, were selected as a tool in order to increase removal volume. The filamentous fungus collected in a soil was cultured in a medium. Then the medium included enzyme was sterile filtered in order to eliminate the filamentous fungus. Thus, crude enzyme solution was prepared. Buffer solution, activator and stabilizer were added to the crude enzyme solution to prepare reaction that has a role to biodegrade biopol as a tool.

Fig.2 shows a schematic diagram of preparation of the crude enzyme solution utilizing the filamentous fungus. A 100 ml medium shown in Table 1 in a flask was autoclaved at 121°C for 20 minutes. The filamentous fungus were seeded to the medium, and cultured at 30°C and 120cpm for 9 days. Then the cultured fluid was filtered by a membrane filter with 0.2 μ m mesh size, in order to eliminate any kinds of microorganisms. Crude enzyme solution without any molds, referred as "biochemical machining solution" hereafter, was prepared being capable of biodegrading biopol.

Table 2 shows components of the biochemical machining solution. The solution prepared was always stored in a refrigerator.

2.3 Biochemical Machining Experiments

The specimen has two types of shape. One is a cylindrical shape with a 2 mm diameter, while the other one is a 1 mm thickness plate. The latter was produced by press forming at 170°C and has a 10×40×1 mm dimension. Fig.3 shows a general view of biochemical machining experiment method. Biochemical machining experiment processes are as follows: the specimens

Table 1 Components of medium

Biopol	20.0g
$(NH_4)_2SO_4$	5.00g
KH_2PO_4	2.00g
$MgSO_4 \cdot 7H_2O$	0.25g
Yeast extract	0.25g
$CaCO_3$	0.30g
Mineral solution	1.00ml
Distilled water	1000ml

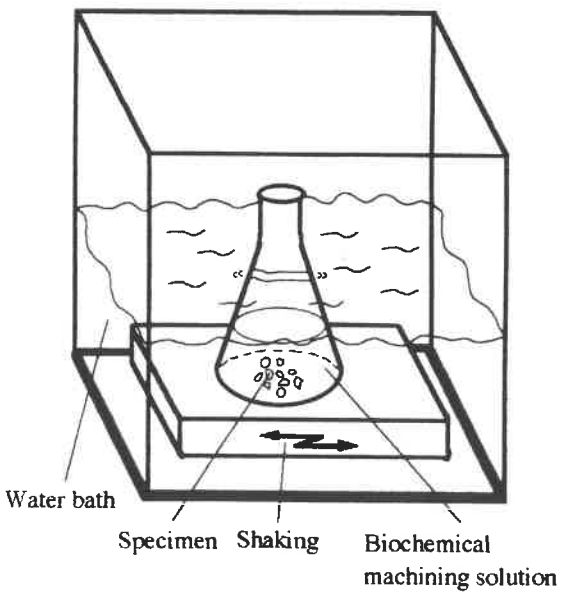

Fig.3 Biochemical machining experiment

having a 1 gram weight were put into a flask including the reaction. The reaction, namely the biochemical machining solution, is composed of buffer solution[3] for maintaining a constant pH value, Ca solution for activating enzyme, and crude enzyme solution. The volumes of three components are shown in Table 2. The biochemical machining experiments were conducted on the flask in a water bath with temperature control. The flask mounted on a shaker was oscillated at 120 cpm under a constant temperature. After the biochemical machining experiment, the specimen was cleaned by distilled water and dried in a desiccator for 24 hours. Then removal weight of the specimen biochemically machined was measured as a removal rate.

3. Experimental Results and Discussion

Enzyme reaction is influenced by pH and the temperature of the reaction, then pH and temperature effects on removal rates was investigated in order to find the maximum removal rate condition. All the data presented here were obtained from the cylindrical specimen. Biochemical machining results showed that the cylindrical biopol specimen could be biochemically machined by neutral lipase and filamentous fungus. The latter had much higher performance than the former on the removal rate. Then the experimental results shown hereafter came from those by the filamentous fungus as a tool.

Fig.4 shows pH effects of the reaction on the removal rate. The biochemical machining conditions are as follows: 30 °C temperature of the reaction, 120cpm shaking rate and 48 biochemical machining hours. The pH of the reaction was always regulated at a constant value by the buffer solution. The experimental results indicate that the maximum removal rate was provided at pH 6.0-7.5. The filamentous fungus can usually thrive under weak acid conditions, hence the enzyme from the filamentous fungus offers highly active under the same conditions. The pH 6.0-7.5 range at which the biochemical machining experiments presented the maximum removal volume is the same as that the filamentous fungus and the enzyme are remarkably activated at.

Fig.5 shows temperature effects of the reaction on the removal rates. The removal rates increased with the reaction temperature up to 45 °C, then decreased over 45 °C. Enzyme reaction usually activates with increasing of temperature, however enzyme loses activity over a certain temperature. The experimental results suggest that the maximum removal rate was obtained at 45 °C.

Fig.6 shows relationship between heat treatment temperature of the enzyme and the removal rate.

Table 2 Components of biochemical machining solution

0.5M Citric acid / trisodium citrate buffer [3]	40ml
0.1M Calcium chloride solution	5ml
Crude enzyme solution	5ml

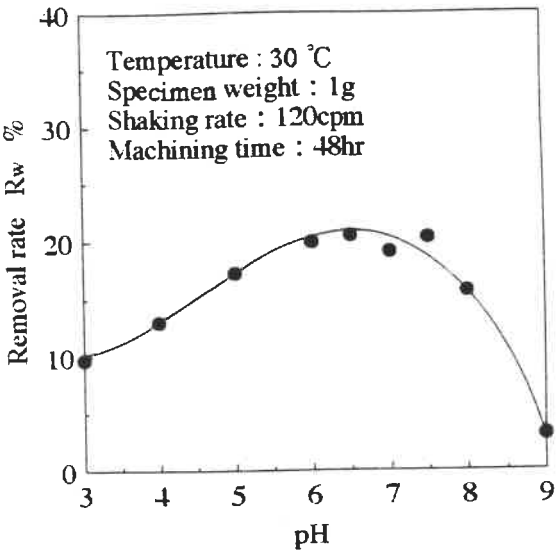

Fig.4 pH effects on removal rates

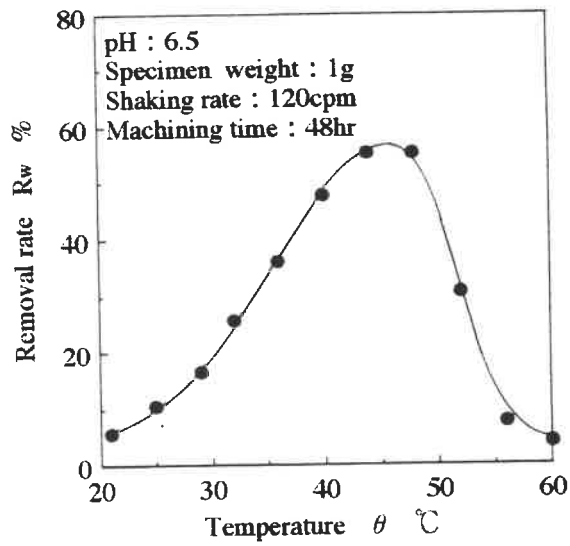

Fig.5 Temperature effects on removal rate

This relationship suggest the activity of the enzyme at the temperature from 40 °C up to 80 °C. The crude enzyme solution containing the enzyme was heat treated at the set temperatures for 15 minutes, then employed as the biochemical machining solution. The removal rates presented high constant values in under 45 °C heat treatment solution, however abruptly decreased in over 50 °C heat treatment solution. These results indicate this kind of enzyme can hold the activity up to 45 °C. The maximum removal rate was obtained at 45 °C, over which the enzyme loses the activity.

Fig.7 shows the relationship between the biochemical machining time and the removal rates. The removal rates proportionally increased with the machining time. Activity of enzyme definitely lowers with the life time because fatty acid generated in biodegrading a biopol specimen reduces pH of the reaction. The same kinds of experiments were conducted for the biopol plates. The experimental results presented about 50 % reduction in the removal rate for 24 hours.

The reason why the plates have larger removal rate than that of cylindrical specimens appears to be thermal history of the plates. The plates may have different mechanical or chemical properties from that of the original biopol pellets because of press temperature or cooling rate in the heat press process.

Fig.8 shows a typical specimen biochemical machined. The specimen size is 10×40×1. The machining time is three hours. The specimen was dyed by rhodamine 6G reagent to contrast the character "ASPE" well with the biochemical machined part.

4. Conclusions

As experimental results of this paper, the followings have been obtained.

1) Biochemical machining solution which is composed of crude enzyme solution mainly can degrade the biodegradable plastics "biopol", therefore, biochemical machining of biopol was realized.
2)The maximum removal rate was provided at pH6.5 and temperature 45°C.
3)The removal rates proportionally increased with the machining time.

References

1)D.Satyanarayana, Biodegradable Polymers: Challenge and Strategies, REV. MACROMOL. CHEM. PHYS., C33,3(1993) 349.
2)ICI Co. Catalogue.
3)K.Tsuji, Buffers for pH and Metal Ion Control (in Japanese), Koudansha (1986)136.

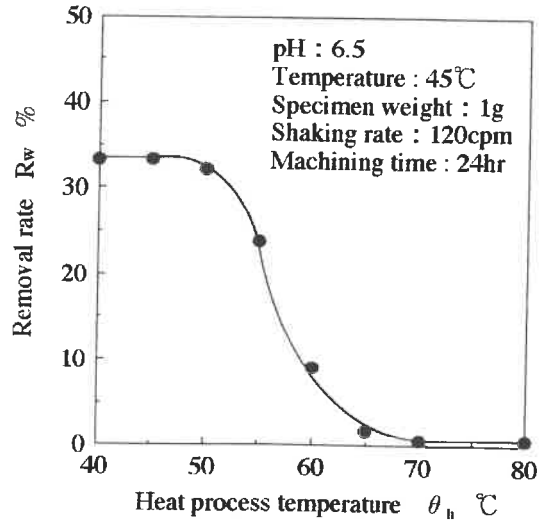

Fig.6 Heat stability of enzyme

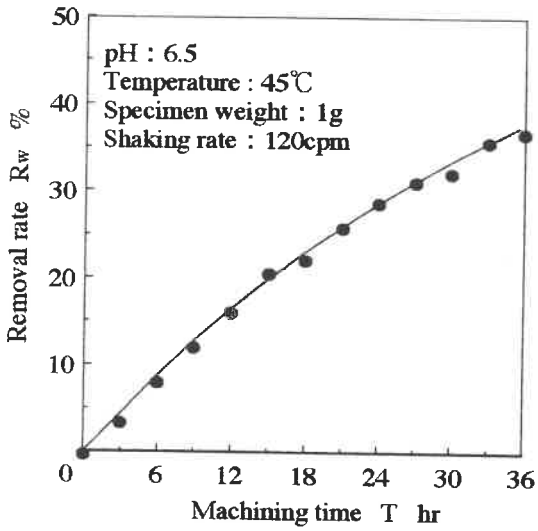

Fig.7 Relationship between machining time and removal rate

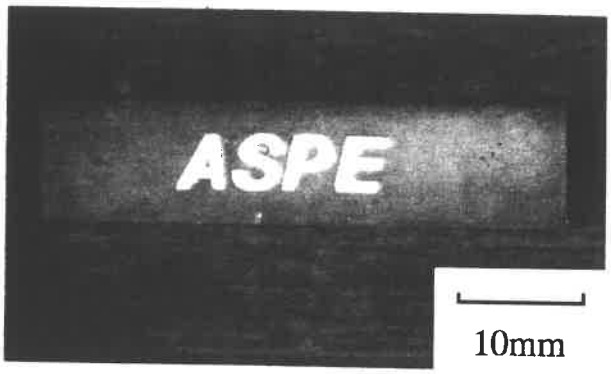

Fig.8 Typical example of biopol biochemical machined

Development of a Micro Machining/Testing System with a Fixed View/Operational Point

Mamoru MITSUISHI, Kazuo KOBAYASHI, Takuro WATANABE, Hirofumi NAKANISHI and Takaaki NAGAO
Department of Engineering Synthesis, Faculty of Engineering
The University of Tokyo
Hongo 7-3-1, Bunkyo-ku, Tokyo 113, Japan

1. Introduction

With the development of LSI fabrication technology, beam machining technology and laser technology, it becomes possible to make very small mechanical parts and high-density wiring patterns on printed circuit boards. Micro handling and testing systems are indispensable for repairing the wiring of printed circuit boards, assembly of micro-machines, testing material, checking LSI circuit wiring, evaluation of the quality of the connections and interfaces in LSI circuits, testing magnetic and optical disk surfaces, and evaluation of the quality of thin films. Not only the engineering area but also the medical area has relevance to micro machining/testing systems. Surgical operation in the micro world, called "micro surgery," including connecting blood vessels and nerves is another application area. When it becomes feasible to realize surgical operations using micro handling/machining technology which are currently executed by a medical doctor's hands under the microscope and which necessitate special expertise, the load on the doctor and the surgical operation time will be much reduced.

To realize a micro-handling/testing system in the micro-world, it is important to acquire, abstract, transmit, complement, emphasize and present multi-dimensional information between operational and operated environments. This paper presents the functions required and a basic structure for realizing a tele-micro-handling/testing system with operational environment transmission capability.

2. Related work

An example of research on micro-machining/testing is micro-operation within an SEM [1]. The SEM employed is specially adapted to produce a stereo image of the object being manipulated in real-time. The system includes a specimen stage with 6 degrees-of-freedom (two pairs of micro-manipulators, each with 3 degrees-of-freedom) and a 3 degree-of-freedom tool-handling robot, equipped with a single axis force sensor. It is driven by piezoelectric actuators and is installed in the vacuum chamber of the SEM. The essential structure of the system is a parallel plate structure inside which piezoelectric actuation elements and strain gauge sensors are mounted. By using the strain gauges for feedback, the non-linearity in the voltage-displacement characteristics of the piezo-elements can be precisely compensated for. The information presentation to the human operator is enhanced by the availability of a stereo view of the object.

Another system concerned with micro-operation is called the "magic wrist" and is used as a master system to control the fine motion of an STM, which serves as a slave system [2]. The master system is hexagonal in shape and is magnetically levitated by installing plate magnets in each surface of the prism. Control of 6 degrees-of-freedom is realized by monitoring the position of the floater using LEDs. The motion of the master wrist is transmitted to the STM with a reduction ratio of from 10^{-6} to 10^{-5}. The analog controller is operated in the PID mode. The tunneling current of the STM is transmitted as force to the master system with a ratio of from 10^{6} to 10^{8}.

Research in micro-handling has also been performed using a six degree of freedom micromanipulator, based on the Stewart Platform, for ophthalmic surgery [3]. In a different approach, a micro-handling system using a rotational axis coincident type micro handling system with a high-precision linear axis to reduce the imprecision caused by the use of the rotational joints has also been proposed [4]. In addition, control strategies for connecting the micro-world and the human world are discussed, for example, in [5].

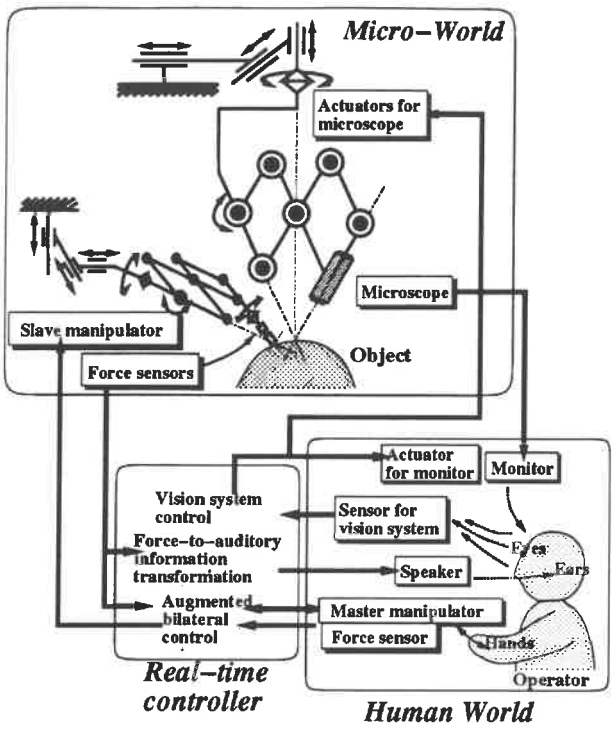

Fig.1 System construction

3. Required functions and a basic structure for a tele-micro-handling/testing system

Fig.1 shows the basic structure of the system. In the system it is assumed that an operator uses left and right hands to operate the system which works in the range from micro-millimeter to millimeter scale with the posture that he/she is looking at the display monitor from top to down, putting his/her elbows on the table. The features of the system are presented in subsequent subsections.

3.1 Operational environment recognition using multiple sensors

Because handling and testing in the micro-world are difficult to perceive for a human operator by normal human sensors, it is required to acquire various kinds of information using multiple sensors and to present integrated and fused multi-sensor information to the operator. In particular, multi-axis force information is essential for the recognition of constraint state, judgement of contact state, measurement of object rigidity and detection of excessive force.

3.2 Transformation and display of multi-axis force information to auditory information

To transmit the operational environment information to an operator, presentation methods should be determined considering the characteristics of the human senses. Multi-axis force-to-auditory information transformation is one of the practical methods for presenting operational environment information with realistic sensation [6, 7]. The features of the transformation is as follows. (a) Auditory information processing ability of human being (1.51^6 bit/s) is higher than force information processing ability (0.21^6 bit/s) [8]. Therefore, auditory display is suitable to present force information in micro-world. (b) The sound level in micro-world is less than the sound acquisition level of microphones. Therefore, transformation of force information-to-auditory information enables virtual sound creation to transmit the reality. Furthermore, to create easily recognizable information, the wave shape of auditory information is synthesized and modulated.

3.3 Augmented multi-axis force information display

One reason why handling, machining and testing in micro-world has been difficult is that the contact force between tool and workpiece is too subtle for human beings to perceive. Therefore, bilateral control with augmented force information display capability is necessary. Vector information in multi-axis force information is fed back to the tactile sense because human being can easily recognize the direction of force. On the other hand, the contact state between the machining tool/testing probe and workpiece is well presented as auditory information. Consequently, multi-axis force information is displayed in a fused way.

3.4 Active sensing of visual information

To obtain the state of the operational environment requires a visual information acquisition system which is high-quality and operates in stereo. Moreover, it needs the ability to adjust vision parameters. More concretely, control of position, zooming and lighting power of the microscope depending on the understanding of the operator's intention is necessary. It is also necessary to reduce an operator's load by automatic visual information display depending on the situation, which is acquired by tracking the end-effector and the object and by automatic adjustment capability of vision parameters.

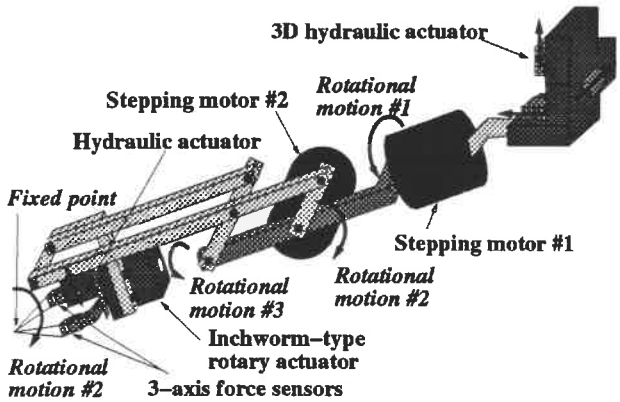

Fig.2 Mechanism of a slave manipulator

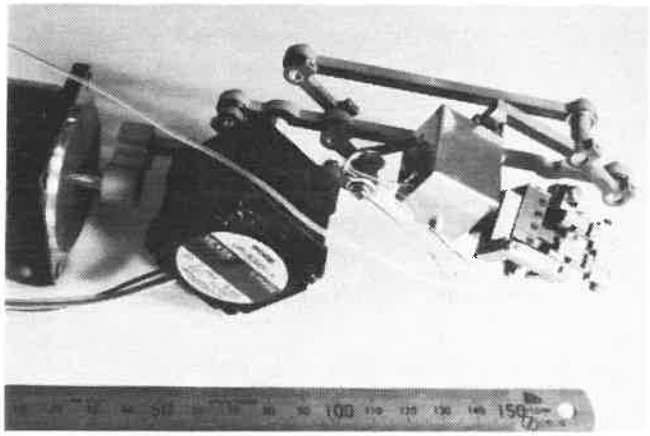

Fig.3 Overview of a slave manipulator

4. Slave manipulator for machining/testing with a fixed point at the end of the tool

4.1 Translational and rotational mechanism

It is effective to separate the translational and rotational degrees of freedom to improve the positioning preciseness and to reduce the computational load. The system described in this paper consists of (i) translational coarse positioner to realize wide range motion, (ii) translational precise positioner for high accuracy, and (iii) rotational mechanism to approach an object from an arbitrary angle. Because an object to be machined and tested by the system is small, the apparatus should be arranged to surround the object. Therefore, (a) the axes of all rotational degrees of freedom should intersect each other at the same point to enable high positionability independent of the approach angle from the manipulator to object. (b) A mechanism which does not occupy too much of the limited small space should be adopted. A parallel-link mechanism was adopted to realize a fixed point at the end effector of the tool/probe (Fig.2, Fig.3).

The precise mechanism for the orthogonal three degrees of freedom is realized by three hydraulic actuators which are located at the outside of the mechanism and have 10mm stroke for each direction. Furthermore, the coarse positioner using stepping motors and linear guides is implemented behind the precise positioner.

4.2 Tweezers

For opening and closing the tweezers, a hydraulic actuator which has 5mm stroke is adopted. As the control part of the actuator can be located at the outer position of the manipulator, the effector part of the slave manipulator, which has the tool/probe, can be compact. The rotational degree of freedom is realized by an inch-worm type piezo-electric actuator. The size and mass of the actuator are approximately 20 × 20 × 25mm and 40g, respectively. The actuator is compact and light compared with a D.C. motor or a stepping motor.

4.3 Multi-axis force sensor

3-axis force sensors are installed on both sides of the tweezers by combining parallel plate structures. The rated value and the natural frequency of the sensor are approximately 40mN for each direction and 1kHz, respectively.

5. Visual information acquisition equipment with a fixed visual point

The basic components of the visual information system are as follows:

(1) fine translational mechanism to move to the working position,

(2) rotational mechanism to get visual information from an arbitrary direction, keeping the center of the rotation in the visual field,

(3) zoom function for an arbitrary magnification ratio,

(4) lighting equipment which does not disturb operation,

(5) wide range motion ability, and

(6) compactness to leave room for manipulators.

In the system described in this paper, the visual system with a microscope has 5 degrees of freedom, including 3 translational degrees and 2 rotational degrees. For an operator to be able to obtain visual information from an arbitrary

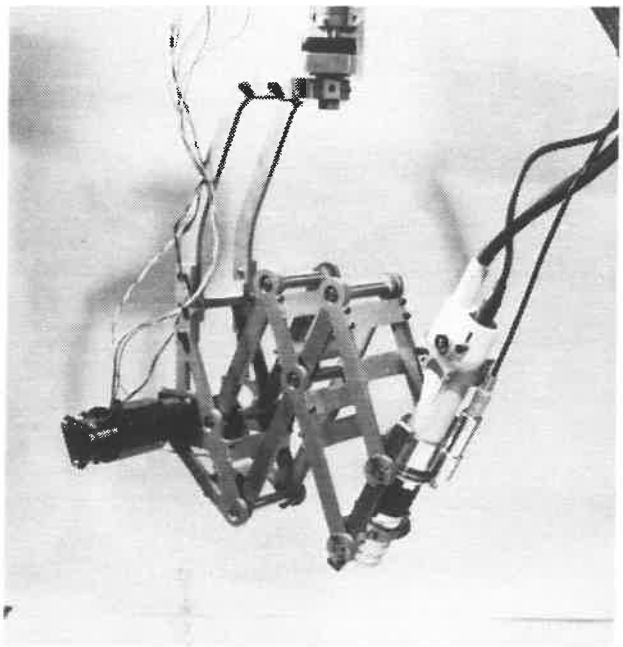

Fig.4 Overview of the visual information acquisition system

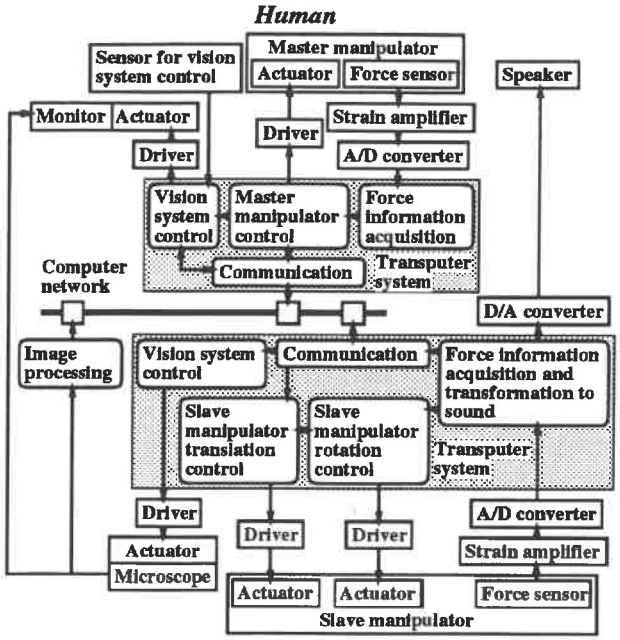

Fig.5 Schematic diagram of control system

direction, the visual point is controlled to become a fixed point by implementing the system such that the axes of all rotational degrees of freedom intersect at the focal point of the microscope. A zoom function with an arbitrary magnification ratio can also be controlled from the outside control system.

6. System controller

The controller implemented for the system consists of the following parts: (1) master and slave manipulators' controller to realize augmented force feedback, (2) force-to-auditory information transformation controller, and (3) visual system controller. Because it is required to control many of degrees of freedom with a high communication frequency, a transputer system is employed. The overview of the control system is shown in Fig.5.

7. Conclusions

Necessary functions and a basic structure for realizing a micro-machining/testing system were presented. In particular, a slave manipulator which has a fixed point at the end of the tool and a vision system which has a fixed visual point are described. Furthermore, a multi-axis force information to auditory information transformation technique is used to enhance the operability of the system.

References

[1] Hatamura,Y. et al., "Direct Coupling System Between Nanometer World and Human World," *Proc. IEEE Micro Electro Mechanical Systems*, pp.203–208, Napa Valley, California, 1990.

[2] Hollis,R.L. et al., "Toward a tele-nanorobotic manipulation system with atomic scale force feedback and motion resolution," *Proc. IEEE Micro Electro Mechanical Systems*, pp.115–119, Napa Valley, California, 1990.

[3] Grace,K.W. et al., "A Six Degree of Freedom Micromanipulator for Ophthalmic Surgery," *Proc. IEEE Intern. Conf. on Robotics and Automation*, vol.1, pp.630–635, Atlanta, 1993.

[4] Sato,T. et al., "Novel Manipulation for Micro Object Handling as Interface between Micro and Human Worlds," *Proc. IEEE/RSJ Intern. Conf. on Intelligent Robots and Systems*, pp.1674–1681, Japan, 1993.

[5] Yokokoji,Y., et al., "Analysis of maneuverability and stability of micro-teleoperation systems," *Proc. IEEE Intern. Conf. on Robotics and Automation*, pp.237–243, Atlanta, 1993.

[6] Mitsuishi,M., et al., "Development of Tele-Operated Micro-Handling/Machining System Based on Information Transformation," *Proc. IEEE/RSJ Intern. Conf. on Intelligent Robots and Systems*, pp.1473–1478, Japan, 1993.

[7] Mitsuishi,M., et al., "Information Transformation-Based Tele-Micro-Handling/Machining System," *Proc. IEEE Micro Electro Mechanical Systems*, pp.303–308, Japan, 1994.

[8] The society of biomechanism, "Biomechanism of human ability," *Industrial Research Society*, 1987.

Focused Ion Beam Machining of Diamond Probes
— Simulation for Profile Change of Probes —

Iwao **Miyamoto**, Shuji **Kiyohara** and Masahiro **Ide**
Department of Applied Electronics, Science University of Tokyo
2641 Yamazaki, Noda, Chiba 278, Japan

1 Introduction

Focused ion beam (FIB) technology is becoming increasingly important for submicron device processing such as mask and device repairs due to maskless etching and depositioning, and lithography. The technology may also be important for the microfabrication of fine mechanical parts and sensors. Those are usually made of single- or polycrystalline silicon, and are mainly fabricated by anisotoropic chemical etching. For the fabrication of fine mechanical parts made of metallic materials, diamond turning, electron beam machining, and electrodischarge machining are usually used. It is, however, difficult to make three dimensional devices with free shapes and to etch a hole or a line at any position by chemical etching and other machining methods without masks. In contrast to those machining methods, the FIB machining method can be used for the fabrication of those three dimensional device without masks. On the other hand, diamond which has a high thermal conductivity and a large specific stiffness is more suitable than silicon as a material for micro-mechanical parts such as a stylus, probe, spring, cantilever, dies and so on. The fabrication of diamond probes using a FIB has been investigated. Furthermore, a simulation methods for profile change of probes during FIB machining was investigated theoretically.

2 Apparatus and procedures

Diamond chips with (100) surface were used as specimens. The specimens were machined using a FIB apparatus having a liquid metal ion source with Au-Si alloy as a source material of Au metal ions. In this case, various ions were emitted from the Au-Si liquid metal ion source. Therefore, the mass filter was used to select Au^+ ions from various ions such as Au^+, Au^{++}, Si^+, Si^{++} and etc. Inspite of the use of the E×B mass filter, the appratus can generate a 30 keV Au ion beam with a diameter of 0.25 μm at an ion current density in the order of A/cm^2.

The apparatus also has two secondary electron detectors and an analog image processor for the in situ observation of the surface micro-topography of the processed specimen, and for the measurement of the cross-sectional profile of etched patterns into the specimen with FIB. The image processor provides sum and sub. (subtract) of signal images through calculation of signals from two secondary electron detectors by a electronic analog circuitry. The obtained cross-sectional profile of the patterns may be useful for the feedback control of the FIB during etching patterns into the specimen by the FIB.

3 The computer simulation scheme

In order to simulate profile changes of a probe with a conical tip during FIB machining, the following assumptions were made:

1. We can simulate the profile changes of the three dimensional tip (specimen) during machinig in a two dimensional manner, because there is no significant profile change during one scan due to fast rotating or scanning of the FIB around the tip axis.

2. Usually, the distribution of the current density of a FIB has three components[1]. The first is the Gaussian distribution. The second component concerns the lens chromatic aberration. The FIB tail is dominated by this component. The third is the distribution tail brought by FIB collisions with the residual gas. In the simulation, however, the ion current density I_b(A/cm^2) in the ion beam spot which incidents along the tip axis and focuses on the tip is assumed to have a Gaussian distribution which is given by

$$I_b = \left(\frac{I}{2\pi\sigma^2}\right) exp\left(-\frac{x^2+y^2}{2\sigma^2}\right) \tag{1}$$

   where, I is total ion beam current [A], σ is standard deviation [m].

3. The tangential lines to the curved line of the specimen move parallel to themselves during FIB machining (Two dimensional approximation).

4. The sputtering yields $S(\theta)$ of diamond (100) single crystal chips obtained experimentally for 30 keV Au ions can be used for the simulation of profile changes of diamond tips.

5. There are no secondary effects such as redepositioning of sputtered atoms from the bottom to the side walls of the etched pattern and/or from the side walls to the bottom.

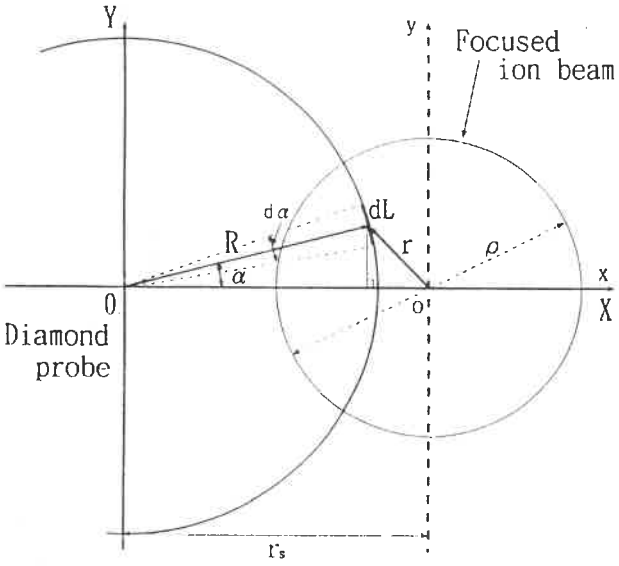

Fig.1: Schematic configuration of a diamond probe and a FIB being rotated around the probe axis with rotation radius of r for calculating I_a by equ.(5) (top view)

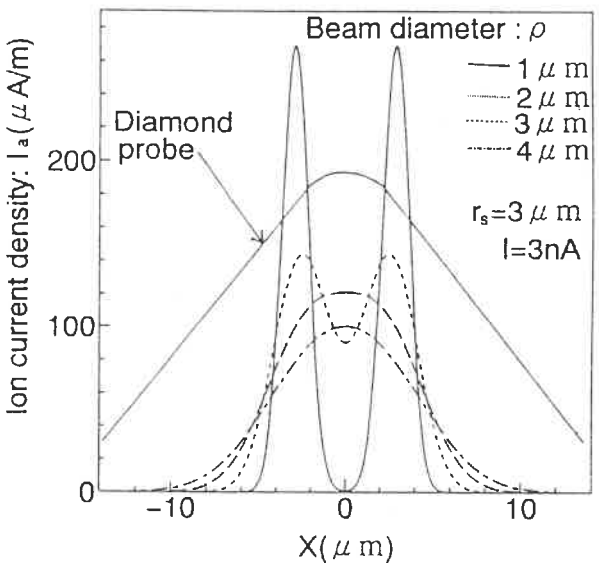

Fig.2: Relationship between the X and ion current density I_a at various beam diameters with rotation radius of 3 μm

Under the above assumptions, we consider the case of machining of the diamond probe with conical tip by a FIB, which incidents on the tip along the tip axis and describes a circle with a scanning radius of r_s[m], as shown in Fig.1

If the rotating or describing speed of the FIB around tip axis is high, there is no significant change in the profile of the tip during one revolution of the beam. The ion current density dI_a at the line element dL on the probe can be derived as follows:

Relation among r,R,α and r_s is expressed by following equation:

$$r^2 = {r_s}^2 - 2r_s R\cos\alpha + R^2 \tag{2}$$

By substituting $\rho = \sigma\sqrt{8\ln 2}$, $x^2 + y^2 = r^2$ and equ.(2) for equ.(1), dI_a is then expressed by the following equation.

$$dI_a = \left(\frac{4\ln 2}{\pi\rho^2} I\right) \exp\left\{-\frac{4ln2}{\pi\rho^2}\left(r_s^2 - 2r_s R\cos\alpha + R^2\right)\right\} dL \tag{3}$$

where, dL is the length of line element given by

$$dL = Rd\alpha \tag{4}$$

By integration of equ.(3) with respect to α from 0 to 2π then the ion current density at the X can be obtained as follows:

$$I_a = \int_0^{2\pi} \left(\frac{2\ln 2}{\pi^2\rho^2} I\right) \exp\left\{-\frac{4\ln 2}{\pi\rho^2}\left(r_s^2 - 2r_s R\cos\alpha + R^2\right)\right\} d\alpha \tag{5}$$

Fig.2 shows the relationship between the X (distance from the center of the probe axis along the X axis) and the ion current density I_a at various beam diameters, rotating the FIB around the probe axis (center of the rotation of FIB) with radius r_s of 3 μm. As shown in the figure, when the diameter of FIB is enough smaller than r_s, the ion current density distribution curves as a function of X has two peaks at the position of nearly X= r_s. The peaks of the ion current density curves shift to the center of beam rotation (X=0) and come together when the diameter of the FIB is larger than the r_s.

4 Results and discussion

Fig.3 shows SEM photos of the diamond probes with conical tip processed by a FIB (30 keV Au ions, ion current; 0.10 nA, beam diameter; 4 μm). In this case the FIB incidents on the tip along the tip axis and swings a circle with a radius of 5 μm. After machining of the diamond probe for 12 h, a protrusion was formed at the tip of the diamond probes as shown in the figure (SEM photos). The protrusion of the tip machined for 24 h became dull compared with the prefinished one. Reasons of this are considered as follows:

1. Ion current density distribution which was assumed to be Gaussian has a tail so that the tip of the probe may be machined with the tail of the FIB.

2. It takes a long time to find the center of the tip by the monitor, because the secondary electron yield of the diamond probes is very low. The tip of the probe then may be machined.

Fig.4 shows results obtained by the computer simulation which was done under the same machining conditions as in the experiment. As shown in Figs.3 and 4, the results of the simulation fairly coincide with results of the experiments. However, the height of the protrusion by the simulation is somewhat higher than that by the experiments. This difference may be caused

due to the secondary effects such as redepositioning which were ignored in the simulation model and/or the difference between initial shape of the tip of the diamond probe used for an experiment and that of the simulation model.

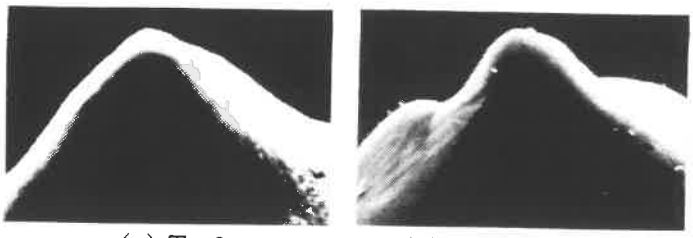

(a) T=6 (b) T=12

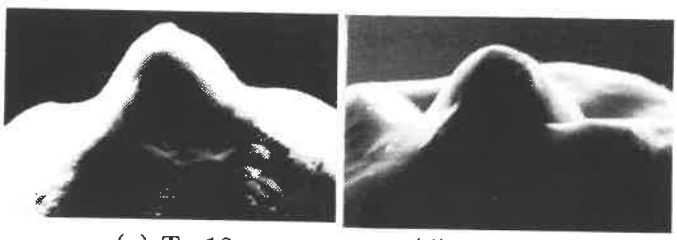

(c) T=18 (d) T=24

Fig.3: Experimental result
(T: hours)

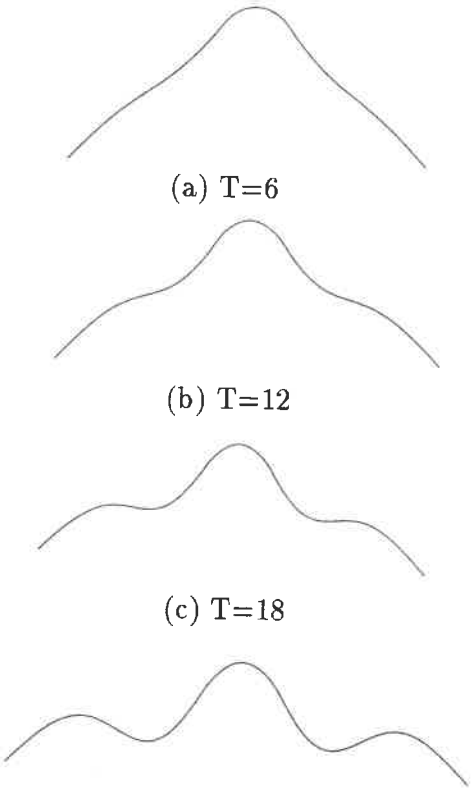

(a) T=6 (b) T=12 (c) T=18 (d) T=24

Fig.4: Simulation result
(T: hours)

5 Conclusions

From experimental and theoretical (computer simulation) results, the conclusions are summarized as follows:

1. After machining of a diamond probe with 30 keV Au ion at ion current of 0.10 nA for 12 h, the profile of the protrusion at the tip of the diamond probe changed little.
2. The protrusion of the diamond probe machined for 24 h became dull compared with the tip of the prefinished one.
3. The developed simulation method can predict the profile change of the tip during FIB machinig of the diamond probe.

References

[1] T. Ishitani et al: *J. Vac. Sci. and Technol.*, B6, No.3, (1988), pp.931–935

[2] I. Miyamoto and S.T. Davies: *Annals of the CIRP.*, No.37, (1988), pp.171–174

Analytic and Experimental Investigation on Deep Hole Formation Process of Covalent Bond-Ceramics Using Pulsed YAG Laser

Noboru MORITA, Takehiro WATANABE and Yoshitaro YOSHIDA
Department of Mechanical Engineering, Faculty of Engineering, Chiba University
1-33, Yayoi-cho, Inage-ku, Chiba, 263, Japan

Introduction

A deep hole above 20 in the aspect ratio, which is the ratio of a depth and a diameter, is easily formed in laser machining of covalent bond-ceramics [1,2]. This can be explained by assuming that drilling progresses as the laser beam is multiply reflected by the wall of the hole and convergently carried to the bottom of the hole. To verify the machining model mentioned above, the present study investigated the effect of reflection in laser drilling of ceramics by analyzing the drilling process using a laser intensity distribution simulation with reflections from the walls of the hole under a ray tracing method combined with thermal analysis using the method of finete differences.

Analysis Method

Figure 1 presents the ray tracing model simulated in this study. It is assumed here that a YAG laser beam of 6mm in diameter is condensed by a lens, reflected by the walls of hole at a constant reflectance and passed to the bottom of the hole.

Figure 2 illustrates the flow chart of analysis. The first step is to determine laser irradiating condition and the initial values of material properties. This is followed by thermal analysis under difference method. When the hole is 0.5mm depth, the work enters a laser intensity distribution analysis program. Here, the first step is to obtain the laser intensity at the bottom of the hole under a ray tracing method. The determined distribution is then thrown again into thermal analysis. When analysis comes to the end of the preset laser irradiating time the ultimate hole shape is determined.

The laser irradiating conditions are pulse duration: 1.7ms and irradiation energy: 3J. The material is silicon nitride ceramics having covalent bonding. For further details of analysis method, the reader should refer to Ref.[3].

Results of Analysis

Figure 3 illustrates the dependency of hole depth on laser irradiation times at various reflectances of the wall of the hole. The hole depth increases with increasing the laser irradiation time. This behavior is distinguished as the reflectance increases.

This result means that the deep hole drilling is affected directly by multiple reflectance, which characterizes the delivering of laser beam to the bottom of the hole.

Figure 4 shows the results of hole shape analysis. The hole shapes depend on the reflectance. The higher reflectance makes hole shape conical and pointed toward the bottom. Figure 5 illustrates the results of laser intensity distribution in the holes shown in Fig.4. In the case of reflectance 20 per cent, the intensity becomes higher as the hole is deeper because the laser beam reflected from the wall of the hole is condensed efficiently to the bottom of the hole, allowing power density to increase. This explains how a sharp and deep hole is produced.

Figure 6 shows the dependency of hole depth on laser irradiation times using various focal length of a lens. The focal length of a lens dominates the hole depth. It is understood that this results can be explained by the variation of reflection characteristics due to a difference of focusing angle and spot size of laser beam on the material surface.

Results of Experiment

To check the validity of the results of analysis, drilling test was attempted in hot-press sintered silicon nitride ceramics using a pulse pumped YAG laser [1]. Table 1 lists the properties of the workpieces. The irradiation conditions are the same as those of analysis.

Figure 7 illustrates the dependency of hole depth on laser irradiation times using various focal length of a lens, and Fig.8 shows the cross sections of the holes. The dependency of hole depth on laser irradiation times is quantitatively similar to that of analysis. The hole shapes are sharp and deep, and agree with those of analysis.

Conclusions

Combining intensity distribution analysis by ray tracing with a thermal analysis program by a difference method with the multiple reflection of laser beam from the walls of the hole taken into account, a method for analyzing the processes of drilling was developed. The obtained results are summarized as follows:

(1) Drilling in silicon nitride ceramics by the YAG laser is primarily executed by energy being propagated to the bottom of the hole by laser beam reflections from the walls of the hole.

(2) In laser drilling, the laser beam is reflected by the walls of the hole and converged, causing the power density to be increased at the center of the hole. This allows drilling to progress at the bottom of the hole, producing a sharp shape.

References

1. Noboru MORITA, "Influence of Defocusing on Hole Features in Laser Drilling of Ceramics", J. Ceramic Society of Japan, Int. Edition, Vol.102(1994)189.
2. N.MORITA, H.SAKAMOTO, T.WATANABE and Y.YOSHIDA,"Crack-FreeProcessing of Hot-Pressed Silicon Nitride Ceramics Using Pulsed YAG Laser", MD-Vol.16, ASME(1989)9.
3. N.MORITA, "Crack-Free Processing of Hot-Pressed Silicon Nitride Ceramics Using Pulsed YAG Laser",Proceedings of the International Conference on Machining of Advanced Materials NISTSpecial Publication 847(1993)517.

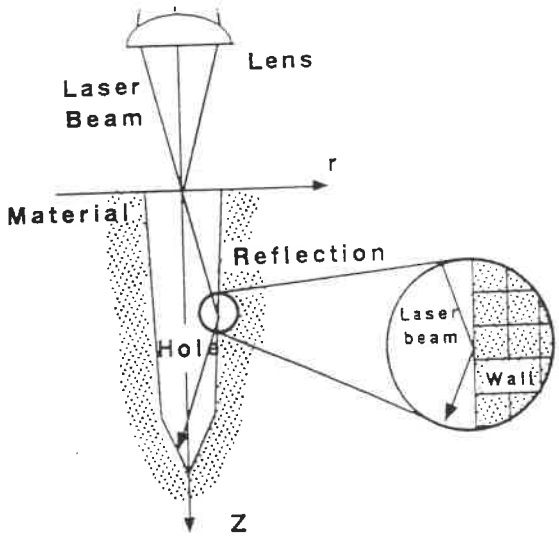

Fig.1 The ray tracing model simulated in this study

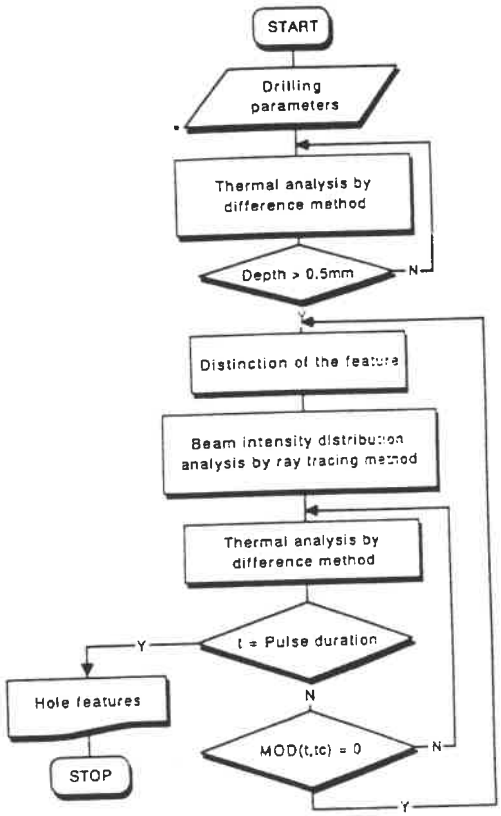

Fig.2 The flow chart of analysis

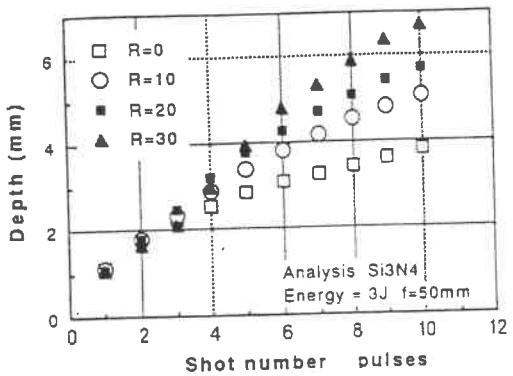

Fig.3 The dependency of hole depth on laser irradiation times at various reflectances

Table 1 The properties of the workpieces

Density [g / cm^3]	2.70
Bending strength [kg /mm^2]	28 ~35
Thermal expansion coefficient [10^{-6} / ° C]	3.1
Thermal conductivity [W/m · K]	12.8
Young's modulus [kg / mm^2]	2.0×10^4

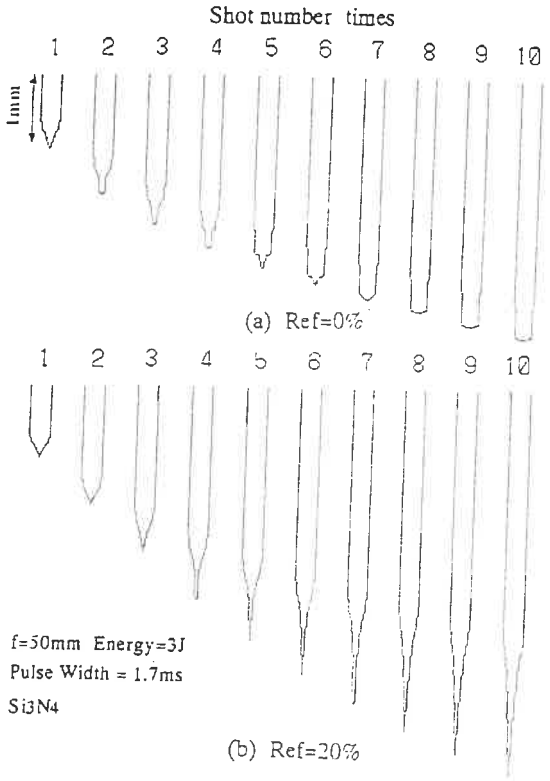

Fig.4 The results of hole shape analysis

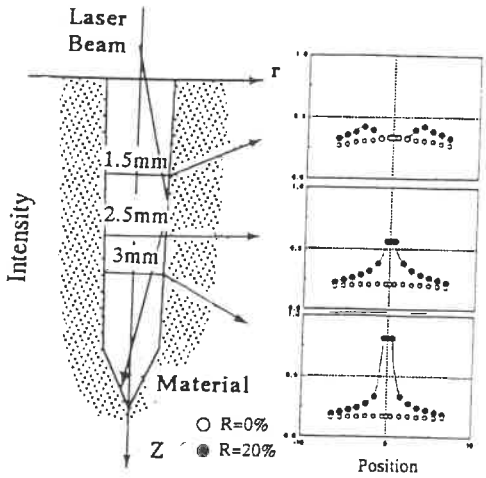

Fig.5 The results of laser intensity distribution in the holes shown in Fig.4

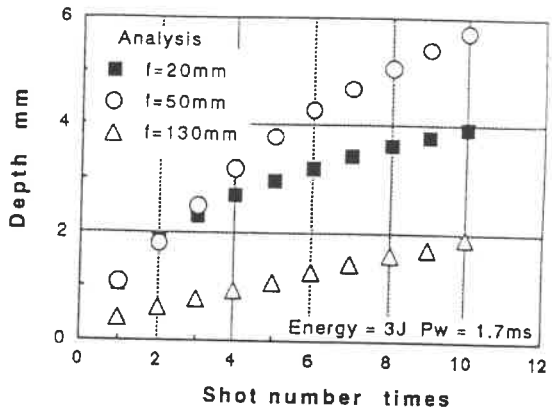

Fig.6 The dependency of hole depth on laser irradiation times using various focal length

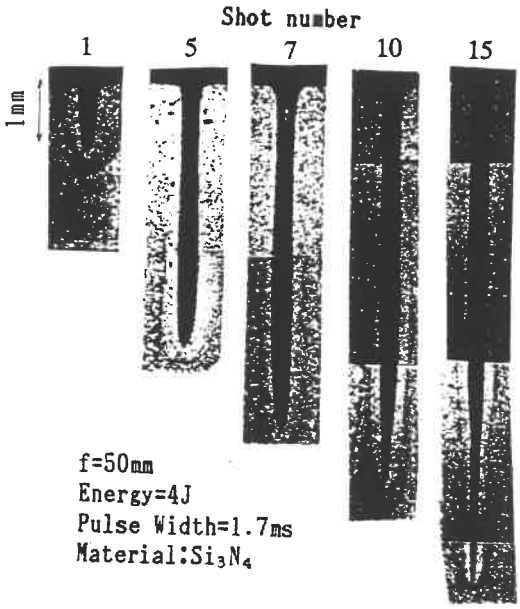

Fig.8 The cross sections of the holes

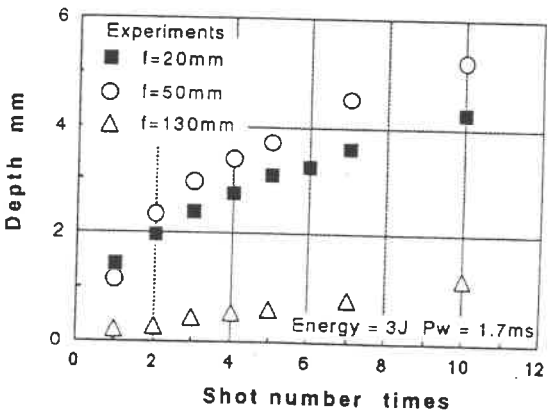

Fig.7 The dependency of hole depth on laser irradiation times using various focal length (experiment)

Manufacturing Economics and Removal Mechanisms in the Forming and Finishing of Reflective Optical Surfaces

Arthur José Vieira Porto[1]
Jaime Gilberto Duduch[1]
Anthony E Gee[2]

1 Escola de Engenharia de São Carlos - Universidade de São Paulo
Av. Dr. Carlos Botelho, 1465 Caixa Postal 359
13560-254 São Carlos SP BRAZIL Tel.: 162-726222 ext 3235 Fax (162)719241

2 School of Industrial and Manufacturing Science Building 40 Cranfield University
Cranfield Bedford MK43 0AL UK Tel.: 234-750111ext2386/2389 Fax (234)750875

1. Summary

This work addresses the feasibility limits of material removal in diamond turning of non-ferrous materials (aluminium and copper) in order to stabilish a planned economical production process of optical surfaces which require fine forms and surface finishes. Cutting tests were carried out aiming at the establishment of an economical process to attain the required specifications. It is anticipated that such an approach will be required in respect of production process. Samples were cut on a Pneumo ASG 2500 Aspheric Generator at several cutting conditions and subsequently analysed on a Wyko 6000 Fizeau Interferometer and a Rank Taylor Hobson Form Talysurf.

2. Introduction

Ultra-precision of optical components may involve a combination of the following aspects: accurate form, low surface roughness and low sub-surface damage. Whereas at low demand a process may not require a great deal of investigation, as demand increases it becomes necessary to anticipate the material removal sequence in order to reduce machining time and cost and to improve tool life.

Although not generally susceptible to edge build-up, with some materials, eg, aluminium, some built-up edge can occur, which affects the surface finish. Diamond turning of metals is not (generally) sensitive to cutting speed and depth of cut so that some authors indicate that optics should be machined in only two passes: rough cutting and fine finishing to produce specularly reflecting surfaces. However, large initial cuts may incur sub-surface damage (strain hardened material) and, as a consequence, figure errors. Finish feedrates can be determined by the required peak-to-valley for the finished surface and the

and the geometry of the tool. The theoretical peak-to-valley may be expressed as $f^2/8R$, where f is the feedrate and R is the tool nose radius[1]. But spurious motion caused by tool/workpiece vibration and thermal and geometric errors must be considered. The finish feedrate will be less than that set only by the theoretical peak-to-valley.

3. Description of the Experiments

The components were cut on a Pneumo ASG 2500 Aspheric Generator at Machine Tool Laboratory, São Carlos[1]. The samples were in the form of 75 mm diameter, 25 mm thick cylinders of aluminium Kobe M2B and copper 99,9 %. The samples received a series of roughing cuts followed by a single finishing cut. A CONTOUR[2] diamond tool, with nose radius 1.524 mm, 0° rake angle and 11.5° clearance angle, was used.

For the aluminium samples, the roughing cuts were as follows: Sample 1 received a single 30 m deep cut; sample 2 had 2 passes of 15 m each; sample 3, 3 passes of 10 m and sample 4 had 5 passes of 6 m, so that the total depth of roughing cuts was always 30 m for each part. All four samples had the same feedrate of 50 m/rev at 1000 rpm spindle rotational speed.

Similarly, for the copper samples the number of roughing passes increased from one single pass 15 m deep to 5 passes 3 m deep. Four samples were cut with the same 15 m total depth of cut, 50 m/rev feedrate at 1000 rpm spindle speed.

All samples received only one 3 m deep finishing cut. The finishing feedrate was 5 m/rev at 1000 rpm spindle speed.

The specimens were analysed on a Fizeau interferometer (Wyko 6000) and a RTH Form Talysurf series 120L, both after the series of roughing cuts and after the finishing cut.

4. Results and Discussion

The tests are summarized in tables 1 (aluminium samples) and 2 (copper samples)

---

[1]Escola de Engenharia de São Carlos - Univ. de S. Paulo
Depto de Eng. Mecanica
13560-254 São Carlos SP Brazil

[2] Contour Fine Tooling
39, Wedgewood Way, Stevenage, Herts, SG1 4QT

The analysis of the Wyko Interferometer plots showed that, although the total roughing cut depth and finishing cut depth were the same, the final form of the surfaces varied substantially from sample to sample (increasing number of roughing passes), for both the aluminium and copper samples. The maximum peak-to-valley deviations from the Wyko traces are summarized in Tables 3 and 4.
The surfaces were assessed after the last roughing cut and after the finishing cut.

Material:aluminiumKobeM2B,n=1000rpmroughingcut

sample#	#passes	depthofcut (μm)	feedrate (μm/rev)
1	1	30	50
2	2	15	50
3	3	10	50
4	5	6	50

Table 1 Aluminium samples roughing cuts. Finishing cut: 1 pass 3m deep, feedrate 5m/rev.

Material: copper 99.9%, n = 1000 rpmroughing cut

sample#	#passes	depthofcut (μm)	feedrate (μm/rev)
1	1	15	50
2	2	7.5	50
3	3	5	50
4	4	3	50

Table 2 Copper samples roughing cuts. Finishing cut: 1 pass 3m deep, feedrate 5m/rev.

Material: aluminium Kobe M2B, n = 1000 rpm

Sample#	roughing cuts p-v (μm)	finishing cut p-v (μm)
1	0.82	0.45
2	0.59	1.09
3	0.62	0.63
4	0.52	0.96

Table 3 Peak-to-valley deviations of aluminium samples as a function of the number of roughing passes.

Material: copper 99.9%, n = 1000 rpm

Sample#	roughing cuts p-v(μm)	finishing cut p-v(μm)
1	0.60	0.43
2	0.53	0.45
3	0.51	0.22
4	0.49	0.65

Table 4 Peak-to-valley deviations of copper samples as a function of the number of roughing passes.

The results indicate a dependence of the form of the surface on the number of passes and the depth of cut. It would appear that, as the number of passes changes, the final damaged (strain hardened layer) would reach different depths and hardness, resulting in unequal surface deformations.

There seems to be an optimum number of passes associated with an optimum depth of cut for roughing where the depth of remaining plastic work would more easily be reduced or removed by the finishing cut. This will require further investigation as relatively few surfaces have hitherto been tested.

The surface finish (Ra) as well as the average slope (degrees) were assessed on a RTH Form Talysurf. The results were grouped in graphs as a function of the roughing depth of cut shown in Figures 1 and 2. The three curves on the graphs correspond to Ra (no filter used), Ra Rough (Roughness filter/gauss/18x0.25 mm) and Ra wave (waviness filter/gauss/19x0.25 mm).

As can be seen from the graphs, for the same feedrate and depth of finishing cut, the surface roughness varies with the number of roughing cuts. This may be correlated with the degree of 'burnishing' caused by the clearance face and sub-surface damage which might still be associated with unequal grain elastic recovery and damage caused by subsequent strain relief[2].

The average slope (Figures 3 and 4) of the surface behaves similarly, ie, varies with the number of passes, and is presented as a measure of reflectivity of the surface.

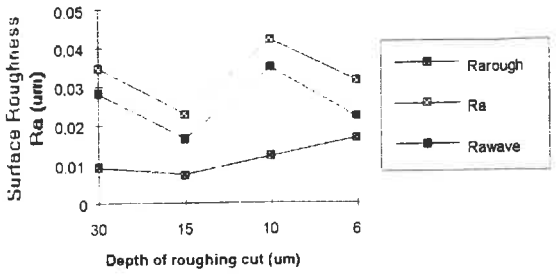

Figure 1. Finishing Al 1000rpm / 5 um/rev / dc= 3 um

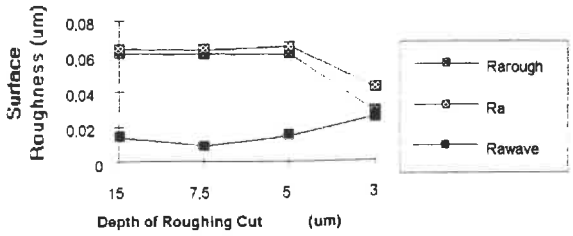

Figure 2 Finishing Cu 1000 rpm/5um/rev/dc=3um

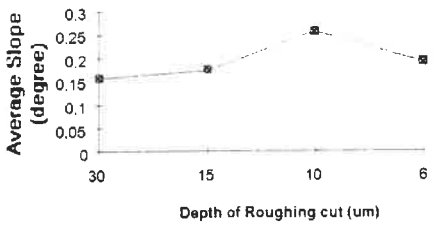

Figure 3. Finishing Al 1 pass / 1000rpm / 5um/rev / dc= 3 um

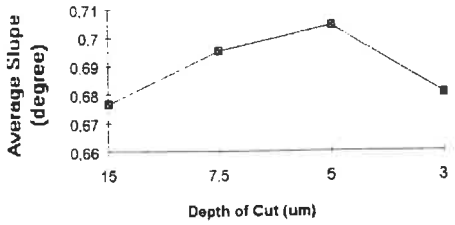

Figure 4. Finishing Cu 1 pass / 1000rpm/5um/rev/dc=3um

References

1 C. Evans, R. Polvani, M. Postek and R. Rhorer, Some Observations on Tool Sharpness and Sub-Surface Damage in Single Point Diamond Turning. SPIE Vol. 802 In-Process Optical Metrology for Precision Machining, 1987, pp52-66.

2 Ikawa N. and Shimada S., Cutting Tool for Ultraprecision Machining. Proceedings of the 3rd International Conference on Production Engineering, Kyoto, July, 1977.

ELECTROCHEMICAL DISCHARGE MACHINING - A NEW APPROACH

V. Raghuram
Department of Mechanical Engineering
Indian Institute of Technology Kanpur
Kanpur, India

T. Pramila
Department of Physics
Christ Church College
Kanpur, India

INTRODUCTION

Machining of brittle, hard and non-conducting materials such as glass and ceramics poses a problem that needs to be solved, because, the difficulty faced in the handling of these materials has resulted in the utilization of these materials in a limited number of fields. Among the techniques developed for machining these materials are ion beam machining (IBM), laser beam machining (LBM) and electrochemical discharge machining (ECDM). In electrochemical discharge machining, an electrical discharge is used for machining these materials. The electrochemical discharge (ECD), is the discharge which occurs in an electrochemical cell containing two electrodes which are vastly different in size. This discharge takes place inside the electrolyte around the smaller of the two electrodes which is used as the tool for machining.

ECDM is concluded to be a low efficiency process as regards to its material removal capacity by all the previous researchers [1-5]. It was also seen to exhibit a limiting depth characteristic i.e. machining no longer progressed after the tool penetrated upto a certain depth into the workpiece. In all these studies, gravity feed was given to the tool and materials of relatively low melting points were used as tool. In this paper, we discuss a new and successful electrochemical discharge machining configuration after presenting,in breif, the results of various studies on ECD, which led to the development of this machining technique.

HIGH RESOLUTION SPECTROSCOPY OF ELECTROCHEMICAL DISCHARGE

The high resolution emission spectrum of the electrochemical discharge in the region (3000-8000Å) was recorded using a monochromator (SPEX 1403) with PMT (RCA C31034) and digital photon counter combination. The emission spectrum of the ECD in this region clearly showed it to be a gaseous discharge comprising primarily of line spectra characteristic of emission from atomic species. Using KOH electrolyte,intense spectral lines due to atomic hydrogen, atomic potassium and singly ionised potassium(K^+) are observed. The determination of the gaseous nature of ECD is very helpful in its utilisation for machining purpose. The thickness of the gaseous medium through which the discharge is striking is observed to be around 200 μm. .

EFFECT OF THE EXTERNAL CIRCUIT CONFIGURATION AND ESTIMATION OF ELECTRON TEMPERATURE

A careful and extensive study of the instantaneous behaviour of the voltage and the current through the ECD cell showed that the energy input to the system not only got

enhanced but stayed constant when a circuit with a series inductor,L, is used. Using smooth DC and a series inductor, a very intense discharge which surrounded all the portion of the tool that is dipped inside the electrolyte is obtained.A new technique used to obtain this discharge is momentary increasing of the voltage to about 90V and bringing it down to normal operating voltages (60V) once the discharge is formed. This kind of discharge is not obtained by the previous researchers.

The atomic lines of potassium at 4044, 4048, 7664 and 7698Å were recorded for 1M, 5M, 7M and 10M concentrations of KOH and the electron temperatures present in the discharge column are determined spectroscopically, incorporating the measured spectral line intensities in the standard relations [6]. The electron temperatures in ECD for KOH electrolyte concentrations between 1M and 10M are estimated to be in the range of 8000°K - 12000°K.

MACHINING OF QUARTZ GLASS

The tool is always in contact with the workpiece due the gravity feed mechanism employed by previous researchers. Machining of glass using this configuration did not yield satisfactory results.The present studies carried out on ECD showed it to be a gaseous discharge. The gas envelope around the tool is having considerable thickness and electron temperatures of the order of 10000 °K are existing inside the discharge column. Based on these reults, it was reasoned out that better machining conditions could be obtained through better utilization of the discharge column. For this purpose, the machining configuration is modified in order to keep the workpiece always stay within the discharge column instead of in contact with the tool (Fig. 1).

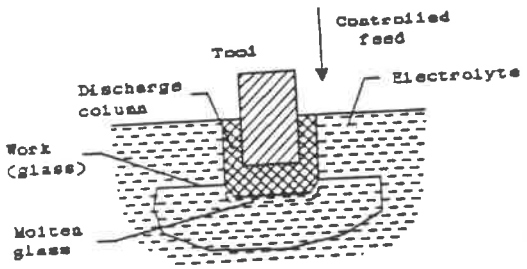

Fig. 1

Experimental Details

To achieve precisely controlled tool feed, a stepper motor was connected to the screw-slide mechanism as shown in Fig. 2. The rotational speed of the stepper motor was controlled through a microprocessor. Delay time routines were incorporated in the programme to achieve different rotational speeds of the stepper motor. The programme was written in Intel 8085 based microprocessor machine language. The pitch of the screw is 1 mm. The tool was moved at regular intervals, always ensuring that the discharge was lying above the surface of the workpiece. Quartz glass plate of 3mm

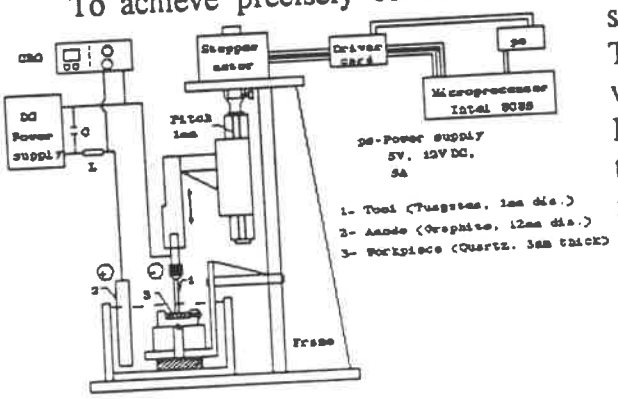

Fig. 2

thickness and 1 mm tungsten wire were used as workpiece and tool. The machined depth and diameter in various samples were measured using an optical microscope with 10X and 40X magnification. The machined surfaces were photographed, using the camera attachment provided.

Results and Discussion

Machining of the workpieces was carried out with concentrations of 2M, 5M and 10M of KOH electrolyte. The operating voltage in all the experiments was kept fixed at 60V. Fig. 3 shows the variation of the machined depth with time at feed rates of 0.15 mm/min and 0.3 mm/min. It can clearly be seen that the machined depth is increasing linearly with time and that there is no evidence of the limited depth characteristic which was observed by the previous researchers. A comparison of the plots for each concentration shows that faster feed rate is resulting in more efficient machining. This is because of the fact that the discharge column is having a thickness of about 200 μm and smaller feeds do not make effective use of the discharge.

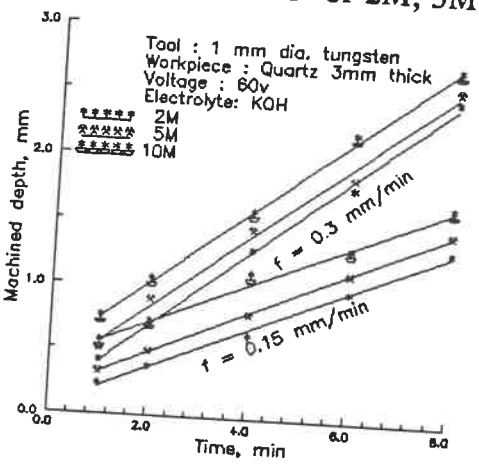

Fig. 3

The variation of observed hole diameter, top and bottom surfaces of the workpiece, with molarity is as shown in Fig.4 when machining was carried out for 8 min. It is observed that the hole diameter at the top is larger than that at the bottom and that the rate of variation of hole diameter decreases with increasiing molarity. This disparity is due to the material loss in the tool during discharge giving a taper to the tool. The volume of the material removed is plotted against molarity in Fig. 5. Though the volume of material removed is increasing with molarity the rate of this increase is decreasing with molarity. Plate 1 shows the bottom surface of one of the blind holes machined using this new

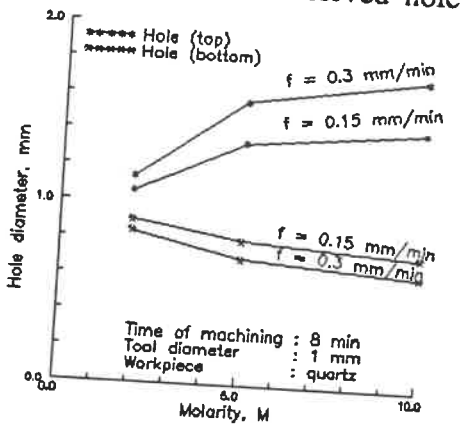

Fig. 4

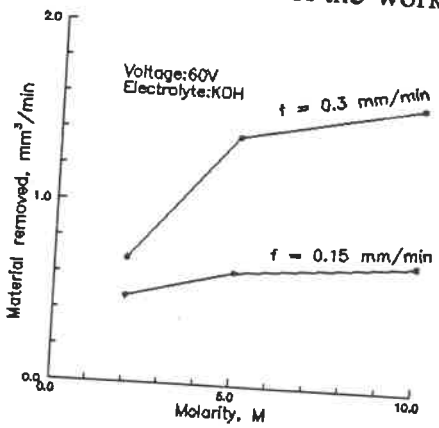

Fig. 5

machining configuration. Successful machining of through holes was achieved in 3 mm thick quartz glass plates (Plate 2).

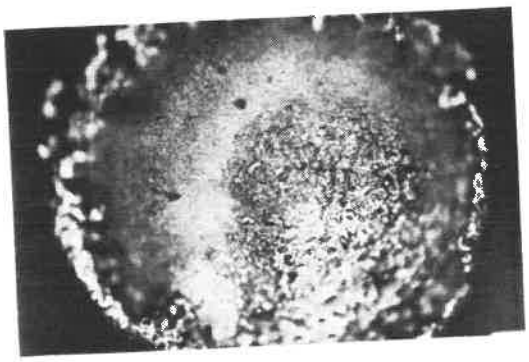

Plate 1

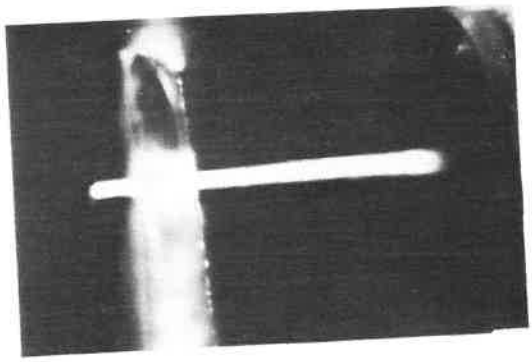

Plate 2

Limited Depth Characteristic

A microscopic study of the machined surfaces using smooth DC through inductor shows that the material removal is taking place by melting, evaporation and atomisation of the workpiece material. When smooth DC only is used, the discharge is limited to the bottom edge of the tool and is very weak. Due to the discharge at the bottom of the tool, workpiece undergoes melting initially and the tool penetrates into the glass melt due to gravity feed which results in the extinguishing of discharge. Once the discharge is extinguished the molten glass gets resolidified in its site. This is as observed through a travelling microscope and is supported by Plate 3. In this plate, it can be seen that the machined depth is very minimal and the central portion of the tool is left unmachined. The texture of the surface clearly indicates that resolidification of molten glass has taken place whereas Plate 1 shows that the material removal is more uniform even at the bottom of the tool and that melting only is not the factor causing material removal.

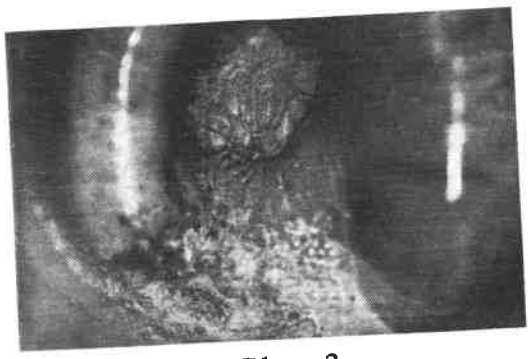

Plate 3

REFERENCES

1. Kellog, H.H., J. of Elec. Chem. Soc., No.97, pp.132-142 (1950).
2. Kurafuji, H and Suda, K., Ann. CIRP, Vol.XVI, pp.415-419 (1968).
3. Cook,N.H, Foote, G.B, Jordon, P and Kalyani, B.N.,J. of Engg. for Ind., Trans. ASME, No.95, pp. 945-950 (1973).
4. Allesu, K, Muju, M.K, and Ghosh, A., Proc. Int. Symp. for Electro-machining (ISEM-9), Nagoya, Japan, pp. 94-99 (1989).
5. Tokura, M, Kondoh, I and Yoshikswa., J. of Matl. Science, Vol.24, pp. 991-998 (1988).
6. Howatson, A.M.,An Introduction to Gas Dishcharges, Pergamon Press, Oxford (1965).

Abrasive Wear Characteristics under Three-body Conditions of CFRP in Vibratory Environment

Sadakazu TERAOKA *, Ken-ichi ISHIKAWA **, Tatuo NAKAGAWA **
* Kanazawa Technical College, ** Kanazawa Institute of Technology
* 2-270 Hisayasu Kanazawa Japan, ** 7-1 Ohgigaoka Nonoich Kanazawa Japan

1. Introduction

Carbon fiber reinforced plastics (CFRP) have been widely used in industry because of their attractive mechanical characteristics. Such CFRP parts are invariably subjected to three-body wear due to small indentation[1] and machine vibrations.

In this study, the abrasive wear characteristics of CFRP were investigated using a vibrating environment and the silicon carbide abrasive grains. The wear characteristics and the wear process was examined.

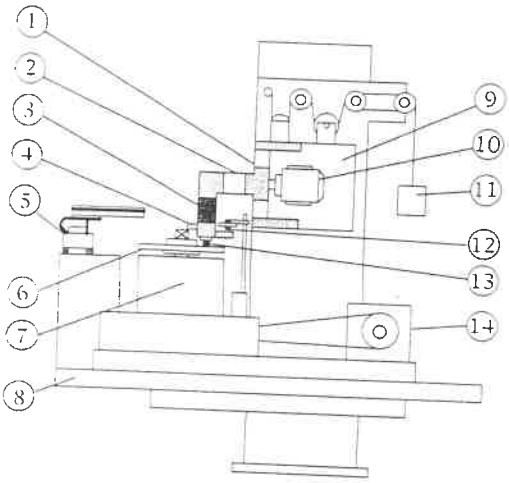

Fig. 1 Experimental apparatus

2. Experimental apparatus and method

The abrasive wear apparatus was based on the pin-on-disk method as shown in Fig. 1. The CFRP testpeace (diameter of 4mm) (13) was machined from CFRP plate by a lath. The abrasive grain was used as the green carborundum grain (GC#600). A constant amount of the grain was passed in front of friction surface using the parts feeder(5), and it collected after a passed surface, then the new one was supplied always. The testpeace was loaded by the dead weight. Frictional force was detected by means of strain gauges on the parallel spring (3), and the wear volume was detected by displacement of the testpeace using the uncontact displace-meter (12).

The relation between sliding direction and lines of carbon fiber is defined as the rubbing direction in Fig. 2. The X- and Y-direction axes denote the direction parallel and perpen-

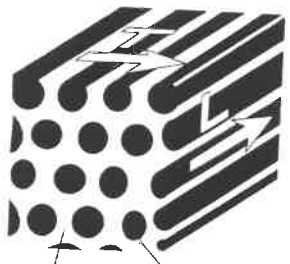

Fig. 2 Rubbing directions

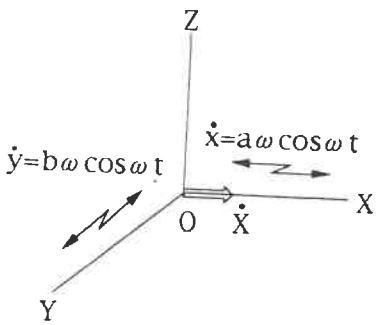

Fig. 3 Vibrational directions

dicular to the sliding direction respectively. (Fig. 3) The sliding distance, when the vibration acts, was not considered the moving length of the frictional surface, but was dealt with as a "real sliding distance". [2]

The velocity ratio(V and U) was defined as the velocity amplitude of vibration ($a\omega$ or $b\omega$) of the testpiece per sliding speed($\dot{X}$) of the disk. The velocity ratio ($a\omega$ or $b\omega$)/$\dot{X}$) was changed to examine the influence of the vibration action. The experimental conditions are shown in Table 1.

Table 1 Experimental Conditions

Sliding Speed : $\dot{X}$	40, 200 mm/s
Frequency : f	60 Hz
Amplitude : a, b	0-0.95 mm
Load : W	0-9.8 N
Abrasive grain	GC#600

3. Results and considerations

Fig. 4 shows the relationship between the load and the wear rate under non-vibration. Fig. 5 shows observation on worn surface of CFRP. It was clear that the wear rate became larger in the order of :L → T. In the T-direction the breakage of fiber was sever, and as a result it was considered that the wear rate of the L-direction was smaller. The wear rate increased according to the load, and the increasing rate of the wear rate under a high load was smaller than the case of a low load. In a consideration of this phenomenon, it is said that wear rate was related to the indentation depth of abrasive grad which have some limit of the high load.

Fig. 6 shows the relationship between the velocity ratio(V) and wear rate in the X-direction vibration. Fig. 7 and 8 show observation on worn surface of CFRP and schematic illustration of wear mechanisms. The real line shows the calculated wear rate, considering wear volumes of the non vibration and the over-lapping ratio.

The wear rate was calculated by the following Eqs. (1), (2).

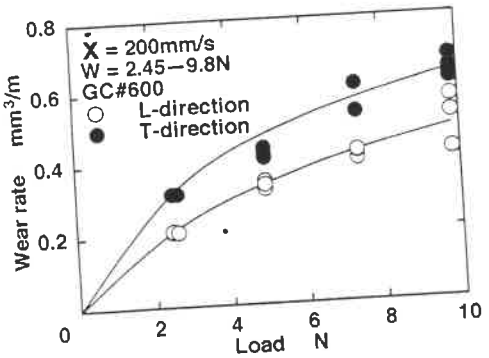

Fig. 4 Relationship between load and wear rate

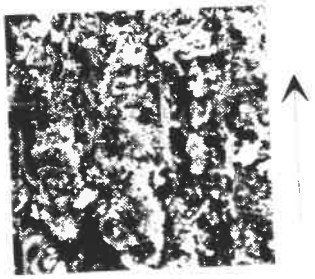

(a) L-direction

20 μ m

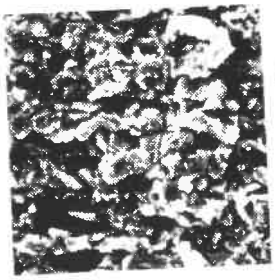

(b) T-direction

Fig. 5 Observation on worn surface of CFRP (non vibration)

Over-rapping ratio:

$$Q_r=\frac{\bar{V}-\dot{X}}{V} \qquad (1)$$

Wear rate:

$$W=W_n(1-Q_r) \qquad (2)$$

where:

$\bar{V}$: mean sliding speed, $\dot{X}$: sliding speed in frictional surface, W_n: wear rate in non vibration

When the velocity ratio is from 0 to 1 in the L- and T-directions, the wear rate is subjected to no vibrational effects, because the vibrational speed of test piece exited is smaller than that of the frictional surface. When the velocity ratio is from 1 to 3, the wear rate decreases rectilinearly, and the calculate value is also similar. In this case, the wear rate is proportional to the distance that the frictional surface moved. When the velocity ratio is more than 3, the wear rate shows a constant value, and these values are large in comparison with the calculated values. In this case, the movement of the abrasive grains are more complex, and the wear rate is proportional to the real sliding distance of the testpiece.

Fig. 9 shows the relationship between velocity ratio(U) and wear rate in Y-direction vibration. Fig. 10 and 11 show observation on worn surface of CFRP and schematic illustration of wear mechanisms. When the velocity ratio is from 0 to 3 in the L-direction, the wear rate volume gently increases in comparison with the calculated value. In this case, the wear rate is strongly subjected to the effect of the T-direction. When the velocity ratio is from 0 to 3 in the T-direction, the wear rate rapidly decreases and the calculated value is also similar.

In this case, the wear rate is strongly subjected to the effect of the L-direction.

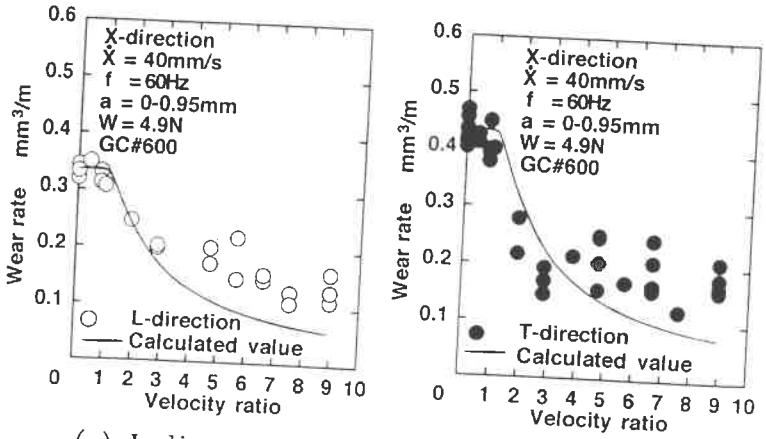

(a) L-direction (b) T-direction

Fig. 6 Relationship between velocity ratio and wear rate

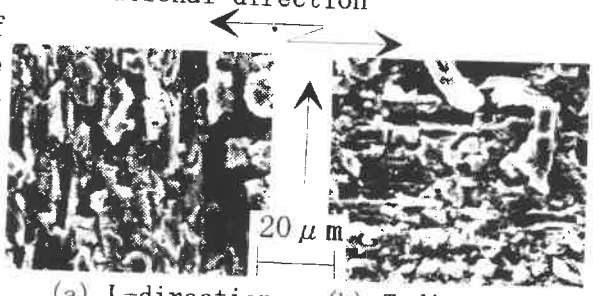

(a) L-direction (b) T-direction

Fig. 7 Observation on worn surface of CFRP (X-direction)

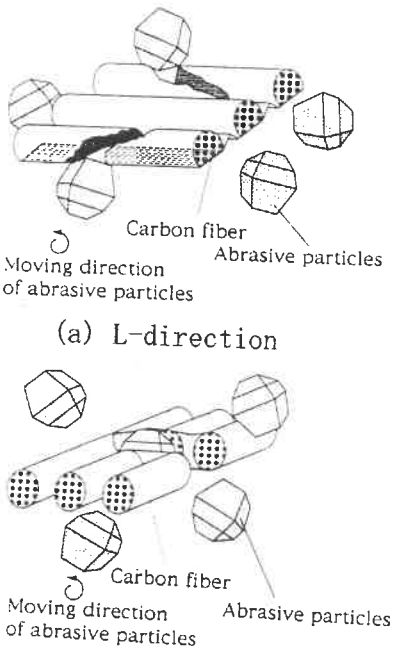

(a) L-direction

(b) T-direction

Fig. 8 Wear mechanism

When the velocity ratio is more than 3, the wear rate shows a constant in the L- and the T-directions and these values are larger in comparison with the calculated values.
Therefore, the movement of the abrasive grains are more complex, the wear rate is proportional to the real sliding distance of the testpiece.

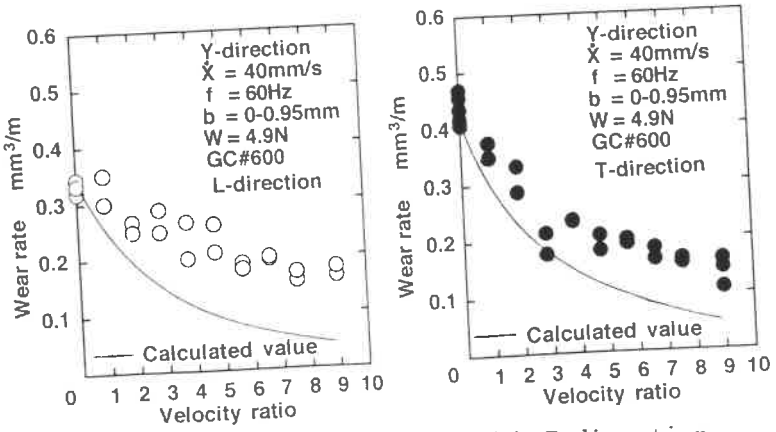

(a) L-direction (b) T-direction

Fig. 9 Relationship between velocity ratio and wear rate

4. Conclusions

1) The wear rate becomes larger in the order of :L < T.
2) In the X-direction vibration, when the velocity ratio 3 or less, the wear rate is dependent on the overlapping by being rubbed repeatedly the same place, and when more than 3, the wear rate is dependent on vibrational velocity.
3) In the Y-direction vibration, the wear rate is dependent on the overlapping as well as the X-direction. In addition, it was influenced by the direction of carbon fiber's orientation. When the velocity ratio is more than 3, the wear rate is dependent on vibrational velocity.
4) It was clarified that the rolling action had a larger influence than the scratch action of the grains under the three-body conditions on CFRP.

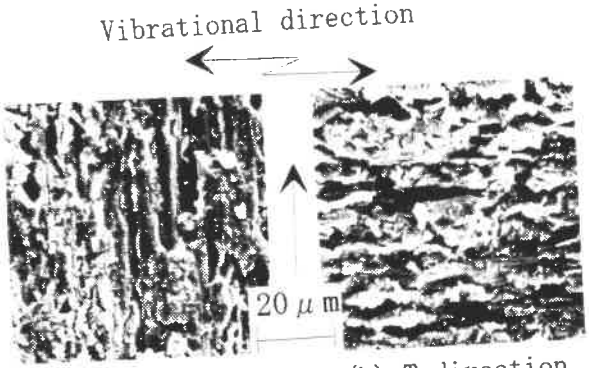

(a) L-direction (b) T-direction

Fig. 10 Observation on worn surface of CFRP (Y-direction)

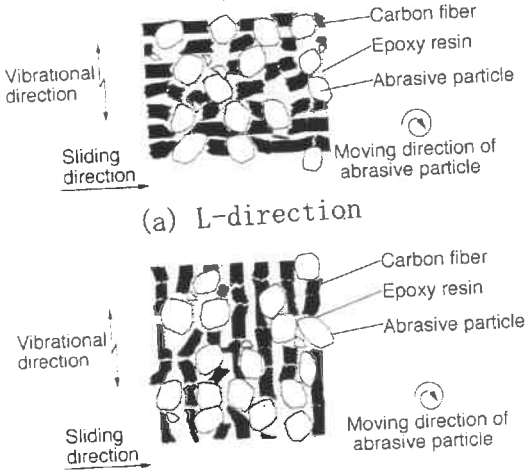

(a) L-direction

(b) T-direction

Fig. 11 Wear mechanism

References
1) E. Rabinowicz, L. A. Dunn and P. G. Rusell: A Study of Abrasive Wear under Three-Body Conditions, Wear, 4(1961)345
2) K. Ishikawa : Applied Vibration Engineering, Kanazawa Institute of Technology Press(1988)47

A New Biological Machining Technique with Chemolithotrophic Bacteria

Yoshiyuki UNO* 1, Toshiaki KANEEDA* 2, Seiichi YOKOMIZO* 3,
Akira OKADA* 1 and Takahiko YOSHIMURA* 1

* 1 Okayama University, 3-1-1, Tsushimanaka, Okayama 700, Japan
* 2 Okayama University of Science, 1-1, Ridaicho, Okayama 700, Japan
* 3 Industrial Technology Center of Okayama Prefecture

1. Introduction

Conventional material processings are classified roughly into physical processing and chemical one according to energy used in the process. However, biological processing has never been developed in the field of material processing. Recently the biotechnology has remarkably developed and the possibility of its application for many fields has been examined. Therefore, it is necessary to investigate the effective application of biotechnology in the field of material processing. This paper deals with the possibility of biological machining of metal with a chemolithotrophic bacteria[1].

2. What is chemolithotrophic bacteria?

There are many bacteria in the natural world. Chemolithotrophic bacteria is a very peculiar one. Life in the world is classified into two groups from the viewpoint of carbon source necessary for the body of life: organotroph and lithotroph as shown in Table 1. Organotroph gains carbon from organic matter and lithotroph from carbon dioxide in the air. Each group is also divided into two groups according to the energy source used for the activity of life. Animal and many bacteria are included in chemoorganotroph which gains energy from organic matter, while plant is included in photolithotroph which uses light as energy source. Chemolithotroph is very rare life in the world, which uses energy in oxidizing of inorganic matter and fixes carbon dioxide in the air. In this category, there are Thiobacillus ferrooxidans and Thiobacillus thiooxidans, which"eat"metals. For example, Thiobacillus ferrooxidans gains energy as follows:

$$4Fe^{2+} + O_2 + 4H^+ \rightarrow 4Fe^{3+} + 2H_2O$$

In this reaction, about 8 kcal per mol is generated[1].

Table 1 Classification of life from the viewpoint of carbon source and energy source

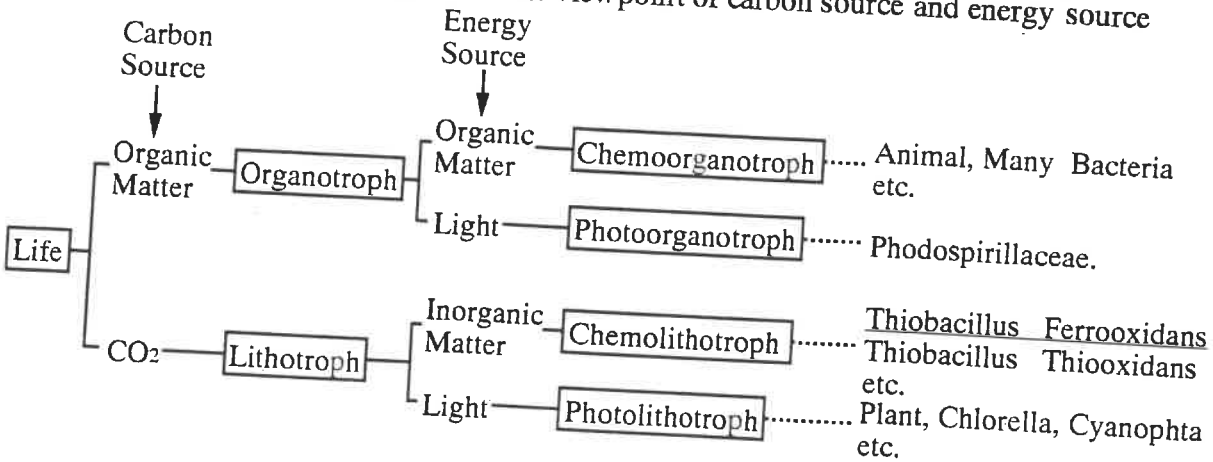

We investigate the possibility of the utilization of Thiobacillus ferrooxidans for metal removal processing.

3. Metal removal by bacteria Thiobacillus ferrooxidans

Fig.1 shows a SEM photograph of Thiobacillus ferrooxidans. As can be seen from the figure, the size of this bacteria is about 0.5 μm in diameter and 1 μm in length. The cultured fluid of this bacteria is used for metal removal experiment.

Fig.2 shows the variations of the number of bacteria with the cultured time. As shown in this figure, the number of bacteria increases with the cultured time. It reaches about 10^8/mL for 100 hours and keeps approximately constant. We used three kinds of Thiobacillus ferrooxidans registered by American Type Culture Collection[2] in this study.

Fig.3 shows a schematic diagram used for the metal removal experiment. The mask pattern for machining was formed on the workpiece in advance by the photolithography process. Pure copper, pure iron, zinc and brass were used as the workpiece. The workpiece was set in the cultured fluid and shaken on the rotary shaker in the incubator controlled at the constant temperature. The machined profile of workpiece was measured by a surface profile meter.

Fig.4 shows a SEM photograph and a measured example of machined grooves on copper. As shown in the figure, the workpiece was grooved approximately at a constant depth. The mean depth of groove is defined as the removal amount.

Fig.5 shows the variations of depth of groove with the machining time for pure copper. The solid circles in the figure show the removal amount in 9K medium that does not contain bacteria, which was negligible small even after 10 hours. On the other hand, the depth of groove increased approximately proportional to the machining time in the cultured fluid. This suggests that Thiobacillus ferrooxidans has the ability to machine copper, and the removal amount can be controlled by the machining time. We named this new metal removal processing "biomachining". As shown in the figure, there were no marked differences among the three types of bacteria used here, then their abilities to machine copper appear to be similar. The mean removal rate for pure copper reached about 20 μm per hour. It proved that this bacteria has also the ability to machine iron, zinc and brass, while the mean removal rate differs according to the kind of metal.

Fig.6 is the example of letters produced by biomachining on copper showing "BIOMACHINING OKAYAMA". The width of letters is about 20 μm.

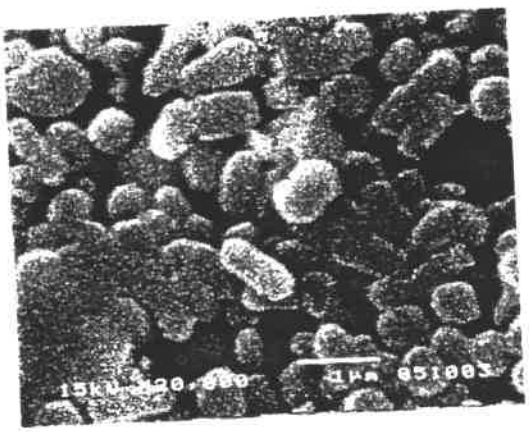

Fig.1 SEM photograph of Thiobacillus ferrooxidans

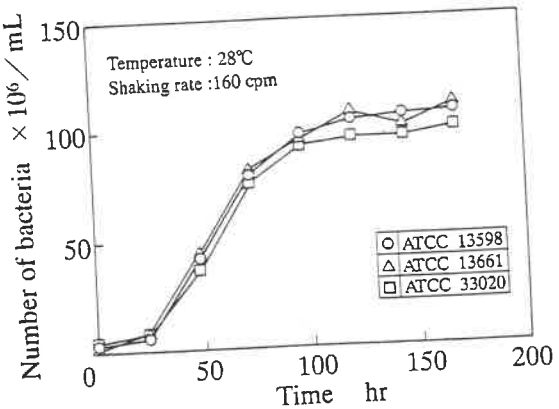

Fig.2 Variations of the number of bacteria with the cultured time

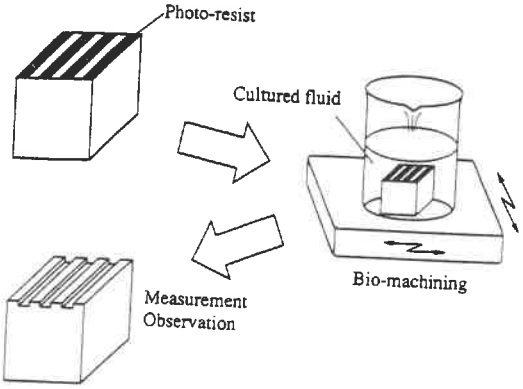

Fig.3 Schematic diagram of the metal removal experiment

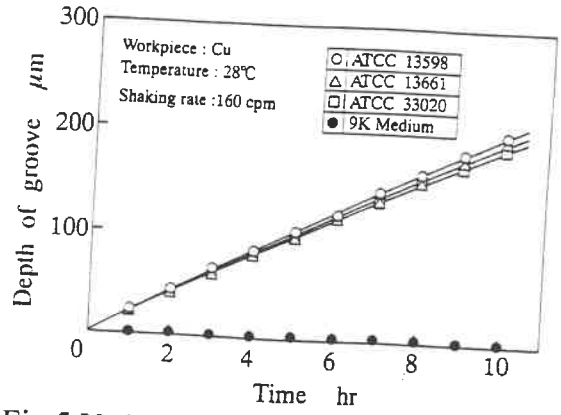

Fig.5 Variations of depth of groove with the machining time for pure copper

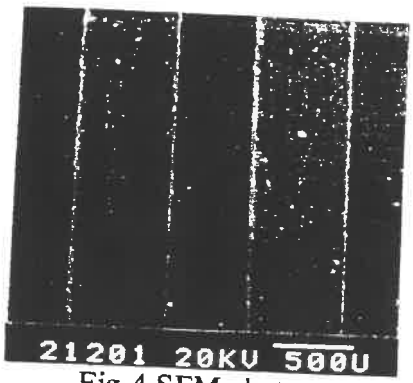

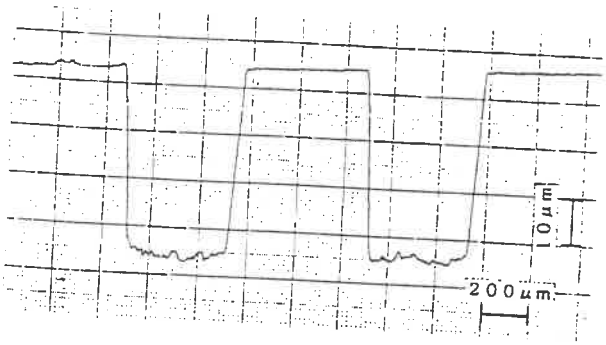

Fig.4 SEM photograph and measured example of machined grooves

Fig.6 Example of letters produced by biomachining

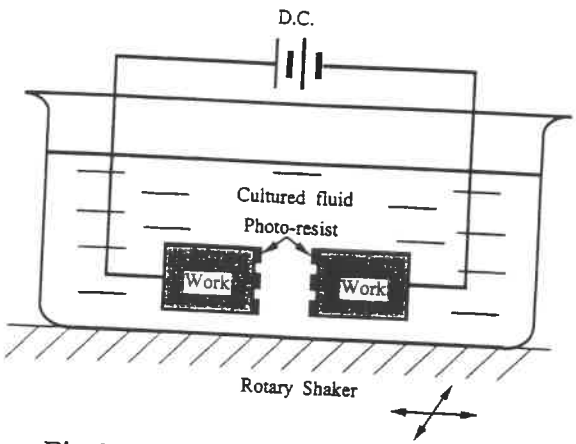

Fig.7 Schematic diagram of electric field assisted biomachining

4. Electric field assisted biomachining

Fig.7 shows a schematic diagram of experimental apparatus for investigating the effect of electric field on biomachining. As shown in the figure, two workpieces connected to cathode and anode were set facing each other and some direct current was applied. We named this method "electric field assisted biomachining".

Fig.8 shows the variations of depth of groove with the machining time when 0.5V D.C was applied between two workpieces for pure copper at 28° C and 160 cpm with bacteria

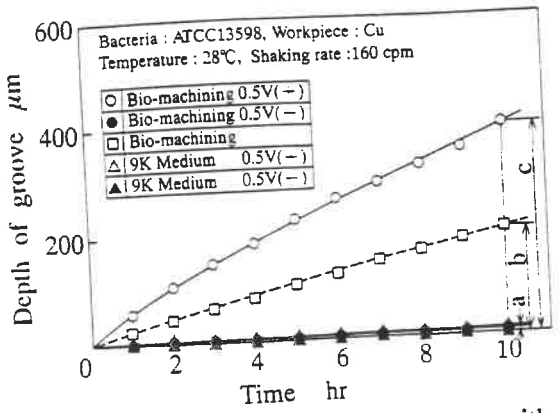

Fig.8 Variations of depth of groove with the machining time in electric field assisted biomachining

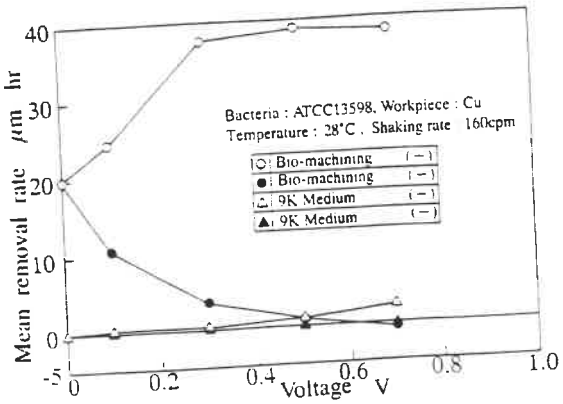
Bacteria : ATCC13598, Workpiece : Cu
Temperature : 28°C , Shaking rate 160cpm
○ Bio-machining (−)
● Bio-machining (−)
△ 9K Medium (−)
▲ 9K Medium (−)
Mean removal rate μm hr
Voltage V

Fig.9 Relationship between the mean removal rate and applied voltage

ATCC13598. The dashed line in the figure represents the depth of groove in normal biomachining without electric field, then "b" means the depth of groove for 10 hours. When the electric field was applied between two workpieces, the depth of groove generated on the anodic workpiece was about twice as deep as that in normal biomachining, while that on the cathodic workpiece became very small. On the other hand, when the same electric field was applied in 9K medium without bacteria, the anodic workpiece was slightly electropolished. In this case the electropolished depth for 10 hours is "a" in the figure. If the additional rule can be applied to these results, the depth of groove under an electric field should be "a+b". However, the depth of groove in this case (represented as "c") was much larger than the depth calculated by the additional rule (c > (a+b)). This result indicates that the electric field produces a kind of multiplication effect between biomachining and electrolytic machining.

Fig.9 shows the relationship between the mean removal rate and the applied voltage for pure copper with bacteria ATCC13598. As shown in the figure, the removal amount on the anodic workpiece increases with an increase of the applied voltage, reaching a certain constant value at about 0.5V, while that on the cathodic workpiece decreases. When the electric field was applied between two workpieces without bacteria, the removal rate in electropolishing is very small. The difference between symbols ○ and △ represents the effect of electric field assisted biomachining.

5. Conclusions

A new metal removal process "biomachining" is proposed, using chemolithotrophic bacteria Thiobacillus ferrooxidans as a tool for machining. Main conclusions are as follows:

(1) Thiobacillus ferrooxidans in cultured fluid showed the ability to machine some metals.

(2) The removal depth in biomachining was approximately proportional to the machining time.

(3) In electric field assisted biomachining, the removal rate at the anodic workpiece became much higher than that in normal biomachining.

Acknowledgement

The authors would like to express their gratitude to Prof.Sugio, Okayama University for supplying bacteria as well as useful information on the culture of bacteria.

References

1) K.Imai, Chemolithotrophic Bacteria, Kogaku Dojin(1984)4.

2) ATCC, Catalogue of Bacteria and Bacteriophages, 17th ed.,(1988)250.

DEFLECTION COMPENSATION MODEL FOR THE MACHINING OF MICROSHAFTS

(Initial Results)

by
Craig R. Friedrich and Balaji Kithiganahalli
Complementary Micromachining Processes Laboratory
Institute for Micromanufacturing
Louisiana Tech University
Ruston, LA 71272 USA

Introduction

Micromachining has traditionally been associated with the fabrication of components by lithography and etching of silicon. More recently, electroplating and micro injection molding have been used in the LIGA process. As micro- and mini- machines develop, there is also a need for the traditional machining techniques (metal cutting) to be developed for the microscale. The processes of precision diamond machining, microdrilling and micromilling, micro electrical discharge machining, laser ablative and ion beam machining, and others are being grouped into the complementary micromachining processes. Diamond machining is presently being used for the production of parts such as microshafts.

For the purpose of this study, a microshaft is a cylindrical component with a major diameter of 200 micrometers or less as shown in Figure 1. Microshafts are machined using a precision air-bearing spindle, high resolution tool positioners, and single crystal or polycrystalline diamond cutting tools. The shaft is produced by a process very similar to conventional turning on a lathe, except that the process must be monitored microscopically and machining parameters (depth of cut, tool feed, work rotational speed, etc.) are altered accordingly because of the small size of the shaft. As the diameter of a shaft is reduced, the forces generated during the cutting operation have a large influence on the accuracy of the resulting part. Because the deflection is a function of the fourth power of the diameter, the microshaft tends to deflect during machining. The deflection is a function of a number of material and machining parameters. The purpose of this study was to identify those parameters most important to the development of a model of the shaft deflection so that dimensional accuracy could be better maintained.

The Deflection Equations

A shaft which is being turned will behave as a simple cantilever beam. The free end of the shaft, along with the appropriate geometry and forces, is shown in Figure 2. Because of the cutting forces involved, there will be two primary components of force causing deflections. The deflections will be maximum at the free end of the shaft and may be described by

$$Y_x = \frac{l^3}{3EI}(F_p \sin\gamma^* + F_q \cos\gamma^*); \qquad Y_y = \frac{l^3}{3EI}(F_p \cos\gamma^* - F_q \sin\gamma^*)$$

and

$$F_p = \frac{\cos(\beta - \gamma^*)\tau_s A^*}{\cos(\phi^* + \beta - \gamma^*)\sin\phi^*}; \qquad F_q = \frac{\sin(\beta - \gamma^*)\tau_s A^*}{\cos(\phi^* + \beta - \gamma^*)\sin\phi^*}$$

Where γ^* is the instantaneous rake angle, β is the tool-workpiece friction angle, τ_s is the workpiece shear strength during machining, A^* is the instantaneous chip area, and ϕ^* is the instantaneous shear plane angle.

These equations are used for orthogonal metal cutting and a perfectly sharp cutting edge is assumed. The expression for the uncut chip area becomes considerably more complex for the microscale situation. Assuming a small depth of cut and tool feed per revolution, when compared to the tool nose radius, the equation for the uncut chip area becomes,

$$A^* = \sin(\cos^{-1}(1 - \frac{d^*}{R}))(\frac{aR}{2}\cos^{-1}(1 - \frac{d^*}{R}) + \frac{a^2}{2}(1 - \frac{d^*}{R}))$$

Where d^* is the instantaneous depth of cut which is the difference of the indicated depth of cut and shaft deflection, and R is the tool nose radius.

A second important deviation from the macroscale cutting is shown in Figure 3. At the macroscale, a tool with zero rake angle is aligned with the rake face radial to the workpiece. With no shaft deflection, the cutting force vectors would be aligned with the global axes. At the microscale, the shaft will deflect away form the tool in the horizontal direction, due to the thrust force (Fq), reducing the effective depth of cut. The shaft will also deflect upward, due to the cutting force (Fp), adding to the dimensional error. The actual depth of cut will be less than the indicated depth of cut.

In macroscale machining, the inclination and primary rake angles of the tool are treated separately. At the microscale, most of the uncut chip is located at the apex of the tool nose. This allows the inclination angle to be treated as the primary rake angle. The upward deflection changes the rake angle of the tool relative to the velocity vector of the incoming, uncut chip. As a result, the cutting force (Fp) has a component in the horizontal direction which increases the shaft deflection even more. These two compound effects can cause the microshaft to "ride up" onto the rake face of the tool causing shaft breakage. To eliminate that effect, the tool must be initially placed above the center of the shaft with a positive rake angle so that after deflection the tool rake face is near the horizontal radial of the shaft (zero rake angle). Because of the vertical deflection of the shaft, the

rake angle varies and this must be accounted for in the cutting force equation. The expression for the instantaneous rake angle becomes,

$$\gamma^* = \sin^{-1}\left(\frac{Y_i - Y_y}{R_i^*}\right)$$

Where Y_i is the initial tool setting position above the horizontal radial, Y_y is the vertical shaft deflection, and R_i^* is the instanteous machined radius of the shaft.

One of the last modifications for the microscale problem is in the orientation of the shear plane angle within the workpiece. This is the plane along which the material shears during the cutting process. The orientation of this plane contributes to the relative magnitudes of the cutting and thrust force components. Using the simplified Ernst-Merchant model, the shear plane angle is also a function of the rake angle and is given by,

$$\phi = 45^o - 0.5(\beta - \gamma^*)$$

Results

The deflection equations are transcendental and can not be solved in closed form. An iterative approach was taken and an algorithm implemented based upon the successive substitution method. The algorithm typically converged in less than 50 iterations with a criteria of less than 1% of the shaft diameter.

Acknowledging that the mechanics-based cutting force equations are not wholly accurate at the macroscale, apart from the microscale, the primary unknowns were varied to determine which are most sensitive in determining the cutting forces. Using polycrystalline diamond and 4043-0 aluminum as the materials, it was found that variations in the friction angle, shear plane angle, depth of cut, initial tool setting position, shaft diameter and feed all resulted in a deflections which were larger in the vertical-direction. The slopes of plots were greater for the vertical direction than the horizontal direction, thus showing a larger influence on the cutting force.

One experiment was performed to determine the applicability of the model. Future experiments will be conducted when a micrometrology system, currently under development, is completed. For a 90 μm diameter shaft, the one experiment did indicate that the model was able to predict the vertical deflection with an accuracy of more than 85%. The model predicted a much lower horizontal deflection than was obtained by the experiment. This was obviously due to the less than perfectly sharp cutting edge of the tool. In fact, the cutting edge radius was on the order of the depth of cut resulting in a very large negative rake angle. Results of cutting tests by Lucca, et al [1] and Moriwaki and Okuda [2] will be incorporated in the next iteration of the model.

1. Lucca, D. A., Rhorer, R. L., and Komanduri, R. "Energy Dissipation in Ultraprecision Machining of Copper." Annals of CIRP, Vol. 40, pp. 69-71, January, 1991.

2. Moriwaki, T., Okuda, K. "Machinability of Copper in Ultra Precision Micro Diamond Cutting." Annals of CIRP, Vol 38, pp. 115-118, January, 1989.

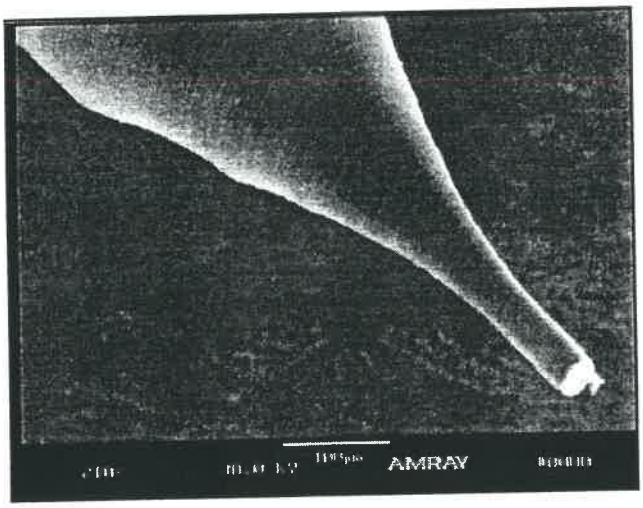

Figure 1 25μm Diameter Diamond machined Microshaft (4043-0A1)

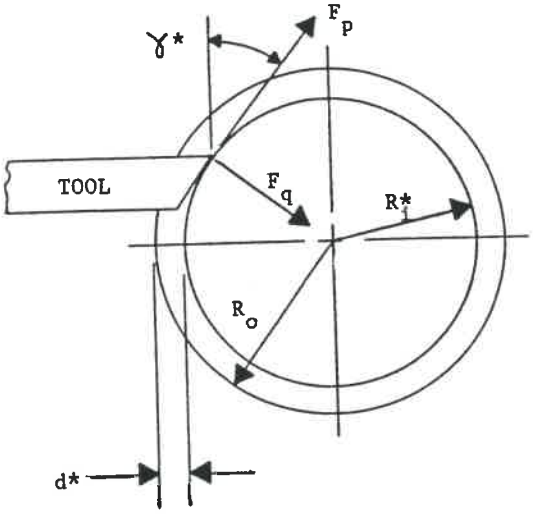

Figure 2 Geometry and forces on Free End of Microshaft

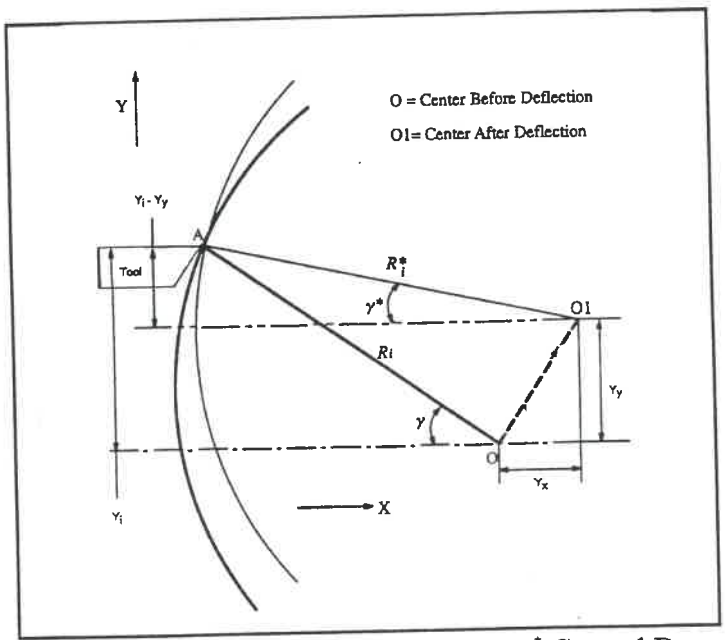

Figure 3 Instantaneous Rake Angle γ^* Caused By Shaft Deflection

Authors Index

Abou-Kandil, Hisham 214
Aoyama, Hisayuki. 125, 238
Aoyama, Tojiro 53, 250
Arcona, Chris 404
Arnold, W. 167
Ascanio, G.. 297
Atherton, Paul D. 23
Badami, V. G.. 230
Balasubramaniam, S.. 49
Bell, David J. 394
Bierden, Paul 113
Bifano, Thomas G. 113, 145, 424
Boudreau, Brian D.. 18
Bradshaw, Alan 334
Brinksmeier, Ekkard 167
Brohl, M.. 234
Buchard, Celine 218
Carr, Kirsten 137
Carrington, Tom 358
Case, Steven 194
Chen, C. J.. 206
Chen, Jenq-Shyong 88
Chollet, Patrice. 218
Cuttino, James F. 326
Daito, Masamichi 366
DeBra, Daniel B. 84
Delbrugge, G. Vincent * 262
Dow, Thomas A. 45, 101, 105, 326, 374, 404, 420
Drueding, Thomas W. 424
Duduch, Jaime G. 444
Dufraigne, J-O. 218
Edamura, K. 53
Egert, Charles M. 121
Eguchi, I. 61
Evans, Chris* 96, 202
Falter, K. J.. 45
Farabaugh, F.. 178
Fawcett, Steven C.. . . . . 346, 424
Fechner, R.. 167
Ferreira, Placid. 137
Friedrich, Craig R. 117, 461
Fukaya, J. 238
Funkenbusch, P. D. 370
Gans, R. F.. 370
Gao, Robert X.. 416
Garrard, Kenneth P. 45
Gartner, Joseph R.. 390
Gee, Anthony E.. 444
Goto, Takayuki 242
Gracewski, S. M. 370
Hachiga, S.. 289
Hachiuma, Hirokuni 186
Hahn, P. O.. 234
Han, Dong-Chul 263
Harary, Howard 218
Hasegawa, Masahiko. 190
Hashimoto, Katsuro 129
Hatakeyama, Minoru 378
Hatamura, Yotaro 61, 186, 254
Hatheway, Alson E. 246
Hirosaki, Kenichi 342
Hisada, Jiro 267
Hocken, Robert J.. . . . . 18, 49, 178, 230
Hockenberger, W. * 262
Hogg, M. 109
Horio, Ken'ichiro. 350
Howard, Lowell P.. 13
Hsu, R. H. 206
Huang, H. C. 206
Huang, Peisen S. 149
Huber, A. 234
Hylton, K. W. 121
Ide, Masahiro 436
Ikezoe, Keigo 250
Inaba, F. 92
Inasaki, Ichiro. 378
Ishikawa, Ken-ichi 453
Ishiyama, M. 53
Ives, Lewis K. *. 96
Iwata, F. 238
Jahanmir, Said *. 96
Jayaraman, V. 141
Jenkins, Hodge E. 408
Jones, R. 23
Judge, Thomas R. 23
Kahl, W. Keith. 362
Kaiser, Steve 358
Kanai, Akira 92, 267, 366
Kane, N.. . . . . 57, 275
Kaneeda, Toshiaki 428, 457
Kaneko, Kazushi 254
Kasai, Toshio 350
Kato, Shigeo. 271
Kerstan, Michael 234
King, Tim 258
Kithiganahalli, Balaji. 461
Kiyohara, Shuji. 436
Kobayashi, Kazuo 432
Kohno, Tsuguo. 182
Koike, Makoto 153
Kramar, John A. 29
Kubo, Takahiro. 125, 238

*Extended abstract not available at press time.

Kurfess, Thomas R. . . . 408
Kuroda, Akio. . . . 412
L'Heritier, Pascal . . . 218
Lambropoulos, John C. . . . 97, 370
Leaf, Kathy . . . 402
Lee, Kyoil . . . 222
Lee, W. B. . . . 354
Leung, T. P. . . . 354
Li, James C. M. . . . 301
Li, Kangjie . . . 301
Lindquist, Arne . . . 398
Ling, C. C. . . . 88
Lombardo, L. . . . 398
Lu, S. H. . . . 206
Lu, X. M. . . . 354
Lucca, Don A. . . . 49
Luderich, J. . . . 281
Ludwick, Stephen J. . . . 408
Lundt, Holger . . . 234
Luo, Z. . . . 317
Ma, Q. . . . 37
Mackie, B. R. . . . 313
Mai, Y-W. . . . 109
Mandak, Josef . . . 210
Margrave, Frank . . . 334
Marinescu, Ioan D.* . . . 129
Maruyama, Kazuo . . . 29, 174
McWaid, Thomas H. . . . 214
Mestre, Manuel . . . 41
Miller, Jr., Arthur C. . . . 101, 374
Miller, Michele H. . . . 289, 330
Mishima, Nozomu . . . 153, 242
Mitsui, Kimiyuki. . . . 428
Mitsuishi, Kazuta . . . 338, 432
Mitsuishi, Mamoru . . . 428
Miwa, Akio . . . 412, 436
Miyamoto, Iwao . . . 92, 267, 366
Miyashita, Masakazu . . . 330
Mizuhara, Kiyoshi. . . . 45
Moorefield, II, George M. . . . 342
Morimoto, Yoshitaka. . . . 428
Morioka, Hiroyuki . . . 305, 440
Morita, Noboru . . . 338, 432
Nagao, Takaaki . . . 453
Nakagawa, Tatuo . . . 432
Nakanishi, Hirofumi . . . 238
Nakano, H. . . . 61, 186, 254
Nakao, Masayuki . . . 297
Nava, R. . . . 398
Nemechek, John . . . 149
Ni, J. . . . 338
Ohta, Takashi . . . 457
Okada, Akira . . . 330
Okazaki, Yuichi. . . . 222
Pahk, Heuijae . . . 263
Park, Sang-Shin . . . 18
Patten, John A. . . . 80
Patterson, Steven R. . . . 109
Payor, S. . . . 84
Peirce, Scott B. . . . 157
Pistecky, Peter V. . . . 285
Polijaniuk, Andrzej . . . 96
Polvani, Robert S. * . . . 449
Pramila, T. . . . 167
Preuß, Werner R. . . . 370
Quesnel, D. J. . . . 167
Rabe, U. . . . 449
Raghuram, V. . . . 18, 141, 230
Raja, Jay . . . 416
Rao, B. C. . . . 297
Rickards, J. . . . 194
Riddle, Michael . . . 167
Riemer, O. . . . 37
Ro, Paul I. . . . 317
Rong, Y. . . . 133
Rosielle, P. C. J. N. . . . 125
Santo, T. . . . 33
Sato, M. . . . 238
Sasaki, Akira . . . 57, 275
Scagnetti, Paul . . . 374
Scattergood, Ronald O. . . . 358
Schaefer, John P. . . . 69, 133, 161
Schellekens, Piet H. . . . 167
Scherer, V. . . . 167
Schindler, A. . . . 80
Schmidt, D. M. . . . 29, 174
Schneir, Jason . . . 301
Shapiro, Yelena . . . 194
Skunes, Tim . . . 57, 275
Slocum, Alexander H. . . . 198
Smith, Steven K. . . . 23, 230
Smith, Stuart T. . . . 69
Soons, J. A. . . . 69
Spaan, H. A. . . . 178
Srinivasan, Nandakumar . . . 105, 374, 420
Storz II, Gene E. . . . 289
Sugimura, N. . . . 33
Sugita, T. . . . 202
Sullivan, Paul . . . 109
Sun, Jie . . . 242
Suzuki, Norio . . . 350
Takei, Hiroyuki . . . 254
Tanaka, Shuji . . . 242
Tawara, Satoshi . . . 45
Taylor, Lauren W. . . . 13, 29
Teague, E. Clayton . . . 453
Teraoka, Sadakazu . . . 121
Thomas, K. A. . . . 262
Titcomb, F. * . . . 125
Tokutomi, E. . . .

*Extended abstract not available at press time.

Trejo, R. 297
Trumper, David L. 65
Tsubono, Toyokazu 342
Tsuji, Hirokazu 129
Tsukamoto, Hidehiko 153
Uda, Yutaka 182
Ueda, T. 33
Ueno, Shigeru 289
Uno, Yoshiyuki 428, 457
van Dop, E. 157
Vermeulen, Marc M. P. A. 133
Vieira Porto, Arthur J. 444
Visvanathan, K. 117
Vos, Markus 281
Warisawa, Shin'ichi 338
Watanabe, Munemori 254
Watanabe, Takehiro 440
Watanabe, Takuro 432
Webster , John A. 386
Weck, Manfred 281
Wetzels, S. F. C. L. 161
Wieners, Andreas. 281
Wilhelm, Robert 178, 322
Williams, M. E. 65
Wright, Peter 402
Xu, Wei 258
Xu, Ying 23
Yajima, Minoru 153
Yang, W. L. 206
Yasui, Kunihiro 378
Yasui, Takeshi 342
Yazawa, Takanori 182
Yokomizo, Seiichi 428, 457
Yoshida, Yoshitaro 305, 440
Yoshimura, Kazuhiro 412
Yoshimura, Takahiko 457
Yuan, Z. J. 354
Zhang, Bi 293, 309, 382
Zhang, Chengrui 334
Zhang, Liangchi 109
Zheng, You. 226
Zhou, S. Steven 390
Zhou, Shihui. 386
Zhu, Y. 317
Zhu, Zhen Qi 293
Ziegert, John C. 76